Effective field theories for low-energy reactions

Effektive Feldtheorien für Niederenergie-Reaktionen

Vom Fachbereich Physik der Technischen Universität Darmstadt
zur Erlangung des Grades eines Doktors der Naturwissenschaften (Dr. rer. nat.)
genehmigte Dissertation von Marcel Schmidt, M.Sc., geb. in Bad Hersfeld

Tag der Einreichung:	21. Mai 2019
Tag der Prüfung:	5. Juni 2019

Darmstadt 2019 - D17

1. Gutachten:	Professor Dr. Hans-Werner Hammer
2. Gutachten:	Professor Dr. Jens Braun

TECHNISCHE
UNIVERSITÄT
DARMSTADT

Fachbereich Physik
AG Hammer, Institut für Kernphysik

Effective field theories for low-energy reactions
Effektive Feldtheorien für Niederenergie-Reaktionen

Genehmigte Dissertation von Marcel Schmidt, M.Sc., geb. in Bad Hersfeld

Tag der Einreichung: 21. Mai 2019
Tag der Prüfung: 5. Juni 2019

Darmstadt 2019 - D17

1. Gutachten: Professor Dr. Hans-Werner Hammer
2. Gutachten: Professor Dr. Jens Braun

Bitte zitieren Sie dieses Dokument als:
URN: urn:nbn:de:tuda-tuprints-87789
URL: http://tuprints.ulb.tu-darmstadt.de/8778

Erklärung gemäß §9 Promotionsordnung

Hiermit versichere ich, dass ich die vorliegende Dissertation selbstständig angefertigt und keine anderen als die angegebenen Quellen und Hilfsmittel verwendet habe. Alle wörtlichen und paraphrasierten Zitate wurden angemessen kenntlich gemacht. Die Arbeit hat bisher noch nicht zu Prüfungszwecken gedient.

Datum: ______________________ Unterschrift: ______________________

(Marcel Schmidt)

Abstract

Quantum-mechanical reactions can be used to probe the nature of composite particles if relations between reaction and structure observables are known. Such correlations are, however, often hard to obtain theoretically, especially when constituent particles participate in the reaction or when interactions involve many parameters. Effective field theories (EFTs) provide a promising way to reduce the number of relevant particles and interaction parameters in the low-energy limit. At the same time, EFT correlations come along with quantitative uncertainty estimates and can be improved systematically if needed. We exemplify this approach at the example of three systems in hadron, nuclear, and atomic physics.

The first system is the exotic charmonium state $X(3872)$. Its mass lies less than 200 keV away from the $D^0\bar{D}^{0*}$ threshold, reinforcing its interpretation as a loosely bound dimeson. To confirm this picture, the mass has to be measured with a high precision, for example in the $B^\pm \to K^\pm + X(3872) \to K^\pm + D^0\bar{D}^0\pi^0$ decay reaction. Threshold effects, however, are known to disguise the true pole position in this process. For this reason, we propose a novel EFT to extract the mass and width of the $X(3872)$ from its line shape. The theory uses Galilean-invariant contact interactions among D^0, $\bar{D}^0$, and π^0 fields. The D^{0*} enters as a $D^0\pi^0$ p-wave resonance, allowing for a systematization of pion interactions.

The second part is a pilot study exploring the potential of halo effective field theory to describe nuclear (d, p) reactions. As a test case, we use the neutron transfer reaction ^{10}Be (d, p) ^{11}Be. The relevant degrees of freedom for this process are the ^{10}Be core nucleus, the neutron, and the proton, which we treat as point-like particles. In contrast, the halo nucleus ^{11}Be and the deuteron are generated by contact interactions using experimental and *ab initio* input. As opposed to the $X(3872)$ system, Coulomb repulsion occurs in addition to strong interactions in the ^{10}Be-proton sector. The leading photon exchange diagrams are identified in a scaling analysis and iterated in a Faddeev equation.

In the third part, we investigate loss effects in an ultracold polarized ^{6}Li Fermi gas due to three-body recombination $3\,^6\text{Li} \to {}^6\text{Li}_2(\text{d}) + {}^6\text{Li}$ into deeply bound molecules. This process is enhanced in the presence of a p-wave Feshbach resonance. In leading order, atom-atom interactions can then be described by the large scattering volume and the initially unknown p-wave effective range only. By fitting our leading-order theory to data for the loss coefficient at nonzero temperature, we predict a value for the p-wave effective range. Moreover, our results suggest the existence of a low-energy three-body state.

Kurzfassung

In vielen Gebieten der Physik kann die Struktur zusammengesetzter Teilchen durch quantenmechanische Reaktionsprozesse untersucht werden. Voraussetzung hierfür ist die Kenntnis über Zusammenhänge einzelner Reaktions- und Strukturobservablen. Die theoretische Ermittlung solcher Korrelationen erweist sich oft als schwierig, insbesondere wenn einzelne Teilchenkomponenten aktiv an der Reaktion beteiligt sind und Wechselwirkungen viele freie Parameter aufweisen. Effektive Feldtheorien (EFTen) bieten eine vielversprechende Methode, die Zahl aktiv beteiligter Teilchen und freier Parameter bei niedrigen Energien zu reduzieren. Zugleich gehen EFT-Korrelationen einher mit quantifizierbaren Unsicherheiten und können, falls benötigt, systematisch verbessert werden. In dieser Arbeit werden EFTen zur Beschreibung von Systemen der Hadronen-, Kern- und Atomphysik verwandt.

Zunächst wird der exotische Charmonium-Zustand $X(3872)$ untersucht. Da seine Masse weniger als 200 keV entfernt ist von der $D^0\bar{D}^{0*}$-Schwelle, liegt es nahe, das $X(3872)$ als schwach gebundenes Dimeson zu interpretieren. Um dieses Bild überprüfen zu können, muss die $X(3872)$-Masse mit hoher Genauigkeit ermittelt werden, z. B. mithilfe der Zerfallsreaktion $B^\pm \to K^\pm + X(3872) \to K^\pm + D^0\bar{D}^0\pi^0$. Schwelleneffekte verschleiern jedoch bekanntermaßen die wahre Position des $X(3872)$-Pols in diesem Prozess. Mithilfe der in dieser Arbeit entwickelten EFT können Masse und Zerfallsbreite des $X(3872)$ aus seiner experimentellen Signalform extrahiert werden. Die Theorie verwendet Galilei-invariante Wechselwirkungen zwischen D^0-, $\bar{D}^0$-, and π^0-Feldern. Das D^{0*} tritt als p-Wellen-Resonanz im $D^0\pi^0$-Sektor in Erscheinung. Dies ermöglicht eine rigorose Systematisierung von Pion-Wechselwirkungen.

Der zweite Teil der Arbeit ist eine Pilotstudie, die die Anwendbarkeit von Halo-EFT auf kernphysikalische (d, p)-Reaktionen untersucht. Als Fallbeispiel dient die Reaktion $^{10}\mathrm{Be}(\mathrm{d},\mathrm{p})\,^{11}\mathrm{Be}$. Sie wird beschrieben durch einen ^{10}Be-Rumpfkern, ein Neutron und ein Proton. Diese Teilchen werden als punktförmig betrachtet. Der ^{11}Be-Halokern und das Deuteron werden dynamisch durch Kontaktwechselwirkungen der drei Teilchen erzeugt. Hierbei kommen Input-Parameter aus experimentellen Messungen und Resultate aus *ab initio*-Rechnungen zum Einsatz. Im Gegensatz zum $X(3872)$-System muss zusätzlich zur starken Wechselwirkung auch die Coulomb-Abstoßung von Rumpfkern und Proton berücksichtigt werden. Die führenden Photon-Austauschdiagramme werden im Rahmen einer Skalenanalyse identifiziert und dann in einer Faddeev-Gleichung iteriert.

Der dritte Teil der Arbeit beschäftigt sich mit Teilchenverlusten eines ultrakalten polarisierten ^{6}Li-Fermigases aufgrund von Dreiteilchenrekombination $3\,^6\mathrm{Li} \to {}^6\mathrm{Li}_2(\mathrm{d}) + {}^6\mathrm{Li}$ in tiefgebundene Moleküle. Dieser Prozess tritt gehäuft in Anwesenheit einer p-Wellen-Feshbach-Resonanz auf. In führender Ordnung werden Wechselwirkungen zwischen den Atomen durch das Streuvolumen und die zunächst unbekannte p-Wellen-effektive Reichweite parametrisiert. Durch einen Fit der Theorie an Daten für den Verlustkoeffizienten bei nichtverschwindenden Temperaturen ergibt sich ein Wert für die p-Wellen-effektive Reichweite. Zugleich legen die Fitresultate die Existenz eines niederenergetischen Dreiteilchenzustands nahe.

Contents

1 Introduction

Most physical phenomena can ultimately be traced back to the standard model (SM) of particle physics, until today the most fundamental theory of nature [1]. One of its cornerstones, quantum chromodynamics (QCD), describes strong interactions among quarks and gluons; see the left-most sketch in Fig. 1.1. Nowadays, the light hadron spectrum, including the nucleon, can be correctly predicted using a nonperturbative approach called lattice QCD [2, 3]. However, precise calculations of light nuclei or threshold states like the exotic $X(3872)$ meson are still challenging [4, 5]. The main reason is the large value of the QCD coupling constant at low energies. It renders perturbative approaches impossible and thus requires expensive supercomputer calculations.

Effective field theories (EFTs) provide an alternative promising gateway to the low-energy regime [6, 7]. These systematic approximations of the SM make explicit use of the relevant degrees of freedom at a certain length or energy scale. Interactions are described by low-energy constants which can be matched to experiments or to more fundamental theories. In this sense, EFTs are complementary to microscopic approaches like lattice QCD. The idea of developing phenomenological Lagrangians arose from Weinberg's insight that a quantum field theory has no other content but analyticity, unitarity, cluster decomposition, and symmetry [8]. Details on how EFTs can be constructed will be given in Chapter 2.

A prominent example of an EFT is chiral perturbation theory (χPT); see Refs. [9, 10] for reviews. It describes strong interactions if relevant momenta are of the order of the pion mass[1] $m_\pi \approx 135\,\mathrm{MeV}$. At the corresponding length scale $1/m_\pi \sim 1.5\,\mathrm{fm}$, quarks and gluons cannot be resolved anymore. Hadrons, e.g., the proton, neutron, and pion shown in the second sketch of Fig. 1.1, become the new relevant particles. Upon being developed for pions exclusively by Gasser and Leutwyler in the mid-80s [11, 12], χPT was extended to nucleons (N) in the early 90s [13–15]. This important achievement enabled a systematic calculation of effective N-N potentials for application to larger nuclei and even nuclear matter [16, 17]. Nowadays, χPT can be used to describe strong interactions of a variety of hadrons, including also heavy D and B mesons [18].

As soon as typical momenta become smaller than m_π, further simplifications can be made. Firstly, all hadrons then behave nonrelativistically and Lorentzian symmetry can be replaced by Galilean symmetry. Secondly, particle number conservation becomes a new symmetry since pair creation is suppressed. Thirdly, if pions only occur as exchange particles in a certain process, they represent short-range physics

---

[1] We use natural units $\hbar = c = 1$ in this thesis; see Appendix A.

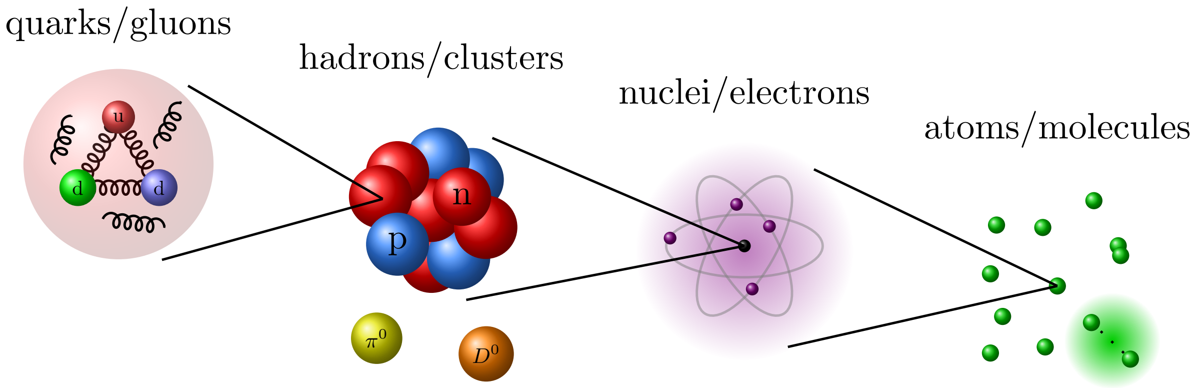

Figure 1.1.: Composition of visible matter (sketches not to scale). The relevant degrees of freedom needed to describe the four depicted systems are named above.

and can be integrated out. For example, pionless effective field theory (EFT($\not\pi$)) describes N-N scattering at low momenta in terms of contact terms, i.e., delta-type interactions, which incorporate the effect of pions *effectively* [19]. In a Galilean-invariant framework with contact interactions, one then recovers the well-known effective range expansion (ERE) of nonrelativistic quantum mechanics [20]. It states that scattering at low energies is described accurately by only a few observables, usually given by the scattering length and the effective range parameter.

If certain ERE coefficients are enhanced, then weakly bound states and near-threshold resonances fall into the scope of the short-range EFT [21]. In nuclear physics, such states are, for example, given by the deuteron [19] and by so-called halo nuclei which have a small one- or two-nucleon separation energy [22]. Short-range EFTs were also used to describe threshold states in quarkonium spectra like the $X(3872)$ [23] and even to describe few-body physics in ultracold atomic gases [21]; see the right-most sketch in Fig. 1.1.

1.1 Joining structure and reaction theory

Traditional reaction theories often suffer from the fact that their structure and reaction parts are described by separate unconnected models. A great advantage of EFTs is that they treat these parts on the same footing. That allows for the calculation of systematic correlations between structure and reaction observables. At some predefined calculation accuracy, theoretical uncertainties can be expressed in terms of typical momentum scales. The description can be improved by increasing the amount of inputs.

Correlations obtained from an EFT can then be used to extract structure information from scattering-related observables like phase shifts. For example, Ji *et al.* used low-energy neutron-neutron and ^{4}He-neutron scattering data to calculate the binding energy of the Borromean halo nucleus ^{6}He in Halo EFT [24]. Vice versa, EFTs enable predictions for reaction rates at experimentally unaccessible low energies, given structure input. For example, the neutron-proton fusion reaction $\mathrm{n}+\mathrm{p}\to\mathrm{d}+\gamma$, as part of big-bang nucleosynthesis, happens at low kinetic energies $\leq 1\,\mathrm{MeV}$. Its cross section was predicted in EFTs both with and without explicit pions, using, among other structure observables, the deuteron binding energy [25–27].

It is the goal of this thesis to develop short-range EFTs for three, at first glance totally different reactions in hadron, nuclear, and atomic physics. Below, we introduce the three systems phenomenologically and motivate the respective studies.

1.2 $X(3872)$

The novel charmonium state $X(3872)$ was initially observed as a narrow peak in the $B^\pm\to K^\pm J/\psi\,\pi^+\pi^-$ decay by the Belle Collaboration in 2003 [28]. The signal was quickly confirmed by the CDF II Collaboration in 2004 [29]. At the time, the new state attracted much attention since it does not fit into the conventional quark model. In particular, it cannot be a pure $c\bar{c}$ state since it violates isospin symmetry. This attribute can be seen from its decay channels. On the one hand, the two pions in the discovery mode predominantly result from a ρ meson (isospin $T=1$) [30]. On the other hand, in the decay mode $J/\psi\,\pi^+\pi^-\pi^0$, which has a comparable branching ratio, pions result from an ω meson (isospin $T=0$). Many assignments have been discussed for the $X(3872)$, including a tetraquark explanation [31–33]. For over a decade, also the quantum numbers remained unknown, until the LHCb Collaboration finally determined them to be $J^{PC}=1^{++}$ in 2013 [34].

A remarkable feature of the $X(3872)$ is its extreme vicinity to the neutral $D^0\bar{D}^{0*}$ threshold. The current mass[2] value $m_X=3871.69(17)\,\mathrm{MeV}$ implies a tiny mass difference

$$\delta_X\equiv(m_{D^0}+m_{D^{0*}})-m_X=(-0.01\pm0.2)\,\mathrm{MeV}\,,\tag{1.1}$$

---

[2] In this thesis, we define the mass m (and also binding/resonance energy) of a particle by the real part of its energy pole in the S matrix. The width Γ of a state is defined by the pole's imaginary part $-i\Gamma/2$.

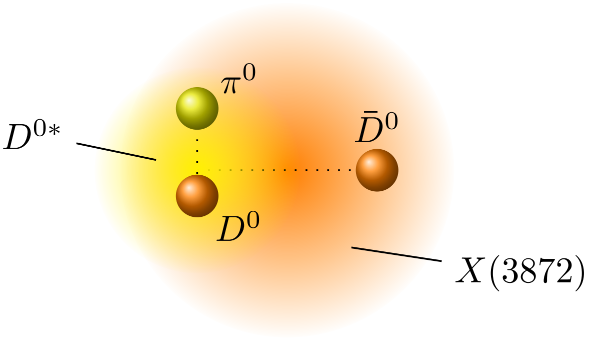

Figure 1.2.: Sketch of the exotic $X(3872)$ particle as a $D^0\bar{D}^0\pi^0$ resonance. The antiparticle configuration is omitted.

which could be positive or negative [35,36]. The small value of δ_X and the quantum numbers give rise to a large s-wave $D^0\bar{D}^{0*}$ molecule component, an interpretation discussed by many authors [23,37–41]. The possible existence of dimeson states around 4 GeV was already pointed out by Voloshin *et al.* in 1976 [42]. The molecular assignment

$$X(3872) \equiv \frac{1}{\sqrt{2}}\left(D^0\bar{D}^{0*} + \bar{D}^0 D^{0*}\right) \tag{1.2}$$

is in line with $J^{PC} = 1^{++}$ since D^0 ($\bar{D}^0$) and $\bar{D}^{0*}$ (D^{0*}) are pseudoscalar ($J^{PC} = 0^-$) and vector ($J^{PC} = 1^-$) mesons, respectively. The isospin violation follows from the fact that the splitting $\nu \approx 8$ MeV between the neutral channel and the charged channel $(D^+D^{-*} + D^-D^{+*})/\sqrt{2}$ is much larger than $|\delta_X|$ [36].

The $X(3872)$ has a large branching ratio for decays to D meson final states [36]. It follows naturally from constituent decays $D^{0*} \to D^0\pi^0$ and $D^{0*} \to D^0\gamma$ ($\bar{D}^{0*}$ analogous). The small energy release $\delta \approx 7$ MeV in the pionic channel will allow us to treat the vector mesons as nonrelativistic p-wave resonances of $D^0\pi^0$ ($\bar{D}^0\pi^0$). It follows that the $X(3872)$ can be seen as a $D^0\bar{D}^0\pi^0$ three-body resonance; see Fig. 1.2.

At the moment, neither the mass difference δ_X nor the width $\Gamma_X < 1.2$ MeV of the $X(3872)$ are known accurately [30].[3] Both are, however, needed to test the molecular picture. In particular, Braaten pointed out in Ref. [43] that a dimeson-type $X(3872)$ would either be bound or virtual ($\delta_X > 0$) due to s-wave universality [21]. A negative value for δ_X would contradict this claim as it would imply a resonance above the $D^0\bar{D}^{0*}$ threshold. A definite answer could be obtained by precisely measuring $X(3872)$ line shapes in different decay modes. In addition, one needs an appropriate theory to extract the values of δ_X and Γ_X.

In this thesis, we propose such a theory for the line shape in the $B^\pm \to K^\pm + X(3872) \to K^\pm + D^0\bar{D}^0\pi^0$ decay rate. Braaten and Lu showed in a zero-range approximation[4] that it is strongly enhanced above the $D^0\bar{D}^{0*}$ threshold due to the finite D^{0*} width [44]. This effect disguises the true pole position for small δ_X, such that it cannot be identified by the peak position and the full width at half maximum (FWHM). In 2007, Fleming *et al.* calculated the partial decay width $\Gamma[X(3872) \to D^0\bar{D}^0\pi^0]$, i.e., the pole position, in XEFT, a newly developed EFT including D and π meson fields. They showed that pions can be treated perturbatively. The connection between the pole and the line shape, however, was not studied. XEFT was later improved by Braaten who restored explicit Galilean invariance [45]. For details on both versions of XEFT, we refer to Chapter 3. Another important study was performed by Baru *et al.* [46]. They calculated the line shape in a coupled channel Faddeev approach, including neutral and charged D and π mesons to all orders. The peak position and FWHM were identified with the pole position for $\delta_X \geq 0.1$ MeV. We will see that this approximation is no more valid for smaller δ_X values due to the threshold enhancement.

---

[3] The upper bound for Γ_X stems from the detector resolution.

[4] The zero-range limit is defined by vanishing higher-order coefficients in the effective range expansion. s-wave scattering is then determined only by the scattering length; see Chapter 2 for details.

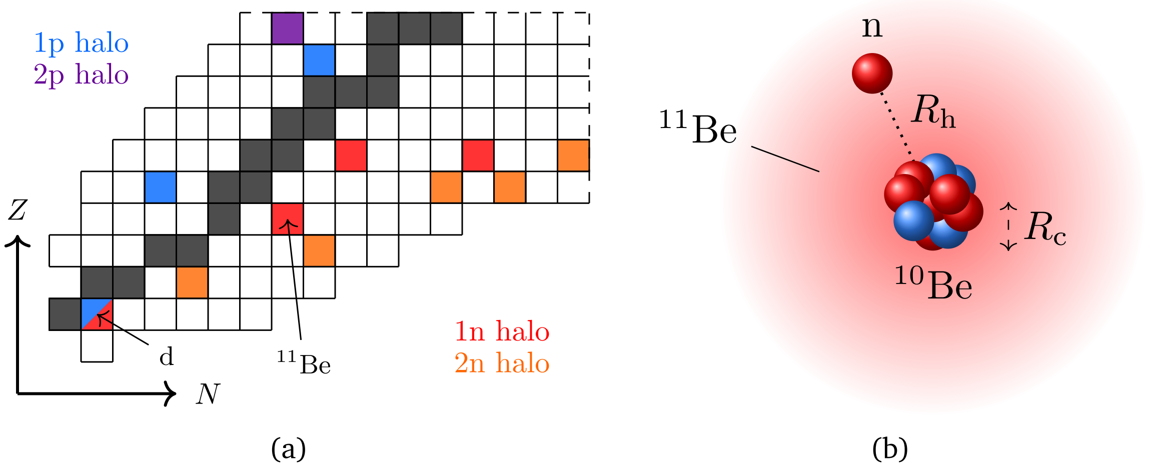

Figure 1.3.: (a) Excerpt of the nuclear chart. Neutron and proton halo nuclei (colored) lie away from the valley of stability (black). (b) Sketch of the one-neutron halo nucleus ^{11}Be. Compared to the radius $R_\mathrm{c} \sim 2.6\,\mathrm{fm}$ of the tightly bound core ^{10}Be, the radius $R_\mathrm{h} \approx 7\,\mathrm{fm}$ of the halo is unnaturally large.

The EFT we propose in this thesis uses explicit Galilean invariance to treat the $X(3872)$ as an effective $D^0\bar{D}^0\pi^0$ resonance. For simplicity, we will call it "$D^0\bar{D}^0\pi^0$ EFT". Both pole position and line shape are calculated at next-to-leading order accuracy. In doing so, we provide correlations between the peak maximum, the FWHM, the binding energy δ_X, and the width Γ_X.

1.3 Halo nuclei

Near-threshold ("shallow") states like the $X(3872)$ can also be found in nuclear physics. Since the 1980s, a bunch of nuclei with unusually large matter radius have been observed near the neutron dripline at radioactive beam facilities [47]; see Fig. 1.3(a). Jonson and Hansen identified the large spatial extend as a consequence of their comparably small one- or two-neutron separation energies [48]. In many of these so-called halo nuclei, the valence neutrons reside mostly outside the radius of the inert core [49–52]. More generally, the term halo nucleus can be used for ground or excited states which are weakly bound with respect to the one- or two-nucleon separation threshold.[5] This picture also includes the deuteron (d), the lightest of all halo nuclei.

Figure 1.3(b) shows a prime example of a one-neutron halo nucleus, the ground state ^{11}Be of Beryllium-11.[6] The neutron-core distance ("halo radius") $R_\mathrm{h} \sim 7\,\mathrm{fm}$ is large compared to the core radius $R_\mathrm{c} \sim$ 2-3 fm and to matter radii of other Beryllium isotopes [53]. In line with the explanation of Jonson and Hansen, the neutron separation energy $B_\sigma = 0.50\,\mathrm{MeV}$ is unusually small, for example compared to the core's excitation energy $E_\mathrm{x} = 3.37\,\mathrm{MeV}$. Based on this separation of scales, Hammer and Phillips developed a short-range EFT description for Beryllium-11 (and other halo nuclei) called Halo EFT [54]. It treats the ^{10}Be core as an explicit degree of freedom and the ground and first excited levels of Beryllium-11 as one-neutron halo states. The theory was used to calculated electromagnetic properties and transitions in an $R_\mathrm{c}/R_\mathrm{h}$ expansion. The Halo EFT formalism has also been applied to Coulomb dissociation and radiative capture processes. It has also been extended to two-neutron halo nuclei, one-proton halo nuclei, and even shallow resonances. For a recent review, see Ref. [22].

Studying halo nuclei experimentally is a challenging task as they undergo radioactive decay. Thus, ongoing effort is put into improving measurement techniques at existing radioactive beam facilities and

---

[5] We will specify the term "weak" in Chapter 4.

[6] By writing out the full isotope name we collectively refer to all relevant energy levels.

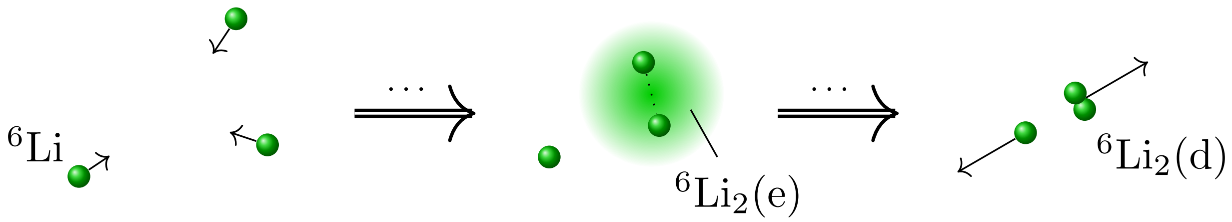

Figure 1.4.: Sketch of the three-body recombination reaction $3{}^6\mathrm{Li} \to {}^6\mathrm{Li}_2(\mathrm{d}) + {}^6\mathrm{Li}$. The large binding energy of the deeply bound diatom $^6\mathrm{Li}_2(\mathrm{d})$ is released as kinetic energy, such that the diatom-atom pair leaves the optical trap. Recombination is enhanced at energies close to the Feshbach resonance-induced shallow diatom state $^6\mathrm{Li}_2(\mathrm{e})$.

new facilities like NUSTAR at FAIR are on the way [55, 56]. One technique to probe halo structures directly is to populate them in neutron transfer reactions [57, 58]. For example, Schmitt *et al.* measured the differential cross section of the reaction $^{10}\mathrm{Be}(\mathrm{d},\mathrm{p})\,^{11}\mathrm{Be}$ in inverse kinematics at comparably low deuteron beam energies $E_\mathrm{d} \leq 21.4\,\mathrm{MeV}$ [59, 60].

Traditional reaction models have been successful in describing nearly all experimental data points of the Schmitt *et al.* data. However, they do not provide information on theoretical uncertainties. How to obtain such uncertainties for reaction models remains subject to ongoing research [61, 62]. Moreover, reaction models have limited predictive power due to energy-dependent fitting parameters. A desirable reaction theory would predict cross sections over a large energy and angular range from minimal experimental input. Tremendous progress in achieving this goal for lighter systems was made by Navrátil *et al.* who combined the variational approach of the resonating group model and the no-core shell model into the no-core shell model with continuum [63]. The microscopic N-N interaction needed for the *ab initio* calculation was obtained from χPT. Recently, Capel *et al.* combined the dynamical eikonal approximation with a Halo EFT description of ^{11}Be to calculate ^{11}Be breakup on Pb and C targets [64].

In this thesis, we go one step further compared to the study by Capel *et al.* by using only Halo EFT to describe reactions at low energies. In particular, we explore the potential of Halo EFT to describe neutron transfer reactions at the example of $^{10}\mathrm{Be}(\mathrm{d},\mathrm{p})\,^{11}\mathrm{Be}$. In doing so, we provide a theory predicting low-energy cross sections – including uncertainty estimates – from only a few input observables, e.g., binding energies and ERE coefficients.

1.4 Ultracold Fermi gases

Ultracold gases provide a versatile playground to study universal aspects of shallow quantum states. As opposed to hadron or nuclear physics systems, Feshbach resonances in different partial wave channels can be used to artificially tune low-energy scattering observables [65]. For example, in s-wave interacting gases, the scattering length a_0 can be brought near divergence by an external magnetic field B. For $a_0 > 0$, the binding energy $\propto a_0^{-2}$ of the corresponding shallow diatom state is then exactly determined by the large scattering length since short-range corrections become arbitrarily small (zero-range limit) [21].

In general, two-body interactions depend on the atoms' polarizations. Consequently, there can be several Feshbach resonances per partial wave type, corresponding to equal- or opposite-spin pairs. For example, the ^{6}Li Fermi gas exhibits several s-wave resonances at $B \in [690, 834]\,\mathrm{G}$ and p-wave resonances at $B \in [159, 215]\,\mathrm{G}$ [66, 67]. They can be used to study remarkable features of condensed matter. For example, an opposite-spin s-wave Feshbach resonance has been used by Yi and Duan to implement a BEC-BCS phase transition experimentally [68, 69]. In Ref. [70], Waseem *et al.* polarized ^{6}Li atoms to obtain a gas of identical fermions, in which s-wave interactions are forbidden. One of the p-wave Feshbach resonances was then used to study universal aspects of p-wave interactions; see below.

Typically, ultracold gases are studied in optical traps [71]. One difficulty that arises then is the loss of particles from the trapping potential. A main loss source is often given by three-body recombination, i.e., a reaction in which two atoms form a bound diatom in the presence of a third atom; see Fig. 1.4. The binding energy is released as kinetic energy, which leads to the loss of three atoms per recombination event. Close to a Feshbach resonance, the process is particularly strong since it can proceed through the channel related to the shallow diatom state. In general, the recombination rate depends on the temperature of the gas, i.e., on typical kinetic energies of the atoms. It can be obtained experimentally by measuring the density profile of the gas in time-of-flight experiments [70].

Recombination of three identical spinless bosons close to an s-wave Feshbach resonance has been studied thoroughly using short-range EFT. The recombination rate K_3 at zero temperature is a function of a_0. One then has to distinguish between recombination into shallow and deep diatoms. The rescaled rate $K_3 a_0^{-4}$ for recombination into a shallow diatom state is log-periodic in $a_0 \kappa_*$ if $a_0 > 0$ (diatom is bound) and zero if $a_0 < 0$ (diatom is unbound) [72]. Here, κ_* is a three-body parameter. The rescaled rate for recombination into deep diatom states is almost constant if $a_0 > 0$ [73]. For $a_0 < 0$, it has consecutive maxima whenever an Efimov state hits the three-atom threshold [74]. Zero-range results at nonzero temperatures in Ref. [75] agree with data for the ^{133}Cs gas.

In this thesis, we use short-range EFT to calculate the three-body recombination rate for identical ^{6}Li fermions near a p-wave Feshbach resonance. Suno *et al.* calculated the recombination rate using model potentials [76]. They focussed on the total angular momentum channel $J^P = 1^+$ which is dominant at low enough energies [77]. We also focus on this channel and on magnetic fields B above the Feshbach resonance, where data for the loss coefficient[7] is available [70]. On this side, the shallow diatom ^{6}Li$_2$(e) is a p-wave resonance and atoms only recombine into deep states ^{6}Li$_2$(d). By fitting our theory to data at nonzero temperature, we predict the existence of a low-energy three-body state and extract a value for the p-wave effective range parameter in the two-body sector.

1.5 Overview

This thesis is structured as follows. In Chapter 2, we give a theoretical introduction to low-energy scattering. The concept of fine-tuning and universal aspects of shallow two-body states are explained using short-range potentials in configuration space and the scattering amplitude in momentum space. Moreover, we explain how to construct an EFT for a given physical system. Afterwards, we develop EFTs for low-energy reactions in different physical systems. The first reaction in Chapter 3 is a high-energy B meson decay, followed by a low-energy $D^0 \bar{D}^0 \pi^0$ decay of the exotic $X(3872)$ particle. Here, we use a short-range EFT to extract the mass and width of the $X(3872)$ from its experimental line shape. In Chapter 4, we present a pilot study for the direct calculation of nuclear (d, p) cross sections from structure input. As a first application, we benchmark the theory using data for the reaction ^{10}Be(d, p)^{11}Be [59,60]. Lastly, we calculate the loss rate due to the three-body recombination process $3\,{}^6\mathrm{Li} \rightarrow {}^6\mathrm{Li}_2(\mathrm{d}) + {}^6\mathrm{Li}$ in an ultracold ^{6}Li Fermi gas in Chapter 5. The diatom state related to the Feshbach resonance is described using a short-range EFT for shallow p-wave states. Results are compared using data from Ref. [70]. We conclude this thesis with a summary for all three studies. Based on the findings, we formulate open issues for future projects.

---

[7] The loss coefficient is proportional to the thermally averaged recombination rate; see Chapter 5.

2 Theoretical foundations

Before we start calculating reaction processes, we briefly summarize relevant theoretical concepts of nonrelativistic scattering in this chapter. In particular, we argue that the low-energy limit implies a reduction of relevant degrees of freedom and partial wave channels. Moreover, we explain the occurrence of weakly bound states and near-threshold resonances by means of fine-tunings in the underlying interaction.

Firstly, we choose the vivid picture of an isotropic short-range potential to explain the above points. Afterwards, we quantify our arguments by discussing the two-body scattering amplitude in the low-energy limit. Finally, we introduce the concept of an effective field theory. This theoretical framework will be used in subsequent chapters to systematize relevant contributions to the amplitude – and thus to reaction observables – in tailor-made low-momentum expansions.

2.1 Low-energy simplifications

In general, quantum-mechanical reactions represent complicated many-body processes between the fundamental particles of the standard model (quarks, leptons, etc.). However, a microscopic derivation of cross sections and other reaction observables is usually very complicated and computationally not viable. Fortunately, it is not at all necessary if the relevant degrees of freedom are given by cluster states, i.e., by nucleons, nuclei, or even atoms. The reaction can then be described as a sequence of effective interactions between these states, i.e., it thus reduces to a few-body problem.

The cluster picture is particularly appropriate when typical momenta p are small. In particular, if the (reduced) de Broglie wave length $\lambda = 1/p$ is larger than the interaction range R of the clusters' constituents, then the constituents themselves are not resolved. For example, the ^{10}Be nucleus in Fig. 1.3(b) will be treated as a structureless (pointlike) "particle", even though it consists of many individual nucleons. In this thesis, all considered reactions are effective three-body problems.

If the typical momentum p of a single particle is smaller than its rest mass m, the relativistic dispersion relation can be expanded in the ratio $p^2/m^2 \ll 1$ yielding

$$E_{\text{tot}} = \sqrt{\boldsymbol{p}^2 + m^2} = m + \frac{\boldsymbol{p}^2}{2m} + \mathcal{O}\left(\boldsymbol{p}^4/m^3\right) . \tag{2.1}$$

In this thesis, relativistic corrections in Eq. (2.1) will be largest for the neutral pion π^0, the lightest of all hadrons. An analysis in Chapter 3 will reveal that π^0 can still be treated nonrelativistically to a good approximation in the reaction of interest. Thus, in the following, we neglect relativistic corrections.

In the rest of this chapter, we will work in the center-of-mass system of two nonrelativistic particles with masses m_1, m_2. The total kinetic energy in this frame,

$$E_{\text{cm}} \equiv E_{\text{tot},1} + E_{\text{tot},2} - m_1 - m_2 - \frac{(\boldsymbol{k}_1 + \boldsymbol{k}_2)^2}{2(m_1 + m_2)} , \tag{2.2}$$

is simply referred to as "center-of-mass energy".

2.1.1 Short-range interactions

Having identified the relevant degrees of freedom, the remaining task is to define appropriate two-body interaction potentials $V(\boldsymbol{r}, \boldsymbol{r}')$ between them.[1] Here, $\boldsymbol{r}$ and $\boldsymbol{r}'$ denote distance vectors. Given such an

---

[1] Two-body forces alone will not be sufficient to calculate physical observables in this thesis. Explicit three-body forces will be introduced where needed.

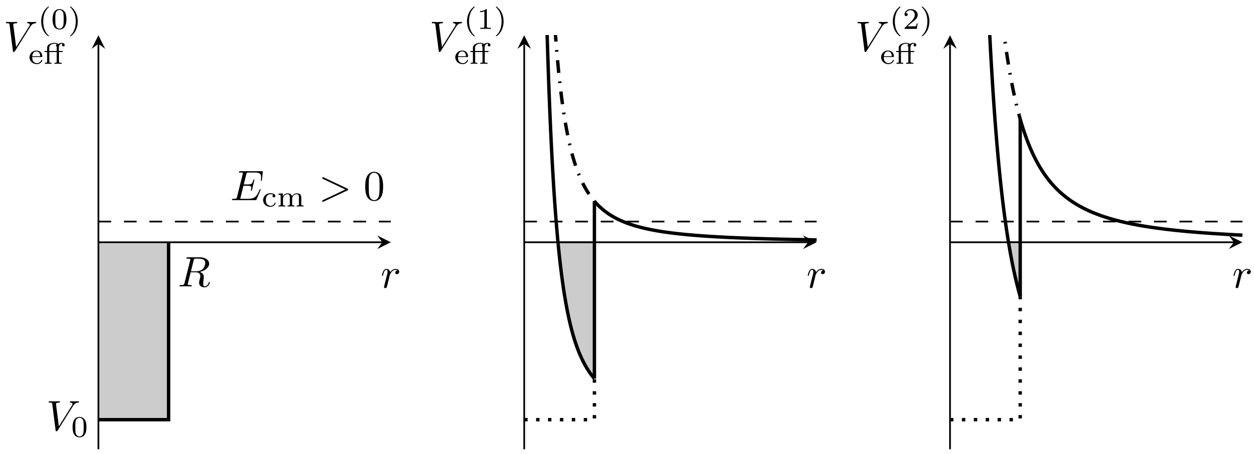

Figure 2.1.: Sketches of the effective potential $V_{\text{eff}}^{(l)}$ (solid curves) for a spherical square well potential as functions of the particle distance r for $l \leq 2$. For low center-of-mass energies E_{cm} (dashed curves), the angular momentum barrier (dash-dotted curves) lowers the probability of scattering via the short-range potential $V(r) = V_0\,\theta(R-r)$ with $V_0 < 0$ (dotted curves). Two-body bound states also become less likely since the region $V_{\text{eff}}^{(l)}(r) < 0$ shrinks (gray areas).

interaction, the two-body wave function in the center-of-mass frame is then determined by the stationary Schrödinger equation[2]

$$-\frac{\boldsymbol{\nabla}_{\boldsymbol{r}}^2}{2\mu}\,\psi(\boldsymbol{r}) + \int \mathrm{d}^3 r'\; V(\boldsymbol{r}, \boldsymbol{r}')\,\psi(\boldsymbol{r}') = E_{\text{cm}}\,\psi(\boldsymbol{r}), \tag{2.3}$$

with reduced mass $\mu \equiv m_1 m_2/(m_1 + m_2)$.

Since fundamental interactions happen only at small ranges R, the potential is essentially zero for $r > R$ or $r' > R$. In fact, it is possible to construct a potential only from delta functions and their derivatives[3], i.e., from contact terms. It will be written

$$\begin{aligned} V(\boldsymbol{r}, \boldsymbol{r}') = {} & \delta^{(3)}(\boldsymbol{r}) \left[c_0^{(0)} - \frac{c_0^{(2)}}{2} \left(\overleftarrow{\boldsymbol{\nabla}}_{\boldsymbol{r}}^2 + \overrightarrow{\boldsymbol{\nabla}}_{\boldsymbol{r}'}^2 \right) + \cdots \right] \delta^{(3)}(\boldsymbol{r}') \\ & + \delta^{(3)}(\boldsymbol{r})\, \overleftarrow{\boldsymbol{\nabla}}_{\boldsymbol{r}} \cdot \overrightarrow{\boldsymbol{\nabla}}_{\boldsymbol{r}'} \left[c_1^{(0)} - \frac{c_1^{(2)}}{2} \left(\overleftarrow{\boldsymbol{\nabla}}_{\boldsymbol{r}}^2 + \overrightarrow{\boldsymbol{\nabla}}_{\boldsymbol{r}'}^2 \right) + \cdots \right] \delta^{(3)}(\boldsymbol{r}') + \cdots . \end{aligned} \tag{2.4}$$

The coefficients $c_l^{(2n)}$ $(l, n \geq 0)$ contribute to the l^{th} partial wave.[4] Operators with additional derivatives are typically less important since they introduce momentum factors which are small.[5] Thus, for each l, the series is usually truncated at some small n. The remaining coefficients are chosen such that they reproduce certain low-energy observables like binding energies or scattering phase shifts. In this thesis, all interactions will be described by contact terms of Eq. (2.4). They represent a complete set of interactions in the sense that they describe every phase shift analytic in the energy; see the subsequent chapters.

Note that partial wave contributions $l \geq 1$ in Eq. (2.4) introduce at least $2l$ momentum factors. Thus, by construction, scattering at higher l usually becomes negligible at lower energies. This behavior is

---

[2] The symbol $\boldsymbol{\nabla}_{\boldsymbol{r}}$ denotes the gradient operator with respect to $\boldsymbol{r}$. If not further specified, it acts to the right.

[3] The derivative of a delta function is defined via its action $\int \mathrm{d}^3 r [\boldsymbol{\nabla}_{\boldsymbol{r}} \delta^{(3)}(\boldsymbol{r})] f(\boldsymbol{r}) \equiv -\boldsymbol{\nabla}_{\boldsymbol{r}} f(\boldsymbol{r})|_{\boldsymbol{r}=0}$.

[4] Truncations of this series can in general not be written in the form $V(\boldsymbol{r})\,\delta^{(3)}(\boldsymbol{r} - \boldsymbol{r}')$. They are still local in the sense that they vanish everywhere but at $\boldsymbol{r} = \boldsymbol{r}' = 0$.

[5] We will specify this statement when having introduced the knowledge of an effective field theory.

a generic feature of short-range potentials. It can be understood more vividly using a local, isotropic potential $V(\boldsymbol{r}, \boldsymbol{r}') \equiv V(r)\,\delta^{(3)}(\boldsymbol{r} - \boldsymbol{r}')$. The suppression of $l \geq 1$ scattering is due to the presence of a repulsive centrifugal barrier in the effective potential

$$V_{\text{eff}}^{(l)}(r) = V(r) + \frac{1}{2\mu}\frac{l(l+1)}{r^2} \tag{2.5}$$

of the l^{th} partial wave [78]. Here, μ denotes the reduced mass. In Fig. 2.1, we illustrate the impact of the barrier using a square well potential $V(r) \equiv V_0\,\theta(R - r)$ with $V_0 < 0$ (attractive). For $l = 0$, no barrier exists. The particles can approach each other down to short distances and scatter via the attractive potential. For $l \geq 1$, however, scattering at low center-of-mass energies E_{cm} implies that the particles must tunnel through the barrier. The tunneling probability becomes smaller as l increases and eventually vanishes for large l.

2.1.2 Shallow bound and resonance states

In some physical systems, scattering observables are significantly smaller or larger than expected from the scale of the interaction range R. Such systems often exhibit two-body bound states very close to threshold. For example, ^{11}Be is a bound ^{10}Be-n state; see Fig. 1.3. Its small binding energy can be translated into the length scale $\approx 7\,\text{fm}$ which is much larger than the typical range $R \sim 2$-$3\,\text{fm}$ of the nuclear force. Such states will be called "shallow". They have a significant impact on reaction observables and need to be reproduced by the coefficients in Eq. (2.4).

The "unnaturalness" of certain observables can be explained by a fine-tuning in the underlying theory [79]. How such a fine-tuning can lead to shallow bound states can be exemplified using the square well potential of Fig. 2.1. For this interaction, bound state solutions $E_{\text{cm}} = -B$ in the s-wave channel fulfill the transcendental equation

$$\sqrt{b} = \sqrt{b - v_0}\,\cot\left(\sqrt{b - v_0}\right) \geq 0 \tag{2.6}$$

with $b \equiv R^2\,2\mu B$ and $v_0 \equiv R^2\,2\mu V_0$. In order to have a shallow bound state with $B \ll R^{-2}/(2\mu) \Leftrightarrow b \approx 0$, the quantity v_0 has to be sufficiently close to one of the values $-\pi^2(1/2 + n)^2$ $(n \geq 0)$. To fulfill this condition, V_0 and R have to be highly correlated ("fine-tuned").

Asymptotically, the wave function of an s-wave bound state falls off exponentially like $\exp(-\gamma r)$ with binding momentum $\gamma \equiv (2\mu B)^{1/2}$. In the shallow case $\gamma \ll R^{-1}$, this tail extends far beyond the interaction range R. The two particles are then predominantly found in the classically forbidden region outside the potential. In nuclear physics, this quantum physical phenomenon explains why the root-mean-square radius of weakly bound halo nuclei is often much larger than expected from a naive $A^{1/3}$ estimation.

Most shallow bound states in hadron, nuclear, and atom physics correspond to a small orbital angular momenta $l \leq 2$. The reason is again the angular momentum barrier. Bound states require that there are regions where $V_{\text{eff}}^{(l)} < 0$. As indicated in Fig. 2.1, these regions quickly shrink as l increases (gray areas). The formation of a shallow bound state thus becomes less and less likely. In order to still have a shallow bound state, one usually needs further fine-tunings [80].

For $l \geq 1$, the effective potential can also support quasi-bound states ("resonances") at $E_{\text{cm}} = \delta > 0$ below the barrier maximum. In cross sections, they occur as peaks with a width Γ. Resonances have a finite life time $\tau \sim 1/\Gamma$ since they eventually tunnel through the barrier into the two-particle continuum. Note, however, that for very thick barriers, resonances can become long-lived. The width Γ is then small and the resonance is called "narrow". In this thesis, we will encounter two examples of shallow (and narrow) p-wave resonances, namely the D^{0*} dimeson and the ^{6}Li$_2$(e) diatom.

2.2 Scattering amplitude

The connection between bound and resonance states and the concept of fine-tuning can be formulated more quantitatively in terms of the scattering amplitude. Throughout this thesis, this quantity will be used as a starting point for the calculation of reaction rates and cross sections. In this section, we define it for the simple case of two nonrelativistic, distinguishable, and spinless particles, following Ref. [78]. Moreover, we assume that no other scattering channel is present and interactions are short-ranged. In subsequent chapters, we will then extend the concept of the scattering amplitude to spin structures, indistinguishable particles, inelastic channels, particles with substructure, and long-range forces.

Elastic scattering in the center-of-mass system maps an incident plain wave state onto an asymptotic scattering wave function $\psi_{\boldsymbol{k}}(\boldsymbol{r})$ with r much larger than the interaction range R. The asymptotic wave is a superposition of the plain wave and a scattered radial wave,

$$\psi_{\boldsymbol{k}}(\boldsymbol{r}) = e^{i\boldsymbol{k}\cdot\boldsymbol{r}} + \frac{\mu}{2\pi} t\left(\boldsymbol{k}, \boldsymbol{k}'\right) \frac{e^{i\bar{k}r}}{r} \quad (r \gg R) . \tag{2.7}$$

The complex-valued function t is called (on-shell) scattering amplitude.[6] It depends on the incoming and outgoing relative momenta $\boldsymbol{k}$ and $\boldsymbol{k}' \propto \boldsymbol{r}$. In elastic scattering, kinetic energy is conserved. The momenta then fulfill $\boldsymbol{k}^2 = \boldsymbol{k}'^2 = 2\mu E_{\mathrm{cm}} \equiv \bar{k}^2$, where $\bar{k}$ is called “on-shell relative momentum”.[7]

To calculate the scattering amplitude directly from a given potential, we introduce abstract position and momentum eigenstates with normalization properties

$$\left\langle \boldsymbol{r}' \,\middle|\, \boldsymbol{r} \right\rangle = \delta^{(3)}\left(\boldsymbol{r} - \boldsymbol{r}'\right), \tag{2.8a}$$

$$\left\langle \boldsymbol{l}' \,\middle|\, \boldsymbol{l} \right\rangle = (2\pi)^3 \, \delta^{(3)}\left(\boldsymbol{l} - \boldsymbol{l}'\right), \tag{2.8b}$$

such that $\langle \boldsymbol{r} \,|\, \boldsymbol{l} \rangle = \exp(i\boldsymbol{l} \cdot \boldsymbol{r}) = \langle \boldsymbol{l} \,|\, \boldsymbol{r} \rangle^*$. Momentum states are eigenstates of the free Hamiltonian $\hat{H}_0$ with eigenvalues $E_{\mathrm{cm}} = \boldsymbol{l}^2/(2\mu)$, i.e., $(E_{\mathrm{cm}} - \hat{H}_0)\,|\boldsymbol{l}\rangle = 0$.

Let $|\boldsymbol{k}\rangle$ be the incident state (on shell). In the presence of the potential $V(\boldsymbol{r}, \boldsymbol{r}') \equiv \langle \boldsymbol{r}' | \hat{V} \,| \boldsymbol{r} \rangle$, the asymptotic state $|\psi_{\boldsymbol{k}}\rangle$ fulfills $(E_{\mathrm{cm}} - \hat{H}_0 - \hat{V})\,|\psi_{\boldsymbol{k}}\rangle = 0$. We demand $|\psi_{\boldsymbol{k}}\rangle \to |\boldsymbol{k}\rangle$ in the limit of no interaction ($\hat{V} \to 0$) and obtain the self-consistent Lippmann-Schwinger equation

$$|\psi_{\boldsymbol{k}}\rangle = |\boldsymbol{k}\rangle + \left(E_{\mathrm{cm}} - \hat{H}_0 + i\epsilon\right)^{-1} \hat{V} \,|\psi_{\boldsymbol{k}}\rangle \tag{2.9}$$

for the asymptotic state. The quantity

$$\hat{G}_0(E_{\mathrm{cm}}) \equiv \left(E_{\mathrm{cm}} - \hat{H}_0 + i\epsilon\right)^{-1} \tag{2.10}$$

is the Green’s function operator of $\hat{H}_0$. In configuration and momentum space, it reads

$$\left\langle \boldsymbol{r}' \middle| \hat{G}_0(E_{\mathrm{cm}}) \,|\boldsymbol{r}\rangle = -\frac{\mu}{2\pi} \frac{e^{i\bar{k}|\boldsymbol{r}-\boldsymbol{r}'|}}{|\boldsymbol{r} - \boldsymbol{r}'|}, \tag{2.11a}$$

$$\left\langle \boldsymbol{l}' \middle| \hat{G}_0(E_{\mathrm{cm}}) \,|\boldsymbol{l}\rangle = \frac{(2\pi)^3 \, \delta^{(3)}(\boldsymbol{l} - \boldsymbol{l}')}{E_{\mathrm{cm}} - \frac{\boldsymbol{l}^2}{2\mu} + i\epsilon}; \tag{2.11b}$$

see for example Ref. [78].

---

[6] Note that in text books, the term scattering amplitude is often used for the function $f(\boldsymbol{k}, \boldsymbol{k}') \equiv \mu/(2\pi)\, t(\boldsymbol{k}, \boldsymbol{k}')$.

[7] Throughout the thesis, we treat E_{cm} and $\bar{k}$ synonymously. Later, we generalize relative momenta $\boldsymbol{k}$ to off-shell values $\boldsymbol{k}^2 \neq 2\mu E_{\mathrm{cm}}$.

Equation (2.9) can be translated to an equation for $\psi_{\boldsymbol{k}}(\boldsymbol{r})$ by multiplying $\langle\boldsymbol{r}|$ from the left. We obtain

$$\psi_{\boldsymbol{k}}(\boldsymbol{r}) = e^{i\boldsymbol{k}\cdot\boldsymbol{r}} - \frac{\mu}{2\pi}\int \mathrm{d}^3r'\, \frac{e^{i\bar{k}|\boldsymbol{r}-\boldsymbol{r}'|}}{|\boldsymbol{r}-\boldsymbol{r}'|}\left\langle\boldsymbol{r}'\right|\hat{V}\left|\psi_{\boldsymbol{k}}\right\rangle \tag{2.12a}$$

$$\xrightarrow{r\to\infty} e^{i\boldsymbol{k}\cdot\boldsymbol{r}} - \frac{\mu}{2\pi}\frac{e^{i\bar{k}r}}{r}\int \mathrm{d}^3r'\, e^{-i\boldsymbol{k}'\cdot\boldsymbol{r}'}\left\langle\boldsymbol{r}'\right|\hat{V}\left|\psi_{\boldsymbol{k}}\right\rangle \tag{2.12b}$$

$$= e^{i\boldsymbol{k}\cdot\boldsymbol{r}} - \frac{\mu}{2\pi}\left\langle\boldsymbol{k}'\middle|\hat{V}\middle|\psi_{\boldsymbol{k}}\right\rangle\frac{e^{i\bar{k}r}}{r}\,, \tag{2.12c}$$

since $\bar{k}|\boldsymbol{r}-\boldsymbol{r}'| \to \bar{k}(r-\hat{\boldsymbol{r}}\cdot\boldsymbol{r}') = \bar{k}r - \boldsymbol{k}'\cdot\boldsymbol{r}'$. By comparing this result with Eq. (2.7), we find that the scattering amplitude is connected to the potential via $t(\boldsymbol{k},\boldsymbol{k}') = -\left\langle\boldsymbol{k}'\middle|\hat{V}\middle|\psi_{\boldsymbol{k}}\right\rangle$. We can now interpret the scattering amplitude as the on-shell matrix element[8]

$$t\left(\boldsymbol{k},\boldsymbol{k}'\right) \equiv t\left(\boldsymbol{k},\boldsymbol{k}';E_{\mathrm{cm}}\right) \equiv \left\langle\boldsymbol{k}'\middle|\hat{T}(E_{\mathrm{cm}})\middle|\boldsymbol{k}\right\rangle \tag{2.13}$$

of the scattering operator $\hat{T} \equiv \hat{T}(E_{\mathrm{cm}})$. Per definition, it obeys the relation $\hat{T}(E_{\mathrm{cm}})\left|\boldsymbol{k}\right\rangle = -\hat{V}\left|\psi_{\boldsymbol{k}}\right\rangle$ for on-shell momenta $\boldsymbol{k} = \bar{k}\,\hat{\boldsymbol{k}}$. Equation (2.9) for the wave function holds if $\hat{T}$ fulfills the Lippmann-Schwinger equation

$$\hat{T} = -\hat{V} + \hat{V}\,\hat{G}_0(E_{\mathrm{cm}})\,\hat{T} = -\hat{V} + \hat{T}\,\hat{G}_0(E_{\mathrm{cm}})\,\hat{V}\,. \tag{2.14}$$

In subsequent chapters, we will recover the momentum space representation

$$t\left(\boldsymbol{k},\boldsymbol{k}';E_{\mathrm{cm}}\right) = -V\left(\boldsymbol{k},\boldsymbol{k}'\right) + \int\frac{\mathrm{d}^3l}{(2\pi)^3}\,V\left(\boldsymbol{k},\boldsymbol{l}\right)\left[E_{\mathrm{cm}} - \frac{\boldsymbol{l}^2}{2\mu} + i\epsilon\right]^{-1} t\left(\boldsymbol{l},\boldsymbol{k}';E_{\mathrm{cm}}\right) \tag{2.15}$$

of Eq. (2.14) using diagrammatic methods. The momenta $\boldsymbol{k}$, $\boldsymbol{k}'$, $\boldsymbol{l}$ are then firstly off shell.

Note that one of the two particles will be a two-body state itself. The potential will then be generalized to an energy-dependent particle exchange interaction $\hat{V}(E)$ and E will be the energy with respect to the three-particle threshold. The scattering equation might then still look like a Lippmann-Schwinger equation, but it really includes the full three-body dynamics. For this reason, it will be called a Faddeev equation.

2.2.1 Unitarity

Let us postpone the description of three-body systems to later chapters and come back to two particles without substructure. Now that we know how to obtain the on-shell amplitude $t(\boldsymbol{k},\boldsymbol{k}')$ from a given potential, we can discuss its mathematical properties.

The amplitude only depends on E_{cm} (or equivalently $\bar{k}$) and the scattering angle $\theta = \angle(\boldsymbol{k},\boldsymbol{k}')$. In terms of Legendre polynomials P_l, its partial wave expansion thus reads

$$t\left(\boldsymbol{k},\boldsymbol{k}'\right) = \sum_{l\geq 0}(2l+1)\,t^{(l)}\left(\bar{k}\right)\,P_l(\cos\theta)\,. \tag{2.16}$$

If l is a good quantum number, we can relate the partial wave amplitudes to the S matrix element

$$s^{(l)}(\bar{k}) = 1 + 2i\bar{k}\,\frac{\mu}{2\pi}\,t^{(l)}\left(\bar{k}\right) \equiv \exp\left(2i\delta_l(\bar{k})\right) \tag{2.17}$$

---

[8] Note that our definition of $\hat{T}$ includes a relative minus sign compared to the one in Ref. [78].

with phase shift $\delta_l(\bar{k})$ [78]. In the absence of inelastic channels, probability in the l^{th} partial wave is conserved and $s^{(l)}(\bar{k})$ is constraint to unitarity, i.e., $|s^{(l)}(\bar{k})| = 1$. The phase shift parametrization then implies $\delta_l(k) \in \mathbb{R}$.[9]

The relation between partial wave amplitude and phase shift can be rewritten in the form

$$t^{(l)}\left(\bar{k}\right) = \frac{2\pi}{\mu} \frac{\bar{k}^{2l}}{\bar{k}^{2l+1}\cot\delta_l(\bar{k}) - i\bar{k}^{2l+1}}. \tag{2.18}$$

Note that unitarity places an upper bound on the amplitude at $E_{\text{cm}}, \bar{k} > 0$. In particular, we have

$$\left|t^{(l)}(\bar{k})\right|^2 \overset{\delta_l(\bar{k})\in\mathbb{R}}{\propto} \bar{k}^{4l}\left[\left|\bar{k}^{2l+1}\cot\delta_l(\bar{k})\right|^2 + \left|-i\bar{k}^{2l+1}\right|^2\right]^{-1} \xrightarrow{\max} \bar{k}^{4l}\left|-i\bar{k}^{2l+1}\right|^{-2}. \tag{2.19}$$

Correspondingly, one speaks of the "unitary limit" if $\bar{k}^{2l+1}\cot\delta_l(\bar{k}) \to 0$. Note that this limit cannot always be reached due to causality restrictions; see below.

2.2.2 Analytic properties and the effective range expansion

The first denominator term in Eq. (2.18), $\bar{k}^{2l+1}\cot\delta_l(\bar{k})$, carries all information on the scattering process. In the years 1947-1950, Schwinger and Bethe independently proved for nucleon-nucleon s-wave scattering that $\bar{k}\cot\delta_0(\bar{k})$ is analytic in $E_{\text{cm}} \propto \bar{k}^2$ [20, 81, 82]. This important finding holds for scattering in higher partial waves if the interaction potential is short-ranged in the sense that it falls of exponentially as $r \to \infty$ [83]. The corresponding Taylor series

$$\bar{k}^{2l+1}\cot\delta_l(\bar{k}) \equiv -a_l^{-1} + \frac{r_l}{2}\bar{k}^2 + \mathcal{O}\left(\bar{k}^4\right). \tag{2.20}$$

is called "effective range expansion".[10]

For $l = 0$, the coefficients a_0 and r_0 are called "scattering length" and "effective range", respectively. They both have dimensions of a length. For $l = 1$, the terms "scattering volume" and "p-wave effective range" are used. They have dimensions of a spatial volume and a momentum, respectively. At low momenta, higher-order terms in the series become unimportant and scattering is determined only by a few scalar parameters. This remarkable finding implies that the specific shape of the short-range potential is irrelevant for low-energy scattering, as long as the numbers a_l, r_l, etc. are reproduced to some accuracy.

Note that the analyticity of Eq. (2.20) implies that partial wave amplitudes $t^{(l)}(\bar{k})$ become proportional to $\bar{k}^{2l}$ for small $\bar{k}$. This finding reproduces our earlier claim that $l \geq 1$ scattering is negligible for short-range interactions at small enough energies.

The so-called "unitary cut term" $-i\bar{k}^{2l+1}$ in Eq. (2.18) is not analytic in E_{cm} at $E_{\text{cm}} = 0$. It introduces a square root cut to $t^{(l)}$. The mapping $E_{\text{cm}} \mapsto \bar{k}$ is well defined using the definition

$$\bar{k} \equiv i\sqrt{-2\mu E_{\text{cm}} - i\epsilon} \tag{2.21}$$

with implicit limit $\epsilon \searrow 0$ [78]. For $E_{\text{cm}} > 0$, one has $\bar{k} > 0$ and for $E_{\text{cm}} < 0$, the imaginary part of the momentum $\bar{k} = +i|\,\bar{k}\,|$ is positive.

---

[9] In Chapter 3, unitarity in p-wave elastic $D^0\pi^0$ scattering will be violated due to the inelastic channel $D^0\gamma$. In this case, the phase shift will be generalized to complex values.

[10] If the potential, however, has a power-law tail $1/r^\nu$ ($\nu \geq 1$), analyticity in E_{cm} is in general not given. For example, the van der Waals interaction between two ultracold atoms induces a term linear in $\bar{k}$ for $l = 1$ due to its $1/r^6$ tail [84]. We will come back to this point in Chapter 5.

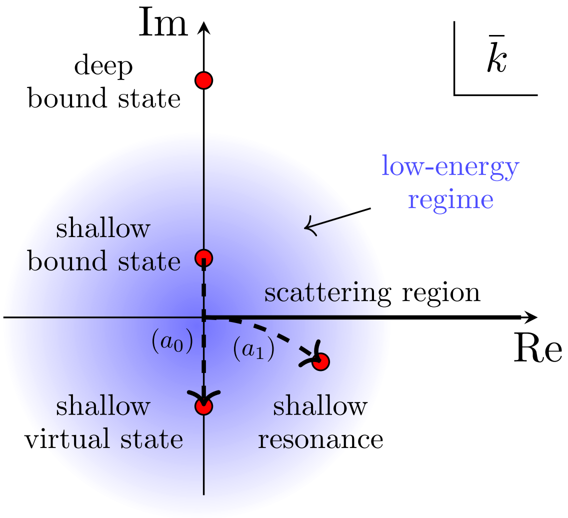

Figure 2.2.: Pole structure of the scattering amplitude. Bound (virtual) states occur on the positive (negative) imaginary axis of $\bar{k}$. Resonances lie in the fourth quadrant. States in the low-energy regime (blue) are called shallow. In this thesis, bound states of s-wave (p-wave) type can be transferred into virtual states (resonances) by tuning the scattering length a_0 (scattering volume a_1).

2.2.3 Pole structure

Two-body states[11] of l-wave type can be identified as poles in the partial wave amplitude $t^{(l)}$. We illustrate the locations of the different types of states as red dots in the complex $\bar{k}$ plane in Fig. 2.2. Bound states live on the positive imaginary axis, i.e., at $\bar{k} = i\gamma$ with some binding momentum $\gamma > 0$. Resonance poles lie in the fourth quadrant. Their imaginary part is connected to the resonance width. Poles on the negative imaginary axis, i.e., at $\bar{k} = i\gamma$ with $\gamma < 0$, correspond to virtual states. One such pole occurs in neutron-neutron scattering; see Chapter 4. If a pole lies in the low-energy regime (blue), the state is called shallow.

Shallow s-wave states usually result from a fine-tuning of the scattering length $a_0 \gg R$ [78]. For large enough a_0 and low momenta $\bar{k} \sim a_0^{-1}$, the partial wave amplitude becomes proportional to $[-a_0^{-1} - i\bar{k}]^{-1}$. The fine-tuning thus leads to a shallow pole at $\bar{k} = i\gamma$ with $\gamma \approx a_0^{-1}$. Depending on the sign of a_0, the s-wave state is bound ($a_0 > 0$) or virtual ($a_0 < 0$). The transition through $\gamma \approx a_0^{-1} = 0$ is indicated as a dashed arrow in Fig. 2.2.

For shallow $l \geq 1$ states, the manifestation of the fine-tuning differs from system to system [85]. In this thesis, we will discuss three different shallow p-wave states. In Chapter 3, the resonance D^{0*} will be due to an enormously large p-wave effective range $|r_1| \gg R^{-1}$. In contrast, the bound state $^{11}\mathrm{Be}^*$ in Chapter 4 results from a large scattering volume $a_1 \gg R^3$. The third p-wave state will be the diatom $^6\mathrm{Li}_2$(e) in Chapter 5. Its scattering volume a_1 is driven to arbitrarily large values by an external magnetic field, i.e., by an experimental fine-tuning. We will find that $^6\mathrm{Li}_2$(e) can be transferred from a bound state to a resonance if a_1^{-1} crosses the value 0 from above; see Fig. 2.2.

In the E_{cm} plane, bound states lie at negative energies $-B$ ($B > 0$). Resonances and virtual states are hidden on the second Riemann sheet due to the nonanalyticity of the unitary cut term.

---

[11] In this thesis, the term “two-body state” refers to bound, resonance, or virtual states specifically.

2.2.4 Unitary limit and universality

As mentioned above, the unitary limit corresponds to the hypothetical situation in which the term $\bar{k}^{2l+1} \cot \delta_l(\bar{k})$ can be neglected against the unitary cut term. If the limit can be taken, the resulting partial wave amplitude looses all information on the specific physical system. For short-range interactions, the unitary limit implies vanishing threshold parameters a_l^{-1}, r_l, etc. Some physical s-wave systems come pretty close to this situation. For example, the modulus of the scattering length $a_0 \approx -23.71\,\text{fm}$ in ${}^1s_0$ nucleon-nucleon scattering is much larger then the effective range $r_0 = 2.75\,\text{fm}$ [86]. The latter is of the order of the nuclear interaction range R. If typical momenta fulfill $r_0 < \bar{k}^{-1} < |a_0|$, the unitary limit is a good approximation. König *et al.* demonstrated that such a description for the ${}^1s_0$ channel yields good results for the ^{3}H and ^{3}He binding energies [87].

In systems with $\bar{k} \sim a_0^{-1}$, the unitary limit may not be a good approximation. Still, if r_0 can be neglected against a_0, the theory greatly simplifies. All low-energy observables, e.g., binding energies or cross sections, are then determined by a_0 alone. Such a system has universal properties in the sense that it is insensitive to short-range details of the interaction. Since r_0 typically represents the interaction range R, a theory only including a_0 is called zero-range theory.

For $l \geq 1$, the unitary limit $a_1^{-1}, r_1 \to 0$ cannot be reached completely. In fact, it violates causality as was shown by Hammer and Lee [88]. For example, the p-wave effective range is restricted by the Wigner bound $r_1 \leq -2/R$ if $a_1^{-1} = 0$ and R is the interaction range. Similar bounds can be calculated for $a_1^{-1} \neq 0$ and for $l \geq 2$. The Wigner bound shows that scattering in higher partial waves is more sensitive to short-range physics than in the s-wave case. Still, we will demonstrate in subsequent chapters that systems with shallow p-wave states can be described using only the two parameters a_1 and r_1.

2.3 Effective field theories

Above we saw that different short-range interactions can describe the same low-energy physics in terms of scattering lengths, binding energies, etc. This observation has led to the more modern approach to build a theory not upon some microscopic interaction model, but solely upon observables accessible at the (low) energy scale of interest.

Nucleon-nucleon (N-N) scattering is a perfect example to illustrate this paradigm shift. Over the years, many different N-N potentials like Nijmegen I, II [86], AV18 [89], and CD-Bonn [90] have been constructed, accurately describing phase shifts up to momenta of order 350 MeV. They all mimic the effect of microscopic meson-exchange interactions (π, ρ, etc.) relevant at kinetic energies of order $m_\pi \approx 135\,\text{MeV}$. At low energies of a few MeV, however, N-N physics is described to very good accuracy by the ${}^3s_1$ and ${}^1s_0$ scattering lengths a_0 and effective ranges r_0 only. In the ${}^3s_1$ channel, these two parameters reproduce the deuteron binding momentum (a low-energy phenomenon) with an accuracy of $\approx 95\,\%$. Precise knowledge of microscopic physics is then irrelevant for the low-energy theory.[12]

This point brings us back to the start of this chapter, where we stated that physics related to high-energy degrees of freedom (here: meson exchanges) cannot be resolved at low energies. Kaplan and Wise demonstrated in Ref. [19] that all short-range details of meson exchanges can be absorbed into a series of local N-N operators. Just one of them is needed to reproduce a_0 and a second one can be used for r_0.[13] These two operators are nothing but the first two contact terms of the short-range "potential" of Eq. (2.4) ($c_0^{(0)}$ and $c_0^{(2)}$).

The theory of Kaplan and Wise is an example of an effective field theory (EFT). Such quantum field theories provide a systematic way to describe physics at a certain energy scale at a desired accuracy. In the following, we elucidate how to construct such a theory "bottom-up", i.e., starting directly from

---

[12] It is true that the values of a_0 and r_0 are ultimately determined by microscopic physics. For a low-energy description of the N-N system, however, the precise origin is irrelevant and the values can be treated much like natural constants.

[13] More generally, one needs a single operator for each effective range coefficient.

observables at a certain energy scale. Afterwards, we discuss the "top-down" approach, in which an existing microscopic theory is simplified by an EFT expansion at low energies.

2.3.1 Bottom-up

The bottom-up approach can be chosen if the values (or at least the scalings) of all relevant low-energy observables are known. In this thesis, we use it to describe the transfer reaction $^{10}\mathrm{Be}\,(\mathrm{d},\,\mathrm{p})\,^{11}\mathrm{Be}$ and the three-body recombination process $3^6\mathrm{Li} \longrightarrow {}^6\mathrm{Li}_2(\mathrm{d}) + {}^6\mathrm{Li}$.

1. *First of all, one identifies particles and symmetries which describe the system at the energy scale under consideration.*

   For example, to describe the deuteron, one needs only a proton and a neutron. Important symmetries in nonrelativistic theories are Galilean invariance, i.e., frame independence, and particle number conservation.

2. *A (spinor) quantum field is assigned to each particle. One then writes down a Lagrangian containing all local operators which respect the analyticity and unitarity properties of the scattering amplitude. The operators also have to be compliant with the proposed symmetries.*

   In this thesis, we use nonrelativistic Schrödinger fields

   $$\phi_\alpha(x) = \int \frac{\mathrm{d}^3 p}{(2\pi)^3}\, \hat{a}_{\boldsymbol{p},\alpha}\, e^{-i\left(\frac{p^2}{2m}t - \boldsymbol{p}\cdot\boldsymbol{x}\right)}, \quad \phi^\dagger_\alpha(x) = \int \frac{\mathrm{d}^3 p}{(2\pi)^3}\, \hat{a}^\dagger_{\boldsymbol{p},\alpha}\, e^{i\left(\frac{p^2}{2m}t - \boldsymbol{p}\cdot\boldsymbol{x}\right)}. \tag{2.22}$$

   They annihilate and create a particle at space-time $x \equiv (\boldsymbol{x},\, t)$, respectively, with polarization α. For indistinguishable bosons (fermions), the fields obey certain (anti)commutation relations; see subsequent chapters.

   Galilean-invariant operators only depend on relative momenta $\boldsymbol{k}, \boldsymbol{k}'$. Thus, local operators for two-body scattering of (spinless, equal-mass) particles ϕ, ψ have the form

   $$\mathscr{L}_{\phi\psi} = c_0^{(0)}(\phi\psi)^\dagger(\phi\psi) + \frac{c_0^{(2)}}{2}\left[(\phi\psi)^\dagger\left(\phi\,\frac{\overleftarrow{\boldsymbol{\nabla}} - \overrightarrow{\boldsymbol{\nabla}}}{2}\psi\right) + \mathrm{H.c.}\right] + \cdots \tag{2.23a}$$

   $$\xrightarrow{\text{momentum space}} c_0^{(0)} + \frac{c_0^{(2)}}{2}\left(k^2 + k'^2\right) + \cdots . \tag{2.23b}$$

   The ellipses in Eq. (2.23a) include further derivatives and "H.c." is the Hermitian conjugate. The momentum space form in Eq. (2.23b) is nothing but a Fourier transform of Eq. (2.4).

3. *Usually, an infinite amount of terms obey the symmetry restrictions. To obtain reasonable predictions with only a finite number of terms, a "power counting" must be developed which orders the terms according to their importance.*

   If the ϕ-ψ scattering length a_0 is much larger than the effective range r_0, then they define the typical low and high momentum scales $K_{\mathrm{lo}} \sim a_0^{-1}$ and $K_{\mathrm{hi}} \sim r_0^{-1}$. In this case, the system exhibits an intrinsic "separation of scales". The scattering amplitude can then be expanded in terms of $\chi_2 \equiv K_{\mathrm{lo}}/K_{\mathrm{hi}} < 1$. In particular, for scattering at $k \sim K_{\mathrm{lo}}$, the first two operators scale like $c_0^{(0)} \sim a_0 \sim K_{\mathrm{lo}}^{-1}$ (leading order) and $c_0^{(2)}k^2 \sim a_0^2 r_0 k^2 \sim K_{\mathrm{hi}}^{-1}$ (next-to-leading order) [19]. By truncating at a fixed power counting order, the remaining uncertainty is some power of $\chi_2 = K_{\mathrm{lo}}/K_{\mathrm{hi}}$. Additional expansion parameters in the three-body sector will be denoted χ_3.

Due to the fact that the effective Lagrangian has usually infinitely many terms, EFTs are not renormalizable in the classical sense. In fact, infinitely many counterterms are needed to absorb ultraviolet divergences in amplitudes. However, at fixed power counting order, only a finite number of counterterms is needed. EFTs in this thesis are then renormalizable "order by order".

2.3.2 Top-down

Sometimes, a given (effective) quantum field theory contains too many short-range details for an efficient computation of low-energy observables. One then expands this theory in terms of low momenta or an intrinsic separation of scales to obtain a simpler EFT. In this process, one produces a series of low-energy constants which can be matched to parameters of the underlying theory.

A prominent example is Fermi's theory for the nuclear beta decay [91]. It is an approximation for the weak interaction if momenta are smaller than the W boson mass $m_W \approx 80\,\text{GeV}$ [36]. After expanding the W boson propagator at low momenta, the leading low-energy constant (Fermi's constant G_F) is sufficient to describe nuclear beta decay accurately. It can be matched to the underlying theory by expressing it in terms of the weak coupling and m_W.

The first reaction described in this thesis is $D^0\bar{D}^0\pi^0$ production at energies around the $X(3872)$. Here, we will choose a top-down approach to match the unknown D^{0*} decay width to a coupling constant of Heavy Hadron Chiral Perturbation theory.

3 $X(3872)$ line shape in $D^0\bar{D}^0\pi^0$ production

In this chapter, we develop a novel EFT for the charmonium state $X(3872)$, based on its interpretation as a $D^0\bar{D}^0\pi^0$ three-body resonance. The theory is used to relate the mass m_X and width Γ_X of the $X(3872)$ to its asymmetric line shape in the $D^0\bar{D}^0\pi^0$ production reaction

$$B^\pm \to K^\pm + X(3872) \to K^\pm + D^0\bar{D}^0\pi^0 \,. \tag{3.1}$$

Note that the total mass difference $m_{B^\pm} - m_{K^\pm} - 2m_{D^0} - m_{\pi^0} \approx 921\,\mathrm{MeV}$ is larger than the masses of the outgoing π^0 and $K^\pm$ mesons [36]. Thus, it might seem counterintuitive to study the process in a nonrelativistic theory. In fact, it was shown that the line shape, i.e., the form of its experimental peak, is fully determined by the three-body decay of the $X(3872)$ [44, 92]. This subprocess is of nonrelativistic nature since it involves only a tiny energy excess $\approx 7\,\mathrm{MeV} \ll m_{\pi^0} \ll m_{D^0}$; see Fig. 3.1.

We start by deriving a Galilean-invariant EFT Lagrangian for pseudoscalar D and π mesons in the kinematic region of the $X(3872)$ from heavy-hadron chiral perturbation theory (HHχPT). Afterwards, we calculate the $X(3872)$ line shape, closely following the lines of our publication "*Threshold effects and the line shape of the* $X(3872)$ *in effective field theory*" in Physical Review D **98**, 014032 (2018) [93]. We obtain results for the $X(3872)$ width Γ_X and its line shape up to NLO in the equally small expansion parameters

$$\underbrace{\chi_2 \approx \frac{\delta}{m_\pi/2}}_{\text{2-body}} \quad \sim \quad \underbrace{\chi_3 = \sqrt{\frac{|\delta_X|}{\delta}} \sim \sqrt{\frac{|\delta_X|}{\nu}} \sim \frac{\mu_{D\pi}}{\mu_*}}_{\text{3-body}} \quad \lesssim \quad 0.13 \tag{3.2}$$

of the two- ($D\pi$) and three-body ($DD\pi$) sectors.[1] In Eq. (3.2),

$$\delta \equiv m_{D^{0*}} - (m_{\pi^0} + m_{D^0}) = 7.04(3)\,\mathrm{MeV}\,, \tag{3.3a}$$

$$\nu \equiv (m_{D^+} + m_{D^{+*}}) - (m_{D^0} + m_{D^{0*}}) = 8.16(9)\,\mathrm{MeV} \sim \delta\,, \tag{3.3b}$$

are the small mass differences between $D^0\bar{D}^0\pi^0 \longleftrightarrow D^0\bar{D}^{0*} \longleftrightarrow D^+D^{-*}$ and $\delta_X = (-0.01 \pm 0.2)\,\mathrm{MeV}$ is the tiny mass difference of the $X(3872)$ with respect to $D^0\bar{D}^{0*}$; see Fig. 3.1. Moreover, $\mu_{D\pi}$ and μ_* denote reduced masses defined in Eqs. (3.23a)-(3.23b). We conclude the chapter by extending the theory to virtual $X(3872)$ states.

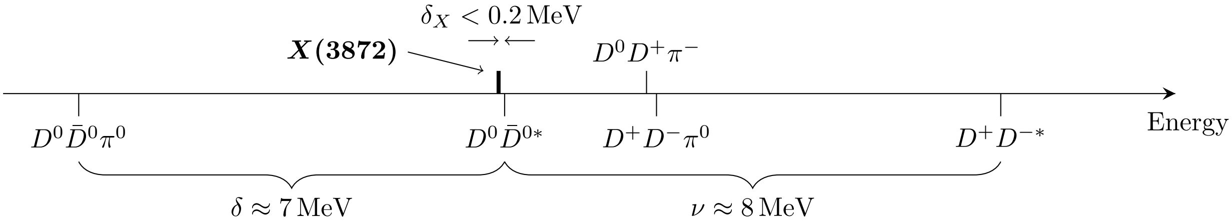

Figure 3.1.: Thresholds close to the $X(3872)$ (to scale, antiparticle states omitted). The $X(3872)$ occurs near the $D^0\bar{D}^{0*}$ threshold at a tiny separation δ_X. The mass splitting δ in the decay $D^{0*} \to D^0\pi^0$ and the distance ν between the neutral and charged DD^* thresholds are also small compared to the particle masses. Precise values are given in Eqs. (1.1), (3.3a), and (3.3b).

---

[1] Whenever superscripts "0" or "±" are omitted, we refer collectively to all relevant meson combinations.

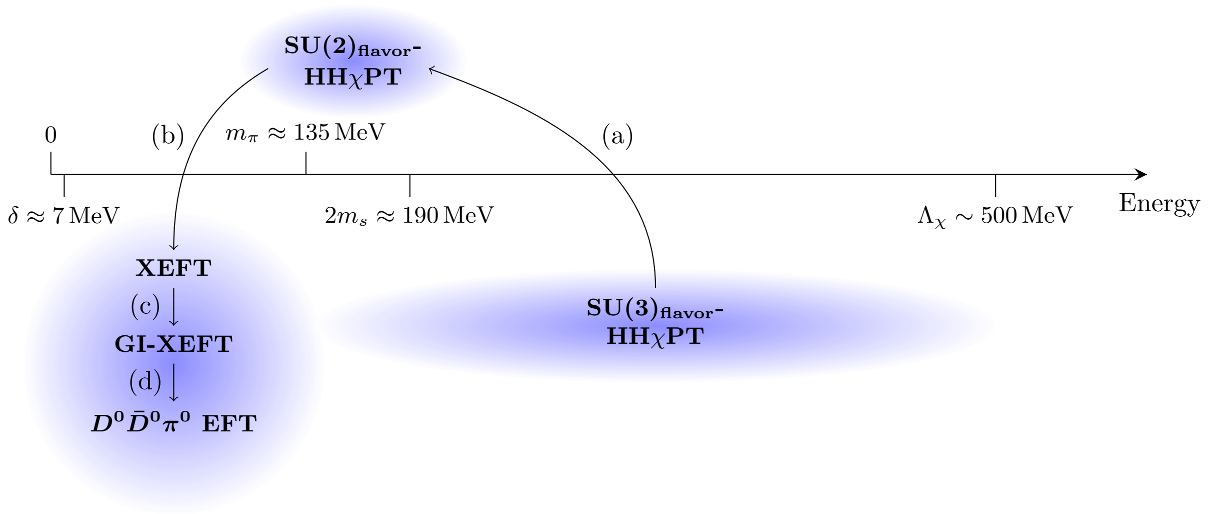

Figure 3.2.: The "$D^0\bar{D}^0\pi^0$ EFT" used in this thesis follows from (a) HHχPT after integrating out the high scales (b) $2m_s$ (mass of two strange quarks) and (c) m_π (pion mass), (d) restoring Galilean invariance, and (e) reformulating vector D mesons as pure p-wave $D\pi$ resonances. These steps are explained in the sections below.

3.1 Top-down derivation of $D^0\bar{D}^0\pi^0$ EFT

Given the quantum numbers, masses, and widths of the particles in Fig. 3.1, one could in principle write down a bottom-up EFT for the $X(3872)$ line shape only from phenomenological observations. At the moment, however, this approach would suffer from the fact that the width $\Gamma_{0*} \equiv \Gamma[D^{0*}] < 2.1\,\text{MeV}$ [36], on which the line shape crucially depends, has not been measured accurately yet. Thus, one would need to estimate Γ_{0*}, e.g., using naturalness arguments, already at LO.

In order to gain more predictive power, we will instead determine Γ_{0*} from the well-known width $\Gamma_{c*} \equiv \Gamma[D^{+*}] = 82(2)\,\text{keV}$ of the charged vector mesons [36]; see also Table 3.2. As pointed out by Braaten in Ref. [94], the two widths can be connected assuming isospin symmetry between the vertices of the neutral and charged $D^* \to D\pi$ decays; see Sec. 3.2.2. To implement this constraint, we choose a top-down approach and derive the EFT directly from HHχPT [18, 95–97] by conducting the steps in Fig. 3.2.

3.1.1 SU(2)$_{\text{flavor}}$ heavy-hadron chiral perturbation theory

HHχPT is an approximation of QCD formulated to describe interactions between mesons containing one light and one heavy (anti)quark ($\bar{q}Q$ or $\bar{Q}q$). At LO, the theory takes the limit $m_Q \to \infty$, where u-, d-, and also s-quarks can be considered light. Forces are then mediated by the Goldstone bosons of the SU(3)$_{\text{flavor}}$ group (π, η, and K mesons). The breakdown scale of HHχPT is set by the chiral scale $\Lambda_\chi \sim 500\,\text{MeV}$ as indicated in Fig. 3.2.

For the $X(3872)$, we set $Q = c$ ($\bar{Q} = \bar{c}$), where c denotes the charm quark with mass $m_c \approx 1275\,\text{MeV}$ [36]. Each heavy-light pair $\bar{q}c$ ($\bar{c}q$) then couples either to a pseudoscalar ($J^P = 0^-$) or a vector ($J^P = 1^-$) meson. Thus, for $\bar{q} \in \{\bar{u}, \bar{d}, \bar{s}\}$, three $\bar{q}c$-type D meson pairs can be constructed. They are given by (D^0, D^{0*}), (D^+, D^{+*}), and (D_s^+, D_s^{+*}), respectively, and the antiparticles ($\bar{c}q$) read ($\bar{D}^0$, $\bar{D}^{0*}$), (D^-, D^{-*}), and (D_s^-, D_s^{-*}). Potentially, all these particles contribute to the $X(3872)$ wave function. However, due to the large strange meson mass $m_s \approx 95\,\text{MeV}$, the physical $D_s^+D_s^{-*}$ threshold lies roughly $208\,\text{MeV} \sim 2m_s \gg \delta \sim \nu$ away from the $X(3872)$ [36]. Thus, while being important in the original $1/m_Q$ counting, strange mesons can be safely integrated out in an expansion in $\chi_2 \sim \chi_3$ in Eq. (3.2); see step (a) in Fig. 3.2. The remaining theory then has SU(2)$_{\text{flavor}}$ symmetry.

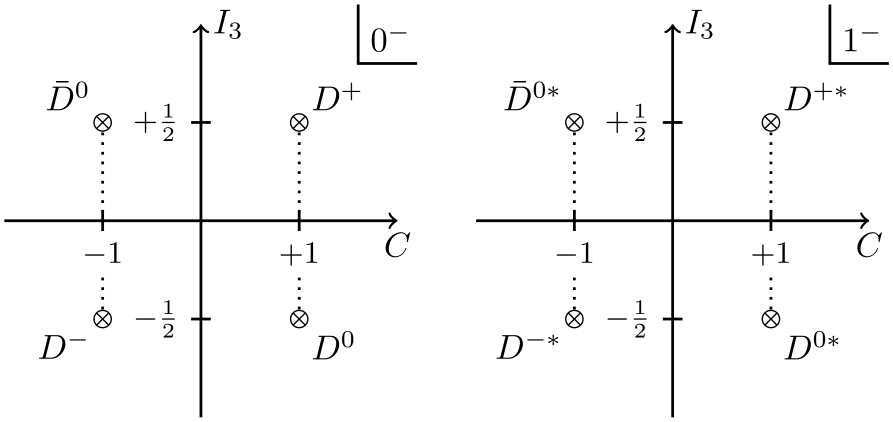

Figure 3.3.: Isospin doublets (dotted lines) of pseudovector (0^-) and vector (1^-) D mesons (charmness $C = \pm 1$). Charge conjugation corresponds to a reflection at the origin.

As suggested by Hu and Mehen, we begin our derivation with a version of $\mathrm{SU}(2)_{\mathrm{flavor}}$-HH$\chi$PT which is formulated explicitly in the heavy meson rest frame [98]. The fact that this choice breaks Lorentzian invariance is no problem for our purposes since we aim at a nonrelativistic description of the $X(3872)$. At the end of the derivation, we will restore the correct nonrelativistic symmetry, which is Galilean invariance. The Lagrangian will be divided into a part for the heavy $D^{(*)}$ mesons, a part for the pions, and an interaction part by writing

$$\mathscr{L}_{\mathrm{HM}} = \mathscr{L}_{\mathrm{HM},H} + \mathscr{L}_{\mathrm{HM},\pi} + \mathscr{L}_{\mathrm{HM},H\pi} \,. \tag{3.4}$$

Three-body terms will be neglected until the very end of our derivation.

D mesons

The $\mathrm{SU}(2)_{\mathrm{flavor}}$ doublet fields for the heavy pseudoscalar and vector mesons are denoted by

$$\begin{pmatrix} P_1 \\ P_2 \end{pmatrix} \equiv \begin{pmatrix} D^0 \\ -D^+ \end{pmatrix}, \quad \begin{pmatrix} \boldsymbol{P}_1 \\ \boldsymbol{P}_2 \end{pmatrix} \equiv \begin{pmatrix} \boldsymbol{D}^0 \\ -\boldsymbol{D}^+ \end{pmatrix}, \tag{3.5a}$$

$$\begin{pmatrix} \bar{P}_1 \\ \bar{P}_2 \end{pmatrix} \equiv \begin{pmatrix} D^- \\ \bar{D}^0 \end{pmatrix}, \quad \begin{pmatrix} \bar{\boldsymbol{P}}_1 \\ \bar{\boldsymbol{P}}_2 \end{pmatrix} \equiv \begin{pmatrix} -\boldsymbol{D}^- \\ -\bar{\boldsymbol{D}}^0 \end{pmatrix}. \tag{3.5b}$$

Upper (lower) entries in Eqs. (3.5a)–(3.5b) correspond to isospin projections $I_3 = -1/2$ ($I_3 = +1/2$) [99]. The sign convention coincides with Ref. [100]. It is chosen such that meson and antimeson states fulfill the charge conjugation relation

$$\hat{C}\,|M\rangle = \left|\bar{M}\right\rangle . \tag{3.6}$$

Appropriate interpolating di-quark fields[2] can be found in Ref. [46]. Figure 3.3 summarizes the above D mesons in charmness and isospin space.

The mass splittings $\Delta_H \equiv m_{D^*} - m_D$ between the pseudoscalar and vector mesons are small compared to the masses themselves (some GeV). Thus, HHχPT exhibits approximate heavy-quark spin symmetry and the quantum fields of the pairs are typically treated as heavy-quark spin doublets. They are summarized into superfields

$$H_a \equiv P_a + \boldsymbol{P}_a \cdot \boldsymbol{\sigma} \,, \tag{3.7a}$$

$$\bar{H}_a \equiv \bar{P}_a + \bar{\boldsymbol{P}}_a \cdot \boldsymbol{\sigma} \,, \tag{3.7b}$$

---

[2] The global minus sign between $(P_1, P_2)^T$ and $(\boldsymbol{P}_1, \boldsymbol{P}_2)^T$ in Eq. (3.5b) follows from the charge conjugation relations $\hat{C}^{-1}\gamma_5\hat{C} = \gamma_5$ and $\hat{C}^{-1}\gamma_\mu\hat{C} = -\gamma_\mu$ of the gamma matrices appearing in the interpolating fields.

where $\boldsymbol{\sigma}$ is the vector of Pauli matrices and $a \in \{1, 2\}$. The Lagrangian formulated by Hu and Mehen in Ref. [98] then reads

$$\mathcal{L}_{\mathrm{HM},H} = \mathrm{Tr}\left[H_a^\dagger (iD_0)_{ba} H_b\right] + \frac{\Delta_H}{4}\mathrm{Tr}\left[H_a^\dagger \boldsymbol{\sigma} H_a \boldsymbol{\sigma}\right] + \text{c.c.}\,, \tag{3.8}$$

where "c.c." denotes the charge conjugate. The second term of Eq. (3.8) explicitly breaks heavy-quark spin symmetry by introducing the mass splitting Δ_H. In the following, we choose the masses to be the physical neutral meson masses, i.e., $m_{D^{(*)}} \equiv m_{D^{0(*)}}$ with $\Delta_H \approx 142\,\mathrm{MeV}$; see also Table 3.1.

Pions

We summarize the relativistic pion fields into an isovector $\pi \equiv (\pi^-, \pi^0, \pi^+)^T$ with uniform pion mass $m_\pi \equiv m_{\pi^0} \approx 135\,\mathrm{MeV}$. The pion term in Eq. (3.4) then reads

$$\mathcal{L}_{\mathrm{HM},\pi} = \frac{1}{2}\pi_i\left[-\partial^2 - m_\pi^2\right]\pi_i + \mathcal{O}\left(\pi^4\right). \tag{3.9}$$

Interactions between D and π mesons are described by the Lagrangian term

$$\mathcal{L}_{\mathrm{HM},H\pi} = -g_{\mathrm{HH}\chi\mathrm{PT}}\,\mathrm{Tr}\left[H_a^\dagger H_b\, \boldsymbol{\sigma}\cdot \boldsymbol{A}_{ba}\right] \tag{3.10}$$

being proportional to the coupling constant $g_{\mathrm{HH}\chi\mathrm{PT}} \sim 1$. The interaction involves the axial vector field

$$\boldsymbol{A}_{ab} \equiv -\frac{1}{f_\pi}\boldsymbol{\nabla} M_{ab} + \mathcal{O}\left(\pi^3\right) \tag{3.11}$$

with the $\mathrm{SU}(2)_{\mathrm{flavor}}$ pion matrix

$$M = \frac{1}{\sqrt{2}}\begin{pmatrix} \pi^0 & \sqrt{2}\,\pi^+ \\ \sqrt{2}\,\pi^- & -\pi^0 \end{pmatrix} \tag{3.12}$$

and the pion decay constant[3] $f_\pi \approx 130\,\mathrm{MeV}$ [98].

Higher-order terms in Eqs. (3.9) and (3.11) involve at least two more pion fields. Nonrelativistically, they induce many-body forces, e.g., $\pi\pi \longleftrightarrow \pi\pi$ or $D\pi\pi \longleftrightarrow D^*\pi$, not appearing in the $X(3872)$ sector. Moreover, the $\mathcal{O}\left(\pi^2\right)$ part of the chiral covariant derivative

$$(iD_0)_{ab} = i\partial_0\,\delta_{ab} + \mathcal{O}\left(\pi^2\right) \tag{3.13}$$

in Eq. (3.8) induces Weinberg-Tomozawa vertices of types $D^*\pi \longleftrightarrow D^*\pi$ and $D\pi \longleftrightarrow D\pi$ (s-wave) with at least one charged pion [101]. While the first type is again irrelevant for the $X(3872)$ amplitude, contributions from the second type involve two or more virtual charged pions. Such diagrams are at least suppressed by multiples[4] of $(\mu_{D\pi}/\mu_*)^2 \approx 0.01$ (N^{2}LO in the $\chi_2 \sim \chi_3$ counting of Eq. (3.2)); see Sec. 3.3.4. Further suppression is expected to come from the fact that there is no resonant s-wave $D\pi$ state near the $X(3872)$. Thus, Weinberg-Tomozawa vertices are expected to be negligible in this work.

After field redefinitions $H_a \to H_a \exp(i\,3\Delta_H t/4)/\sqrt{2}$, the Lagrangian takes the form

$$\begin{aligned}\mathcal{L}_{\mathrm{HM}} = {}& \boldsymbol{P}_a^\dagger\left[i\partial_0 - \Delta_H\right]\boldsymbol{P}_a + P_a^\dagger\left[i\partial_0\right]P_a + \text{c.c.} + \mathcal{L}_{\mathrm{HM},\pi} \\ & - g_{\mathrm{HH}\chi\mathrm{PT}}\left(\boldsymbol{P}_a^\dagger \boldsymbol{A}_{ba} P_b + \text{H.c.}\right) - i\,g_{\mathrm{HH}\chi\mathrm{PT}}\,\boldsymbol{P}_a^\dagger\cdot\left(\boldsymbol{P}_b \times \boldsymbol{A}_{ba}\right) + \text{c.c.}\,,\end{aligned} \tag{3.14}$$

where "H.c." denotes the Hermitian conjugate.

---

[3] The pion decay constant always comes along with $g_{\mathrm{HH}\chi\mathrm{PT}}$ in this thesis. Its precise value is not relevant for our purposes since $f_\pi/g_{\mathrm{HH}\chi\mathrm{PT}}$ will be matched to the experimental D^{+*} width; see Eqs. (3.35) and (3.49).

[4] For definitions of the reduced masses see Eqs. (3.23a)-(3.23b).

3.1.2 XEFT for neutral and charged mesons

The Lagrangian in Eq. (3.14) is appropriate for energies of the order $E \sim \Delta_H \sim m_\pi$. However, as can be seen from Fig. 3.1, the process $X(3872) \to D^0\bar{D}^0\pi^0$ is sensitive to much smaller energies $\delta \sim \nu$. Thus, the scales $\Delta_H \sim m_\pi$ will be integrated out; see step (b) in Fig. 3.2. We identify parts in Eq. (3.14) related to the large scales by introducing creation/annihilation operators $\hat{\pi}^{0\,(\dagger)}$ and $\hat{\pi}^{\pm\,(\dagger)}$, which do not involve the time-dependent rest mass phase. They fulfill

$$\pi^0 \equiv \frac{1}{\sqrt{2m_\pi}}\left(\hat{\pi}^0\, e^{-im_\pi t} + \hat{\pi}^{0\,\dagger}\, e^{im_\pi t}\right), \tag{3.15a}$$

$$\pi^\pm \equiv \frac{1}{\sqrt{2m_\pi}}\left(\hat{\pi}^\pm\, e^{-im_\pi t} + \hat{\pi}^{\mp\,\dagger}\, e^{im_\pi t}\right). \tag{3.15b}$$

Afterwards, we perform field redefinitions $\boldsymbol{P}_a^{(\dagger)} \to \boldsymbol{P}_a^{(\dagger)} \exp(\mp i m_\pi t)$ and $\bar{\boldsymbol{P}}_a^{(\dagger)} \to \bar{\boldsymbol{P}}_a^{(\dagger)} \exp(\mp i m_\pi t)$. Those Lagrangian terms still involving powers of the phase factor $\exp(i m_\pi t)$ are dropped. The result reads

$$\begin{aligned}\mathscr{L}_{\mathrm{HM},\cancel{m_\pi}} = {}& \boldsymbol{P}_a^\dagger\left[i\partial_0 - \delta\right]\boldsymbol{P}_a + P_a^\dagger\left[i\partial_0\right]P_a + \text{c.c.} + \hat{\pi}_i^\dagger\left[i\partial_0 + \frac{\boldsymbol{\nabla}^2}{2m_\pi} + \frac{(i\partial_0)^2}{2m_\pi}\right]\hat{\pi}_i \\ & + \frac{g_{\mathrm{HH}\chi\mathrm{PT}}}{f_\pi\sqrt{2m_\pi}}\left[\boldsymbol{P}_a^\dagger\cdot\left(\boldsymbol{\nabla}\hat{M}\right)_{ba} P_b + \text{H.c.}\right] + \text{c.c.}\end{aligned} \tag{3.16}$$

The rest masses of the pions and pseudoscalar D mesons are now set to zero and the vector D mesons possess the small rest mass $\delta = \Delta_H - m_\pi \ll \Delta_H, m_\pi$. In Eq. (3.16), the hats in $\hat{M}_{ba}$ and $\hat{\pi}_i$ are to be applied to each $\mathrm{SU(2)}_{\text{flavor}}$ component.

Note that the pion kinetic term in Eq. (3.16) involves a piece quadratic in the energy. It summarizes relativistic corrections to the pion propagators. We show in Appendix D.3, that in the region of the $X(3872)$, this piece is suppressed by $\delta/(m_\pi) \sim \chi_2$ compared to the linear term. Moreover, in Sec. 3.3.4 we show that the overall impact of dynamical pions on the $X(3872)$ pole is further suppressed by $\mu_{D\pi}/\mu_* \sim \chi_3$. Thus, the quadratic piece is at most of N^{2}LO size in the $\chi_2 \sim \chi_3$ counting of Eq. (3.2) and will be neglected in this thesis.

Rest masses

Up to this point, neutral and charged mesons possess equal rest masses. However, in order to describe physics at energies $E \sim \delta$ correctly, we need to break $\mathrm{SU(2)}_{\text{flavor}}$ symmetry explicitly by adding the physical mass splittings

$$\Delta m_{\mathrm{c},D^*} \equiv m_{D^{+*}} - m_{D^{0*}} = 3.41(7)\,\mathrm{MeV}, \tag{3.17a}$$

$$\Delta m_{\mathrm{c},D} \equiv m_{D^+} - m_{D^0} = 4.75(8)\,\mathrm{MeV}, \tag{3.17b}$$

$$\Delta m_{\mathrm{c},\pi} \equiv m_{\pi^+} - m_{\pi^0} = 4.5936(5)\,\mathrm{MeV}, \tag{3.17c}$$

to the rest masses of the charged mesons [36]. Thus, we introduce the terms

$$\mathscr{L}_{\Delta m_\mathrm{c}} = -\boldsymbol{D}^{+\dagger}\,\Delta m_{\mathrm{c},D^*}\,\boldsymbol{D}^+ - D^{+\dagger}\,\Delta m_{\mathrm{c},D}\,D^+ - \hat{\pi}^{+\dagger}\,\Delta m_{\mathrm{c},\pi}\,\hat{\pi}^+ + \text{c.c.} \tag{3.18}$$

to the Lagrangian. Moreover, the D mesons' kinetic energy terms, scaling like $1/m_Q$ and thus formerly subleading, have to be restored at small energies [102].

The result of the above modifications,

$$
\begin{aligned}
\mathscr{L}_{\mathrm{XEFT}+,D\pi} = {} & \boldsymbol{D}^{0\dagger}\left[i\partial_0 + \frac{\boldsymbol{\nabla}^2}{2m_{D^{0*}}} - \delta\right]\boldsymbol{D}^0 + \boldsymbol{D}^{+\dagger}\left[i\partial_0 + \frac{\boldsymbol{\nabla}^2}{2m_{D^{+*}}} - (\delta + \Delta m_{\mathrm{c},D^*})\right]\boldsymbol{D}^+ + \mathrm{c.c.}\\
& + D^{0\dagger}\left[i\partial_0 + \frac{\boldsymbol{\nabla}^2}{2m_{D^0}}\right]D^0 + D^{+\dagger}\left[i\partial_0 + \frac{\boldsymbol{\nabla}^2}{2m_{D^+}} - \Delta m_{\mathrm{c},D}\right]D^+ + \mathrm{c.c.}\\
& + \pi^{0\dagger}\left[i\partial_0 + \frac{\boldsymbol{\nabla}^2}{2m_{\pi^0}}\right]\pi^0\\
& + \pi^{+\dagger}\left[i\partial_0 + \frac{\boldsymbol{\nabla}^2}{2m_{\pi^+}} - \Delta m_{\mathrm{c},\pi}\right]\pi^+ + \mathrm{c.c.}\\
& + \frac{g_{\mathrm{HH}\chi\mathrm{PT}}}{\sqrt{2}f_\pi\sqrt{2m_\pi}}\Big[\boldsymbol{D}^{0\dagger}\cdot(\boldsymbol{\nabla}\pi^0)D^0 - \sqrt{2}\boldsymbol{D}^{0\dagger}\cdot(\boldsymbol{\nabla}\pi^-)D^+ + \mathrm{H.c.}\\
& \qquad -\sqrt{2}\boldsymbol{D}^{+\dagger}\cdot(\boldsymbol{\nabla}\pi^+)D^0 - \boldsymbol{D}^{+\dagger}\cdot(\boldsymbol{\nabla}\pi^0)D^+ + \mathrm{H.c.}\Big] + \mathrm{c.c.}\,, \qquad (3.19)
\end{aligned}
$$

recovers the $D\pi$ sector of the well-known XEFT Lagrangian of Fleming *et al.* [102] and generalizes it to charged mesons. For convenience, we dropped the hats of the pion creation/annihilation fields in Eq. (3.19).

Even though neutral and charged particles now have different masses, the $D^* \longleftrightarrow D\pi$ vertices exhibit $\mathrm{SU}(2)_{\mathrm{flavor}}$ symmetry as desired. As a consequence, charged pion couplings exhibit an additional factor $\sqrt{2}$ compared to those with neutral pions. This detail will be important when we relate the widths Γ_{0*} and $\Gamma_{\mathrm{c}*}$ later on.

Note that in addition to the $D\pi$ couplings of Eq. (3.19), original XEFT also involves direct couplings between DD^*-type states [102]. We will show in this thesis that the vector mesons can be interpreted as $D\pi$ p-wave resonances. Their quantum fields could in principle be integrated out, a procedure, which turns DD^*-DD^* couplings into $DD\pi$-$DD\pi$ three-body forces. Indeed, a three-body force will be needed to produce the $X(3872)$ pole. It will be introduced at the end of the derivation.

Power counting and limitations of XEFT

In the power counting of XEFT, the $D^0\pi^0 \longleftrightarrow D^{0*}$ ($\bar{D}^0\pi^0 \longleftrightarrow \bar{D}^{0*}$) energy gap $\delta \approx 7\,\mathrm{MeV}$ is counted[5] as Q^2, where $Q \sim (2m_\pi\delta) \approx 42\,\mathrm{MeV}$ must be compared with the high scale m_π [102]. That yields an XEFT expansion parameter $Q/m_\pi \sim 0.3$. The binding energy $\delta_X < 0.2\,\mathrm{MeV}$ of the $X(3872)$ is also counted like Q. At the time of publication of XEFT, the experimental value for the binding energy, $(\delta_X)_{[102]} = (0.6 \pm 0.6)\,\mathrm{MeV}$, was already smaller than δ, and is has shrunk even further until today. Consequently, in this thesis we will explicitly distinguish between the two scales in the $D^0\bar{D}^0\pi^0$ three-body sector, where δ_X occurs. That yields the two expansion parameters $(\delta_X/\delta)^{1/2} \sim (\delta_X/\nu)^{1/2}$ with $\delta \sim \nu$ in Eq. (3.2).

As its first application, Fleming *et al.* used XEFT in 2007 to calculate the partial decay width $\Gamma[X(3872) \to D^0\bar{D}^0\pi^0]$, i.e., the imaginary part of the $X(3872)$ pole. The LO result was in line with the $D^0\bar{D}^{0*}$ + c.c. zero-range prediction by Voloshin from 2003 [39], justifying the perturbative treatment of dynamical pions at NLO. A major problem of XEFT, however, is its limitation to NLO accuracy. It results from the fact that counterterms in the XEFT Lagrangian can cancel ultraviolet divergences in NLO calculations only if results are expanded in the small mass ratio $(m_\pi/m_D)^{1/2} \sim 0.3 \sim Q/m_\pi$ [45]. Alternatively, one would need to introduce further counterterms leading to less predictive power. Moreover, a preferred frame has to be chosen in each XEFT calculation. As pointed out by Braaten in Ref. [45], the root of these problem lies in the formulation of XEFT as a nonrelativistic theory violating Galilean invariance. The steps needed to restore this symmetry will be performed in the next section.

---

[5] Masses m_{kin} in nonrelativistic kinetic energies $Q^2/(2m_{\mathrm{kin}})$ are not counted since they factor out.

The renormalization scheme of XEFT make it difficult to incorporate the electromagnetic decay width $\Gamma[D^{0*} \to D^0\gamma]$, which has a branching ratio of approximately one third; see Table 3.2. A correct description of the total D^{0*} ($\bar{D}^{0*}$) width

$$\Gamma_{0*} \equiv \Gamma[D^{0*} \to D^0\pi^0] + \Gamma[D^{0*} \to D^0\gamma] \equiv \Gamma_{D^0\pi^0} + \Gamma_{D^0\gamma}\,, \tag{3.20}$$

however, is especially important for the line shape in $X(3872) \to D^0\bar{D}^0\pi^0$ since the $X(3872)$ lies directly at the $D^0\bar{D}^{0*}$ + c.c. threshold. As a solution to the problem, Braaten suggesting the novel "complex on-shell renormalization scheme" [45]. It fixes the complex mass of the vector mesons already at LO, including the full width Γ_{0*}. We will adopt this scheme by expanding the full D^{0*} ($\bar{D}^{0*}$) propagator at the physical pole. The partial width $\Gamma_{D^0\gamma}$ will enter effectively via imaginary $D^0\pi^0$ ($\bar{D}^0\pi^0$) interactions; see below.

3.1.3 Galilean-invariant XEFT

In Ref. [45], Braaten showed how to modify XEFT for neutral mesons in order to implement explicit Galilean invariance. In the following, we will conduct his steps for neutral and charged mesons; see step (c) in Fig. 3.2.

Conservation of kinetic mass

Galilean invariance requires the conservation of "kinetic mass" m_{kin} appearing in the nonrelativistic dispersion relation $E = m_{\text{rest}} + \boldsymbol{k}^2/(2m_{\text{kin}})$, as opposed to the "rest mass" m_{rest}. I.e., a two-body state formed by point-like particles with kinetic masses $m_{\text{kin}\,1}$ and $m_{\text{kin}\,2}$ must have a total kinetic mass $m_{\text{kin}\,12} = m_{\text{kin}\,1} + m_{\text{kin}\,2}$.[6]

In the system at hand, we have to set the kinematic mass of the neutral vector meson D^{0*} ($\bar{D}^{0*}$) to

$$M_{D\pi} \equiv m_D + m_\pi\,. \tag{3.21}$$

The systematic error induced by this modification is of size $\delta/M_{D\pi} \approx 0.35\,\%$ since

$$\frac{\boldsymbol{\nabla}^2}{2m_{D^{0*}}} = \frac{\boldsymbol{\nabla}^2}{2M_{D\pi}}\left(1 - \frac{\delta}{M_{D\pi}}\right). \tag{3.22}$$

This error is comparable to three orders in $\chi_2 \sim \chi_3$ and thus negligible up to N^{2}LO. The necessity of kinetic mass conservation will become immediately visible in Sec. 3.2.1, where divergences from the D^{0*} ($\bar{D}^{0*}$) self-energy can only be cured if $m_{\text{kin}} = M_{D\pi}$. Since reduced masses always result from kinetic masses, we define the $D\pi$ two-body reduced mass and the DD^* three-body reduced mass to be

$$\mu_{D\pi} \equiv m_\pi m_D/(m_\pi + m_D) = 125.8667(5)\,\text{MeV} \tag{3.23a}$$

$$\mu_* \equiv m_D M_{D\pi}/(m_D + M_{D\pi}) = 964.98(2)\,\text{MeV}\,. \tag{3.23b}$$

For two reasons we neglect direct couplings $D^{0*} \to D^+\pi^-$ ($\bar{D}^{0*} \to D^-\pi^+$) in this thesis. Firstly, this channel does not contribute to the D^{0*} ($\bar{D}^{0*}$) width (let alone the $X(3872)$ width) because it is purely virtual in the pole region. Secondly, charged pion exchanges in the $X(3872)$ are suppressed by at least a factor $(\mu_{D\pi}/\mu_*)^2 \approx 0.01$ (∼N^{2}LO). The charged vector meson D^{+*} (D^{-*}), however, does receive partial widths from both combinations $D^0\pi^+$ and $D^+\pi^0$ ($D^0\pi^-$ and $D^-\pi^0$). Galilean invariance then demands that the total kinetic masses of both combinations be equal. One achieves that by neglecting the tiny difference $\Delta m_{c,D} - \Delta m_{c,\pi} = 0.16(8)\,\text{MeV}$ between the mass shifts in Eqs. (3.17b)-(3.17c). In order to keep the systematic error small, we replace $\Delta m_{c,D} \to \Delta m_{c,\pi}$ in the D^+ (D^-) kinetic mass (systematic error 0.009 %, ∼N^{4}LO), while keeping the π^+ (π^-) untouched. The kinetic mass of the D^{+*} (D^{-*}) is then replaced by $m_{D^0} + m_{\pi^+} = M_{D\pi} + \Delta m_{c,\pi}$ (systematic error 0.3 %, ∼N^{3}LO). Table 3.1 summarizes all mass modifications by contrasting the experimental masses with the chosen rest and kinetic masses.

---

[6] The total rest mass of a bound (resonance) state, in contrast, lies below (above) the sum of the components' rest masses.

Table 3.1.: Experimental masses from Ref. [36] and rest/kinetic masses used in calculations. Experimental values of δ_X, δ, and ν are given in Eqs. (1.1), (3.3a), and (3.3b).

Particle	Mass (exp.)	Rest mass (calc.)	Kinetic mass (calc.)
π^0	$m_{\pi^0} \equiv 134.9770(5)\,\text{MeV}$	0	$m_\pi \equiv m_{\pi^0}$ (exp.)
D^0 $(\bar{D}^0)$	$m_{D^0} \equiv 1864.83(5)\,\text{MeV}$	0	$m_D \equiv m_{D^0}$ (exp.)
D^{0*} $(\bar{D}^{0*})$	$m_{D^{0*}} \equiv 2006.85(5)\,\text{MeV}$	$\delta \equiv m_{D^{0*}} - m_{\pi^0} - m_{D^0}$	$M_{D\pi} \equiv m_D + m_\pi$
π^+ (π^-)	$m_{\pi^+} \equiv 139.57061(24)\,\text{MeV}$	$\Delta m_{\text{c},\pi} \equiv m_{\pi^+} - m_{\pi^0}$	m_{π^+} (exp.)
D^+ (D^-)	$m_{D^+} \equiv 1869.58(9)\,\text{MeV}$	$\Delta m_{\text{c},D} \equiv m_{D^+} - m_{D^0}$	$m_D + \Delta m_{\text{c},\pi}$
D^{+*} (D^{-*})	$m_{D^{+*}} \equiv 2010.26(5)\,\text{MeV}$	$\delta + \Delta m_{\text{c},D^*} \equiv \delta + (m_{D^{+*}} - m_{D^{0*}})$	$M_{D\pi} + \Delta m_{\text{c},\pi}$
$X(3872)$	$m_X \equiv 3871.69(17)\,\text{MeV}$	$\delta - \delta_X$ (see results)	–

Frame independence

The $D^* \longleftrightarrow D\pi$ vertices exhibit spatial derivatives for the pion field, resulting from the axial vector in Eq. (3.11). Applied to plain wave states, they produce powers factors of the pion momentum $\boldsymbol{k}_\pi$. This quantity, however, is not conserved under Galilean boosts of the total $D\pi$ two-body system. To ensure Galilean invariance, the vertices must instead produce factors of the $D\pi$ relative momentum

$$\boldsymbol{k} \equiv \frac{1}{m_D + m_\pi}(m_D \boldsymbol{k}_\pi - m_\pi \boldsymbol{k}_D) = \xi \boldsymbol{k}_\pi - (1-\xi)\boldsymbol{k}_D \tag{3.24}$$

with mass ratio

$$\xi \equiv \frac{m_D}{m_D + m_\pi} \approx 0.93\,. \tag{3.25}$$

Thus, we replace all vertex terms of type $\boldsymbol{D}^\dagger \cdot (\boldsymbol{\nabla}\pi) D + \text{H.c.}$ by expressions $\boldsymbol{D}^\dagger \cdot (\pi \overleftrightarrow{\boldsymbol{\nabla}} D) + \text{H.c.}$ The Galilean-invariant derivative is generically defined as

$$\overleftrightarrow{\boldsymbol{\nabla}} \equiv \frac{1}{\overleftarrow{m_\text{kin}} + \overrightarrow{m_\text{kin}}}\left(\overrightarrow{m_\text{kin}}\,\overleftarrow{\boldsymbol{\nabla}} - \overleftarrow{m_\text{kin}}\,\overrightarrow{\boldsymbol{\nabla}}\right). \tag{3.26}$$

It involves spatial derivatives $\overleftarrow{\boldsymbol{\nabla}}$ $(\overrightarrow{\boldsymbol{\nabla}})$ and kinetic mass operators $\overleftarrow{m_\text{kin}}$ $(\overrightarrow{m_\text{kin}})$ acting to the left (right). These replacements recover terms of order $1/m_Q$, which are subleading in the power counting of HHχPT.

3.1.4 $D^0\bar{D}^0\pi^0$ EFT

With the above modifications, the Lagrangian of Eq. (3.19) is now explicitly Galilean-invariant. However, it does not represent the most general Lagrangian compliant with the symmetry. In the following we implement higher-order corrections by reformulating the vector meson fields as p-wave resonance auxiliary fields; see step (d) in Fig. 3.2.

From now on we focus explicitly on the neutral sector $D^0\bar{D}^0\pi^0$ as done in Refs. [45, 93, 102]. It is the only three-body state lying below the $X(3872)$ and thus directly contributing to the $X(3872)$ width. Virtual contributions from the charged channels will be discussed in Sec. 3.3.4.

Higher-order terms

Higher-order corrections could in principle be implemented via vertices with multiples $\overleftrightarrow{\boldsymbol{\nabla}}^{2n} \sim (\boldsymbol{k}^2)^n$ $(n \geq 1)$ of the Galilean derivative. However, it is more convenient to introduce them in the vector meson kinetic term; see for example [103]. Due to the above modifications, the kinetic term now involves the derivative combination

$$i\partial_{\rm cm} \equiv i\partial_0 + \frac{\boldsymbol{\nabla}^2}{2\overrightarrow{m_{\rm kin}}} \tag{3.27}$$

with $\overrightarrow{m_{\rm kin}} \simeq M_{D\pi}$. We call this operator “center-of-mass derivative” since its eigenvalues are the center-of-mass-energies

$$E_{\rm cm} \equiv p^0 - \frac{\boldsymbol{p}^2}{2M_{D\pi}} \tag{3.28}$$

of a constituent $D^0\pi^0$ pair with total energy p^0 and total momentum $\boldsymbol{p} = \boldsymbol{k}_\pi + \boldsymbol{k}_D$. In the on-shell case, $E_{\rm cm} = \boldsymbol{k}^2/(2\mu_{\pi D})$ (+ constituent rest masses), where $\boldsymbol{k}$ is the relative momentum of Eq. (3.24). Thus, a Lagrangian with higher powers in $i\partial_{\rm cm}$ is on-shell equivalent to a Lagrangian with higher powers in $\overleftrightarrow{\boldsymbol{\nabla}}^2$ [104]. Consequently, the vector meson kinetic term is now generalized to the series

$$\boldsymbol{D}^{0\dagger}\left[\Delta_0 + \Delta_1 i\partial_{\rm cm} + \sum_{n\geq 2}\Delta_n\,(i\partial_{\rm cm})^n\right]\boldsymbol{D}^0 + \text{c.c.} \tag{3.29}$$

with sign $\Delta_1 = \pm 1$. The coefficients $\Delta_n \in \mathbb{R}$ $(n \geq 0)$ with mass units MeV^{1-n} will reproduce the effective range expansion (ERE) of the $D^0\pi^0$ $(\bar{D}^0\pi^0)$ scattering matrix; see Sec. 3.2.

Note that the sign Δ_1 cannot be changed by field redefinitions and has to be determined in the renormalization procedure. If $\Delta_1 = -1$, the vector meson fields would, in the absence of interactions, create/annihilate states of negative norm. In order not to loose the connection to GI-XEFT, the two-body power counting we develop in Sec. 3.2 should yield $\Delta_0 \approx -\delta$ and $\Delta_1 = +1$. Moreover, it should state that $\boldsymbol{D}^{0\,\dagger}[i\partial_{\rm cm} - \delta]\boldsymbol{D}^0$ is the LO kinetic term and that higher-order terms $\propto \Delta_n$ are strongly suppressed. All these relations will indeed be fulfilled in the $\delta/(m_\pi/2)$ power counting of Sec. 3.2.

Extension to radiative decays

The D^{0*} $(\bar{D}^{0*})$ does not only decay to $D^0\pi^0$, but also radiatively to $D^0\gamma$ $(\bar{D}^0\gamma)$. The respective branching ratio $\mathscr{B}_{D^0\gamma} \equiv 35.3(9)\,\%$ is large; see Table 3.2. Thus, the partial decay width $\Gamma_{D^0\gamma} = 18.9(9)\,\text{keV}$ is of LO if one wants to develop a theory for the $X(3872)$ pole position near the $D^0\bar{D}^{0*}$ threshold. At this point, it might seem problematic that radiative decays involve relative momenta $\sim 137\,\text{MeV} \sim m_\pi$ outside the order of our EFT [36]. In fact, one can implement effects of the “deep” $D^0\gamma$ $(\bar{D}^0\gamma)$ channel effectively by complexifying the coefficients $\Delta_n \to \Delta_n + iW_n$ in Eq (3.29) [94]. As shown in Fig. 3.4, the coefficients W_n represent imaginary D^{0*} $(\bar{D}^{0*})$ self-interactions, which result from integrating out the deep state. At LO in the $\delta/(m_\pi/2)$ power counting, the radiative decay width is given by $W_0 \approx \Gamma_{D^0\gamma}/2$. Thus, the above substitutions implement the radiative decay width at Lagrangian level.

Instead of $\Gamma_{D^0\gamma}$, Braaten directly introduced the full D^{0*} width Γ_{0*} to the Lagrangian [45]. This choice makes it particularly easy to identify the LO D^{0*} propagator $\sim [E_{\rm cm} - \delta + i\Gamma_{0*}/2]^{-1}$ in the vicinity of the $X(3872)$. However, it might convey the impression that the pionic part of $\Gamma_{0*} = \Gamma_{D^0\pi^0} + \Gamma_{D^0\gamma}$ results from imaginary couplings just like the radiative part. In fact, $\Gamma_{D^0\pi^0}$ follows from $D^0\pi^0$ self-energy bubbles in the full D^{0*} propagator. We note that our scheme indeed reproduces the LO propagator of Braaten, but based on the $\delta/(m_\pi/2)$ power counting.

Table 3.2.: Experimental widths and branching ratios from Ref. [36] and widths used in calculations. The D^{0*} ($\bar{D}^{0*}$) width Γ_{0*} is predicted in Sec. 3.2.2. The $X(3872)$ width $\Gamma_X(\delta_X)$ depends on the binding energy δ_X of the $X(3872)$; see Sec. 3.3.5.

Particle	Width (exp.)	Width (calc.)	Branching ratios (exp.)
D^{0*} ($\bar{D}^{0*}$)	$\Gamma[D^{0*}] < 2.1\,\text{MeV}$	$\Gamma_{0*} = (53.6 \pm 1.0)\,\text{keV}$ (our prediction)	$\mathscr{B}_{D^0\pi^0} \equiv 64.7(9)\,\%$ $\mathscr{B}_{D^0\gamma} \equiv 35.3(9)\,\%$
D^{+*} (D^{-*})	$\Gamma[D^{+*}] = (83.4 \pm 1.8)\,\text{keV}$	$\Gamma_{c*} \equiv \Gamma[D^{+*}]$ (exp.)	$\mathscr{B}_{D^0\pi^+} \equiv 67.7(5)\,\%$ $\mathscr{B}_{D^+\pi^0} \equiv 30.7(5)\,\%$ $\mathscr{B}_{D^+\gamma} \equiv 1.6(4)\,\%$
$X(3872)$	$\Gamma[X(3872)] < 1.2\,\text{MeV}$	$\Gamma_X = \Gamma_X(\delta_X)$ (see results)	–

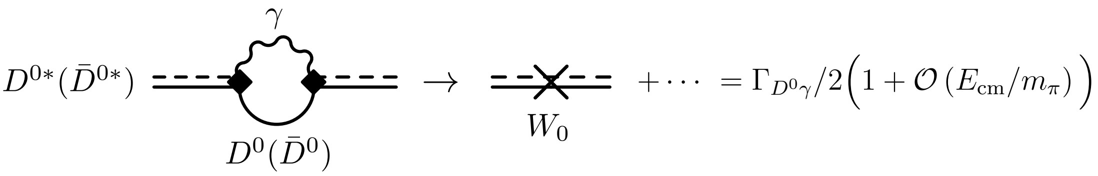

Figure 3.4.: Integrating out the deep-lying $D^0\gamma$ state. The induced imaginary D^{0*} self-interactions iW_n ($n \geq 0$) effectively describe the partial decay width $\Gamma_{D^0\gamma} \equiv \Gamma[D^{0*} \to D^0\gamma]$ with its large branching ratio $\mathscr{B}_{D^0\gamma} = 35.3(9)\,\%$. Due to Galilean invariance, higher-order terms involve powers of $E_{\text{cm}} \sim \delta$, as defined in Eq. (3.28), divided by the large scale m_π. The same picture can be drawn for the $\bar{D}^{0*} \to \bar{D}^0\gamma$ channel. Radiative decays of charged $D^{\pm*}$ mesons are neglected due to the small branching ratio $\mathscr{B}_{D^+\gamma} = 1.6(4)\,\%$; see Table 3.2.

Lagrangian

For clarity, the Lagrangian used in this thesis,

$$\mathscr{L} \equiv \mathscr{L}_{\text{kin}} + \mathscr{L}_{D\pi} + \mathscr{L}_{DD\pi}\,, \tag{3.30}$$

is divided into one-, two- and three-body parts. The kinetic part

$$\mathscr{L}_{\text{kin}} = D^{0\dagger}\left[i\partial_0 + \frac{\boldsymbol{\nabla}^2}{2m_D}\right]D^0 + \text{c.c.} + \pi^{0\dagger}\left[i\partial_0 + \frac{\boldsymbol{\nabla}^2}{2m_\pi}\right]\pi^0 \tag{3.31}$$

involves only pseudoscalar mesons D^0 ($\bar{D}^0$) and π^0 with nonrelativistic propagators

$$iG_a(k^0, \boldsymbol{k}) = i\left[k^0 + i\epsilon - \frac{\boldsymbol{k}^2}{2m_a}\right]^{-1} \qquad (a \in \{D^0, \pi^0\})\,. \tag{3.32}$$

In Feynman diagrams, they are represented by solid and dashed lines, respectively; see Fig. 3.5.

In contrast, the vector meson fields $\boldsymbol{D}^0$ and $\bar{\boldsymbol{D}}^0$ represent two-body auxiliary fields, similar to the one used in Ref. [85] for the p-wave-type neutron-alpha resonance. Thus, they enter the two-body part of the Lagrangian,

$$\begin{aligned}\mathscr{L}_{D\pi} = \boldsymbol{D}^{0\dagger}&\left[(\Delta_0 + iW_0) + (1 + iW_1)\,i\partial_{\text{cm}} + \sum_{n\geq 2}(\Delta_n + iW_n)(i\partial_{\text{cm}})^n\right]\boldsymbol{D}^0 + \text{c.c.}\\ &+ g\left[\boldsymbol{D}^{0\dagger}\cdot\left(\pi^0\overleftrightarrow{\boldsymbol{\nabla}}D^0\right) + \text{H.c.}\right] + \text{c.c.}\,.\end{aligned} \tag{3.33}$$

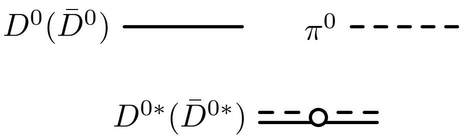

Figure 3.5.: The propagators of the D^0 ($\bar{D}^0$) and π^0 mesons are depicted by solid and dashed lines, respectively. The vector mesons D^{0*} ($\bar{D}^{0*}$) represent $D^0\pi^0$ ($\bar{D}^0\pi^0$) two-body states and are consequently depicted by solid-dashed double lines. The empty circle tells that the propagator is "bare", i.e., it does not contain $D^0\pi^0$ ($\bar{D}^0\pi^0$) self-energy bubbles yet.

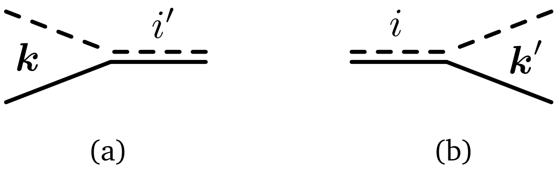

Figure 3.6.: (a) The $D^0\pi^0 \to D^{0*}$ ($\bar{D}^0\pi^0 \to \bar{D}^{0*}$) vertex has the Feynman rule $-g\,k_{i'}$, where $\boldsymbol{k}$ and $i' \in \{1, 2, 3\}$ denote the relative incoming momentum and vector meson polarization, respectively. (b) The Feynman rule for the time-reversed process reads $+g\,k'_i$.

In Appendix D.1 we show that $\boldsymbol{D}^0$ ($\bar{\boldsymbol{D}}^0$) could in principle be eliminated using the equation of motion.[7] That corresponds to performing the Gaussian path integral, i.e., a Hubbard-Stratonovich transformation. However, for our purposes the auxiliary field formalism is more convenient. It allows us to treat the $D^0\bar{D}^0\pi^0$ three-body system as an effective $D^0\bar{D}^{0*}$ + c.c. two-body problem.

The first row in Eq. (3.33) defines the bare D^{0*} ($\bar{D}^{0*}$) propagator

$$i\,G_*^{(\mathrm{b})}(E_{\mathrm{cm}}) = i\left[(\Delta_0 + iW_0) + (1 + iW_1)(E_{\mathrm{cm}} + i\epsilon) + \sum_{n\geq 2}(\Delta_n + iW_n)(E_{\mathrm{cm}} + i\epsilon)^n\right]^{-1}, \tag{3.34}$$

which is represented by a solid-dashed double line with empty circle; see Fig. 3.5.[8] The $D^{0*} \longleftrightarrow D^0\pi^0$ ($\bar{D}^{0*} \longleftrightarrow \bar{D}^0\pi^0$) transition vertex term in the second row of Eq. (3.33) is proportional to the overall coupling constant

$$g \equiv \frac{g_{\mathrm{HH}\chi\mathrm{PT}}}{\sqrt{2}\,f_\pi\sqrt{2m_\pi}}, \tag{3.35}$$

which has units $\mathrm{MeV}^{-3/2}$. Note that g must not be confused with the same-named one used by Baru *et al.* [46]. The two are connected via $g \equiv g_{\mathrm{Baru}}(2\pi)^{3/2}$ since the momentum state normalization $\langle \boldsymbol{p}_1\,|\,\boldsymbol{p}_2\rangle = \delta^{(3)}(\boldsymbol{p}_1 - \boldsymbol{p}_2)$ in Ref. [46] lacks a factor $(2\pi)^3$. Due to the Galilean-invariant derivative, the transition vertices involve the incoming/outgoing relative momentum of $D^0\pi^0$ ($\bar{D}^0\pi^0$); see caption of Fig. 3.6.

As the last step in our derivation, we equip our theory with a three-body force C_0, depicted by an empty square in Fig. 3.7. Its vertex is defined by the Lagrangian part

$$\mathscr{L}_{DD\pi} = -C_0\,\frac{1}{2}\left[D^0\bar{\boldsymbol{D}}^0 + \bar{D}^0\boldsymbol{D}^0\right]^\dagger \cdot \left[D^0\bar{\boldsymbol{D}}^0 + \bar{D}^0\boldsymbol{D}^0\right] + \cdots, \tag{3.36}$$

which connects states $(D^0\bar{D}^{0*} + \bar{D}^0D^{0*})/\sqrt{2}$ with positive charge conjugation $C = +$ in relative s-waves. This specific choice respects the quantum numbers $J^{PC} = 1^{++}$ of the $X(3872)$. Later, C_0 will renormalize the three-body amplitude by generating the $X(3872)$ pole near the $D^0\bar{D}^{0*}$ + c.c. threshold.

---

[7] In doing so, one recovers $D^0\pi^0$ contact terms given by the second row of Eq. (2.4).

[8] In Feynman diagrams, vector meson propagators have to be multiplied by the polarization-conserving factor $\delta^{ii'}$, which we omit in the following.

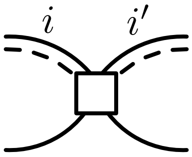

Figure 3.7.: The vertex $-iC_0\delta^{ii'}$, depicted by an empty square, connects $(D^0\bar{D}^{0*}+\bar{D}^0D^{0*})/\sqrt{2}$ combinations in a relative s-wave.

Let us note that the vertex structure of C_0 in Eq. (3.36) coincides with the one used in XEFT [102]. At LO, XEFT is a DD^* zero-range theory with contact force C_0 and no explicit pions. In fact, our LO three-body amplitude will look very similar to the one of LO-XEFT. The important difference, however, is that the vector mesons' rest mass will contain the constant width term $-i\Gamma_{0*}/2$. A large part of the width results from pion interactions *within* the vector meson propagators. Thus, as opposed to XEFT, we do include pions already at LO.

Another conceptual difference between $D^0\bar{D}^0\pi^0$ EFT and XEFT lies in the treatment of higher-order terms summarized into the ellipses of Eq. (3.36). In XEFT, such terms are included in order to estimate NLO corrections from the unknown DD^* ERE coefficients. In order to gain more predictive power, we include higher-order three-body terms only if needed to eliminate divergences from higher-order $D\pi$ two-body interactions. In fact, it turns out that C_0 is sufficient to renormalize the theory up to NLO. Higher-order three-body forces will thus be neglected in this work.

3.2 Two-body system: the D^{0*} resonance

Due to the extreme proximity of the $X(3872)$ to the $D^0\bar{D}^{0*}+$c.c. threshold, the width and line shape of the $X(3872)$ crucially depend on the chosen vector meson propagator. Consequently, in this section, we identify the leading D^{0*} ($\bar{D}^{0*}$) propagator in the kinematic region of the $X(3872)$.

Given the EFT Lagrangian of Eq. (3.30), we implement the D^{0*} as a p-wave resonance in $D^0\pi^0$ scattering. Due to charge conjugation symmetry of the $X(3872)$, all steps in this section equally apply to the $\bar{D}^{0*}$ resonance in $\bar{D}^0\pi^0$ scattering. After recovering the p-wave ERE from (real) interactions in the Lagrangian, we analyze its coefficients in terms of characteristic momentum scales. This analysis lays the ground for the $D^0\pi^0$ power counting with its expansion parameter $\delta/(m_\pi/2)$, which gives a natural explanation for the narrowness of the D^{0*} resonance. The scheme is then extended to complex D^{0*} self-interactions capturing effects of the deep channel $D^0\gamma$. At the end of the section, we derive an appropriate expansion for the D^{0*} propagator in the vicinity of the $X(3872)$.

3.2.1 Self-energy and effective range expansion

The full D^{0*} propagator can be obtained by dressing the bare one in Eq. (3.34) with self-energy bubbles $-i\Sigma_*(E_{\text{cm}})$ to all orders. The corresponding Dyson series is depicted in Fig. 3.8. Due to Galilean invariance, each ingredient depends only on the D^{0*} center-of-mass energy E_{cm} as defined in Eq. (3.28). Let us for the moment neglect all imaginary D^{0*} self-interactions W_n in Eq. (3.34). The resummation procedure then yields the full propagator[9]

$$iG_*^{(\text{f})}(E_{\text{cm}}) = i\left[G_*^{(\text{b})\,-1}(E_{\text{cm}})-\Sigma_*(E_{\text{cm}})\right]^{-1} \tag{3.37a}$$

$$= i\left[\Delta_0+(E_{\text{cm}}+i\epsilon)-\Sigma_*(E_{\text{cm}})+\sum_{n\geq 2}\Delta_n\,(E_{\text{cm}}+i\epsilon)^n\right]^{-1}. \tag{3.37b}$$

---

[9] The superscripts "(f)" and "(b)" indicate full and bare propagators, respectively, throughout the thesis.

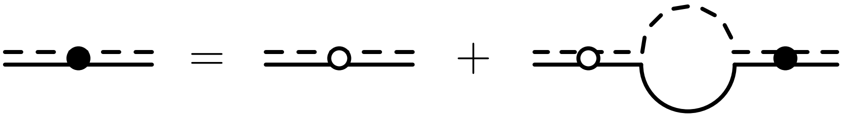

Figure 3.8.: The full D^{0*} propagator $iG_*^{(\mathrm{f})}(E_{\mathrm{cm}})$ is depicted by a solid-dashed double line with filled circle. It can be expressed as a Dyson series of the bare propagator $iG_*^{(\mathrm{b})}(E_{\mathrm{cm}})$ (with empty circle) and the $D^0\pi^0$ self-energy $-i\Sigma_*(E_{\mathrm{cm}})$.

An explicit expression for the self-energy can be obtained by applying the Feynman rules in the caption of Fig. 3.6 and integrating over the relative $D^0\pi^0$ momentum $\boldsymbol{l}$ and energy l^0 in the bubble.[10] We perform this calculation in Appendix D.2.

Note that the loop integral is divergent and has to be regularized. For example, one could use dimensional regularization and the Power Divergence Subtraction (PDS) scheme with mass scale Λ_{PDS} [19]. In this scheme, the integral's linear divergence in $d = 2$ dimensions is removed, which introduces a term $\propto \Lambda_{\mathrm{PDS}} E_{\mathrm{cm}}$ in the self-energy.[11] At this point one sees that Galilean invariance is needed for a consistent renormalization. Would we choose the D^{0*} kinetic mass different from $M_{D\pi}$, e.g., to be $m_{D^{0*}} > M_{D\pi}$, the bare propagator part in Eq. (3.37b) would not represent a series in E_{cm} anymore. The $\Lambda_{\mathrm{PDS}} E_{\mathrm{cm}}$ term of the self-energy could then not be eliminated. For further details, we refer to Appendix D.2.

For convenience, we use Minimal Subtraction (MS) instead of PDS for all practical calculations, which is obtained from PDS by taking the limit $\Lambda_{\mathrm{PDS}} \to 0$. This choice renders the scaling analysis below much more transparent since all Lagrangian parameters can be directly analyzed in terms of physical scales. In any case, observables do not dependent on the choice of renormalization scheme. In MS, the self-energy takes the form

$$\Sigma_*(E_{\mathrm{cm}}) = -g^2 \frac{\mu_{D\pi}}{6\pi} [-2\mu_{D\pi}(E_{\mathrm{cm}} + i\epsilon)]^{3/2} \tag{3.38a}$$

$$= g^2 \frac{\mu_{D\pi}}{6\pi} \left(-i\bar{k}^3\right). \tag{3.38b}$$

In Eq. (3.38b), we express the self-energy in terms of the on-shell relative momentum

$$\bar{k} \equiv i[-2\mu_{D\pi}(E_{\mathrm{cm}} + i\epsilon)]^{1/2}, \tag{3.39}$$

a form, which will be convenient for the following analysis. Note that the self-energy is purely imaginary for $E_{\mathrm{cm}} > 0 \Leftrightarrow \bar{k} > 0$. It will thus introduce the nonzero pionic partial width $\Gamma_{D^0\pi^0}$ to the D^{0*} pole; see Fig. 3.9.

In the auxiliary field formalism, the full $D^0\pi^0$ scattering amplitude it_* can be obtained by attaching external $D^0\pi^0$ legs to the full propagator as shown in Fig. 3.10. In doing so, we recover the ERE for p-wave scattering [79]

$$it_*(\boldsymbol{k}, \boldsymbol{k}'; E_{\mathrm{cm}}) = -g^2 \boldsymbol{k} \cdot \boldsymbol{k}'\, iG_*^{(\mathrm{f})}(E_{\mathrm{cm}}) \tag{3.40a}$$

$$= i\frac{6\pi}{\mu_{D\pi}} \boldsymbol{k} \cdot \boldsymbol{k}' \left[-a_*^{-1} + \frac{r_*}{2}\bar{k}^2 - i\bar{k}^3 + \sum_{n\geq 2} \mathscr{P}_*^{(2n)} \bar{k}^{2n} \right]^{-1}. \tag{3.40b}$$

---

[10] This choice of integration variables is convenient since it exploits the EFT's explicit Galilean invariance.

[11] A hard cutoff $\lambda \geq |\boldsymbol{l}|$ would lead to a similar term $\propto \lambda E_{\mathrm{cm}}$. In addition, one obtained a scale-less cubic term $\propto \lambda^3$.

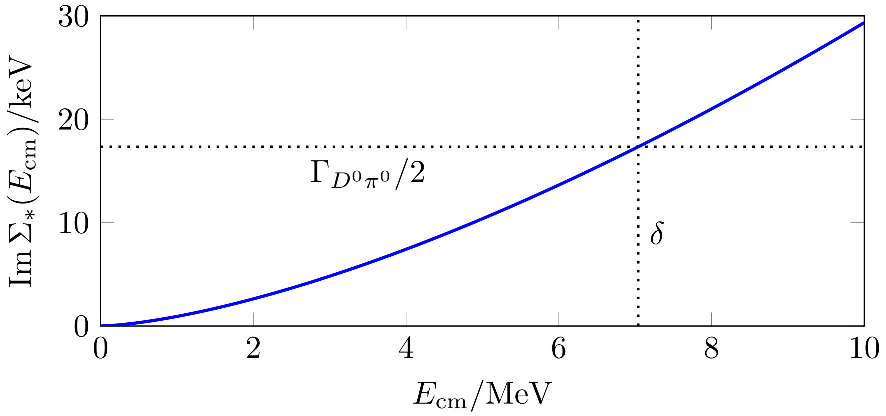

Figure 3.9.: Imaginary part of the self-energy $\Sigma_*(E_\mathrm{cm})$ as function of the center-of-mass energy E_cm. At resonance ($E_\mathrm{cm} = \delta$), it yields the pionic partial width $\Gamma_{D^0\pi^0}$; see Eq. (3.48b). Values for g^2 and $\Gamma_{D^0\pi^0}$ can be found in Eqs. (3.50a)-(3.50b).

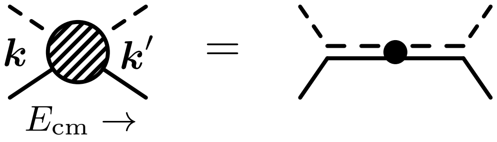

Figure 3.10.: The full $D^0\pi^0$ scattering amplitude $it_*(\boldsymbol{k}, \boldsymbol{k}'; E_\mathrm{cm})$ is given by the full D^{0*} propagator, attached with external $D^0\pi^0$ legs.

The p-wave unitary cut term $-i\bar{k}^3$ in Eq. (3.40b) is nothing but the rescaled self-energy. The scattering volume a_* (in MeV^{-3}), the p-wave effective range r_* (in MeV), and higher-order shape coefficients $\mathscr{P}_*^{(2n)}$ (in MeV^{3-2n}) can be matched to the Lagrangian parameters via

$$-a_*^{-1} = -\frac{6\pi}{\mu_{D\pi}}\frac{\Delta_0}{g^2}\,, \tag{3.41a}$$

$$\frac{r_*}{2} = -\frac{6\pi}{\mu_{D\pi}}\frac{1}{2\mu_{D\pi}g^2}\,, \tag{3.41b}$$

$$\mathscr{P}_*^{(2n)} = -\frac{6\pi}{\mu_{D\pi}}\frac{\Delta_n}{(2\mu_{D\pi})^n\, g^2} \quad (n \geq 2)\,. \tag{3.41c}$$

These ERE coefficients will be analyzed in terms of characteristic momentum scales in the following.

3.2.2 Scaling analysis at threshold

It is known from experiment that the D^{0*} resonance occurs at a $D^0\pi^0$ center-of-mass energy of $\delta = 7.04(3)\,\mathrm{MeV}$ [36]; see Fig. 3.1. This energy is much smaller than the already smallest meson mass $m_\pi \approx 135\,\mathrm{MeV}$. As a consequence, we decided to integrate out high energy modes $\sim m_\pi$ in the derivation of $D^0\bar{D}^0\pi^0$ EFT in Sec. 3.1. The energy scale separation $\delta/m_\pi \ll 1$ can be explained by an accidental fine-tuning in the underlying theory, which is QCD.

As usual, we express the scale separation in terms of momenta. The small relative $D^0\pi^0$ momentum K_lo required to see the resonance and the natural (high) scale K_hi are set by

$$K_\mathrm{lo} \equiv \sqrt{2\mu_{D\pi}\delta} \approx 42\,\mathrm{MeV}\,, \tag{3.42a}$$

$$K_\mathrm{hi} \equiv m_\pi \approx 135\,\mathrm{MeV}\,. \tag{3.42b}$$

Due to the fact that we use a nonrelativistic theory, the relativistic momentum $K_{\mathrm{lo}} = m_\pi$ represents also its breakdown point. Given $\mu_{D\pi} \approx m_\pi$, the scale separation can be expressed by the number

$$\frac{K_{\mathrm{lo}}}{K_{\mathrm{hi}}} \approx \sqrt{\frac{\delta}{m_\pi/2}} \sim 0.3\,, \tag{3.43}$$

which is not particularly small. Note, however, that the actual expansion parameter in the two-body system will be $\chi_2 = (K_{\mathrm{lo}}/K_{\mathrm{hi}})^2 \approx \delta/(m_\pi/2) \approx 0.1$, as proposed in Eq. (3.2). This will be a consequence of the ERE in Eq. (3.40b) being a series in $\bar{k}^2$. Thus, we expect quick convergence of the final D^{0*} propagator expansion. Below, we perform a scaling analysis for the leading resonance parameters [steps a)-e)].

a) Natural higher-order parameters

We may allocate to each ERE term and to the unitary cut a certain scaling behavior in K_{lo} and K_{hi}. Firstly, near the D^{0*} pole, the on-shell relative momentum $\bar{k} \sim K_{\mathrm{lo}}$ and thus $|-i\bar{k}^3| \sim K_{\mathrm{lo}}^3$. Secondly, due to the fine-tuning $\delta \ll m_\pi$, also some ERE coefficients will involve the unnaturally small scale K_{lo}. We assume that these parameters are either a_*, $r_*/2$, or both of them. Thirdly, we assume that each higher-order parameters $\mathscr{P}_*^{(2n)}$ scales with appropriate powers of the natural scale K_{hi}, i.e.,

$$\mathscr{P}_*^{(2n)} \sim K_{\mathrm{hi}}^{3-2n} \quad (n \geq 2)\,. \tag{3.44}$$

If the parameters $\mathscr{P}_*^{(2n)}$ would also involve powers of K_{lo}, the theory exhibited even more fine-tunings, a scenario unlikely to occur in nature [85, 105]. Higher-order terms are consequently suppressed by at least one order in $K_{\mathrm{lo}}/K_{\mathrm{hi}}$ compared to the unitary cut. The relation holds for higher-order coefficients in the D^{0*} propagator compared to the self-energy at resonance, i.e.,

$$\mathscr{P}_*^{(2n)}\bar{k}^{2n} \sim |-i\bar{k}^3| \left(\frac{K_{\mathrm{lo}}}{K_{\mathrm{hi}}}\right)^{1+2(n-2)} \quad (n \geq 2)\,. \tag{3.45a}$$

$$\Leftrightarrow \Delta_n(E_{\mathrm{cm}} + i\epsilon)^n \sim |-\Sigma_*(E_{\mathrm{cm}})| \left(\frac{K_{\mathrm{lo}}}{K_{\mathrm{hi}}}\right)^{1+2(n-2)} \quad (n \geq 2)\,. \tag{3.45b}$$

The remaining scalings of a_* and $r_*/2$ will be discussed below.

b) Consequences from the small D^{0*} width

Given that higher-order terms $\propto \Delta_n$ in the propagator are small compared to the self-energy, we can now match the remaining Lagrangian parameters, Δ_0 and g, to the D^{0*} pole position. Without imaginary interactions iW_n, the D^{0*} decays only hadronically. We may thus demand

$$G_*^{(\mathrm{f})\,-1}(E_{\mathrm{cm}} = \delta - i\Gamma_{D^0\pi^0}/2) \equiv 0\,. \tag{3.46}$$

While a value for the partial width $\Gamma_{D^0\pi^0}$ has not been determined yet, an upper bound $\Gamma_{D^0\pi^0} < 1.4\,\mathrm{MeV}$ is known from experiment [36]. Thus, the ratio of the pole's imaginary and real parts,

$$\mathscr{N} \equiv \frac{\Gamma_{D^0\pi^0}/2}{\delta} < 0.1\,, \tag{3.47}$$

which indicates the "narrowness" of the resonance, is small. It can be used to derive approximate relations for Δ_0 and g^2. Using Eqs. (3.46) and (3.45b), we obtain

$$\Delta_0 = -\delta\left(1 + \mathscr{O}(\mathscr{N} K_{\mathrm{lo}}/K_{\mathrm{hi}})\right), \tag{3.48a}$$

$$|\Sigma_*(\delta)| = g^2\,\frac{\mu_{D\pi}}{6\pi}(2\mu_{D\pi}\,\delta)^{3/2} = \frac{\Gamma_{D^0\pi^0}}{2}\left(1 + \mathscr{O}(\mathscr{N} K_{\mathrm{lo}}/K_{\mathrm{hi}})\right). \tag{3.48b}$$

These relations are exact up to tiny corrections $\mathcal{N} K_{\text{lo}}/K_{\text{hi}} < 3\,\%$. In order for the approximations to fail, the higher-order parameter $\mathscr{P}_*^{(4)}$ would have to be enhanced by a factor of order $(\mathcal{N} K_{\text{lo}}/K_{\text{hi}})^{-1} > 33$ which is unlikely. Later, we will obtain a narrowness parameter $\mathcal{N} \approx 0.0025 \ll 0.1$, which secures the validity of the above approximations. Equation (3.48a) shows that our power counting fulfills the demand of Sec. 3.1.4, that $\boldsymbol{D}^{0\dagger}[i\partial_{\text{cm}} - \delta]\boldsymbol{D}^0$ be the LO kinetic term. Moreover, we see that the width is given by $2|\Sigma(\delta)|$ to excellent accuracy; see also Fig. 3.9.

c) Parameter fixing: a value for the D^{0*} width

While Eq. (3.48a) is determined by the experimental value of δ, Eq. (3.48b) contains two unknowns g^2 and $\Gamma_{D^0\pi^0}$. One possibility to resolve this problem is to use the latest Lattice QCD (LQCD) value for the HHχPT coupling $(g_{\text{HH}\chi\text{PT}})_{\text{LQCD}} = 0.53(3)(3)$ from Ref. [106], defined with $(f_\pi)_{\text{LQCD}} = 120\,\text{MeV}$. Using Eqs. (3.35) and (3.48b), we would obtain $(g^2)_{\text{LQCD}} \approx 3.6(4)\cdot 10^{-8}\,\text{Mev}^{-3}$ and $(\Gamma_{D^0\pi^0})_{\text{LQCD}} = 36(4)\,\text{keV}$.[12] Apparently, LQCD suggest that the width is many orders smaller than the upper bound 1.4 MeV.

Similar results are obtained if one decides to use the experimentally known width $\Gamma_{c*} = 83.4(18)\,\text{keV}$ of the charged vector mesons as input. As shown in Table 3.2, the D^{+*} obtains partial widths from its *two* decay channels $D^0\pi^+$ and $D^+\pi^0$ with branching ratios $\mathscr{B}_{D^0\pi^+} = 67.7(5)\,\%$ and $\mathscr{B}_{D^+\pi^0} = 30.7(5)\,\%$. The respective $D^* \longleftrightarrow D\pi$ couplings read $-\sqrt{2}g$ and $-g$, respectively, as was shown in Sec. 3.1. Just like the D^{0*}, it can be interpreted as a p-wave resonance of its constituents. The respective rest mass differences[13] $\delta_{+0} \equiv m_{D^{+*}} - m_{D^0} - m_{\pi^+} = 5.855(2)\,\text{MeV}$ and $\delta_{++} \equiv m_{D^{+*}} - m_{D^+} - m_{\pi^0} = 5.69(8)\,\text{MeV}$ scale like δ and are much larger than the partial widths $\Gamma_{D^0\pi^+}$ and $\Gamma_{D^+\pi^0}$. Thus, the power counting above can be applied to the charged two-body sectors. The analogue of Eq. (3.48b) reads

$$|\Sigma_*(\delta_{+0})|\,\Big|_{g\to-\sqrt{2}g} + |\Sigma_*(\delta_{++})|\,\Big|_{g\to-g} = \frac{\Gamma_{c*}\big(1-\mathscr{B}_{D^+\gamma}\big)}{2}\Big(1+\mathcal{O}\big(\mathcal{N} K_{\text{lo}}/K_{\text{hi}}\big)\Big) \tag{3.49}$$

with $\mathscr{B}_{D^+\gamma} = 1.6(4)\,\%$; see Table 3.2. This relation implies the values

$$g^2 = \frac{3\pi}{\sqrt{2}}\,\frac{(\Gamma_{D^0\pi^+}+\Gamma_{D^+\pi^0})/2}{2\,\mu_{D^0\pi^+}^{5/2}\,\delta_{+0}^{3/2} + \mu_{D^+\pi^0}^{5/2}\,\delta_{++}^{3/2}}\Big(1+\mathcal{O}\big(\mathcal{N} K_{\text{lo}}/K_{\text{hi}}\big)\Big) = 3.48(8)\cdot 10^{-8}\,\text{MeV}^{-3}\,, \tag{3.50a}$$

$$\Gamma_{D^0\pi^0} = 34.7(9)\,\text{keV}\,, \tag{3.50b}$$

which are in excellent agreement with the lattice results. The kinetic masses entering the reduced masses $\mu_{D^0\pi^+}$ and $\mu_{D^+\pi^0}$ are given in Table 3.1.

Uncertainties indicated in Eqs. (3.50a)-(3.50b) are due to the experimental uncertainty of Γ_{c*}. As proposed above, the narrowness parameter $\mathcal{N} = \Gamma_{D^0\pi^0}/(2\delta) \approx 0.0025 \ll 0.1$ is extremely small and yields negligible theory uncertainties $\mathcal{N}K_{\text{lo}}/K_{\text{hi}} \sim 0.075\,\%$ ($\sim$N^{3}LO). For this reason, we use the central values of g^2 and $\Gamma_{D^0\pi^0}$ in Eqs. (3.50a)-(3.50b) in all later calculations. Our prediction for the full D^{0*} width thus reads

$$\Gamma_{0*} \equiv \Gamma_{D^0\pi^0}/\mathscr{B}_{D^0\pi^0} = (53.6 \pm 1.0)\,\text{keV}\,. \tag{3.51}$$

d) Fine-tuning scenarios for a_* and $r_*/2$

We are now in the position to give predictions for the leading ERE coefficients in Eqs. (3.41a)-(3.41b). Using the calculated values for g^2 and Δ_0 of Eqs. (3.48a) and (3.50a), we obtain

$$a_*^{-1/3} = -312(3)\,\text{MeV} \tag{3.52a}$$

$$\frac{r_*}{2} = -17.1(4)\,\text{GeV}\,. \tag{3.52b}$$

---

[12] Here, we neglect the second, fitting-related uncertainty of $(g_{\text{HH}\chi\text{PT}})_{\text{LQCD}}$.

[13] Per convention, the first subscript refers to the decaying vector meson, the second to the resulting pseudoscalar D meson.

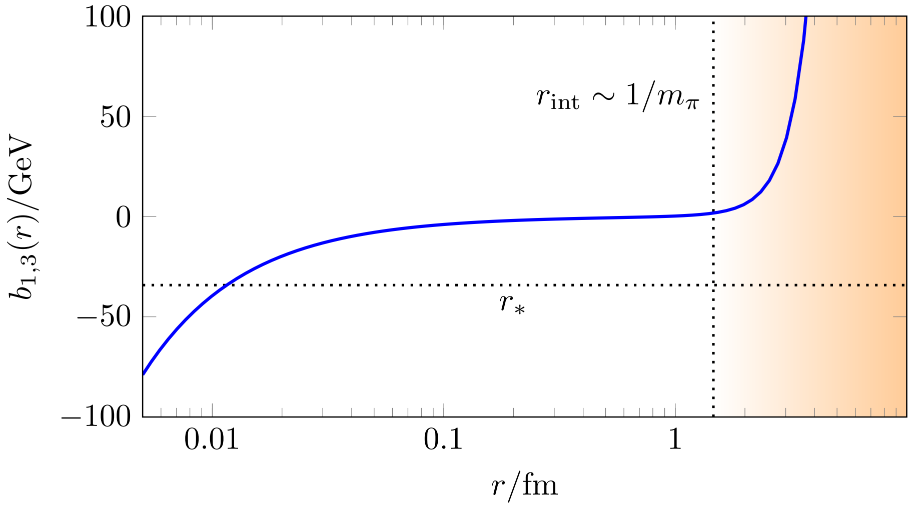

Figure 3.11.: The predicted value of r_* in Eq. (3.52b) (horizontal grid line) fulfills Wigner's causality bound for p-wave scattering in $d = 3$ as given in Ref. [88]. The restriction states that $r_* \leq b_{1,3}(r)$ (blue curve) must hold outside the interaction region, i.e., for $r \geq r_{\mathrm{int}} \sim 1/m_\pi$ (orange area and vertical grid line).

As a first step, we may check if these values fulfill Wigner's causality bound for p-wave scattering $(l = 1)$ in $d = 3$ dimensions, which was determined in Ref. [88]. It states that r_* is bound from above by the function

$$b_{1,3}(r) = -2\,r^{-1} - \frac{2}{3}\,a_*^{-1}\,r^2 + \frac{2}{45}\,a_*^{-2}\,r^5 \tag{3.53}$$

outside the interaction region, i.e., for $r \geq r_{\mathrm{int}}$. As can be seen in Fig. 3.11, the restriction is fulfilled for $r_{\mathrm{int}} \sim 1/m_\pi$ and even for much smaller choices of r_{int}.

Apparently, both a_* and $r_*/2$ are much larger than the small momentum scale $K_{\mathrm{lo}} \approx 42\,\mathrm{MeV}$. As for a_*, this circumstance is a direct consequence of the small width $\Gamma_{D^0\pi^0}$. Due to Eqs. (3.48a)-(3.48b) and the matching conditions of Eqs. (3.41a)-(3.41b), the separation of the inverse scattering volume and the unitary cut at resonance is determined by the narrowness parameter like $|-i\bar{k}^3/a_*^{-1}| \approx |\Sigma(\delta)/\Delta_0| \approx \Gamma_{D^0\pi^0}/(2\delta) = \mathscr{N}$. Higher-order terms are further suppressed in our power counting. Thus, the existence of a shallow resonance pole implies also a large p-wave effective range

$$\frac{r_*}{2} \sim a_*^{-1}\,K_{\mathrm{lo}}^{-2}\,. \tag{3.54}$$

The resonance condition of Eq. (3.54) only fixes the relative scaling of the two parameters, but not how they individually scale. In fact, infinitely many options are possible. One scenario that respects the resonance condition is $a_*^{-1} \sim K_{\mathrm{lo}}^3$, $r_*/2 \sim K_{\mathrm{lo}}$. It has been discussed by Bertulani *et al.* in order to describe the shallow neutron-alpha p-wave resonance [79]. A disadvantage of this scheme is that it requires two combinations of Lagrangian parameters, Δ_0/g^2 and $1/g^2$, to scale unnaturally. According to Bedaque *et al.*, a scenario with less fine-tuning should be preferred instead. They suggested the modified scheme $a_*^{-1} \sim K_{\mathrm{lo}}^2 K_{\mathrm{hi}}$, $r_*/2 \sim K_{\mathrm{hi}}$, in which only the combination Δ_0/g^2 is unnaturally small [85]. However, none of the two schemes seems to be able to explain the extremely large value of $r_*/2$ in Eq. (3.52b), which exceeds K_{hi} by many magnitudes.

There is exactly one more scaling scenario which requires a single fine-tuning, being

$$a_*^{-1} \sim K_{\mathrm{hi}}^3\,, \tag{3.55a}$$

$$\frac{r_*}{2} \sim K_{\mathrm{lo}}^{-2} K_{\mathrm{hi}}^3\,. \tag{3.55b}$$

This scheme assumes that $r_*/2$ is enhanced, while a_* scales naturally. Given that $|a_*^{-1/3}| \approx 2.3\, m_\pi$, these choices are in agreement with the numerical values of Eq. (3.52a)-(3.52b). We thus suggest this scaling scenario for the $D^0\pi^0$ sector. Let us emphasize that other scenarios compliant with Eq. (3.54) may be possible, but they would inevitable involve more than one fine-tuning.

In the new scheme, the coupling is unnaturally small,

$$\frac{1}{2\mu_{D\pi} g^2} \sim K_{\mathrm{lo}}^{-2} K_{\mathrm{hi}}^{3} \frac{\mu_{D\pi}}{6\pi}\,, \tag{3.56}$$

while Δ_0/g^2 scales naturally. Consequently, we obtain for the narrowness parameter and the widths

$$\mathcal{N} \sim \left(\frac{K_{\mathrm{lo}}}{K_{\mathrm{hi}}}\right)^3 \Leftrightarrow \frac{\Gamma_{D^0\pi^0}}{2} \sim \frac{\Gamma_{0*}}{2} \sim \frac{K_{\mathrm{lo}}^5 K_{\mathrm{hi}}^{-3}}{2\mu_{D\pi}}\,. \tag{3.57}$$

We see that the narrowness of the D^{0*} resonance can be explained naturally in terms of typical $D^0\pi^0$ momentum scales. For the rest of the thesis, however, we keep the narrowness parameter $\mathcal{N}$ in all scaling analyses explicit, in order to ensure that power counting predictions for the $X(3872)$ width do not dependent on a certain scaling scheme for a_* and $r_*/2$.

3.2.3 Extension for radiative D^{0*} decays

The radiative partial width $\Gamma_{D^0\gamma} = 18.9(9)\,\mathrm{keV} \approx 0.55\, \Gamma_{D^0\pi^0}$ is of the order of the hadronic partial width. Thus, it is as important for the $X(3872)$ width, and we count $\Gamma_{D^0\gamma} \sim \Gamma_{D^0\pi^0}$. In order to implement $\Gamma_{D^0\gamma}$ in the D^{0*} propagator, we now allow the Lagrangian parameters to be complex, i.e., we allow for $W_n \neq 0$ $(n \geq 0)$. The former scaling relations of the coefficients Δ_n $(n \geq 0)$ shall not be affected by this procedure. The new pole position will then be given by

$$E_* \equiv \delta - i\frac{\Gamma_{0*}}{2}\,. \tag{3.58}$$

Since $\Gamma_{D^0\gamma}/2 \sim \mathcal{N}\delta \sim \mathcal{N}(K_{\mathrm{lo}}/K_{\mathrm{hi}})^2 K_{\mathrm{hi}}^2/(2\mu_{D\pi})$, all imaginary parts W_n are expected to be at least suppressed by a common factor $\mathcal{N}(K_{\mathrm{lo}}/K_{\mathrm{hi}})^2$. Other than that, no fine-tunings between different W_n are assumed. It follows that

$$iW_n\,(E_{\mathrm{cm}} + i\epsilon)^n \sim i\mathcal{N}\left(\frac{K_{\mathrm{lo}}}{K_{\mathrm{hi}}}\right)^{2n} \delta \quad (n \geq 0) \tag{3.59}$$

near the pole. Demanding the pole to sit at $E_{\mathrm{cm}} = E_*$, we recover Eqs. (3.48a)-(3.48b) and additionally

$$iW_0 = i\frac{\Gamma_{D^0\gamma}}{2}\left(1 + \mathcal{O}\left(K_{\mathrm{lo}}^2/K_{\mathrm{hi}}^2\right)\right). \tag{3.60}$$

3.2.4 Propagator expansion at resonance

In the previous section, we saw that the unitary cut is many times smaller than the leading ERE terms $a_*^{-1} \sim r_*/2\bar{k}^2$. When working close to $E_{\mathrm{cm}} = 0$, it can consequently be neglected at LO. However, Bedaque *et al.* pointed out that this is no longer true if one studies physics close to the resonance, as is the case for the $X(3872)$. In this region, the two leading terms almost cancel and the unitary cut becomes the new leading quantity. Due to this "kinematic fine-tuning" $|E_{\mathrm{cm}} - \delta|/\delta \ll 1$, the resonance value of the unitary cut, i.e., the nonzero D^{0*} width, has to be included nonperturbatively at LO. The LO D^{0*} propagator in the vicinity of the $X(3872)$ is thus given by the Breit-Wigner form

$$iG_*^{(\mathrm{LO})}(E_{\mathrm{cm}}) \equiv i\,[E_{\mathrm{cm}} - E_* + i\epsilon]^{-1} \tag{3.61}$$

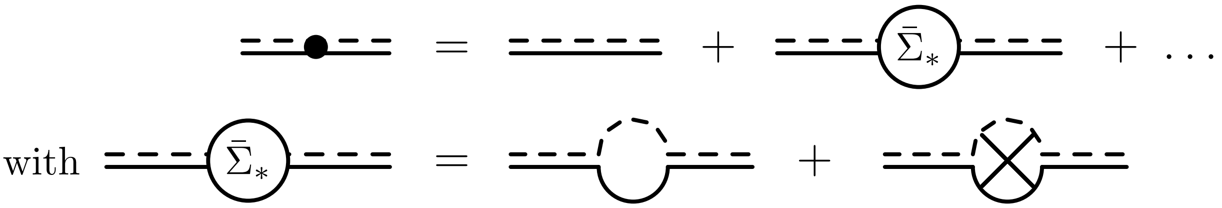

Figure 3.12.: Pole expansion of the full D^{0*} propagator. The first correction to the LO propagator $iG_*^{(\mathrm{LO})}(E_\mathrm{cm})$ (without a circle) contains the self-energy insertion $-i\bar{\Sigma}_*(E_\mathrm{cm})$. It is given by the self-energy loop $-i\Sigma_*(E_\mathrm{cm})$ and a counter term $+i\Sigma_*(E_*)$ (second row).

with pole position E_* given in Eq. (3.58). In Feynman diagrams, it will be represented by a simple solid-dashed double line; see Fig. 3.12.

Subleading corrections to this expression can be obtained by expanding the full propagator around $E_\mathrm{cm} = E_*$. In order to do so, we write the propagator in the form

$$iG_*^{(\mathrm{f})}(E_\mathrm{cm}) = i\left[\left(1+i\,W_1\right)(E_\mathrm{cm}+i\epsilon) - \Sigma_*(E_\mathrm{cm}) + \sum_{n\geq 2}(\Delta_n + i\,W_n)(E_\mathrm{cm}+i\epsilon)^n - [E_\mathrm{cm}\to E_*]\right]^{-1} \tag{3.62a}$$

$$= iG_*^{(\mathrm{LO})}(E_\mathrm{cm})\cdot\left[1\ \underbrace{-i\bar{\Sigma}_*(E_\mathrm{cm})\cdot iG_*^{(\mathrm{LO})}(E_\mathrm{cm})}_{=\mathcal{O}\left(\mathcal{N}^2\right)+i\mathcal{O}(\mathcal{N})} + \mathcal{O}(\mathcal{N}K_\mathrm{lo}/K_\mathrm{hi}) + i\,\mathcal{O}\left(\mathcal{N}K_\mathrm{lo}^2/K_\mathrm{hi}^2\right)\right]. \tag{3.62b}$$

Note that the expression $[E_\mathrm{cm} \to E_*]$ in Eq. (3.62a) is nothing but the constant $-(\Delta_0 + iW_0) = \delta - i\Gamma_{D^0\gamma}/2 + \cdots$. All “propagator corrections” in the brackets of Eq. (3.62b) are at least suppressed by the narrowness parameter $\mathcal{N} = \Gamma_{D^0\pi^0}/(2\delta) \ll 1$ and possibly also by powers of $K_\mathrm{lo}/K_\mathrm{hi}$; see Eqs. (3.45b), (3.48b) and (3.59). Such corrections involving higher order parameter Δ_n $(n \geq 2)$ or iW_n $(n \geq 1)$ are condensed into the expression $\mathcal{O}(\mathcal{N}K_\mathrm{lo}/K_\mathrm{hi}) + i\mathcal{O}\left(\mathcal{N}K_\mathrm{lo}^2/K_\mathrm{hi}^2\right)$.

The first correction,

$$-i\bar{\Sigma}_*(E_\mathrm{cm})\cdot iG_*^{(\mathrm{LO})}(E_\mathrm{cm}) \equiv \frac{\Sigma_*(E_\mathrm{cm}) - \Sigma_*(E_*)}{E_\mathrm{cm} - E_*} \sim \Sigma_*'(E_*) = \mathcal{O}\left(\mathcal{N}^2\right) + i\mathcal{O}(\mathcal{N}), \tag{3.63}$$

is given by the self-energy and a counterterm $+i\Sigma_*(E_*)$ as shown in Fig. 3.12. The scalings $\sim \mathcal{N}^2$ and $\sim \mathcal{N}$ of real and imaginary part in Eq. (3.63) follow from $E_* \sim \delta(1 + i\mathcal{O}(\mathcal{N}))$ and $\Sigma_*'(E_*) \sim \Sigma_*(E_*)/E_*$. For illustration, we plot the self-energy correction for complex E_cm in Fig. 3.13 using the values of g^2 and E_* obtained above. Indeed, the scaling predictions are correct in the region of the D^{0*} pole (indicated by red dots).

Remarkably, the scalings of Eq. (3.63) do not only hold close to $E_\mathrm{cm} = E_*$, but also close to $E_\mathrm{cm} = 0$; see Fig. 3.13. That is due to the fact that the difference quotient in Eq. (3.63) collapses to $\Sigma_*(E_*)/E_*$ at this point. All propagator corrections exhibit this feature since they also represent difference quotients of the terms in Eq. (3.62a). This observation is crucial for this work because *both* regions are important for the $X(3872)$ width power counting in Sec. 3.3.

For the $X(3872)$ width, only imaginary parts of the propagator corrections are relevant. The self-energy correction with its scaling $i\mathcal{O}(\mathcal{N})$ will thus be the most important one. It will modify the $X(3872)$ width at NLO. All other imaginary corrections are suppressed by even powers of $K_\mathrm{lo}/K_\mathrm{hi}$. That is a direct consequence of the fact that the ERE is analytic in $E_\mathrm{cm} \sim K_\mathrm{lo}^2/(2\mu_{D\pi})$. It follows that two-body corrections to the $X(3872)$ width are actually suppressed by the expansion parameter

$$\chi_2 \equiv \left(\frac{K_\mathrm{lo}}{K_\mathrm{hi}}\right)^2 \approx \frac{\delta}{m_\pi/2}, \tag{3.64}$$

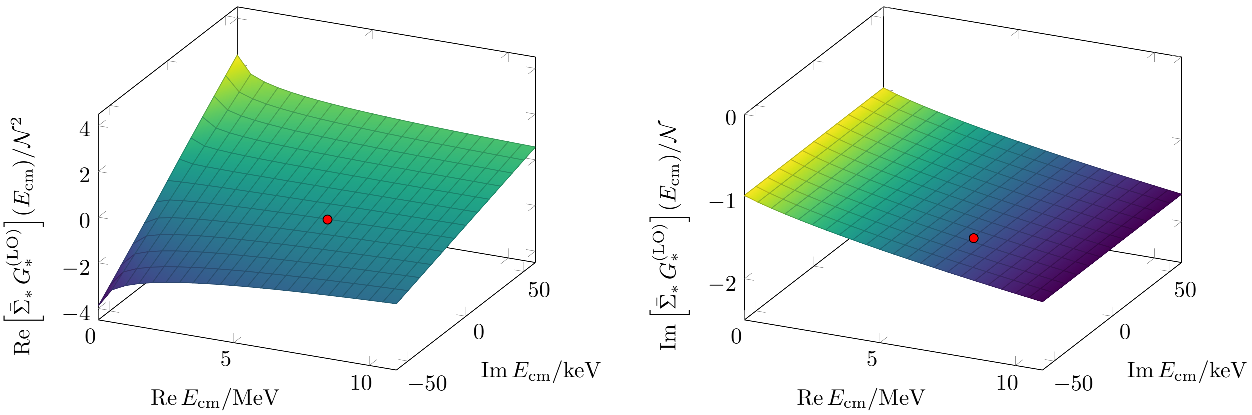

(a) (b)

Figure 3.13.: (a) Real part and (b) imaginary part of the self-energy correction $-i\bar{\Sigma}_*(E_{\mathrm{cm}}) \cdot iG_*^{(\mathrm{LO})}(E_{\mathrm{cm}})$ in Eq. (3.63), in units of $\mathcal{N}^2$ and $\mathcal{N}$. For clarity, we continued $\bar{\Sigma}_*(E_{\mathrm{cm}})$ to the second sheet ($\mathrm{Im}\, E_{\mathrm{cm}} < 0$), where the D^{0*} pole position $E_* = \delta - i\Gamma_{0*}/2$ lies (indicated by red dots).

as proposed already in Eq. (3.2).

A convenient side-effect of the expansion in Eq. (3.62b) is that at each power counting order, there is only one energy pole representing the D^{0*}. If one instead directly truncated the denominator of the full propagator at some higher-order, one would find unphysical deep poles [79]. For example, a propagator $\sim [E_{\mathrm{cm}} - \delta - \Sigma_*(E_{\mathrm{cm}})]^{-1}$, which includes the full self-energy nonperturbatively, exhibits a pole at $E_{\mathrm{cm}} \approx -\delta/\mathcal{N}^2 \approx -1.13\,\mathrm{TeV}$, which lies far outside the EFT's region of applicability.[14] Such artifacts are avoided when choosing the pole expansion above.

Before we turn to the three-body system, let us mention that relativistic corrections to the D^{0*} propagator are strongly suppressed by multiples of the inverse total mass $M_{D\pi}^{-1}$ and can be neglected at the order we are working; see Appendix D.3.

3.3 Three-body system: the $X(3872)$ resonance

In this section, we implement the $X(3872)$ as an energy pole in the $D^0\bar{D}^{0*}$ + c.c. Faddeev amplitude. Firstly, we construct the nonperturbative amplitude in the 1^{++} channel from Feynman diagrams. For renormalization, we introduce the three-body force defined in Eq. (3.36).

Secondly, we identify the relevant expansion parameters of the three-body system (χ_3 in Eq. (3.2)). Based on a diagrammatic power counting for the $X(3872)$ width Γ_X, we decompose the Faddeev amplitude into an LO part and three NLO corrections, the latter being suppressed by powers of $\chi_2 \sim \chi_3 \sim 0.13$. The power counting exploits the D^{0*} ($\bar{D}^{0*}$) propagator expansion of Eq. (3.62b).

Lastly, we give predictions for the width Γ_X of the $X(3872)$ at LO and NLO in the case of a bound $X(3872)$. It turns out that the LO width is just given by the D^{0*} width, i.e., $\Gamma_X^{(\mathrm{LO})} = \Gamma_{0*}$. At NLO, Γ_X obtains a mild dependence on the binding energy δ_X. Remarkably, the three NLO corrections cancel near the experimentally reasonable value $\delta_X = 50\,\mathrm{keV}$. This observation gives rise to high accuracy of the width already at LO.

3.3.1 Faddeev amplitude

Due to the fact that the vector mesons are unstable, they can never appear as asymptotic states. Still, we may define a transition amplitude iT, which connects intermediate $D^0\bar{D}^{0*}$ + c.c. states, for example in

---

[14] This pole is unphysical because it its residue is negative.

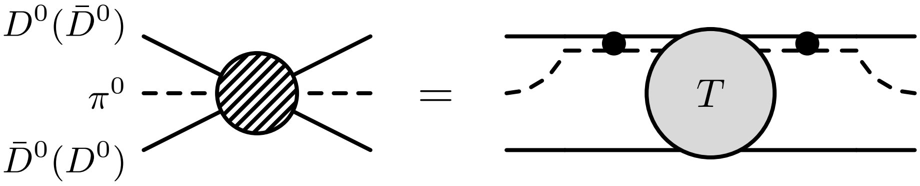

Figure 3.14.: The full $D^0\bar{D}^{0*}$ + c.c. Faddeev amplitude iT can be used to calculate the full $D^0\bar{D}^0\pi^0$ three-body amplitude in the $C = +$ channel.

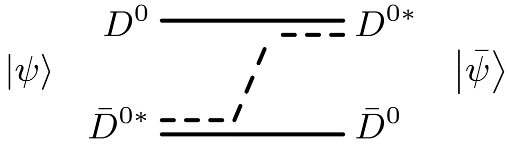

Figure 3.15.: The pion exchange diagram $-iV$ connects different flavor eigenstates $|\psi\rangle$, $|\bar{\psi}\rangle$.

$D^0\bar{D}^0\pi^0$ three-body scattering as shown in Fig. 3.14. In this thesis, we use iT to calculate the $D^0\bar{D}^0\pi^0$ production amplitude.

Construction

The $X(3872)$ can be interpreted as a $C = +$ superposition

$$|\psi_+\rangle \equiv \frac{1}{\sqrt{2}}\left(|\psi\rangle + |\bar{\psi}\rangle\right) \tag{3.65}$$

of the flavor eigenstates

$$|\psi\rangle \equiv \left|D^0\bar{D}^{0*}\right\rangle, \quad |\bar{\psi}\rangle \equiv \left|\bar{D}^0 D^{0*}\right\rangle. \tag{3.66}$$

Let $\hat{T}$ be the scattering operator and $iT_{\phi_\text{in}\phi_\text{out}} \equiv \langle\phi_\text{out}|\, i\hat{T}\, |\phi_\text{in}\rangle$ the amplitudefor a specific transition. The desired $C = +$ amplitude $iT \equiv iT_{\psi_+\psi_+}$ then fulfills

$$iT = \langle\psi_+|\, i\hat{T}\, |\psi_+\rangle = \frac{1}{2}\left(iT_{\psi\psi} + iT_{\bar{\psi}\bar{\psi}} + iT_{\bar{\psi}\psi} + iT_{\psi\bar{\psi}}\right) = iT_{\psi\psi} + iT_{\bar{\psi}\psi}\,. \tag{3.67}$$

In Eq. (3.67), we applied the relations $T_{\bar{\psi}\bar{\psi}} = T_{\psi\psi}$ and $T_{\psi\bar{\psi}} = T_{\bar{\psi}\psi}$, which follow from charge conjugation symmetry of the Lagrangian in Eq. (3.30). In the following, we discuss the three DD^* interactions, from which iT will be constructed up to NLO.

Firstly, different flavor eigenstates are connected via pion exchange. The respective tree-level diagram for $|\psi\rangle \to |\bar{\psi}\rangle$, denoted $-iV_{\psi\bar{\psi}}$, is shown in Fig. 3.15. The process is invariant under charge conjugation. Thus, $-iV \equiv -iV_{\bar{\psi}\psi} = -iV_{\psi\bar{\psi}}$ be the generic pion exchange diagram. For incoming (outgoing) polarization i (j), relative DD^* momentum[15] $\boldsymbol{p}$ ($\boldsymbol{q}$), and total energy E, it is given by

$$V^{ij}(\boldsymbol{p},\boldsymbol{q};E) = g^2 \frac{(\xi\boldsymbol{p} + \boldsymbol{q})^i\,(\xi\boldsymbol{q} + \boldsymbol{p})^j}{E - \frac{\boldsymbol{p}^2}{2\mu_{D\pi}} - \frac{\boldsymbol{q}^2}{2\mu_{D\pi}} - \frac{\boldsymbol{p}\cdot\boldsymbol{q}}{m_\pi} + i\epsilon}\,, \tag{3.68}$$

with $\xi \equiv m_D/M_{D\pi} \approx 0.93$. The function V will be called "pion exchange potential" in the following.

---

[15] Relative DD^* momenta are defined via $\boldsymbol{p} \equiv \mu_*\left(m_D^{-1}\boldsymbol{p}_D - M_{D\pi}^{-1}\boldsymbol{p}_{D^*}\right)$. In the center-of-mass system, this expression equals the momentum of the pseudoscalar meson (spectator) $\boldsymbol{p} = \boldsymbol{p}_D = -\boldsymbol{p}_{D^*}$.

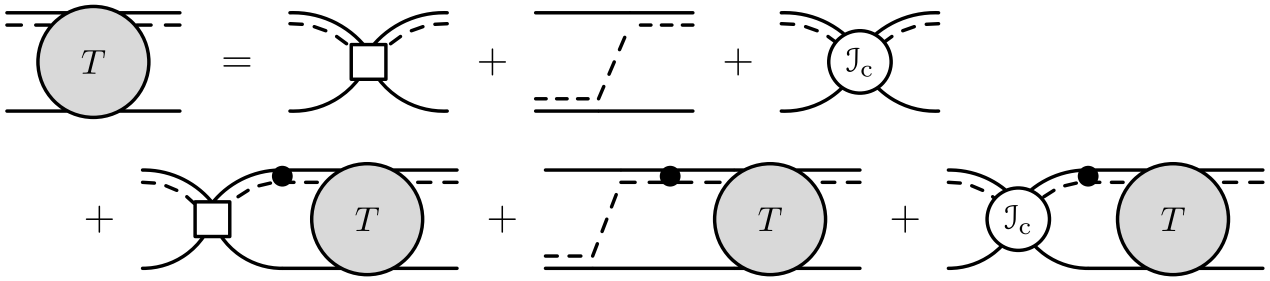

Figure 3.16.: The full Faddeev equation for the $C=+$ amplitude iT includes the three-body vertex $-iC_0$ (white square), the pion exchange potential $-iV$, and an effective s-wave interaction $-i\mathcal{J}_\mathrm{c}$ from charged mesons. Loop integrals in the second row involve the full D^{0*} ($\bar{D}^{0*}$) propagator $iG_*^{(\mathrm{f})}$.

Secondly, the three-body vertex of Eq. (3.36) connects all combinations of $|\psi\rangle$ and $|\bar{\psi}\rangle$ with equal strength $-iC_0/2\,\delta^{ij}$. Thirdly, we allow for an additional DD^* s-wave interaction $-i\mathcal{J}_\mathrm{c}(E)/2\,\delta^{ij}$ which takes into account NLO contributions from the charged DD^* threshold; see Fig. 3.1. The full analytic form of $\mathcal{J}_\mathrm{c}$ will be given at the end of Sec. 3.3.4.

Symbolically[16], we then obtain the coupled amplitude system

$$T_{\psi\psi} = -\frac{C_0+\mathcal{J}_\mathrm{c}}{2} + \frac{C_0+\mathcal{J}_\mathrm{c}}{2}\,G_*^{(\mathrm{f})}\,T_{\psi\psi} + \left(V_{\psi\bar{\psi}} + \frac{C_0+\mathcal{J}_\mathrm{c}}{2}\right) G_*^{(\mathrm{f})}\,T_{\bar{\psi}\psi}\,, \tag{3.69a}$$

$$T_{\bar{\psi}\psi} = -V_{\bar{\psi}\psi} - \frac{C_0+\mathcal{J}_\mathrm{c}}{2} + \left(V_{\bar{\psi}\psi} + \frac{C_0+\mathcal{J}_\mathrm{c}}{2}\right) G_*^{(\mathrm{f})}\,T_{\psi\psi} + \frac{C_0+\mathcal{J}_\mathrm{c}}{2}\,G_*^{(\mathrm{f})}\,T_{\bar{\psi}\psi}\,. \tag{3.69b}$$

Due to Eq. (3.67), an equation for T can be obtained by adding Eqs. (3.69a) and (3.69b), yielding

$$T = -(C_0+V+\mathcal{J}_\mathrm{c}) + (C_0+V+\mathcal{J}_\mathrm{c})\,G_*^{(\mathrm{f})}\,T\,. \tag{3.70}$$

Thus, the two-channel Faddeev amplitude system simplifies to a single equation for T. Diagrammatically, Eq. (3.70) is shown in Fig. 3.16.

We evaluate the Faddeev equation in the center-of-mass system at energy E (relative to the $D^0\bar{D}^0\pi^0$ threshold). The integrals are performed over the four-momentum $q^\mu \equiv (q^0, \boldsymbol{q})$ of the respective spectator particle (D meson). In the center-of-mass system, $\boldsymbol{q}$ represents also the relative DD^* momentum. The q^0 integrals are performed using the residue theorem, similar to the D^{0*} self-energy calculation in Appendix D.2. For example, the pion exchange loop diagram in the second row of Fig. 3.16 yields

$$\sum_{j=1}^{3}\int\frac{\mathrm{d}^4q}{(2\pi)^4}\,\frac{i^2\left(+g\,(-\xi\boldsymbol{p}-\boldsymbol{q})^i\right)\left(-g\,(-\xi\boldsymbol{q}-\boldsymbol{p})^j\right)\,iG_*^{(\mathrm{f})}\left(E-q^0-\frac{\boldsymbol{q}^2}{2M_{D\pi}}\right)\,iT^{ji'}(\boldsymbol{q},\boldsymbol{p}';E)}{\left[q^0-\frac{\boldsymbol{q}^2}{2m_D}+i\epsilon\right]\left[\left(E-\frac{\boldsymbol{p}^2}{2m_D}-q^0\right)-\frac{(\boldsymbol{p}+\boldsymbol{q})^2}{2m_\pi}+i\epsilon\right]} \tag{3.71a}$$

$$= i\sum_{j=1}^{3}\int\frac{\mathrm{d}^3q}{(2\pi)^3}\,\frac{g^2\,(\xi\boldsymbol{p}+\boldsymbol{q})^i\,(\xi\boldsymbol{q}+\boldsymbol{p})^j}{E-\frac{\boldsymbol{p}^2}{2m_D}-\frac{\boldsymbol{q}^2}{2m_D}-\frac{(\boldsymbol{p}+\boldsymbol{q})^2}{2m_\pi}+i\epsilon}\,G_*^{(\mathrm{f})}\left(E-\frac{\boldsymbol{q}^2}{2\mu_*}\right)T^{ji'}\left(\boldsymbol{q},\boldsymbol{p}';E\right), \tag{3.71b}$$

where lifting the pole at $q^0=\boldsymbol{q}^2/(2m_D)-i\epsilon$ introduces a factor $-i$. In Eq. (3.71b), we recover the pion exchange potential of Eq. (3.68). The full Faddeev equation for T then reads

$$\begin{aligned} T^{ii'}\left(\boldsymbol{p},\boldsymbol{p}';E\right) = &-\left(C_0\,\delta^{ii'}+V^{ii'}\left(\boldsymbol{p},\boldsymbol{p}';E\right)+\mathcal{J}_\mathrm{c}(E)\,\delta^{ii'}\right)\\ &+\sum_{j=1}^{3}\int\frac{\mathrm{d}^3q}{(2\pi)^3}\,\frac{C_0\,\delta^{ij}+V^{ij}(\boldsymbol{p},\boldsymbol{q};E)+\mathcal{J}_\mathrm{c}(E)\,\delta^{ij}}{G_*^{(\mathrm{f})\,-1}\left(E-\boldsymbol{q}^2/(2\mu_*)\right)}\,T^{ji'}\left(\boldsymbol{q},\boldsymbol{p}';E\right). \end{aligned} \tag{3.72}$$

---

[16] We omit intermediate spectator propagators, loop integrals, and polarization sums in this short-hand notation. As exemplified below, loop integrals effectively introduce a factor $-i$.

An important feature of the given process is that exchanged pions can go on shell for $E > 0$. That is the case whenever the exchange potential in Eq. (3.68) has a pole, i.e., at

$$E_\pi - \frac{\boldsymbol{k}_\pi^2}{2m_\pi} = E - \frac{\boldsymbol{p}^2}{2m_D} - \frac{\boldsymbol{q}^2}{2m_D} - \frac{(\boldsymbol{p}+\boldsymbol{q})^2}{2m_\pi} = 0 \tag{3.73a}$$

$$\Leftrightarrow x \equiv \frac{\boldsymbol{p}\cdot\boldsymbol{q}}{pq} = -\frac{\frac{1}{2\xi}(p^2+q^2) - m_\pi(E+i\epsilon)}{pq}\,. \tag{3.73b}$$

As a consequence, pion exchanges modify the $X(3872)$ width at NLO (see below).

Partial wave projection

In principle, one could solve Eq. (3.72) for fixed i', $\boldsymbol{p}'$, and E in three spatial dimensions. However, this equation contains contributions from all spin-parity channels J^P, of which only $J^P = 1^+$ exhibits the $X(3872)$ as a pole. Consequently, we perform a partial wave projection onto $J = 1$ and $L \in \{0, 2\}$, where the total angular momentum $\boldsymbol{J} \equiv \boldsymbol{L} + \boldsymbol{S}$ is build from the orbital angular momentum $\boldsymbol{L}$ and the total spin $\boldsymbol{S}$ (with $S = 1$).

Our partial wave projection procedure is inspired by Ref. [46], in which Baru *et al.* defined projection operators based on vector spherical harmonics. For each individual interaction in Eq. (3.72) and the amplitude, these operators absorb dependencies on the polarizations as well as the angular parts $\hat{\boldsymbol{p}} \equiv \boldsymbol{p}/p$ of the momenta (similar $\hat{\boldsymbol{p}}'$ and $\hat{\boldsymbol{q}}$). For a general definition of the projectors and their properties, we refer to Appendix C. Let $\mathcal{J}^{ij}$ be an interaction or amplitude in Eq. (3.72). The partial wave decomposition then reads

$$\mathcal{J}^{ij}(\boldsymbol{p},\boldsymbol{q};E) \equiv \sum_J \sum_{L,L'} \mathcal{J}^{{}^3L_J,{}^3L'_J}(p,q;E)\; P^{ij}_{{}^3L_J,{}^3L'_J}(\hat{\boldsymbol{p}},\hat{\boldsymbol{q}})\,, \tag{3.74a}$$

$$\begin{aligned}
&= \mathcal{J}^{{}^3S_1,{}^3S_1}(p,q;E)\,\delta^{ij} \\
&\quad + \mathcal{J}^{{}^3D_1,{}^3S_1}(p,q;E)\,\frac{1}{\sqrt{2}}\left(\delta^{ij} - 3\hat{\boldsymbol{p}}^i\hat{\boldsymbol{p}}^j\right) + \mathcal{J}^{{}^3S_1,{}^3D_1}(p,q;E)\,\frac{1}{\sqrt{2}}\left(\delta^{ij} - 3\hat{\boldsymbol{q}}^i\hat{\boldsymbol{q}}^j\right) \\
&\quad + \mathcal{J}^{{}^3D_1,{}^3D_1}(p,q;E)\,\frac{1}{2}\left(\delta^{ij} - 3\left(\hat{\boldsymbol{p}}^i\hat{\boldsymbol{p}}^j + \hat{\boldsymbol{q}}^i\hat{\boldsymbol{q}}^j\right) + 9\hat{\boldsymbol{p}}^i\hat{\boldsymbol{q}}^j(\hat{\boldsymbol{p}}\cdot\hat{\boldsymbol{q}})\right) \\
&\quad + \cdots\,,
\end{aligned} \tag{3.74b}$$

where L (L') denotes the orbital angular momentum in the incoming (outgoing) channel. Note that the s-wave projector exhibits the simple form $P^{ij}_{{}^3S_1,{}^3S_1}(\hat{\boldsymbol{p}},\hat{\boldsymbol{q}}) = \delta^{ij}$ in our convention.[17] Thus, projections of the interactions $C_0\,\delta^{ij}$ and $\mathcal{J}_c(E)\,\delta^{ij}$ in Eq. (3.72) are trivial.

We aim at the calculation of the s-wave amplitude $T^{{}^3S_1,{}^3S_1}$. Through pion exchanges, it couples to the s-d-mixing amplitude $T^{{}^3D_1,{}^3S_1}$. We summarize these two amplitudes into the $J^P = 1^+$ vector

$$\vec{T}^{1^+}(p,q;E) \equiv \begin{pmatrix} T^{{}^3S_1,{}^3S_1} \\ T^{{}^3D_1,{}^3S_1} \end{pmatrix}(p,q;E)\,. \tag{3.75}$$

After projection, one obtains the equation system

$$\begin{aligned}
\vec{T}^{1^+}(p,p';E) &= -\underline{\underline{K}}^{1^+}(p,p';E)\cdot\vec{e}_1 \\
&\quad + \frac{1}{2\pi^2}\int_0^\Lambda \mathrm{d}q\,q^2\,\underline{\underline{K}}^{1^+}(p,q;E)\,\mathcal{G}_*^{(\mathrm{f})}(q;E)\cdot\vec{T}^{1^+}\left(q,p';E\right)\,,
\end{aligned} \tag{3.76}$$

---

[17] In Ref. [46], the projectors exhibit an additional factor $1/(4\pi)$.

which we regularize with a cutoff $\Lambda \geq q$. The dependence of the amplitude $T^{{}^3S_1,{}^3S_1}$ on Λ will be absorbed into the three-body force $C_0(\Lambda)$. In order to capture all relevant low-energy physics, we will choose $\Lambda \gg (2\mu_*\delta)^{1/2} \approx 117\,\mathrm{MeV}$. In Eq. (3.76), we define the interaction matrix

$$\underline{\underline{K}}^{1^+}(p,q;E) \equiv \begin{pmatrix} C_0(\Lambda) + V^{{}^3S_1,{}^3S_1} + \mathcal{J}_\mathrm{c} & V^{{}^3S_1,{}^3D_1} \\ V^{{}^3D_1,{}^3S_1} & V^{{}^3D_1,{}^3D_1} \end{pmatrix}(p,q;E) \tag{3.77}$$

and the D^{0*} $(\bar{D}^{0*})$ propagator function

$$\mathcal{G}_*^{(\mathrm{f})}(q;E) \equiv G_*^{(\mathrm{f})}\left(E - \frac{q^2}{2\mu_*}\right). \tag{3.78}$$

The partial wave components $V^{{}^3L_1,{}^3L_1'}$ of the pion exchange potential appearing in the interaction matrix are calculated in App. D.4. They read

$$V^{{}^3S_1,{}^3S_1}(p,q;E) = -\frac{1}{6}g^2 m_\pi\left[\xi\left(p^2+q^2\right)\hat{t}_0 + \left(\xi^2+1\right)pq\,\hat{t}_1\right]I^{(\cdot)}_{\pi;D,D}(p,q;E), \tag{3.79a}$$

$$V^{{}^3S_1,{}^3D_1}(p,q;E) = \frac{\sqrt{2}}{6}g^2 m_\pi\left[\xi\, q^2\,\hat{t}_0 + \left(\xi^2+1\right)pq\,\hat{t}_1 + \xi\, p^2\,\hat{t}_2\right]I^{(\cdot)}_{\pi;D,D}(p,q;E), \tag{3.79b}$$

$$V^{{}^3D_1,{}^3S_1}(p,q;E) = V^{{}^3S_1,{}^3D_1}(q,p;E), \tag{3.79c}$$

$$V^{{}^3D_1,{}^3D_1}(p,q;E) = -\frac{1}{3}g^2 m_\pi\left[\left(\xi^2+\frac{1}{10}\right)pq\,\hat{t}_1 + \xi\left(p^2+q^2\right)\hat{t}_2 + \frac{9}{10}pq\,\hat{t}_3\right]I^{(\cdot)}_{\pi;D,D}(p,q;E), \tag{3.79d}$$

with integral functions $\hat{t}_L\, I^{(\cdot)}_{\pi;D,D}(p,q;E) \equiv I^{(L)}_{\pi;D,D}(p,q;E)$ $(L \geq 0)$ defined in Appendix C.2. For large loop momenta $q \gg p,\, (m_\pi E)^{1/2}$, the s-wave component

$$V^{{}^3S_1,{}^3S_1}(p,q;E) = -\frac{1}{6}g^2 m_\pi\left[2\left(\xi^2+1\right) + \int_{-1}^{1}\mathrm{d}x\,\frac{\frac{1}{2\xi}\left(\xi^2-1\right)\left(p^2+q^2\right) - \left(\xi^2+1\right)m_\pi E}{\frac{1}{2\xi}\left(p^2+q^2\right) - m_\pi E + pq\,x - i\epsilon}\right] \tag{3.80a}$$

$$\xrightarrow{q\to\infty} -\frac{1}{6}g^2 m_\pi\left[2\left(\xi^2+1\right) + 2\left(\xi^2-1\right)\right] = -\frac{2}{3}g^2\frac{\mu_{D\pi}^2}{m_\pi} \equiv V^{(\infty)} \tag{3.80b}$$

approaches the constant $V^{(\infty)} \approx -2.72\,\mathrm{GeV}^{-2} < 0$.[18] The associated divergence in $\Lambda \to \infty$ can be cured by shifting the three-body force $C_0(\Lambda)$ by the amount $-V^{(\infty)}$ whenever pion exchanges are present; see Fig. 3.24.

Renormalization

The system in Eq. (3.76) can be solved after $T^{{}^3S_1,{}^3S_1}$ (and $T^{{}^3D_1,{}^3S_1}$) numerically. More precisely, we perform an exponential transformation $[0,\Lambda] \to [0,1]$ of the integration region putting emphasis onto momenta $q \ll \Lambda$ and then discretize the interval using Gaussian quadrature.

At this stage, however, we are not so much interested in the amplitudes themselves, but rather in their pole structure. In particular, for fixed binding energy $\delta_X > 0$ and cutoff Λ, we wish to adjust $C_0(\Lambda)$ such that the amplitudes exhibits a pole at

$$E_X \equiv (\delta - \delta_X) - i\,\frac{\Gamma_X(\delta_X)}{2}. \tag{3.81}$$

---

[18] In Eq. (3.80b), we used relations for the $I^{(l)}_{\pi;D,D}$ functions given in Appendix C.2.

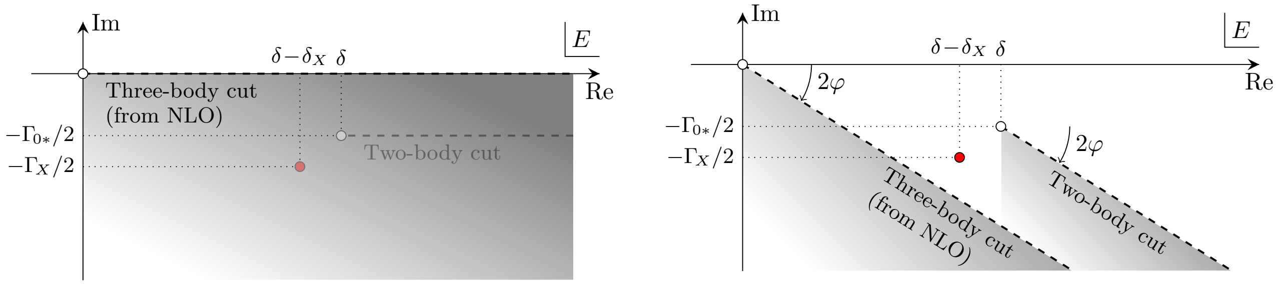

(a) (b)

Figure 3.17.: (a) From NLO, the integration kernel exhibits a three-body cut at $E=0$ along the real axis, stemming from dynamical pion interactions. The two-body cut, starting at $E_* = \delta - i\Gamma_{0*}/2$ (white dot), and the $X(3872)$ pole at $E_X = \delta - \delta_X - i\Gamma_X/2$ (red dot) are hidden on the second energy sheet, which lies below the first sheet (shaded area). (b) By rotating the loop momenta $q \to q\exp(-i\varphi)$ with $\varphi > 0$, we partially reveal the second energy sheet. That allows for a direct computation of the Fredholm determinant at the $X(3872)$ pole. Dimensions on the two sketches are not to scale.

More precisely, we demand a certain real part for the pole, while the imaginary part should come out as a prediction. Numerically, we determine the pole position E_X by searching the complex energy root of the Fredholm determinant of Eq. (3.76). This procedure is explained in detail in Appendix D.5.1. We expect that for $\Lambda \to \infty$, the width $\Gamma_X(\delta_X)$ does not depend on the cutoff. Similarly, the δ_X dependence of $C_0(\Lambda)$ will vanish as $\Lambda \to \infty$.

Note that the functions $I^{(l)}_{\pi;D,D}(p,q;E)$ in the partial wave components Eq. (3.79a)-(3.79d) exhibit logarithmic divergences for $E > 0$. That is a consequence of the possibility for exchanged pions to go on shell; see Eq. (3.73a). The logarithmic divergences introduce a three-body cut along the positive real energy axis to the amplitudes. This cut hides the $X(3872)$ pole and the two-body cut starting at E_*, which both lie on the second energy sheet; see Fig. 3.17(a). The cut also shows up in the Fredholm determinant which we need to calculate in the renormalization procedure. Thus, from NLO, when pion exchanges are included, we cannot directly access the pole position of the $X(3872)$ anymore.

We circumvent this obstacle by rotating the loop momenta into the complex plane, i.e., we let $q \to q\exp(-i\varphi)$ with small angle $\varphi > 0$. The rotated integration path, which now ends at $\Lambda\exp(-i\varphi) \in \mathbb{C}$, is followed by a closing arc back to $\Lambda \in \mathbb{R}$. This procedure partially reveals the second sheet as can be seen in Fig. 3.17(b). If we choose $2\varphi > \arg(E_X)$, we can directly access the $X(3872)$ pole at E_X.

3.3.2 Three-body momentum scales

In the following, we will decompose the 1^{++} Faddeev equation (3.76) into a LO part, some NLO contributions and negligible higher-order ingredients. This simplification procedure is based on a scaling analysis, which uses the typical momentum scales of the two- and three-body system. In Sec. 3.2, we already showed that the D^{0*} propagator can be expanded in the energy ratio $\chi_2 \sim \delta/(m_\pi/2) \approx 0.1$, where $\delta \approx 7\,\text{MeV}$ is an unnaturally small energy scale.

The three-body sector, however, exhibits *two* small energy scales, given by δ and also the binding energy $\delta_X = (-0.01 \pm 0.2)\,\text{MeV}$. These scales define the typical DD^* momenta[19]

$$P_* \equiv \sqrt{2\mu_*\delta} \approx 117\,\text{MeV}\,, \tag{3.82a}$$

$$P_X \equiv \sqrt{2\mu_*\delta_X} \in [0,\,20]\,\text{MeV}\,. \tag{3.82b}$$

---

[19] In Eq. (3.82b) and in the following we assume $\delta_X \geq 0$.

The P_X range given in Eq. (3.82b) follows from the experimental uncertainty of δ_X. Apparently, the two scales are strongly separated. Their ratio defines the small three-body expansion parameter

$$\chi_3 \equiv \frac{P_X}{P_*} = \sqrt{\frac{\delta_X}{\delta}} \leq 0.17\,. \tag{3.83}$$

XEFT counts powers of P_X and P_* collectively like a small momentum Q [102]. Our scheme improves upon this point by distinguishing the two scales. At NLO, we will encounter contributions from the charged DD^* threshold, which lies at an energy $\nu \approx 8\,\mathrm{MeV}$ above the $X(3872)$. This number is of the same order as δ. Consequently, we will count

$$\sqrt{\frac{\delta_X}{\nu}} \sim \chi_3 \tag{3.84}$$

in this thesis.

Given that the centroid of the experimental range $\delta_X \in [-0.21, 0.19]\,\mathrm{MeV}$ is close to 0, the actual value of δ_X is likely smaller than $0.19\,\mathrm{MeV}$. That means that the expansion parameter χ_3 is probably smaller than the upper bound 0.17 indicated in Eq. (3.83). It could even be of the same order as $\chi_2 = (K_{\mathrm{lo}}/K_{\mathrm{hi}})^2 \sim 0.3^2 = 0.09$. Thus, for simplicity, we count $\chi_3 \sim \chi_2$ in this thesis. This choice corresponds to the representative binding energy

$$(\delta_X)_{\chi_3=\chi_2} = \delta\chi_2^2 \sim 0.09^2\,\delta \sim 57\,\mathrm{keV}\,, \tag{3.85}$$

i.e., $(P_X)_{\chi_3=\chi_2} \approx 11\,\mathrm{MeV}$, which we will take as a reference value in calculations.

Let us emphasize that $P_* \approx 117\,\mathrm{MeV}$ represents a *low* momentum scale describable by our EFT, given that it results from the unnaturally small energy scale δ. Thus, it must not be misinterpreted as a breakdown point of the theory, even though the value of P_* is close to the relativistic momentum scale $K_{\mathrm{hi}} = m_\pi \approx 135\,\mathrm{MeV}$ of the two-body system. Nonrelativistic charm mesons dynamics can be neglected as long as momenta are much smaller than $m_D \approx 1865\,\mathrm{MeV}$. That is the case for momenta of the order P_*. A breakdown point for the DD^* system is expected to lie in the chiral breakdown regime $\Lambda_\chi \sim 500\,\mathrm{MeV}$ of HHχPT.

The reason why P_* seems large is that it is calculated using the three-body reduced mass $\mu_* \approx 965\,\mathrm{MeV}$. It is much larger than $\mu_{D\pi}$ with a ratio

$$r \equiv \frac{\mu_{D\pi}}{\mu_*} \approx 0.13 \sim \chi_3 \tag{3.86}$$

comparable to χ_3. Thus, one should not directly compare two- and three-body momenta in strongly mass-imbalanced systems. It is due to the small mass ratio that multi-pion exchanges will be negligible at NLO. We systematize such mass ratio suppressions by counting $r \sim \chi_3$ in this thesis.

3.3.3 $X(3872)$ width at LO

In Sec. 3.2 we showed that D^{0*} propagator corrections are suppressed by the narrowness parameter $\mathcal{N}$ and possibly powers of χ_2. Moreover, we claimed that pion exchanges involve powers of the small mass ratio $\mu_{D\pi}/\mu_*$ and charged meson contributions are suppressed by $(\delta_X/\nu)^{1/2}$. All these claims will be confirmed in the detailed NLO analysis below.

Let us use the short-hand notation

$$T_{00} \equiv T^{{}^3S_1,{}^3S_1} \tag{3.87}$$

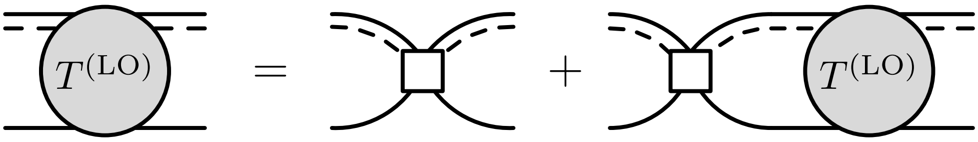

Figure 3.18.: Amplitude $T^{(\mathrm{LO})\,ij} = T_{00}^{(\mathrm{LO})}\delta^{ij}$ for the calculation of the $X(3872)$ width at LO.

in the following. The LO amplitude $T_{00}^{(\mathrm{LO})}$ can then be obtained by neglecting all suppressed ingredients of T_{00}. It is given by an iteration of the LO D^{0*} propagator $iG_*^{(\mathrm{LO})}$ of Eq. (3.61) alongside the three-body force C_0. The corresponding Faddeev equation is shown in Fig. 3.18.

Since we switched of pion exchanges in Fig. 3.18, the LO amplitude does not depend on relative momenta, but only on the energy. Moreover, the s-d-mixing component $T^{{}^3D_1,{}^3S_1}$ vanishes. The Faddeev equation can then be solved analytically. It reduces to the simple form

$$T_{00}^{(\mathrm{LO})}(E) = -C_0(\Lambda) + \frac{1}{2\pi^2}\int_0^\Lambda \mathrm{d}q\, q^2 \frac{C_0(\Lambda)}{E - \frac{q^2}{2\mu_*} - E_* + i\epsilon}\, T_{00}^{(\mathrm{LO})}(E), \tag{3.88a}$$

$$= -C_0(\Lambda)\Big[1 + 2\mu_* J_{3,0}^{(\Lambda)}\Big(-2\mu_*\,(E + i\epsilon - E_*)\Big)\, T_{00}^{(\mathrm{LO})}(E)\Big], \tag{3.88b}$$

with s-wave integral function $J_{3,0}^{(\Lambda)}$ given in Eq. (B.11f).

We obtain

$$T_{00}^{(\mathrm{LO})}(E) = -\left[C_0^{-1}(\Lambda) + \frac{\mu_*}{2\pi}\left(\frac{2}{\pi}\Lambda - \sqrt{2\mu_*\,(E_* - E - i\epsilon)} + \mathcal{O}\left(\Lambda^{-1}\right)\right)\right]^{-1}. \tag{3.89}$$

Renormalization can also be done analytically. By demanding a pole at $E = E_X$, one directly obtains

$$\Gamma_X^{(\mathrm{LO})} = \Gamma_{0*}\,, \tag{3.90a}$$

$$C_0^{(\mathrm{LO})\;-1}(\Lambda) = -\frac{\mu_*}{2\pi}\left(\frac{2}{\pi}\Lambda - \sqrt{2\mu_*\delta_X} + \mathcal{O}\left(\Lambda^{-1}\right)\right), \tag{3.90b}$$

if C_0 is chosen real. As stated above, the LO width is given by the full D^{0*} width, independently of δ_X.

By plugging Eq. (3.90b) into Eq. (3.89), we obtain the renormalized LO amplitude

$$T_{00}^{(\mathrm{LO})}(E) = -\frac{2\pi}{\mu_*}\left[\sqrt{2\mu_*\delta_X} - \sqrt{2\mu_*(E_* - E - i\epsilon)}\right]^{-1} \equiv \mathrm{reg} + \frac{Z^{(\mathrm{LO})}}{E - E_X^{(\mathrm{LO})} + i\epsilon}\,, \tag{3.91}$$

with LO pole position $E_X^{(\mathrm{LO})} = E_* - \delta_X$ and LO residue

$$Z^{(\mathrm{LO})} = \left[\left.\frac{\partial T_{00}^{(\mathrm{LO})\;-1}}{\partial E}\right|_{E=E_X}\right]^{-1} = -\frac{2\pi}{\mu_*^2}P_X\,. \tag{3.92}$$

Note that the residue is proportional to the small momentum $P_X = (2\mu_*\delta_X)^{1/2}$ defined in Eq. (3.82b). This observation implies that all corrections to the LO $X(3872)$ pole will at least involve one suppression factor P_X; see below.

The LO amplitude resembles a zero-range s-wave amplitude of two point-like particles, but with complex rest mass E_*. Thus, at LO, the substructure of the vector mesons, reflects itself only in the constant width. In contrast to the result of Braaten and Lu in Ref. [44], the width is energy-independent. The energy dependence, which is given by the full D^{0*} self-energy, will be introduced at NLO through self-energy corrections in the D^{0*} propagator.

3.3.4 Scaling analysis and NLO width corrections

Given the momentum scales of the two- and three-body sectors, we are now in the position to demonstrate the NLO nature of self-energy corrections, pion exchanges, and charged meson states for the $X(3872)$ width. In principle, these corrections do not only modify the width, but also the binding energy of the $X(3872)$ pole. Our renormalization scheme, however, keeps the real part of the pole fixed in each calculation by readjusting the three-body force. Consequently, we focus explicitly on the width in the subsequent analysis.

In this thesis, we calculate the width only up to NLO. N^{2}LO corrections can be neglected for two reasons. Firstly, the small expansion parameters $\chi_2 \sim \chi_3 \lesssim 0.13$ give rise to a fast convergence of the power counting scheme. NLO predictions are thus already much more accurate compared to EFTs with larger expansion parameters. Secondly, N^{2}LO corrections $\sim 0.13^2 \lesssim 2\,\%$ are expected to be of the order of the experimental uncertainties of input parameters like the charged width Γ_{c*} ($\sim 3\,\%$). For this reason, a detailed N^{2}LO does not yield any predictive power. In order to demonstrate the convergence of the power counting scheme, we show that partial N^{2}LO corrections from the d-wave channel are of expected size.

a) Power counting

We investigate diagrammatic corrections to the LO system of Fig. 3.18 in a comprehensive power counting analysis. The power counting attributes certain mass and momentum factors to propagators, vertices, integral measures, etc. Given that *two* low-momentum scales P_X and P_* exist in the three-body system, we investigate the overall scaling of a loop integral for loop momenta in both regions, i.e., for $q \sim P_X$ and $q \sim P_*$.

In nonrelativistic EFTs, energies are typically counted like squared momenta. That is a consequence of the nonrelativistic dispersion relation. Consequently, for a relative DD^* four-momentum $q^\mu = (q^0, \boldsymbol{q})$, we count integral measures $\mathrm{d}q^4 \sim q^0 q^3 \sim q^5/(2\mu_*)$, where $q \equiv |\boldsymbol{q}|$. For clarity, however, we won't keep track of reduced mass factors like $2\mu_*$ in the power counting since they can be factored out. Charm meson propagators are then counted like

$$G_D \sim G_*^{(\mathrm{LO})} \sim q^{-2} \quad (q \in \{P_X, P_*\})\,. \tag{3.93}$$

For pion propagators, the governing mass factor is $2\mu_{D\pi} \ll 2\mu_*$. That can be seen from the pion exchange potential in Eq. (3.68). Factoring out this factor effectively introduces an overall suppression of $r = \mu_{D\pi}/\mu_*$ for each exchanged pion. Moreover, the pion propagator depends on both the incoming and outgoing relative momenta p_{in} and p_{out} [p and q in Eq. (3.68)], such that we count

$$G_\pi \sim \frac{r}{p_{\mathrm{in}}^2 + p_{\mathrm{out}}^2} \quad (p_{\mathrm{in}}, p_{\mathrm{out}} \in \{P_X, P_*\})\,. \tag{3.94}$$

In Eq. (3.56) of the two-body sector, we expressed the magnitude of the coupling g in terms of two-body quantities $K_{\mathrm{lo}}, K_{\mathrm{hi}}$, and $\mu_{D\pi}$. In the three-body sector, however, one has to do so using the quantities P_X, P_*, and μ_*. Numerically, we find $1/(2\mu_* g^2) \approx 0.8\, P_*\, \mu_*/(2\pi)$. Thus, we effectively count

$$g \sim P_*^{-1/2}\,. \tag{3.95}$$

Let us, for illustration, apply the above power counting scheme to the two-pion exchange diagram in Fig. 3.19. In this specific diagram, the momentum factors of the four vertices cancel with those of the pion exchange propagators, e.g., $(p+q)^2/(p^2+q^2) \sim 1$ on the left-hand side. For fixed q, one then obtains the expression $g^4 r^2 q$ with $g^4 \sim P_*^{-2}$. We now pick up contributions from the two low-momentum regions by formally summing over $q \in \{P_X, P_*\}$. That yields an overall scaling $r^2 P_*^{-1}$ of the diagram. Certainly, this simple scheme yields only a rough estimation of the true integral value. Still, we will see that it correctly predicts the power counting order of the pionic NLO contributions and even of the N^{2}LO contribution from DD^* d-wave states.

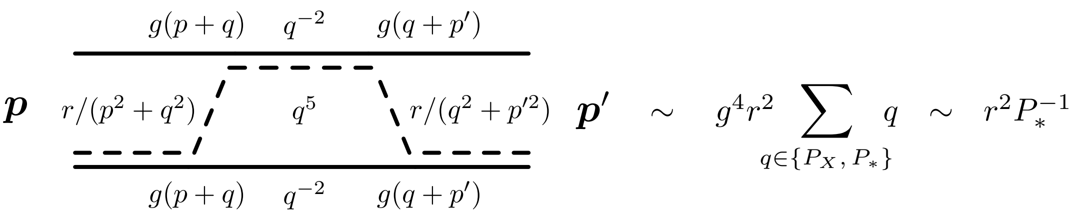

Figure 3.19.: Exemplary power counting of a two-pion exchange diagram.

b) Diagrammatic width estimation

Let $\mathcal{J}$ be an arbitrary interaction other than C_0. In particular, $\mathcal{J}$ could either be an effective $D^0\bar{D}^{0*}$ + c.c. interaction or a certain D^{0*} ($\bar{D}^{0*}$) propagator correction. Resumming $\mathcal{J}$ to all orders leads to a shift in the LO pole position, i.e., $E_X^{(\mathrm{LO})} = \delta - \delta_X - i\Gamma_{0*}/2 \to E_X^{(\mathcal{J})} \equiv E_X^{(\mathrm{LO})} + \Delta E_X^{(\mathcal{J})}$. Similarly, the LO residue of Eq. (3.92) gets shifted like $Z^{(\mathrm{LO})} \to Z^{(\mathcal{J})} \equiv Z^{(\mathrm{LO})} + \Delta Z^{(\mathcal{J})}$. Our goal is now to determine these shifts diagrammatically for given $\mathcal{J}$.

In the first step, we compare the new amplitude

$$T_{00}^{(\mathcal{J})} = \mathrm{reg} + \frac{Z^{(\mathcal{J})}}{E - E_X^{(\mathcal{J})} + i\epsilon} = \mathrm{reg} + \frac{Z^{(\mathrm{LO})} + \Delta Z^{(\mathcal{J})}}{E - E_X^{(\mathrm{LO})} + i\epsilon} + \frac{\left(Z^{(\mathrm{LO})} + \Delta Z^{(\mathcal{J})}\right)\Delta E_X^{(\mathcal{J})}}{\left(E - E_X^{(\mathrm{LO})} + i\epsilon\right)^2} + \cdots \tag{3.96}$$

with the generic form

$$T_{00}^{(\mathcal{J})} \equiv T_{00}^{(\mathrm{LO})} + \mathrm{reg} + a^{(\mathcal{J})}\, T_{00}^{(\mathrm{LO})} + b^{(\mathcal{J})} \left(T_{00}^{(\mathrm{LO})}\right)^2 + \cdots, \tag{3.97}$$

where “reg” stands for terms regular at $E_X^{(\mathrm{LO})}$. That yields the shifts

$$\Delta E_X^{(\mathcal{J})} = Z^{(\mathrm{LO})} \frac{b^{(\mathcal{J})}}{1 + a^{(\mathcal{J})}}, \tag{3.98a}$$

$$\Delta Z^{(\mathcal{J})} = Z^{(\mathrm{LO})}\, a^{(\mathcal{J})}. \tag{3.98b}$$

The coefficients $a^{(\mathcal{J})}, b^{(\mathcal{J})}$, etc. summarize $\mathcal{J}$-dependent parts of the different diagrams contributing to $T_{00}^{(\mathcal{J})}$, evaluated at $E = E_X^{(\mathrm{LO})}$. For example, the term $b^{(\mathcal{J})}\left(T_{00}^{(\mathrm{LO})}\right)^2$ in Eq. (3.97) stands for all diagrams induced by the interaction $\mathcal{J}$ that include exactly two powers of the LO amplitude.

In Ref. [107], Jansen *et al.* used the above relations to determine NLO contributions to the binding energy δ_X in XEFT. Our renormalization scheme, however, fixes δ_X by resumming an appropriate correction term $\Delta C_0^{(\mathcal{J})}$ alongside $\mathcal{J}$, such that $\mathrm{Re}\,\Delta E_X^{(\mathcal{J})} = 0$ at every order.

Note that the coefficients $a^{(\mathcal{J})}, b^{(\mathcal{J})}$ generally dependent on momenta. At the same time, Eq. (3.98a) demands that the combination $b^{(\mathcal{J})}/(1 + a^{(\mathcal{J})})$ be just a number. In Ref. [108], this property of the coefficients was explicitly checked for XEFT at NLO. More generally, however, it follows from the momentum independence of the LO amplitude; see Eq. (3.91). Since $T_{00}^{(\mathrm{LO})}$ depends only on E, two loop momentum integrals connected by $T_{00}^{(\mathrm{LO})}$ always factorize. Omitting the energy dependence of $T_{00}^{(\mathrm{LO})}$, we may write

$$\left[\left(1 + a^{(\mathcal{J})}\right) T_{00}^{(\mathrm{LO})}\right](p, p') = f_{\mathrm{in}}^{(\mathcal{J})}(p)\, T_{00}^{(\mathrm{LO})}\, f_{\mathrm{out}}^{(\mathcal{J})}(p') = f_{\mathrm{in}}^{(\mathcal{J})}(p) f_{\mathrm{out}}^{(\mathcal{J})}(p') \times T_{00}^{(\mathrm{LO})}, \tag{3.99a}$$

$$\left[b^{(\mathcal{J})}\left(T_{00}^{(\mathrm{LO})}\right)^2\right](p, p') = f_{\mathrm{in}}^{(\mathcal{J})}(p)\, T_{00}^{(\mathrm{LO})}\, \bar{b}^{(\mathcal{J})}\, T_{00}^{(\mathrm{LO})}\, f_{\mathrm{out}}^{(\mathcal{J})}(p') = f_{\mathrm{in}}^{(\mathcal{J})}(p) f_{\mathrm{out}}^{(\mathcal{J})}(p') \times \bar{b}^{(\mathcal{J})}\left(T_{00}^{(\mathrm{LO})}\right)^2. \tag{3.99b}$$

The functions $f_{\mathrm{in}}^{(\mathcal{J})}(p)$, $f_{\mathrm{out}}^{(\mathcal{J})}(p')$ dress incoming and outgoing channels with interactions $\mathcal{J}$. Moreover, due to integral factorization, the intermediate factor $\bar{b}^{(\mathcal{J})}$ is just a number. By comparison of Eqs. (3.99a)-(3.99b), one then finds immediately that $b^{(\mathcal{J})}/(1 + a^{(\mathcal{J})}) = \bar{b}^{(\mathcal{J})}$ is independent of momenta.

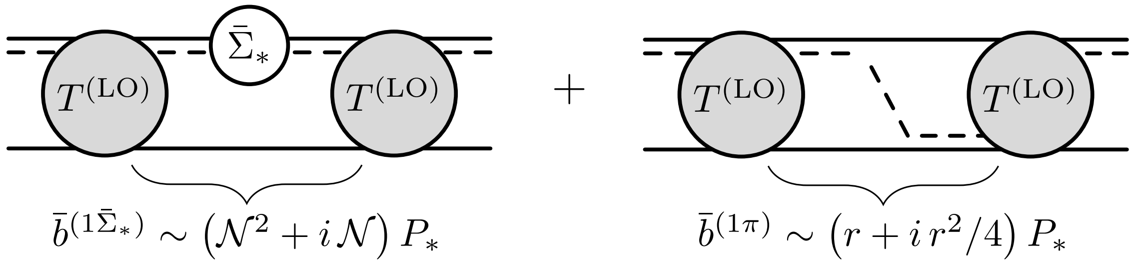

(a) (b)

Figure 3.20.: Pion interaction diagrams contributing to Γ_X at NLO: The width shift due to single self-energy corrections is proportional to diagram (a). Diagram (b) determines the shift due to one-pion exchanges. The indicated scalings are derived in the text.

It follows that the width shift induced by $\mathcal{I}$ is given by

$$\Delta\Gamma_X^{(\mathcal{I})} = -2\,\mathrm{Im}\,\Delta E_X^{(\mathcal{I})} = -2\,Z^{(\mathrm{LO})}\,\mathrm{Im}\,\bar{b}^{(\mathcal{I})}\,. \tag{3.100}$$

The expression $\bar{b}^{(\mathcal{I})}$ in Eq. (3.100) can be obtained by considering all diagrams with interactions $\mathcal{I}$ *between* two LO amplitudes, like in Fig. 3.20. As proposed above, all corrections to the width are at least proportional to the small LO residue, i.e., to $P_X = (2\mu_*\delta_X)^{1/2}$. For a given interaction $\mathcal{I}$, we now conduct the following steps:

1. Identify all diagrams induced by $\mathcal{I}$ that contribute to $\bar{b}^{(\mathcal{I})}\,(T_{00}^{(\mathrm{LO})})^2$.
2. Determine their scaling using the power counting above.
3. Estimate $\Delta\Gamma_X^{(\mathcal{I})}$ using Eq. (3.100).

c) Propagator corrections

In order to estimate corrections to the LO width from D^{0*} ($\bar{D}^{0*}$) self-interactions, we make use of the expansion derived in Eq. (3.62b). The most important such interaction is given by the self-energy insertions $\bar{\Sigma}_*$ of Eq. (3.63).

The width shift $\Delta\Gamma_X^{(1\bar{\Sigma}_*)}$ induced by single self-energy insertions[20] is proportional to the diagram shown in Fig. 3.20(a), evaluated at $E = E_X^{(\mathrm{LO})} = E_* - \delta_X$; see above. Let q be the loop momentum. In the kinematics of Fig. 3.20(a) the low-momentum regions $q \sim P_X$ and $q \sim P_*$ correspond to D^{0*} ($\bar{D}^{0*}$) center-of-mass energies

$$E_{\mathrm{cm}} = E_X^{(\mathrm{LO})} - \frac{q^2}{2\mu_*} \approx \begin{cases} E_*\,, & q \sim P_X \\ 0\,, & q \sim P_* \end{cases}\,. \tag{3.101}$$

In these two E_{cm} regions, the self-energy correction $[\bar{\Sigma}_* G_*^{(\mathrm{LO})}](E_{\mathrm{cm}}) \sim \mathcal{N}^2 + i\mathcal{N}$ is suppressed by powers of the narrowness parameter $\mathcal{N} = \Gamma_{D^0\pi^0}/(2\delta) \approx 0.0025$; see Sec. 3.2. The two remaining propagators and the integral measure in Fig. 3.20(a) contribute a factor q, such that the main contribution to the integral stems from $q \sim P_*$. We obtain the overall scaling $\bar{b}^{(1\bar{\Sigma}_*)} \sim (\mathcal{N}^2 + i\mathcal{N})P_*$. That leads to

$$\Delta\Gamma_X^{(1\bar{\Sigma}_*)} = -2\,Z^{(\mathrm{LO})}\,\mathrm{Im}\,\bar{b}^{(1\bar{\Sigma}_*)} \sim 2\,P_X\,\mathcal{N}P_* = 2\,\frac{P_X}{P_*}\,\mathcal{N}P_*^2 \sim 2\,\chi_3\,\mathcal{N}\delta \sim \chi_3\,\Gamma_X^{(\mathrm{LO})}\,, \tag{3.102}$$

---

[20] The term “single” means that we discard diagrams with two or more subsequent self-energy insertions.

where we used the relations $Z^{(\mathrm{LO})} \sim P_X$ [Eq. (3.92)], $\delta \sim P_*^2$ [Eq. (3.82a)], $P_X/P_* = \chi_3$ [Eq. (3.83)], and $2\mathcal{N}\delta = \Gamma_{D^0\pi^0} \sim \Gamma_{0*} = \Gamma_X^{(\mathrm{LO})}$ [Eq. (3.57)]. Thus, we expect single self-energy corrections to modify the width at NLO in the $\chi_2 \sim \chi_3$ expansion.

The sign of the width shift can also be inferred from Eq. (3.100). After performing the q^0 integral, we can symbolically write $\operatorname{sign} \bar{b}^{(1\bar{\Sigma}_*)} = -\operatorname{sign} \operatorname{Im}[G_*^{(\mathrm{LO})}\,\bar{\Sigma}_*\,G_*^{(\mathrm{LO})}]$. For $E = E_X^{(\mathrm{LO})}$, we have $G_*^{(\mathrm{LO})} < 0$. Moreover, the self-energy correction has a negative imaginary part; see Fig. 3.13. It follows that the width correction is negative decreases the overall width.

Let us note that the integral $\bar{b}^{(1\bar{\Sigma}_*)}$ can in fact also be obtained analytically. We perform this calculation in Appendix D.6. Neglecting higher powers in $\mathcal{N}$ and χ_3, the analytic result for the width shift is $\Delta\Gamma_X^{(1\bar{\Sigma}_*)} = -3\chi_3\,\Gamma_{D^0\pi^0}$. This expression confirms the scaling and sign predictions above.

The imaginary parts of all higher-order propagator corrections (including subsequent self-energy insertions) are further suppressed by powers of χ_2; see Sec. 3.2. They can safely be neglected at NLO. Relativistic corrections to the propagator are even more suppressed; see Appendix D.3.

d) Pion exchanges

Three-body $D^0\bar{D}^0\pi^0$ dynamics does not only modify the $X(3872)$ width through self-energy insertions $\bar{\Sigma}_*$, but also through pion exchanges between DD^* states. The modification caused by one-pion exchange interactions is governed by the two-loop integral in Fig. 3.20(b). Let q^μ and s^μ be the four-momenta of the left-hand and right-hand loop, respectively. In the above power counting, the pion propagator scales like $G_\pi \sim r/(q^2+s^2)$ with $r = \mu_*/\mu_{D\pi}$. Moreover, the vertices contribute two factors of $g(q+s)$ with $g \sim P_*^{-1/2}$. Together with the charm meson propagators ($\sim q^{-4}s^{-4}$) and the integral measures ($\sim q^5s^5$), one obtains an overall product $rqsP_*^{-1}$. The absolute value of the integral is thus again governed by the region $q \sim P_* \sim s$ and we find $|\bar{b}^{1\pi}| \sim rP_*$.

The imaginary part of the integral, however, turns out to be much smaller than the absolute value. The reason is that it only occurs when the pion goes on shell. Thus, not all regions of the two integrals contribute to the width. The on-shell condition can be read off from Eq. (3.73b). For the given loop momenta, one finds the restriction

$$x = \frac{\boldsymbol{q}\cdot\boldsymbol{s}}{qs} = \frac{m_\pi}{qs}\left(E - \frac{q^2+s^2}{2\mu_{D\pi}}\right) \sim \frac{r\,P_*^2 - q^2 - s^2}{2\,qs} \in [-1,\,1]\,, \tag{3.103}$$

with $m_\pi \sim \mu_{D\pi}$. This condition is not fulfilled for the option $P_X \sim q \ll s \sim P_*$ or vice versa, because $x < 1$ in this case. Apparently, on-shell pions require $q \sim s$. For small loop momenta $q \sim s \gtrsim r^{1/2}P_*/2 \approx 2P_X$, one obtains $x \lesssim +1$. The overall scaling of the imaginary part in this region is then $rqsP_*^{-1} \sim r^2P_*/4$. In the region $q \sim s \sim P_*$, which was responsible for the overall scaling of the absolute value, one instead finds $x \approx -1$. This antiparallel configuration of $\boldsymbol{q}$ and $\boldsymbol{s}$ leads to a near cancellation of the two vertices in the pion exchange potential in Eq. (3.68). For $\boldsymbol{q} = -\boldsymbol{s}$, it is proportional to the suppression factor $(1-\xi)^2 \approx r^2/4$. For this reason, the region $q \sim s \sim P_X$ contributes the largest imaginary part and we find $\bar{b}^{(1\pi)} \sim (r + ir^2/4)P_*$. We conclude that the width shift caused by one-pion exchange scales like

$$\Delta\Gamma_X^{(1\pi)} = -2\,Z^{(\mathrm{LO})}\operatorname{Im}\bar{b}^{(1\pi)} \sim P_X\,\underbrace{(r^2/4)}_{\approx 1.7\,\mathcal{N}}\,P_* \sim \chi_3\,\mathcal{N}\delta \sim \chi_3\,\Gamma_X^{(\mathrm{LO})}/2\,, \tag{3.104}$$

which is an NLO correction.

The sign of the shift can be inferred as follows. Firstly, the pion propagator produces a negative imaginary part, which follows from the $+i\epsilon$ prescription. Secondly, the product of the two pion vertices is always negative $[(-g)\cdot(+g) = -g^2]$. Together with the remaining phase factors $\pm i$, one obtains $\operatorname{sign}\Delta\Gamma_X^{(1\pi)} = +1$. The fact that this width shift is positive will lead to a near cancellation with the negative self-energy correction $\Delta\Gamma_X^{(1\bar{\Sigma}_*)}$.

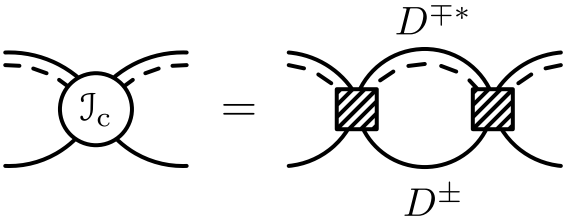

Figure 3.21.: Effective $D^0\bar{D}^{0*}$ + c.c. interaction $-i\,\mathcal{J}_c(E)\,\delta^{ii'}$ for the leading contribution of intermediate charged states D^+D^{-*} + c.c.: The shaded vertex $-i\tilde{C}_0\delta^{ii'}$ is defined in Eq. (3.105).

Due to the small mass ratio r occurring in each pion propagator, subsequent pion exchanges could be neglected at NLO. This observation confirms the perturbative nature of pion exchanges for the $X(3872)$ stated in Ref. [102]. In a strict EFT sense, one has to discard such multi-pion exchanges in the Faddeev amplitude. Doing so, however, requires an explicit calculation of the integral in Fig. 3.20(b), which is much more involved than the one of Fig. 3.20(a). For convenience, we keep the pion exchange potential as is in the integration kernel. This procedure resums partial contributions of N^{2}LO or even higher orders. However, given that r is very small, our NLO predictions should not be spoiled. Intermediate d-wave contributions, however, will be discarded at NLO since they involve at least two pion exchanges (N^{2}LO).

We note that relativistic corrections to the pion exchange propagator enter at N^{2}LO; see Appendix D.3. They will be neglected in this thesis.

e) Charged meson contributions

So far, we have neglected contributions from the charged threshold D^+D^{-*} + c.c. to the Faddeev amplitude. In Ref. [46], Baru *et al.* calculated such contributions by iterating charged pion exchanges between the DD^* states to all orders. However, for a single charged state to occur in the Faddeev equations, already two charged pion exchanges are needed. Just as for neutral ones, each such exchange introduces a mass suppression factor $\sim r$. It follows that charged pions can be neglected at NLO in our power counting.

Instead of iterating charged pion exchanges, we introduce a contact force $\tilde{C}_0$ directly connecting neutral and charged DD^* combinations in the $C = +$ channel. Such an effective three-body force was also used in Ref. [46] to renormalize the charged pion exchange part. The effective $D^0\bar{D}^{0*}$ + c.c. interaction $-i\mathcal{J}_c(E)$ entering the Faddeev equation (3.72) is then given by a single charged meson bubble as shown in Fig. 3.21. This perturbative treatment of charged mesons has several advantages. Firstly, we do not have to introduce an additional scattering channel, which keeps the kernel matrix small. Secondly, we will see that the system becomes renormalizable for arbitrary cutoffs, which was not the case in Ref. [46].

We follow the lines of Baru *et al.* in demanding that the contact force $\tilde{C}_0$ be isospin symmetric to the term C_0 in the neutral sector. It follows, that $\tilde{C}_0$ involves a factor of 2 compared to C_0 [46]. However, recall that C_0 contains a counterterm $-V^{(\infty)} = 2/3\, g^2\mu_{D\pi}^2/m_\pi$ [see (3.80b)] whenever neutral pion exchanges enter the calculation. Such a counterterm must not be part of $\tilde{C}_0$ since charged pions are excluded. Consequently, we subtract the counterterm in the definition

$$\tilde{C}_0 \equiv 2\left(C_0 + V^{(\infty)}\right). \tag{3.105}$$

In order to calculate the diagram in Fig. 3.21, we need to write down propagators for the charged charm mesons first. Kinetic and rest masses for these particles are given in Table 3.1. For the charged pseudoscalars $D^\pm$, we find

$$iG_{D^+}\left(k^0, \boldsymbol{k}\right) = i\left[k^0 - \frac{\boldsymbol{k}^2}{2(m_D + \Delta m_{c,\pi})} - \Delta m_{c,D}\right]^{-1}. \tag{3.106}$$

The charged vector mesons $D^{\pm*}$ are constructed as p-wave resonances similar to the neutral ones. as discussed above, we may apply the p-wave power counting developed in Sec. 3.2 also to the charged two-body systems. The self-energy loops and higher-order $D\pi$ are then strongly subleading for $D\pi$ center-of-mass energies $\sim \delta$. Thus, we write

$$iG_{*,\mathrm{c}}^{(\mathrm{LO})}\left(p^0, \boldsymbol{p}\right) = i\left[p^0 - \frac{\boldsymbol{p}^2}{2(M_{D\pi} + \Delta m_{\mathrm{c},\pi})} - (\delta + \Delta m_{\mathrm{c},D^*})\right]^{-1} \tag{3.107}$$

for the LO charged vector meson propagator. The effective interaction is then proportional to the s-wave integral function $J_{3,0}^{(\Lambda)}$ of Appendix B.2 like

$$\begin{aligned}
\mathcal{J}_\mathrm{c}(E) &= -\tilde{C}_0^2\, 2\mu_{*,\mathrm{c}}\, J_{3,0}^{(\Lambda)}\Big(2\mu_{*,\mathrm{c}}\,(\delta + \nu - E - i\epsilon)\Big) && \text{(3.108a)}\\
&= -\tilde{C}_0^2\,\frac{\mu_{*,\mathrm{c}}}{2\pi}\left(\frac{2}{\pi}\Lambda - \sqrt{2\mu_{*,\mathrm{c}}\,(\delta + \nu - E - i\epsilon)} + \mathcal{O}\left(\Lambda^{-1}\right)\right), && \text{(3.108b)}
\end{aligned}$$

where $\nu = \Delta m_{\mathrm{c},D} + \Delta m_{\mathrm{c},D^*} \approx 8\,\mathrm{MeV}$ and the D^+D^{-*} reduced mass $\mu_{*,\mathrm{c}} \approx 967\,\mathrm{MeV}$ is defined using the kinetic masses indicated in Eqs. (3.106)-(3.107). In calculations we neglect vanishing terms $\mathcal{O}\left(\Lambda^{-1}\right)$ in Eq. (3.108b).

The width shift caused by $\mathcal{J}_\mathrm{c}(E)$ can be calculated analytically, which is done in Appendix D.6. The result

$$\Delta\Gamma_X^{(\mathcal{J}_\mathrm{c})} \approx \underbrace{-\sqrt{\frac{\mu_{*,\mathrm{c}}}{\mu_*}}\left(1 + 2\frac{1+\sqrt{1+16\,\mu_{*,\mathrm{c}}/\mu_*}}{16\,\mu_{*,\mathrm{c}}/\mu_*}\right)^{-1}}_{\approx -0.6}\sqrt{\frac{\delta_X}{\nu}}\,\Gamma_{0*} \tag{3.109}$$

lowers the width. This observation is in line with the findings of Baru *et al.* [46]. Due to $\nu \sim \delta$, the ratio $(\delta_X/\nu)^{1/2}$ scales like χ_3. Consequently, charged mesons have to be included at NLO.

Summary

We conclude that NLO contributions to the $X(3872)$ width are given by self-energy corrections $\bar{\Sigma}_*$ to the D^{0*} propagator, pion exchanges between $D^0\bar{D}^0$ + c.c. s-wave states, and the charged meson loop. We may now write done the final NLO Faddeev equation. It can be obtained from Eq. (3.76) by switching off the d-wave parts of the pion exchange potential and replacing the full propagator function $\mathcal{G}_*^{(\mathrm{f})}(q;\,E)$ by its NLO form

$$\mathcal{G}_*^{(\mathrm{NLO})}(q;\,E) \equiv \frac{1}{E - \frac{q^2}{2\mu_*} - E_* + i\epsilon}\left(1 + \frac{\bar{\Sigma}_*\left(E - \frac{q^2}{2\mu_*}\right)}{E - \frac{q^2}{2\mu_*} - E_* + i\epsilon}\right). \tag{3.110}$$

The final NLO Faddeev equation then reads

$$\begin{aligned}
T_{00}^{(\mathrm{NLO})}\left(p, p';\,E\right) = &-\left(C_0(\Lambda) + V^{{}^3S_1,{}^3S_1}\left(p, p';\,E\right) + \mathcal{J}_\mathrm{c}(E)\right)\\
&+ \frac{1}{2\pi^2}\int_0^\Lambda \mathrm{d}q\, q^2\left(C_0(\Lambda) + V^{{}^3S_1,{}^3S_1}(p, q;\,E) + \mathcal{J}_\mathrm{c}(E)\right)\mathcal{G}_*^{(\mathrm{NLO})}(q;\,E)\; T_{00}^{(\mathrm{NLO})}\left(q, p';\,E\right).
\end{aligned} \tag{3.111}$$

Recall that along our derivation so far, we have made use of several experimental input parameters, which we arranged in Fig. 3.22 and Table 3.3. In the following, we briefly summarize these parameters and the predictions our theory makes.

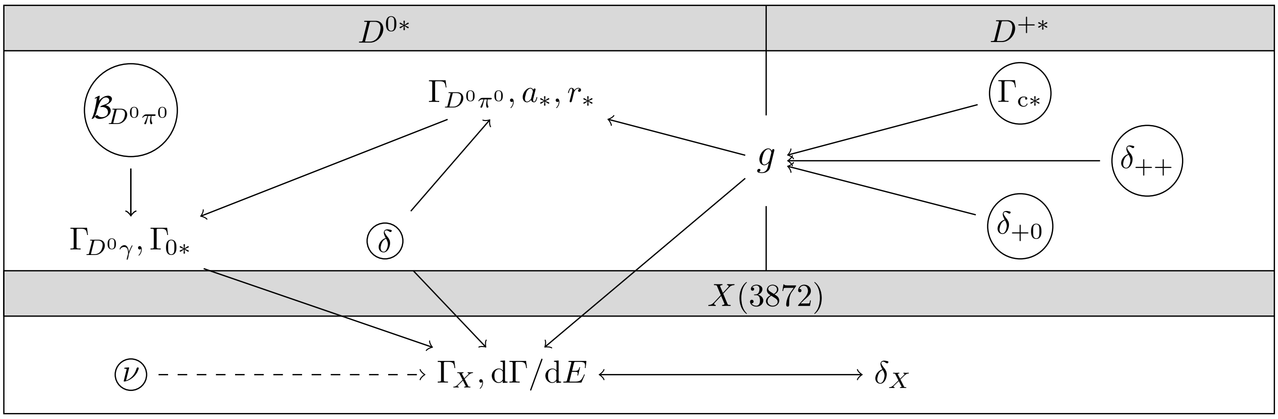

Figure 3.22.: Input parameters (circled) and predictions (uncircled) in the two-body sectors (D^{0*}, D^{+*}) and the three-body sector ($X(3872)$). The meaning of each parameter is explained in the text. From LO (~ 1) to NLO ($\sim \chi_2 \sim \chi_3 \lesssim 0.13$), there is only one additional parameter ν.

Table 3.3.: Input parameter values taken from Ref. [36]. The expansion parameters are $\chi_2 \sim \chi_3 \lesssim 0.13$.

Order	D^{0*}	D^{+*}	$X(3872)$
LO [$\mathcal{O}(1)$]	$\delta = 7.04(3)\,\mathrm{MeV}$	$\Gamma_{c*} = 82(2)\,\mathrm{keV}$	[$\delta_X < 0.2\,\mathrm{MeV}$]
	$\mathcal{B}_{D^0\pi^0} = 64.7(9)\,\%$	$\delta_{+0} = 5.855(2)\,\mathrm{MeV}$	
		$\delta_{++} = 5.69(8)\,\mathrm{MeV}$	
NLO [$\mathcal{O}(\chi_2 \sim \chi_3)$]	–	–	$\nu = 8.16(9)\,\mathrm{MeV}$

Initially, we used the charged decay width $\Gamma_{c*} = \Gamma[D^{+*}]$ and the resonance energies δ_{++}, δ_{+0} to determine the coupling g. Its value is in agreement with recent lattice results; see Sec. 3.2. Assuming isospin symmetry, we then inferred from g and the resonance energy δ the neutral pionic decay width $\Gamma_{D^0\pi^0}$ and the $D^0\pi^0$ ($\bar{D}^0\pi^0$) threshold parameters a_*, r_*. Afterwards, the radiative width $\Gamma_{D^0\gamma}$ and total width $\Gamma_{0*} = \Gamma[D^{0*}]$ were inferred from $\Gamma_{D^0\pi^0}$ using the branching ratio $\mathcal{B}_{D^0\pi^0}$. In the renormalization of the three-body system, neither of these two-body values changes from LO to NLO. The reason is that at NLO the D^{0*} ($\bar{D}^{0*}$) propagator expansion does not introduce new parameters; see Eq. (3.62b).

Already at LO, the three-body system requires a value for the binding energy δ_X of the $X(3872)$. Since its physical value is not precisely known, all three-body predictions will be functions of δ_X. Given a fixed δ_X, we will be able to infer the width Γ_X. At NLO, we also need the mass difference ν between the neutral and charged DD^* thresholds as input. Later, we will also predict the line shape $\mathrm{d}\Gamma/\mathrm{d}E$ of the $X(3872)$ in $D^0\bar{D}^0\pi^0$ production.

3.3.5 Numerical renormalization and width predictions

In this section, we numerically renormalize the three-body system up to NLO ($\sim \chi_2 \sim \chi_3$) using the three-body force $C_0(\Lambda)$. In doing so, we obtain predictions for the $X(3872)$ width $\Gamma_X(\delta_X)$, which verify the power counting analysis of the previous section. NLO corrections to the LO system of Fig. 3.18 are given by single D^{0*} ($\bar{D}^{0*}$) self-energy corrections, neutral pion exchanges, and the charged meson loop. The system will be renormalizable for arbitrary cutoffs Λ. To illustrate the convergence of the power counting scheme, we will moreover demonstrate that the influence of D^0D^{0*} d-wave states is indeed of N^{2}LO. Other corrections like higher-order self-energy insertions, charged pion exchanges, relativistic effects, etc. are neglected at NLO.

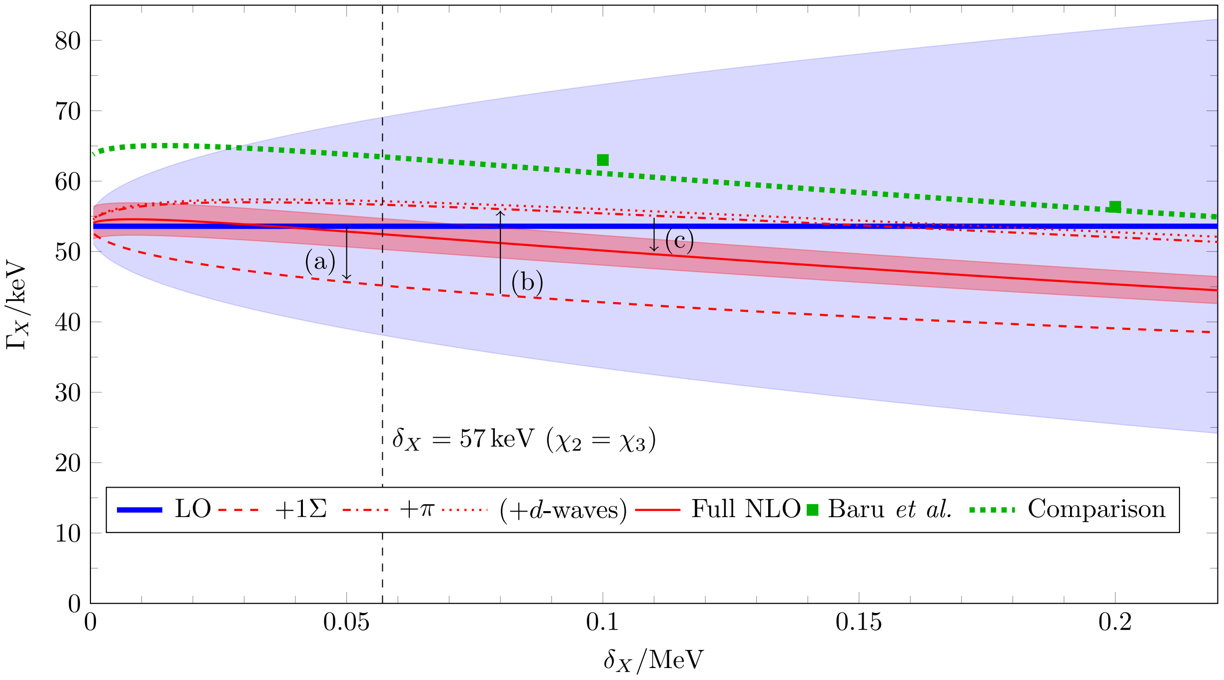

Figure 3.23.: Width Γ_X as a function of δ_X up to NLO compared to the results of Baru *et al.* in Ref. [46]. The three arrows indicate the NLO corrections (a) $\Delta\Gamma_X^{(1\Sigma)}$, (b) $\Delta\Gamma_X^{(\pi)}$ and (c) $\Delta\Gamma_X^{(\mathcal{J}_c)}$. For the representative binding energy $\delta_X = 57\,\text{keV}$ of Eq. (3.85) (vertical dashed grid line), we find the NLO result $\Gamma_X^{(\text{NLO})} = (52.5 \pm 2.2)\,\text{keV}$.

$X(3872)$ width

We begin by applying the numerical renormalization procedure of Appendix D.5.1 to the LO system of Fig. 3.18. The numerical result $\Gamma_X^{(\text{LO})} = \Gamma_{0*} = 53.6\,\text{keV}$ verifies the analytical findings above. The corresponding blue bold line in Fig. 3.23 is independent of the binding energy, which we vary in the positive part of the experimental uncertainty range, i.e., $\delta_X \in [0, 0.2]\,\text{MeV}$.

Subleading width contributions are at least proportional to $\chi_3 = (\delta_X/\delta)^{1/2}$. Thus, without explicitly calculating NLO corrections, we can estimate them by multiplying the constant D^{0*} width by $(1 \pm a\chi_3)$. Here, a is numerical factor of order 1, which we choose to be 3.[21] On top, we take into account experimental uncertainties by varying the parameters $g^2 \in [3.40, 3.56] \cdot 10^{-8}\,\text{MeV}^{-3}$ and $\mathscr{B}_{D^0\pi^0} \in [63.8, 65.6]\,\%$ in their uncertainty ranges. The resulting LO uncertainty band is shown in blue in Fig. 3.23. For the representative value $\delta_X = 57\,\text{keV}$ of Eq. (3.85), we obtain an LO uncertainty of $\pm 15\,\%$, i.e., $\Gamma_X^{(\text{LO})} = 54(8)\,\text{keV}$.

To demonstrate the convergence of our power counting scheme, we add the three NLO contributions step by step. Firstly, the self-energy insertion yields a negative width shift proportional to $\delta_X^{1/2}$ as expected. The resulting red dashed curve lies within the LO band. Secondly, pion exchanges between DD^* s-wave states shift the width up as proposed in the power counting analysis; see the red dot-dashed line. Note that these first two corrections almost cancel such that the red dot-dashed curve lies only 3 keV above the LO result.

At this point, we may address the overall influence of s-d mixing caused by pion exchanges. Theoretically, its influence is of N^{2}LO size $[(\mu_{D\pi}/\mu_*)^2\Gamma_{0*} \approx 1\,\text{keV}]$; see Sec. 3.3.4. In addition to s-wave pion exchange, we include the mixing amplitude $T^{{}^3D_1,{}^3S_1}$ in Eq. (3.76) to the system. The red dot-dashed result then turns into the red dotted curve, which lies only 0.5 keV above. This observation confirms

---

[21] This number is inspired by the analytic self-energy shift in Appendix D.6, which exhibits a factor 3.

the power counting and ensures that d-waves can be neglected at NLO. Thus, we exclude them from all following calculations.

We complete the NLO Faddeev equation of Eq. (3.111) by introducing the charged meson loop of Eq. (3.108b). Figure 3.23 shows the final NLO result as a red solid line. In agreement with the analytic findings above, charged mesons lower the width. For the value $\delta_X = 57\,\text{keV}$, the shift is approximately $-4\,\text{keV} \approx -(\delta_X/\nu)^{1/2}$ (NLO size). As a result, the final NLO curve lies now only 1 keV below the LO width at this binding energy. After varying g and $\mathscr{B}_{D^0\pi^0}$ in their uncertainty ranges (red band in Fig. 3.23), we obtain the NLO width prediction

$$\Gamma_X^{(\text{NLO})} = (52.6 \pm 2.2)\,\text{keV}\,. \tag{3.112}$$

The band is of N^{2}LO size as expected. Note that due to experimental uncertainties, the LO and NLO results are not distinguishable for the large range $\delta_X \in [0, 75]\,\text{keV}$ of binding energies. We conclude that the LO prediction *de facto* holds up to NLO and that the power counting is fast converging.

Let us emphasize that our NLO calculation neglects many higher-order interactions that have been taken into account in the multi-channel calculation of Baru *et al.* [46]. These interactions include charged pion exchanges and d-waves in both the neutral and charged channel. Moreover, in Ref. [46] the D^{0*} self-energy was not treated perturbatively, but resummed to all orders. Thus, by comparing the NLO width curve to the one obtained in Ref. [46], we can verify their subleading nature without calculating them explicitly. For that, we choose

$$(\Gamma_{0*})_{\text{Baru}} = 63\,\text{keV} \tag{3.113a}$$

$$(g)_{\text{Baru}} = 1.29 \cdot 10^{-5}\,\text{MeV}^{3/2} \tag{3.113b}$$

and set the vector meson kinetic masses to their physical values. The result of this comparison calculation is shown in Fig. 3.23 as a green bold-dotted curve. The curve reproduces the two green points of Ref. [46] up to deviations of 2 keV at $\delta_X = 0.1\,\text{keV}$ and 0.5 keV at $\delta_X = 0.2\,\text{keV}$ (N^{2}LO). This observation verifies our power counting arguments.

Note that deviations seem to become larger for smaller binding energies. The reason could lie in the way Baru *et al.* determined Γ_X. Instead of calculating the complex pole, they fitted a Breit-Wigner shape to the $X(3872)$ peak in $D^0\bar{D}^0\pi^0$ production. This procedure is reasonable for binding energies $\delta_X \gg \Gamma_{0*}$. For smaller δ_X, however, threshold effects are expected to systematically enhance the full width at half maximum (FWHM) [44]. We will show that this is indeed the case in the next section.

Three-body force

Results for the three-body force $C_0(\Lambda)$ are shown in Fig. 3.24 for a large range of cutoffs $\Lambda \in [0.5, 50]\,\text{GeV}$. At LO, the bold blue curve reproduces the analytic result of Eq. (3.90b). Modifications of self-energy insertions to the real part of the pole are highly suppressed ($\sim \mathcal{N}^2$). Thus, they do not influence $C_0(\Lambda)$ notably. In contrast, the pion exchanges introduce the constant counterterm $-V^{(\infty)} \approx -2.72\,\text{GeV}^{-2}$ to C_0. Charged mesons solely suppresses parts of C_0 vanishing as $\Lambda \to \infty$ by a factor ≈ 0.4. This suppression factor was also derived in Appendix D.6.

Remarkably, the three-body force in the exemplary d-wave calculation (dotted line in Fig. 3.23) shows a totally different signature than in all other calculations. It exhibits consecutive singularities for high cutoffs $\Lambda > 11\,\text{GeV}$ also observed in Ref. [46]. These singularities are due to deep three-body states, a generic feature of three-body systems with resonant p-wave interactions [109, 110]. We have checked that the additional states lie outside the EFT's region of applicability. Thus, they do not influence low-energy physics.

However, when taking into account both d-waves and charged mesons in one calculation, the deep states lead to renormalization artifacts. In particular, Baru *et al.* saw in their multi-channel calculation that there are cutoffs for which the system cannot be renormalized [46]. At NLO, these problems do

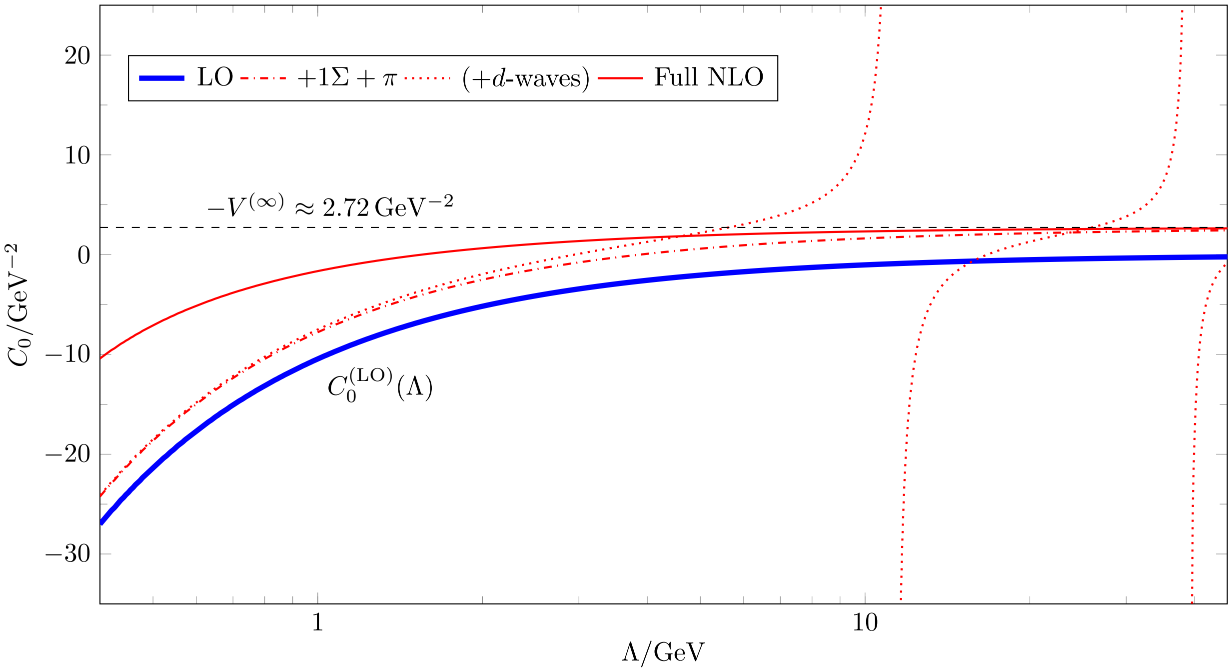

Figure 3.24.: Three-body force $C_0(\Lambda)$ for the different LO and NLO calculations at $\delta_X = 0.1\,\mathrm{MeV}$.

not occur and the system can be renormalized for all cutoffs. We note that resumming d-waves to all orders should not be done in a strict N^{2}LO calculation. Instead, one would include them perturbatively, similarly to the treatment of charged mesons. It remains to be seen if this approach would help avoiding renormalization artifacts such that C_0 alone could produce the $X(3872)$ for arbitrary cutoffs.

3.4 Line shape of the $X(3872)$

Having renormalized the amplitude T, we are finally in the position to calculate the $D^0\bar{D}^0\pi^0$ production rate $\mathrm{d}\Gamma/\mathrm{d}E$ of the decay in Eq. (3.1), in which the $X(3872)$ occurs as a pronounced peak. The rate can be measured and thus represents an important link between theory and experiment.

We will see that there are monotonic relations connecting δ_X to the $X(3872)$ peak's maximum position (E_{max}) and full width at half maximum (FWHM), which we denote by

$$E_{\mathrm{max}} \equiv \delta - \tilde{\delta}_X\,, \tag{3.114a}$$

$$\mathrm{FWHM} \equiv \tilde{\Gamma}_X\,. \tag{3.114b}$$

Baru *et al.* used the approximate relations $\tilde{\delta}_X \approx \delta_X$ and $\tilde{\Gamma}_X \approx \Gamma_X$ to determine $\Gamma_X(\delta_X)$ in a Breit-Wigner fit [46]. For $X(3872)$ peaks close to the $D^0\bar{D}^{0*}$ + c.c. threshold, however, we will find $\tilde{\delta}_X < \delta_X$ and $\tilde{\Gamma}_X > \Gamma_X$.

After investigating the line shape for bound $X(3872)$, we calculate it for virtual $X(3872)$ states. That will be done by linearly extrapolating the three-body force C_0.

3.4.1 $D^0\bar{D}^0\pi^0$ production rate

The $D^0\bar{D}^0\pi^0$ production process is described by the matrix element in Fig. 3.25. As stated in the beginning, the line shape is insensitive to how exactly the $X(3872) \equiv (D^0\bar{D}^{0*} + \text{c.c.})/\sqrt{2}$ gets produced at short distances [44]. Such details can be absorbed into a single factor $F \in \mathbb{R}$, diagrammatically represented by a crossed circle in Fig. 3.25. We derive the mathematical form of the matrix element in Appendix D.7.

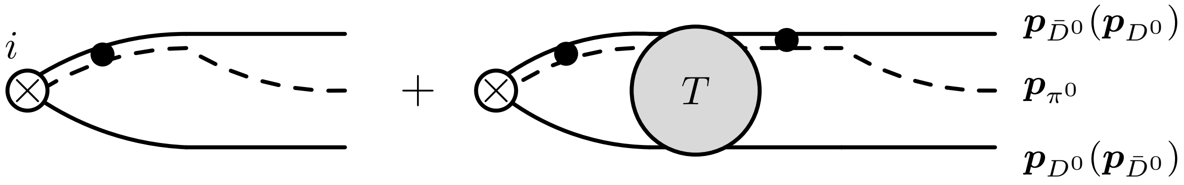

Figure 3.25.: Diagrams contributing to the $D^0\bar{D}^0\pi^0$ production matrix element $i\mathcal{M}^i_{\to D^0\bar{D}^0\pi^0}$ close to the $X(3872)$. Short-range processes are absorbed into the factor F indicated by the crossed circle. All intermediate states are in $C = +$ superpositions.

In order to calculate the $D^0\bar{D}^0\pi^0$ production rate from the matrix element, one has to integrate its squared modulus over the phase space of the three mesons and average over the incoming polarization $i \in \{1, 2, 3\}$. This calculation is done in Appendix D.7 as well. The final rate then reads

$$\frac{\mathrm{d}\Gamma}{\mathrm{d}E}(E) = \frac{g^2F^2m_\pi\mu_{D\pi}}{12\pi^3}\int_0^{\sqrt{2\mu_*E}}\mathrm{d}p_{D^0}\,p_{D^0}\int_0^{\sqrt{2\mu_*E}}\mathrm{d}p_{\bar{D}^0}\,p_{\bar{D}^0}\,\theta(1-x_0)\,\theta(1+x_0)$$
$$\times\Bigg[\left(E-\frac{p_{D^0}^2}{2\mu_*}\right)|\mathcal{J}_*(p_{D^0};E)|^2+\left[p_{D^0}\longleftrightarrow p_{\bar{D}^0}\right]$$
$$+\xi^{-1}\left((1+\xi^2)E-\frac{p_{D^0}^2+p_{\bar{D}^0}^2}{2\mu_*}\right)\mathrm{Re}\left(\mathcal{J}_*(p_{D^0};E)[\mathcal{J}_*(p_{\bar{D}^0};E)]^*\right)\Bigg] \tag{3.115}$$

with Heaviside step function $\theta(\cdot)$ and expressions

$$\mathcal{J}_*(p;E) \equiv \mathcal{G}_*^{(\mathrm{f})}(p;E)\left(1-\frac{1}{2\pi^2}\int_0^\Lambda \mathrm{d}q\,q^2\,\mathcal{G}_*^{(\mathrm{f})}(q;E)\,T_{00}(q,p;E)\right), \tag{3.116a}$$

$$x_0 \equiv \frac{m_\pi}{p_{D^0}p_{\bar{D}^0}}\left(E-\frac{p_{D^0}^2+p_{\bar{D}^0}^2}{2\mu_{D\pi}}\right). \tag{3.116b}$$

In each calculation, we will choose the vector meson propagators in Eq. (3.116a) like the ones entering the amplitude.

Note that the short-range factor F is an unknown parameter governed by physics outside the EFT's scope. In fact, F will have to absorb a Λ divergence stemming from the loop integral in Fig. 3.25. In this thesis, however, we are not interested in the line shape's overall size, but only in its maximum position and FWHM. Thus, we follow Braaten and Lu by normalizing the peak. In particular, we choose the maximum of the $\delta_X = 0$ line shape to be 1 [44]. Normalized line shapes will then be independent of the cutoff as $\Lambda \to 0$.

3.4.2 Bound $X(3872)$

In Fig. 3.26, we present numerical results for the normalized production rates at LO (blue) and NLO (red) for three binding energies $\delta_X \in \{0.5, 57, 100\}$ keV. All curves are calculated for $\Lambda = 1$ GeV and are converged in Λ. Due to the near cancellation of NLO width contributions, the NLO curves lie exactly on top of the LO curves. Thus, in Fig. 3.26 one sees only the uncertainty bands of the LO results.

In order to demonstrate the asymmetry of the line shapes, we compare them to Breit-Wigner shapes

$$\mathrm{BW}(E;\delta_X) \equiv \frac{(\mathrm{d}\Gamma/\mathrm{d}E)^{(\mathrm{NLO})}_{\max}\Big|_{\delta_X}}{1+[E-(\delta-\delta_X)]^2/\left[\Gamma_X^{(\mathrm{NLO})}(\delta_X)/2\right]^2} \tag{3.117}$$

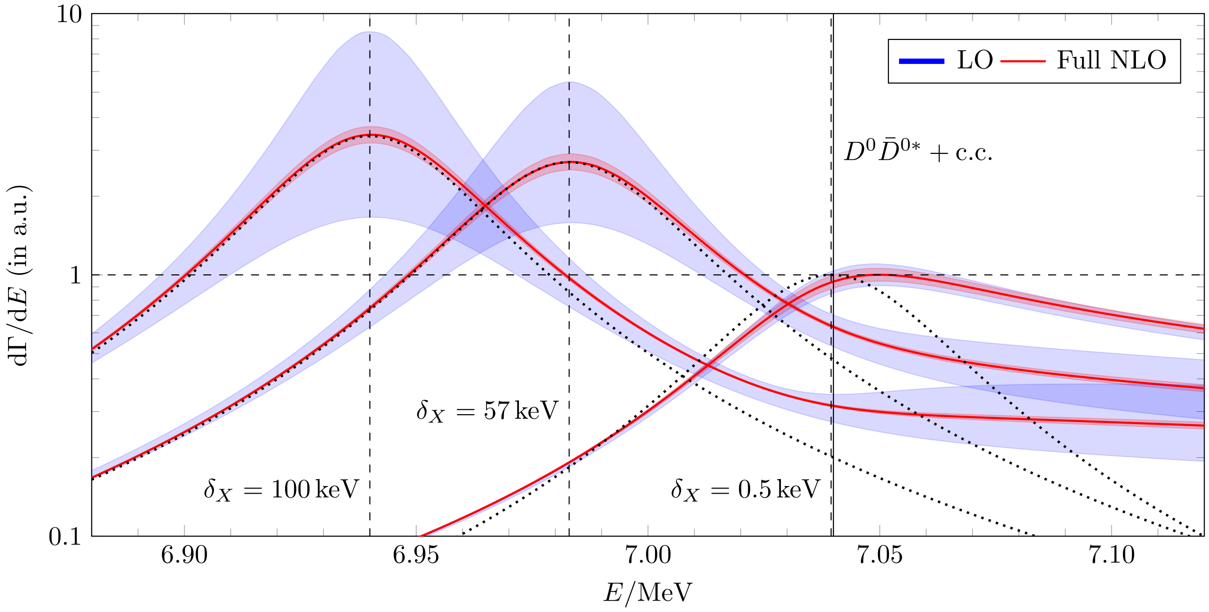

Figure 3.26.: Normalized line shapes $\mathrm{d}\Gamma/\mathrm{d}E$ as functions of the energy E for $\delta_X \in \{0.5, 57, 100\}\,\mathrm{keV}$ (dashed grid lines right to left) up to NLO: The $D^0\bar{D}^{0*}$ + c.c. threshold is indicated by a solid grid line. The black dotted curves show Breit-Wigner shapes with maximum positions $\delta - \delta_X$ and widths $\Gamma_X^{(\mathrm{NLO})}(\delta_X)$. All curves are converged in the cutoff, which we take to be $\Lambda = 1\,\mathrm{GeV}$.

with FWHM value $\Gamma_X^{(\mathrm{NLO})}(\delta_X)$ and maximum position $\delta - \delta_X$. In Fig. 3.26, they are shown as dotted curves. Apparently, all three line shapes are strongly enhanced at the $D^0\bar{D}^0$ + c.c. threshold, as was also seen by Braaten and Lu [44]. For $\delta_X \geq 50\,\mathrm{keV} \approx \Gamma_{0*}$, however, the peaks are still well separated from the $D^0\bar{D}^0$ + c.c. threshold. For that reason, deviations of the peak parameters $\tilde{\delta}_X$ and $\tilde{\Gamma}_X$ from δ_X and Γ_X are negligible at NLO.

As soon as δ_X becomes smaller, however, threshold effects become more an more important. In the limit of extremely small binding energies ($\delta_X = 0.5\,\mathrm{keV}$ in Fig. 3.26), the FWHM value $\tilde{\Gamma}_X$ is much larger than the width Γ_X. We investigate this phenomenon in more detail in Fig. 3.27. Indeed, threshold effects set in as soon as δ_X is as large as $\Gamma_X \approx \Gamma_{0*} \approx 50\,\mathrm{keV}$. The line width then increases up to about $\tilde{\Gamma}_X \approx 2.8\,\Gamma_X$. The function $\tilde{\Gamma}_X(\delta_X)$ turns out to be strictly monotonic. Thus, it could be inverted in order to determine the binding energy from an experimental line shape.

The approximation $\tilde{\delta}_X \approx \delta_X$ is valid down to binding energies $\delta_X \approx 10\,\mathrm{keV}$; see upper-most red curve in Fig. 3.28. Below this value, the peak maximum crosses the $D^0\bar{D}^{0*}$ + c.c. threshold such that $\tilde{\delta}_X < 0$. That can also be seen in Fig. 3.26 for the case $\delta_X = 0.5\,\mathrm{keV}$. That shows that even if the $X(3872)$ were bound with $\delta_X > 0$, it could be confused with a shallow $D^0\bar{D}^{0*}$ + c.c. resonance.

This effect becomes even stronger for a nonzero experimental resolution. We may mimic the detector resolution by convoluting the production rate with a Gaussian

$$g_\sigma(E) = \frac{1}{\sigma\sqrt{2\pi}}\, e^{-E^2/(2\sigma^2)}. \tag{3.118}$$

The smeared production rate is then given by

$$\left(\frac{\mathrm{d}\Gamma}{\mathrm{d}E}\right)_\sigma(E) \equiv \int_{-\infty}^{\infty} \mathrm{d}E'\; g_\sigma(E-E')\, \frac{\mathrm{d}\Gamma}{\mathrm{d}E'}(E'). \tag{3.119}$$

Since the line shape is much larger above $E = \delta$, the peak maximum moves almost linearly upwards when σ is turned on; see Fig. 3.28. For $\delta_X = 57\,\mathrm{keV}$, a resolution of $\sigma \approx 0.2\,\mathrm{MeV}$ is enough to shift the peak onto the $D^0\bar{D}^{0*}$ + c.c. threshold; see Fig. 3.29.

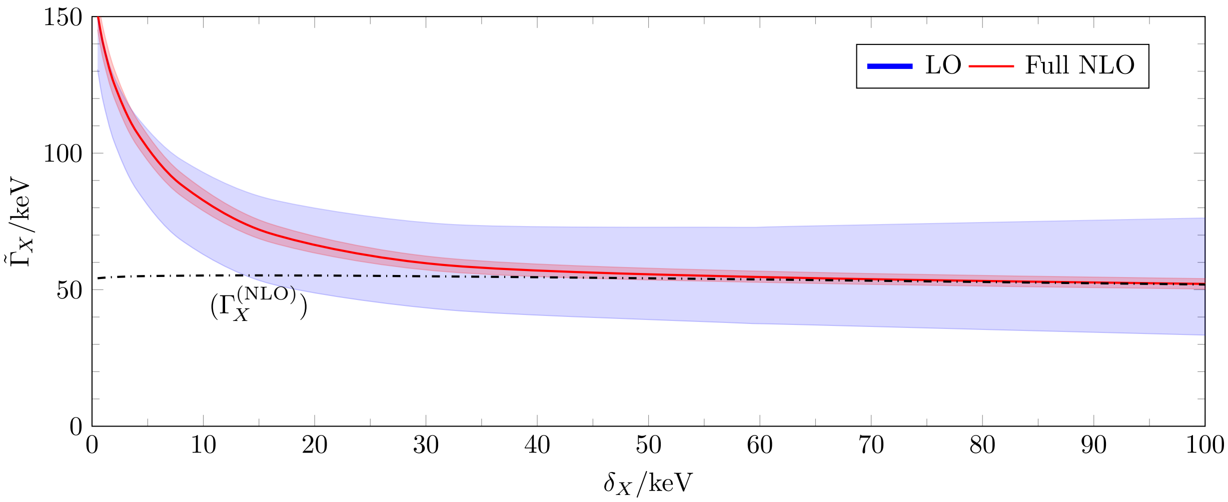

Figure 3.27.: FWHM $\tilde{\Gamma}_X$ as a function of δ_X. Without threshold effects, $\tilde{\Gamma}_X = \Gamma_X^{(\mathrm{NLO})}(\delta_X)$ (dot-dashed line); cf. Fig. 3.23.

We conclude that the pole position of the $X(3872)$ can only be correctly inferred from an experimental line shape if the detector resolves peaks with a width of $\Gamma_X \approx 50\,\mathrm{keV}$. For comparison, the energy resolution of the $\bar{\mathrm{P}}$ANDA experiment at FAIR will be of the order $100\,\mathrm{keV}$ [111].

3.4.3 Virtual $X(3872)$

We conclude our study of the $X(3872)$ resonance by extending the theoretical framework to virtual $X(3872)$ states. Generally, a "virtual" state is represented by a pole on the second energy sheet with respect to the constituents' unitary cut.

LO system

Let us exemplify the possibility of a virtual pole for the LO system. In order to eliminate the cutoff dependence of the LO amplitude in Eq. (3.89), the three-body force must have the generic form

$$C_0^{(\mathrm{LO})\ -1}(\Lambda;\gamma_X) = -\frac{\mu_*}{2\pi}\left(\frac{2}{\pi}\Lambda - \gamma_X + \mathcal{O}\left(\Lambda^{-1}\right)\right) \in \mathbb{R}\,, \tag{3.120}$$

with some $\gamma_X \in \mathbb{R}$. So far, the positive choice $\gamma_X = (2\mu_*\delta_X)^{1/2} > 0$ ensured that the $X(3872)$ occurs at some energy $E_X^{(\mathrm{LO})} = E_* - \delta_X$. More generally, however, $C_0^{(\mathrm{LO})\ -1}$ can be tuned such that γ_X takes any real value. The LO amplitude

$$T_{00}^{(\mathrm{LO})}(E) = -\frac{2\pi}{\mu_*}\left[\gamma_X - \sqrt{2\mu_*(E_* - E - i\epsilon)}\right]^{-1} \tag{3.121}$$

then has a pole at the one energy $E_X^{(\mathrm{LO})}$ for which the momentum variable

$$\bar{p}(E) \equiv i\sqrt{2\mu_*(E_* - E - i\epsilon)} \tag{3.122}$$

takes the value $i\gamma_X$. For $\gamma_X < 0$, that requires that $E_X^{(\mathrm{LO})}$ lies on the second energy sheet with respect to E_*. In this particular case, the LO system exhibits a virtual pole.

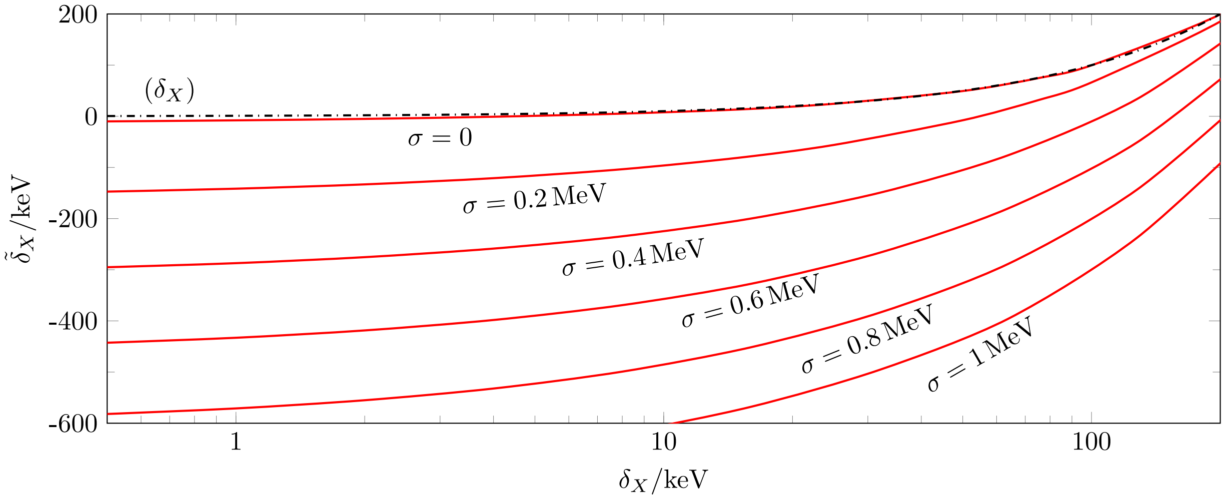

Figure 3.28.: Distance $\tilde{\delta}_X = \delta - E_{\text{max}}$ between maximum position E_{max} of the $X(3872)$ peak and the $D^0\bar{D}^{0*}$ + c.c. threshold. LO and NLO results coincide. Without threshold effects, $\tilde{\delta}_X = \delta_X$ (dot-dashed line). After convoluting the line shape with a Gaussian of standard deviation σ, the peak maximum lies above the $D^0\bar{D}^{0*}$ + c.c. threshold ($\tilde{\delta}_X < 0$).

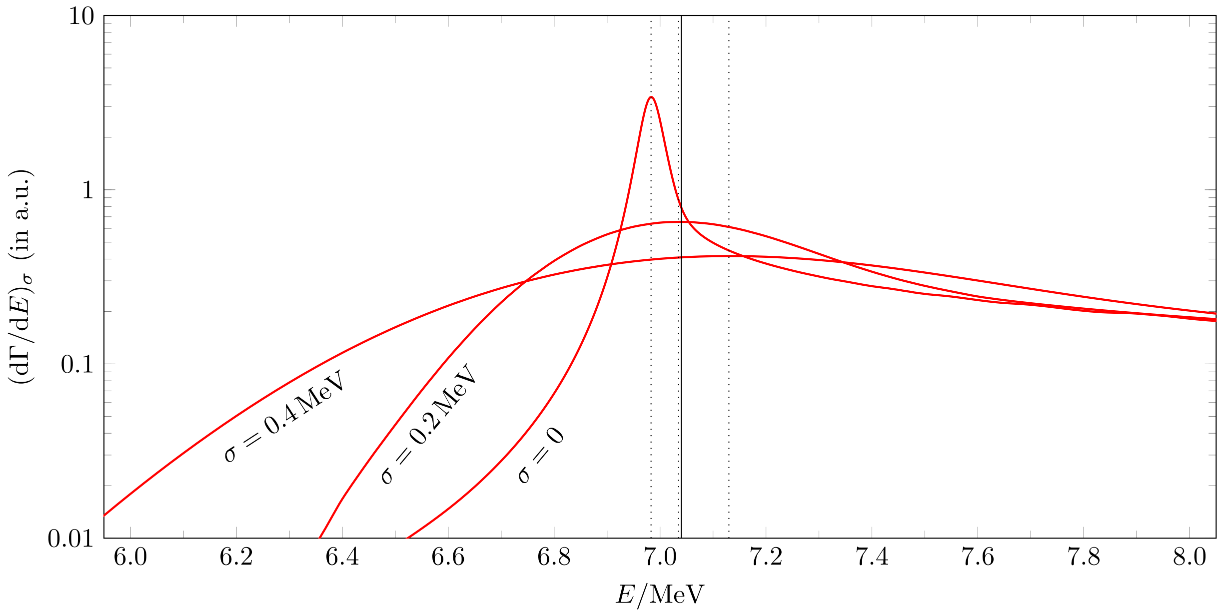

Figure 3.29.: Smeared production rate $(\mathrm{d}\Gamma/\mathrm{d}E)_\sigma$ as a function of E for $\delta_X = 57\,\mathrm{keV}$ at NLO: The solid grid line represents the $D^0\bar{D}^{0*}$+c.c. threshold, the dotted ones mark the maximum positions $E_{\text{max}} = \delta - \tilde{\delta}_X$.

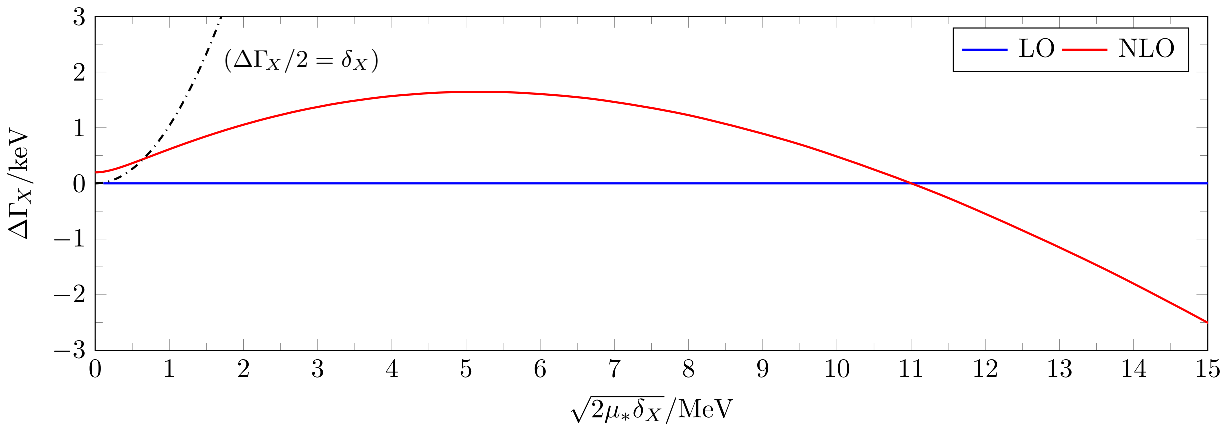

Figure 3.30.: Difference $\Delta\Gamma_X = \Gamma_X - \Gamma_{0*}$ for small binding energies δ_X at LO and NLO. The dot-dashed curve shows that $\Delta\Gamma_X/2 < \delta_X$ always but at NLO for $(2\mu_*\delta_X)^{1/2} < 1\,\mathrm{MeV}$ ($\delta_X < 0.5\,\mathrm{keV}$).

Numerically, we may produce a virtual pole at some $\gamma_X < 0$ by implementing the LO three-body force of Eq. (3.120) into the Faddeev kernel. As long as $|\gamma_X| \ll \Lambda$, we can moreover linearize the three-body force in γ_X, yielding

$$C_0^{(\mathrm{LO})}(\Lambda;\,\gamma_X) \approx C_0^{(\mathrm{LO})}(\Lambda;\,0)\left(1 + \beta^{(\mathrm{LO})}\frac{\gamma_X}{\Lambda}\right) \tag{3.123}$$

with parameters

$$C_0^{(\mathrm{LO})}(\Lambda;\,0) = -\frac{\pi^2}{\mu_*}\Lambda^{-1}\,, \tag{3.124a}$$

$$\beta^{(\mathrm{LO})} = \frac{\pi}{2}\,. \tag{3.124b}$$

NLO system

From NLO on, the $X(3872)$ width Γ_X can be different from Γ_{0*}, i.e., $\Delta\Gamma_X \equiv \Gamma_X - \Gamma_{0*} \neq 0$. The parameter

$$\gamma_X \equiv \sqrt{2\mu_*(E_* - E_X)} \in \mathbb{C}\,, \tag{3.125}$$

defined by the pole position E_X, is then in general complex. For this reason, we call γ_X a “generalized binding momentum”. When the $X(3872)$ is bound at $E_X = E_* - \delta_X - i\Delta\Gamma_X(\delta_X)/2$ on the first sheet, the generalized binding momentum reads

$$\gamma_X = \sqrt{2\mu_*(\delta_X + i\Delta\Gamma_X(\delta_X)/2)} \tag{3.126a}$$

$$= \sqrt{\mu_*}\left[\sqrt{\delta_X + \sqrt{\delta_X^2 + (\Delta\Gamma_X(\delta_X)/2)^2}} + i\,\mathrm{sign}\,(\Delta\Gamma_X(\delta_X))\sqrt{-\delta_X + \sqrt{\delta_X^2 + (\Delta\Gamma_X(\delta_X)/2)^2}}\right] \tag{3.126b}$$

$$\xrightarrow{\Delta\Gamma_X(\delta_X)/2 \ll \delta_X} \sqrt{2\mu_*\delta_X} + i\sqrt{2\mu_*\delta_X}\,\frac{1}{2}\,\frac{\Delta\Gamma_X(\delta_X)/2}{\delta_X}\,. \tag{3.126c}$$

The approximation in Eq. (3.126c) is valid for all $\delta_X > 0.5\,\mathrm{keV}$; see Fig. 3.30 For complex γ_X, the LO definition $\gamma_X < 0$ of virtualness must be modified. Note that for bound states, one always has $\mathrm{Re}\,\gamma_X > 0$. Thus, we say a pole is virtual if $\mathrm{Re}\,\gamma_X < 0$.

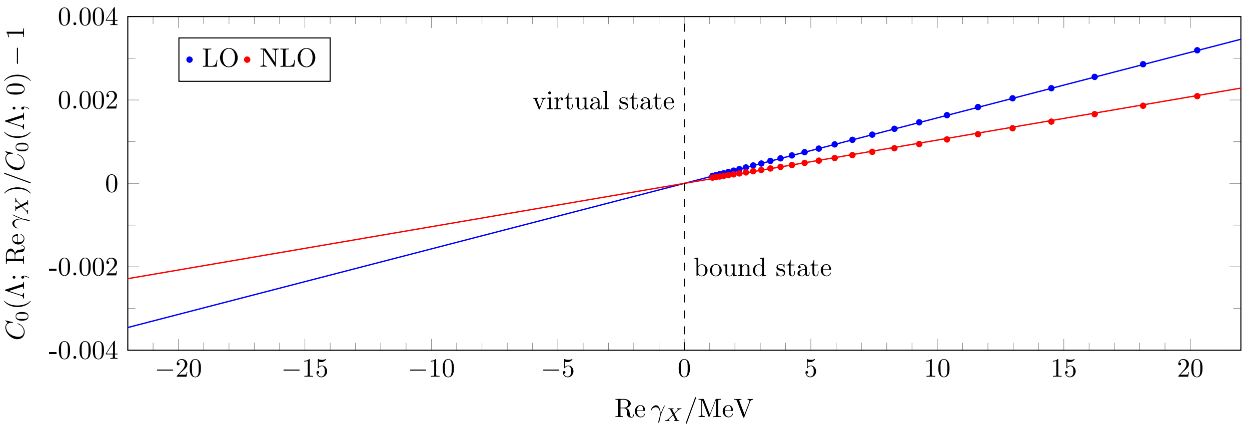

Figure 3.31.: Normalized three-body force as function of $\mathrm{Re}\,\gamma_X$ for $\Lambda = 10\,\mathrm{GeV}$. The straight lines show linear fits of the numerical results at LO (blue points) and NLO (red points). The slope of the LO line is known to be $\beta^{(\mathrm{LO})}/\Lambda = \pi/(2\Lambda)$. At NLO, the fit yields $\beta^{(\mathrm{NLO})}/\Lambda \approx 0.6611\pi/(2\Lambda)$. The lines are used to extrapolate the three-body force to virtual $X(3872)$ states ($\mathrm{Re}\,\gamma_X < 0$).

Since $C_0 \in \mathbb{R}$, the three-body force can now be written as the real part of a polynomial in γ_X. For example, if $\mathcal{I}_c(E)$ was the only NLO interaction, the three-body force would take the form

$$C_0^{(\mathcal{I}_c)}(\Lambda;\,\gamma_X) = C_0^{(\mathcal{I}_c)}(\Lambda;\,0)\ \mathrm{Re}\left(1 + \frac{\pi}{2}(1-\eta)\frac{\gamma_X}{\Lambda} + \eta\frac{\pi}{2}\frac{\gamma_X^2}{2\Lambda\sqrt{2\mu_*\nu}} + \mathcal{O}\left(\frac{\gamma_X\sqrt{2\mu_*\nu}}{\Lambda^2}\right)\right) \tag{3.127}$$

with $(2\mu_*\nu)^{1/2} \approx P_* \approx 117\,\mathrm{MeV}$ and $\eta \approx 0.38$; see Appendix D.6. By including pion exchanges, also terms involving the momentum $(2\mu_*\delta)^{1/2} = P_*$ itself would come into play. As long as $|\gamma_X| \sim P_X \ll P_*$ and also $P_* \ll \Lambda$, however, we can neglect all terms besides those linear in γ_X/Λ. The NLO three-body force is then linear in $\mathrm{Re}\,\gamma_X/\Lambda$ up to corrections of order $P_X/P_* \sim \chi_3$.

Consequently, we may fit the NLO three-body force of Fig. 3.24 to the functional form

$$C_0^{(\mathrm{NLO})}(\Lambda;\,\mathrm{Re}\,\gamma_X) \approx C_0^{(\mathrm{NLO})}(\Lambda;\,0)\left(1 + \beta^{(\mathrm{NLO})}\frac{\mathrm{Re}\,\gamma_X}{\Lambda}\right) \tag{3.128}$$

for a fixed cutoff. This procedure allows us to infer the three-body force needed to produce a virtual pole with certain $\mathrm{Re}\,\gamma_X < 0$. In order to keep corrections to the linear form small, we perform the fit at the large cutoff $\Lambda = 10\,\mathrm{GeV}$. Moreover, we keep $\mathrm{Re}\,\gamma_X$ much smaller than $P_* \approx 117\,\mathrm{MeV}$. Data points $(\mathrm{Re}\,\gamma_X,\, C_0)$ for the fit are produced by calculating three-body force and $X(3872)$ width for a set of δ_X in the developed renormalization procedure. We then reconstruct the respective $\mathrm{Re}\,\gamma_X$ values from δ_X and $\Delta\Gamma_X(\delta_X) = \Gamma_X(\delta_X) - \Gamma_{0*}$ using Eq. (3.126b).

Figure 3.31 shows results of the fits at LO and NLO. At LO, we recover the analytic values of $C_0^{(\mathrm{LO})}(\Lambda;\,0)$ and $\beta^{(\mathrm{LO})}$ above. At NLO, we obtain

$$C_0^{(\mathrm{NLO})}(\Lambda = 10\,\mathrm{GeV};\,0) \approx -0.3865\,\frac{\pi^2}{\mu_*}\Lambda^{-1}\,, \tag{3.129a}$$

$$\beta^{(\mathrm{NLO})} \approx 0.6611\,\frac{\pi}{2}\,. \tag{3.129b}$$

This fit can be used to extrapolate the three-body force to virtual states ($\mathrm{Re}\,\gamma_X < 0$) at NLO.

Extrapolation results

We calculate line shapes of the $X(3872)$ in $D^0\bar{D}^0\pi^0$ production for virtual states using the linearized three-body forces of Eqs. (3.123) and (3.128). The curves are normalized such that the maximum of the $\mathrm{Re}\,\gamma_X = 0$ curve equals 1.

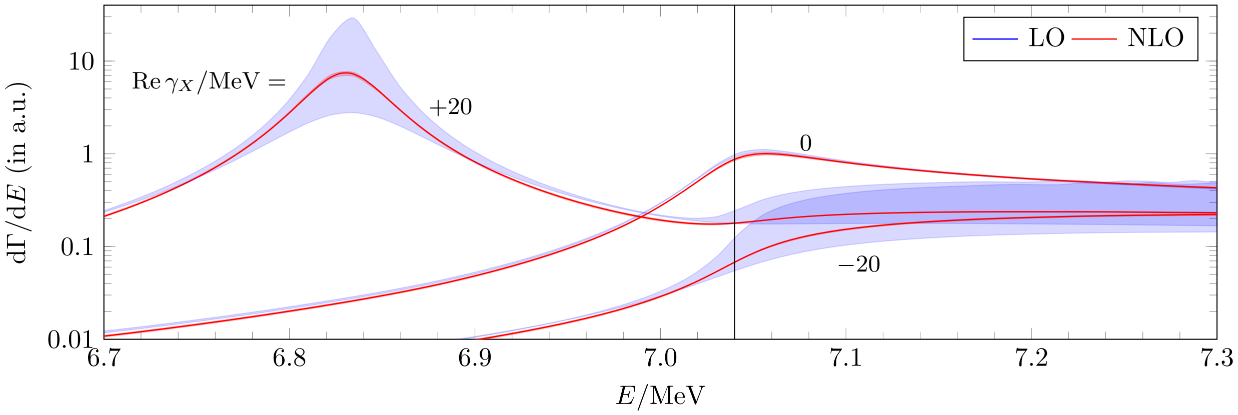

Figure 3.32.: Normalized line shapes up to NLO for $\Lambda = 10\,\mathrm{GeV}$ (converged). The solid grid line represents the $D^0\bar{D}^{0*}$ + c.c. threshold.

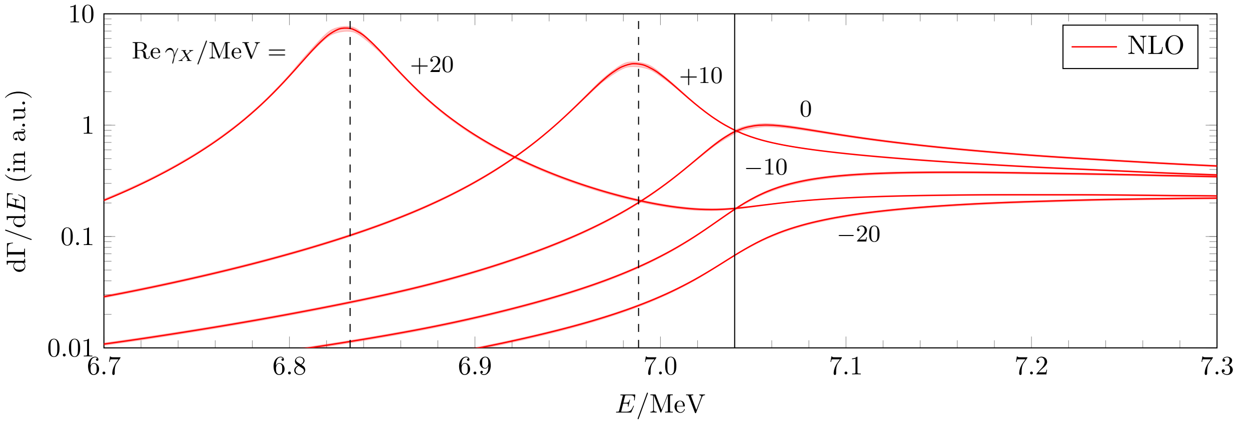

Figure 3.33.: Normalized line shapes at NLO for $\Lambda = 10\,\mathrm{GeV}$ (converged). Above $E = \delta$, productions rates for bound and virtual states with equal modulus $|\mathrm{Re}\,\gamma_X|$ coincide. The dashed grid lines shows the respective energies $\delta - \delta_X$ for the bound state cases.

Figure 3.32 shows results for $\mathrm{Re}\,\gamma_X \in \{-20, 0, 20\}\,\mathrm{MeV}$ at LO and NLO. For the virtual state, the line shape does not possess a maximum anymore. Instead, it becomes a monotonically increasing function with maximum slope near the $D^0\bar{D}^0$ + c.c. threshold. This signature was also seen in the zero-range calculation by Braaten and Lu [44], which is similar to our LO calculation. As a consequence, it is no longer possible to determine an FWHM value of the line shape.

In the bound state case, NLO contributions to the width turned out to be very small. As a consequence, line shapes for both cases coincide for $\mathrm{Re}\,\gamma_X = 20\,\mathrm{MeV}$. For the virtual state case, we observe the same feature. That confirms that the developed power counting is also appropriate for virtual state poles not to far away from the $D^0\bar{D}^0$ + c.c. threshold. In Figure 3.33 we plot line shapes for more values of $\mathrm{Re}\,\gamma_X$ at NLO. Note that the $\mathrm{Re}\,\gamma_X = \pm 20\,\mathrm{MeV}$ and the $\mathrm{Re}\,\gamma_X = \pm 10\,\mathrm{MeV}$ curves coincide for energies $E > 7.3\,\mathrm{MeV}$ above δ. Apparently, at these energies above the threshold, the line shapes are no more sensitive to the sign of $\mathrm{Re}\,\gamma_X$.

We conclude that the nature of the $X(3872)$, i.e., if it is bound, virtual, or a different kind of state, can only be answered by measuring the line shape with a high precision.

4 Nuclear (d, p) reactions

In this chapter, we explore the potential of EFT to describe nuclear transfer reactions at low energies. Being a pilot project, our study focuses on nuclei that can be described using only a small number of observables. Such a simplified treatment is justified for one-neutron halo nuclei (including the deuteron). Due to their remarkable scale separations, they can be described as two-body systems whose constituents interact only via short-range forces. Consequently, we focus on deuteron-induced transfer reactions ${}^{A}\mathrm{X}(\mathrm{d},\,\mathrm{p})^{A+1}\mathrm{X}$, where ${}^{A+1}\mathrm{X}$ represents a one-neutron halo nucleus with tightly bound core ${}^{A}\mathrm{X}$. Our EFT builds upon EFT($\not\pi$) for nucleon-nucleon scattering and Halo EFT for the description of the halo nucleus [19, 22, 79, 112].

In the first section, we develop the general formalism for a ${}^{A}\mathrm{X}$-neutron-proton three-body calculation including both strong contact interactions and Coulomb repulsion. Afterwards, we apply our framework to the transfer reaction

$$^{10}\mathrm{Be}\,(\mathrm{d},\,\mathrm{p})\,^{11}\mathrm{Be}\,, \tag{4.1}$$

which involves the halo nucleus ${}^{11}\mathrm{Be}$; see Fig. 1.3(b). We calculate the reaction cross section up to NLO in the expansion parameters

$$\underbrace{\chi_2 \equiv r_\mathrm{d}\gamma_\mathrm{d} \approx 0.4 \sim \frac{R_\mathrm{c}}{R_\mathrm{h}}}_{\text{2-body}}\,,\quad \underbrace{\chi_3 \equiv \frac{p_\mathrm{C}}{p_E} \leq 0.2}_{\text{3-body}} \tag{4.2}$$

of the two- and three-body system. Here, $\gamma_\mathrm{d}, r_\mathrm{d}$ are the deuteron binding momentum and effective range, $R_\mathrm{c}, R_\mathrm{h}$ denote the radii of ${}^{10}\mathrm{Be}$ and ${}^{11}\mathrm{Be}$, p_C is a so-called Coulomb momentum [see Eq. (4.72)], and p_E is the typical three-body relative momentum. Results are compared to cross-section data of Schmitt *et al.* from Ref. [60]. Similar to the previous chapter, we follow the lines of our publication "*Neutron transfer reactions in halo effective field theory*" in Physical Review C **99**, 054611 (2019) [113].

4.1 EFT formalism

In this first section, we show how the deuteron $\mathrm{d} \equiv {}^{2}\mathrm{H}\ (1^+)$ and the generic one-neutron halo state $\mathrm{h} \equiv {}^{A+1}\mathrm{X}$ emerge dynamically from contact interactions between p (proton, $1/2^+$), n (neutron, $1/2^+$), and $\mathrm{c} \equiv {}^{A}\mathrm{X}$ (core, 0^+); see Fig. 4.1. Afterwards, we calculate elementary three-body diagrams induced by the contact interactions and discuss the treatment of the Coulomb force.

Often, one-neutron halo states are defined as such states in which the probability for the valence neutron to be found outside the nuclear interaction range is larger than some value [50]. Our EFT, however, is formulated in momentum space. For this reason, we will use a different definition of the term "halo state", which rather builds upon typical momentum scales of the system:

Definition (Halo state): *A one-neutron halo state is an energy level in* ${}^{A+1}\mathrm{X}$ *which represents a* c-n *bound state below the* c-n *separation threshold, such that the* c-n *binding momentum* γ_h *is smaller than the natural momentum scale of the* c-n *system. The binding momentum is defined by the binding energy* B_h *and the* c-n *reduced mass*[1] μ_Nc *via* $\gamma_\mathrm{h} \equiv (2\mu_\mathrm{Nc}B_\mathrm{h})^{1/2}$.

---

[1] See Eq. (4.36) for definition of μ_Nc.

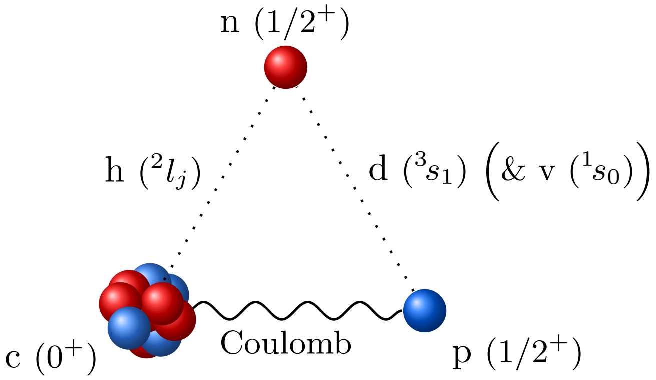

Figure 4.1.: The three-body system is given by a proton (p), a neutron (n), and a 0^+ core (c). The c-n system exhibits (possibly more than) one bound state h. The p-n system involves the deuteron and a virtual state. The latter can be neglected in the reaction $^{10}\text{Be}\,(\text{d, p})\,^{11}\text{Be}$ up to NLO. All these two-body states emerge from strong contact interactions. We assume no shallow state in the c-p subsystem. Instead, these particles interact only via Coulomb repulsion.

The natural momentum scale K_hi is typically estimated using the excitation energy $E_\text{x} > B_\text{h}$ of the core, i.e., $K_\text{hi} = (2\mu_\text{Nc}E_\text{x})^{1/2} > \gamma_\text{h}$. As a consequence of the scale separation, the radius of the halo state $R_\text{h} \sim \gamma_\text{h}^{-1}$ is typically enhanced compared to the small core radius $R_\text{c} \sim K_\text{hi}^{-1}$ [54]. One thus often expresses the scale separation in terms of the ratio

$$\frac{R_\text{c}}{R_\text{h}} \sim \frac{\gamma_\text{h}}{K_\text{hi}} < 1 \tag{4.3}$$

in Halo EFT.

The above definition does not put any constraint on the c-n orbital angular momentum l. For example, both the ground state ^{11}Be $(1/2^+)$ and first excited state $^{11}\text{Be}^*$ $(1/2^-)$ of Beryllium-11 fulfill the definition; see Fig. 4.7. They represent s- and p-wave halo states ($l = 0$ and $l = 1$) of ^{10}Be and n [54]. Another example is Carbon-15, whose ground state ^{15}C $(1/2^+)$ and first excited state $^{15}\text{C}^*$ $(5/2^+)$ can be interpreted as s- and d-wave halo states ($l = 0$ and $l = 2$) [80, 114].

Moreover, the definition can be applied to the deuteron. It represents a halo state with core c = p ($A = 1$) and binding energy $B_\text{d} = 2.22\,\text{MeV}$ [86]. The typical momentum scale is set by the pion mass $m_\pi \approx 135\,\text{MeV}$, which is larger than the binding momentum $\gamma_\text{d} = (m_\text{N}B_\text{d})^{1/2} \approx 46\,\text{MeV}$. As a consequence, dynamical pions will be neglected in this chapter. Note that the *de facto* expansion parameter in the deuteron sector is slightly larger than $\gamma_\text{d}/m_\pi \approx 0.34$. It is given by

$$\chi_2 \equiv r_\text{d}\gamma_\text{d} \approx 0.4\,, \tag{4.4}$$

where $r_\text{d} = 1.74\,\text{fm} \sim 1/m_\pi$ denotes the $^3s_1$ effective range [86]; see Eq. (4.2). In the following, we will discuss the EFT($\not{\pi}$) treatment of p-n scattering in more detail.

4.1.1 Proton-neutron scattering in EFT($\not{\pi}$)

Our treatment of the p-n sector is equivalent to the one in EFT($\not{\pi}$). Usually, proton and neutron are comprised into a nucleon field $N = (p, n)^T$ with spinors $p = (p_{+1/2}, p_{-1/2})^T$, $n = (n_{+1/2}, n_{-1/2})^T$ and average nucleon mass $m_N = 938.918\,\text{MeV}$ [112]. The relative mass difference $(m_\text{p} - m_\text{n})/m_\text{N} \approx 0.005$

between proton and neutron enters only at high orders in the γ_d/m_π power counting of EFT($\not{\pi}$) [36]. The nucleon field obeys the equal-time anticommutation relations

$$\left\{N_{a,\alpha}(x), N^\dagger_{\beta,b}(y)\right\} = \delta^{ab}\delta^{\alpha\beta}\,\delta^{(3)}(\boldsymbol{x}-\boldsymbol{y})\,, \tag{4.5a}$$

$$\left\{N_{a,\alpha}(x), N_{\beta,b}(y)\right\} = 0\,, \tag{4.5b}$$

where $a, b \in \{+1/2, -1/2\}$ and $\alpha, \beta \in \{+1/2, -1/2\}$ are isospin and spin indices, respectively.

The field N will be treated nonrelativistically since we want to describe (d, p) reactions at low center-of-mass energies $E \ll m_\mathrm{N}$.[2] We thus write

$$\mathscr{L}_{\mathrm{EFT}(\not{\pi}),\mathrm{kin}} = N^\dagger\left[iD_0 + \frac{\boldsymbol{D}^2}{2m_\mathrm{N}}\right]N \tag{4.6}$$

with rest masses set to zero. The covariant derivative

$$D_\mu \equiv \partial_\mu + ieA_\mu\hat{Q} \tag{4.7}$$

induces couplings to the photon field A_μ, which we introduce in Sec. 4.1.3. In Eq. (4.7), e denotes the elementary charge and $\hat{Q}$ the charge operator. For nucleons, $\hat{Q}$ can be written in the form

$$\hat{Q} \equiv \frac{1}{2}(\mathbb{1} + \tau_3)\,, \tag{4.8}$$

where $\tau_3 = \mathrm{diag}\,(1, -1)$ is an isospin Pauli matrix.

Shallow poles and higher partial waves

In p-n scattering, the two s-wave channels ${}^3s_1$ and ${}^1s_0$ exhibit unnaturally large scattering lengths compared to the natural nuclear physics length scale $1/m_\pi \sim 1.46\,\mathrm{fm}$. As a consequence, both states can be treated in EFT($\not{\pi}$), as will be explained in the following.

For low center-of-mass energies E_cm, the elastic p-n amplitude in the ${}^3s_1$ (isospin singlet) channel can be written in the effective range expansion (ERE) form

$$it_\mathrm{d}^{1m_j,1m'_j}(\boldsymbol{k}, \boldsymbol{k}'; E_\mathrm{cm}) = i\frac{4\pi}{m_\mathrm{N}}\left[-a_\mathrm{d}^{-1} - i\bar{k} + \frac{r_\mathrm{d}}{2}\bar{k}^2 + \mathscr{O}\left(\bar{k}^4 m_\pi^{-3}\right)\right]^{-1}\delta^{mm'}\,. \tag{4.9}$$

Here, $m \in \{+1, 0, -1\}$ and $\boldsymbol{k}$ ($m' \in \{+1, 0, -1\}$ and $\boldsymbol{k}'$) denote the incoming (outgoing) total spin projection and relative momentum. Moreover,

$$\bar{k} \equiv i\left[-m_\mathrm{N}(E_\mathrm{cm} + i\epsilon)\right]^{1/2} \tag{4.10}$$

is the on-shell momentum. The scattering length $a_\mathrm{d} = 5.42\,\mathrm{fm}$ is much larger than the naturally scaling effective range $r_\mathrm{d} = 1.74\,\mathrm{fm}$ [86]. Higher-order coefficients in the ERE of Eq. (4.9) are assumed to be natural as well. It follows that the amplitude exhibits a shallow bound state with positive binding momentum $\gamma_\mathrm{d} \sim a_\mathrm{d}^{-1} \ll m_\pi$. This state is the deuteron. Due to the scale separation, the amplitude can be described using only few parameters. At LO, we will demand the pole to sit at the well-known deuteron binding energy $B_\mathrm{d} = 2.22\,\mathrm{MeV}$ [86], i.e., $\gamma_\mathrm{d} \equiv (m_\mathrm{N}B_\mathrm{d})^{1/2} \approx 46\,\mathrm{MeV}$ and $a_\mathrm{d}^{(\mathrm{LO})} = \gamma_\mathrm{d}^{-1}$. At NLO, also r_d enters and $a_\mathrm{d}^{(\mathrm{NLO})} = \gamma_\mathrm{d}^{-1}(1 + r_\mathrm{d}\gamma_\mathrm{d}/2)$. We note that ${}^3s_1$-${}^3d_1$ mixing enters first at N^{2}LO in EFT($\not{\pi}$) [112] and thus also in this thesis.

---

[2] For example, in Ref. [60] the reaction cross section of ${}^{10}\mathrm{Be}(\mathrm{d},\mathrm{p})\,{}^{11}\mathrm{Be}$ was measured for $E \leq 15.61\,\mathrm{MeV} \ll m_\mathrm{N}$.

In our notation, the amplitude[3] it_{v} of the ${}^1s_0$ (isospin triplet) channel can be obtained from Eq. (4.9) by replacing all subscripts d → v. The scattering length $a_{\mathrm{v}} = -23.71\,\mathrm{fm}$ has a negative sign [86], indicating the existence of a shallow virtual pole. Again, the effective range $r_{\mathrm{v}} = 2.75\,\mathrm{fm}$ is natural [86] and the ${}^1s_0$ channel can be treated using EFT($\not{\pi}$) as well. Later, however, we will show that the ${}^1s_0$ channel decouples from the reaction process ${}^A\mathrm{X}(\mathrm{d},\,\mathrm{p})^{A+1}\mathrm{X}$ when all two-body interactions are of s-wave type. That is the case when the only halo state h in the reaction has quantum numbers ${}^2l_j = {}^2s_{1/2}$. For example, our LO description of the reaction ${}^{10}\mathrm{Be}\,(\mathrm{d},\,\mathrm{p})\,{}^{11}\mathrm{Be}$ in Sec. 4.2.4 will involve only the s-wave halo state ${}^{11}\mathrm{Be}$. The additional p-wave halo state ${}^{11}\mathrm{Be}^*$, entering at NLO, indeed couples to the ${}^1s_0$ channel, but this effect will be of N^{2}LO size. For this reason, the ${}^1s_0$ channel will never enter three-body calculations in this thesis. Still, we keep it for the moment in order to show how the virtual state would enter other (d, p) reaction calculations.

Using dibaryon auxiliary fields $\boldsymbol{d} = (d_1,\, d_2,\, d_3)^T$ for the deuteron and v for the virtual state, the p-n interaction part of EFT($\not{\pi}$) can be written

$$\begin{aligned}\mathscr{L}_{\mathrm{EFT}(\not{\pi}),\mathrm{pn}} = {} & \boldsymbol{d}^\dagger\left[\Delta_{\mathrm{d},0} + \Delta_{\mathrm{d},1}\, iD_{\mathrm{cm}} + \cdots\right]\boldsymbol{d} + v^\dagger\left[\Delta_{\mathrm{v},0} + \Delta_{\mathrm{v},1}\, iD_{\mathrm{cm}} + \cdots\right]v \\ & - g_{\mathrm{d}}\left[d_i^\dagger\left(N^T P_i^{{}^3s_1} N\right) + \mathrm{H.c.}\right] - g_{\mathrm{v}}\left[v^\dagger\left(N^T P_3^{{}^1s_0} N\right) + \mathrm{H.c.}\right] \\ & + \cdots\,. \end{aligned} \tag{4.11}$$

The covariant center-of-mass derivative

$$iD_{\mathrm{cm}} \equiv i\partial_{\mathrm{cm}}\Big|_{\partial_\mu \to D_\mu} = iD_0 + \frac{\boldsymbol{D}^2}{2\overrightarrow{m_{\mathrm{kin}}}} \tag{4.12}$$

is defined via $i\partial_{\mathrm{cm}}$. Both auxiliary fields have kinetic masses $2m_{\mathrm{N}}$. In contrast to the dimeson auxiliary fields $\boldsymbol{D}^0, \bar{\boldsymbol{D}}^0$ of Sec. 3.1.4, the dibaryon fields $\boldsymbol{d}$ and v are ghosts with negative signs $\Delta_{\mathrm{d},1} = \Delta_{\mathrm{v},1} = -1$. These signs are needed to ensure $r_{\mathrm{d}}, r_{\mathrm{v}} > 0$ [115]. The ellipses in the first row of Eq. (4.11) indicate that higher-order ERE coefficients scale naturally, i.e., with powers of m_π. Thus, higher orders in iD_{cm} can be neglected at NLO.

The vertices in the second row of Eq. (4.11) involve spin-isospin projection operators

$$P_i^{{}^3s_1} \equiv \frac{1}{\sqrt{8}}\sigma_2\sigma_i\tau_2 \quad (i \in \{1,\,2,\,3\})\,, \tag{4.13a}$$

$$P_A^{{}^1s_0} \equiv \frac{1}{\sqrt{8}}\sigma_2\tau_2\tau_A \quad (A \in \{1,\,2,\,3\})\,, \tag{4.13b}$$

with (cartesian) Pauli matrices σ_i and τ_A acting in spin and isospin space, respectively. The couplings $g_{\mathrm{d}}, g_{\mathrm{v}}$ (mass units $\mathrm{MeV}^{-1/2}$) and the parameters $\Delta_{\mathrm{d},0}, \Delta_{\mathrm{v},0}$ (mass units MeV) can be related to the scattering lengths and effective ranges; see Eqs. (4.29a)-(4.29b) below.

The ellipses in the last row of Eq. (4.11) indicate interactions in partial wave sectors $l \geq 1$, which are neglected up to N^{2}LO in Halo EFT. Due to the absence of fine-tunings, there are no states near the p-n threshold in these channels and ERE coefficients are assumed to scale naturally. The naturalness statement can be checked using the Nijmegen partial wave analysis for N-N scattering of Ref. [116]; see Fig. 4.2. The red phase shifts in the ${}^3p_0$, ${}^1p_1$, ${}^3p_1$, and ${}^3p_2$ channels yield scattering volumes

$$a_1 = -\left[\lim_{\bar{k}\to 0}\bar{k}^3\cot\delta_1(\bar{k})\right]^{-1} \tag{4.14}$$

of sizes $(145\,\mathrm{MeV})^{-3}$, $(141\,\mathrm{MeV})^{-3}$, $(-171\,\mathrm{MeV})^{-3}$, and $(302\,\mathrm{MeV})^{-3}$, all being of the order $\sim m_\pi^{-3}$. For general $l \geq 1$, the partial wave amplitude then behaves like $\bar{k}^{2l}/m_\pi^{2l+1}$ for small $\bar{k} \sim \gamma_{\mathrm{d}}$ (orange region

---

[3] The subscript “v” stands for “virtual”.

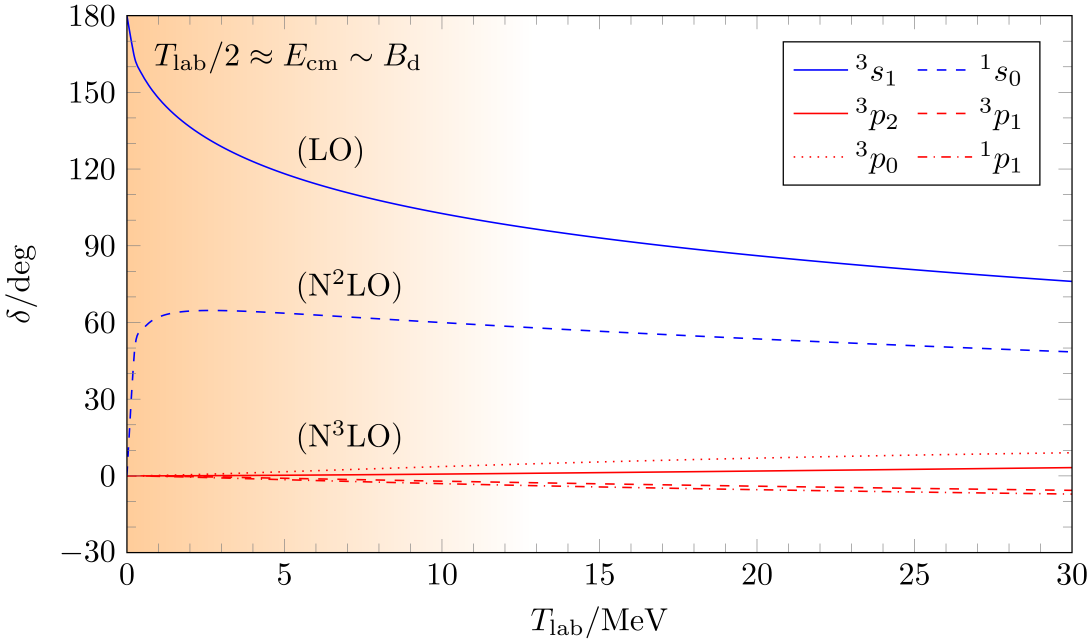

Figure 4.2.: p-n scattering phase shifts for $l = 0$ (blue) and $l = 1$ (red) as functions of the p-n lab energy $T_{\mathrm{lab}} \approx 2E_{\mathrm{cm}}$. Data is taken from the Nijmegen analysis of Ref. [116]. The indicated power counting classifications refer to the importance of the channels for the reaction $^{10}\mathrm{Be}\,(\mathrm{d},\,\mathrm{p})\,^{11}\mathrm{Be}$; see discussions in the text. Power counting classifications of higher partial waves base on their suppressions in the orange region, where $E_{\mathrm{cm}} \sim B_{\mathrm{d}}$. For example, $l = 1$ phase shifts (and scattering amplitudes) enter at N^{3}LO.

in Fig. 4.2). In contrast, the s-wave amplitudes behave like $|a_{\mathrm{v}}| \gtrsim a_{\mathrm{d}} \sim \gamma_{\mathrm{d}} \gg m_\pi^{-1}$ ($b \in \{\mathrm{d}, \mathrm{v}\}$). The overall suppression of higher partial waves is then given by $(\bar{k}^{2l}/m_\pi^{1+2l})/|a_b| \lesssim (\gamma_{\mathrm{d}}/m_\pi)^{2l+1} \sim \chi_2^{2l+1}$ and corresponds to N^{3}LO or higher.

The importance of partial waves $l \geq 0$ at nonzero energies can also be estimated using the phase shifts. Given two specific l- and s- wave amplitudes t_l, t_0, one finds

$$\left|\frac{t_l(\bar{k})}{t_0(\bar{k})}\right| = \left|\frac{\exp\left(2i\,\delta_l(\bar{k})\right) - 1}{\exp\left(2i\,\delta_0(\bar{k})\right) - 1}\right| \tag{4.15a}$$

$$= \left|\frac{2i\left(\delta_l(\bar{k}) - \delta_l(0)\right) + \mathcal{O}\left(\left(\delta_l(\bar{k}) - \delta_l(0)\right)^2\right)}{2i\left(\delta_0(\bar{k}) - \delta_0(0)\right) + \mathcal{O}\left(\left(\delta_0(\bar{k}) - \delta_0(0)\right)^2\right)}\right| \approx \left|\frac{\delta_l(\bar{k}) - \delta_l(0)}{\delta_0(\bar{k}) - \delta_0(0)}\right| \tag{4.15b}$$

Let us consider such center-of-mass energies $E_{\mathrm{cm}} = \bar{k}^2/m_{\mathrm{N}}$ smaller or equal to the largest c-n-p center-of-mass energy $E = 15.61\,\mathrm{MeV}$ in the $^{10}\mathrm{Be}\,(\mathrm{d},\,\mathrm{p})\,^{11}\mathrm{Be}$ measurement of Schmitt *et al.* [60]. The p-n lab kinetic energy

$$T_{\mathrm{lab}} = \frac{(E_{\mathrm{cm}} + 2m_{\mathrm{N}})^2}{2m_{\mathrm{N}}} - 2m_{\mathrm{N}} \approx 2E_{\mathrm{cm}}\left(1 + \mathcal{O}\left(\frac{E_{\mathrm{cm}}}{2m_{\mathrm{N}}}\right)\right) \tag{4.16}$$

is then smaller than 30 MeV, which is the upper energy limit in Fig. 4.2. The red p-wave phase shifts then give rise to suppressions stronger than $9\,\% \sim \chi_2^3 \approx 6.4\,\%$ compared to the dominating $^3s_1$ channel. That again corresponds to N^{3}LO in the χ_2. In this thesis, we calculate the reaction cross section up to NLO. Thus, higher p-n partial waves will be neglected.

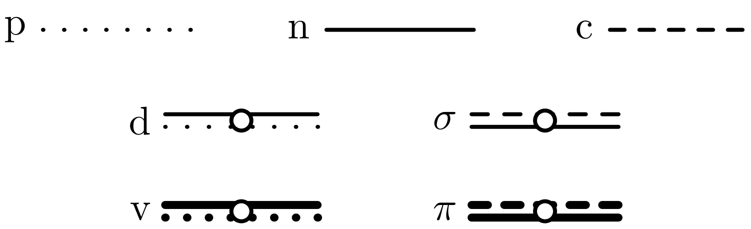

Figure 4.3.: The propagators iG_p of the proton and iG_n of the neutron are depicted by dotted and solid lines, respectively. The bare deuteron and virtual state propagators $iG_\mathrm{d}^{(\mathrm{b})}$ and $iG_\mathrm{v}^{(\mathrm{b})}$ are represented by solid-dotted (thickened) double lines with an empty circle. For completeness, we show here also the dashed propagator iG_c of the ^{10}Be core and the (thickened) solid-dashed bare propagators $iG_\sigma^{(\mathrm{b})}$ and $iG_\pi^{(\mathrm{b})}$ for the ^{11}Be and ^{11}Be* bound states.

Particle representation and spherical basis

In this thesis, the proton and the neutron have very different relations to the core $\mathrm{c} = {}^{A}\mathrm{X}$. The c-n subsystem interacts only via strong interactions and even involves one or more shallow bound states $\mathrm{h} = {}^{A+1}\mathrm{X}$. In contrast, core and proton do not interact strongly up to NLO; see Sec. 4.1.3. Instead, they repel each other via the Coulomb force. We make the difference between proton and neutron explicit by writing out the nucleon field N. The nucleon kinetic term then reads

$$\mathscr{L}_{\mathrm{EFT}(\not{\pi}),\mathrm{kin}} = p_\alpha^\dagger\left[iD_0+\frac{\boldsymbol{D}^2}{2m_\mathrm{N}}\right]p_\alpha + n_\alpha^\dagger\left[i\partial_0+\frac{\boldsymbol{\nabla}^2}{2m_\mathrm{N}}\right]n_\alpha \tag{4.17}$$

with $\alpha \in \{+1/2, -1/2\}$. The propagators iG_p and iG_n of proton and neutron will be depicted by dotted and solid lines, respectively; see Fig. 4.3.

Moreover, it will be beneficial to work in the spherical spin basis due to nontrivial spin-orbit couplings later on. We thus transform the deuteron field and the $^3s_1$ projection operator to the spherical spin basis with indices $m \in \{+1, 0, -1\}$. That can be done using the basis transformation matrix A given in Eq. (C.8). The scalar products $\boldsymbol{d}^\dagger \cdot \boldsymbol{d} = d_i^\dagger d_i$ and $d_i^\dagger P_i^{{}^3s_1}$ in Eq. (4.11) are invariant under this transformation. For example,

$$d_i^\dagger P_i^{{}^3s_1} = (A_{im}d_m)^\dagger A_{im'}P_{m'}^{{}^3s_1} = d_m^\dagger \underbrace{A^*_{mi}A_{im'}}_{=\delta_{mm'}} P_{m'}^{{}^3s_1} = d_m^\dagger P_m^{{}^3s_1}\,. \tag{4.18}$$

The new projection operators $P_m^{{}^3s_1}$ involve spherical Pauli matrices $\sigma_m = (A^{-1})_{mi}\,\sigma_i$, which are given in Appendix C.

After writing out the new projection operators, the vertex terms

$$-g_\mathrm{d}\,\mathrm{C}^{1m}_{1/2\alpha,1/2\beta}\left[d_m^\dagger\frac{p_\alpha n_\beta - n_\alpha p_\beta}{2} + \mathrm{H.c.}\right] - g_\mathrm{v}\,\mathrm{C}^{00}_{1/2\alpha,1/2\beta}\left[v^\dagger\frac{p_\alpha n_\beta + n_\alpha p_\beta}{2} + \mathrm{H.c.}\right] \tag{4.19}$$

exhibit Clebsch-Gordan coefficients, which make the spin couplings explicit. Further simplification can be achieved using the anticommutation relation of the nucleon field N,

$$n_\alpha p_\beta = \left\{n_\alpha, p_\beta\right\} - p_\beta n_\alpha = \left\{N_{-1/2,\alpha}, N_{+1/2,\beta}\right\} - p_\beta n_\alpha = -p_\beta n_\alpha\,, \tag{4.20}$$

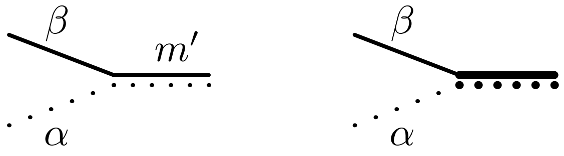

(a) (b)

Figure 4.4.: The vertices for (a) pn → d and (b) pn → v transitions have Feynman rules $-ig_\mathrm{d}\mathsf{C}^{1m'}_{1/2\alpha,1/2\beta}$ and $-ig_\mathrm{v}\mathsf{C}^{00}_{1/2\alpha,1/2\beta}$, respectively. These expressions are invariant under time reversal.

and the (anti)symmetry relations

$$\mathsf{C}^{1m}_{1/2\alpha,1/2\beta} = \mathsf{C}^{1m}_{1/2\beta,1/2\alpha}\,, \tag{4.21a}$$

$$\mathsf{C}^{00}_{1/2\alpha,1/2\beta} = -\,\mathsf{C}^{00}_{1/2\beta,1/2\alpha} \tag{4.21b}$$

of the Clebsch-Gordan coefficients. The final p-n interactions part of the EFT Lagrangian then reads

$$\begin{aligned}\mathscr{L}_\mathrm{pn} = {} & d_m^\dagger\left[\Delta_{\mathrm{d},0}+\Delta_{\mathrm{d},1}\,iD_\mathrm{cm}+\cdots\right]d_m + v^\dagger\left[\Delta_{\mathrm{v},0}+\Delta_{\mathrm{v},1}\,iD_\mathrm{cm}+\cdots\right]v \\ & -g_\mathrm{d}\,\mathsf{C}^{1m}_{1/2\alpha,1/2\beta}\left[d_m^\dagger\left(p_\alpha n_\beta\right)+\mathrm{H.c.}\right]-g_\mathrm{v}\,\mathsf{C}^{00}_{1/2\alpha,1/2\beta}\left[v^\dagger\left(p_\alpha n_\beta\right)+\mathrm{H.c.}\right] \\ & +\cdots\,. \end{aligned} \tag{4.22}$$

The bare deuteron propagator $iG_\mathrm{d}^{(\mathrm{b})}$ is depicted by a solid-dotted (thick) double line with an empty circle; see Fig. 4.3. The bare virtual state propagator $iG_\mathrm{v}^{(\mathrm{b})}$ looks similar, but is drawn using thick lines.

Feynman rules for the vertices in Eq. (4.22) are given in Fig. 4.4. They involve Clebsch-Gordan coefficients coupling the proton and neutron spins to total spins 1 (${}^3s_1$) or 0 (${}^1s_0$).

Self-energies and dibaryon propagators

At LO in EFT($\not{\pi}$), the deuteron and virtual state poles are produced by the scattering lengths and the s-wave unitary cut terms alone. It is thus necessary to resum p-n self-energy loops $-i\Sigma_b(E_\mathrm{cm})$ ($b \in \{\mathrm{d},\mathrm{v}\}$) to all orders already at LO; see Fig. 4.5. In the PDS scheme, the self-energies are given by[4]

$$\Sigma_b^{(\mathrm{PDS})}(E_\mathrm{cm}) = -\,g_b^2\frac{m_\mathrm{N}}{4\pi}\left(\Lambda_\mathrm{PDS}-\sqrt{-m_\mathrm{N}\left(E_\mathrm{cm}+i\epsilon\right)}\right) \tag{4.23a}$$

$$= -\,g_b^2\frac{m_\mathrm{N}}{4\pi}\left(\Lambda_\mathrm{PDS}+i\bar{k}\right) \quad (b\in\{\mathrm{d},\mathrm{v}\})\,. \tag{4.23b}$$

The calculation is done in Appendix E.1.1. As done for the vector mesons D^{0*} and $\bar{D}^{0*}$ in Sec. 3.2.1, resummation of the self-energy leads to full dibaryon propagators

$$iG_b^{(\mathrm{f})}(E_\mathrm{cm}) = i\left[G_b^{(\mathrm{b})\,-1}(E_\mathrm{cm})-\Sigma_b^{(\mathrm{PDS})}(E_\mathrm{cm})\right]^{-1} \quad (b\in\{\mathrm{d},\mathrm{v}\})\,. \tag{4.24}$$

It turns out that the above relations hold when p_α and n_β obey the commutation relations

$$\left[p_\alpha(x),\, n_\beta^{(\dagger)}(y)\right] = 0\,. \tag{4.25}$$

---

[4] In calculations, the deuteron self-energy Σ_d and propagator G_d have to be multiplied by spin projection-conserving factors $\delta^{mm'}$, which we omit here.

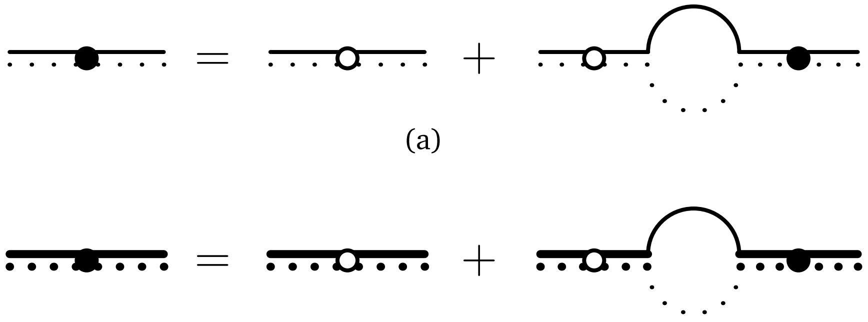

Figure 4.5.: The full dibaryon propagators (a) $iG_{\mathrm{d}}^{(\mathrm{f})}$ and (b) $iG_{\mathrm{v}}^{(\mathrm{f})}$ include p-n self-energy loops $-i\Sigma_{\mathrm{d}}$ and $-i\Sigma_{\mathrm{v}}$, respectively, to all orders. The PDS counter terms $-i\Delta\Sigma_b^{(\mathrm{PDS})}$ are omitted; see Appendix E.1.1.

We show the validity of this statement in Appendix E.1.1. For simplicity, we will treat the proton and the neutron as commuting, distinguishable particles for the rest of the thesis.

The elastic p-n amplitude can be obtained by attaching external nucleon fields $p_\alpha n_\beta$ and $p_{\alpha'} n_{\beta'}$ to the full dibaryon propagators, i.e.,

$$\begin{aligned}\left\langle p_{\alpha'}\mathrm{n}_{\beta'}\right| i\hat{T}\left|p_\alpha \mathrm{n}_\beta\right\rangle\left(\boldsymbol{k},\boldsymbol{k}';E_{\mathrm{cm}}\right) = &-g_{\mathrm{d}}^2\,\mathrm{C}^{1m}_{1/2\alpha,1/2\beta}\;iG_{\mathrm{d}}^{(\mathrm{f})}(E_{\mathrm{cm}})\delta^{mm'}\;\mathrm{C}^{1m'}_{1/2\alpha',1/2\beta'}\\ &-g_{\mathrm{v}}^2\,\mathrm{C}^{00}_{1/2\alpha,1/2\beta}\;iG_{\mathrm{v}}^{(\mathrm{f})}(E_{\mathrm{cm}})\;\mathrm{C}^{00}_{1/2\alpha',1/2\beta'}\\ &+\cdots\,.\end{aligned} \tag{4.26}$$

The ellipses again denote higher partial waves negligible at NLO. For p-n scattering in the ${}^3s_1$ (${}^1s_0$) channel, one needs to couple the external p-n states to total spins $j = 1$ ($j = 0$). That yields the amplitudes

$$it_{\mathrm{d}}^{1m,1m'}\left(\boldsymbol{k},\boldsymbol{k}';E_{\mathrm{cm}}\right) = \langle(\mathrm{pn})_{1m'}|\,i\hat{T}\,|(\mathrm{pn})_{1m}\rangle\left(\boldsymbol{k},\boldsymbol{k}';E_{\mathrm{cm}}\right) \tag{4.27a}$$

$$= \mathrm{C}^{1m}_{1/2\alpha,1/2\beta}\mathrm{C}^{1m'}_{1/2\alpha',1/2\beta'}\left\langle p_{\alpha'}\mathrm{n}_{\beta'}\right| i\hat{T}\left|p_\alpha \mathrm{n}_\beta\right\rangle\left(\boldsymbol{k},\boldsymbol{k}';E_{\mathrm{cm}}\right) \tag{4.27b}$$

$$= -ig_{\mathrm{d}}^2\,G_{\mathrm{d}}^{(\mathrm{f})}(E_{\mathrm{cm}})\,\delta^{mm'} \tag{4.27c}$$

and similarly

$$it_{\mathrm{v}}\left(\boldsymbol{k},\boldsymbol{k}';E_{\mathrm{cm}}\right) = -ig_{\mathrm{v}}^2 G_{\mathrm{d}}^{(\mathrm{f})}(E_{\mathrm{cm}})\,. \tag{4.28}$$

By comparison to Eq. (4.9), we can match the Lagrangian parameters to the ERE. Up to NLO, we obtain the relations

$$\Delta_{b,0}(\Lambda_{\mathrm{PDS}})\,g_b^{-2} = \frac{m_{\mathrm{N}}}{4\pi}\left(a_b^{-1}-\Lambda_{\mathrm{PDS}}\right)\quad(b\in\{\mathrm{d},\mathrm{v}\}), \tag{4.29a}$$

$$\Delta_{b,1}\,g_b^{-2} = -\frac{m_{\mathrm{N}}^2}{8\pi}r_b\quad(b\in\{\mathrm{d},\mathrm{v}\})\,. \tag{4.29b}$$

The MS renormalization scheme can be recovered by sending $\Lambda_{\mathrm{PDS}} \to 0$. At LO ($r_b = 0 = \Delta_{b,1}$), the coupling is not independent of $\Delta_{b,0}$. Instead, the only free parameter is the combination $\Delta_{b,0}g_b^{-2}$, which is fine-tuned to yield an unnaturally small value for a_b^{-1}. Being a Hermitian theory, the couplings of EFT($\not\pi$) are real, i.e., $g_b^2 > 0$. Thus, in order to ensure $r_b > 0$ at NLO, the signs $\Delta_{b,1}$ have to be negative as claimed above. The final dibaryon propagators then read

$$iG_b^{(\mathrm{f})}(E_{\mathrm{cm}}) = -ig_b^{-2}\,\frac{4\pi}{m_{\mathrm{N}}}\left[-a_b^{-1}-i\bar{k}+\frac{r_b}{2}\bar{k}^2+\mathcal{O}\left(\bar{k}^4 m_\pi^{-3}\right)\right]^{-1}\quad(b\in\{\mathrm{d},\mathrm{v}\})\,. \tag{4.30}$$

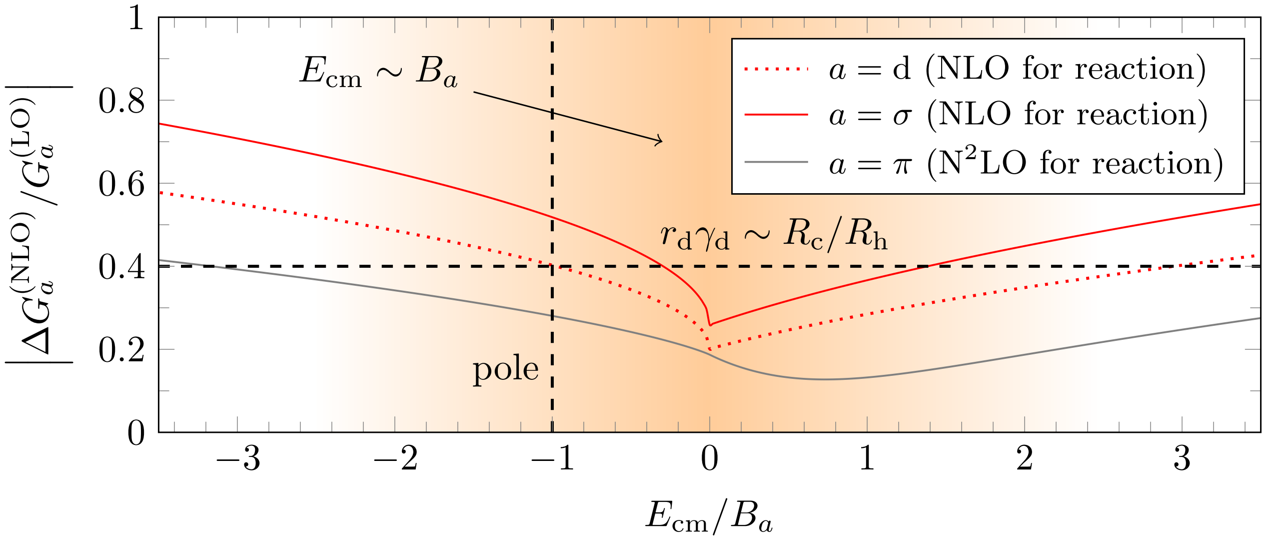

Figure 4.6.: The red dotted curve shows the ratio $|\Delta G_{\mathrm{d}}^{(\mathrm{NLO})}/G_{\mathrm{d}}^{(\mathrm{LO})}|$ between the leading deuteron propagator terms of Eq. (4.33b) around the pole at $E_{\mathrm{cm}} = -B_{\mathrm{d}}$ (vertical grid line) and for $E_{\mathrm{cm}} \sim B_{\mathrm{d}}$ (orange region). In both regions, the ratio is of order $r_{\mathrm{d}}\gamma_{\mathrm{d}} \sim R_{\mathrm{c}}/R_{\mathrm{h}}$ (horizontal grid line). The solid curves show ratios for the propagators of ^{11}Be (red) and ^{11}Be* (gray), which scale more or less similarly. Red (gray) curves indicate that the respective correction $i\Delta G_a^{(\mathrm{NLO})}$ ($a \in \{\mathrm{d}, \sigma, \pi\}$) enters the reaction ^{10}Be(d, p)^{11}Be at NLO (N^{2}LO).

In the deuteron channel, we will use the binding energy $B_{\mathrm{d}} = \gamma_{\mathrm{d}}^2/m_{\mathrm{N}} = 2.22\,\mathrm{MeV}$ as input at each power counting order. It is thus beneficial to make the pole at $\bar{k} = i\gamma_{\mathrm{d}}$ explicit by writing

$$iG_{\mathrm{d}}^{(\mathrm{f})}(E_{\mathrm{cm}}) = i g_{\mathrm{d}}^{-2}\frac{4\pi}{m_{\mathrm{N}}}\left[\gamma_{\mathrm{d}} + i\bar{k} - \frac{r_b}{2}\left(\bar{k}^2 + \gamma_{\mathrm{d}}^2\right) + \mathcal{O}\left(\bar{k}^4 m_\pi^{-3}\right)\right]^{-1} \quad (b \in \{\mathrm{d}, \mathrm{v}\}). \tag{4.31}$$

In this scheme, the scattering length becomes a prediction. Its expansion in the $\chi_2 = r_{\mathrm{d}}\gamma_{\mathrm{d}} \sim 0.4$ power counting reads

$$a_{\mathrm{d}}^{-1} = \gamma_{\mathrm{d}}\left(1 - \underbrace{\frac{1}{2}r_{\mathrm{d}}\gamma_{\mathrm{d}}}_{\text{NLO}} + \underbrace{\mathcal{O}\left((r_{\mathrm{d}}\gamma_{\mathrm{d}})^2\right)}_{\text{N}^2\text{LO, etc.}}\right). \tag{4.32}$$

Even though $iG_{\mathrm{d}}^{(\mathrm{f})}$ contains more information on physics in the $^3s_1$ channel than only the position of the deuteron pole, let us call refer to it as the “deuteron propagator” in the following.

Three-body calculations will involve loop integrals over the deuteron propagator. We utilize the fact that the largest contribution to loop integrals comes from the pole region and thus expand the deuteron propagator at $\bar{k} = i\gamma_{\mathrm{d}}$, i.e.,

$$iG_{\mathrm{d}}^{(\mathrm{f})}(E_{\mathrm{cm}}) = i g_{\mathrm{d}}^{-2}\frac{4\pi}{m_{\mathrm{N}}}\left[\gamma_{\mathrm{d}} + i\bar{k}\right]^{-1}\left(1 + \frac{r_{\mathrm{d}}}{2}\left(\gamma_{\mathrm{d}} - i\bar{k}\right) + \mathcal{O}\left((\gamma_{\mathrm{d}}r_{\mathrm{d}})^2\right)\right) \tag{4.33a}$$

$$= \underbrace{iG_{\mathrm{d}}^{(\mathrm{LO})}(E_{\mathrm{cm}})}_{\sim\gamma_{\mathrm{d}}^{-1}} + \underbrace{i\Delta G_{\mathrm{d}}^{(\mathrm{NLO})}(E_{\mathrm{cm}})}_{\sim\gamma_{\mathrm{d}}^{-1}\cdot r_{\mathrm{d}}\gamma_{\mathrm{d}}} + \cdots, \tag{4.33b}$$

where we count $\bar{k} \sim \gamma_{\mathrm{d}}$. Beyond LO, we moreover write $iG_{\mathrm{d}}^{(\mathrm{NLO})} \equiv iG_{\mathrm{d}}^{(\mathrm{LO})} + i\Delta G_{\mathrm{d}}^{(\mathrm{NLO})}$, etc. The scaling relation $i\Delta G_{\mathrm{d}}^{(\mathrm{NLO})} \sim r_{\mathrm{d}}\gamma_{\mathrm{d}} \cdot iG_{\mathrm{d}}^{(\mathrm{LO})}$ holds not only around the pole $E_{\mathrm{cm}} = -B_{\mathrm{d}}$, but also for small $E_{\mathrm{cm}} \sim B_{\mathrm{d}}$ in general. That can be seen from Fig. 4.6, where the red dotted line represents the ratio between the leading two expansion terms.

The residue

$$Z_{\mathrm{d}} \equiv \left[\frac{\partial G_{\mathrm{d}}^{(\mathrm{f})\,-1}}{\partial E_{\mathrm{cm}}} \bigg|_{E_{\mathrm{cm}}=-B_{\mathrm{d}}} \right]^{-1} = g_{\mathrm{d}}^{-2} \frac{8\pi}{m_{\mathrm{N}}^2} \gamma_{\mathrm{d}} \left(1 + r_{\mathrm{d}}\gamma_{\mathrm{d}} + \mathcal{O}\left((r_{\mathrm{d}}\gamma_{\mathrm{d}})^2\right)\right) \tag{4.34a}$$

$$\equiv \underbrace{Z_{\mathrm{d}}^{(\mathrm{LO})}}_{\sim\gamma_{\mathrm{d}}} + \underbrace{\Delta Z_{\mathrm{d}}^{(\mathrm{NLO})}}_{\sim\gamma_{\mathrm{d}}\cdot r_{\mathrm{d}}\gamma_{\mathrm{d}}} + \cdots \tag{4.34b}$$

with $Z_{\mathrm{d}}^{(\mathrm{NLO})} \equiv Z_{\mathrm{d}}^{(\mathrm{LO})} + \Delta Z_{\mathrm{d}}^{(\mathrm{NLO})}$, etc. has a similar expansion. In three-body calculations, each external deuteron state must be normalized with an appropriate factor $(Z_{\mathrm{d}})^{1/2}$. As done in Chapter 3, the LO propagator $iG_{\mathrm{d}}^{(\mathrm{LO})}$ will be drawn without a circle.

4.1.2 Core-neutron scattering in Halo EFT

As done for the p-n system, we start by considering the elastic c-n amplitude in the ${}^2l_j$ channel of the halo state $\mathrm{h} \equiv {}^{A+1}\mathrm{X}$. For small E_{cm}, it may be written in the ERE form

$$it_{\mathrm{h}}^{\alpha,\alpha'}\left(\boldsymbol{k},\boldsymbol{k}';E_{\mathrm{cm}}\right) = i\,\frac{2\pi}{\mu_{\mathrm{Nc}}}\,T_{l,j}^{\alpha,\alpha'}\left(\hat{\boldsymbol{k}},\hat{\boldsymbol{k}}'\right)|\boldsymbol{k}|^l\,|\boldsymbol{k}'|^l \left[-a_{\mathrm{h}}^{-1} + \frac{r_{\mathrm{h}}}{2}\bar{k}^2 + \sum_{n\geq 2}\mathscr{P}_{\mathrm{h}}^{(2n)}\bar{k}^{2n} - i\bar{k}^{2l+1}\right]^{-1}. \tag{4.35}$$

Equation (4.35) involves the c-n reduced mass

$$\mu_{\mathrm{Nc}} \equiv \frac{m_{\mathrm{c}} m_{\mathrm{N}}}{m_{\mathrm{c}} + m_{\mathrm{N}}} = \frac{m_{\mathrm{N}}}{1 + 1/A}\,, \tag{4.36}$$

ERE coefficients a_{h}^{-1} (in MeV^{2l+1}), r_{h} (in MeV^{2l-1}), $\mathscr{P}_{\mathrm{h}}^{(2n)}$ (in $\mathrm{MeV}^{2l+1-2n}$), the on-shell relative momentum

$$\bar{k} \equiv i\sqrt{-2\mu_{\mathrm{Nc}}\left(E_{\mathrm{cm}} + i\epsilon\right)} \tag{4.37}$$

and relative c-n momenta $\boldsymbol{k}^{(\prime)}$ defined below. Since the core has spin-parity 0^+, the amplitude only depends on the neutron spins $\alpha, \alpha' \in \{1/2, -1/2\}$. The respective spin tensor $T_{l,j}^{\alpha,\alpha'}\left(\hat{\boldsymbol{k}},\hat{\boldsymbol{k}}'\right)$ in Eq. (4.35) is discussed below.

The scalings of the various ERE coefficients will not be specified in this section since they differ from system to system. At this point, we only assume the existence of a shallow bound state at $E_{\mathrm{cm}} = -B_{\mathrm{h}}$. Due to some fine-tuning, the binding momentum $\gamma_{\mathrm{h}} = (2\mu_{\mathrm{Nc}}B_{\mathrm{h}})^{1/2}$ be unnaturally small compared to some natural high momentum scale K_{hi}, such that only a few ERE coefficients are needed to produce the pole at LO. For s-wave halo states, the fine-tuning typically occurs in the scattering length $a_{\mathrm{h}} \sim \gamma_{\mathrm{h}}^{-1}$, while higher order coefficients scale naturally [19]. This scheme has been used to describe various one-neutron halo states, including ${}^{11}\mathrm{Be}$ [54], ${}^{15}\mathrm{C}$ [114], ${}^{19}\mathrm{C}$ [117], and the first excited state ${}^{17}\mathrm{C}^*$ [118]. For p-wave halo states like ${}^{11}\mathrm{Be}^*$, the shallow pole can for example be produced by an unnaturally small scattering volume [54, 85]. Moreover, also d-wave halo states have been described in the literature. One example is the first excited state ${}^{15}\mathrm{C}^*$ ($j^P = 5/2^+$) [114]. Different d-wave scaling schemes were proposed in [79, 85, 114].

Lagrangian for the halo state ${}^{A+1}\mathrm{X}$

The 0^+ core $\mathrm{c} = {}^{A}\mathrm{X}$ enters Halo EFT via the nonrelativistic scalar field c with kinetic mass $m_{\mathrm{c}} \equiv Am_{\mathrm{N}}$ and vanishing rest mass. The neutron field is the same as in Eq. (4.17). The Halo EFT kinetic term thus reads

$$\mathscr{L}_{\text{Halo EFT, kin}} = c^\dagger\left[iD_0 + \frac{\boldsymbol{D}^2}{2m_{\mathrm{c}}}\right]c + n_\alpha^\dagger\left[i\partial_0 + \frac{\boldsymbol{\nabla}^2}{2m_{\mathrm{N}}}\right]n_\alpha\,. \tag{4.38}$$

The core propagator is represented by a dashed line in this chapter; see Fig. 4.3. In the following, the charge of the core is denoted $Q_c \geq 1$.

Together with the neutron field n_α of Eq. (4.17), c couples to the halo auxiliary field h_{m_j}.[5] It exhibits a spherical index $m_j \in \{j, \cdots, -j\}$. The respective Lagrangian term is written

$$\begin{aligned}\mathscr{L}_{\mathrm{cn}} = h^\dagger_{m_j} &\left[\sum_{n\geq 0} \Delta_{\mathrm{h}}^{(n)} \left(iD_{\mathrm{cm}}\right)^n\right] h_{m_j} \\ &- g_{\mathrm{h}}\, \mathrm{C}^{jm_j}_{1/2\alpha, lm_l} \left[h^\dagger_{m_j} \left(n_\alpha \left\{-i\overleftrightarrow{\nabla}\right\}_{lm_l} c\right) + \mathrm{H.c.}\right] \\ &+ \cdots . \end{aligned} \tag{4.39}$$

The propagator term in the first row resembles previous Lagrangian terms in this thesis. Due to Galilean invariance, the halo state possesses kinetic mass

$$M_{\mathrm{Nc}} \equiv m_{\mathrm{c}} + m_{\mathrm{N}} = (A+1)\, m_{\mathrm{N}} \,. \tag{4.40}$$

Due to the scale separation of h, only a finite number of parameters $\Delta_{\mathrm{h}}^{(n)}$ (mass units $\mathrm{MeV}^{1-\mathrm{n}}$) are needed at fixed power counting order. Again, we define the auxiliary field such that $\Delta_{\mathrm{h}}^{(1)} = \pm 1$ is a sign.

The vertex term requires a bit more explanation. In contrast to the p-n sector, angular momentum coupling takes place not between two spins but between the neutron spin 1/2 and the orbital angular momentum $l \geq 0$. Thus, the vertex involves the Galilean-invariant derivative defined in Eq. (3.26). Applied to c-n momentum states, the operator[6] $-i\overleftrightarrow{\nabla}$ yields the c-n relative momentum

$$\boldsymbol{k} = \xi \boldsymbol{k}_{\mathrm{n}} - (1-\xi)\, \boldsymbol{k}_{\mathrm{c}} \tag{4.41}$$

with mass ratio

$$\xi \equiv \frac{m_{\mathrm{c}}}{m_{\mathrm{c}} + m_{\mathrm{N}}} = \frac{1}{1+1/A} \,. \tag{4.42}$$

The Galilean-invariant derivative is embedded in an l-wave tensor structure $\{\cdot\}_{lm_l}$. Since we work in the spherical representation this structure can conveniently be expressed in terms of spherical harmonics. For an arbitrary vector (operator) $\boldsymbol{\mathcal{O}}$, we write

$$\{\boldsymbol{\mathcal{O}}\}_{lm_l} \equiv \sqrt{\frac{4\pi}{2l+1}}\, |\boldsymbol{\mathcal{O}}|^l\, Y_l^{m_l}\left(\hat{\boldsymbol{\mathcal{O}}}\right) \tag{4.43}$$

with $\hat{\boldsymbol{\mathcal{O}}} \equiv \boldsymbol{\mathcal{O}}/|\boldsymbol{\mathcal{O}}|$. This expression is normalized such that it gives 1 in the s-wave case ($l = 0$). The tensors can be translated to the cartesian basis. For example, one obtains the relations

$$\{\boldsymbol{k}\}_{00} = 1\,, \tag{4.44a}$$

$$\{\boldsymbol{k}\}_{1m_l} = \begin{cases} (\mp k_1 - ik_2)/\sqrt{2}, & m_l = \pm 1 \\ k_3, & m_l = 0 \end{cases} . \tag{4.44b}$$

$$\{\boldsymbol{k}\}_{2m_l} = \begin{cases} \sqrt{3/2}\,(\mp k_1 - ik_2)^2/2, & m_l = \pm 2 \\ \sqrt{3/2}\,(\mp k_1 - ik_2)\, k_3, & m_l = \pm 1 \\ \left(2k_3^2 - k_1^2 - k_2^2\right)/2, & m_l = 0 \end{cases} . \tag{4.44c}$$

---

[5] Different halo states will be distinguished by their quantum number l. Following Ref. [54], we write $h = \sigma, \pi, \cdots$ for s-waves, p-waves, etc.

[6] The factor $-i$ could in principle be removed by applying field redefinitions $h^{(\dagger)}_{m_j} \to (\pm i)^l\, h^{(\dagger)}_{m_j}$. The "kinematic" term of the halo state is not affected by such a phase since it is proportional to $h^\dagger_{m_j} h_{m_j}$.

The Feynman rule for transitions cn ⟷ h then read

$$\left\langle h_{m_j'} \middle| i\hat{T} \middle| (n_\alpha c)_{\boldsymbol{k}} \right\rangle_{\mathcal{O}(g_\mathrm{h})} = -i g_\mathrm{h} \mathrm{C}^{jm_j'}_{1/2\alpha,lm_l} \{\boldsymbol{k}\}_{lm_l} \,, \tag{4.45a}$$

$$\left\langle (n_{\alpha'} c)_{\boldsymbol{k}'} | i\hat{T} \middle| h_{m_j} \right\rangle_{\mathcal{O}(g_\mathrm{h})} = -i g_\mathrm{h} \mathrm{C}^{jm_j}_{1/2\alpha',lm_l'} \{\boldsymbol{k}'\}^*_{lm_l'} \tag{4.45b}$$

and summations over $m_l^{(\prime)}$ are implicit. We will see below that the tensor structure produces the correct angular dependence for the c-n scattering amplitude.

c-n scattering channels which do not exhibit a shallow state will be neglected in this thesis. They are assumed to be suppressed due to the lack of further fine-tunings, similar to higher p-n partial wave channels. Possible interactions at higher power counting orders are condensed in the ellipses at the end of Eq. (4.39).

Self-energy and full halo-state propagator

The self-energy of h is calculated in Appendix E.1.2. In the PDS scheme it reads[7]

$$\Sigma_\mathrm{h}^{(\mathrm{PDS})}(E_\mathrm{cm}) = -g_\mathrm{h}^2 \frac{\mu_\mathrm{Nc}}{2\pi(2l+1)} [2\mu_\mathrm{Nc}(E_\mathrm{cm}+i\epsilon)]^l \left(\Lambda_\mathrm{PDS} - [-2\mu_\mathrm{Nc}(E_\mathrm{cm}+i\epsilon)]^{1/2}\right) \tag{4.46a}$$

$$= -g_\mathrm{h}^2 \frac{\mu_\mathrm{Nc}}{2\pi(2l+1)} \bar{k}^{2l} \left(\Lambda_\mathrm{PDS} + i\bar{k}\right) \tag{4.46b}$$

and the full propagator is given by

$$iG_\mathrm{h}^{(\mathrm{f})}(E_\mathrm{cm}) = -i g_\mathrm{h}^{-2} \frac{2\pi(2l+1)}{\mu_\mathrm{Nc}} \left[\bar{k}^{2l+1}\cot\delta_l(\bar{k}) - i\bar{k}^{2l+1}\right]^{-1} \tag{4.47}$$

with phase shift term

$$\bar{k}^{2l+1}\cot\delta_l(\bar{k}) = -g_\mathrm{h}^{-2} \frac{2\pi(2l+1)}{\mu_\mathrm{Nc}} \sum_{n=0}^{\infty} \Delta_\mathrm{h}^{(n)} \left(\frac{\bar{k}^2}{2\mu_\mathrm{Nc}}\right)^2 - \Lambda_\mathrm{PDS}\bar{k}^{2l} \tag{4.48a}$$

$$\equiv -a_\mathrm{h}^{-1} + \frac{r_\mathrm{h}}{2}\bar{k}^2 + \sum_{n\geq 2} \mathscr{P}_\mathrm{h}^{(2n)} \bar{k}^{2n} \,. \tag{4.48b}$$

Moreover, the full residue at the pole $E_\mathrm{cm} = -B_\mathrm{h}$ reads

$$Z_\mathrm{h} \equiv \left[\left.\frac{\partial G_\mathrm{h}^{(\mathrm{f})\text{ -1}}}{\partial E_\mathrm{cm}}\right|_{E_\mathrm{cm}=-B_\mathrm{h}} \right]^{-1} = g_\mathrm{h}^{-2} \frac{2\pi(2l+1)}{\mu_\mathrm{Nc}^2} \left[(-1)^l (2l+1)\gamma_\mathrm{h}^{2l-1} + 2\sum_{n\geq 1}(-1)^n n \mathscr{P}_\mathrm{h}^{(2n)} \gamma_\mathrm{h}^{2n-2} \right]^{-1} \tag{4.49}$$

with $\mathscr{P}_\mathrm{h}^{(2)} \equiv r_\mathrm{h}/2$.

As usual, the elastic two-body amplitude can be calculated by attaching external c-n legs to the propagator. We find

$$it_\mathrm{h}^{\alpha,\alpha'}(\boldsymbol{k}, \boldsymbol{k}'; E_\mathrm{cm}) = \left(-i g_\mathrm{h} \mathrm{C}^{jm_j}_{1/2\alpha,lm_l} \{\boldsymbol{k}\}_{lm_l}\right) iG_\mathrm{h}^{(\mathrm{f})}(E_\mathrm{cm}) \delta^{m_j m_j'} \left(-i g_\mathrm{h} \mathrm{C}^{jm_j'}_{1/2\alpha',lm_l'} \{\boldsymbol{k}'\}_{lm_l'}\right) \tag{4.50a}$$

$$= i\frac{2\pi}{\mu_\mathrm{Nc}} |\boldsymbol{k}|^l \left|\boldsymbol{k}'\right|^l \frac{(j+1/2)P_l(x)\delta^{\alpha\alpha'} - 2i(j-l)P_l'(x)\boldsymbol{\nu}\cdot\boldsymbol{\sigma}_{\alpha\alpha'}}{\bar{k}^{2l+1}\cot\delta_l(\bar{k})} \tag{4.50b}$$

---

[7] Spin-projection conserving factor $\delta^{m_j m_j'}$ for self-energy and propagator are again omitted here.

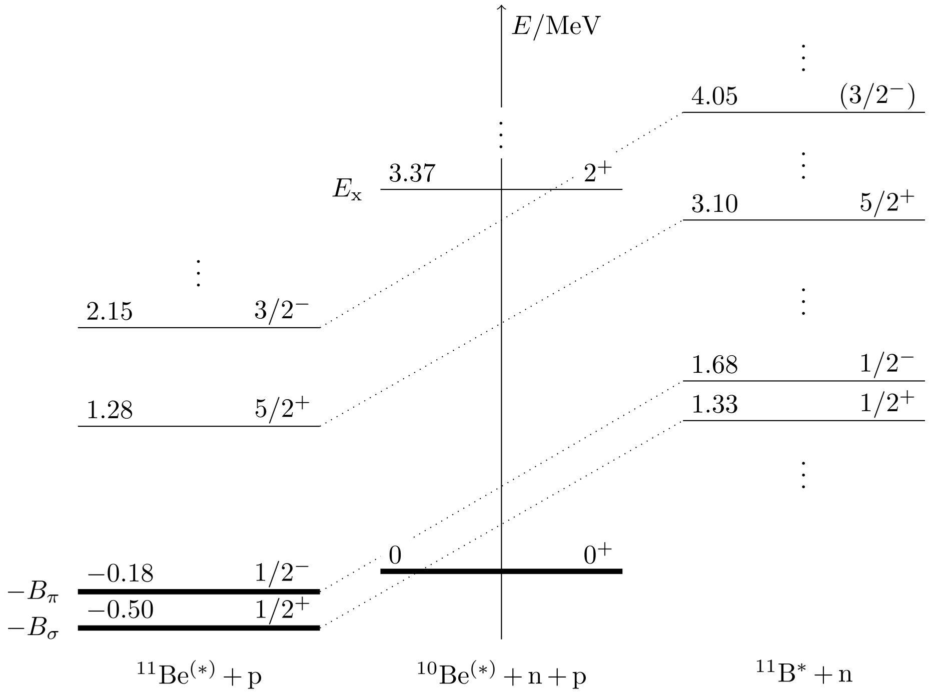

Figure 4.7.: Level scheme of the three-body system ^{10}Be-n-p [120–122]. The center column shows the ground and first excited state of the core ^{10}Be. Bound and resonance states of the c-n (^{11}Be) and c-p (^{11}B) systems are depicted in the left and right columns, respectively. We only show ^{11}B levels, which have been seen in the ^{10}Be(p, γ)^{11}B experiment of Ref. [123]. They can be interpreted as isobaric analog state of the lowest ^{11}Be levels [124]. In this thesis, we explicitly include those states with thick lines.

with $x \equiv \hat{\boldsymbol{k}} \cdot \hat{\boldsymbol{k}}'$ and $\boldsymbol{v} \equiv \hat{\boldsymbol{k}} \times \hat{\boldsymbol{k}}'$. The spin tensor $T^{\alpha,\alpha'}_{l,j}$ above is now given by the enumerator of Eq. (4.50b). It was derived using Eq. (34) of Ref. [119]. The first term of the spin tensor represents spin transitions $\alpha = \alpha'$ and the second term allows spin flips for $l \geq 1$. In the first case, the chosen interaction vertices recover the familiar $P_l(x)$ dependence one also gets for scattering of two spinless particles.

Note that Halo EFT can be extended to shallow resonance states above the c-n separation threshold. In fact, such states are treated just like the D^{0*} resonance in Chapter 3 [93]. For example, the $^2p_{3/2}$ channel of αn scattering exhibits a shallow "Helium-5" resonance. As shown by Bedaque *et al.*, its existence can be explained by a single fine-tuning [85]. The only conceptual difference to $D^0\pi^0$ scattering is that the fine-tuning occurs in the scattering volume and not in the p-wave effective range of αn scattering. The scheme was later adopted by Ji *et al.*, who used the αn resonance to calculate structure properties of the two-neutron halo state ^{6}He in an αnn Faddeev calculation [24]. However, in the generic ^{A}X(d, p)$^{A+1}$X reaction we want to study, at least the outgoing $^{A+1}$X has to be a bound c-n state. We thus focus on the description of bound halo states in this thesis.

Application 1: the ground state of Beryllium-11

Let us in the following apply the c-n formalism developed so far to the Beryllium-11 system. Both the ground state $\sigma \equiv {}^{11}$Be ($^2s_{1/2}$) and the first excited state $\pi \equiv {}^{11}$Be* ($^2p_{1/2}$) lie extremely close to the ^{10}Be-n threshold; see Fig. 4.7. The respective binding energies $B_\sigma = 0.50\,\mathrm{MeV}$ and $B_\pi = 0.18\,\mathrm{MeV}$ are much smaller than the excitation energy $E_\mathrm{x} = 3.37\,\mathrm{MeV}$ of the ^{10}Be core [120, 121]. In other words, the binding momenta $\gamma_\sigma = (2\mu_\mathrm{Nc}B_\sigma)^{1/2} \approx 29\,\mathrm{MeV}$ and $\gamma_\pi = (2\mu_\mathrm{Nc}B_\pi)^{1/2} \approx 18\,\mathrm{MeV}$ are smaller than the typical high momentum scale $K_\mathrm{hi} \equiv (2\mu_\mathrm{Nc}E_\mathrm{x})^{1/2} \approx 76\,\mathrm{MeV}$ and both states fulfill the above definition of a halo state.

As a consequence of the scale separation, the experimentally measured radius $R_\mathrm{h} \approx 7\,\mathrm{fm}$ of the Beryllium-11 ground state is unnaturally large. In contrast, the core radius represents a natural nuclear physics length scale, i.e., $R_\mathrm{c} \sim K_\mathrm{hi}^{-1} \approx 2.6\,\mathrm{fm}$ [53]; see Fig. 1.3(a) for illustration. In Halo EFT it is common to express all ERE coefficients of the Beryllium-11 nucleus in terms of the two radii [54]. The expansion parameter

$$\frac{R_\mathrm{c}}{R_\mathrm{h}} \sim 0.4 \approx \chi_2 \tag{4.51}$$

is then as small as the expansion parameter $\chi_2 = r_\mathrm{d}\gamma_\mathrm{d}$ of the p-n system.

For example, the inverse binding momentum $\gamma_\sigma^{-1} \approx 6.8\,\mathrm{fm}$ is almost exactly as large as R_h and thus one counts $\gamma_\sigma \sim R_\mathrm{h}^{-1}$ in Halo EFT. In contrast, the effective range r_σ is counted like R_c. Hammer and Phillips used Halo EFT to relate the effective range to the low-energy E1 strength of ^{11}Be breakup. Using theory predictions for the E1 strength of Ref. [125], the effective range was determined to be $2.7\,\mathrm{fm} \sim R_\mathrm{c}$. This value confirms the scaling assumption of Halo EFT. Higher-order ERE coefficients $\mathscr{P}_\sigma^{(2n)} \sim R_\mathrm{c}^{2n-1}$ $(n \geq 2)$ are assumed to scale naturally as well.

(a) (b)

Figure 4.8.: The vertices for (a) c n → σ and (b) c n → π transitions have Feynman rules $-ig_\sigma\delta^{\alpha m'_j}$ and $-ig_\pi \mathrm{C}^{1/2m'_j}_{1/2\alpha,1m_l}\,\{\boldsymbol{k}\}_{1m_l}$, respectively. The vertex in (a) is invariant under time reversal. Vertices for $\pi \to$ c n involve a complex-conjugated momentum tensor $\{\boldsymbol{k}'\}^*_{1m_l}$.

Using the vertex given in Fig. 4.8(a), we calculate the c-n self-energy loop and resum it; see Fig. 4.9(a). The full propagator

$$iG_\sigma^{(\mathrm{f})}(E_\mathrm{cm}) = ig_\sigma^{-2}\,\frac{2\pi}{\mu_\mathrm{Nc}}\left[\gamma_\sigma + i\bar{k} - \frac{r_\sigma}{2}\left(\bar{k}^2+\gamma_\sigma^2\right) + \mathcal{O}\left(\bar{k}^4 R_\mathrm{c}^3\right)\right]^{-1}. \tag{4.52}$$

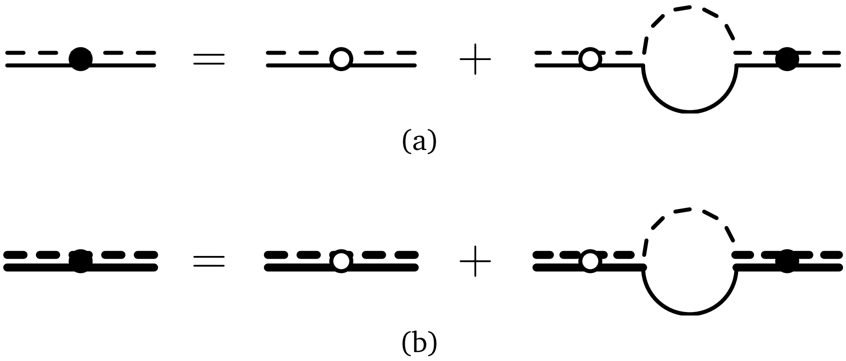

(a)

(b)

Figure 4.9.: The full dibaryon propagators (a) $iG_\sigma^{(\mathrm{f})}$ and (b) $iG_\pi^{(\mathrm{f})}$ include ^{10}Be-n self-energy loops $-i\Sigma_\sigma$ and $-i\Sigma_\pi$, respectively, to all orders. Dashed lines represent the ^{10}Be core, solid lines the neutron. The PDS counter terms $-i\Delta\Sigma_\mathrm{h}^{(\mathrm{PDS})}$ (h $\in \{\sigma, \pi\}$) are omitted; see Appendix E.1.2.

has the same structure as the deuteron propagator. The propagator is represented by a solid-dashed double line; see Fig. 4.3. The expansion of the inverse scattering length reads

$$a_\sigma^{-1} = \gamma_\sigma \left(1 - \frac{r_\sigma \gamma_\sigma}{2} + \mathcal{O}\left((R_\mathrm{c}/R_\mathrm{h})^2\right)\right) \sim R_\mathrm{h}^{-1} \,. \tag{4.53}$$

In three-body calculations, we will use the propagator expansion

$$\begin{aligned} iG_\sigma^{(\mathrm{f})}(E_\mathrm{cm}) &= i g_\sigma^{-2} \frac{2\pi}{\mu_\mathrm{Nc}} \left[\gamma_\sigma + i\bar{k}\right]^{-1} \left(1 + \frac{r_\sigma}{2}\left(\gamma_\sigma - i\bar{k}\right) + \mathcal{O}\left((R_\mathrm{c}/R_\mathrm{h})^2\right)\right) && \text{(4.54a)} \\ &= \underbrace{iG_\sigma^{(\mathrm{LO})}(E_\mathrm{cm})}_{\sim R_\mathrm{h}} + \underbrace{i\Delta G_\sigma^{(\mathrm{NLO})}(E_\mathrm{cm})}_{\sim R_\mathrm{h} \cdot R_\mathrm{c}/R_\mathrm{h}} + \cdots \,, && \text{(4.54b)} \end{aligned}$$

where we count momenta $\bar{k} \sim \gamma_\sigma \sim R_\mathrm{h}^{-1}$. As for the deuteron, we use the notations $iG_\sigma^{(\mathrm{NLO})} \equiv iG_\sigma^{(\mathrm{LO})} + i\Delta G_\sigma^{(\mathrm{NLO})}$, etc.

The residue expansion reads

$$\begin{aligned} Z_\sigma \equiv \left[\left.\frac{\partial G_\sigma^{(\mathrm{f})\,-1}}{\partial E_\mathrm{cm}}\right|_{E_\mathrm{cm}=-B_\sigma}\right]^{-1} &= g_\sigma^{-2} \frac{2\pi}{\mu_\mathrm{Nc}^2} \gamma_\sigma \left(1 + r_\sigma\gamma_\sigma + \mathcal{O}\left((R_\mathrm{c}/R_\mathrm{h})^2\right)\right) && \text{(4.55a)} \\ &\equiv \underbrace{Z_\sigma^{(\mathrm{LO})}}_{\sim R_\mathrm{h}^{-1}} + \underbrace{\Delta Z_\sigma^{(\mathrm{NLO})}}_{\sim R_\mathrm{h}^{-1} \cdot R_\mathrm{c}/R_\mathrm{h}} + \cdots && \text{(4.55b)} \end{aligned}$$

and $Z_\sigma^{(\mathrm{NLO})} \equiv Z_\sigma^{(\mathrm{LO})} + \Delta Z_\sigma^{(\mathrm{NLO})}$, etc. The LO propagator $iG_\sigma^{(\mathrm{LO})}$ will be drawn without a circle.

So far, we have identified ^{11}Be with a pure ^{10}Be-n state ($^2s_{1/2}$). However, in principle, ^{11}Be also couples to the $^4d_{1/2}$ and $^6d_{1/2}$ channels of an excited 2^+ core ^{10}Be* and a neutron. Note that the ^{10}Be*-n threshold resides far away from the pole at an energy distance $E_\mathrm{x} + B_\sigma \gg B_\sigma$; see Fig. 4.7. Close to the pole ($E_\mathrm{cm} \approx -B_\sigma$), the propagator is insensitive to nonanalyticities of this remote threshold. In fact, residual modifications to $iG_\sigma^{(\mathrm{f})}$ are automatically taken into account by reproducing ERE observables and the physical pole position. Thus, core excitation effects enter our *effective* single-channel description implicitly through renormalization. In Appendix E.3, we show that our approach is equivalent to a theory with a dynamical core excitation field.

Lately, the role of core excitations in transfer reactions was also addressed in the context of traditional reaction model calculations; see for example Refs. [126–130]. In Ref. [126], Deltuva *et al.* found that dynamical core excitations in the ^{11}Be bound state do not influence the ^{10}Be(d, p)^{11}Be cross section. That confirms our claim that they can be treated effectively in the ^{11}Be propagator.[8] In general, reaction models have been very successful in reproducing experimental cross sections for various energies [59, 60]. Still, the utilized two-body potentials (usually complex-valued Wood-Saxon shapes) are often not motivated by the respective physical systems and involve many fitting parameters. Moreover, model calculations typically start from the traditional shell model (SM) picture. Here, the ^{11}Be wave function is defined as a superposition

$$\left|{}^{11}\mathrm{Be}\right\rangle_\mathrm{SM} \equiv C_{^2s_{1/2}} \left|\left({}^{10}\mathrm{Be} + \mathrm{n}\right)_{^2s_{1/2}}\right\rangle_\mathrm{SM} + C_{^4d_{1/2}} \left|\left({}^{10}\mathrm{Be}^* + \mathrm{n}\right)_{^4d_{1/2}}\right\rangle_\mathrm{SM} + C_{^6d_{1/2}} \left|\left({}^{10}\mathrm{Be}^* + \mathrm{n}\right)_{^6d_{1/2}}\right\rangle_\mathrm{SM} \tag{4.56}$$

of SM states; see for example Ref. [131]. The absolute squares of the coefficients are called “spectroscopic factors”. These nonobservable quantities depend on the choice of two-body potentials; see for example Ref. [64] by Capel *et al.*. In model calculations, the spectroscopic factors have to be extracted from data by globally rescaling cross-section predictions [60].

---

[8] Note that breakup can lead to core excitations outside the ^{11}Be propagator. Such contributions have to be analyzed separately; see Sec. 4.2.3.

Spectroscopic factors are not needed to obtain cross sections in Halo EFT. Once physics in the pole region is reproduced at a desired accuracy, the ^{11}Be ground state wave function is fully determined by low-energy observables [22]. In particular, Eq. (4.52) yields a systematic low-energy expansion for the asymptotic normalization factor (ANC)

$$A_\sigma = \sqrt{\frac{2\gamma_\sigma}{1 - r_\sigma\gamma_\sigma + \mathcal{O}((R_\mathrm{c}/R_\mathrm{h})^3)}}\,, \tag{4.57}$$

which normalizes the radial wave function $u_\sigma(r) = A_\sigma \exp(-\gamma_\sigma r)$ [22]. Recently, Calci *et al.* obtained the ANC value $A_\sigma = 0.786\,\mathrm{fm}^{-1}$ in the no-core shell model with continuum (NCSMC) [132]. Yang and Capel extracted a similar value $A_\sigma = (0.785 \pm 0.03)\,\mathrm{fm}^{-1}$ from cross-section data [133]. The value was also confirmed in analyses of ^{11}Be breakup at intermediate and high energies in Refs. [64, 134].

Given the strong evidence for the validity of the ANC of Calci *et al.*, we use it as input parameter at NLO. Equation (4.57) then yields an effective range

$$r_\sigma = \left(\gamma_\sigma^{-1} - \frac{2}{A_\sigma}\right)\left(1 + \mathcal{O}\left((Rc/R_\mathrm{h})^2\right)\right) \approx 3.5\,\mathrm{fm} \tag{4.58}$$

which is larger than the one obtained by Hammer and Phillips in Ref. [54]. We will still count $r_\sigma \sim R_\mathrm{c}$, since $r_\sigma\gamma_\sigma \approx 0.52$ differs only by $12\,\% \approx (R_\mathrm{c}/R_\mathrm{h})^2$ from $R_\mathrm{c}/R_\mathrm{h} \sim 0.4$. From Fig. 4.6 one sees that the scaling relation $i\Delta G_\sigma^{(\mathrm{NLO})} \sim R_\mathrm{c}/R_\mathrm{h}\, iG_\sigma^{(\mathrm{LO})}$ is still appropriate for the slightly larger value of r_σ (red solid curve), both around the pole $E_\mathrm{cm} \approx -B_\sigma$ and for $E_\mathrm{cm} \sim B_\sigma$ in general.

Application 2: the first excited state of Beryllium-11

The excited halo state $\pi \equiv {}^{11}\mathrm{Be}^*$ represents a c-n p-wave state. We evaluate Eq. (4.47) for $l = 1$ and make the pole at $\bar{k} = i\gamma_\pi$ explicit, which yields

$$iG_\pi^{(\mathrm{f})}(E_\mathrm{cm}) = -ig_\pi^{-2}\frac{6\pi}{\mu_\mathrm{Nc}}\left[\frac{r_\pi}{2}\left(\bar{k}^2 + \gamma_\pi^2\right) - \left(i\bar{k}^3 - \gamma_\pi^3\right) + \mathcal{O}\left(\bar{k}^4 R_\mathrm{c}\right)\right]^{-1}. \tag{4.59}$$

This propagator is represented by a thickened solid-dashed double line with filled circle; see Figs. 4.9(b) and 4.3.

As was shown in the previous chapter for the D^{0*} ($\bar{D}^{0*}$) resonance, shallow p-wave states require the inclusion of *two* low-energy parameters, in this case γ_π and the p-wave effective range r_π, already at LO. Again, we assume naturally scaling higher-order ERE coefficients $\mathscr{P}_\pi^{(2n)} \sim R_\mathrm{c}^{2n-3}$ $(n \geq 2)$. While $\gamma_\pi \approx 18\,\mathrm{MeV} \sim R_\mathrm{h}^{-1}$, the p-wave effective length $r_\pi \sim R_\mathrm{c}^{-1}$ in Halo EFT. Thus, the fine-tuning needed to produce the shallow pole at LO does not occur in r_π, as opposed to the D^{0*} ($\bar{D}^{0*}$) case. Instead, the inverse scattering volume

$$a_\pi^{-1} = -\frac{r_\pi}{2}\gamma_\pi^2\left(1 + \frac{2\gamma_\pi}{r_\pi} + \mathcal{O}\left((R_\mathrm{c}/R_\mathrm{h})^2\right)\right) \sim R_\mathrm{c}^{-1}R_\mathrm{h}^{-2} \tag{4.60}$$

is assumed to be unnaturally small. This claim is confirmed by the large value $a_\pi = (457 \pm 67)\,\mathrm{fm}^3$ predicted by Typel and Baur [125], which is comparable with $R_\mathrm{c}\gamma_\pi^{-2} \sim 312\,\mathrm{fm}^3$. Similar to the ground state, a value for r_π can be obtained from the respective ANC A_π [54]. Using the value $A_\pi = 0.129\,\mathrm{fm}^{-1/2}$ obtained by Calci *et al.* [132], we find

$$r_\pi = -\frac{2\gamma_\pi^2}{A_\pi^2}\left(1 + \mathcal{O}\left(R_\mathrm{c}/R_\mathrm{h}\right)\right) \approx -0.95\,\mathrm{fm}^{-1}\,. \tag{4.61}$$

The pole expansion we use in three-body calculations reads

$$iG_\pi^{(\mathrm{f})}(E_\mathrm{cm}) = i g_\pi^{-2}\frac{6\pi}{\mu_\mathrm{Nc}}\frac{2}{-r_\pi}\left[\bar{k}^2+\gamma_\pi^2\right]^{-1}\left(1-\frac{2}{r_\pi}\left(\gamma_\pi-\frac{\bar{k}^2}{\gamma_\pi-i\bar{k}}\right)+\mathcal{O}\left((R_\mathrm{c}/R_\mathrm{h})^2\right)\right) \tag{4.62a}$$

$$= \underbrace{iG_\pi^{(\mathrm{LO})}(E_\mathrm{cm})}_{\sim R_\mathrm{c}R_\mathrm{h}^2}+\underbrace{i\Delta G_\pi^{(\mathrm{NLO})}(E_\mathrm{cm})}_{\sim R_\mathrm{c}R_\mathrm{h}^2\cdot R_\mathrm{c}/R_\mathrm{h}}+\cdots\,, \tag{4.62b}$$

with $\bar{k}\sim\gamma_\pi\sim R_\mathrm{h}^{-1}$, $iG_\pi^{(\mathrm{NLO})}\equiv iG_\pi^{(\mathrm{LO})}+i\Delta G_\pi^{(\mathrm{NLO})}$, etc., residue

$$Z_\pi \equiv \left[\left.\frac{\partial G_\pi^{(\mathrm{f})-1}}{\partial E_\mathrm{cm}}\right|_{E_\mathrm{cm}=-B_\pi}\right]^{-1} = -g_\pi^{-2}\frac{6\pi}{\mu_\mathrm{Nc}^2}r_\pi^{-1}\left(1-\frac{3\gamma_\pi}{r_\pi}+\mathcal{O}\left((R_\mathrm{c}/R_\mathrm{h})^2\right)\right) \tag{4.63a}$$

$$\equiv \underbrace{Z_\pi^{(\mathrm{LO})}}_{\sim R_\mathrm{c}}+\underbrace{\Delta Z_\sigma^{(\mathrm{NLO})}}_{\sim R_\mathrm{c}\cdot R_\mathrm{c}/R_\mathrm{h}}+\cdots\,, \tag{4.63b}$$

and $Z_\pi^{(\mathrm{NLO})}\equiv Z_\pi^{(\mathrm{LO})}+\Delta Z_\pi^{(\mathrm{NLO})}$, etc. The LO propagator $iG_\pi^{(\mathrm{LO})}$ will be drawn without a circle.

Note that the LO propagator is already proportional to one order of $R_\mathrm{c}<R_\mathrm{h}$. That means that the c-n p-wave amplitude $it_\pi\sim kk'\,iG_\pi\sim R_\mathrm{h}^{-2}\cdot R_\mathrm{c}R_\mathrm{h}^2\sim R_\mathrm{c}$ is one order smaller than the c-n s-wave amplitude $it_\pi\sim iG_\sigma\sim R_\mathrm{h}$ for small momenta. Thus, the excited state itself enters three-body calculations for $^{10}\mathrm{Be}\,(\mathrm{d},\mathrm{p})\,^{11}\mathrm{Be}$ not before NLO in Halo EFT. Corrections to $iG_\pi^{(\mathrm{LO})}$ will consequently be neglected in this thesis. That comprises the correction $i\Delta G_\pi^{(\mathrm{NLO})}$, which stems from the unitary cut term, i.e., the self-energy. It only enters at N^{2}LO since $i\Delta G_\pi^{(\mathrm{NLO})}\sim R_\mathrm{c}/R_\mathrm{h}\,iG_\pi^{(\mathrm{LO})}$. This scaling relation is confirmed numerically; see gray curve in Fig. 4.6.

In contrast to the $^2p_{1/2}$ channel, we do not include interactions in the $^2p_{3/2}$ sector. The reason is that it does not exhibit a shallow state like $^{11}\mathrm{Be}^*$. The lowest $j^P=3/2^-$ level of Beryllium-11 lies 2.65 MeV $\sim K_\mathrm{hi}^2/(2\mu_\mathrm{Nc})$ above the ground state; see Fig. 4.7. This much higher energy gives rise to naturally scaling ERE parameters in the $^2p_{3/2}$ sector [54]. Thus, interactions in the $^2p_{3/2}$ channel are of order N^{3}LO for $^{10}\mathrm{Be}\,(\mathrm{d},\mathrm{p})\,^{11}\mathrm{Be}$, similar to p-n p-wave interactions; see above.

4.1.3 Core-proton interactions in the presence of Coulomb repulsion

We now let $^A\mathrm{X}$ be again a generic core and discuss the remaining two-body sector, given by the core and the proton. Both particles are charged ($Q_\mathrm{c}\geq 1$ and $Q_\mathrm{p}=1$). Thus, they do not only interact strongly, but also electromagnetically. In fact, the long-ranged Coulomb repulsion turns out to suppress strong c-p interactions, such that they become negligible at NLO.

Coulomb scattering

In Coulomb gauge, the photon kinetic part can be written

$$\mathcal{L}_\gamma = -\frac{1}{4}F_{\mu\nu}F^{\mu\nu}-\frac{1}{2\Xi}\left(\partial_\mu A^\mu-\eta_\mu\eta_\nu\partial^\nu A^\mu\right)^2\,, \tag{4.64}$$

where $\eta_\mu=(1,\mathbf{0})^T$ is a time-like unit vector and Ξ is a gauge parameter [135,136]. Photon couplings of c and p are introduced in Eqs. (4.17) and (4.38) by the covariant derivative D_μ defined in Eq. (4.7). In particular, couplings to A_0 photons read $-iQ_\mathrm{c}\,e$ and $-ie$, respectively. They induce the repulsive Coulomb potential [136]. In contrast, couplings to transverse photons are strongly suppressed by the tiny kinetic mass factors $1/(2m_\mathrm{N})$ and $1/(2m_\mathrm{c})$ [136]. They can be neglected at the order we are working.

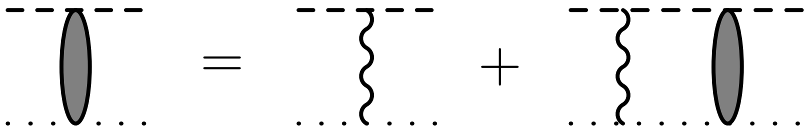

Figure 4.10.: The full c-p Coulomb amplitude $it_{\rm cp}^{\rm (C)}$ (dark ellipses) is given by iterations of the Coulomb interaction (tree-level diagram).

As done in Ref. [87], we introduce a screened Coulomb photon propagator

$$iG_\gamma(\boldsymbol{q}) \equiv i\left[\boldsymbol{q}^2 + \lambda^2 - i\epsilon\right]^{-1}, \tag{4.65}$$

which is represented by a curvy line.[9] The artificial photon mass λ has to be taken to zero at the end of each calculation. The tree-level diagram

$$-iV_{\rm C}\left(\boldsymbol{k},\boldsymbol{k}'\right) = (-iQ_{\rm c}\,e)\,iG_\gamma(\boldsymbol{k}-\boldsymbol{k}')(-ie) = -i\frac{4\pi Q_{\rm c}\,\alpha}{(\boldsymbol{k}-\boldsymbol{k}')^2+\lambda^2-i\epsilon} \tag{4.66}$$

of Fig. 4.10 depends on the incoming (outgoing) relative c-p momentum $\boldsymbol{k}$ ($\boldsymbol{k}'$) and represents the screened Coulomb potential in momentum space. It is proportional to the fine-structure constant

$$\alpha \equiv \frac{e^2}{4\pi} \approx \frac{1}{137}\,. \tag{4.67}$$

By iterating $-iV_{\rm C}$, one obtains the full c-p Coulomb amplitude $it_{\rm cp}^{\rm (C)}$ (dark ellipses in Fig. 4.10). For finite photon mass, it has been calculated analytically by König *et al.*; see for example Ref. [87]. We show the expression in Appendix E.4.1. By expanding $it_{\rm cp}^{\rm (C)}$ in α, one recovers iterations of the one-photon exchange $\sim \alpha^n$ ($n \geq 1$). Multi-photon exchanges have to be included nonperturbatively if the typical c-p momentum $\bar{k}$ is small or at least of the same order as the so-called Coulomb momentum

$$p_{\rm C} \equiv \mu_{\rm Nc}\,Q_{\rm c}\alpha\,. \tag{4.68}$$

In the three-body sector, the typical $\bar{k}$ for pure Coulomb scattering will be of the order of the large three-body relative momentum $p_E > p_{\rm C}$. Corrections to the tree-level one-photon exchange are then suppressed by powers of the Sommerfeld parameter $\eta \equiv p_{\rm C}/\bar{k}$ [137, 138]. This suppression will be used to classify multi-photon exchanges in a Coulomb power counting.

Strong interactions

The full c-p scattering amplitude

$$it_{\rm cp} = it_{\rm cp}^{\rm (C)} + it_{\rm cp}^{\rm (SC)} \tag{4.69}$$

is depicted in the first row of Fig. 4.11 as a hatched blob [139]. The pure Coulomb scattering part $it_{\rm cp}^{\rm (C)}$ will induce certain Coulomb diagrams later on in the three-body sector. The remaining part, $it_{\rm cp}^{\rm (SC)}$, mixes strong and Coulomb interactions. Its s-wave part is proportional to the c-p two-body propagator $iG_{({\rm cp})_0}^{\rm (f)}(E_{\rm cm})$ (dotted-dashed double line). Note that we describe strong c-p interactions using contact interactions, as done in the c-n sector.

---

[9] Note that A_0 photons do not really “propagate”, i.e., their Feynman Green’s function vanishes [136]. Still, they induce the Coulomb potential as a nonlocal cn → cn interaction, which is proportional to the expression $iG_\gamma(\boldsymbol{q})$. One sees that by integrating out A_0, i.e., by using its time-independent equation of motion $\boldsymbol{\nabla}^2 A_0 = -e\,p_\alpha^\dagger p_\alpha - Q_{\rm c}\,e\,c^\dagger c$.

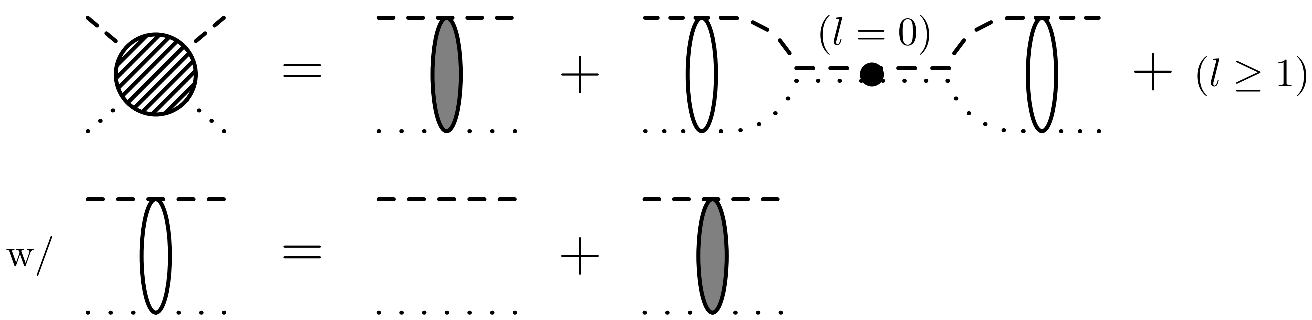

Figure 4.11.: The full c-p amplitude (hatched blob in the upper row) can be split into a pure Coulomb amplitude $it^{(\mathrm{C})}_{\mathrm{cp}}$ (filled ellipses) and a part $it^{(\mathrm{SC})}_{\mathrm{cp}}$ containing both strong and Coulomb interactions. The empty ellipses are c-p Coulomb propagators defined in the lower row. The dotted-dashed double line represents the Coulomb-modified c-p propagator $iG^{(\mathrm{f})}_{(\mathrm{cp})_0}$ in the s-wave sector. It contains intermediate Coulomb propagators to all orders.

The c-p propagator obeys the Coulomb-modified ERE form

$$iG^{(\mathrm{f})}_{(\mathrm{cp})_0}(E_{\mathrm{cm}}) = -i\frac{2\pi}{\mu_{\mathrm{Nc}}}\left[-a^{(\mathrm{C})-1}_{(\mathrm{cp})_0} + \frac{r^{(\mathrm{C})}_{(\mathrm{cp})_0}}{2}\bar{k}^2 + \cdots - 2p_{\mathrm{C}}\left[\psi\left(i\frac{p_{\mathrm{C}}}{\bar{k}}\right) - \ln\left(i\frac{p_{\mathrm{C}}}{\bar{k}}\right)\right] + i\bar{k}\right]^{-1} \tag{4.70}$$

with Coulomb-modified ERE coefficients $a^{(\mathrm{C})-1}_{(\mathrm{cp})_0}, r^{(\mathrm{C})}_{(\mathrm{cp})_0}/2$, etc. [139, 140]. The denominator of Eq. (4.70) includes the digamma function $\psi(x) \equiv \Gamma'(x)/\Gamma(x)$. Moreover, it depends on the Coulomb momentum p_{C} defined in Eq. (4.72), which determines the strength of the Coulomb repulsion. In the limit $p_{\mathrm{C}} \to 0$, the nonanalytic part of the denominator yields the usual unitarity cut term $-i\bar{k}$. In this thesis, we count all ERE coefficients in Eq. (4.70) and in higher partial waves naturally, i.e., with powers of R_{c}. The p-n propagator $iG^{(\mathrm{f})}_{(\mathrm{cp})_0} \sim R_{\mathrm{c}}$ is then natural as well.

In order to see at which order strong c-p interactions enter Halo EFT, we may compare $it^{(\mathrm{SC})}_{\mathrm{cp}}$ to an enhanced c-n amplitude $it_{\mathrm{h}} \sim R_{\mathrm{h}}$ in the halo state channel.[10] In particular, we consider the s-wave part of $it^{(\mathrm{SC})}_{\mathrm{cp}}$ which we expect to dominate at low energies. Compared to the enhanced c-n propagator, the natural c-p propagator is suppressed by one order in $R_{\mathrm{c}}/R_{\mathrm{h}}$. Further suppression of $it^{(\mathrm{SC})}_{\mathrm{cp}}$ comes from the Coulomb repulsion in the initial and final states, i.e., from the two loop integrals over Coulomb propagators (empty ellipses) in Fig. 4.11. In the on-shell region, i.e., near $E_{\mathrm{cm}} = k^2/(2\mu_{\mathrm{Nc}}) = k'^2/(2\mu_{\mathrm{Nc}})$, the product of these two integrals yields the so-called Gamow factor

$$C^2_{\eta,0} \equiv \frac{2\pi\eta}{\exp(2\pi\eta) - 1} \in [0,\, 1], \quad \eta \equiv p_{\mathrm{C}}/\bar{k}\,; \tag{4.71}$$

see for example Ref. [139]. It describes the probability to find two charged particles at zero separation. Thus, it can be interpreted as the probability of core and proton to interact via strong interactions. We expect strong c-p interactions to contribute strongest in the region of (nonshallow) two-body poles, i.e., close to c-p resonance states occurring at some relative momenta $\bar{k} \sim K_{\mathrm{hi}}$. As long as the typical $\bar{k}$ is not too large, the Gamow factor suppresses strong c-p interactions as compared to the c-n sector. Depending on p_{C} and the typical momentum $\bar{k}$ under consideration, the suppression can be read off from Fig. 4.12.

---

[10] For example, the ^{11}Be propagator has this scaling.

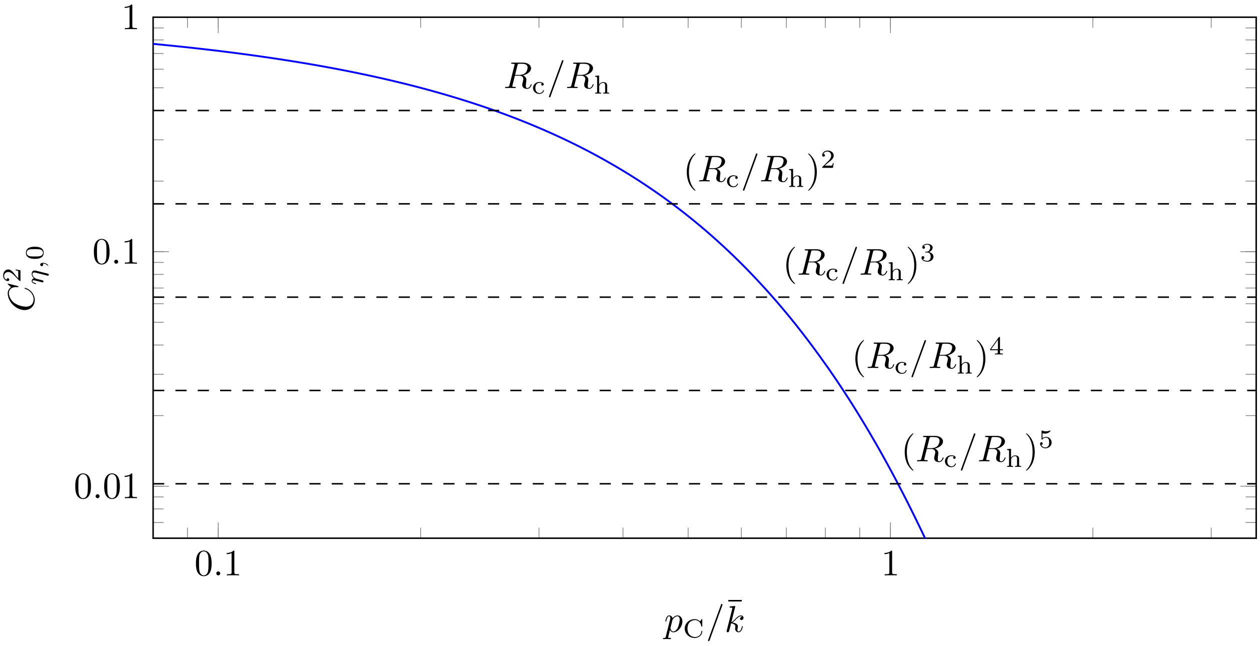

Figure 4.12.: The s-wave Gamow factor $C_{\eta,0}$ as a function of the ratio $\eta = p_C/\bar{k}$ between the Coulomb momentum $p_C = \mu_{Nc} Q_c e$ and the on-shell relative momentum $\bar{k}$. We compare the exponential suppression of the Gamow factor to the expansion parameter $R_c/R_h \sim 0.4$ of the Beryllium-11 sector.

Application: strong ^{10}Be-p interactions

The core c = ^{10}Be has charge number $Q_c = 4$. The corresponding Coulomb momentum

$$p_C \equiv \mu_{Nc} Q_c \alpha \approx 25\,\text{MeV} \tag{4.72}$$

is of the order of the ^{11}Be binding momentum $\gamma_\sigma \approx 29\,\text{MeV}$. For small c-p momenta $\bar{k} \sim \gamma_\sigma$, the Gamow factor takes the small value 2.4 % which is comparable to four orders in $R_c/R_h \sim 0.4$; see Fig. 4.12.

At larger $\bar{k}$, several ^{10}Be-p resonances have been found in the ^{10}Be(p, γ)^{11}B experiment by Goosman *et al.* [123]. These excited ^{11}B levels have branching ratios for decay to ^{10}Be-p of order 1 and can be interpreted as isobaric analog states of the lowest ^{11}Be levels [124]; see the level scheme of Fig. 4.7. The lowest one[11] occurs in the ^{10}Be-p s-wave channel ($j^P = 1/2^+$) at a center-of-mass energy $E_{r,(cp)_0} = (1.33 \pm 0.04)\,\text{MeV}$ with a width $\Gamma_{(cp)_0} = (230 \pm 65)\,\text{keV}$ [123]. The c-p momentum needed to see this resonance is given by $(2\mu_{Nc} E_{r,(cp)_0})^{1/2} \approx 48\,\text{MeV}$.

Let us take a look at the scaling of $it^{(SC)}_{cp}$ close to this resonance. By demanding a pole at $E_{cm} = E_{r,(cp)_0} - i\Gamma_{(cp)_0}/2$ in the c-p propagator of Eq. (4.70), one obtains ERE terms $a^{(C)-1}_{(cp)_0} = [(-2.7 \pm 0.8)\,\text{fm}]^{-1}$ and $r^{(C)}_{(cp)_0}/2\,\bar{k}^2_r = [(-3.5 \pm 1.4)\,\text{fm}]^{-1}$, both scaling like R_c^{-1}. Thus, the propagator $iG^{(f)}_{(cp)_0} \sim R_c$ scales naturally. Moreover, the Gamow factor $C^2_{\eta,0}$ has the small value $0.13 \sim (R_c/R_h)^2$ in the vicinity of the resonance. We conclude that strong ^{10}Be-p interactions are at least of order N^{3}LO and can be neglected in this thesis.

There are in fact more ^{11}B levels around the ^{10}Be-p threshold not shown in Fig. 4.7. Since they were not seen in Ref. [123], we assume they do not couple strongly to ^{10}Be-p. Moreover, transitions of ^{10}Be-p to such states would involve even smaller Gamow factors.

---

[11] This state could also have spin-parity $3/2^+$ according to Ref. [141]. This possibility should, however, not change the subleading nature of the state for the reaction ^{10}Be (d, p) ^{11}Be.

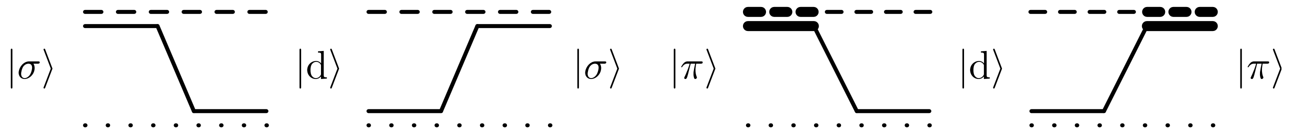

(a) (b)

Figure 4.13.: Neutron exchange diagrams for the reaction $^{10}\mathrm{Be}\,(\mathrm{d,\,p})\,^{11}\mathrm{Be}$. (a) At LO in $R_\mathrm{c}/R_\mathrm{h}$, the diagrams $-iV_{\sigma\mathrm{d}}$ and $-iV_{\mathrm{d}\sigma}$ connect the halo channel $|\sigma\rangle \equiv \left|\mathrm{p} + {}^{11}\mathrm{Be}\right\rangle$ and the deuteron channel $|\mathrm{d}\rangle \equiv \left|{}^{10}\mathrm{Be} + \mathrm{d}\right\rangle$. At NLO, also transfer to the excited halo state channel $|\pi\rangle \equiv \left|\mathrm{p} + {}^{11}\mathrm{Be}^*\right\rangle$ is included using the diagrams $-iV_{\pi\mathrm{d}}$ and $-iV_{\mathrm{d}\pi}$.

4.1.4 Three-body sector

Once more, we go back to the generic case $\mathrm{c} = {}^A\mathrm{X}$ and finally turn to the three-body sector. In Chapter 3, two-body $D^0\pi^0$ ($\bar{D}^0\pi^0$) interactions induced a pion exchange interaction in the three-body system. Similarly, c-n and p-n interactions induce a neutron exchange interaction, which will be discussed in the following. Afterwards, we discuss which Coulomb diagrams are induced by c-p Coulomb scattering.

Neutron exchanges

The reaction $^A\mathrm{X(d,\,p)}^{A+1}\mathrm{X}$ describes a transition between the two states[12]

$$|\mathrm{h}\rangle \equiv \left|\mathrm{p} + {}^{A+1}\mathrm{X}\right\rangle, \tag{4.73a}$$
$$|\mathrm{d}\rangle \equiv \left|{}^{A}\mathrm{X} + \mathrm{d}\right\rangle. \tag{4.73b}$$

As far as strong interactions are concerned, these states are connected by iterations of neutron exchange diagrams $-iV_\mathrm{hd}$ and $-iV_\mathrm{dh}$. For example, the LO amplitude for $^{10}\mathrm{Be}\,(\mathrm{d,\,p})\,^{11}\mathrm{Be}$ will contain the exchange diagrams $-iV_{\sigma\mathrm{d}}$ and $-iV_{\mathrm{d}\sigma}$ of Fig. 4.13(a). At NLO, we will also include transitions to intermediate excited states $^{11}\mathrm{Be}^*$ using the exchange diagrams $-iV_{\pi\mathrm{d}}$ and $-iV_{\mathrm{d}\pi}$ in Fig. 4.13(b).

In the following, we calculate $-iV_\mathrm{hd}$ and $-iV_\mathrm{dh}$ for arbitrary quantum numbers $l \geq 0$ and $j = l \pm 1/2$ of the halo state h. Neutron exchange diagrams $-iV_\mathrm{hv}$ and $-iV_\mathrm{vh}$ connecting $|\mathrm{h}\rangle$ to the virtual state channel $|\mathrm{v}\rangle = \left|{}^A\mathrm{X} + (\mathrm{pn})_{^1\mathrm{S}_0}\right\rangle$ can be calculated similarly; see Appendix E.2.2. However, they are negligible at NLO for the reaction $^{10}\mathrm{Be}\,(\mathrm{d,\,p})\,^{11}\mathrm{Be}$.

We choose the center-of-mass system at energy E and let $\boldsymbol{p}$ ($\boldsymbol{q}$) be the momentum of the incoming (outgoing) spectator. Moreover, in each channel we couple the particle spins to a total spin S (S') with projection m_S ($m_{S'}$). Using the Feynman rules of Eq. (4.45a)-(4.45b), we then obtain the exchange diagrams

$$\begin{aligned}
-iV_\mathrm{hd}^{Sm_S,S'm_{S'}}(\boldsymbol{p},\boldsymbol{q};E) &\equiv \mathrm{C}^{Sm_S}_{1/2\alpha,jm_j}\mathrm{C}^{S'm_{S'}}_{00,1m'}\left\langle (cd_{m'})_{\boldsymbol{q}}\left| i\hat{T}\right|(p_\alpha h_{m_j})_{\boldsymbol{p}}\right\rangle_{\mathcal{O}(g^2)} \\
&= ig_\mathrm{d}g_\mathrm{h}m_\mathrm{N}(-1)^l\sqrt{3(2j+1)}\,\mathrm{C}^{Sm_S}_{lm_l,1m_{S'}}\begin{Bmatrix} S & l & 1 \\ 1/2 & 1/2 & j\end{Bmatrix}\delta^{S'1}\frac{\{\xi\boldsymbol{p}+\boldsymbol{q}\}^*_{lm_l}}{\boldsymbol{p}\cdot\boldsymbol{q}+U_{\mathrm{n;p,c}}(p,q;E)}, && (4.74a) \\
-iV_\mathrm{dh}^{Sm_S,S'm_{S'}}(\boldsymbol{p},\boldsymbol{q};E) &\equiv \mathrm{C}^{Sm_S}_{00,1m}\mathrm{C}^{S'm_{S'}}_{1/2\alpha',jm_j'}\left\langle (p_{\alpha'}h_{m_j'})_{\boldsymbol{q}}\right| i\hat{T}\left|(cd_m)_{\boldsymbol{p}}\right\rangle_{\mathcal{O}(g^2)} \\
&= -i\left[V_\mathrm{hd}^{S'm_{S'},Sm_S}(\boldsymbol{q},\boldsymbol{p};E)\right]^*. && (4.74b)
\end{aligned}$$

---

[12] Three-body states in this chapter are labeled by the respective two-body state, for example by $\sigma = {}^{11}\mathrm{Be}$, $\pi = {}^{11}\mathrm{Be}^*$ or $\mathrm{d} = {}^2\mathrm{H}$.

In Eq. (4.74a), $\xi = 1/(1+1/A)$ is the mass ratio and the function $U_{\mathrm{n;p,c}}$ is defined in Eq. (C.14). For a derivation of the tensor structure in Eq. (4.74a), we refer to Appendix E.2.

In the following, we will refer to the functions V_{dh} and V_{hd} as "neutron exchange potentials". They will enter the Faddeev amplitude for the desired reaction. Note, however, that these functions are more than just effective interaction potentials. In fact, they involve a dynamical intermediate three-body state $\left|{}^{A}\mathrm{X}+\mathrm{n}+\mathrm{p}\right\rangle$ due to two-body state breakup and recombination. For $E>0$, this state can go on shell, just like the $D^0\bar{D}^0\pi^0$ three-body state in the previous chapter. Thus, by iterating the exchange potentials, one automatically includes three-body continuum states to all orders.

The partial wave projections of Eqs. (4.74a)-(4.74b) on total angular momentum $\boldsymbol{J} = \boldsymbol{L}+\boldsymbol{S}$ can be done analytically; see Appendix E.2. Using the short-hand notations $\hat{S} \equiv 2S+1$, $\hat{j} \equiv 2j+1$, etc., we find

$$
\begin{aligned}
V_{\mathrm{hd}}^{\hat{S}L_J,\hat{S}'L'_J}(p,q;E) = {} & \frac{g_{\mathrm{d}}g_{\mathrm{h}}m_{\mathrm{N}}}{2}(-1)^{J+l}\sqrt{3\,\hat{S}\,\hat{L}\,\hat{L}'\,\hat{j}\,(\hat{l}\,!)}\begin{Bmatrix} S & 1 & l \\ L' & L & J \end{Bmatrix}\begin{Bmatrix} S & l & 1 \\ 1/2 & 1/2 & j \end{Bmatrix}\delta^{S'1} \\
& \times \sum_{l_1+l_2=l} (\xi p)^{l_1} q^{l_2} \frac{1}{\sqrt{(2l_1!)(2l_2!)}} \\
& \times \sum_k (-1)^k \, \mathrm{C}^{k0}_{l_1 0, L0}\mathrm{C}^{k0}_{l_2 0, L'0}\begin{Bmatrix} l_1 & l_2 & l \\ L' & L & k \end{Bmatrix} I^{(k)}_{\mathrm{n;p,c}}(p,q;E)\,, \qquad (4.75) \\
V_{\mathrm{dh}}^{\hat{S}L_J,\hat{S}'L'_J}(p,q;E) = {} & V_{\mathrm{hd}}^{\hat{S}'L'_J,\hat{S}L_J}(q,p;E)\,. \qquad (4.76)
\end{aligned}
$$

The functions $I^{(k)}_{\mathrm{n;p,c}}$ are defined in Eq. (C.15).

Let us take a quick break here and analyze the tensor structure of (4.75). Firstly, the total spin of the $|\mathrm{d}\rangle$ state must trivially be equal to 1 since the core is spinless. For fixed $J \geq 0$, that implies three possible orbital angular momenta in the $|\mathrm{d}\rangle$ channel, being

$$L_{\mathrm{d}} \in \{J+1, J, J-1\}\,. \qquad (4.77)$$

In the halo channel $|\mathrm{h}\rangle$, the $6j$ symbol in Eq. (4.74a) demands total spins $S_{\mathrm{h}} = j \pm 1/2$ and thus

$$L_{\mathrm{h}} \in \{J+j+1/2, J+j-1/2, \cdots, J-j-1/2\}\,. \qquad (4.78)$$

Secondly, the last row of Eq. (4.75) puts certain restrictions on the possible changes $\Delta L \equiv L_{\mathrm{d}} - L_{\mathrm{h}}$ in the orbital angular momentum. In particular, the $6j$ symbol in Eq. (4.74a) dictates that $|\Delta L|$ cannot be larger than the halo state's quantum number $l \geq 0$. In addition, the two Clebsch-Gordan coefficients demand that $(-1)^{l_1+L_{\mathrm{h}}} = (-1)^k = (-1)^{l_2+L_{\mathrm{d}}}$. Since $l = l_1 + l_2$, this relation implies parity conservation $(-1)^{L_{\mathrm{h}}+l} = (-1)^{L_{\mathrm{d}}}$. The two findings can be summarized into the selection rule

$$|\Delta L| \in \begin{cases} \{l, l-2, \cdots, 0\}, & l \text{ even} \\ \{l, l-2, \cdots, 1\}, & l \text{ odd} \end{cases}. \qquad (4.79)$$

Another convenient feature of the neutron exchange potentials is more subtle: It comes into play if only p-n interactions in the ${}^3s_1$ channel are included in the calculation, i.e., if one can neglect p-n interactions in the ${}^1s_0$ channel and in higher partial waves. If that is the case, then the orbital angular momentum L_{d} is conserved throughout the scattering process. That can be be seen as follows. If $L_{\mathrm{d}} = J$ at some point in the reaction, the statement is trivial since the other two options $L_{\mathrm{d}} = J \pm 1$ decouple due to parity conservation. Thus, we only have to check that transitions $L_{\mathrm{d}} = J+1 \longleftrightarrow L'_{\mathrm{d}} = J-1$ are forbidden. Such a transition would be a two-step process

$$\left|\mathrm{d}, {}^3L_{\mathrm{d}\,J}\right\rangle \rightarrow \left\{ \left|\mathrm{h}, {}^{\hat{S}_{\mathrm{h}}}L_{\mathrm{h}J}\right\rangle \right\} \rightarrow \left|\mathrm{d}, {}^3L'_{\mathrm{d}\,J}\right\rangle, \qquad (4.80)$$

where one has to sum over all allowed S_h and L_h in the intermediate state. Let us consider a fixed L_h in the intermediate state. The two-step amplitude for this L_h is then proportional to the sum

$$\begin{aligned}\sum_{S_\mathrm{h}} V_{\mathrm{dh}}^{{}^3L_\mathrm{d}\,J,\,{}^{\hat{S}_\mathrm{h}}L_\mathrm{h}\,J} V_{\mathrm{hd}}^{{}^{\hat{S}_\mathrm{h}}L_\mathrm{h}\,J,\,{}^3L'_\mathrm{d}\,J} &\propto \sum_{S_\mathrm{h}} \begin{Bmatrix} S_\mathrm{h} & 1 & l \\ L_\mathrm{d} & L_\mathrm{h} & J \end{Bmatrix} \left[\sqrt{2S_\mathrm{h}+1} \begin{Bmatrix} S_\mathrm{h} & l & 1 \\ 1/2 & 1/2 & j \end{Bmatrix} \right]^2 \begin{Bmatrix} S_\mathrm{h} & 1 & l \\ L'_\mathrm{d} & L_\mathrm{h} & J \end{Bmatrix} \\ &= \begin{Bmatrix} - & 1/2 & 1 & 1/2 \\ L_\mathrm{h} & - & L_\mathrm{d} & l \\ l & 1/2 & - & j \\ L'_\mathrm{d} & 1 & J & - \end{Bmatrix} . \end{aligned} \tag{4.81}$$

The bracket in the lower row is a $12j$-symbol of second kind. It is only nonzero if certain quadrupels (j_1, j_2, j_3, j_4) of its entries fulfill the tetragonal condition $j_a \leq \sum_{b\neq a} j_b$ [142]. That includes the four entries $(L'_\mathrm{d}, 1/2, L_\mathrm{d}, 1/2)$ on the antidiagonal. However, for $L_\mathrm{d} = J+1$ and $L'_\mathrm{d} = J-1$, we find $L_\mathrm{d} = J+1 \not\leq J = L'_\mathrm{d} + 1/2 + 1/2$ and thus the symbol vanishes. We conclude that L_d is conserved if only p-n interactions in the ${}^3s_1$ channel are present. Thus, for fixed total J, the scattering equations can be decomposed into three decoupled systems $L_\mathrm{d} \in \{J+1, J, J-1\}$.

In order to calculate a differential cross section for intermediate energies, one needs to take into account projections of the neutron exchange potentials up to some orbital angular momentum $L_\mathrm{max} \gg 1$ between p-${}^{A+1}$X and ^{A}X-d. In doing so, one then automatically introduces two-body continua in all partial waves up to $l = L_\mathrm{max}$ to the reaction since the neutron exchange diagrams involve dynamical three-body states. For example, consider $L = 1$ in the initial $|\sigma\rangle = |\mathrm{p} + {}^{11}\mathrm{Be}\rangle$ state of Fig. 4.13(a). After ^{11}Be breakup (first, upper vertex), the intermediate state exhibits a ^{10}Be-n pair in $l = 0$ and $L = 1$ between the pair and the proton. This configuration can for example be recoupled to $L = 0$ between ^{10}Be and an $l = 1$ p-n pair. In this specific case, the exchange diagram takes care of the p-n p-wave continuum, described by plane waves. By including projections up to L_max, all p-n, ^{A}X-n, and ^{A}X-p continua up to $l = L_\mathrm{max}$ are included.

Coulomb diagrams

Having discussed strong interactions in the three-body sector, we turn to the Coulomb force. Its repulsion is expected to lower the reaction probability. In reaction model calculations, e.g., the distorted wave Born approximation (DWBA) or the continuum-discretized coupled channel (CDCC) model, the Coulomb force is usually included as a static two-body potential in addition to some nuclear model interaction. In EFT language, such calculations include Coulomb effects to all orders. In contrast to most model calculations, however, EFT calculations are performed in momentum space. Here, a nonperturbative Coulomb treatment proves difficult due to the photon propagator's infrared singularity at vanishing momentum transfer; see Eq. (4.66). Fortunately, the thorough usage of scale separations often enables a (semi-)perturbative treatment of Coulomb effects [87, 139].

Recall that we separated the pure Coulomb scattering part of the c-p amplitude from negligible strong interactions in Sec. 4.1.3. This part now induces three-body diagrams with photon exchanges. By analyzing them in terms of typical momenta, one identifies leading diagrams, which can typically be solved analytically [87]. Afterwards, they enter a Faddeev equation as effective interactions between the different scattering states. In this way, it is possible to include Coulomb effects *effectively* with reliable uncertainty estimates.

To give an example, the s-wave states $|\mathrm{d}\rangle$ and $|\sigma\rangle$ of the ${}^{10}\mathrm{Be}(\mathrm{d},\mathrm{p})\,{}^{11}\mathrm{Be}$ reaction are connected by the Coulomb diagrams shown in Fig. 4.14. They resemble those diagrams considered by König *et al.* for the three-nucleon system [87]. However, they exhibit nontrivial dependencies on the mass ratio $y \equiv m_\mathrm{N}/m_\mathrm{c} = 1/A \ll 1$. We will discuss them in detail in Sec. 4.2.3.

Independently of the halo type, one can classify the induced Coulomb diagrams according to their topology. One important class is given by so-called "bubble diagrams", which describe c-p Coulomb

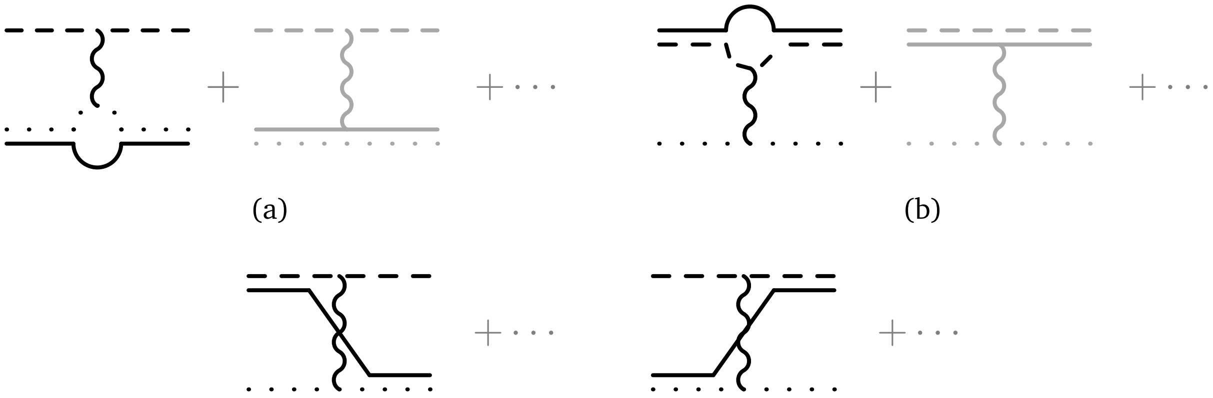

(a) (b)

(c) (d)

Figure 4.14.: Coulomb diagram series (a) $-i\Gamma_{\mathrm{dd}}$ in the $|\mathrm{d}\rangle$ channel, (b) $-i\Gamma_{\sigma\sigma}$ in the $|\sigma\rangle$ channel, and (c, d) $-i\Gamma_{\sigma\mathrm{d}}$, $-i\Gamma_{\mathrm{d}\sigma}$ in the transfer channels of the ${}^{10}\mathrm{Be}\,(\mathrm{d},\,\mathrm{p})\,{}^{11}\mathrm{Be}$ reaction. Grayed-out parts are either induced by direct couplings of the photon to the two-body states (a) deuteron and (b) ^{11}Be, or they involve multiple-photon exchanges. They will be negligible up to NLO for the experimental energies used by Schmitt *et al.* [60]. In cross-section calculations, we will iterate the black LO diagrams to all orders.

scattering in between breakup and recombination of a two-body state; see for example Fig. 4.14(a) and (b). At order $\mathcal{O}\,(\alpha)$, these diagrams are proportional to a single Coulomb photon propagator. Due to its infrared divergence for vanishing photon mass, such diagrams have to be handled with care in numerical calculations. We will follow König *et al.* by steadily decreasing the photon mass towards convergence [87]. For the reaction cross section, convergence takes place around $\lambda \approx 0.1\,\mathrm{MeV}$. Such small photon masses require a large amount of sampling points in the momentum region around 0.

The next diagram class includes direct couplings of the photon to the two-body auxiliary fields d_m and h_{m_j}; see the grayed out diagrams in Fig. 4.14(a) and (b). These couplings result from higher-order ERE terms in the Lagrangians of Eqs. (4.22) and (4.39). If the ERE coefficients related to these terms, e.g., the effective ranges r_{d} and r_σ, are small, then the couplings enter only at higher orders compared to the bubble diagrams. In this thesis, the "ERE-photon diagrams" are negligible, which is why we grayed them out. Further details will be given in Sec. 4.2.3.

The third class comprises diagrams with simultaneous photon and neutron exchange; see Figs. 4.14(c) and (d). They are called "box diagrams". As opposed to the bubble diagrams, the photon propagator appears now inside a loop integral. For this reason, the diagram does not exhibit an infrared divergence.

The grayed out terms $\mathcal{O}\left(\alpha^2\right)$ in Fig. 4.14 summarize diagrams with multiple photon exchanges in between two-body state breakup and recombination. They can be neglected in this thesis due to the large energies used in the experiment by Schmitt *et al.* [60]. Note, however, that this simplification cannot always be made. In particular, it might fail when the typical external momentum p_E is of the order p_{C}.

4.2 Transfer reaction ${}^{10}\mathrm{Be}\,(\mathrm{d},\,\mathrm{p})\,{}^{11}\mathrm{Be}$

In this section, we apply the developed EFT framework to the neutron transfer reaction ${}^{10}\mathrm{Be}\,(\mathrm{d},\,\mathrm{p})\,{}^{11}\mathrm{Be}$, which was studied experimentally by Schmitt *et al.* in Ref. [60]. In particular, we construct a Faddeev equation for the transfer amplitude up to NLO in $\chi_2 = r_{\mathrm{d}}\gamma_{\mathrm{d}} \sim r_\sigma\gamma_\sigma \sim R_{\mathrm{c}}/R_{\mathrm{h}}$ and to zeroth order in $\chi_3 = p_{\mathrm{C}}/p_E \sim \chi_2^2$, where p_E is a relative momentum; see below. The amplitude is then used to calculate the reaction cross section.

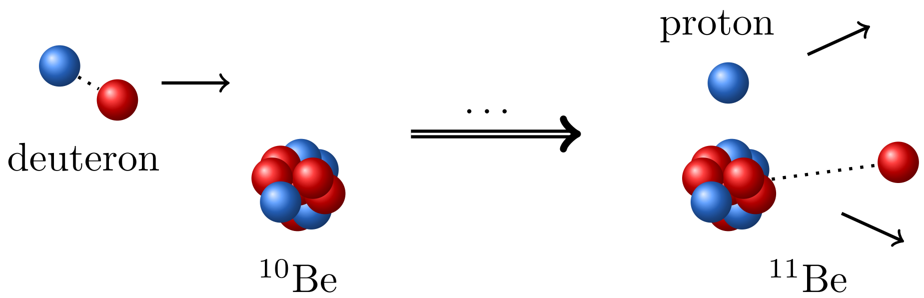

Figure 4.15.: Sketch of the reaction $^{10}\text{Be}(\text{d},\text{p})\,^{11}\text{Be}$. The incident deuteron transfers its neutron (red) onto a tightly bound ^{10}Be nucleus, such that a weakly bound halo nucleus ^{11}Be is formed. In the experiment of Schmitt *et al.* [59, 60], the cross section of the reaction was measured in inverse kinematics. The angular distribution of the outgoing protons (blue) was measured at different ^{10}Be beam energies.

Firstly, we discuss the reaction kinematics and identify the typical momentum scales. Secondly, we write down the EFT Lagrangian and analyze the induced three-body diagrams (neutron exchanges and Coulomb diagrams) for $^{10}\text{Be}(\text{d},\text{p})\,^{11}\text{Be}$ in terms of the momentum scales. Thirdly, we construct the LO transfer amplitude and present results for the reaction cross section. The influence of single Coulomb diagrams is discussed in detail. At the end of the section, we discuss NLO corrections.

4.2.1 Kinematics

The reaction $^{10}\text{Be}(\text{d},\text{p})\,^{11}\text{Be}$ describes the transfer of a neutron from an incoming deuteron to a ^{10}Be nucleus; see Fig. 4.15. This process was studied by Schmitt *et al.* in inverse kinematics [59,60]. A beam of long-lived ^{10}Be ions was accelerated onto a deuteron target at beam energies $E_\text{c} \in \{60, 75, 90, 107\}\,\text{MeV}$ (kinetic energy in the lab frame). These energies are equivalent to deuteron beam energies $E_\text{d} = 0.2\,E_\text{c} \in \{12, 15, 18, 21.4\}\,\text{MeV}$. That can can be seen by expressing both E_c and E_d in terms of the c-p-n center-of-mass energy E. In the rest frame of the deuteron with $\tilde{\boldsymbol{p}}_\text{d} = 0$, the beam energy $E_\text{c} = \tilde{p}_\text{c}^2/(2m_\text{c})$ is determined by the core momentum $\tilde{\boldsymbol{p}}_\text{c}$. In the rest frame of the core, we have $E_\text{d} = p_\text{d}^2/(4m_\text{N})$ and $\boldsymbol{p}_\text{c} = 0$. Transformations of both frames to the center-of-mass system yields

$$E + B_\text{d} = E_\text{c} - \frac{(\tilde{\boldsymbol{p}}_\text{c} + \tilde{\boldsymbol{p}}_\text{d})^2}{2(m_\text{c} + 2m_\text{N})} = E_\text{c} - \frac{\tilde{p}_\text{c}^2}{2(m_\text{c} + 2m_\text{N})} = \frac{\mu_\text{d}}{m_\text{c}} E_\text{c} \tag{4.82a}$$

$$= E_\text{d} - \frac{(\boldsymbol{p}_\text{c} + \boldsymbol{p}_\text{d})^2}{2(m_\text{c} + 2m_\text{N})} = E_\text{d} - \frac{p_\text{d}^2}{2(m_\text{c} + 2m_\text{N})} = \frac{\mu_\text{d}}{2m_\text{N}} E_\text{d} \tag{4.82b}$$

$$\Longleftrightarrow E_\text{d} = (1 + 2y)(E + B_\text{d}) = 2y\,E_\text{c} \tag{4.82c}$$

with $y = 1/A = 0.1$ and $B_\text{d} = 2.22\,\text{MeV}$. The experimental center-of-mass energies are then given by

$$E \in \{7.78, 10.28, 12.78, 15.61\}\,\text{MeV}\,. \tag{4.83}$$

The EFT expansion discussed above is expected to converge fastest for energies $E < E_\text{x}$, where $E_\text{x} = 3.37\,\text{MeV}$ denotes the excitation energy of the ^{10}Be core. However, in the absence of appropriate data, we will compare our theory to the Schmitt *et al.* data at $E \geq 7.78\,\text{MeV}$. In other words, we perform an extrapolation of a low-energy theory to intermediate and high energies. The extrapolation is appropriate if couplings of the states $\left|^{10}\text{Be} + \text{d}\right\rangle$ and $\left|\text{p} + {}^{11}\text{Be}\right\rangle$ to higher-energy states like $\left|^{10}\text{Be}^* + \text{p} + \text{n}\right\rangle$ are comparably weak. This assumption is supported by the fact that scattering parameters are large in two-body sectors with weakly-bound states.

In fact, previous studies suggest that, at least for the lowest beam energies of Schmitt *et al.*, high-energy states are negligible and the low-energy expansion of Halo EFT is still appropriate. In particular, Deltuva *et al.* addressed the role of dynamical core excitations on the cross section in a Faddeev approach [126]. It turned out that they are negligible for energies $\lesssim 10\,\mathrm{MeV}$. More recently, Yang and Capel reanalyzed the data by Schmitt *et al.* by combining the adiabatic distorted wave approximation reaction model with a Halo EFT description of ^{11}Be [133]. For lower beam energies and forward angles, the reaction was found to be purely peripheral. That means that the cross section predominantly depends on the asymptotic form of the ^{11}Be wave function, while being independent of short-range (high energy) details.

Typical momentum scales

Above we saw that NLO corrections $r_\sigma\gamma_\sigma \gtrsim r_\mathrm{d}\gamma_\mathrm{d} \approx 0.40$ to the weakly-bound state ^{11}Be and the deuteron are roughly of the same size. To simplify the power counting, we thus introduce a generic small binding energy scale $\gamma \sim \gamma_\mathrm{d} \sim \gamma_\sigma \sim \gamma_\pi \sim R_\mathrm{h}^{-1}$ and count $r_\mathrm{d} \sim r_\sigma \sim R_\mathrm{c}$. The largest subleading corrections in the strong sector are then suppressed by the two-body expansion parameter

$$\chi_2 \approx 0.4 \sim R_\mathrm{c}/R_\mathrm{h}\,. \tag{4.84}$$

If indeed scattering channels at high energies can be neglected to good approximation, then the largest part of the available energy E goes into the relative movement of the two-body states and their spectators. I.e., the typical relative momentum

$$p_E \equiv (2m_\mathrm{N}E)^{1/2} \geq 120\,\mathrm{MeV} \tag{4.85}$$

between these two is large in the experiment by Schmitt *et al.*. It was pointed out by Rupak and Kong in Ref. [143] that one has to keep track of this new momentum scale in Coulomb diagrams. In our case, p_E is much larger than the Coulomb momentum $p_\mathrm{C} \approx 25\,\mathrm{MeV} \sim \gamma$ of Eq. (4.72). These momenta form a second expansion parameter

$$\chi_3 \equiv \frac{p_\mathrm{C}}{p_E} \leq 0.2 \sim \chi_2^2 \tag{4.86}$$

in the three-body sector. It will be the reason why multi-photon exchange diagrams can be neglected in this work.

4.2.2 Lagrangian

The Lagrangian for $^{10}\mathrm{Be}\,(\mathrm{d},\mathrm{p})\,^{11}\mathrm{Be}$ can then be written as the sum

$$\mathscr{L} = \mathscr{L}_\mathrm{kin} + \mathscr{L}_\mathrm{pn} + \mathscr{L}_\mathrm{cn} + \mathscr{L}_\mathrm{cpn} + \mathscr{L}_\gamma\,. \tag{4.87}$$

The "kinetic" part

$$\mathscr{L}_\mathrm{kin} = c^\dagger\left[i\partial_0 - 4eA_0 + \frac{\boldsymbol{\nabla}^2}{2m_\mathrm{c}}\right]c + p_\alpha^\dagger\left[i\partial_0 - eA_0 + \frac{\boldsymbol{\nabla}^2}{2m_\mathrm{N}}\right]p_\alpha + n_\alpha^\dagger\left[i\partial_0 + \frac{\boldsymbol{\nabla}^2}{2m_\mathrm{N}}\right]n_\alpha \tag{4.88}$$

involves also couplings to Coulomb photons A_0. The photon part $\mathscr{L}_\gamma$ is given by Eq. (4.64).

In the p-n sector, the virtual state occurs only at N^{2}LO and p-wave interactions are further suppressed; see Sec. 4.3.2. Up to NLO, we may then write the p-n interaction part in the form

$$\mathscr{L}_\mathrm{pn} = g_\mathrm{d}^{-2}\,\tilde{d}_m^\dagger\left[\Delta_{\mathrm{d},0} - i\partial_\mathrm{cm} + \cdots\right]\tilde{d}_m - \mathrm{C}_{1/2\alpha,1/2\beta}^{1m}\left[\tilde{d}_m^\dagger\left(p_\alpha n_\beta\right) + \mathrm{H.c.}\right]. \tag{4.89}$$

By using the redefined deuteron fields $\tilde{d}_m^{(\dagger)} \equiv g_\mathrm{d}\, d_m^{(\dagger)}$, we effectively remove the unphysical coupling g_d from interaction vertices. As a consequence, we have to multiply the propagator iG_d in Eq. (4.33a) and the residue Z_d in Eq. (4.34a) by g_d^2, which removes their g_d dependencies. Direct couplings of the deuteron field to the photon occur at N^{2}LO; see below. As a consequence, we use the usual center-of-mass derivative $i\partial_\mathrm{cm}$ instead of iD_cm in Eq. (4.89).

The c-n system involves two shallow Beryllium-11 states, ^{11}Be and ^{11}Be*. Up to NLO in $R_\mathrm{c}/R_\mathrm{h}$, only the corresponding channels $^2s_{1/2}$ and $^2p_{1/2}$ enter the reaction. The Lagrangian term reads

$$\begin{aligned}\mathscr{L}_\mathrm{cn} = {} & g_\sigma^{-2}\,\tilde{\sigma}_\alpha^\dagger\left[\Delta_{\sigma,0} - i\partial_\mathrm{cm} + \cdots\right]\tilde{\sigma}_\alpha - \left[\tilde{\sigma}_\alpha^\dagger\,(n_\alpha\, c) + \mathrm{H.c.}\right] \\ & + g_\pi^{-2}\,\tilde{\pi}_\alpha^\dagger\left[\Delta_{\pi,0} + i\partial_\mathrm{cm} + \cdots\right]\tilde{\pi}_\alpha - \mathrm{C}^{1\alpha'}_{1/2\alpha,1m_l}\left[\tilde{\pi}_{\alpha'}^\dagger\left(n_\alpha\left\{-i\overleftrightarrow{\nabla}\right\}_{1m_l} c\right) + \mathrm{H.c.}\right].\end{aligned} \tag{4.90}$$

The prefactor of $i\partial_\mathrm{cm}$ in the π_α “kinetic” term is positive as it was for the p-wave state D^{0*} in the previous chapter. Similar to the p-n sector, we removed the couplings g_σ and g_π from the interaction vertices by using redefined fields and neglected photon couplings to the auxiliary fields.

The reaction cross section will need a single three-body force for renormalization at LO. We implement it in the $|\mathrm{d}\rangle$ channel by writing

$$\mathscr{L}_\mathrm{cpn} = -C_0\left(\tilde{d}_m c\right)^\dagger\left(\tilde{d}_m c\right) + \cdots\,. \tag{4.91}$$

A complete NLO renormalization lies beyond the scope of the thesis. Further three-body forces required at NLO are summarized into the ellipses.

4.2.3 Three-body diagrams up to NLO and beyond

The reaction $^{10}\mathrm{Be}\,(\mathrm{d},\,\mathrm{p})\,^{11}\mathrm{Be}$ will be described by the transfer amplitude $T_{\mathrm{d}\sigma}$, which connects the two states

$$|\mathrm{d}\rangle \equiv \left|{}^{10}\mathrm{Be} + \mathrm{d}\right\rangle\,, \tag{4.92a}$$

$$|\sigma\rangle \equiv \left|\mathrm{p} + {}^{11}\mathrm{Be}\right\rangle \tag{4.92b}$$

via neutron exchange potentials V_{ab} and Coulomb diagram interactions Γ_{ab}. At NLO, also the state

$$|\pi\rangle \equiv \left|\mathrm{p} + {}^{11}\mathrm{Be}^*\right\rangle \tag{4.93}$$

will contribute intermediately. The on-shell relative momenta in these channels are given by

$$\bar{p}_\mathrm{d} \equiv i\sqrt{-2\mu_\mathrm{d}\,(E + B_\mathrm{d} + i\epsilon)}\,, \tag{4.94a}$$

$$\bar{p}_\sigma \equiv i\sqrt{-2\mu_\sigma\,(E + B_\sigma + i\epsilon)}\,, \tag{4.94b}$$

$$\bar{p}_\pi \equiv i\sqrt{-2\mu_\pi\,(E + B_\pi + i\epsilon)}\,, \tag{4.94c}$$

where the reduced masses

$$\mu_\mathrm{d} \equiv \frac{2m_\mathrm{N}\, m_\mathrm{c}}{2m_\mathrm{N} + m_\mathrm{c}} = \frac{2}{1 + 2/A}\, m_\mathrm{N} = \frac{5}{3}\, m_\mathrm{N}\,, \tag{4.95a}$$

$$\mu_\sigma \equiv \mu_\pi \equiv \frac{m_\mathrm{N}\,(m_\mathrm{N} + m_\mathrm{c})}{2m_\mathrm{N} + m_\mathrm{c}} = \frac{1 + 1/A}{1 + 2/A}\, m_\mathrm{N} = \frac{11}{12}\, m_\mathrm{N} \tag{4.95b}$$

are of order m_N.

Strong interaction diagrams up to NLO

The relevant neutron exchange potentials for the reaction $^{10}\mathrm{Be}\,(\mathrm{d},\,\mathrm{p})\,^{11}\mathrm{Be}$ are given by the diagrams in Fig. 4.13. Their analytic forms can be obtained by evaluating Eqs. (4.74a)-(4.74b) for $l = 0, j = 1/2$ ($|\sigma\rangle$) and $l = 1, j = 1/2$ ($|\pi\rangle$). We then find

$$V_{\sigma\mathrm{d}}^{Sm_S,1m_{S'}}(\boldsymbol{p},\boldsymbol{q};E) = -m_\mathrm{N}\,\delta^{S1}\delta^{m_Sm_{S'}}\left[\boldsymbol{p}\cdot\boldsymbol{q}+p^2+\frac{1}{2\xi}q^2-m_\mathrm{N}(E+i\epsilon)\right]^{-1}, \tag{4.96a}$$

$$V_{\mathrm{d}\sigma}^{1m_S,S'm_{S'}}(\boldsymbol{p},\boldsymbol{q};E) = V_{\sigma\mathrm{d}}^{S'm_{S'},1m_S}(\boldsymbol{q},\boldsymbol{p};E), \tag{4.96b}$$

$$\begin{aligned}V_{\pi\mathrm{d}}^{Sm_S,1m_{S'}}(\boldsymbol{p},\boldsymbol{q};E) &= m_\mathrm{N}\,\sqrt{6}\begin{Bmatrix} S & 1 & 1\\ 1/2 & 1/2 & 1/2\end{Bmatrix}\sum_{m_l}\mathrm{C}_{1m_l,1m_{S'}}^{Sm_S}\\ &\quad\times\{\xi\boldsymbol{p}+\boldsymbol{q}\}_{1m_l}^{*}\left[\boldsymbol{p}\cdot\boldsymbol{q}+p^2+\frac{1}{2\xi}q^2-m_\mathrm{N}(E+i\epsilon)\right]^{-1},\end{aligned} \tag{4.96c}$$

$$V_{\mathrm{d}\pi}^{1m_S,S'm_{S'}}(\boldsymbol{p},\boldsymbol{q};E) = \left[V_{\pi d}^{S'm_{S'},1m_S}(\boldsymbol{q},\boldsymbol{p};E)\right]^{*}, \tag{4.96d}$$

where we explicitly used $S_\mathrm{d} = 1$. The mass ratio reads $\xi = 1/(1+1/A) = 10/11 \approx 0.91$. As a consequence of the field redefinitions, the coupling prefactors in the exchange potentials have been removed.

For the exchange potentials, we use the standard power counting of EFT($\not\pi$), which counts all momenta like small binding momenta $\gamma \sim R_\mathrm{h}^{-1}$. Thus, we have $V_{\sigma\mathrm{d}} \sim V_{\mathrm{d}\sigma} \sim m_\mathrm{N}\gamma^{-2}$ and $V_{\pi\mathrm{d}} \sim V_{\mathrm{d}\pi} \sim m_\mathrm{N}\gamma^{-1}$. In general, loop integrals and one-body propagators propagators are counted like $m_\mathrm{N}^{-1}\gamma^5$ and $m_\mathrm{N}\gamma^{-2}$. The s-wave type deuteron and $^{11}\mathrm{Be}$ propagators are counted like $m_\mathrm{N}^{-1}\gamma^{-1}$ and the $^{11}\mathrm{Be}^*$ propagator scales like $m_\mathrm{N}^{-1}R_\mathrm{c}\gamma^{-2}$. It follows that neutron exchanges between states $|\mathrm{d}\rangle$ and $|\sigma\rangle$ have to be resummed to all orders at LO. Each transfer to an excited state, in contrast, comes along with a suppressed $^{11}\mathrm{Be}^*$ propagator $\sim R_\mathrm{c}$ since $^{11}\mathrm{Be}^*$ occurs only intermediately in $^{10}\mathrm{Be}\,(\mathrm{d},\,\mathrm{p})\,^{11}\mathrm{Be}$. Thus, the excited state enters at NLO.

The partial wave projected potentials are obtained from Eqs. (4.75)-(4.76). We find

$$V_{\sigma\mathrm{d}}^{{}^{2S+1}L_J,{}^3L'_J}(p,q;E) = -\frac{m_\mathrm{N}}{2}\,\delta^{S1}\delta^{LL'}\,I_{\mathrm{n;p,c}}^{(L)}(p,q;E), \tag{4.97a}$$

$$V_{\mathrm{d}\sigma}^{{}^3L_J,{}^{2S'+1}L'_J}(p,q;E) = V_{\sigma\mathrm{d}}^{{}^{2S'+1}L'_J,{}^3L_J}(q,p;E), \tag{4.97b}$$

$$\begin{aligned}V_{\pi\mathrm{d}}^{{}^{2S+1}L_J,{}^3L'_J}(p,q;E) &= \frac{m_\mathrm{N}}{2}(-1)^J\sqrt{2\hat{S}\,\hat{L}\,\hat{L}'}\begin{Bmatrix} S & 1 & 1\\ L' & L & J\end{Bmatrix}\begin{Bmatrix} S & 1 & 1\\ 1/2 & 1/2 & 1/2\end{Bmatrix}\mathrm{C}_{L0,L'0}^{10}\\ &\quad\times\left[\xi p\,\hat{t}_{L'}+q\,\hat{t}_L\right]I_{\mathrm{n;p,c}}^{(\cdot)}(p,q;E),\end{aligned} \tag{4.97c}$$

$$V_{\mathrm{d}\pi}^{{}^3L_J,{}^{2S'+1}L'_J}(p,q;E) = V_{\pi\mathrm{d}}^{{}^{2S'+1}L'_J,{}^3L_J}(q,p;E), \tag{4.97d}$$

with $\hat{t}_L\,I_{\mathrm{n;p,c}}^{(\cdot)}(p,q;E) \equiv I_{\mathrm{n;p,c}}^{(L)}(p,q;E)$ $(L \geq 0)$ defined in Appendix C.2. For transfer between deuteron and $^{11}\mathrm{Be}$ ($^{11}\mathrm{Be}^*$), the selection rule derived above simplifies to $|\Delta L| = 0$ ($|\Delta L| = 1$). In the absence of further exchange diagrams, the quantum numbers of the $|\sigma\rangle$ state are conserved and equal those of the $|\mathrm{d}\rangle$ state, i.e., $S_\sigma = S_\mathrm{d} = 1$ and $L_\sigma = L_\mathrm{d} \in \{J+1, J, J-1\}$. In contrast, the quantum numbers $S_\pi \in \{1, 0\}$ and L_π of the $|\pi\rangle$ state. are not conserved.

At LO, strong interactions in the transfer amplitude will be given by $V_{\sigma\mathrm{d}}$ and $V_{\mathrm{d}\sigma}$ only. Thus, we can obtain a first impression on how many J channels we have to include to describe the reaction $^{10}\mathrm{Be}\,(\mathrm{d},\,\mathrm{p})\,^{11}\mathrm{Be}$ by reconstructing the full potential $V_{\sigma\mathrm{d}}$ from its partial wave components. For that, we calculate the sum in Eq. (C.1) up to some J_max. In Fig. 4.16, we plot partial sums for the lowest experimental energy $E = 7.78\,\mathrm{MeV}$ used by Schmitt *et al.* [60] as functions of the angle θ between $\boldsymbol{p}$ and $\boldsymbol{q}$ (momenta are set on shell). Apparently, the sum converges around $J_\mathrm{max} = 8$. Thus, to describe cross-section data, we have to go high up in J already without Coulomb diagrams.

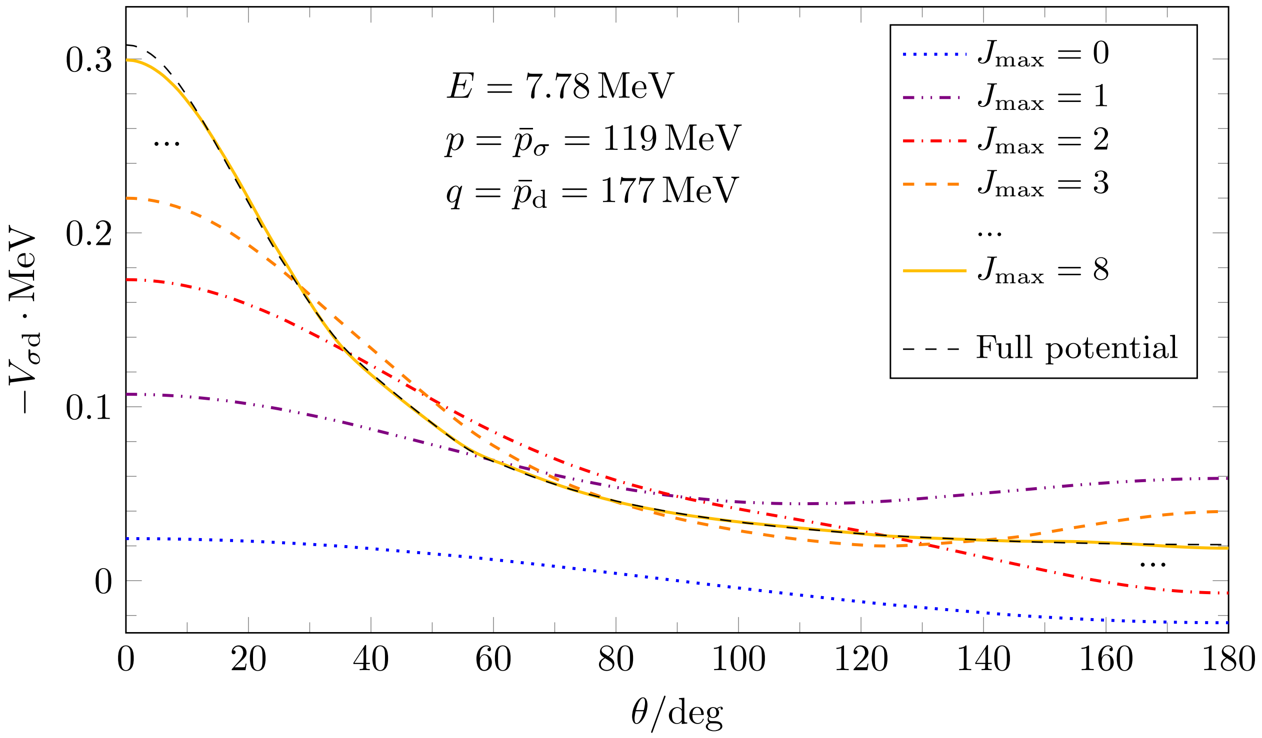

Figure 4.16.: Partial wave decomposition of the LO neutron exchange potential $V_{\sigma\mathrm{d}}$. For the lowest center-of-mass energy $E = 7.78\,\mathrm{MeV}$ used in the experiment of Ref. [60], the partial wave sum converges around $J_\mathrm{max} = 8$. The relative momenta p, q are chosen such that incoming/outgoing channels are on shell.

Next, we analyze, which partial wave channels are connected by the exchange potentials. Let us consider a fixed total angular momentum $J \geq 0$. Due to parity conservation and the decoupling of $L_\mathrm{d} = J \pm 1$ (see above), this channel falls into three subchannels, which we label using the conserved quantum numbers $[L_\mathrm{d}, J]$. The three subchannels read

$$[J+1, J]: \quad \big|\mathrm{d}, {}^3(J+1)\big\rangle \longleftrightarrow \big|\sigma, {}^3(J+1)\big\rangle \vee \big|\pi, {}^3J\big\rangle \vee \big|\pi, {}^1J\big\rangle \quad (J \geq 0), \tag{4.98a}$$

$$[J, J]: \quad \big|\mathrm{d}, {}^3J\big\rangle \longleftrightarrow \big|\sigma, {}^3J\big\rangle \vee \big|\pi, {}^3(J+1)\big\rangle \vee \big|\pi, {}^3(J-1)\big\rangle \quad (J \geq 1), \tag{4.98b}$$

$$[J-1, J]: \quad \big|\mathrm{d}, {}^3(J-1)\big\rangle \longleftrightarrow \big|\sigma, {}^3(J-1)\big\rangle \vee \big|\pi, {}^3J\big\rangle \vee \big|\pi, {}^1J\big\rangle \quad (J \geq 1). \tag{4.98c}$$

For clarity, we omitted the subscripts J in the spectroscopic notations. Each subchannel involves four different scattering channels.

Note that the subchannels $[J \pm 1, J]$ involve the same $|\pi\rangle$ spin states, even though they decouple. Thus, it must be possible to define superpositions of the two $|\pi\rangle$ spin states such that the first occurs only in $[J+1, J]$ and the second only in $[J-1, J]$. That is achieved by defining rotated spin states

$$\begin{pmatrix} \big|\pi, {}^{\bar{3}}J_J\big\rangle \\ \big|\pi, {}^{\bar{1}}J_J\big\rangle \end{pmatrix} \equiv \frac{1}{\sqrt{2J+1}} \begin{pmatrix} \sqrt{J+1} & \sqrt{J} \\ -\sqrt{J} & \sqrt{J+1} \end{pmatrix} \begin{pmatrix} \big|\pi, {}^3J_J\big\rangle \\ \big|\pi, {}^1J_J\big\rangle \end{pmatrix}, \tag{4.99}$$

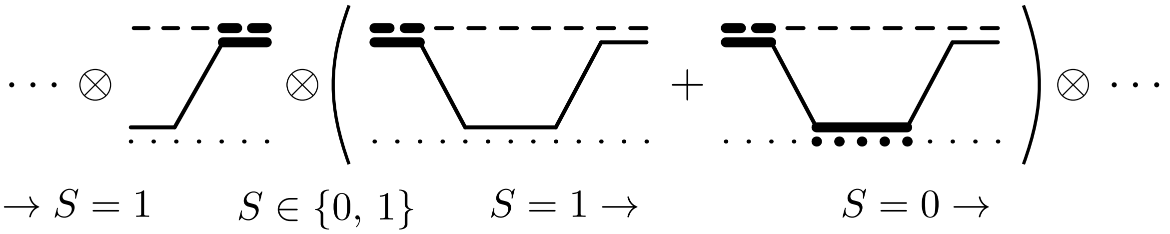

Figure 4.17.: The excited state $^{11}\mathrm{Be}^*$ allows transitions from total spin $S = 1$ to $S = 1$ ($|\mathrm{d}\rangle \to |\pi\rangle \to |\mathrm{d}\rangle$) or to $S = 0$ ($|\mathrm{d}\rangle \to |\pi\rangle \to \left|\mathrm{np}(^1s_0) + {}^{10}\mathrm{Be}\right\rangle$). The thickened solid-dotted double line represents the neutron-proton $^1S_0$ virtual state. Multiple transitions via $|\pi\rangle$ are negligible at NLO.

which we label with barred multiplicities $\hat{\bar{S}} \in \{\bar{3}, \bar{1}\}$. For $J = 0$, we have no rotation and $\bar{3} = 3$ and $\bar{1} = 1$. The only nonvanishing exchange potentials then read

$$\begin{aligned} V_{\pi\mathrm{d}}^{\overline{2\mp1}J_J,\,^3(J\pm1)_J}(p, q; E) &= \sqrt{\frac{2J+1}{J+1}}\, V_{\pi\mathrm{d}}^{^{2\mp1}J_J,\,^3(J\pm1)_J}(p, q; E) \\ &= \pm\frac{m_\mathrm{N}}{2\sqrt{3}}\left[\xi p\,\hat{t}_{J\pm1} + q\,\hat{t}_J\right] I^{(\cdot)}_{\mathrm{n;\,p,\,c}}(p, q; E)\,, \end{aligned} \tag{4.100a}$$

$$V_{\mathrm{d}\pi}^{^3(J\pm1)_J,\,\overline{2\mp1}J_J}(p, q; E) = V_{\pi\mathrm{d}}^{\overline{2\mp1}J_J,\,^3(J\pm1)_J}(q, p; E)\,. \tag{4.100b}$$

The new subchannels are given by

$$[J+1, J]: \quad \left|\mathrm{d}, {}^3(J+1)\right\rangle \leftrightarrow \left|\sigma, {}^3(J+1)\right\rangle \vee \left|\pi, {}^{\bar{1}}J\right\rangle \quad (J \geq 0)\,, \tag{4.101a}$$

$$[J, J]: \quad \left|\mathrm{d}, {}^3J\right\rangle \leftrightarrow \left|\sigma, {}^3J\right\rangle \vee \left|\pi, {}^3(J+1)\right\rangle \vee \left|\pi, {}^3(J-1)\right\rangle \quad (J \geq 1)\,, \tag{4.101b}$$

$$[J-1, J]: \quad \left|\mathrm{d}, {}^3(J-1)\right\rangle \leftrightarrow \left|\sigma, {}^3(J-1)\right\rangle \vee \left|\pi, {}^{\bar{3}}J\right\rangle \quad (J \geq 1)\,. \tag{4.101c}$$

Due to the rotation, $[J \pm 1, J]$ have been reduced to three scattering channels each.

Strong interaction diagrams beyond NLO

In Sec. 4.1.1 we claimed that the p-n virtual state in the $^1s_0$ sector can be neglected for the reaction $^{10}\mathrm{Be}\,(\mathrm{d, p})\,^{11}\mathrm{Be}$ up to NLO. One reason is that neutron exchanges and Coulomb diagrams between s-wave states conserve the total spin $S = 1$ of the system. Transitions $|\mathrm{d}\rangle \to |\sigma\rangle \to |\mathrm{v}\rangle \equiv \left|\mathrm{np}(^1s_0) + {}^{10}\mathrm{Be}\right\rangle$ are thus forbidden. In the presence of the p-wave state $^{11}\mathrm{Be}^*$, however, S can change and transitions $|\mathrm{d}\rangle \to |\pi\rangle \to |\mathrm{v}\rangle$ become possible; see Fig. 4.17. However, the virtual state is not only suppressed due to the small $^{11}\mathrm{Be}^*$ propagator, which precedes it. Since multiple spin changes ($\sim (R_\mathrm{c}/R_\mathrm{h})^2$ or smaller) are negligible at NLO, a virtual state leads to $S = 0$ in the final state of $^{10}\mathrm{Be}\,(\mathrm{d, p})\,^{11}\mathrm{Be}$. The corresponding phase space is $1/3$ the size of the $S = 1$ phase space, yielding an overall suppression of $R_\mathrm{c}/(3R_\mathrm{h}) \lesssim (R_\mathrm{c}/R_\mathrm{h})^2$ (N^{2}LO).

We saw in Sec. 4.1.2 that core excitations within the $^{11}\mathrm{Be}$ propagator are effectively taken care of by renormalization onto low-energy observables (γ_σ, r_σ, etc.). However, a $^{11}\mathrm{Be}$ propagator could also break up into a $^{10}\mathrm{Be}^*$-n pair, followed by a transfer of the neutron to the spectator proton. This process would introduce an intermediate $\left|^{10}\mathrm{Be}^* + \mathrm{d}\right\rangle$ scattering channel. In Halo EFT, the coupling between $^{11}\mathrm{Be}$ and the $^{10}\mathrm{Be}^*$-n pair is assumed to be of natural order. It follows that dynamical core excitations are at most of N^{4}LO in the low-energy counting; see Appendix E.3 for details.

In this thesis, we consider such Coulomb diagrams in Fig. 4.14, which are not grayed out. They represent effective interactions between the states $|\mathrm{d}\rangle$ and $|\sigma\rangle$. In the following, we analyze them using the Coulomb power counting developed by Rupak and Kong [143] and calculate them analytically.

Bubble diagrams

Figures 4.14(a) and (b) show Coulomb diagram series in the $|\mathrm{d}\rangle$ and the $|\sigma\rangle$ channel. They are collectively denoted by $-i\Gamma_{\mathrm{dd}}$ and $-i\Gamma_{\sigma\sigma}$, respectively. In both cases, the leading bubble diagram involves a photon exchange, scaling like $p_{\mathrm{C}}\,p_E^{-2}$. Loop momenta within the bubble can be counted like γ because the p-n (c-n) subsystem is governed by the deuteron (^{11}Be) pole. This statement is supported by on-shell evaluation of the bubble diagrams; see below. The overall diagram scalings read $m_{\mathrm{N}}\gamma^{-1}p_{\mathrm{C}}p_E^{-2} \sim \gamma p_{\mathrm{C}}/p_E^2\, V_{\sigma\mathrm{d}}$ with $p_E > \gamma \sim p_{\mathrm{C}}$. Thus, the bubble diagrams are expected to have much smaller influence on the cross section than neutron exchanges.

However, one important feature of the bubble diagrams is not captured by the Rupak and Kong counting, namely the photon propagator's infrared divergence at small momentum transfers. In principle, this enhancement could compensate for the discussed suppression. We account for this possibility by including the bubble diagrams already at LO as was done in Ref. [87]. We will then critically assess our choice by comparing the numerical influence of all Coulomb diagrams on the cross section. This comparison will reveal that the influence of the bubble diagrams is *de facto* of NLO, but they improve the overall LO result significantly; see discussion in Sec. 4.2.4.

The bubble diagrams will be denoted $-i\Gamma_{\mathrm{dd}}^{(\mathrm{LO})}$ and $-i\Gamma_{\sigma\sigma}^{(\mathrm{LO})}$. They can be calculated analytically for arbitrary particle masses. We find

$$\Gamma_{\mathrm{dd}}^{(\mathrm{LO})\,1m_S,S'm_{S'}}(\boldsymbol{p},\boldsymbol{q};E) = \frac{Q_{\mathrm{c}}\alpha\, m_{\mathrm{N}}^2\,\delta^{S'1}\,\delta^{m_Sm_{S'}}}{(\boldsymbol{p}-\boldsymbol{q})^2+\lambda^2-i\epsilon}\, f\Big(\boldsymbol{p}-\boldsymbol{q};\, \mathscr{A}_{\mathrm{d}}(p;E),\, \mathscr{A}_{\mathrm{d}}(q;E)\Big), \tag{4.102a}$$

$$\Gamma_{\sigma\sigma}^{(\mathrm{LO})\,Sm_S,S'm_{S'}}(\boldsymbol{p},\boldsymbol{q};E) = \frac{Q_{\mathrm{c}}\alpha\,(2\mu_{\mathrm{Nc}})^2\,\delta^{SS'}\,\delta^{m_Sm_{S'}}}{(\boldsymbol{p}-\boldsymbol{q})^2+\lambda^2-i\epsilon}\, \underbrace{f\left(\frac{2y}{1+y}(\boldsymbol{p}-\boldsymbol{q});\, \mathscr{A}_\sigma(p;E),\, \mathscr{A}_\sigma(q;E)\right)}_{=\left(\sqrt{\mathscr{A}_\sigma(q;E)}-\sqrt{\mathscr{A}_\sigma(p;E)}\right)/\left(\mathscr{A}_\sigma(q;E)-\mathscr{A}_\sigma(p;E)\right)+\mathscr{O}\left(y^2\right)}, \tag{4.102b}$$

with core charge $Q_{\mathrm{c}} = 4$, mass ratio $y = m_{\mathrm{N}}/m_{\mathrm{c}} = 1/A = 0.1$. The ellipses indicate higher-order diagrams. Both bubble diagrams depend on the function

$$f(\boldsymbol{\Delta};\, \mathscr{A}_1,\, \mathscr{A}_2) \equiv \frac{1}{|\boldsymbol{\Delta}|}\tan^{-1}\left(\frac{\mathscr{A}_1-\mathscr{A}_2+\boldsymbol{\Delta}^2/4}{|\boldsymbol{\Delta}|\sqrt{\mathscr{A}_2}}\right) + [\mathscr{A}_1 \longleftrightarrow \mathscr{A}_2], \tag{4.103}$$

evaluated at expressions

$$\mathscr{A}_{\mathrm{d}}(p;E) \equiv \frac{1+2y}{4}\,p^2 - m_{\mathrm{N}}(E+i\epsilon) = m_{\mathrm{N}}\,\frac{p^2-\bar{p}_{\mathrm{d}}^2}{2\mu_{\mathrm{d}}} + \gamma_{\mathrm{d}}^2 \xrightarrow{\text{on shell}} \gamma_{\mathrm{d}}^2, \tag{4.104a}$$

$$\mathscr{A}_\sigma(p;E) \equiv \frac{1+2y}{(1+y)^2}\,p^2 - \frac{2}{1+y}m_{\mathrm{N}}(E+i\epsilon) = 2\mu_{\mathrm{Nc}}\,\frac{p^2-\bar{p}_\sigma^2}{2\mu_\sigma} + \gamma_\sigma^2 \xrightarrow{\text{on shell}} \gamma_\sigma^2\,. \tag{4.104b}$$

The form of $\Gamma_{\sigma\sigma}^{(\mathrm{LO})}$ can be simplified significantly by neglecting terms of order $\mathscr{O}\left(y^2\right)$; see Eq. (4.102b). This approximation is justified since $y^2 = 0.01$ is a tiny number. The only angular dependence then comes from the photon propagator, which can be projected onto certain partial waves analytically; see below.

Rupak and Kong suggested an even stronger approximation to the bubble diagram expressions for scattering at momenta $p < \gamma$ [143]. In this limit, the values of f in Eqs. (4.102a)-(4.102b) approach $1/(2\gamma_a)$

($a \in \{\mathrm{d}, \sigma\}$). König *et al.* applied this approximation also for larger external momenta $p \gtrsim \gamma$ [144]. They argued that the main contribution from the diagrams comes from the region $\boldsymbol{p} - \boldsymbol{q} = 0$, where the values of f yield $\mathscr{A}_a(p; E)^{-1/2}/2$ ($a \in \{\mathrm{d}, \sigma\}$). If off-shell contributions are small, it should be allowed to replace this expression by $\mathscr{A}_a(\bar{p}_a; E)^{-1/2}/2 = 1/(2\gamma_a)$ everywhere; see Eqs. (4.104a)-(4.104b). Indeed, each intermediate bubble diagram comes along with a propagator $iG_a(E_{\mathrm{cm}})$, which is strongly peaked at $E_{\mathrm{cm}} = -B_a = E - p^2/(2\mu_a) \Leftrightarrow p = \bar{p}_a$. In subsequent studies, however, König *et al.* avoided this so-called "bubble approximation" as it cannot be systematized in the EFT's power counting [87]. Still, it strongly supports the claim that the bubble is governed by small momenta γ as stated above.

Since Coulomb couplings do not change particle spins, the diagrams are diagonal in the spin quantum numbers S and m_S. It follows that partial wave projections are also diagonal in L and

$$\Gamma_{aa}^{(\mathrm{LO})\,{}^{2S+1}L_J,{}^{2S'+1}L_J}(p, q; E) = \delta^{LL'}\,\frac{1}{2}\int_{-1}^{1} \mathrm{d}x\; P_L(x)\,\Gamma_{aa}^{S0,S'0}(\boldsymbol{p}, \boldsymbol{q}; E) \quad (a \in \{\mathrm{d}, \sigma\}), \tag{4.105}$$

where $x \equiv \boldsymbol{p}\cdot\boldsymbol{q}/(pq)$. For $a = \sigma$, we can use $y \ll 1$ to obtain the analytic approximation

$$\begin{aligned}\Gamma_{\sigma\sigma}^{(\mathrm{LO})\,{}^{2S+1}L_J,{}^{2S'+1}L_J}(p, q; E) = {}& \frac{\delta^{LL'}\,\delta^{SS'}}{2pq}\,Q_L\!\left(\frac{p^2+q^2+\lambda^2}{2pq}\right)\\ &\times\left(\frac{\sqrt{\mathscr{A}_\sigma(q; E)} - \sqrt{\mathscr{A}_\sigma(p; E)}}{\mathscr{A}_\sigma(q; E) - \mathscr{A}_\sigma(p; E)} + \mathcal{O}\left(y^2\right)\right)\end{aligned} \tag{4.106}$$

with Legendre function Q_L defined in Eq. (C.16).

Box diagrams

Coulomb diagrams in the transfer channels are shown in Figs. 4.14(c) and (d). As opposed to the bubble diagrams, the photon propagators of the box diagrams are part of loop integrals. For this reason, it is not immediately clear if momenta in the loop have to be counted like γ or like p_E. Since in our case $p_E > \gamma$, it is safe to count them like γ, such that the loop $\sim m_{\mathrm{N}}\gamma^{-3}$ is not suppressed. This scheme coincides with the one in Ref. [145]. The overall scaling $m_{\mathrm{N}}p_{\mathrm{C}}\gamma^{-3}$ implies that box diagrams have to be resummed to all orders for the reaction cross section.

The analytic forms of the bubble diagrams read

$$\begin{aligned}\Gamma_{\sigma\mathrm{d}}^{(\mathrm{LO})\,Sm_S,S'm_{S'}}(\boldsymbol{p}, \boldsymbol{q}; E) = {}& -Q_{\mathrm{c}}\alpha\, m_{\mathrm{N}}\, V_{\sigma\mathrm{d}}^{Sm_S,S'm_{S'}}(\boldsymbol{p}, \boldsymbol{q}; E)\\ &\times\Bigg[f\left(\boldsymbol{p} - y\boldsymbol{q};\, \frac{(1+y)^2}{4}\,\mathscr{A}_\sigma(p; E),\, \mathscr{A}_{\mathrm{d}}(q; E)\right)\\ &\qquad - \frac{\lambda}{\boldsymbol{p}\cdot\boldsymbol{q} + p^2 + \frac{1}{2\xi}q^2 - m_{\mathrm{N}}(E + i\epsilon)} + \mathcal{O}\left(\lambda^2\right)\Bigg],\end{aligned} \tag{4.107a}$$

$$\Gamma_{\mathrm{d}\sigma}^{(\mathrm{LO})\,Sm_S,S'm_{S'}}(\boldsymbol{p}, \boldsymbol{q}; E) = \Gamma_{\sigma\mathrm{d}}^{(\mathrm{LO})\,S'm_{S'},Sm_S}(\boldsymbol{q}, \boldsymbol{p}; E)\,. \tag{4.107b}$$

Apparently, they are proportional to the simple neutron exchange diagrams, but exhibit an opposite overall sign. This observation suggests that box diagrams strongly suppress the reaction cross section at LO. Partial wave projections of the box diagrams have to be performed numerically. The angular integration works analogous to the one in Eq. (4.105).

Coulomb diagrams beyond NLO

Apart from the bubble and box diagrams discussed above, there are many more Coulomb diagrams, which we neglect at NLO.

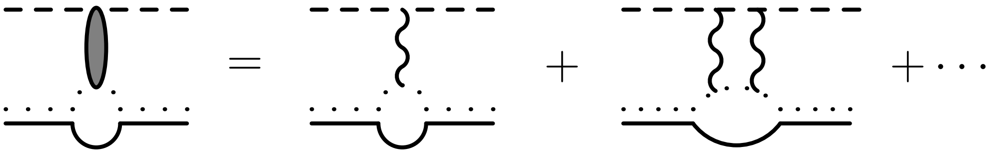

Figure 4.18.: Deuteron bubble diagrams with full Coulomb amplitude between breakup and recombination. Multi-photon terms are negligible in this thesis.

ERE-photon diagrams

First of all, we omit diagrams with direct couplings between photon and two-body fields. These couplings are introduced by the ERE terms of the Lagrangian. One example is the grayed-out diagram in Fig. 4.14(a). It represents a single Coulomb photon exchange between deuteron and proton stemming from the first ERE term. By restoring the covariant derivative in the deuteron Lagrangian, one would get

$$g_{\mathrm{d}}^{-2} d_m^\dagger \left[\Delta_{\mathrm{d},0} - i\partial_{\mathrm{cm}} + \cdots\right] d_m \to g_{\mathrm{d}}^{-2} d_m^\dagger \left[\Delta_{\mathrm{d},0} - \left(i\partial_0 - eA_0 + \frac{\boldsymbol{D}^2}{4m_{\mathrm{N}}}\right) + \cdots\right] d_m \,. \tag{4.108}$$

The Feynman rule for the A_0 coupling would read $-ie\left(-g_{\mathrm{d}}^{-2}\right) = iem_{\mathrm{N}}^2 r_{\mathrm{d}}/(8\pi)$; see Eq. (4.29b). It follows, that the grayed-out diagram in 4.14(a) has the same form as Eq. (4.102a), but with the function $f \sim 1/(2\gamma_{\mathrm{d}})$ replaced by the small constant $r_{\mathrm{d}}/2$; see also Ref. [145]. That corresponds to a $R_{\mathrm{c}}/R_{\mathrm{h}}$ suppression. The same suppression is obtained in Fig. 4.14(b). A_0 couplings due to higher-order ERE terms involve further powers of $R_{\mathrm{c}}/R_{\mathrm{h}}$.[13] Recall that bubble diagrams are suppressed due to the photon propagator (*de facto* NLO; see Sec. 4.3.1). Thus, we neglect direct photon-two-body state couplings, which are at most of N^{2}LO.

Multi-photon diagrams

Moreover, we neglect bubble and box diagrams with multiple Coulomb photon exchanges in between two-body breakup and recombination. In principle, one could include such contributions by replacing the single photon propagator by the full Coulomb scattering amplitude $it_{\mathrm{cp}}^{(\mathrm{C})}$ shown in Fig. 4.10. We assume that multi-photon exchanges within $it_{\mathrm{cp}}^{(\mathrm{C})}$ are suppressed by $\chi_3 = p_{\mathrm{C}}/p_E \leq 0.2$ (a Sommerfeld parameter). It represents the three-body expansion parameter χ_3 of our EFT.

Let us check the proposed $\chi_3 \leq 0.2$ suppression by recalculating $-i\Gamma_{\mathrm{dd}}$ numerically, but this time including full Coulomb scattering. The corresponding diagram is shown in Fig. 4.18. Its mathematical expression (as well as the one of $-i\Gamma_{\sigma\sigma}$) can be simplified to a one-dimensional momentum integral; see Appendix E.4. Results are given in Fig. 4.19, where we plot the ratio between multi-photon ($\mathcal{O}\left(\alpha^2\right)$) contributions to the full result and the single-photon (LO) approximation. We plot this ratio as a function of on-shell momenta $p = q = \bar{p}_{\mathrm{d}}$ for different angles $\theta = \boldsymbol{p}\cdot\boldsymbol{q}/(pq)$. First of all, for $\theta = 0°$ (zero momentum transfer, blue curve) the terms $\mathcal{O}\left(\alpha^2\right)$ are arbitrarily unimportant. For larger angles, the ratio initially increases almost linearly for $\theta \leq 30°$, before it starts to saturate. For experimental on-shell momenta (vertical grid lines) the ratio hits the proposed suppression 0.2 around 60° (red curve). Thus, more or less for the full forward scattering regime, multi-photon contributions scale as proposed and are negligible. Multi-photon corrections for backward scattering may be less suppressed ($\lesssim 0.28$), but in this regime Coulomb scattering itself is much weaker.

The decreasing behavior of the ratio for large $\bar{p}_{\mathrm{d}}$ is in line with $\chi_3 \propto p_E^{-1} \sim \bar{p}_{\mathrm{d}}^{-1}$; see the decreasing dashed curve in Fig. 4.18. Note, however, that the ratio has a different power law behavior in the low-energy regime $\bar{p}_{\mathrm{d}} \sim p_E \leq \gamma_{\mathrm{d}}$. Here, it is proportional to $\bar{p}_{\mathrm{d}}$ and dimensional analysis yields a suppression $p_{\mathrm{C}}\,\bar{p}_{\mathrm{d}}/\gamma_{\mathrm{d}}^2$ (increasing dashed curve in Fig. 4.18). This second low-energy suppression was used by König *et al.* to neglect multi-photon exchanges in d-p scattering [145]. The transition between

---

[13] Couplings to transverse photons induced by $\boldsymbol{D}^2/(4m_{\mathrm{N}})$ are negligible due to $4m_{\mathrm{N}} \gg p_E > p_{\mathrm{C}}$.

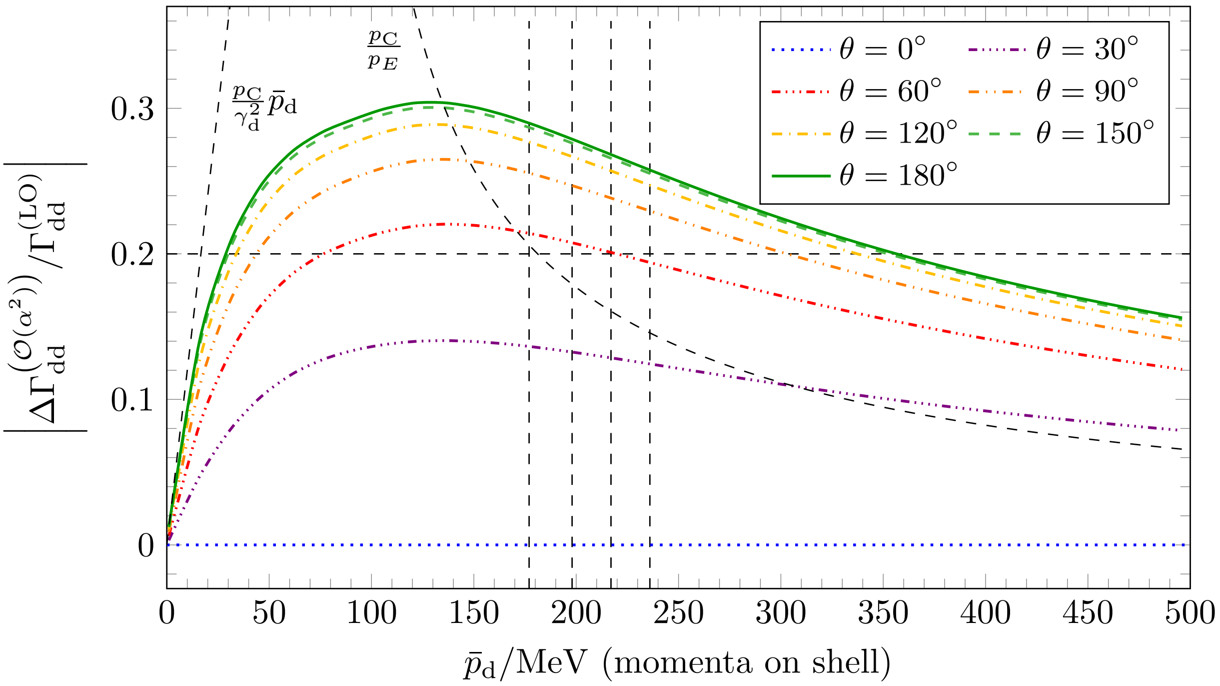

Figure 4.19.: Suppression of multi-photon exchanges in the bubble diagram of $-i\Gamma_{\mathrm{dd}}$ for different on-shell momenta $p = q = \bar{p}_{\mathrm{d}}$. Direct photon-two-body state couplings are neglected here. The vertical grid lines show the on-shell momenta used by Schmitt *et al.* [60]. The horizontal grid line indicates the suppression order 0.2 predicted by the power counting. The thick dashed curves indicate the scaling behaviors for the low-energy ($p_E < \gamma$) and higher-energy ($p_E > \gamma$) regimes; see text.

the two scalings can be understood from the two-photon exchange diagram in Fig. 4.19. This diagram has two loops, of which the upper one is governed by p_E and the lower one by γ. The only propagator which depends on both scales is the proton propagator in between the two photon exchanges. If $p_E > \gamma$, it may be counted like $m_{\mathrm{N}} p_E^{-2}$, leading to an overall suppression p_{C}/p_E of this diagram. If $p_E < \gamma$, we may count the propagator like $m_{\mathrm{N}} \gamma_{\mathrm{d}}^{-2}$ and obtain the suppression $p_{\mathrm{C}}\, p_E/\gamma_{\mathrm{d}}^2 \sim p_{\mathrm{C}}\, \bar{p}_{\mathrm{d}}/\gamma_{\mathrm{d}}^2$.

A direct calculation of multi-photon box diagrams is much more difficult since the loop integral has to be solved with Monte-Carlo methods [145]. This task is particularly challenging for $E > 0$, where three-body singularities need to be taken into account. In this thesis, we assume that multi-photon contributions are suppressed by p_{C}/p_E (N^{2}LO).

Excited-state Coulomb diagrams

Coulomb diagrams including $^{11}\mathrm{Be}^*$ states are subleading because they come along with at least one suppressed $^{11}\mathrm{Be}^*$ propagator.[14] A selection of such diagrams is given in Fig. 4.20.

The diagrams in (b) induce E1 transitions between the Beryllium-11 states. They involve a small photon propagator and are thus negligible at NLO. Note that the photon in the second diagram arises directly from the derivative-type strong interaction vertex [54]. This photon is transverse and thus the photon-proton vertex $\sim 1/(2m_{\mathrm{N}})$ is strongly suppressed. Diagrams in (c) come along with at least two suppressed $^{11}\mathrm{Be}^*$ propagators and can also be neglected at NLO.

For the box diagram $-i\Gamma_{\mathrm{d}\pi}^{(\mathrm{LO})}$ in (a), the situation is not as clear. In order to estimate its importance, we compare it numerically to the neutron exchange diagram $-iV_{\mathrm{d}\pi}$ in Fig. 4.13(b); see Appendix E.4.3.

---

[14] This statement is not true if $^{11}\mathrm{Be}^*$ is an external state, for example in the reaction $^{10}\mathrm{Be}(\mathrm{d},\mathrm{p})\,^{11}\mathrm{Be}^*$. In such a reaction, certain Coulomb diagrams we can neglect for $^{10}\mathrm{Be}(\mathrm{d},\mathrm{p})\,^{11}\mathrm{Be}$ would enter already at lower orders.

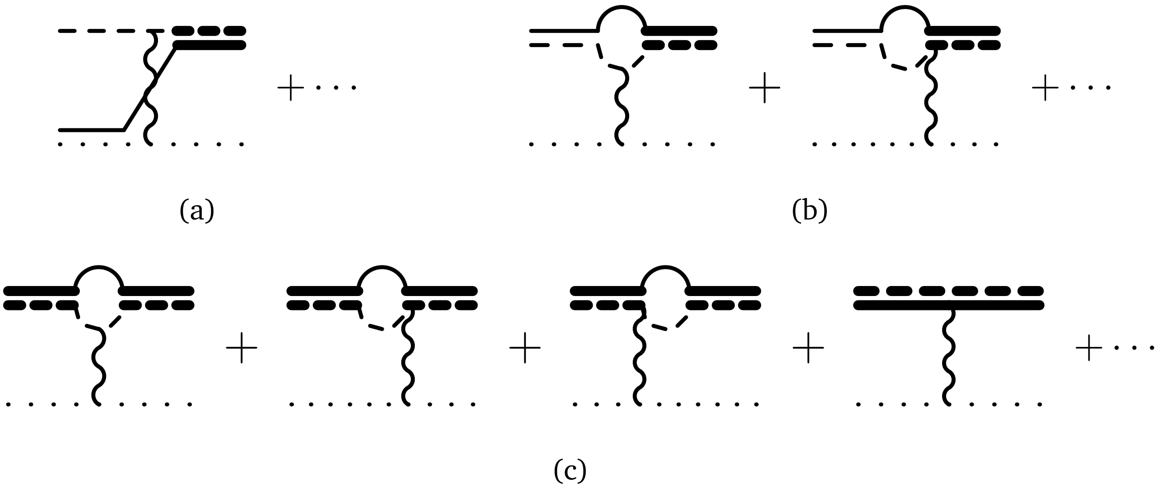

Figure 4.20.: Photon diagrams involving $^{11}\mathrm{Be}^*$ in the (a) $|d\rangle \to |\pi\rangle$, (b) $|\sigma\rangle \to |\pi\rangle$, and (c) $|\pi\rangle \to |\pi\rangle$ channel. Time-reversed diagrams of (a, b) are omitted. All these diagrams can be neglected at NLO; see text.

Table 4.1.: EFT inputs for the calculation of the reaction cross section up to NLO in $\chi_2 \sim 0.4$.

Order	deuteron	$^{11}\mathrm{Be}$	$^{11}\mathrm{Be}^*$
LO [$\mathcal{O}(1)$]	$B_\mathrm{d} = 2.22\,\mathrm{MeV}$ [86]	$B_\sigma = 0.50\,\mathrm{MeV}$ [120]	–
NLO [$\mathcal{O}(\chi_2)$]	$r_\mathrm{d} = 1.75\,\mathrm{fm}$ [86]	$A_\sigma = 0.786\,\mathrm{fm}^{-1/2}$ [132]	$B_\pi = 0.18\,\mathrm{MeV}$ [120] , $A_\pi = 0.129\,\mathrm{fm}^{-1/2}$ [132]

For the smallest experimental energy and on-shell momenta, it turns out to be suppressed by roughly two orders in $R_\mathrm{c}/R_\mathrm{h}$. We conclude that the overall influence of the diagram is of N^{3}LO.

Summary

To conclude this section, let us summarize the scattering channels, three-body diagrams, and EFT input parameters required to calculate the reaction cross section up to NLO. At LO, strong interactions have to be included in the $^3s_1$ channel of p-n and the $^2s_{1/2}$ channel of c-n. The only input parameters in these channels are the binding energies B_d for the deuteron and B_σ for $^{11}\mathrm{Be}$. In the three-body sector, we iterate neutron exchange, bubble and box diagrams (single-photon approximations) between the scattering states $|\mathrm{d}\rangle$ and $|\sigma\rangle$.

At NLO, the deuteron and $^{11}\mathrm{Be}$ propagators involve also the effective ranges r_d, r_σ, the latter being inferred from the *ab initio* ANC A_σ. Moreover, strong interactions in the $^2p_{1/2}$ channel of c-n enter. Here, we use the $^{11}\mathrm{Be}^*$ binding energy B_π and the *ab initio* ANC A_π as inputs. In the three-body sector, the scattering state $|\pi\rangle$ is introduced by neutron exchanges between $|\mathrm{d}\rangle$ and $|\pi\rangle$.

4.2.4 Transfer amplitude

Having identified the relevant diagrams in the strong and Coulomb sectors up to NLO, we now construct the transfer amplitude at LO and show the necessity of a three-body force. NLO corrections will be included at a later point in Sec. 4.3.2.

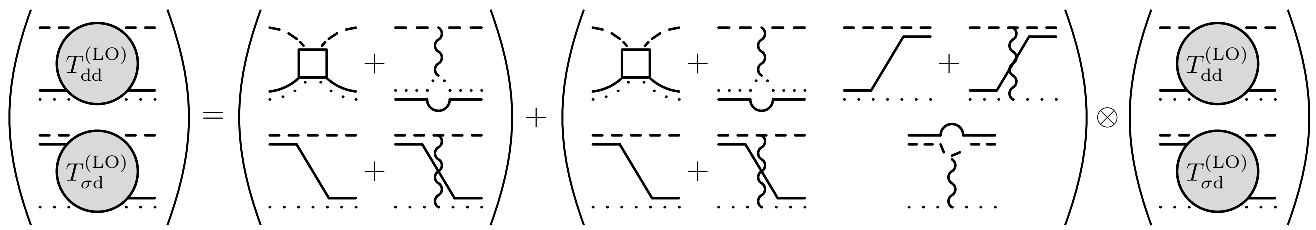

Figure 4.21.: The Faddeev equation for the LO transfer amplitude $T^{(\mathrm{LO})}_{\sigma\mathrm{d}}$ is constructed from neutron exchange, bubble, and box diagrams as well as a three-body force diagram $-iC_0(\Lambda)\delta^{mm'}$ (white square). The diagram multiplication on the right-hand side induces loop integrals over LO two-body propagators $iG^{(\mathrm{LO})}_a$ ($a \in \{\mathrm{d}, \sigma\}$) (drawn without circles).

Construction at LO

The LO transfer amplitude for the transition $|\sigma\rangle \to |\mathrm{d}\rangle$ will be denoted $T^{(\mathrm{LO})}_{\sigma\mathrm{d}}$.[15] The corresponding Faddeev amplitude is shown in Fig. 4.21. It is constructed from neutron exchange diagrams $-iV_{\sigma\mathrm{d}}$, $-iV_{\mathrm{d}\sigma}$, Coulomb box diagrams $-i\Gamma^{(\mathrm{LO})}_{\sigma\mathrm{d}}$, $-i\Gamma^{(\mathrm{LO})}_{\mathrm{d}\sigma}$, and Coulomb bubble diagrams $-i\Gamma^{(\mathrm{LO})}_{\mathrm{dd}}$, $-i\Gamma^{(\mathrm{LO})}_{\sigma\sigma}$. Recall that the bubble diagrams are actually subleading in the Rupak and Kong counting; see Sec. 4.2.3. We still include them already at LO since the infrared-divergent Coulomb propagators could lead to an enhancement. Moreover, we include the three-body force $C_0(\Lambda)$ (white square vertex) in the $|\mathrm{d}\rangle$ sector for renormalization. All these diagrams are iterated to all orders.

As indicated in Fig. 4.21 the LO transfer amplitude and the corresponding elastic amplitude $T^{(\mathrm{LO})}_{\mathrm{dd}}$ can be summarized into an amplitude vector $\vec{T}^{(\mathrm{LO})}$. As discussed in Sec. 4.2.3, the total angular momentum J and the orbital angular momentum $L \equiv L_{\mathrm{d}} = L_\sigma \in \{J+1, J, J-1\}$ are conserved. We label the different scattering channels with the superscript "$[L, J]$" and find

$$\begin{aligned}\vec{T}^{(\mathrm{LO})\,[L,J]}\big(p,p';E\big) &= -\underline{\underline{K}}^{(\mathrm{LO})\,[L,J]}\big(p,p';E\big)\cdot\vec{e}_1\\ &\quad+\frac{1}{2\pi^2}\int_0^{\Lambda}\mathrm{d}q\,q^2\,\underline{\underline{K}}^{(\mathrm{LO})\,[L,J]}(p,q;E)\,\underline{\underline{\mathcal{G}}}^{(\mathrm{LO})\,[L,J]}(q;E)\cdot\vec{T}^{(\mathrm{LO})\,[L,J]}\big(q,p';E\big)\,,\end{aligned} \tag{4.109}$$

with LO amplitude vector, interaction and propagator matrices

$$\vec{T}^{(\mathrm{LO})\,[L,J]} \equiv \begin{pmatrix} T^{(\mathrm{LO})}_{\mathrm{dd}} \\ T^{(\mathrm{LO})}_{\sigma\mathrm{d}} \end{pmatrix}^{{}^3L_J,{}^3L_J}\,, \tag{4.110a}$$

$$\underline{\underline{K}}^{(\mathrm{LO})\,[L,J]} \equiv \begin{pmatrix} C_0(\Lambda)\,\delta^{L0}+\Gamma^{(\mathrm{LO})}_{\mathrm{dd}} & V_{\mathrm{d}\sigma}+\Gamma^{(\mathrm{LO})}_{\mathrm{d}\sigma} \\ V_{\sigma\mathrm{d}}+\Gamma^{(\mathrm{LO})}_{\sigma\mathrm{d}} & \Gamma^{(\mathrm{LO})}_{\sigma\sigma} \end{pmatrix}^{{}^3L_J,{}^3L_J}\,, \tag{4.110b}$$

$$\underline{\underline{\mathcal{G}}}^{(\mathrm{LO})\,[L,J]} \equiv \mathrm{diag}\big[\mathcal{G}^{(\mathrm{LO})}_{\mathrm{d}},\,\mathcal{G}^{(\mathrm{LO})}_{\sigma}\big]\,, \tag{4.110c}$$

and $\vec{e}_1 \equiv (1, 0)^T$ in channel space. The outer superscripts in Eqs. (4.110a)-(4.110b) are to be understood component-wise. For convenience, we introduced the new functions

$$\mathcal{G}^{(\mathrm{N}^n\mathrm{LO})}_a(q;E) \equiv G^{(\mathrm{N}^n\mathrm{LO})}_a\big(E-q^2/(2\mu_a)\big)\;\;(a\in\{\mathrm{d},\sigma\},\,n\in\mathbb{N}_0)\,. \tag{4.111}$$

The reduced masses μ_a are given in Eqs. (4.95a)-(4.95b). Moreover, we equip the Faddeev equation with a momentum cutoff $\Lambda \gg (2m_{\mathrm{N}}|E|)^{1/2} \gg \gamma_{\mathrm{d}}, \gamma_\sigma, p_{\mathrm{C}}$.

---

[15] For the cross section, we in fact need the absolute square of the time-reversed amplitude $T_{\mathrm{d}\sigma}$. However, it is easily obtained using $|T_{\mathrm{d}\sigma}|^2 = |T_{\sigma\mathrm{d}}|^2$.

The full transfer amplitude is given as the sum over the partial wave amplitudes and projection operators as explained in Appendix C. In all calculations, we truncate the partial wave sum at some maximal orbital angular momentum L_{max} and increase this value until the cross section can be considered converged. At the same time, we steadily decrease the photon mass $\lambda \to 0$ in calculations with Coulomb diagrams. We find that the cross section converges at $L_{\text{max}} = 12$ and $\lambda = 0.1\,\text{MeV}$. For cross-section calculations, we moreover have to multiply the full transfer amplitude by a residue factor $(Z_{\text{d}}^{(\text{LO})} Z_{\sigma}^{(\text{LO})})^{1/2}$.

At NLO, we will replace the LO propagator functions and the LO residues by their NLO analogues. In doing so, we take into account range corrections in the deuteron and $^{11}\text{Be}^*$ sectors. Moreover, the excited state will introduce further scattering channels, thereby enlarging the interaction matrix. Respective Faddeev equations will be given in Sec. 4.3.2.

Numerical treatment

In the previous chapter, the two-body propagator of the D^{0*} meson had a pole in the complex plane. This circumstance allowed us to simply integrate along the real axis from $q = 0$ to $q = \Lambda$. In the system at hand, however, the two-body poles of the propagator functions $\mathscr{G}_a^{(\text{LO})}(q;\,E)$ lie on the real axis at $q = \bar{p}_a < \Lambda$ $(a \in \{\text{d}, \sigma\})$ if $E > -B_a$. In the NLO system, the functions $\mathscr{G}_a^{(\text{NLO})}(q;\,E)$ $(a \in \{\text{d}, \sigma\})$ will have the same pole structure and the excited state propagator function $\mathscr{G}_{\pi}^{(\text{LO})}(q;\,E)$ will have a pole at $q = \bar{p}_{\pi} < \Lambda$ if $E > -B_{\pi}$.

We subtract the two-body poles using

$$\mathscr{G}_a(q;\,E) \equiv \tilde{\mathscr{G}}_a(q;\,E)\,\frac{1}{q - \bar{p}_a - i\epsilon} = \tilde{\mathscr{G}}_a(q;\,E)\left(\frac{\mathscr{P}}{q - \bar{p}_a} + i\pi\,\delta(q - \bar{p}_a)\right) \quad (a \in \{\text{d}, \sigma, \pi\})\,. \tag{4.112}$$

The operator $\mathscr{P}$ denotes a principle value integration. The functions $\tilde{\mathscr{G}}_a(q;\,E)$ are regular at $q = \bar{p}_a$. For a specific loop integral transition $a \to b \to c$ $(a, b, c \in \{\text{d}, \sigma, \pi\})$, one then obtains

$$\begin{aligned}
&\int_0^{\Lambda} \mathrm{d}q\, q^2\, K_{ab}(p, q;\,E)\,\mathscr{G}_b(q;\,E)\,T_{bc}\big(q, p';\,E\big) \\
&= \int_0^{\Lambda} \mathrm{d}q\, \frac{q^2 K_{ab}(p, q;\,E)\,\tilde{\mathscr{G}}_b(q;\,E)\,T_{bc}(q, p';\,E) - [q \to \bar{p}_b]\,\theta(E + B_b)\,\theta(\Lambda - \bar{p}_b)}{q - \bar{p}_b} \\
&\quad + \bar{p}_b^2\, K_{ab}(p, \bar{p}_b;\,E)\,\tilde{\mathscr{G}}_b(\bar{p}_b;\,E)\,T_{bc}\big(\bar{p}_b, p';\,E\big)\left[\ln\left(\frac{\Lambda - \bar{p}_b}{\bar{p}_b}\right) + i\pi\right]\theta(E + B_b)\,\theta(\Lambda - \bar{p}_b)\,.
\end{aligned} \tag{4.113}$$

The remaining integral in Eq. (4.113) has an integrand regular at $q = \bar{p}_b$.

By discretizing the integral to loop momenta $\{q_i,\, 1 \le i \le N\} \subseteq [0, \Lambda]$, one obtains a linear system of equations for the amplitude values $\{T_{ab}(q_i, p';\,E),\, a, b \in \{\text{d}, \sigma, \pi\},\, 1 \le i \le N + 3\}$ with $q_{N+1} \equiv \bar{p}_{\text{d}}$, $q_{N+2} \equiv \bar{p}_{\sigma}$, $q_{N+3} \equiv \bar{p}_{\pi}$.

Unphysical deep three-body states

The necessity of a three-body force can be seen by setting $C_0(\Lambda) \equiv 0$ performing an asymptotic analysis for large incoming and loop momenta $p, q \gg (2m_{\text{N}}|E|)^{1/2} \gg \gamma_{\text{d}}, \gamma_{\sigma}, p_{\text{C}}$, similar to Ref. [146]. In this limit, the Coulomb diagrams ($\sim p_{\text{C}}\, q^{-3}$) are negligible against neutron exchange diagrams ($\sim q^{-2}$); see Eqs. (4.96a)-(4.96b), (4.102a)-(4.102b), and (4.107a)-(4.107b). They should leave the qualitative UV behavior unaltered and can be neglected for the moment.

In Appendix E.5.1 we perform the asymptotic analysis for arbitrary $L \ge 0$.[16] It turns out that the transfer and elastic amplitudes are governed by power law behaviors $\sim p^{-1-s^{(L)}}$ with $s^{(0)} = \pm i s_0 =$

---

[16] Note that LO interactions are independent of J.

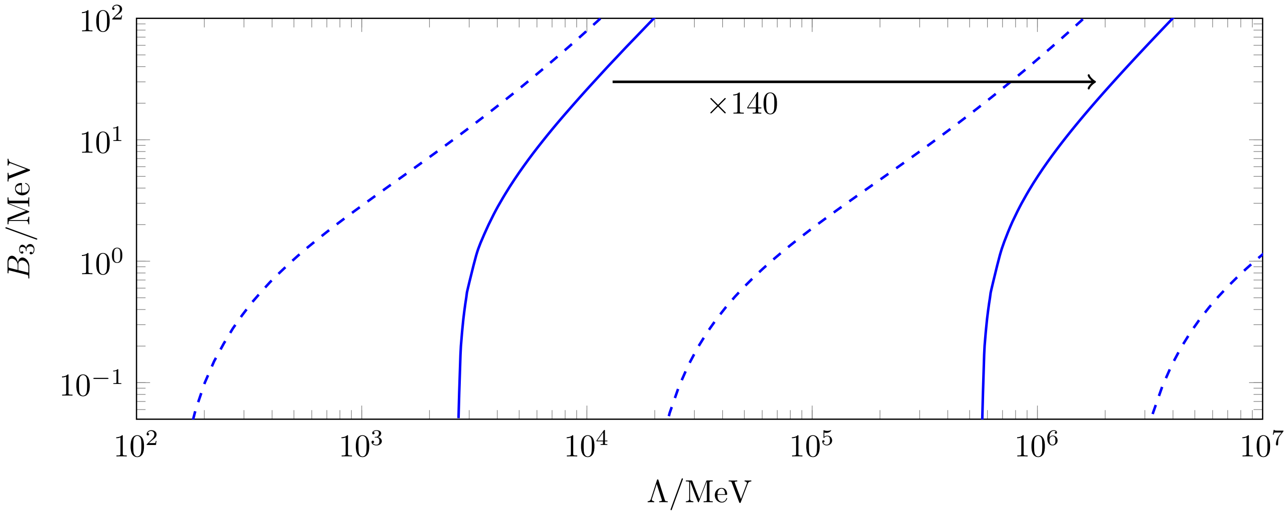

Figure 4.22.: Unrenormalized three-body spectra at LO without (dashed lines) and with (solid lines) Coulomb diagrams ($\lambda = 0.1\,\mathrm{MeV}$, converged) for cutoffs $\Lambda \gg (2m_\mathrm{N}|E|)^{1/2} \gg \gamma_\mathrm{d}, \gamma_\sigma, p_\mathrm{C}$.

$\pm 0.6357i$ for $L = 0$ and $s^{(L)} > 1$ otherwise. It follows that the Faddeev equations produce unique amplitude solutions, converging for $\Lambda \to \infty$, only for $L \geq 1$. The $L = 0$ system, in contrast, needs a three-body force. In fact, it exhibits an Efimov effect, i.e., a geometric spectrum of three-body bound states at energies $E = -B_\mathrm{d} - B_3$ and $B_3 > 0$ [21, 147, 148]. For $C_0(\Lambda) \equiv 0$, the spectrum is log-periodic in Λ, with a scaling factor $\exp(\pi/s_0) \approx 140$. This number reproduces the universal scaling factor of three distinguishable particles (light-light-heavy with mass ratio $y = 0.1$) and large scattering lengths for the light-heavy pairs, presented in Ref. [21].

The three-body spectrum can be calculated numerically by searching the root of the Fredholm determinant of the LO Faddeev equation at $E < -B_\mathrm{d}$. In this region, the Faddeev equation is purely real. Thus, the root finding is performed in one dimension, as opposed to the one in Chapter 3. We show the spectrum of the unrenormalized $L = 0$ system without Coulomb diagrams in Fig. 4.22 as dashed lines. It exhibits the proposed log-periodicity in Λ. Coulomb diagrams do not influence the large momentum behavior qualitatively. Three-body bound states are only pushed to higher cutoffs (solid lines in Fig. 4.22).

The Efimov states have quantum numbers $J^P = 1^+$, $A = 12$ and $Z = 5$. Were they physical, they would correspond to $J^P = 1^+$ levels of ^{12}B. Three such states are known by experiment, corresponding to binding energies $B_3 = 2.374\,\mathrm{MeV}$ (^{12}B ground state), $B_3 = 7.384\,\mathrm{MeV}$ and $B_3 = 5.774\,\mathrm{MeV}$ [149]. These energies correspond to spatial separations $R_{3,\mathrm{d}} \sim (2\mu_\mathrm{d} B_3)^{-1/2} < 1.47\,\mathrm{fm}$ in a deuteron-^{10}Be picture and $R_{3,\sigma} \sim (2\mu_\sigma(B_3 + B_\mathrm{d} - B_\sigma))^{-1/2} < 1.74\,\mathrm{fm}$ in a ^{11}Be-p picture. Both of these numbers are of natural order R_c. Thus, they do not give rise to a scale separation in the three-body sector and the cluster pictures are not justified. As a consequence, the Efimov states are unphysical artifacts of our short-range approach. Fortunately, they only occur at cutoffs $\Lambda \geq 2.5\,\mathrm{GeV}$, which are much larger than all relevant energy scales of the three-body calculation. Moreover, after renormalization onto cross-section data, the three-body states will be pushed to binding energies $B_3 > 19\,\mathrm{MeV}$, which lie outside the EFT' region of applicability; see Fig. 4.24(b). Thus, the existence of three-body states does not impose a problem for our approach.

4.3 Cross-section results

In this final section, we calculate the cross section of ^{10}Be(d, p)^{11}Be and compare it to data by Schmitt *et al.* [59, 60]. Firstly, we assess the performed Coulomb power counting by analyzing the cross-section suppressions caused by the relevant Coulomb diagrams. Secondly, we discuss angular and energy regions where the reaction can be considered peripheral, i.e., independent of short-range details. Moreover, we demonstrate the renormalizability of the LO system. Finally, we discuss NLO corrections to the cross section.

4.3.1 LO study

The reaction cross section is a function of the center-of-mass angle θ_cm, which lies between the incoming deuteron momentum $\bar{\boldsymbol{p}}_\mathrm{d} = -\bar{p}_\mathrm{d}\hat{\boldsymbol{p}}_\mathrm{d}$ and the outgoing proton momentum $\bar{\boldsymbol{p}}_\sigma = \bar{p}_\sigma\hat{\boldsymbol{p}}'_\mathrm{p}$ (both on shell). By averaging over initial spin configurations $S = 1, m_S \in \{+1, 0, -1\}$ and summing over final configurations $S' = 1, m_{S'} \in \{+1, 0, -1\}$ and $S' = 0 = m_{S'}$, we obtain

$$\left(\frac{\mathrm{d}\sigma}{\mathrm{d}\Omega}\right)^{(\mathrm{LO})}(\theta_\mathrm{cm}; E) = \frac{1}{3}\sum_{m_S, S', m_{S'}} \frac{\mu_\mathrm{d}\mu_\sigma}{4\pi^2}\frac{\bar{p}_\sigma}{\bar{p}_\mathrm{d}} Z_d^{(\mathrm{LO})} Z_\sigma^{(\mathrm{LO})} \left| T_{\sigma\mathrm{d}}^{(\mathrm{LO})\,S' m_{S'}, 1 m_S}(\bar{\boldsymbol{p}}_\sigma, \bar{\boldsymbol{p}}_\mathrm{d}; E)\right|^2 . \tag{4.114}$$

This expression is derived in Appendix E.6. Cross sections are expressed in units of mb = 0.1 fm^2; see Appendix A.

Coulomb suppression and improved LO system

In the Coulomb power counting above we decided to include both bubble and box diagrams already at LO. We will now critically assess this choice by comparing cross-section results with and without the two diagram types for experimental center-of-mass energies E in Eq. (4.83). Moreover, we estimate the potential impact of the three-body force $C_0(\Lambda)$ by varying Λ in the large range $[300, 1500]$ MeV in each calculation.

The first calculation is performed without any Coulomb diagram. The corresponding cross sections are shown in Fig. 4.23 as hatched bands. Each single curve is converged at percent level for $L_\mathrm{max} = 12$. Apparently, the bands strongly overestimate the reaction cross section. For all four energies, they lie roughly three times higher than the data. At the same time, the band widths (10-20 mb) are small compared to the average sizes. These observations indicate that the strong interaction does not produce enough repulsion between the scattering partners, even in the presence of a three-body force. We conclude that the Coulomb force has to be included already at LO.

The relative importance of the Coulomb box and bubble diagrams can be understood by successively introducing them to the Faddeev equation. Firstly, we include the box diagrams $-i\Gamma_{\sigma\mathrm{d}}^{(\mathrm{LO})}$ and $-i\Gamma_{\mathrm{d}\sigma}^{(\mathrm{LO})}$, which are expected to suppress the cross section on a LO scale. This claim is in agreement with numerical results, shown as light bands surrounded by dotted lines. They are only half the hatched bands' sizes. Further suppression is achieved after inclusion of the bubble diagrams $-i\Gamma_{\mathrm{dd}}^{(\mathrm{LO})}$ and $-i\Gamma_{\sigma\sigma}^{(\mathrm{LO})}$; see the dark lowermost bands. Apparently, their influence is $\lesssim 40\,\% \sim \chi_2$ smaller than the one of the box diagrams. *A posteriori*, the bubble diagrams are of NLO, as opposed to the LO box diagrams. That means that we have overestimated the influence of the bubble diagrams' infrared divergences by one order in χ_2. In principle, these diagrams could be neglected at LO. The "pure" LO system would then only contain neutron exchanges and box diagrams. It follows that ERE-coupling diagrams, which are one order smaller than the bubble diagrams, can indeed be neglected at NLO.

Even though they are subleading in a strict EFT sense, the bubble diagrams lead to a surprisingly good agreement with data at the lower beam energies and for forward angles. In other words, they improve the overall convergence of the EFT expansion. This statement will be confirmed by NLO calculations later. As a consequence, we refer to the Faddeev equation system in Fig. 4.21 as the "improved LO system". Moreover, in contrast to the pure LO system, the improved system can be renormalized onto cross-section data at $E_\mathrm{d} = 12$ MeV since the cutoff-variation bands comprise all data points.

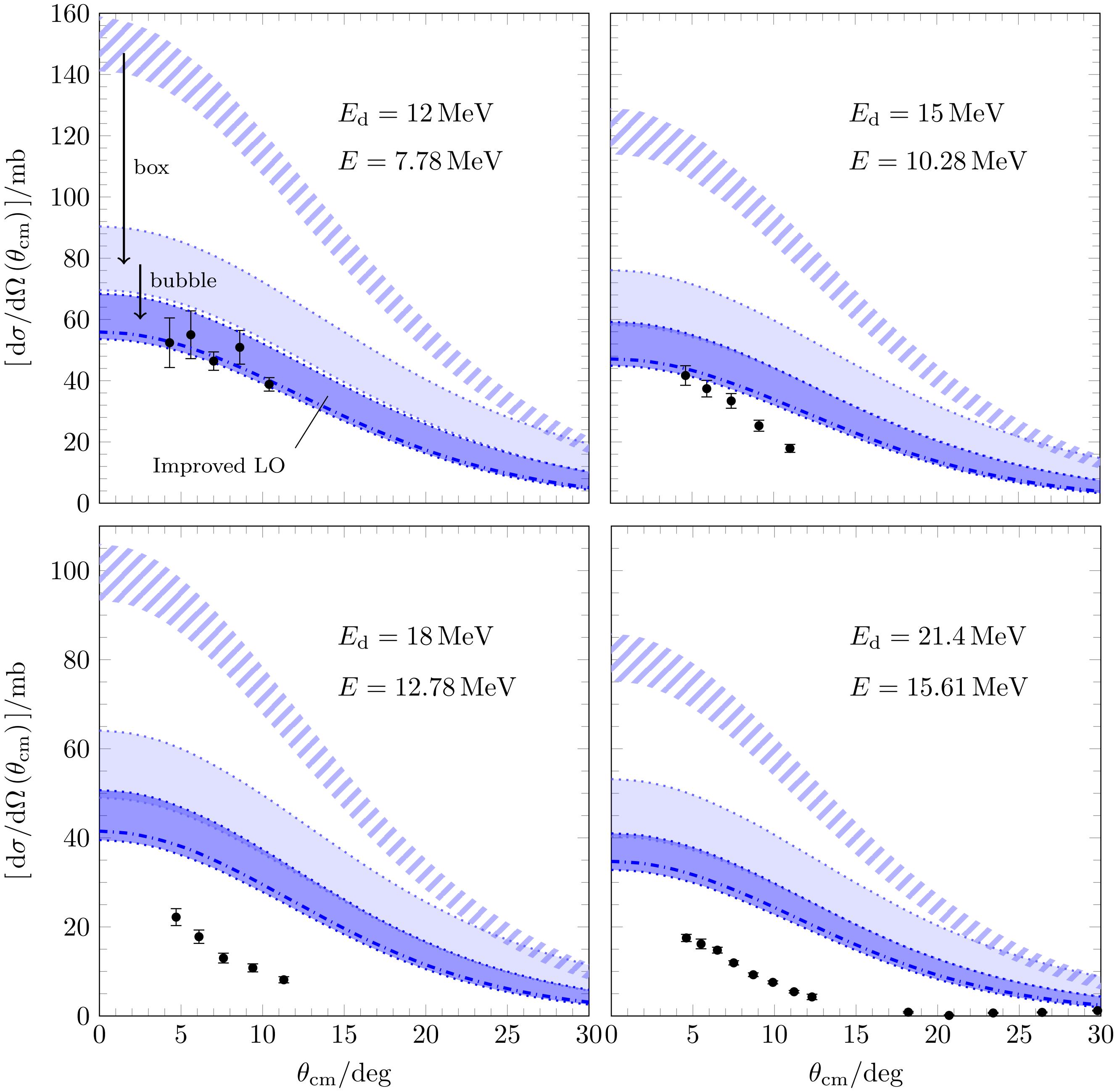

Figure 4.23.: Calculations for the LO cross section of ${}^{10}\mathrm{Be}\,(\mathrm{d},\,\mathrm{p})\,{}^{11}\mathrm{Be}$. The cross section is a function of the center-of mass angle θ_{cm} between deuteron and proton. For different deuteron beam energies E_{d} (lab frame), the results are compared to data (black points) of Schmitt *et al.* [60]. All bands are due to cutoff variations $\Lambda \in [300,\,1500]\,\mathrm{MeV}$. They do not include EFT uncertainties of order 40 % due to neglected NLO contributions. Calculations with hatched bands exclude Coulomb contributions. Such with light (dark) bands include the Coulomb box (and bubble) diagrams. Dash-dotted curves represent a χ^2 fit of the full equation system in Fig. 4.21 onto the $E_{\mathrm{d}} = 12\,\mathrm{MeV}$ data using the three-body force $C_0(\Lambda)$; see also Fig. 4.24. The fit is cutoff-independent for $\Lambda \geq 500\,\mathrm{MeV}$. All curves are calculated for $L_{\mathrm{max}} = 12$ and $\lambda = 0.1\,\mathrm{MeV}$ (converged).

Peripherality regions

Keeping the bubble diagrams in LO calculations does not lead to a loss of predictive power since they do not introduce any new parameters. Thus, the improved LO system is still independent of any short-range details like higher-order ERE coefficients or high-energy states. Cross sections are then only affected by the tail of the two-body wave functions of deuteron and ^{11}Be. I.e., the reaction description is still purely "peripheral". Yang and Capel showed that such a theory could be appropriate at lower beam energies and at forward angles [133]. This claim is supported by our improved LO results, which reproduce data at the lowest beam energy $E_\mathrm{d} = 12\,\mathrm{MeV}$ over the whole angular data range $4.7^\circ \leq \theta_\mathrm{cm} \leq 10.4^\circ$.

According to Yang and Capel, the peripherality region decreases in size by going to higher energies. We indeed observe that data at $E_\mathrm{d} = 15\,\mathrm{MeV}$ is only reproduced by the improved LO band in the forward scattering region $\theta_\mathrm{cm} \leq 4.6^\circ$. Deviations at higher energies are of NLO size and might become smaller at higher power counting orders.

At $E_\mathrm{d} = 18\,\mathrm{MeV}$, the bands deviate from the available $\theta_\mathrm{cm} \geq 4.6^\circ$ data more strongly ($\sim$ 40-80 %). The strong decrease in the data points, however, suggests that the deviation becomes at least of NLO size for very small angles. Here, the reaction could still be considered peripheral. Note that Schmitt *et al.* identified the $E_\mathrm{d} = 18\,\mathrm{MeV}$ data set to be systematically smaller than the other three [60]. They extracted spectroscopic factors for all four energies using two different reaction models. For both models, the spectroscopic factor for $E_\mathrm{d} = 18\,\mathrm{MeV}$ was 25 % smaller than the respective other three. A similar observation was made by Yang and Capel, who extracted the ^{11}Be ANC from the Schmitt *et al.* data [133]. All values were compatible with the *ab initio* ANC from Calci *et al.* [132], except the one at $E_\mathrm{d} = 18\,\mathrm{MeV}$, which was $\approx$ 15 % smaller. We conclude that our $E_\mathrm{d} = 18\,\mathrm{MeV}$ result could actually be better than suggested by Fig. 4.23.

At very high beam energies $E_\mathrm{d} = 21.4\,\mathrm{MeV}$, we do not expect our low-energy theory to be valid anymore. The steady increase of deviations above $E_\mathrm{d} = 15\,\mathrm{MeV}$ indicates that the current low-energy power counting could fail at these energies. In particular, the counting scheme $\bar{k} \sim \gamma$ in the two-body sectors could become inappropriate as more and more energy could enter the two-body systems.

Cutoff dependence and renormalizability

In Sec. 4.2.4 we saw that out of all partial wave components $L \leq L_\mathrm{max} = 12$, only the $L = 0$ component is cutoff dependent. Moreover, the scaling factor of the unphysical Efimov effect is very large. For these reasons, the improved LO bands (dark in Fig. 4.23) are only 20 % the size of the box diagram shift (LO). Such contributions are negligible up to NLO. In principle, we could thus use for example the bands' average values as LO estimates. Renormalization is thus not really required at LO. Remarkably, the only inputs to our LO calculation are then given by the binding energies B_d and B_σ; see Table 4.1.

At much smaller energies, however, the $L = 0$ channel should be of much greater importance and the cutoff dependence could not be ignored anymore. Thus, we demonstrate that the LO Faddeev equation can indeed be renormalized using $C_0(\Lambda)$ only. For that we consider the improved LO system and perform a χ^2 fit with

$$\chi^2 \equiv \frac{1}{5-1} \sum_{i=1}^{5} \left(\frac{\left(\frac{\mathrm{d}\sigma}{\mathrm{d}\Omega}\right)^{(\mathrm{LO})} - \left(\frac{\mathrm{d}\sigma}{\mathrm{d}\Omega}\right)^{(\mathrm{exp})}}{\left(\Delta\frac{\mathrm{d}\sigma}{\mathrm{d}\Omega}\right)^{(\mathrm{exp})}} \right)^2 \left(\theta_\mathrm{cm}^{(i)};\, E = 7.78\,\mathrm{MeV}\right) \tag{4.115}$$

to the depicted $E_\mathrm{d} = 12\,\mathrm{MeV}$ data set for various cutoffs $\Lambda \geq 300\,\mathrm{MeV}$. We obtain two solutions for $C_0(\Lambda)$, shown in Fig. 4.24(a), which have comparable χ^2 values 2.23 (dot-dashed curve) and 2.29 (solid curve). Both values are constant for $\Lambda \geq 500\,\mathrm{MeV}$. The fit result of the dot-dashed solution is shown in Fig. 4.23 as dot-dashed curves.

After renormalization, the binding energies of the unphysical three-body states become constants for $\Lambda \to \infty$. The lowest binding energy for the solid (dot-dashed) solution occurs around $\Lambda \approx 300\,\mathrm{MeV}$

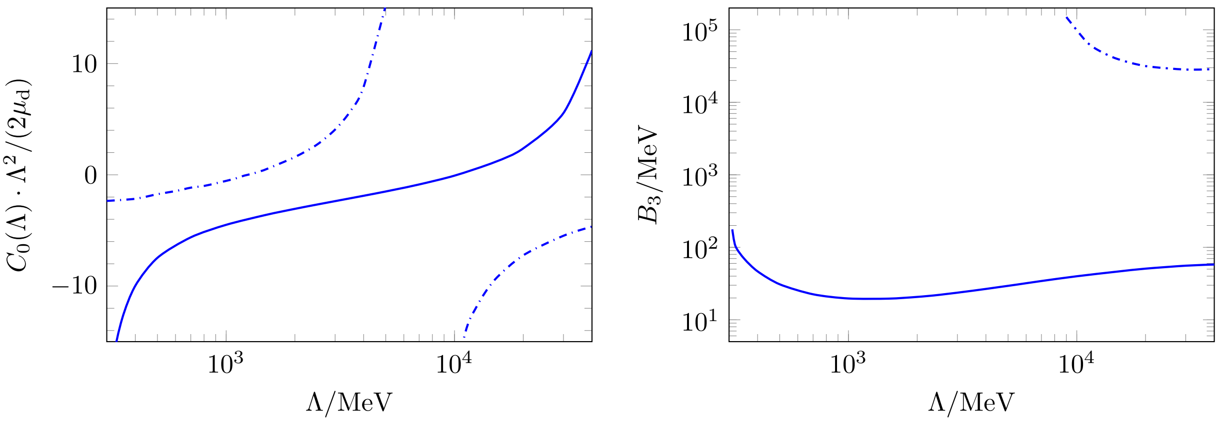

(a) (b)

Figure 4.24.: Renormalization of the improved LO system in Fig. 4.21 using the three-body force $C_0(\Lambda)$. (a) The dot-dashed and solid curves are the two solutions of $C_0(\Lambda)$ of the χ^2 fit with comparable values $\chi^2 \approx 2.23$ and $\chi^2 \approx 2.29$, respectively. (b) Both solutions produce renormalized spectra outside the EFT regime. The smallest binding energies lie above $B_3 \approx 28\,\mathrm{MeV}$ and $B_3 \approx 19\,\mathrm{MeV}$, respectively.

($\Lambda \approx 7\,\mathrm{GeV}$); see Fig. 4.24(b). It lies above $B_3 \approx 19\,\mathrm{MeV}$ ($B_3 \approx 28\,\mathrm{MeV}$) and converges to an even higher value as $\Lambda \to \infty$.

4.3.2 NLO corrections

We conclude our study of the reaction $^{10}\mathrm{Be}(\mathrm{d,p})\,^{11}\mathrm{Be}$ by calculating NLO contributions to the cross section. They comprise effective range corrections in the deuteron and $^{11}\mathrm{Be}$ sectors and intermediate transfer to the excited state $^{11}\mathrm{Be}^*$.

Effective range corrections

We follow Bedaque *et al.* by replacing the LO propagator functions $\mathscr{G}_\mathrm{d}^{(\mathrm{LO})}$ and $\mathscr{G}_\sigma^{(\mathrm{LO})}$ in the Faddeev equation by their NLO forms

$$\begin{aligned}\mathscr{G}_\mathrm{d}^{(\mathrm{NLO})}(q;E) = \frac{4\pi}{m_\mathrm{N}}&\left[\gamma_\mathrm{d} - \sqrt{m_\mathrm{N}\left(\frac{q^2}{2\mu_\mathrm{d}} - E - i\epsilon\right)}\,\right]^{-1} \\ &\times\left[1 + \frac{r_\mathrm{d}}{2}\left(\gamma_\mathrm{d} + \sqrt{m_\mathrm{N}\left(\frac{q^2}{2\mu_\mathrm{d}} - E - i\epsilon\right)}\right)\right], \qquad (4.116\mathrm{a})\\ \mathscr{G}_\sigma^{(\mathrm{NLO})}(q;E) = \frac{2\pi}{\mu_\mathrm{Nc}}&\left[\gamma_\sigma - \sqrt{2\mu_\mathrm{Nc}\left(\frac{q^2}{2\mu_\sigma} - E - i\epsilon\right)}\,\right]^{-1} \\ &\times\left[1 + \frac{r_\sigma}{2}\left(\gamma_\mathrm{d} + \sqrt{2\mu_\mathrm{Nc}\left(\frac{q^2}{2\mu_\sigma} - E - i\epsilon\right)}\right)\right]; \qquad (4.116\mathrm{b})\end{aligned}$$

see Eqs. (4.33b), (4.54b), and (4.111) [150]. Correspondingly, we use NLO residues $Z_a^{(\mathrm{NLO})}$ in the calculation of the cross section; see Eq. (4.114). This straightforward technique is often referred to as "partial resummation" since it induces specific amplitude terms proportional to $r_\mathrm{d}^n, r_\sigma^n$ ($n \geq 2$). However, for natural cutoffs, they are smaller than NLO terms and do not undermine the power counting [151, 152].

More importantly, the new propagator functions behave like q^0 for large loop momenta q, while the LO expressions fell off like q^{-1}. As a consequence, partial resummation modifies the UV behavior of the Faddeev kernel and reintroduces a cutoff dependence to the $L = 0$ channel. In Chapter 3, where we partially resummed self-energy corrections to the D^{0*} propagator at NLO, such a new cutoff dependence was not seen because the NLO correction term was purely imaginary. In principle, the cutoff dependence could be cured by readjusting the three-body force $C_0(\Lambda)$ [153].

In order to see the impact of the additional cutoff dependence, we include effective range corrections in the renormalized improved LO system for various $\Lambda \in [500, 1500]\,\mathrm{MeV}$.[17] That yields the red hatched bands in Fig. 4.25. Apparently, they lie well within the ±40 % uncertainty region (blue bands enclosed by thin solid lines) of the improved LO curves (blue, dot-dashed). The band widths are comparably small, which gives rise to a mild cutoff dependence.

A small fraction of the band widths stems from an unexpected cutoff dependence in the $L = 1$ sector. It is an artifact of the partial resummation technique, which modifies the Faddeev kernels' UV behaviors. In a fully perturbative approach, no such divergence occurs [146]. In Appendix E.5.2 we investigate this issue by performing an asymptotic analysis with effective range corrections. Even though desirable, a fully perturbative NLO treatment lies beyond the thesis' scope. We checked that the cutoff's influence on the $L = 1$ amplitudes is less than 2 % over the chosen Λ range. Thus, we can ignore this issue at NLO.

Contributions from the excited state $^{11}\mathrm{Be}^*$

The second and last NLO contribution comes from the excited state $^{11}\mathrm{Be}^*$. It is introduced via neutron exchange diagrams $-iV_{\pi\mathrm{d}}$ and $-iV_{\mathrm{d}\pi}$ shown in Fig. 4.13(b). Their partial wave-projected forms are given in Eqs. (4.97c)-(4.97d) and (4.100a)-(4.100b). Recall that the excited state is subleading due to the fact that its LO propagator $iG_\pi^{(\mathrm{LO})} \sim R_\mathrm{c}/(\gamma^2 m_\mathrm{N})$ involves one power of the small core radius. Propagator corrections of N^{2}LO or higher will be neglected. Thus, we use the propagator function

$$\mathscr{G}_\pi^{(\mathrm{LO})}(q;\, E) = \frac{6\pi}{\mu_\mathrm{Nc}}\,\frac{2}{-r_\pi}\left[2\mu_\mathrm{Nc}\left(E + i\epsilon - \frac{q^2}{2\mu_\pi}\right) + \gamma_\pi^2\right]^{-1} \tag{4.117}$$

in NLO calculations for the cross section.[18]

As done for the LO system, we label angular momentum channels with superscripts "$[L_\mathrm{d}, J]$", where $J \geq 0$ and $L_\mathrm{d} \in \{J+1, J, J-1\}$ are conserved. The NLO amplitude vectors $\vec{T}^{(\mathrm{NLO})\,[L_\mathrm{d},J]}$ then read

$$\vec{T}^{(\mathrm{NLO})\,[J,J]} = \begin{pmatrix} T_\mathrm{dd}^{(\mathrm{NLO})\,{}^3J_J,{}^3J_J} \\ T_{\sigma\mathrm{d}}^{(\mathrm{NLO})\,{}^3J_J,{}^3J_J} \\ T_{\pi\mathrm{d}}^{{}^3(J-1)_J,{}^3J_J} \\ T_{\pi\mathrm{d}}^{{}^3(J+1)_J,{}^3J_J} \end{pmatrix} \quad (J \geq 1)\,, \tag{4.118a}$$

$$\vec{T}^{(\mathrm{NLO})\,[J\pm1,J]} = \begin{pmatrix} T_\mathrm{dd}^{(\mathrm{NLO})\,{}^3(J\pm1)_J,{}^3(J\pm1)_J} \\ T_{\sigma\mathrm{d}}^{(\mathrm{NLO})\,{}^3(J\pm1)_J,{}^3(J\pm1)_J} \\ T_{\pi\mathrm{d}}^{\overline{2\mp1}J_J,{}^3(J\pm1)_J} \end{pmatrix} \quad (J \geq 0 \text{ and } J \geq 1\text{, respectively})\,. \tag{4.118b}$$

---

[17] We start the variation at $\Lambda = 500\,\mathrm{MeV}$ because the renormalized improved LO results are not yet converged for smaller cutoffs.

[18] The superscript "(LO)" in the propagator function indicates that this expression is the leading term of the $^{11}\mathrm{Be}^*$ pole expansion.

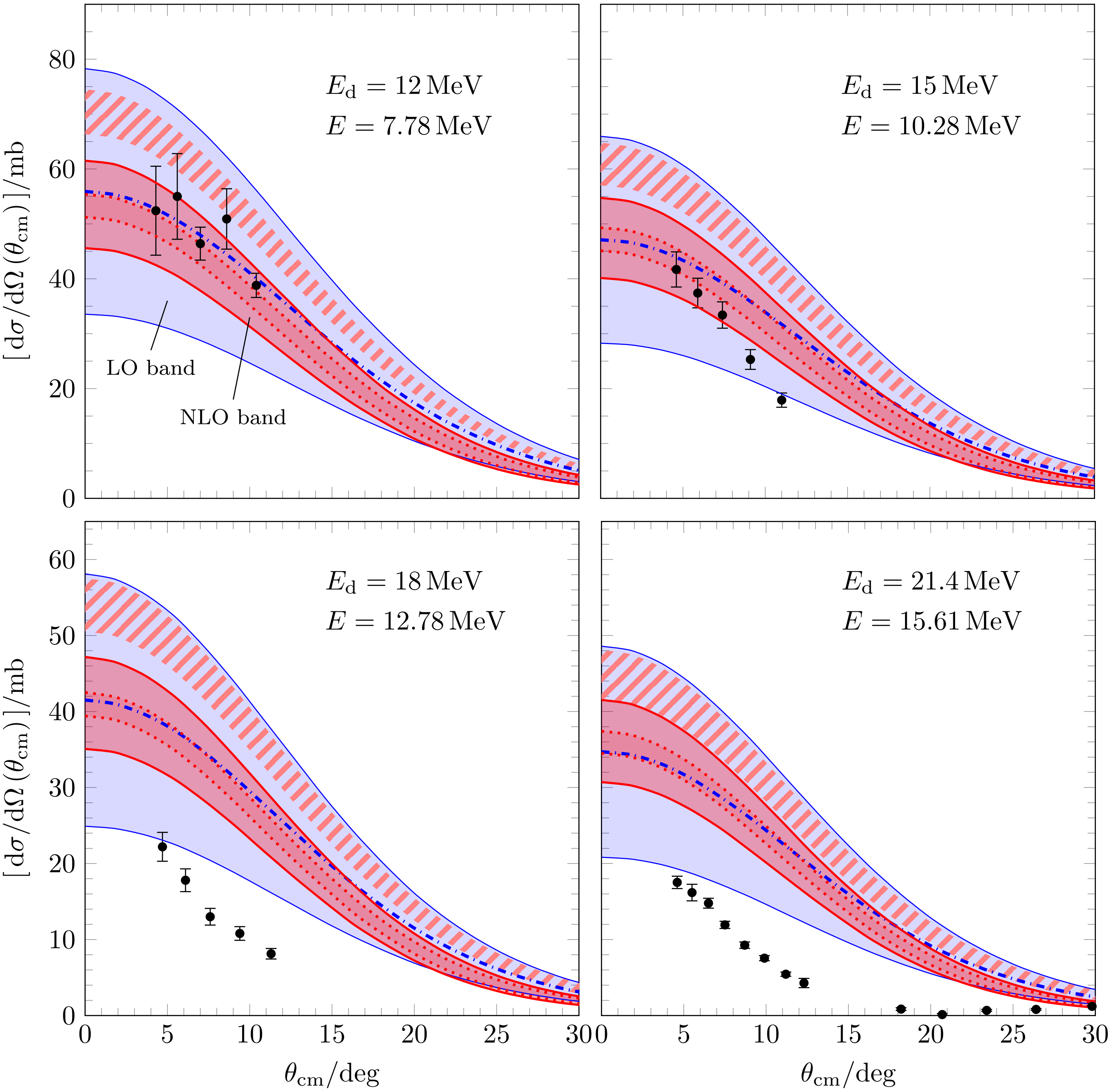

Figure 4.25.: Cross section for $^{10}\mathrm{Be}\,(\mathrm{d},\,\mathrm{p})\,^{11}\mathrm{Be}$ up to NLO as function of the center-of-mass angle θ_cm. Blue bands enclosed by thin solid lines indicate the LO uncertainty regions (±40 %) of the improved LO results (blue dot-dashed curves). By including effective ranges in the deuteron and ^{11}Be sectors one obtains the red hatched bands (cutoff variations), which lie in the proposed LO uncertainty region. The second NLO contribution comes from $^{11}\mathrm{Be}^*$ (red cutoff-variation bands enclosed by dotted lines). The final NLO bands (red, enclosed by thick solid lines) take into account remaining EFT uncertainties (±16 %).

They are determined by the interaction and propagator matrices

$$\underline{\underline{K}}^{(\mathrm{NLO})\,[J,J]} = \begin{pmatrix} \Gamma_{\mathrm{dd}}^{(\mathrm{LO})\,{}^3J_J,{}^3J_J} & (V_{\mathrm{d}\sigma} + \Gamma_{\mathrm{d}\sigma}^{(\mathrm{LO})})^{{}^3J_J,{}^3J_J} & V_{\mathrm{d}\pi}^{{}^3J_J,{}^3(J-1)_J} & V_{\mathrm{d}\pi}^{{}^3J_J,{}^3(J+1)_J} \\ (V_{\sigma\mathrm{d}} + \Gamma_{\sigma\mathrm{d}}^{(\mathrm{LO})})^{{}^3J_J,{}^3J_J} & \Gamma_{\sigma\sigma}^{(\mathrm{LO})\,{}^3J_J,{}^3J_J} & 0 & 0 \\ V_{\pi\mathrm{d}}^{{}^3(J-1)_J,{}^3J_J} & 0 & 0 & 0 \\ V_{\pi\mathrm{d}}^{{}^3(J+1)_J,{}^3J_J} & 0 & 0 & 0 \end{pmatrix}, \tag{4.119a}$$

$$\underline{\underline{\mathscr{G}}}^{(\mathrm{NLO})\,[J,J]} = \mathrm{diag}\big[\mathscr{G}_{\mathrm{d}}^{(\mathrm{NLO})},\, \mathscr{G}_{\sigma}^{(\mathrm{NLO})},\, \mathscr{G}_{\pi}^{(\mathrm{LO})},\, \mathscr{G}_{\pi}^{(\mathrm{LO})}\big], \tag{4.119b}$$

and

$$\underline{\underline{K}}^{(\mathrm{NLO})\,[J\pm1,J]} = \begin{pmatrix} \Gamma_{\mathrm{dd}}^{(\mathrm{LO})\,{}^3(J\pm1)_J,{}^3(J\pm1)_J} & (V_{\mathrm{d}\sigma} + \Gamma_{\mathrm{d}\sigma}^{(\mathrm{LO})})^{{}^3(J\pm1)_J,{}^3(J\pm1)_J} & V_{\mathrm{d}\pi}^{{}^3(J\pm1)_J,{}^{\overline{2\mp1}}J_J} \\ (V_{\sigma\mathrm{d}} + \Gamma_{\sigma\mathrm{d}}^{(\mathrm{LO})})^{{}^3(J\pm1)_J,{}^3(J\pm1)_J} & \Gamma_{\sigma\sigma}^{(\mathrm{LO})\,{}^3(J\pm1)_J,{}^3(J\pm1)_J} & 0 \\ V_{\pi\mathrm{d}}^{{}^{\overline{2\mp1}}J_J,{}^3(J\pm1)_J} & 0 & 0 \end{pmatrix}, \tag{4.120a}$$

$$\underline{\underline{\mathscr{G}}}^{(\mathrm{NLO})\,[J\pm1,J]} = \mathrm{diag}\big[\mathscr{G}_{\mathrm{d}}^{(\mathrm{NLO})},\, \mathscr{G}_{\sigma}^{(\mathrm{NLO})},\, \mathscr{G}_{\pi}^{(\mathrm{LO})}\big]. \tag{4.120b}$$

Similar to previous calculations, we vary $\Lambda \in [500,\, 1500]\,\mathrm{MeV}$ and include the LO three-body force $C_0(\Lambda)$ obtained in the χ^2 fit.[19] The results of the cutoff variations are shown as red bands enclosed by dotted lines in Fig. 4.25. These bands lie very close to the improved LO curves. We conclude that the influence of the excited state is indeed of NLO, in agreement with the power counting. Cutoff dependencies of the $L = 0$ and $L = 1$ sectors are negligible compared to remaining EFT uncertainties of ±16 % (red bands enclosed by thick solid lines). Thus, no further renormalization is required at NLO.

Instead of using the NLO parameters $r_\sigma = 3.5\,\mathrm{fm}$ and $r_\pi = -0.95\,\mathrm{fm}^{-1}$ obtained from the *ab initio* ANCs of Calci *et al.* [132], one could directly use the Halo EFT values $r_\sigma = 2.7\,\mathrm{fm}$ and $r_\pi = -0.66\,\mathrm{fm}^{-1}$ by Hammer and Phillips [54]. The relative differences 30 % and 40 % are of size $R_\mathrm{c}/R_\mathrm{h}$ and should be negligible at NLO. In fact, we have checked that the final NLO bands would only change by about 5 %.

As mentioned earlier, the final NLO results lie almost on top of the improved LO curves. This observation implies two things. Firstly, the inclusion of the bubble diagrams at LO indeed accelerates the EFT's convergence. Secondly, NLO corrections cannot explain the discrepancy between our cross-section results and data at larger angles and energies. This observation provides strong evidence for the assumption that the reaction is peripheral only for beam energies $E_\mathrm{d} \lesssim 15\,\mathrm{MeV}$. Growing short-range sensitivities at higher energies are apparently not appropriately described by our power counting. At this point, one should question the validity of counting all loop momenta like the small scale γ. In a more sophisticated scheme, short-range effects like breakup towards the core excitation might already occur at lower orders in the power counting.

In Ref. [60], also the cross section for transfer to $^{11}\mathrm{Be}^*$ was measured. In principle, it could be obtained from the amplitudes $T_{\pi\mathrm{d}}$ occurring in Eqs. (4.118a)-(4.118b). However, Yang and Capel identified the reaction $^{10}\mathrm{Be}\,(\mathrm{d},\,\mathrm{p})\,^{11}\mathrm{Be}^*$ as less peripheral than $^{10}\mathrm{Be}\,(\mathrm{d},\,\mathrm{p})\,^{11}\mathrm{Be}$ [133]. For this reason, we cannot expect our theory to describe this process correctly for experimental energies. Indeed, naive application of our NLO scheme yields cross sections which strongly overestimate data. At the moment, a modification of the power counting lies beyond the scope of this thesis.

---

[19] Asymptotic analyses of the NLO systems are performed in Appendix (E.5.3). It turns out that the inclusion of the excited state does not qualitatively change the UV behavior of the NLO amplitudes.

5 Three-body losses of a polarized ^{6}Li Fermi gas

In the last two chapters, we developed an EFT framework to describe hadronic and nuclear three-body reactions. The goal of this last topical chapter is to apply the formalism to much larger atomic systems.

In particular, we investigate three-body losses of an ultracold ^{6}Li Fermi gas (μK regime) in the presence of a p-wave Feshbach resonance $^6\mathrm{Li}_2(\mathrm{e})$. The atoms are trapped in the lowest hyperfine ground state $|F = 1/2, m_F = +1/2\rangle$ and are thus fully spin-polarized. Losses are mainly due to recombination into deeply bound molecules $^6\mathrm{Li}_2(\mathrm{d})$.[1] This process is enhanced at the $^6\mathrm{Li}_2(\mathrm{e})$ threshold and can thus be described as a two-step reaction

$$3^6\mathrm{Li} \to {}^6\mathrm{Li}_2(\mathrm{e}) + {}^6\mathrm{Li} \to {}^6\mathrm{Li}_2(\mathrm{d}) + {}^6\mathrm{Li}\,; \tag{5.1}$$

see Fig. 5.1 and also the sketch of Fig. 1.4.

The Feshbach resonance energy κ_e^2/m can be tuned to arbitrarily small values using an external magnetic field B. For this reason, the EFT's expansion parameter

$$\chi_2 \equiv \frac{\kappa_\mathrm{e}}{r_\mathrm{e}} < 0.01 \tag{5.2}$$

is extremely small. It involves the naturally large p-wave effective range r_e. We study recombination at energies E around the Feshbach resonance. Thus, no further scale occurs in the three-body sector. While NLO corrections are very small, the uncertainties of r_e and the scattering volume a_e turn out to be of order 50 % and 11 %, respectively. For this reason, we only perform an LO investigation in this chapter.

Upon presenting the Lagrangian, we infer the LO Faddeev amplitude in the presence of the Feshbach resonance. We then focus on the $J^P = 1^+$ part of the amplitude, which we renormalize using a p-wave three-body force. Afterwards, we calculate the three-body recombination rate, whose thermal average yields the loss coefficient $L_3(T)$. Results for this quantity will be compared to data by Waseem *et al.* [70]. Parts of this chapter will be published under the title "*Three-body losses of a polarized Fermi gas in effective field theory*" in collaboration with L. Platter and H.-W. Hammer in the near future.

---

[1] The letters "d" and "e" stand for "deep" and "excited", respectively.

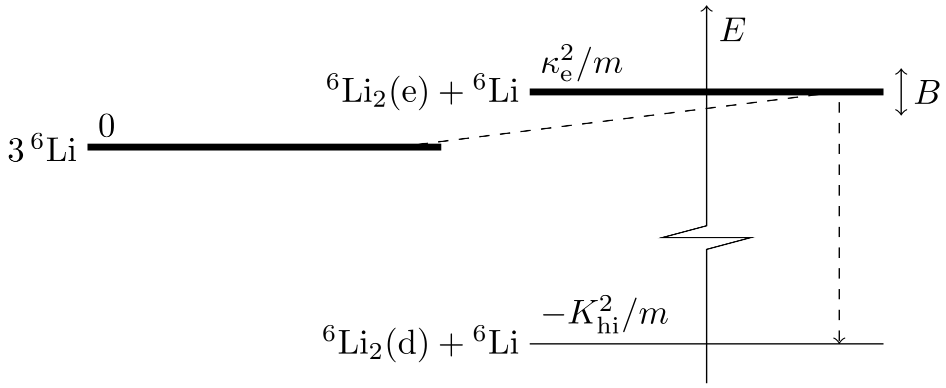

Figure 5.1.: Level scheme of three spin-polarized ^{6}Li atoms in the hyperfine state $|F = 1/2, m_F = +1/2\rangle$. Three-body recombination into a deeply bound state $^6\mathrm{Li}_2(\mathrm{d})$ proceeds through the Feshbach resonance state $^6\mathrm{Li}_2(\mathrm{e})$. Its position $E = \kappa_\mathrm{e}^2/m$ can be tuned by a magnetic field B.

5.1 Building blocks

We start our discussion by writing down the EFT Lagrangian. Afterwards, we calculate the diatom propagator and derive an appropriate LO form in the vicinity of the Feshbach resonance. The propagator is used to construct the LO Faddeev equation for the recombination process in different partial wave channels.

5.1.1 Lagrangian

Due to the fact that the ^{6}Li atoms are fully polarized, they can be treated as spinless, indistinguishable fermions. According to the Pauli principle, the atoms then predominantly interact via p-waves at low energies. Let ψ be the atom's nonrelativistic quantum field with mass $m = 6.0151223(5)\,\mathrm{u} \approx 5.97\, m_\mathrm{N}$ [154]; see also Appendix A. Moreover, let e_{m_l} ($m_l \in \{1, 0, -1\}$) be a diatom field describing the p-wave Feshbach resonance $^6\mathrm{Li}_2(\mathrm{e})$ (spherical representation). We then write

$$\begin{aligned}\mathscr{L} = {}& \psi^\dagger\left[i\partial_0 + \frac{\boldsymbol{\nabla}^2}{2m}\right]\psi \\ & + e^\dagger_{m_l}\left[\Delta_\mathrm{e}^{(0)} + \Delta_\mathrm{e}^{(1)}\, i\partial_\mathrm{cm} + \cdots\right]e_{m_l} - \frac{g_\mathrm{e}}{\sqrt{2}}\left[e^\dagger_{m_l}\left(\psi\ \left\{-i\overleftrightarrow{\boldsymbol{\nabla}}\right\}_{1m_l}\psi\right) + \mathrm{H.c.}\right] \\ & + \mathscr{L}_{\psi\psi\psi}\,. \end{aligned} \tag{5.3}$$

As usual, g_e is the coupling[2] of two atoms to the diatom field and $\Delta_\mathrm{e}^{(0)}$, $\Delta_\mathrm{e}^{(1)} \equiv \pm 1$ introduce the LO effective range expansion (ERE) coefficients a_e and r_e.[3] For equal mass particles, the derivative operators read $i\partial_\mathrm{cm} = i\partial_0 + \boldsymbol{\nabla}^2/(4m)$ and $\overleftrightarrow{\boldsymbol{\nabla}} = (\overleftarrow{\boldsymbol{\nabla}} - \overrightarrow{\boldsymbol{\nabla}})/2$. The tensor structure $\{\cdot\}_{1m_l}$ is defined in Eq. (4.43). Moreover, the three-body part $\mathscr{L}_{\psi\psi\psi}$ contains direct atom-diatom terms. It will be discussed below.

The fermionic nature of the field ψ is encoded in the equal-time anticommutators

$$\left\{\psi(x),\, \psi^\dagger(y)\right\} = \delta^{(3)}(\boldsymbol{x} - \boldsymbol{y})\,, \tag{5.4a}$$

$$\left\{\psi(x),\, \psi(y)\right\} = 0\,. \tag{5.4b}$$

In contrast, the diatom field e_{m_l} is bosonic. It obeys the equal-time commutation relations

$$\left[e_{m_l}(x),\, e^\dagger_{m_l'}(y)\right] = \delta^{m_l m_l'}\,\delta^{(3)}(\boldsymbol{x} - \boldsymbol{y})\,, \tag{5.5a}$$

$$\left[e_{m_l}(x),\, e_{m_l'}(y)\right] = 0. \tag{5.5b}$$

We further assume that atom and diatom fields commute.

5.1.2 Diatom propagator

Similarly to the previous chapters, we resum the atom-atom self-energy $-i\Sigma_\mathrm{e}\delta^{m_l m_l'}$ into the bare propagator. The corresponding Dyson equation is shown in Fig. 5.2. In the calculation of the self-energy, one has to take care of the anticommutation of the indistinguishable fermions. We perform this calculation in Appendix F.1.

---

[2] The coupling comes along with a factor $1/\sqrt{2}$ which compensates for the fermionic symmetry; see Appendix F.1.

[3] Due to the long-range nature of the van der Waals interaction, the ERE expansion is only a good approximation to the scattering amplitude when a_e is enhanced by a Feshbach resonance [84].

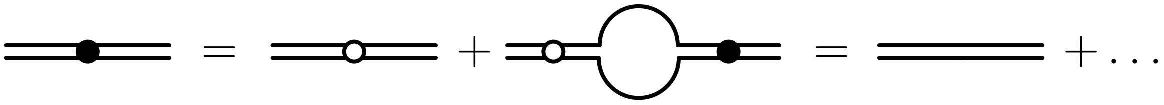

Figure 5.2.: Dyson equation for the full diatom propagator $iG_{\mathrm{e}}^{(\mathrm{f})}$ (double line with filled circle). The bare propagator and the LO propagator at resonance are marked with an empty circle and without a circle, respectively. Single lines in the self-energy loop $-i\Sigma_{\mathrm{e}}$ represent the ^{6}Li atoms.

After resummation, the full propagator

$$iG_{\mathrm{e}}^{(\mathrm{f})}(E_{\mathrm{cm}}) = -ig_{\mathrm{e}}^{-2}\frac{12\pi}{m}\left[-a_{\mathrm{e}}^{-1} + \frac{r_{\mathrm{e}}}{2}\bar{k}^2 - i\,\bar{k}^3 + \mathcal{O}(\bar{k}^4)\right]^{-1} \tag{5.6}$$

obeys the ERE form with on-shell relative momentum $\bar{k} \equiv i(-mE_{\mathrm{cm}} - i\epsilon)^{1/2}$. The scattering volume and p-wave effective range are given by

$$a_{\mathrm{e}}^{-1} = \frac{12\pi}{m}\frac{\Delta_{\mathrm{e}}^{(0)}}{g_{\mathrm{e}}^2}, \tag{5.7a}$$

$$\frac{r_{\mathrm{e}}}{2} = -\left(\frac{12\pi}{m^2}\frac{\Delta_{\mathrm{e}}^{(1)}}{g_{\mathrm{e}}^2} + \Lambda_{\mathrm{PDS}}\right). \tag{5.7b}$$

The value of a_{e} is tunable by an external magnetic field and can be either positive or negative; see below. In contrast, r_{e} is always negative [70].[4] Thus, $\Delta_{\mathrm{e}}^{(1)} = +1$ for not too large $\Lambda_{\mathrm{PDS}} < |r_{\mathrm{e}}/2|$, just as in Chapter 3. In atomic physics, it is common to express momenta and lengths in terms of the Bohr radius $a_{\mathrm{B}} \approx 0.529 \cdot 10^{-10}\,\mathrm{m}$; see Appendix A for definition. Below, we discuss the values of a_{e} and r_{e} in more detail.

As done in Chapter 4, we eliminate the unphysical coupling g_{e} by performing a field redefinition. This time, however, we also eliminate mass factors $m \sim$ MeV which are huge compared to all momentum scales. The field redefinition reads $e_{m_l}^{(\dagger)} \to \tilde{e}_{m_l}^{(\dagger)} \equiv (12\pi/m)^{1/2} g_{\mathrm{e}}^{-1}\, e_{m_l}^{(\dagger)}$.

Feshbach resonance

The scattering volume depends strongly on the external magnetic field B. In particular, it obeys the form

$$a_{\mathrm{e}} = a_{\mathrm{e,bg}}\left(1 + \frac{\Delta B}{B - B_0}\right), \tag{5.8}$$

which diverges at the Feshbach resonance $B_0 = 159.17(5)\,\mathrm{G}$ for ^{6}Li atoms in the lowest hyperfine ground state $|F = 1/2, m_F = +1/2\rangle$ [70]; see Fig. 5.3. The resonant part $a_{\mathrm{e}} - a_{\mathrm{e,bg}}$ of the equation is proportional to the product of the resonance width $\Delta B > 0$ and the background scattering volume $a_{\mathrm{e,bg}} < 0$. Nakasuji *et al.* obtained the value $a_{\mathrm{e,bg}}\Delta B = -2.8(3) \cdot 10^6 a_{\mathrm{B}}^3\,\mathrm{G}$ in a fit to the thermalization rate of the spin-polarized ^{6}Li Fermi gas [155]. Using further the prediction $a_{\mathrm{e,bg}} = (-36\,a_{\mathrm{B}})^3$ of Gautam and Angom from Ref. [156], the resonance width is of the order $\Delta B \sim 60\,\mathrm{G}$. Waseem *et al.* studied ^{6}Li three-body recombination at magnetic field detunings below $B - B_0 = 0.5\,\mathrm{G}$ (orange region in Fig. 5.3). For this reason, the ratio between the nonresonant and the resonant part of Eq. (5.8), i.e., $(B - B_0)/\Delta B$, is below 1 %. We conclude that the nonresonant part $a_{\mathrm{e,bg}}$ can safely be neglected. We then only take $a_{\mathrm{e,bg}}\Delta B = -2.8(3) \cdot 10^6\, a_{\mathrm{B}}^3\,\mathrm{G}$ as input for our calculations.

---

[4] In Ref. [70], Waseem *et al.* denoted the second ERE coefficient $-k_{\mathrm{e}} \equiv r_{\mathrm{e}}/2 < 0$.

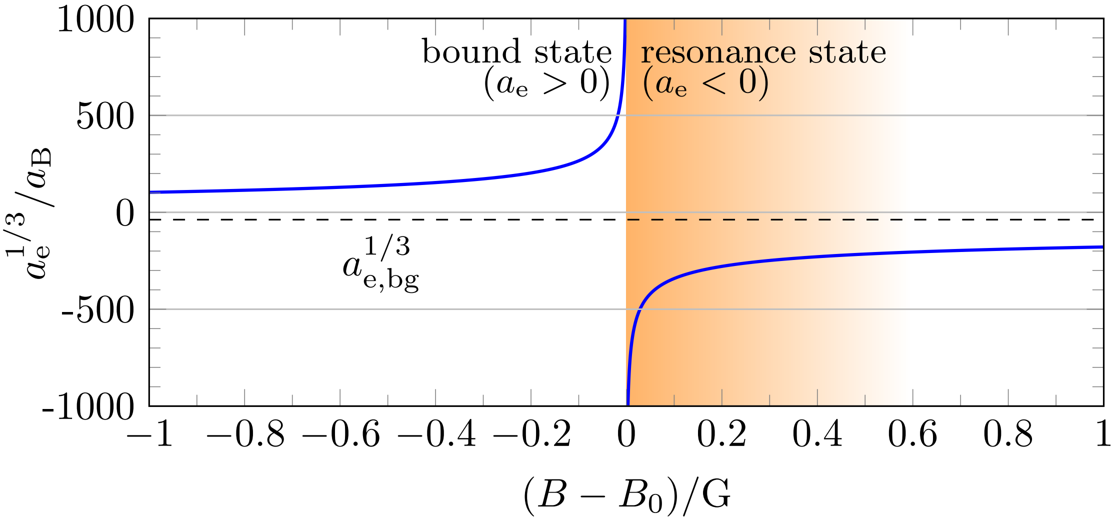

Figure 5.3.: Magnetic field dependence of the scattering volume a_e near the Feshbach resonance at $B = B_0 = 159.17(5)\,\mathrm{G}$. The small background scattering volume $a_{e,bg}$ (horizontal dashed grid line) is negligible at detunings $B - B_0 \in [0,\, 0.5]\,\mathrm{G}$ (orange region) used in the experiment by Waseem *et al.* [70]. In the figure, we use the values $a_{e,bg}\Delta B = -2.8 \cdot 10^6\, a_B^3\,\mathrm{G}$ and $a_{e,bg} = (36\, a_B)^3$; see text.

The p-wave effective range r_e is usually assumed to depend weakly on B in the immediate vicinity of B_0 [70, 155, 157]. Waseem *et al.* suggested the near-resonance estimation value

$$(r_e)_{res} \equiv \frac{2}{m\,\delta\mu\, a_{e,bg}\Delta B} = -0.182(20)\, a_B^{-1} \tag{5.9}$$

and used it in their analysis of the experimental data [70]. In Eq. (5.9), $\delta\mu = 113(7)\, k_B\, \mu\mathrm{K}\,\mathrm{G}^{-1}$ denotes the relative magnetic moment between the states $^6\mathrm{Li}_2(\mathrm{e})$ and $2^6\mathrm{Li}$ and $k_B \approx 8.62 \cdot 10^{-11}\,\mathrm{eV}\,\mu\mathrm{K}^{-1}$ is Boltzmann's constant; see Appendix A. We follow the assumption that r_e is constant in the vicinity of B_0. The estimation $(r_e)_{res}$, however, has to be taken with a grain of salt. Firstly, Eq. (5.9) was derived by Bruun *et al.* for two bosons near an s-wave Feshbach resonance [158]. It is not immediately clear if it can be applied to p-wave Feshbach resonances as well. Secondly, Nakasuji *et al.* obtained a different value $-0.116(10)\, a_B^{-1}$ (roughly 36 % deviation) in their thermalization rate fit [155]. They also cited an even smaller theory prediction $-0.096(6)\, a_B^{-1}$ by Julienne (Ref. [29] in their work). This value deviates by roughly 50 % from the value in Eq. (5.9). Thus, r_e introduces the largest uncertainty to our study and restricts it to LO. For the moment, we will use $(r_e)_{res}$ as input with an uncertainty of ±50 %. At the end of the chapter, we will try to extract r_e from data of the three-body loss coefficient.

In the experiment by Waseem *et al.*, the recombination process was studied at detunings $B - B_0 > 0$, i.e., at scattering volumes $a_e < 0$ [70]. On this side of the Feshbach resonance, $^6\mathrm{Li}_2(\mathrm{e})$ is a resonance state occurring at some center-of-mass energy κ_e^2/m; see Fig. 5.1. The quantity $\kappa_e = \kappa_e(a_e,\, r_e)$ is called resonance momentum in the following. In contrast, for $B - B_0 < 0$, i.e., $a_e > 0$, the state $^6\mathrm{Li}_2(\mathrm{e})$ is bound with a binding momentum $\gamma_e = \gamma_e(a_e,\, r_e)$. Experimentally, three-body recombination was only measured on the resonance side, where the process can be distinguished from background losses [70]. Thus, we restrict ourselves to $a_e < 0$ when calculating the loss rate. In this case, recombination can only take place into the deep diatom state $^6\mathrm{Li}_2(\mathrm{d})$ and not into $^6\mathrm{Li}_2(\mathrm{e})$, which is unstable.

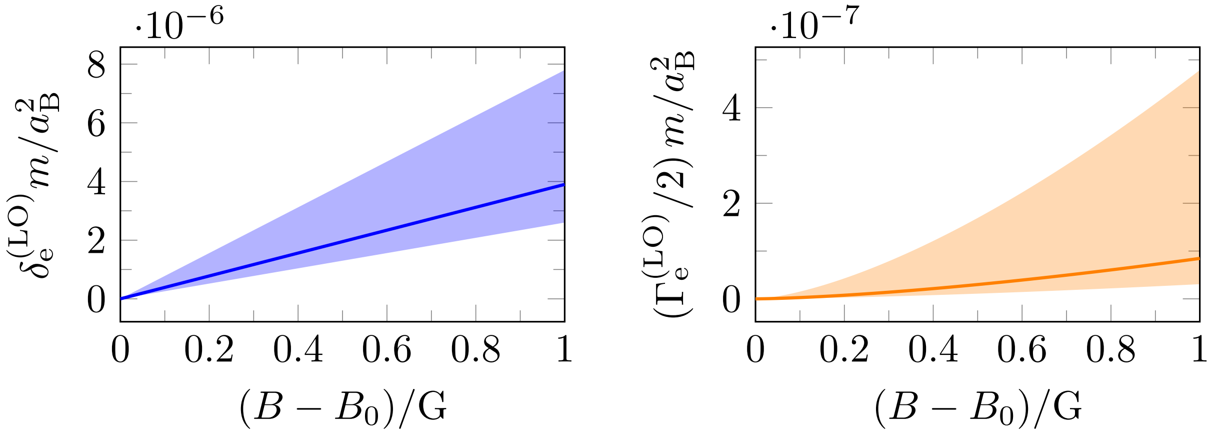

(a) (b)

Figure 5.4.: (a) Real part and (b) negative imaginary part of the LO resonance position $\delta_e^{(LO)} - i\Gamma_e^{(LO)}/2$ as functions of the magnetic field B. The thick lines result from the estimation value $(r_e)_{res} = 0.182\, a_B^{-1}$ and the bands from ±50 % variations of it.

Power counting and LO form

Since r_e is not influenced by the magnetic fine-tuning, it represents the natural high momentum scale K_{hi} of the system. In contrast, the momentum $|a_e|^{-1/3}$ is arbitrarily small and thus contains certain powers of the small momentum scale K_{lo}. The resonance momentum κ_e (binding momentum γ_e) depends on a_e and thus on B. It shall define the small scale K_{lo} in the case $a_e < 0$. For naturally scaling higher-order ERE coefficients, one then obtains

$$\kappa_e = \sqrt{\frac{2}{r_e a_e}}\left(1 + \mathcal{O}\left(K_{lo}^2/K_{hi}^2\right)\right) = \kappa_e^{(LO)} + \cdots \equiv K_{lo} \tag{5.10}$$

and $a_e^{-1} \sim r_e/2\,\kappa_e^2 \sim K_{hi}K_{lo}^2$. For the bound state case ($a_e > 0$), one similarly obtains a binding momentum $\gamma_e = (-2r_e^{-1}a_e^{-1})^{1/2} + \cdots$. Recall that in Chapter 3, the fine-tuning of the D^{0*} resonance occurred in the p-wave effective range and not in the scattering volume. As a consequence, the unitary cut term, corresponding to the resonance width for $a_e < 0$, is now only suppressed by one order compared to the two leading ERE terms, instead of three. The resonance can still be considered narrow since $\chi_2 \equiv \kappa_e/r_e =< 0.01$ (with $r_e \equiv (r_e)_{res}$) is much smaller than in the D^{0*} sector (~ 0.3).

Following the arguments presented in Chapter 3, the unitary cut becomes a leading quantity if $a_e < 0$ and $k \approx \kappa_e$ (“kinematic fine-tuning”); see also Ref. [85]. Indeed, we are going to calculate the recombination rate for energies around the resonance position. However, instead of resumming the full unitary cut, we only include the contribution $-i\kappa_e^3$ as was done in Chapter 3. The rest part $-i(\bar{k}^3 - \kappa_e^3)$ is then suppressed for all $\bar{k} \sim K_{lo}$. For the bound state case ($a_e > 0$), no kinematic fine-tuning occurs and the unitary cut can always be neglected at LO. We thus define

$$iG_e^{(LO)}(E_{cm}) = -i\left[-a_e^{-1} + \frac{r_e}{2}\bar{k}^2 - i\,\kappa_e^{(LO)\,3}\theta(-a_e)\right]^{-1} \tag{5.11}$$

to be the LO propagator.

For the resonance case ($a_e < 0$), the LO ${}^6\mathrm{Li}_2(\mathrm{e})$ propagator exhibits a Breit-Wigner form, just like the one of D^{0*}. The corresponding pole position lies at $E_{cm} = \delta_e^{(LO)} - i\Gamma_e^{(LO)}/2$ with $\delta_e^{(LO)} = \kappa_e^{(LO)\,2}/m \sim K_{lo}^2/m$ and $\Gamma_e^{(LO)}/2 = 2\kappa_e^{(LO)\,3} r_e^{-1}/m \sim K_{lo}^3 K_{hi}^{-1}/m$. The resonance energy δ_e is proportional to the magnetic field; see Fig. 5.4(a) (thick line). The width $\Gamma_e^{(LO)}$ in Fig. 5.4(b) is proportional to $(B - B_0)^{3/2}$ and much smaller

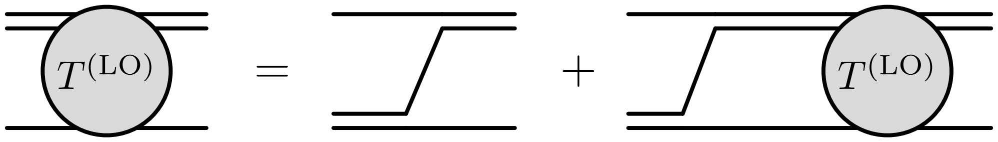

Figure 5.5.: LO atom-dimer amplitude. Possible three-body forces are omitted.

than $\delta_{\mathrm{e}}^{(\mathrm{LO})}$ as proposed by the power counting (thick line). The fact that r_{e} is not known experimentally has to be taken care of when calculating observables. We do so by varying the estimation $(r_{\mathrm{e}})_{\mathrm{res}} = 0.182\, a_{\mathrm{B}}^{-1}$ by Waseem *et al.* by ±50 %, yielding the large bands in Fig. 5.4. Due to the strong dependence $\Gamma_{\mathrm{e}} \propto r_{\mathrm{e}}^{-5/2}$, the uncertainty band width in Fig. 5.4(b) is ≈ 5 times larger than the estimated value (thick line). In the bound state case ($a_{\mathrm{e}} > 0$), the binding energy will be denoted $B_{\mathrm{e}}^{(\mathrm{LO})} \equiv \gamma_{\mathrm{e}}^{(\mathrm{LO})\,2}/m \sim K_{\mathrm{lo}}^2/m$. It is linear in $B - B_0$ just like $\delta_{\mathrm{e}}^{(\mathrm{LO})}$.

5.1.3 LO Faddeev amplitude

Next, we construct the LO atom-diatom amplitude $T^{(\mathrm{LO})}$. Note that one the resonance side $a_{\mathrm{e}} < 0$, the diatom is unstable and cannot occur as an asymptotic state. In the construction of the three-body recombination matrix element, the amplitude will only enter intermediately, similar to the calculation of the $D^0\bar{D}^0\pi^0$ production rate in Chapter 3.

Exchange potential

We construct $T^{(\mathrm{LO})}$ by iterating the interaction vertex defined by Eq. (5.3) to all orders; see Fig. 5.5. Let $\boldsymbol{p}$ ($\boldsymbol{p}'$) be the incoming (outgoing) spectator momentum. The center-of-mass E can be expressed in terms of the momentum

$$p_E \equiv i\sqrt{-m\,E - i\epsilon}\,. \tag{5.12}$$

For an incoming (outgoing) diatom polarization m_l (m_l'), the tree-level exchange diagram reads

$$-\,iV_{\mathrm{e}}^{1m_l,1m_l'}(\boldsymbol{p},\boldsymbol{q};\,E) = -i24\pi\,\frac{\{\boldsymbol{q}+\boldsymbol{p}/2\}^*_{1m_l}\,\{\boldsymbol{p}+\boldsymbol{q}/2\}_{1m_l'}}{p^2+q^2-p_E^2+\boldsymbol{p}\cdot\boldsymbol{q}}\,. \tag{5.13}$$

Note that this function has a different overall sign than the pion exchange potential in Chapter 3. The reason is the fermionic nature of the ^{6}Li atoms. For a derivation of the exchange potential V_{e} we refer to Appendix F.2.

Partial wave projections of the exchange potential V_{e} can be done analytically. Recall that the ^{6}Li atoms are treated as spinless particles. The total angular momentum $\boldsymbol{J}$ is thus the sum of the orbital angular momentum $\boldsymbol{l}$ in the two-body system ($l = 1$) and the atom-dimer orbital angular momentum $\boldsymbol{L}$. The parity is given by $(-1)^{l+L} = (-1)^{1+L}$. In order to use the projection prescription of Eq. (C.12), we identify the total spin $\boldsymbol{S} \equiv \boldsymbol{l}$ with the diatom spin. The partial wave projections then read

$$\begin{aligned}
V_{\mathrm{e}}^{{}^3L_J,{}^3L'_J}(p,q;\,E) &= 12\pi\,\frac{\sqrt{(2L+1)(2L'+1)}}{2J+1}\\
&\times\Bigg[\mathrm{C}^{J0}_{L0,10}\,\mathrm{C}^{J0}_{L'0,10}\,\frac{1}{2}\left(p^2\,\hat{t}_{L'}+q^2\,\hat{t}_L\right)\\
&\qquad+pq\left(\frac{1}{4}\,\mathrm{C}^{J0}_{L0,10}\,\mathrm{C}^{J0}_{L'0,10}\,\hat{t}_J+(2J+1)\sum_k \mathrm{C}^{k0}_{L0,10}\,\mathrm{C}^{k0}_{L'0,10}\begin{Bmatrix}1 & J & L'\\ 1 & k & L\end{Bmatrix}\hat{t}_k\right)\Bigg]\,I^{(\cdot)}_{\psi;\psi,\psi}(p,q;\,E)
\end{aligned} \tag{5.14}$$

with $\hat{t}_L I^{(\cdot)}_{\psi;\psi,\psi} \equiv I^{(L)}_{\psi;\psi,\psi}$ and

$$I^{(L)}_{\psi;\psi,\psi}(p,q;E) = (-1)^L \frac{2}{pq}\, Q_L\left(\frac{p^2+q^2-p_E^2}{pq}\right) \quad (L \geq 0)\,. \tag{5.15}$$

Unrenormalized $J^P = 1^+$ amplitude

In Ref. [77], Esry *et al.* analyzed the low-energy behavior of the three-body recombination rate in different J^P channels. It was shown that for indistinguishable fermions and small enough E, $J^P = 1^+$ ($\sim E^2$) is the dominant channel. In contrast, $J^P = 0^+$ ($\sim E^6$), $J^P = 1^-$ ($\sim E^3$) and the $J \geq 2$ channels are subleading. For this reason, we concentrate on the $J^P = 1^+$ channel in the following, where both $l = L = 1$. It was, however, pointed out that other spin-parity channels might become important in the immediate vicinity of a Feshbach resonance; see also Ref. [76]. This possibility has to be kept in mind when analyzing results for the three-body loss rate.

For simplicity, we denote the ${}^3P_1$ projections of amplitude and exchange potential by $T^{1^+} \equiv T^{(\mathrm{LO})\,{}^3P_1,{}^3P_1}$ and $V_{\mathrm{e}}^{1^+} \equiv V_{\mathrm{e}}^{{}^3P_1,{}^3P_1}$. The LO Faddeev amplitude in the $J^P = 1^+$ channel then reads

$$T^{1^+}\left(p,p';E\right) = -V_{\mathrm{e}}^{1^+}\left(p,p';E\right) + \frac{1}{2\pi^2}\int_0^{\Lambda} \mathrm{d}q\, q^2\, V_{\mathrm{e}}^{1^+}(p,q;E)\, \mathscr{G}_{\mathrm{e}}^{(\mathrm{LO})}(q;E)\, T^{1^+}\left(q,p';E\right) \tag{5.16}$$

with exchange potential projection and LO propagator function

$$V_{\mathrm{e}}^{{}^3P_1,{}^3P_1}(p,q;E) = -4\pi\, pq\left[\hat{t}_0 - \hat{t}_2\right] I^{(\cdot)}_{\psi;\psi,\psi}(p,q;E)\,, \tag{5.17a}$$

$$\mathscr{G}_{\mathrm{e}}^{(\mathrm{LO})}(q;E) = G_{\mathrm{e}}^{(\mathrm{LO})}\left(E - \frac{3}{4m}q^2\right). \tag{5.17b}$$

Moreover, we equip the Faddeev equation with a cutoff Λ of natural order r_{e} or larger.

The amplitude T^{1^+} exhibits a spectrum of three-body poles. Due to the fact that atom and diatom are in a p-wave ($L = 1$), the pole energies E_3 can lie above or below the two-body state threshold $E = \delta_{\mathrm{e}}^{(\mathrm{LO})}$ ($a_{\mathrm{e}} < 0$) or $E = -B_{\mathrm{e}}^{(\mathrm{LO})}$ ($a_{\mathrm{e}} > 0$), respectively. They become complex when lying above the two- or three-body threshold. As the cutoff Λ increases, more three-body states cross the low-energy region from above. In Fig. 5.6, we plot the running of the unrenormalized energies E_3 (blue points) for the bound state case $a_{\mathrm{e}}^{-1/3} = 1/3\,|(r_{\mathrm{e}})_{\mathrm{res}}/2| \approx 0.03\, a_{\mathrm{B}}^{-1} > 0$, i.e., for $\gamma_{\mathrm{e}}^{(\mathrm{LO})} \approx 0.018\, a_{\mathrm{B}}^{-1}$. For simplicity, we only show real-valued three-body state energies below the two-body threshold. The vertical dashed grid lines marks the occurrence of a new three-body state.

Renormalized $J^P = 1^+$ amplitude

For renormalization, we introduce a three-body force in the 1^+ channel. It is part of the general three-body Lagrangian

$$\begin{aligned}\mathscr{L}_{\psi\psi\psi} = &-\sum_J \sum_{L,L'} C_0^{{}^3L_J,{}^3L'_J}(\Lambda) \sum_{m_J} (\psi\,\tilde{e})^{(0)\,\dagger}_{(L',1)Jm_J}\, (\psi\,\tilde{e})^{(0)}_{(L,1)Jm_J} \\ &-\sum_J \sum_{L,L'} \frac{1}{2} C_2^{{}^3L_J,{}^3L'_J}(\Lambda) \sum_{m_J} \Big((\psi\,\tilde{e})^{(0)\,\dagger}_{(L',1)Jm_J}\, (\psi\,\tilde{e})^{(2)}_{(L,1)Jm_J} + \mathrm{H.c.}\Big) \\ &-\cdots\,,\end{aligned} \tag{5.18}$$

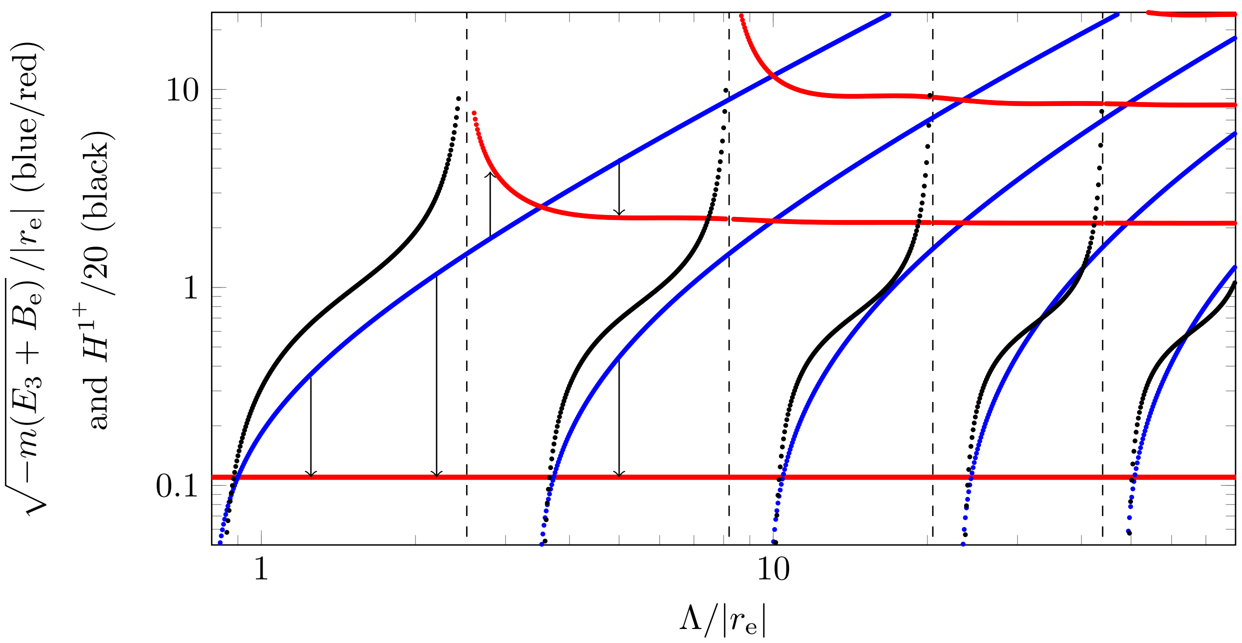

Figure 5.6.: The unrenormalized $J^P = 1^+$ spectrum (blue) exhibits Λ dependent three-body states. We show only such poles $E_3 \in \mathbb{R}$ below the two-body threshold $E = -B_\mathrm{e}^{(\mathrm{LO})}$. Cut-off and energies are scaled by the p-wave effective range estimation $r_\mathrm{e} = (r_\mathrm{e})_\mathrm{res}$. Using the rescaled three-body force $H^{1^+}(\Lambda)$ (black), the spectrum is renormalized onto $E_3^{(1)} \equiv -4\cdot 10^{-4}\, a_\mathrm{B}^{-2}/m \approx -(0.11\, r_\mathrm{e})^2/m$ (lowest red line). After renormalization, the three-body states approach constants as $\Lambda \to \infty$ (red).

which contains three-body forces for all J^P channels. The coupled fields are defined

$$(\psi\,\tilde{e})^{(n)}_{(L,1)Jm_J} \equiv \sqrt{2L+1}\,\mathrm{C}^{Jm_J}_{Lm_L,1m_l}\,\psi\left\{-i\overleftrightarrow{\nabla}\right\}_{Lm_L}\left(-i\overleftrightarrow{\nabla}\right)^{n}\tilde{e}_{m_l}\,. \tag{5.19}$$

In the convention of Eq. (C.1), the sum of three-body forces for fixed L, L', J and incoming (outgoing) relative momentum p (q) reads

$$\left(C_0^{{}^3L_J,{}^3L'_J} + \frac{1}{2}C_2^{{}^3L_J,{}^3L'_J}(p^2+q^2) + \cdots\right)p^L q^{L'}\,. \tag{5.20}$$

The leading three-body force in the $J^P = 1^+$ channel is given by $C_0^{{}^3P_1,{}^3P_1}(\Lambda)pq \equiv H^{1+}(\Lambda)pq/\Lambda^2$. We substitute $V_\mathrm{e}^{1^+}(p,q;E) \to V_\mathrm{e}^{1^+}(p,q;E) + H^{1+}(\Lambda)pq/\Lambda^2$ in Eq. (5.16) and again choose $a_\mathrm{e}^{-1/3} = 1/3\,|r_\mathrm{e}/2| > 0$ (bound two-body state) with $r_\mathrm{e} \equiv (r_\mathrm{e})_\mathrm{res}$. We demonstrate the renormalizability of the 1^+ channel by demanding a fixed three-body pole at $E = E_3^{(1)} \equiv -4\cdot 10^{-4}\, a_\mathrm{B}^{-2}/m \approx -(0.11\, r_\mathrm{e})^2/m$ for various cutoffs $\Lambda \gtrsim |r_\mathrm{e}|$. For convenience, the pole position is chosen to lie below the two-body threshold $E = -B_\mathrm{e}^{(\mathrm{LO})}$, such that it is purely real.

The rescaled three-body force $H^{1^+}(\Lambda)$ is shown in Fig. 5.6 as black points. It exhibits consecutive singularities each time a new three-body state occurs in the unrenormalized spectrum. The three-body force pushes the three-body states onto the red curves, which converge as $\Lambda \to \infty$; see the thin arrows. Thus, a single three-body force is sufficient to renormalize the $J^P = 1^+$ channel. Note that the first three-body state was chosen to be small ($-E_3^{(1)} \sim B_\mathrm{e}^{(\mathrm{LO})} \sim K_\mathrm{lo}^2/m$). All consecutive three-body poles lie outside the EFT's region of applicability ($E_3^{(n)} \gtrsim |r_\mathrm{e}|^2/m$ for $n \geq 2$) and can be considered unphysical.

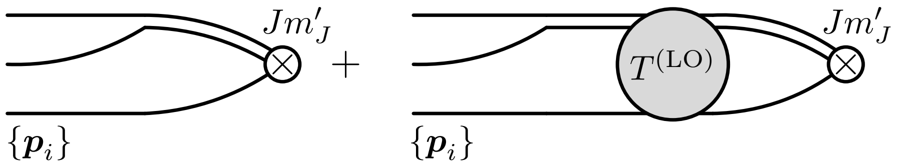

Figure 5.7.: LO diagrams entering the matrix element $i\mathscr{M}^{Jm'_J}_{3\psi\to\mathrm{d}\psi}$ for three-body recombination into a deep state $^6\mathrm{Li}_2(\mathrm{d}) + {}^6\mathrm{Li}$ (crossed short-range vertex).

5.2 Three-body losses

Given the atom-diatom amplitude T^{1^+}, we now calculate the rate of three-body recombination into the deep state $^6\mathrm{Li}_2(\mathrm{d}) + {}^6\mathrm{Li}$ in the $J^P = 1^+$ channel. Afterwards, we apply thermal averaging to obtain the loss coefficient. It will be fitted to data from Ref. [70].

5.2.1 Recombination rate

On the $a_\mathrm{e} < 0$ side of the Feshbach resonance, three-body recombination into $^6\mathrm{Li}_2(\mathrm{e})+{}^6\mathrm{Li}$ is energetically forbidden. Loss effects are thus dominated by recombination into a deep state $^6\mathrm{Li}_2(\mathrm{d}) + {}^6\mathrm{Li}$ outside the EFT's region of applicability. Such a process involves a large excess of kinetic energy, i.e., it is associated with momenta much larger than K_lo. In other words, it happens only at small distances and can be represented by the sum

$$i\sum_L \left(F_0^{^3L_J} + \cdots\right) p^L \sqrt{4\pi}\left(\boldsymbol{Y}_{(L,1)Jm'_J}(\hat{\boldsymbol{p}})\right)^{m_l} = i\sum_L \left(F_0^{^3L_J} + \cdots\right)\sqrt{2L+1}\,\mathrm{C}^{Jm'_J}_{Lm_L,1m_l}\,\{\boldsymbol{p}\}_{Lm_L} \tag{5.21}$$

of sink-like vertices; cf. Eq. (5.19). It is represented by the crossed circle, which enters the recombination matrix element $i\mathscr{M}^{Jm'_J}_{3\psi\to\mathrm{d}\psi}$ in Fig. 5.7. Single components of this sum annihilate field combinations $\psi\,\{-i\overleftrightarrow{\boldsymbol{\nabla}}\}_{Lm_L}\,\tilde{e}_{m_l}$ and create a deep $^6\mathrm{Li}_2(\mathrm{d}) + {}^6\mathrm{Li}$ state with total quantum numbers Jm'_J.

We set all components in Eq. (5.21) to zero, except for $F^{1^+} \equiv F_0^{^3P_1} > 0$. For incoming momenta $\boldsymbol{p}_1$, $\boldsymbol{p}_2$, $\boldsymbol{p}_3$, we then obtain

$$\begin{aligned} i\mathscr{M}^{1m'_J}_{3\psi\to\mathrm{d}\psi}(\{\boldsymbol{p}_i\};\,E) = iF^{1^+}3\sqrt{\frac{2\pi}{m}}\sum_{\pi\in\mathscr{C}_3}\{\boldsymbol{p}_{\pi(1)}-\boldsymbol{p}_{\pi(2)}\}_{1m_l}\,\mathscr{G}^{(\mathrm{LO})}_\mathrm{e}\left(p_{\pi(3)};\,E\right) \\ \times\left(\mathrm{C}^{1m'_J}_{1m_L,1m_l}\,\{\boldsymbol{p}_{\pi(3)}\}_{1m_L} - \int\frac{\mathrm{d}^3q}{(2\pi)^3}\,T^{(\mathrm{LO})\,1m_l,1m'_l}\left(\boldsymbol{p}_{\pi(3)},\boldsymbol{q};\,E\right)\mathscr{G}^{(\mathrm{LO})}_\mathrm{e}(q;\,E)\,\mathrm{C}^{1m'_J}_{1m_L,1m'_l}\,\{\boldsymbol{q}\}_{1m_L}\right). \end{aligned} \tag{5.22}$$

Sums over m_l, m'_l, and m_L are implicit. Moreover, $\mathscr{C}_3$ be the set of even permutations of $(1\,2\,3)$.

To calculate the recombination rate $K_3(E)$, one has to integrate the absolute square of the matrix element over all allowed incoming momenta $\boldsymbol{p}_1$, $\boldsymbol{p}_2$, $\boldsymbol{p}_3$, sum over m'_J and divide by the three-body phase space

$$\phi_{3\psi}(E) = \left(\prod_{i=1}^{3}\int\frac{\mathrm{d}^3p_i}{(2\pi)^3}\right)(2\pi)^4\,\delta^{(3)}\left(\sum_{i=1}^{3}\boldsymbol{p}_i\right)\delta\left(E - \sum_{i=1}^{3}\frac{p_i^2}{2m}\right) = \frac{mp_E^4}{24\sqrt{3}\,\pi^2}\,. \tag{5.23}$$

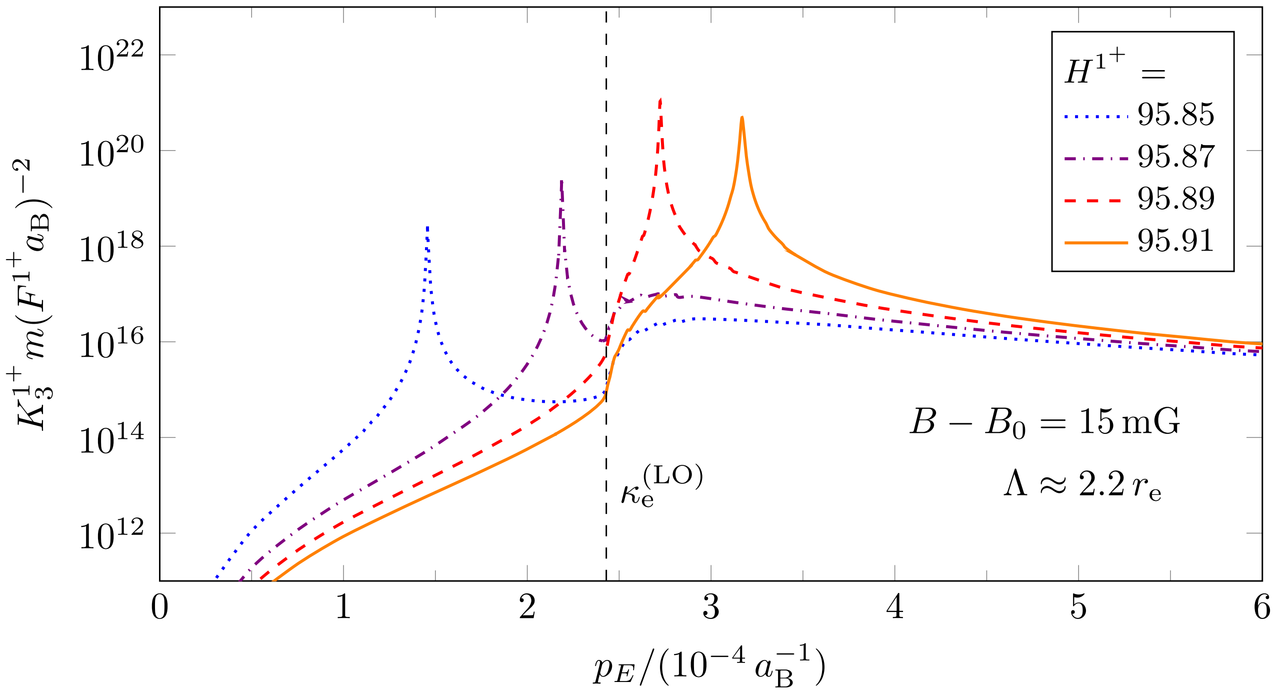

Figure 5.8.: Three-body recombination rate $K_3^{1^+}$ as a function of the energy variable $p_E = (mE)^{1/2}$ for different three-body forces H^{1^+}, $r_\mathrm{e} = (r_\mathrm{e})_\mathrm{res}$, $\Lambda = 0.4\, a_\mathrm{B}^{-1} \approx 2.2\, r_\mathrm{e}$, and $B - B_0 = 15\,\mathrm{mG}$. The unknown factor $(F^{1^+})^2/m$ has been factored out. Around $H^{1^+} \approx 95.88$, a three-body pole penetrates the two-body threshold $p_E = \kappa_\mathrm{e}^{(\mathrm{LO})} \approx 2.43 \cdot 10^{-4} a_\mathrm{B}^{-1}$.

The final expression reads

$$K_3^{1^+}(E) = \frac{1}{\phi_{3\psi}(E)} \left(\prod_{i=1}^{3} \int \frac{\mathrm{d}^3 p_i}{(2\pi)^3} \right) (2\pi)^4 \, \delta^{(3)}\left(\sum_{i=1}^{3} \boldsymbol{p}_i \right) \delta \left(E - \sum_{i=1}^{3} \frac{p_i^2}{2m} \right) \sum_{m_J'} \left| i\mathcal{M}_{3\psi \to \mathrm{d}\psi}^{1 m_J'} (\{\boldsymbol{p}_i\}; E) \right|^2 \tag{5.24a}$$

$$= \frac{(F^{1^+})^2}{m} \frac{432\sqrt{3}}{p_E^4} \int_0^{\sqrt{4/3\, mE}} \mathrm{d}p_A \, p_A \int_0^{\sqrt{4/3\, mE}} \mathrm{d}p_B \, p_B \; \theta(1 - x_0) \theta(1 + x_0)$$
$$\times \left(|p_A \mathcal{J}_\mathrm{e}(p_B; E)|^2 + 2\,\mathrm{Re} \left(p_B \mathcal{J}_\mathrm{e}(p_A; E) \left[p_A \mathcal{J}_\mathrm{e}(p_B; E) \right]^* \right) \right) \tag{5.24b}$$

with

$$x_0 \equiv \frac{1}{p_A p_B} \left(p_E^2 - p_A^2 - p_B^2 \right), \tag{5.25a}$$

$$\mathcal{J}_\mathrm{e}(p; E) \equiv \mathcal{G}_\mathrm{e}^{(\mathrm{LO})}(p; E) \left(p - \frac{1}{2\pi^2} \int_0^\Lambda \mathrm{d}q \, q^2 \; T^{1^+}(p, q; E) \, \mathcal{G}_\mathrm{e}^{(\mathrm{LO})}(q; E) \, q \right). \tag{5.25b}$$

The loop integral in J_e integral diverges as $\Lambda \to \infty$. This cutoff dependence will be absorbed by the short-range factor $F^{1^+} = F^{1^+}(\Lambda)$.

There are two unknown parameters entering the recombination rate, $H^{1^+}(\Lambda)$ and $F^{1^+}(\Lambda)$. The latter only acts as a global factor and does not influence the shape of the rate. Thus, in Fig. 5.8 we show the rescaled rate $K^{1^+} m/(F^{1^+})^2$ as a function of $p_E = (mE)^{1/2}$ for input values $r_\mathrm{e} = (r_\mathrm{e})_\mathrm{res} = 0.182\, a_\mathrm{B}^{-1}$, $B - B_0 = 15\,\mathrm{mG}$, and the natural cutoff $\Lambda = 0.4\, a_\mathrm{B}^{-1} \approx 2.2\, r_\mathrm{e}$. The four curves correspond to three-body forces $H^{1^+} \in \{95.85, 95.87, 95.89, 95.91\}$. They are all significantly enhanced at $p_E = \kappa_\mathrm{e}^{(\mathrm{LO})} \approx$

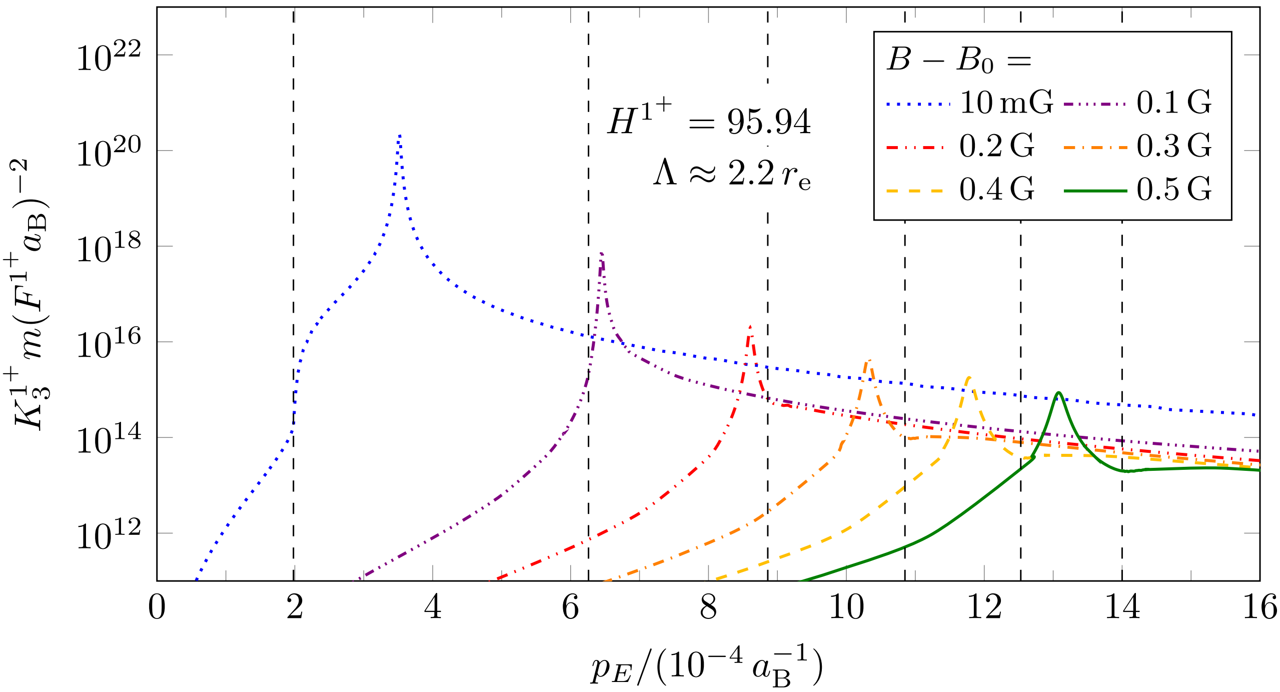

Figure 5.9.: Three-body recombination rate $K_3^{1^+}$ as a function of the energy variable $p_E = (mE)^{1/2}$ for different magnetic field detunings $B - B_0$, $r_e = (r_e)_{\text{res}}$, and $H^{1^+} = 95.94$ at $\Lambda = 2.2\, r_e$. The grid lines mark the different thresholds $p_E = \kappa_e^{(\text{LO})}$.

$2.43 \cdot 10^{-4} a_B^{-1}$ due to the presence of the Feshbach resonance ${}^6\text{Li}_2(\text{e})$. Moreover, the rates vanish like $p_E^4 \propto E^2$ for small E, confirming the threshold law results of Esry *et al.* [77].

By varying the three-body force, the real part $\operatorname{Re} E_3^{(1)}$ of the first pole (approximately given by the peak positions) can be set to arbitrary values. Around $H^{1^+} \approx 95.88$, the pole crosses the two-body threshold; see Fig. 5.8. At this point, the enhancements due the threshold and the three-body pole add up and the rate becomes largest.

The pole position also depends on B. In particular, the peak position changes almost as fast as $\kappa_e^{(\text{LO})}$ when B is increased; see Fig. 5.9. Here, we choose a constant three-body force $H^{1^+} = 95.94$ and the same cutoff as above. We assume that H^{1^+} as a three-body quantity does not to depend on B to first approximation. As $B - B_0$ increases, i.e., when moving away from the unitary regime, the recombination rate drops drastically. The same behavior will be seen at finite temperature.

5.2.2 Thermal averaging

Data for three-body recombination is only available at finite temperature $T \in [1, 8]\,\mu\text{K}$ [70]. For this reason, we have to calculate the thermal average

$$\langle K_3 \rangle (T) = \int_0^\infty \mathrm{d}E\; K_3(E)\, f_B^{(T)}(E) \tag{5.26}$$

in order to benchmark our LO theory. For a fixed T, the energy E is distributed according to the Boltzmann distribution $f_B^{(T)}(E) \propto g(E) \exp[-E/(k_B T)]$, where $g(E)$ denotes the degeneracy of the energy level E. For three-body recombination, $g(E)$ is proportional to the three-particle phase space $\phi_{3\psi}(E) \propto E^2$ given in Eq. (5.23). Normalization then yields

$$f_B^{(T)}(E) = \frac{1}{2(k_B T)^3} E^2 e^{-E/(k_B T)}\,. \tag{5.27}$$

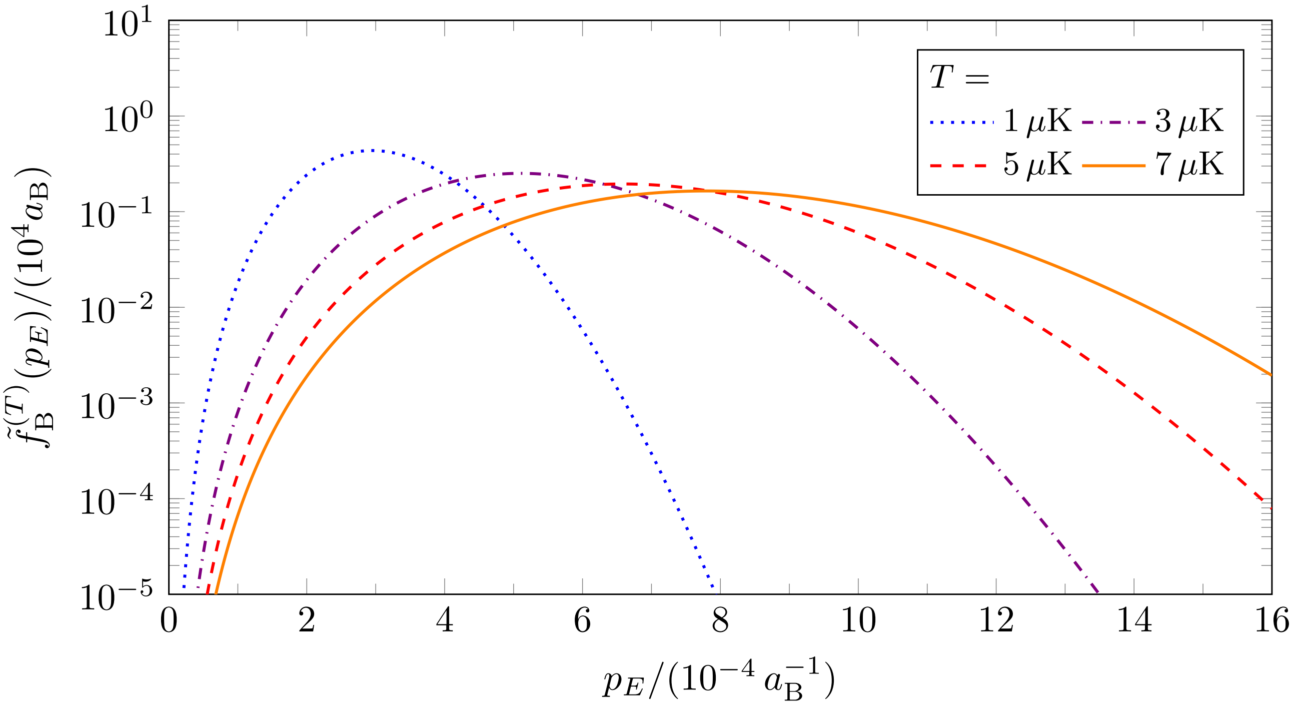

Figure 5.10.: Three-body Boltzmann distribution $\tilde{f}_{\mathrm{B}}^{(T)}(p_E)$ as function of p_E for four temperatures T.

Suno *et al.* and D'Incao *et al.* used this distribution to obtain the three-fermion and three-boson loss rates, respectively, in the adiabatic hyperspherical representation [76, 159].

In order to get a flavor which regions in Figs. 5.8-5.9 are supported by the Boltzmann distribution at experimental temperatures, we consider the equivalent distribution

$$\tilde{f}_{\mathrm{B}}^{(T)}(p_E) \equiv \frac{2p_E}{m} f_{\mathrm{B}}^{(T)}\big(p_E^2/m\big) = \frac{1}{(m\,k_{\mathrm{B}}T)^3}\, p_E^5\, e^{-p_E^2/(m\,k_{\mathrm{B}}T)} \tag{5.28}$$

for the energy variable p_E. Per construction, it fulfills $\tilde{f}_{\mathrm{B}}^{(T)}(p_E)\,\mathrm{d}p_E = f_{\mathrm{B}}^{(T)}(E)\,\mathrm{d}E$. We plot this function in Fig. 5.10 for four different $T \in [1,\,8]\,\mu$K. Its maximum $\tilde{f}_{\mathrm{B,max}}$ lies at $k_T \equiv (5/2\,m\,k_{\mathrm{B}}T)^{1/2}$ and already at $p_E \approx 2.34\,k_T$, its value is as small as $\tilde{f}_{\mathrm{B,max}}/1000$.

Thus, in calculating the thermal average, we proceed as follows. Firstly, we determine the location of the two-body resonance momentum $\kappa_{\mathrm{e}}^{(\mathrm{LO})}$. Secondly, we calculate the position of the three-body pole using standard techniques explained in previous chapters.[5] When sampling the recombination rate we put emphasize on these two regions. The full sampling region goes from $p_E = 0$ up to $p_E = 20\,\kappa_{\mathrm{e}}^{(\mathrm{LO})} \leq 280 \cdot 10^{-4} a_{\mathrm{B}}^{-1}$, where the area under the integrand in Eq. (5.26) can be considered converged. Lastly, we map the energy integral region $[0,\,\infty]$ onto $[0,\,1]$ using the transformation $z \equiv 1/(1+E)$ and numerically integrate an interpolation of the new integrand $z^{-2}[K_3\, f_{\mathrm{B}}^{(T)}](z^{-1}-1)$.

5.2.3 Loss coefficient

The thermal average $\langle K_3\rangle(T)$ in Eq. (5.26) describes the rate at which recombination events take place. It is proportional to the so-called loss coefficient $L_3(T)$ measured by Waseem *et al.* [70]. This quantity occurs in the rate equation

$$\frac{\mathrm{d}}{\mathrm{d}t} N = -L_3(T) \int \mathrm{d}\boldsymbol{x}\ [n(\boldsymbol{x},\,t)]^3 \tag{5.29}$$

---

[5] The three-body pole will lie close to $\kappa_{\mathrm{e}}^{(\mathrm{LO})}$ in calculations for the loss coefficient.

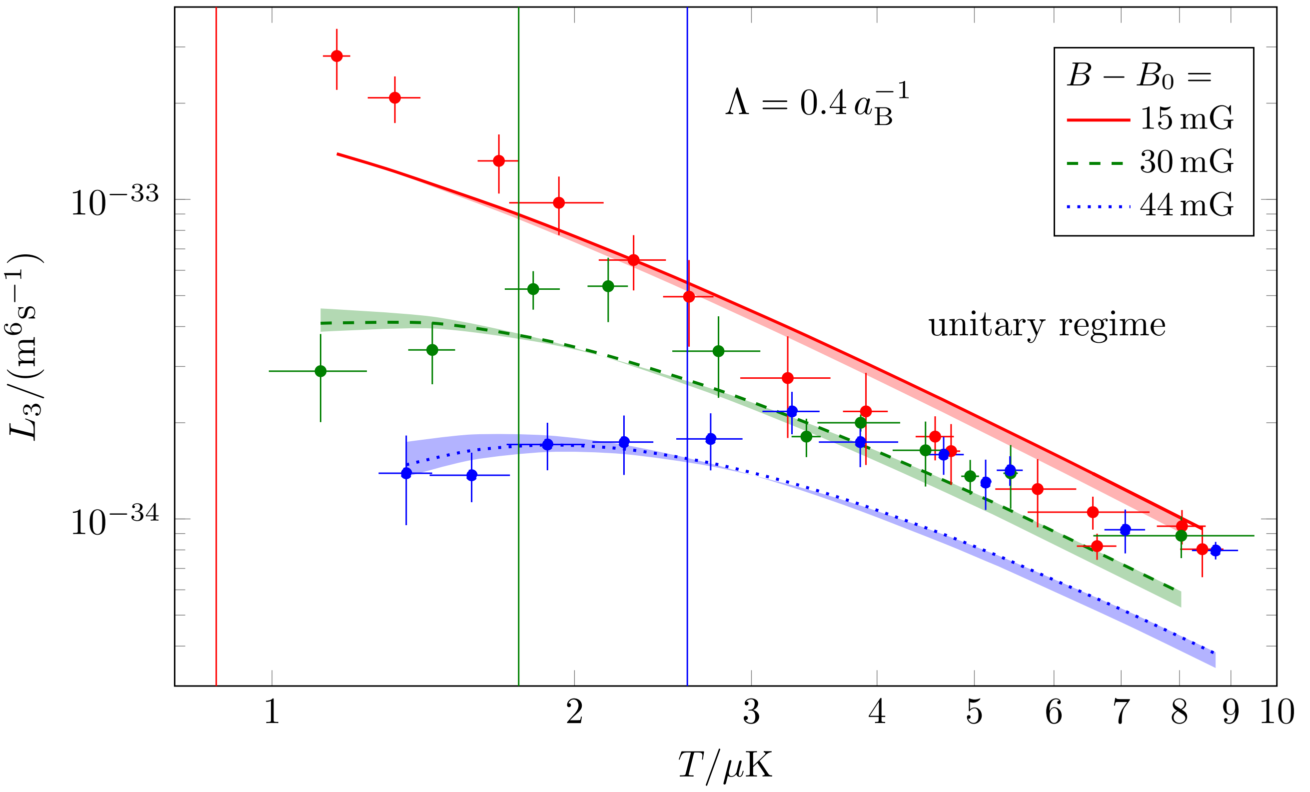

Figure 5.11.: Three-body loss coefficient L_3 as a function of T for three different detunings $B - B_0$. Data is taken from Ref. [70]. The thick lines result from a χ^2 fit in $(r_\mathrm{e}, H^{1^+}, F^{1^+})$ to the data, using $\Lambda = 0.4\, a_\mathrm{B}^{-1}$ and $a_\mathrm{e,bg}\Delta B = -2.8{\cdot}10^6\, a_\mathrm{B}^3\,\mathrm{G}$. The bands are obtained by performing additional fits for $a_\mathrm{e,bg}\Delta B \in \{-3.1, -2.5\} \cdot 10^6 a_\mathrm{B}^3\,\mathrm{G}$. The colored grid lines mark the temperatures T_0 above which the Boltzmann distribution's maximum lies above the two-body threshold (unitary regime).

for the number N of atoms in the trapped gas. Here, $n(\boldsymbol{x}, t)$ denotes the local gas density [70]. Thus, $L_3(T)$ represents the rate at which single atoms leave the trapped gas. Per recombination event, typically each of the 3 atoms gets lost. Moreover, there are $N^3/6$ atom triples per unit volume that potentially undergo recombination. For this reason, the loss coefficient reads

$$L_3(T) = 3\,\langle K_3\rangle(T)/6\,; \tag{5.30}$$

see also Ref. [160].

In Ref. [70], the temperature dependence of L_3 was measured for $T \in [1, 8]\,\mu\mathrm{K}$ at three small detunings $B - B_0 \in \{15, 30, 44\}\,\mathrm{mG}$; see Fig. 5.11. For larger temperatures, the loss coefficient falls off like T^{-2}. As $B - B_0$ decreases, this region becomes larger, until for $B - B_0 = 15\,\mathrm{mG}$ (red) the whole data region obeys this scaling. The T^{-2} region is usually referred to as the unitary regime. It represents the region where $\kappa_\mathrm{e}^{(\mathrm{LO})}$ is smaller than the momentum scale k_T set by the temperature T. If we identify k_T with the Boltzmann distribution's maximum position, then the unitary regime begins at

$$T_0 = \frac{2}{5mk_\mathrm{B}}\,\kappa_\mathrm{e}^{(\mathrm{LO})\,2} \approx \frac{4}{5mk_\mathrm{B}}\,\frac{B - B_0}{a_\mathrm{e,bg}\Delta B\; r_\mathrm{e}} \in \{0.88, 1.76, 2.59\}\,\mu\mathrm{K} \tag{5.31}$$

for $B - B_0 \in \{15, 30, 44\}\,\mathrm{mG}$. These temperatures are depicted as vertical grid lines in Fig. 5.11.

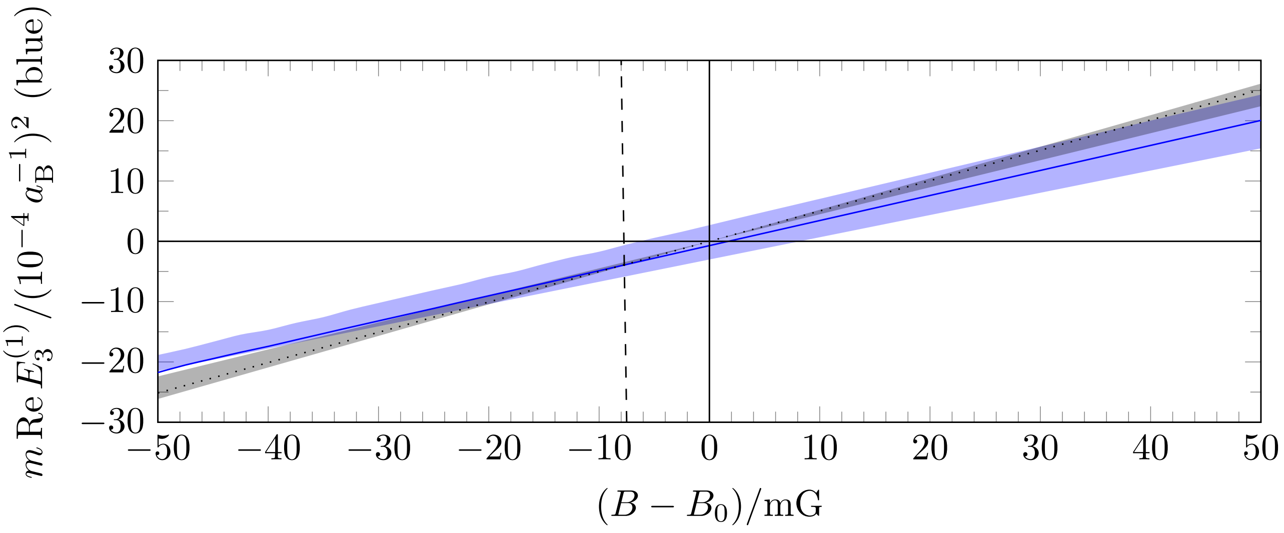

Figure 5.12.: Real part of the three-body state energy $\mathrm{Re}\,E_3^{(1)}$ (blue) as a function of B. For comparison, we show the real part of the two-body state energy, i.e., of $-B_\mathrm{e}^{(\mathrm{LO})}$ $(B < B_0)$ and $\delta_\mathrm{e}^{(\mathrm{LO})}$ $(B > B_0)$ in black. The thick lines and their bands correspond to the three values for $a_{\mathrm{e,bg}}\Delta B$ and (r_e, H^{1^+}) used and obtained in the χ^2 fits. The dashed grid lines marks the point where the two- and three-body energies cross each other.

To benchmark our approach, we perform a simultaneous χ^2 fit to the three data sets by varying the parameter tuple $(r_\mathrm{e}, H^{1^+}, F^{1^+})$ at fixed $\Lambda = 0.4\,a_\mathrm{B}^{-1}$. [6] The χ^2 value is defined[7]

$$\chi^2 = \frac{1}{N_1 + N_2 + N_3 - 1} \sum_{i=1}^{3} \sum_{j=1}^{N_i} \left(\frac{L_3 - L_3^{(\mathrm{exp})}}{\Delta L_3^{(\mathrm{exp})}} \right)^2 \left(T^{(i,j)}, B^{(i)} - B_0 \right). \tag{5.32}$$

In this way, we obtain an LO prediction for r_e. Moreover, the result for H^{1^+} will determine the running of the first three-body pole $E_3^{(1)}$ with the magnetic field B. Note that both predictions will depend on the parameter $a_{\mathrm{e,bg}}\Delta B$ which relates B and a_e; see Eq. (5.8). The input value $a_{\mathrm{e,bg}}\Delta B = -2.8 \cdot 10^6 a_\mathrm{B}^3\,\mathrm{G}$ from Ref. [155] has uncertainties ±11 %. We take them into account by performing separate fits for various values $a_{\mathrm{e,bg}}\Delta B \in [-3.1, -2.5] \cdot 10^6 a_\mathrm{B}^3\,\mathrm{G}$.

The fit results are shown in Fig. 5.11 as colored bands. Their central values (thick lines) correspond to $a_{\mathrm{e,bg}}\Delta B = -2.8 \cdot 10^6 a_\mathrm{B}^3\,\mathrm{G}$ and their borders to $a_{\mathrm{e,bg}}\Delta B \in \{-3.1, -2.5\} \cdot 10^6 a_\mathrm{B}^3\,\mathrm{G}$. All separate fits have comparable χ^2 values of approximately 6.5. Thus, the quality of the fit does not depend strongly on $a_{\mathrm{e,bg}}\Delta B$. The optimal p-wave effective range value reads $r_\mathrm{e} = -0.14^{+0.00}_{-0.01} a_\mathrm{B}^{-1}$. It is comparable to the estimation $(r_\mathrm{e})_\mathrm{res} = -0.182\,a_\mathrm{B}^{-1}$ used by Waseem *et al.* [70] and stable against changes in $a_{\mathrm{e,bg}}\Delta B$. For $\Lambda = 0.4\,a_\mathrm{B}^{-1}$, the three-body force and the recombination rate prefactor read $H^{1^+} = -20.45^{+0}_{-30}$ and $(F^{1^+})^2/m = 1.47^{+3.20}_{-0.06} \cdot 10^{-50} a_\mathrm{B}^{-2}\,\mathrm{m}^6\mathrm{s}^{-1}$. They vary more strongly with $a_{\mathrm{e,bg}}\Delta B$. Given the fit result for H^{1^+}, the running of the three-body state energy $E_3^{(1)}$ with the magnetic field is fixed. The blue band in Fig. 5.12 shows that its real part is linear in B with a slope slightly smaller than the one of the two-body energy $E_\mathrm{e} = -B_\mathrm{e}^{(\mathrm{LO})}$ $(B < B_0)$ and $\mathrm{Re}\,E_\mathrm{e} = \delta_\mathrm{e}^{(\mathrm{LO})}$ $(B > B_0)$.

---

[6] The χ^2 value reacts very strongly on small changes in H^{1^+}. For this reason, we actually vary the position of the three-body pole, which is equivalent to varying H^{1^+}. Moreover, we vary $\ln[(F^{1^+})^2/m]$ instead of F^{1^+}.

[7] In principle, one should also take into account uncertainties $\Delta T^{(i,j)}$ in the experimental temperatures; see Fig. 5.11. One could, for example, translate them into additional contributions to the ΔL_3 values, using an estimation for the slope $\partial L_3/\partial T$. In any case, such contributions would lower the χ^2 value.

Our fits describe data at smaller T farely well. Moreover, in the unitary regime, they reproduce the expected T^{-2} behavior [161]. However, as opposed to data, the curves are not independent of B in the unitary regime. Instead, they are separated by factors of 1.3-1.5. This issue has to be investigated in the future. A straight-forward solution would be to allow for B dependent three-body parameters H^{1^+} and/or F^{1^+}. This approach, however, is undesirable since it reduces the predictive power of the theory significantly. Instead, one should first investigate the importance of spin-parity channels different from $J^P = 1^+$. Even though suppressed close to $E = 0$, they might become LO in the presence of a Feshbach resonance [76]. Their inclusion might improve the χ^2 fit. It would further be instructive to iterate effects of the sink-like short-range factor. A nonperturbative treatment would presumably change the energy/temperature behavior at larger energies.

6 Summary and outlook

In this thesis, we investigated low-energy reactions of three-body systems in hadron, nuclear, and atomic physics. The first reaction, $B^{\pm} \rightarrow K^{\pm} + X(3872) \rightarrow K^{\pm} + D^0\bar{D}^0\pi^0$, is a two-step B meson decay. It can be used to extract the mass and width of the potential dimeson state $X(3872)$. The second one, ${}^{10}\text{Be}\,(\text{d, p})\,{}^{11}\text{Be}$, is a neutron transfer reaction involving the halo nucleus ${}^{11}\text{Be}$. In the third one, $3\,{}^6\text{Li} \rightarrow {}^6\text{Li}_2(\text{e}) + {}^6\text{Li} \rightarrow {}^6\text{Li}_2(\text{d}) + {}^6\text{Li}$, two ${}^6\text{Li}$ atoms recombine into a deep diatom ${}^6\text{Li}_2(\text{d})$ in the presence of a Feshbach resonance state ${}^6\text{Li}_2(\text{e})$. This process occurs in trapped ${}^6\text{Li}$ gases and causes particle losses.

All of these reactions have in common that they exhibit bound and/or resonance states very close to the respective scattering thresholds. In other words, they exhibit intrinsic momentum-scale separations due to certain fine-tunings. The connection between fine-tuned scattering parameters and shallow states was discussed in Chapter 2. We also showed that details of the microscopic interaction have often little influence on low-energy observables. In this case, a short-range EFT can be used to describe the reaction. It bases solely on relevant particles and symmetries needed to describe low-energy observables.

6.1 $X(3872)$ line shape in $D^0\bar{D}^0\pi^0$ production (Chapter 3)

In Chapter 3, the $X(3872)$ was treated as an extremely weakly bound $D^0\bar{D}^{0*}$ + c.c. s-wave molecule (binding energy below 0.2 MeV). At the same time, the vector meson D^{0*} ($\bar{D}^{0*}$) is a shallow p-wave resonance of $D^0\pi^0$ ($\bar{D}^0\pi^0$), turning the $X(3872)$ into a $D^0\bar{D}^0\pi^0$ three-body resonance. Our EFT describes interactions among these three particles and has explicit Galilean invariance. It was derived top-to-bottom from HHχPT [18]. The p-wave power counting needed to describe the D^{0*} as a LO pole in the $D^0\pi^0$ amplitude is inspired by the one of Bedaque *et al.* for ^{5}He [85]. It explains the shallow resonance by a single fine-tuning of the p-wave effective range. Radiative D^{0*} decays were included effectively using an imaginary contact interaction. The LO D^{0*} propagator has a simple Breit-Wigner form. The $D^0\pi^0$ expansion parameter $\chi_2 \sim 0.1$ is small, implying a fast convergence of the EFT expansion.

The $X(3872)$ occurs as a pole in the $D^0\bar{D}^{0*}$ + c.c. amplitude. A thorough analysis revealed that the LO amplitude contains only iterations of the LO D^{0*} propagator and a three-body force. It resembles the zero-range amplitude by Braaten and Lu [44]. NLO corrections are due to D^{0*} self-energy insertions, s-wave pion exchanges, and charged mesons. Only one three-body force is needed for renormalization at NLO. From the amplitude, we calculated the $D^0\bar{D}^0\pi^0$ production rate in which the $X(3872)$ occurs as a sharp peak. Correlations between the binding energy δ_X, the width Γ_X, and the line shape of the $X(3872)$ were extracted at LO and NLO. As predicted by Braaten and Lu [44], the line shape is strongly enhanced above the $D^0\bar{D}^{0*}$ threshold due to the nonzero D^{0*} width. Our theory provides a tool to systematically extract the pole position of the $X(3872)$ from the line shape. It can be extended to virtual $X(3872)$ states. In the following, we list the central findings of our EFT analysis.

1. The D^{0*} width reads $\Gamma_{0*} = (53.6 \pm 1.0)\,\text{keV}$ if higher-order parameters are not strongly enhanced.
2. The LO $X(3872)$ width $\Gamma_X^{(\text{LO})} = \Gamma_{0*}$ is fully determined by the D^{0*} width if only $X(3872) \rightarrow D^0\bar{D}^0\pi^0$ and $X(3872) \rightarrow D^0\bar{D}^0\gamma$ decays are considered. NLO corrections are of the order 13 %. For the representative binding energy $\delta_X = 57\,\text{keV}$ of Eq. (3.85), they are only 2 %.
3. For $\delta_X > 50\,\text{keV}$, the line shape's full width at half maximum (FWHM) can be identified with the width $\Gamma_X(\delta_X)$. For smaller δ_X, however, the FWHM is up to 2.8 times larger.
4. The correlation FHWM(δ_X) is monotonic. It can be inverted to extract $\delta_X > 0$ from an experimental line shape. The correlation $\Gamma_X^{(\text{NLO})}(\delta_X)$ can then be used to infer the width.

5. The line shape's maximum position can be identified by δ_X down to $\delta_X \approx 10\,\text{keV}$. A limited detector resolution, however, can shift the peak above the $D^0\bar{D}^{0*}$ threshold. To confirm the dimeson nature of the $X(3872)$ in $B^\pm \to K^\pm + D^0\bar{D}^0\pi^0$, the detector has to resolve structures of size $50\,\text{keV}$.

Our theory could be used to analyze data from $D^0\bar{D}^{0*}$-type $X(3872)$ decays at Belle [162, 163]. In particular, one could calculate the momentum distribution of $D^0\bar{D}^0\pi^0$, often illustrated in a Dalitz plot. On the theoretical side, the theory could be extended to account for J/ψ-type $X(3872)$ decays. We could then use our framework to predict line shapes to be measured at P̄ANDA [111]. Inelastic channels can be included effectively by allowing for an imaginary three-body force. Note, however, that a value for the branching ratio of $D^0\bar{D}^{0*}$-related decays would be needed then.

6.2 Nuclear (d, p) reactions (Chapter 4)

In Chapter 4, we developed a Halo EFT formalism for transfer reactions ${}^{A}\text{X}(\text{d},\text{p}){}^{A+1}\text{X}$ including one-neutron halo nuclei ${}^{A+1}\text{X}$. The theory uses fields for the core (c) ${}^{A}\text{X}$, neutron (n), and proton (p). Contact interactions between p-n and c-n describe the weakly bound states deuteron and ${}^{A+1}\text{X}$. Photon couplings induce the repulsive Coulomb force between c-p. Upon discussing the general framework, we applied the theory to the reaction ${}^{10}\text{Be}(\text{d},\text{p}){}^{11}\text{Be}$. It includes the one-neutron halo nucleus ${}^{11}\text{Be}$. The two-body expansion parameters, given by the small binding energies and effective ranges of deuteron and ${}^{11}\text{Be}$, are of the order $\chi_2 \sim 0.4$. This number is much larger than in the $D^0\pi^0$ sector, implying important range corrections for the reaction cross section. Using scaling arguments, we showed that c-n/p-n interactions in other partial wave sectors, strong c-p interactions, and dynamical core excitations can be neglected at NLO in Halo EFT power counting.

The reaction amplitude was constructed diagrammatically up to NLO in χ_2. At LO, strong interactions are described by neutron exchanges between deuteron and ${}^{11}\text{Be}$. In addition, we included such Coulomb photon exchange diagrams leading in the three-body expansion parameter $\chi_3 < 0.2 \sim \chi_2^2$. These interactions were iterated to all orders in the Faddeev equation. A three-body force was used to demonstrate renormalizability. At NLO, range corrections and also the first excited state of ${}^{11}\text{Be}^*$ entered the description. To benchmark the EFT, we compared cross-section results to data by Schmitt *et al.* [59, 60] and to the reaction model study by Yang and Capel [133]. Our main findings are the following.

1. Coulomb diagrams significantly lower the cross section at all deuteron beam energies $E_\text{d} \in \{12, 15, 18, 21.4\}\,\text{MeV}$ and have to be included already at LO.

2. NLO corrections from effective ranges and the excited state ${}^{11}\text{Be}^*$ individually modify the cross section by ca. 40 % as predicted. Overall, however, they do not alter the LO results much.

3. The cutoff dependence of the cross section is mild over a large cutoff range. Renormalization is thus not a requirement at these energies. At LO, the cross section is then determined solely by the deuteron/${}^{11}\text{Be}$ binding energies.

4. For beam energies $E_\text{d} \lesssim 15\,\text{MeV}$, our results reproduce data well, especially at forward angles. In these regions, the reaction is peripheral. That is, it predominantly depends on the long-range tails of the deuteron/${}^{11}\text{Be}$ wave functions. This finding confirms earlier claims by Yang and Capel.

5. At larger beam energies, our results strongly overestimate data. This circumstance indicates that the low-energy power counting of Halo EFT may fail at these energies.

In the future, our study could be continued along many possible paths. Firstly, one could try improving the three-body power counting, which, at the moment, counts momenta as small suppression factors. In a power counting tailored to beam energies at and above 15 MeV, so-far neglected higher-order contributions could in principle already enter at NLO. An earlier study by Deltuva *et al.* suggests that dynamical core excitations could be such a high-energy ingredient [126]. Moreover, one should investigate the impact of not explicitly measured loss channels, in particular due to deep Boron-11 states indicated in Fig. 4.7. They could be accounted for similarly to the treatment of the inelastic $D^0\gamma$ channel in $D^0\pi^0$ scattering; see also Ref. [94]. Secondly, since Halo EFT is ideally suited to describe processes at low energies, one could predict the cross section at astrophysical energies. Multi-photon diagrams could then become important. Short-range effects like core excitations, however, should be strongly suppressed. At such low energies, also the less peripheral process ${}^{10}\mathrm{Be}\,(\mathrm{d},\,\mathrm{p})\,{}^{11}\mathrm{Be}^*$ should be describable in Halo EFT.

6.3 Three-body losses of a polarized ^{6}Li Fermi gas (Chapter 5)

In the last study, we described three-body recombination of identical ^{6}Li atoms in an ultracold gas environment in Chapter 5. Due to the Pauli principle, interactions are restricted to the p-wave sector for small energies. Recombination was studied in the presence of a p-wave Feshbach resonance. To describe the corresponding shallow state ${}^6\mathrm{Li}_2(\mathrm{e})$, we used again the power counting of Bedaque *et al.* [85]. As opposed to the $D^0\pi^0$ sector, however, we chose a natural p-wave effective range r_e. Fine-tuning manifests itself in a large scattering volume. This quantity can be tuned near divergence by a magnetic field B. For negative B detunings, ${}^6\mathrm{Li}_2(\mathrm{e})$ is weakly bound and for positive detunings, ${}^6\mathrm{Li}_2(\mathrm{e})$ is a shallow resonance. Since a precise value of r_e is not available, we left it as a free LO parameter. Close to the Feshbach resonance, NLO corrections are below 1 % and thus much smaller than uncertainties due to r_e.

We then calculated the $J^P = 1^+$ diatom-atom amplitude which is leading at low enough energies. It can be renormalized by a p-wave three-body force. Using the amplitude, we calculated the rate for three-body recombination into deeply bound diatoms ${}^6\mathrm{Li}_2(\mathrm{d})$ for positive B field detunings where recombination data is available [70]. Recombination into shallow states is forbidden on this side where ${}^6\mathrm{Li}_2(\mathrm{e})$ is an unbound resonance. Since the deep state lies outside the EFT's range of applicability, the rate includes a sink-like short-range factor. By applying thermal averaging, we inferred the temperature-dependent loss coefficient. It was χ^2-fitted to data from Ref. [70] by varying the three-body force, the short-range factor, and the unknown p-wave effective range. We obtained the following results.

1. The fit result for the p-wave effective range, $r_\mathrm{e} = -0.14^{+0.00}_{-0.01}\,a_\mathrm{B}^{-1}$, agrees with the estimation $(r_\mathrm{e})_\mathrm{res} = -0.182\,a_\mathrm{B}^{-1}$ by Waseem *et al.* [70].
2. The rate exhibits an E^2 behavior at low energies as predicted by Esry *et al.* [77].
3. The rate moreover exhibits a three-body resonance peak near the ${}^6\mathrm{Li}_2(\mathrm{e})$-^{6}Li threshold. The energy of this state increases linearly with B, similarly to the two-body resonance energy.
4. Loss coefficient data is described well for very small temperatures $T \lesssim 3\,\mu\mathrm{K}$ where two atoms do not see the ${}^6\mathrm{Li}_2(\mathrm{e})$ resonance ("nonunitary regime").
5. For larger temperatures ("unitary regime"), loss coefficient results exhibit the expected T^{-2} behavior [161]. However, they are not entirely independent of the B field, as opposed to data.

Further investigations should first of all fathom the unexpected B field dependence of the loss coefficient at larger temperatures. It might be an artifact due to our restriction onto the $J^P = 1^+$ channel. It could also stem from our restriction on B-independent fit parameters. Slight variations of the three-body force with B could have a large impact on the fit results since the three-body state position would be different. Another idea is to iterate effects of the sink-like short-range factor. A nonperturbative approach could be achieved by reformulating the short-range factor as the imaginary part of the three-body force. We plan to publish our results under the title "*Three-body losses of a polarized Fermi gas in effective field theory*" in the near future.

6.4 Comparison and final remarks

The reactions presented in this thesis share many conceptual similarities, although they are not immediately connected physically.

Each study bases upon the observation that certain quantum states relevant for the reaction couple resonantly to an unusually close two-body threshold. In particular, the $X(3872)$ mass is extremely close to the $D^0\bar{D}^{0*}+\text{c.c.}$ threshold and the D^{0*} ($\bar{D}^{0*}$) itself decays to $D^0\pi^0$ ($\bar{D}^0\pi^0$) with a very small energy release. Moreover, the deuteron and the halo states ^{11}Be and $^{11}\text{Be}^*$ lie just below the proton-neutron and ^{10}Be-neutron thresholds, respectively. Most apparently, the diatom state $^6\text{Li}_2(\text{e})$ of Chapter 5 can be tuned arbitrarily close to the threshold of two ^6Li atoms. Related to each small energy difference is a two-body momentum scale K_{lo} much smaller than the natural momentum scale K_{hi} of that system. The EFT power countings we applied to the reactions exploit the scale separations by classifying each contribution to a physical observable according to its suppression in $K_{\text{lo}}/K_{\text{hi}} < 1$.

The scale separations imply two serious simplifications to the reaction mechanisms which are justified at low power counting order. The first simplification is that the D^{0*} ($\bar{D}^{0*}$), deuteron, ^{11}Be, $^{11}\text{Be}^*$, and $^6\text{Li}_2(\text{e})$ can all be treated as pure two-body bound or resonance states. Couplings to other particle channels should be suppressed by powers of $K_{\text{lo}}/K_{\text{hi}}$. For this reason, we could describe each of the three reactions in this thesis as a process of only three particles. It is important to note that the few-body picture fails if typical kinetic energies in the reaction become too large. For example, to describe the reaction $^{10}\text{Be}\,(\text{d, p})\,^{11}\text{Be}$ at larger experimental energies, one might have to include the substructure of the core nucleus, in particular its first excitation state $^{10}\text{Be}^*$, explicitly.

The second simplification is related to the two-body interactions. Compared to the large length scale induced by the shallow bound or resonance state, interactions take place at short distances. Thus, all interactions can be described by contact forces, i.e., derivatives of delta potentials, only. Each contact force determines an ERE coefficient of the two-body system. To describe the low-energy phase shift and the position of the shallow pole, only few ERE coefficients are actually needed. Thus, scale separations do not only reduce the number of relevant degrees of freedom but also the number of relevant interaction parameters.

At LO, the shallow s-wave states deuteron and ^{11}Be are described only by the scattering length. At NLO, also the effective range enters. For the shallow p-wave states D^{0*} ($\bar{D}^{0*}$), $^{11}\text{Be}^*$, and $^6\text{Li}_2(\text{e})$, the scattering volume and the p-wave effective range are both needed at LO. In these systems, the unitary cut term $-i\bar{k}^3$ is an NLO correction. Thus, no new scattering parameter enters at this order. Note that the amount of suppression of the unitary cut term depends on the p-wave power counting. For D^{0*} ($\bar{D}^{0*}$), the unitary cut term is suppressed by three orders in $K_{\text{lo}}/K_{\text{hi}}$. For $^{11}\text{Be}^*$ and $^6\text{Li}_2(\text{e})$, it is suppressed by only one order in $K_{\text{lo}}/K_{\text{hi}}$.

The aforementioned contact forces absorb all short-range interaction details like effects of high-energy scattering channels through renormalization onto real-valued ERE coefficients. That was shown explicitly for the case of ^{11}Be in Appendix E.3. Deep inelastic channels, however, induce imaginary parts to the scattering amplitude which cannot be absorbed by renormalization. Instead, such effects can be included effectively using imaginary contact forces. This approach was used to implement the radiative decay width of $D^{0*} \to D^0\gamma$ into the D^{0*} propagator. Similarly, loss effects due to deep ^{11}B states could be included in the description for $^{10}\text{Be}\,(\text{d, p})\,^{11}\text{Be}$ via imaginary ^{10}Be-proton contact forces. The method is not at all limited to two-body systems. In fact, the three-body recombination process $3\,^6\text{Li} \to {}^6\text{Li}_2(\text{d}) + {}^6\text{Li}$ was described using a sink-like short-range factor F^{1^+}, which could be reformulated as an imaginary $^6\text{Li}_2(\text{e})$-^6Li contact force. Similarly, the $D^0\bar{D}^{0*}+\text{c.c.}$ contact force C_0 could be made complex to account for short-range decays of the $X(3872)$.

We conclude that short-range EFTs provide powerful tools to simplify reaction mechanisms when a system exhibits momentum scale separations. In this way, structure and reaction observables can be treated on equal footing and relations between both types of observables can be obtained in a systematically improvable way.

Appendices

A Units and natural constants

We give a brief overview on the physical units and constants used in this thesis. Numerical values are taken from Ref. [36].

For convenience, we use natural units $\hbar = c \equiv 1$. In this convention, momenta, energies, masses, inverse lengths, and inverse times have the same dimension. In Chapters 3-4, we express them either in MeV or in fm^{-1}. The two alternatives can be converted into each other using the relation

$$\hbar c = 197.3269788(12)\,\mathrm{MeV\,fm} = 1\,. \tag{A.1}$$

Cross sections have dimension $(\text{length})^2$ and will be expressed in

$$\mathrm{mb} = 0.1\,\mathrm{fm}^2\,. \tag{A.2}$$

To convert times from meters to seconds, we use

$$c = 299.792458 \cdot 10^6\,\mathrm{m\,s}^{-1} = 1\,. \tag{A.3}$$

In Chapter 5, we use Bohr radii a_B instead of fm for lengths and inverse momenta. In natural units, one finds

$$a_\mathrm{B} \equiv \frac{1}{m_e \alpha} \approx 0.52917721067(12) \cdot 10^{-10}\,\mathrm{m}\,, \tag{A.4}$$

where $m_e = 0.5109989461(31)\,\mathrm{MeV}$ is the electron mass and

$$\alpha = 1/137.035999139(31) \tag{A.5}$$

is the fine structure constant. The latter is equivalent to the elementary charge $e \equiv (4\pi\alpha)^{1/2} > 0$. Atom masses are expressed in atomic mass units

$$\mathrm{u} = 931.4940954(57)\,\mathrm{MeV}\,. \tag{A.6}$$

Kinetic energies in atom physics have units $a_\mathrm{B}^{-2}\mathrm{u}^{-1} \approx 0.0149\,\mathrm{eV}$. Finally, the Boltzmann constant k_B is used to convert temperatures T (in μK) into kinetic energies $k_\mathrm{B}T$. It reads

$$k_\mathrm{B} = 8.6173303(50) \cdot 10^{-11}\,\mathrm{eV}\,\mu\mathrm{K}^{-1}\,. \tag{A.7}$$

B Analytic two-body integrals

Many multi-dimensional integrals in this thesis have a similar structure. In order to ensure a consistent notation, we discuss how to solve them at this point.

When evaluating Feynman diagrams, we often encounter four-momentum integrals of the form

$$\int \frac{\mathrm{d}^4 l}{(2\pi)^4} \frac{f(\boldsymbol{l})}{[-l^0 + A_1(p^\mu, \boldsymbol{l}) + i\epsilon][l^0 + A_2(p^\mu, \boldsymbol{l}) + i\epsilon]} \,. \tag{B.1}$$

The two denominator factors represent propagators of two particles with kinetic masses $m_{\text{kin},1} \geq m_{\text{kin},2}$, rest masses $m_{\text{rest},1}, m_{\text{rest},2}$, total four-momentum $p^\mu = l_1^\mu + l_2^\mu$, and relative four-momentum $l^\mu = \xi l_2^\mu - (1-\xi) l_1^\mu$. Here, $\xi = m_{\text{kin},1}/(m_{\text{kin},1} + m_{\text{kin},2}) \in [0.5, 1)$ is a mass ratio. Since all particles in this thesis are treated nonrelativistically, the denominator expressions are linear in l^0. The remaining propagator terms are condensed in the functions

$$A_1(p^\mu, \boldsymbol{l}) \equiv \xi p^\mu - \frac{(\xi \boldsymbol{p} - \boldsymbol{l})^2}{2 m_{\text{kin},1}} - m_{\text{rest},1} \tag{B.2a}$$

$$A_2(p^\mu, \boldsymbol{l}) \equiv (1-\xi) p^\mu - \frac{((1-\xi)\boldsymbol{p} + \boldsymbol{l})^2}{2 m_{\text{kin},2}} - m_{\text{rest},2} \,. \tag{B.2b}$$

The enumerator function $f(\boldsymbol{l})$ does only depend on the relative three-momentum since all two-body interactions in this thesis are energy-independent and Galilean-invariant.

At some points in the thesis, we generalize the integral to $D = 1 + d$ space-time dimensions. In order not to change the mass dimension of the integral, however, we introduce an arbitrary mass scale $\Lambda_{\text{PDS}} > 0$. The old integral then transforms to

$$\left(\frac{\Lambda_{\text{PDS}}}{2}\right)^{4-D} \int \frac{\mathrm{d}^D l}{(2\pi)^D} \frac{f(\boldsymbol{l})}{[-l^0 + A_1(p^\mu, \boldsymbol{l}) + i\epsilon][l^0 + A_2(p^\mu, \boldsymbol{l}) + i\epsilon]} \tag{B.3a}$$

$$\equiv \left(\frac{\Lambda_{\text{PDS}}}{2}\right)^{4-D} \int \frac{\mathrm{d}^d l}{(2\pi)^d} \int_{-\infty}^{\infty} \mathrm{d}l^0 \, g(p^\mu, \boldsymbol{l}, l^0) \,. \tag{B.3b}$$

B.1 Residue theorem

The l^0 integral in Eq. (B.3b) can easily be solved using the residue theorem. Instead of integrating over the real axis, let us consider the blue contour shown in Fig. B.1. Due to the l^0 independence of $f(\boldsymbol{l})$, contributions from the contour's arc vanish as the radius r increases. Thus, for $r \to \infty$, we recover the integral from $-\infty$ to ∞. For each finite r, though, the integral is determined only by the enclosed pole. The two poles are located at $l^0 = A_1(p^\mu, \boldsymbol{l}) + i\epsilon$ and $l^0 = -A_2(p^\mu, \boldsymbol{l}) - i\epsilon$. For example, by closing the integral in the upper half of the plane, one gets

$$\int_{-\infty}^{\infty} \mathrm{d}l^0 \, g(p^\mu, \boldsymbol{l}, l^0) = (-2\pi i) \lim_{l^0 \to A_1(p^\mu, \boldsymbol{l}) + i\epsilon} \left[l^0 - A_1(p^\mu, \boldsymbol{l}) - i\epsilon\right] g(p^\mu, \boldsymbol{l}, l^0) \tag{B.4a}$$

$$= i \frac{f(\boldsymbol{l})}{A_1(p^\mu, \boldsymbol{l}) + A_2(p^\mu, \boldsymbol{l}) + i\epsilon} \,. \tag{B.4b}$$

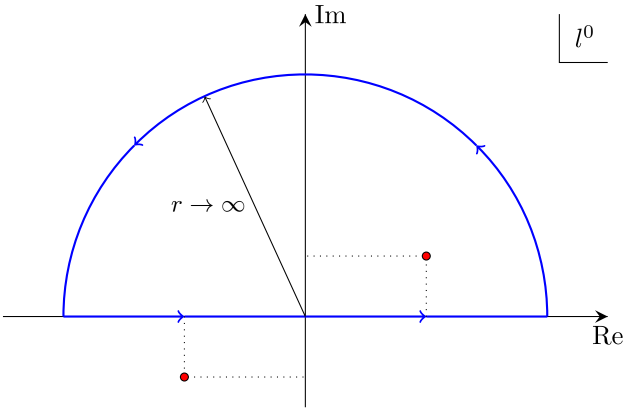

Figure B.1.: Illustration of the residue theorem used to solve l^0 integrals of the type of Eq. (B.3a). The red dots represent the two poles in l^0.

The same result is obtained by closing the contour in the lower half of the plane. Thus, the two denominator factors of Eq. (B.3a) are effectively added. The remaining integral then reads

$$-i\,2\mu\left(\frac{\Lambda_{\text{PDS}}}{2}\right)^{3-d}\int\frac{\mathrm{d}^d l}{(2\pi)^d}\frac{f(\boldsymbol{l})}{\boldsymbol{l}^2-2\mu\left(E_{\text{cm}}-m_{\text{rest,tot}}+i\epsilon\right)} \tag{B.5}$$

with center-of-mass energy

$$E_{\text{cm}}=p^0-\frac{\boldsymbol{p}^2}{2m_{\text{kin,tot}}} \tag{B.6}$$

total kinetic mass $m_{\text{kin,tot}}=m_{\text{kin,1}}+m_{\text{kin,2}}$, reduced mass $\mu=m_{\text{kin,1}}m_{\text{kin,2}}/m_{\text{kin,tot}}$ and total rest mass $m_{\text{rest,tot}}=m_{\text{rest,1}}+m_{\text{rest,2}}$.

B.2 Momentum integrals

In this thesis, the enumerator function $f(\boldsymbol{l})$ in Eq. (B.3b) is typically a tensor involving polarization/spin indices. It can, however, be expressed as a superposition of monomials $\boldsymbol{l}^{2n}$ ($n\geq 0$). The remaining d-dimensional integrals are analytically solvable. They read

$$J_{d,n}(\Delta)\equiv\left(\frac{\Lambda_{\text{PDS}}}{2}\right)^{3-d}\int\frac{\mathrm{d}^d l}{(2\pi)^d}\frac{\boldsymbol{l}^{2n}}{\boldsymbol{l}^2+\Delta} \tag{B.7a}$$

$$=\left(\frac{\Lambda_{\text{PDS}}}{2}\right)^{3-d}\frac{\Gamma\left(1-n-\frac{d}{2}\right)\Gamma\left(n+\frac{d}{2}\right)}{(4\pi)^{d/2}\Gamma\left(\frac{d}{2}\right)}\Delta^{-1+n+d/2} \tag{B.7b}$$

$$=(-1)^{n+1}\frac{1}{4\pi}\times\begin{cases}\Delta^n\Lambda_{\text{PDS}}\left[\frac{1}{d-2}+\gamma_{\text{E}}/2+\ln\left(\frac{\Delta^{1/2}}{\Lambda_{\text{PDS}}\pi^{1/2}}\right)+\mathcal{O}(d-2)\right], & \text{if } d\to 2\\ \Delta^{n+1/2}+\mathcal{O}(d-3), & \text{if } d\to 3\end{cases}\quad (n\geq 0) \tag{B.7c}$$

with $\Delta\in\mathbb{R}$ and Euler-Mascheroni constant $\gamma_{\text{E}}\approx 0.577$.

In the PDS scheme, one introduces a counter term which removes the $d=2$ pole, i.e.,

$$J^{(\text{PDS})}_{d,n}(\Delta)\equiv J_{d,n}(\Delta)-\frac{\lim_{d'\to 2}(d'-2)J_{d',n}(\Delta)}{d-2}\quad (n\geq 0). \tag{B.8}$$

For $d = 3$ spatial dimensions, one then obtains the result

$$J_{3,n}^{(\mathrm{PDS})}(\Delta) = (-1)^{n+1}\frac{1}{4\pi}\Delta^n\left(\Delta^{1/2} - \Lambda_{\mathrm{PDS}}\right) \quad (n \geq 0). \tag{B.9}$$

The MS scheme, in which the $d = 2$ pole is not removed, is recovered by sending $\Lambda_{\mathrm{PDS}} \to 0$.

In three-body calculations, we always calculate integrals in $d = 3$ dimensions. Moreover, we use a cutoff $\Lambda > 0$ instead of dimensional regularization. The integral $J_{3,n}(\Delta)$ above then takes the form

$$J_{3,n}^{(\Lambda)}(\Delta) = \frac{1}{2\pi^2}\int_0^\Lambda \mathrm{d}q\, q^2\, \frac{q^{2n}}{q^2 + \Delta} \quad (n \geq 0)\,. \tag{B.10}$$

The scalar integral $J_n^{(\Lambda)}(\Delta)$ can be solved analytically as well. It reads

$$\begin{aligned}
J_{3,n}^{(\Lambda)}(\Delta) &= \frac{1}{2\pi^2}\int_0^\Lambda \mathrm{d}q\,\left(q^{2n} - \Delta\frac{q^{2n}}{q^2 + \Delta}\right) && \text{(B.11a)}\\
&= \frac{1}{2\pi^2}\frac{\Lambda^{2n+1}}{2n+1} - \Delta\, J_{3,n-1}^{(\Lambda)}(\Delta) && \text{(B.11b)}\\
&= \frac{1}{2\pi^2}\left(\sum_{j=0}^{n}(-\Delta)^{n-j}\,\frac{\Lambda^{2j+1}}{2j+1} + (-\Delta)^{n+1}\int_0^\Lambda \mathrm{d}q\,\frac{1}{q^2 + \Delta}\right) && \text{(B.11c)}\\
&= \frac{1}{2\pi^2}\left(\sum_{j=0}^{n}(-\Delta)^{n-j}\,\frac{\Lambda^{2j+1}}{2j+1} + (-1)^{n+1}\Delta^{n+1/2}\,\mathrm{atan}\left(\frac{\Lambda}{\Delta^{1/2}}\right)\right) && \text{(B.11d)}\\
&= \frac{1}{4\pi}\left(\frac{2}{\pi}\sum_{j=0}^{n}(-\Delta)^{n-j}\,\frac{\Lambda^{2j+1}}{2j+1} + (-1)^{n+1}\Delta^{n+1/2} + \mathcal{O}\left(\Delta^{1/2}/\Lambda\right)\right) \quad (n \geq 0)\,. && \text{(B.11e)}\\
&= \frac{1}{4\pi} \times \begin{cases} \frac{2}{\pi}\Lambda - \Delta^{1/2} + \mathcal{O}\left(\Delta^{1/2}/\Lambda\right), & \text{if } n = 0 \\ \frac{2}{3\pi}\Lambda^3 - \frac{2}{\pi}\Lambda\Delta + \Delta^{3/2}\mathcal{O}\left(\Delta^{1/2}/\Lambda\right), & \text{if } n = 1 \end{cases}\,. && \text{(B.11f)}
\end{aligned}$$

C Partial wave decomposition

Let us consider a three-body interaction $\mathcal{J}^{\alpha\beta}(\boldsymbol{p},\boldsymbol{q};E)$, which connects states with total spins S, S'. The corresponding polarization quantum numbers α, β can be either spherical indices or cartesian indices; see below. Moreover, let $\boldsymbol{J} \equiv \boldsymbol{L} + \boldsymbol{S}$ be the total angular momentum. Dependences of the interaction $\mathcal{J}$ on α, β and on the angular parts $\hat{\boldsymbol{p}} \equiv \boldsymbol{p}/p, \hat{\boldsymbol{q}} \equiv \boldsymbol{q}/q$ can be absorbed into projection operators via

$$\mathcal{J}^{\alpha\beta}(\boldsymbol{p},\boldsymbol{q};E) \equiv \sum_{J} \sum_{L,L'} \mathcal{J}^{{}^{2S+1}L_J,\,{}^{2S'+1}L'_J}(p,q;E)\; P^{\alpha\beta}_{{}^{2S+1}L_J,\,{}^{2S'+1}L'_J}(\hat{\boldsymbol{p}},\hat{\boldsymbol{q}})\,. \tag{C.1}$$

The operators

$$P^{\alpha\beta}_{{}^{2S+1}L_J,\,{}^{2S'+1}L'_J}(\hat{\boldsymbol{p}},\hat{\boldsymbol{q}}) = 4\pi \sum_{m_J} \left(\boldsymbol{Y}_{(L,S)Jm_J}(\hat{\boldsymbol{p}})\right)^{\alpha} \left(\boldsymbol{Y}_{(L',S')Jm_J}(\hat{\boldsymbol{q}})\right)^{\beta\,*} \tag{C.2}$$

are made of tensor spherical harmonics

$$\boldsymbol{Y}_{(L,S)Jm_J}(\hat{\boldsymbol{p}}) = \sum_{m_L,m_S} \mathrm{C}^{Jm_J}_{Lm_L,Sm_S}\, Y^{m_L}_{L}(\hat{\boldsymbol{p}})\, \boldsymbol{\chi}^{m_S}_{S}\,. \tag{C.3}$$

with Clebsch-Gordan coefficient $\mathrm{C}^{Jm_J}_{Lm_L,Sm_S}$ and spherical harmonic $Y^{m_L}_{L}(\hat{\boldsymbol{p}})$ [142].

The vector $\boldsymbol{\chi}^{m_S}_{S}$ is a “spin function”, i.e., an eigenfunction of the spin operators $\hat{\boldsymbol{S}}^2$ and $\hat{S}_z$, with

$$\hat{\boldsymbol{S}}^2\, \boldsymbol{\chi}^{m_S}_{S} = S(S+1)\, \boldsymbol{\chi}^{m_S}_{S}\,, \tag{C.4a}$$

$$\hat{S}_z\, \boldsymbol{\chi}^{m_S}_{S} = m_S\, \boldsymbol{\chi}^{m_S}_{S}\,. \tag{C.4b}$$

In calculations for the halo reaction $^{10}\mathrm{Be}\,(\mathrm{d},\,\mathrm{p})\,^{11}\mathrm{Be}$ and for three-body recombination of fermionic $^{6}\mathrm{Li}$ atoms, we choose a spherical representation

$$\left(\boldsymbol{\chi}^{m_S}_{S}\right)^{m} = \delta_{m_S m} \quad (m \in \{S, S-1, \cdots, -S\}) \tag{C.5}$$

for the spin functions with spherical index m. For the $X(3872)$, however, it is common to express the corresponding $S=1$ spin functions in a cartesian basis by writing

$$\left(\boldsymbol{\chi}^{m_S}_{1}\right)^{i} \equiv \boldsymbol{\chi}^{m_S}_{1} \cdot \boldsymbol{e}_i \quad (i \in \{1,2,3\}) \tag{C.6}$$

with cartesian index i, cartesian basis vectors $\boldsymbol{e}_i$ and

$$\boldsymbol{\chi}^{+1}_{1} = \frac{1}{\sqrt{2}}(-\boldsymbol{e}_1 - i\boldsymbol{e}_2)\,, \quad \boldsymbol{\chi}^{0}_{1} = \boldsymbol{e}_3\,, \quad \boldsymbol{\chi}^{-1}_{1} = \frac{1}{\sqrt{2}}(\boldsymbol{e}_1 - i\boldsymbol{e}_2)\,. \tag{C.7}$$

In Sec. 4.1.1, we transform the deuteron field $\boldsymbol{d}$ and certain projection operators from cartesian basis (d_i) to spherical basis (d_m). Given the above relations, we may do so by using the basis transformation matrix A with $d_i = A_{im} d_m$, $d_m = (A^{-1})_{mi} d_i$ and

$$A_{im} \equiv \frac{1}{\sqrt{2}} \begin{pmatrix} -1 & 0 & 1 \\ -i & 0 & -i \\ 0 & 1 & 0 \end{pmatrix}_{im} \qquad \left(i \in \{1,2,3\},\; m \in \{+1,0,-1\}\right). \tag{C.8}$$

Similarly, the cartesian Pauli matrices σ_i can be transformed to spherical Pauli matrices

$$A^{-1} \begin{pmatrix} \sigma_1 \\ \sigma_2 \\ \sigma_3 \end{pmatrix} = \left(\begin{pmatrix} 0 & 0 \\ -\sqrt{2} & 0 \end{pmatrix}, \begin{pmatrix} 1 & 0 \\ 0 & -1 \end{pmatrix}, \begin{pmatrix} 0 & \sqrt{2} \\ 0 & 0 \end{pmatrix} \right)^{T} = (\sigma_{+1},\, \sigma_0,\, \sigma_{-1})^{T}\,. \tag{C.9}$$

C.1 Projection prescription

By construction, the projection operators $P_{2S+1_{L_J},2S'+1_{L'_J}}$ fulfill important orthogonality relations. In the following, we write $\hat{S} \equiv 2S+1$ for the multiplicity of S. One then finds

$$\begin{aligned}\mathrm{Tr}\left(P_{\hat{S}_{L_J},\hat{S}_{L'_J}}\right) &\equiv \frac{1}{4\pi\,(2J+1)} \sum_{\alpha} \int_{\Omega_{\boldsymbol{q}}} P^{\alpha\alpha}_{\hat{S}_{L_J},\hat{S}_{L'_J}}(\hat{\boldsymbol{q}},\hat{\boldsymbol{q}}) \\ &= \delta_{LL'}\,, \end{aligned} \tag{C.10a}$$

$$\begin{aligned}\left(P_{\hat{S}_1 L_{1\,J_1},\hat{S} L'_{1\,J_1}} \otimes P_{\hat{S}\,L_{2\,J_2},\hat{S}'_2 L'_{2\,J_2}}\right)^{\alpha\beta}(\hat{\boldsymbol{p}}_1,\hat{\boldsymbol{p}}_2) &\equiv \frac{1}{4\pi}\sum_{\gamma}\int_{\Omega_{\boldsymbol{q}}} P^{\alpha\gamma}_{\hat{S}_1 L_{1\,J_1},\hat{S} L'_{1\,J_1}}(\hat{\boldsymbol{p}}_1,\hat{\boldsymbol{q}})\; P^{\gamma\beta}_{\hat{S}\,L_{2\,J_2},\hat{S}'_2 L'_{2\,J_2}}(\hat{\boldsymbol{q}},\hat{\boldsymbol{p}}_2) \\ &= \delta_{L'_1 L_2}\delta_{J_1 J_2}\; P^{\alpha\beta}_{\hat{S}_1 L_{1\,J_1},\hat{S}'_2 L'_{2\,J_1}}(\hat{\boldsymbol{p}}_1,\hat{\boldsymbol{p}}_2)\,, \end{aligned} \tag{C.10b}$$

where α,β,γ can be spherical or cartesian indices. From these relations it follows that the projection operators are orthogonal with respect to the matrix scalar product

$$\left\langle P_{\hat{S}_{L_{1\,J_1}},\hat{S}'_{L'_{1\,J_1}}} \middle| P_{\hat{S}_{L_{2\,J_2}},\hat{S}'_{L'_{2\,J_2}}}\right\rangle \equiv \mathrm{Tr}\left(P_{\hat{S}'_{L'_{1\,J_1}},\hat{S}_{L_{1\,J_1}}} \otimes P_{\hat{S}_{L_{2\,J_2}},\hat{S}'_{L'_{2\,J_2}}}\right) = \delta_{L_1L_2}\,\delta_{L'_1L'_2}\delta_{J_1J_2}\,. \tag{C.11}$$

Equation (C.11) can be used to project out single partial wave components from an interaction. For the components defined in Eq. (C.1), we find

$$\begin{aligned}\mathcal{J}^{2S+1_{L_J},2S'+1_{L'_J}}(p,q;E) &= \left\langle P_{2S+1_{L_J},2S'+1_{L'_J}} \middle| \mathcal{J}\right\rangle(p,q;E) \\ &= \frac{1}{(4\pi)^2\,(2J+1)}\sum_{\alpha,\beta}\int_{\Omega_{\boldsymbol{p}},\Omega_{\boldsymbol{q}}} P^{\beta\alpha}_{2S'+1_{L'_J},2S+1_{L_J}}(\hat{\boldsymbol{q}},\hat{\boldsymbol{p}})\;\mathcal{J}^{\alpha\beta}(\boldsymbol{p},\boldsymbol{q};E) \end{aligned} \tag{C.12}$$

C.2 Particle exchange potentials

Each three-body calculation in this thesis involves at some power counting order a one-particle exchange potential. Generically, it may be denoted $V_{e;s,s'}$, where the subscripts define the exchanged particle e and the incoming (outgoing) spectator particles s (s'). For example, the pion exchange potential used in the calculation for the $X(3872)$ would be written $V_{\pi;D,D}$ in this notation. The generic exchange potential is proportional to the propagator of the exchanged particle e. For incoming (outgoing) relative momenta $\boldsymbol{p}$ ($\boldsymbol{q}$) and a center-of-mass energy E (relative to the respective three-body threshold), it has the form

$$V_{e;s,s'}(\boldsymbol{p},\boldsymbol{q};E) \propto \left[U_{e;s,s'}(p,q;E) + \boldsymbol{p}\cdot\boldsymbol{q}\right]^{-1}\,. \tag{C.13}$$

The polynomial

$$U_{e;s,s'}(p,q;E) \equiv \frac{1+m_e/m_s}{2}\,p^2 + \frac{1+m_e/m_{s'}}{2}\,q^2 - m_e\,(E+i\epsilon) \tag{C.14}$$

depends on kinetic masses $m_e, m_s, m_{s'}$ of the three particles.

The partial wave projected exchange potential is a linear combination of integrals

$$I^{(L)}_{e;s,s'}(p,q;E) \equiv \int_{-1}^{1} \mathrm{d}x\,\frac{P_L(x)}{U_{e;s,s'}(p,q;E)+pq\,x} = -\frac{2}{pq}\,Q_L\left(-\frac{U_{e;s,s'}(p,q;E)}{pq}\right) \quad (L \geq 0)\,, \tag{C.15}$$

whose solutions are Legendre functions of 2$^{\text{nd}}$ kind

$$Q_L(x_0) \equiv -\frac{1}{2}\int_{-1}^{1} \mathrm{d}x\, \frac{P_L(x)}{x-x_0} = (-1)^{L+1}\, Q_L(-x_0)\,. \tag{C.16}$$

Note that we use the convention of Abramowitz and Stegun from Eq. (8.8.3) of Chapter 8.8 in Ref. [164]. In calculations, we use the relations

$$I^{(0)}_{e;s,s'}(p,\,q;\,E) = \frac{1}{pq}\,\ln\!\left(\frac{U_{e;s,s'}(p,\,q;\,E)+pq}{U_{e;s,s'}(p,\,q;\,E)-pq}\right) \xrightarrow{pq\to 0} \frac{2}{U_{e;s,s'}(p,\,q;\,E)}\,, \tag{C.17a}$$

$$\begin{aligned} I^{(L)}_{e;s,s'}(p,\,q;\,E) &= \frac{1}{pq}\left(2\delta_{L1} - \frac{2L-1}{L}\,U_{e;s,s'}(p,\,q;\,E)\;I_{L-1}(p,\,q;\,E) - \frac{L-1}{L}\,pq\,I_{L-2}(p,\,q;\,E)\right) \\ &\xrightarrow{pq\to 0} \frac{2}{U_{e;s,s'}(p,\,q;\,E)}\,\frac{L!}{(2L+1)!!}\left(-\frac{pq}{U_{e;s,s'}(p,\,q;\,E)}\right)^{L} \quad (L\geq 1)\,. \end{aligned} \tag{C.17b}$$

D Calculations for the $X(3872)$ (Chapter 3)

This chapter provides further details on calculations for the $X(3872)$ in $D^0\bar{D}^0\pi^0$ EFT.

D.1 Elimination of vector meson fields

The vector meson fields can be integrated out using the Euler-Lagrange equations, also called equations of motion,

$$\partial_\mu \frac{\delta \mathscr{L}}{\delta\left(\partial_\mu \boldsymbol{D}^{0(\dagger)}\right)} = \frac{\delta \mathscr{L}}{\delta \boldsymbol{D}^{0(\dagger)}}\,, \quad \partial_\mu \frac{\delta \mathscr{L}}{\delta\left(\partial_\mu \bar{\boldsymbol{D}}^{0(\dagger)}\right)} = \frac{\delta \mathscr{L}}{\delta \bar{\boldsymbol{D}}^{0(\dagger)}}\,. \tag{D.1}$$

That leads to an equivalent EFT with only D^0, $\bar{D}^0$, and π^0 fields. In the following, we will focus on the $D\pi$ two-body systems only. Thus, we may set $C_0 = 0$, which decouples the vector meson fields $\boldsymbol{D}^0$ and $\bar{\boldsymbol{D}}^0$. The more general procedure for $C_0 \neq 0$ was performed in the master's thesis [165].

Let us apply the equations of motion for $\boldsymbol{D}^{0\dagger}$ to the Lagrangian in Eq. (3.33). The left-hand side of the equation of motion then vanishes. The right-hand side yields

$$\boldsymbol{D}^0 = -g\,\mathscr{D}^{-1}(i\partial_{\mathrm{cm}})\,\mathscr{G} \tag{D.2}$$

with $i\partial_{\mathrm{cm}} = i\partial_0 - \boldsymbol{\nabla}^2/(2M_{D\pi})$, operators

$$\mathscr{D}(i\partial_{\mathrm{cm}}) \equiv \sum_{n\geq 0} (\Delta_n + iW_n)(i\partial_{\mathrm{cm}})^n\,, \tag{D.3a}$$

$$\mathscr{G} \equiv \pi^0 \overleftrightarrow{\boldsymbol{\nabla}} D^0 = \pi^0\left(\xi\overleftarrow{\boldsymbol{\nabla}} - (1-\xi)\overrightarrow{\boldsymbol{\nabla}}\right)D^0\,, \tag{D.3b}$$

and mass ratio $\xi = m_D/(m_D + m_\pi)$. A similar relation holds for $\bar{\boldsymbol{D}}^0$. By plugging this result into the Lagrangian term $\mathscr{L}_{D\pi}$, it transforms like

$$\mathscr{L}_{D\pi} = \boldsymbol{D}^{0\dagger}\,\mathscr{D}(i\partial_{\mathrm{cm}})\boldsymbol{D}^0 + g\left[\boldsymbol{D}^{0\dagger}\mathscr{G} + \mathrm{H.c.}\right] + \mathrm{c.c.} \tag{D.4a}$$

$$\xrightarrow{\text{e.o.m.}} -g^2\,\mathscr{G}^\dagger\,\mathscr{D}^{-1}(i\partial_{\mathrm{cm}})\,\mathscr{G} + \mathrm{c.c.} \tag{D.4b}$$

$$= -\frac{g^2}{\Delta_0}\left(\pi^0\overleftrightarrow{\boldsymbol{\nabla}}D^0\right)^\dagger\left[1 - iW_0\Delta_0^{-1} - i\partial_{\mathrm{cm}}\Delta_0^{-1} + \cdots\right]\left(\pi^0\overleftrightarrow{\boldsymbol{\nabla}}D^0\right) + \mathrm{c.c.}\,. \tag{D.4c}$$

The ellipses denote terms negligible at NLO.

Equation (D.4c) represents a series

$$\left(\pi^0\overleftrightarrow{\boldsymbol{\nabla}}D^0\right)^\dagger\left(c_1^{(0)} + c_1^{(2)}i\partial_{\mathrm{cm}} + \cdots\right)\left(\pi^0\overleftrightarrow{\boldsymbol{\nabla}}D^0\right) + \mathrm{c.c.} \tag{D.5}$$

of $D^0\pi^0 \to D^0\pi^0$ p-wave interactions. When resummed to all orders and $W_n = 0$, these interactions reproduce the same effective range expansion of the amplitude it_* as shown in Eq. (3.40b). The couplings $c_1^{(0)}$ and $c_1^{(2)}$ both eliminate divergent terms of the $D^0\pi^0$ loop integral; see Ref. [165]. In doing so, they introduce the scattering volume a_* and the p-wave effective range r_*, respectively. The inelastic $D^0\gamma$ channel can be included via imaginary $D^0\pi^0$ interactions $g_n \in \mathbb{C}$ by choosing $W_n \neq 0$. The two-body amplitude then becomes proportional to the full D^{0*} propagator of Eq. (3.62a). Thus, the new Lagrangian yields the same two-body physics as the one with vector meson fields.

It is possible to eliminate the energy dependence in the p-wave vertices of Eq. (D.5) using field redefinitions. At NLO ($g_n = 0$ for $n \geq 2$), these transformations read

$$D^0 \to D^0 - \frac{c_1^{(2)}/2}{2\mu_{D\pi}} \left[\left(\boldsymbol{\nabla} \pi^{0\dagger} \right) \cdot \mathscr{G} + (1-\xi) \pi^{0\dagger} \boldsymbol{\nabla} \cdot \mathscr{G} \right], \tag{D.6a}$$

$$\bar{D}^0 \to \bar{D}^0 - \frac{c_1^{(2)}/2}{2\mu_{D\pi}} \left[\left(\boldsymbol{\nabla} \pi^{0\dagger} \right) \cdot \bar{\mathscr{G}} + (1-\xi) \pi^{0\dagger} \boldsymbol{\nabla} \cdot \bar{\mathscr{G}} \right], \tag{D.6b}$$

$$\pi^0 \to \pi^0 + \frac{c_1^{(2)}/2}{2\mu_{D\pi}} \left[\left(\boldsymbol{\nabla} D^{0\dagger} \right) \cdot \mathscr{G} + \xi D^{0\dagger} \boldsymbol{\nabla} \cdot \mathscr{G} \right] + \frac{c_1^{(2)}/2}{2\mu_{D\pi}} \left[\left(\boldsymbol{\nabla} \bar{D}^{0\dagger} \right) \cdot \bar{\mathscr{G}} + \xi \bar{D}^{0\dagger} \boldsymbol{\nabla} \cdot \bar{\mathscr{G}} \right] \tag{D.6c}$$

with $\bar{\mathscr{G}} \equiv \pi \overleftrightarrow{\boldsymbol{\nabla}} \bar{D}^0$. The new $D^0\pi^0$ interactions

$$c_1^{(0)} \left(\pi^0 \overleftrightarrow{\boldsymbol{\nabla}} D^0 \right)^\dagger \left(\pi^0 \overleftrightarrow{\boldsymbol{\nabla}} D^0 \right) - \frac{c_1^{(2)}}{2} \left[\left(\pi^0 \overleftrightarrow{\boldsymbol{\nabla}} D^0 \right)^\dagger \left(\pi^0 \overleftrightarrow{\boldsymbol{\nabla}} \frac{\overleftrightarrow{\boldsymbol{\nabla}}^2}{2\mu_{D\pi}} D^0 \right) + \text{H.c.} \right] + \text{c.c.} \tag{D.7}$$

are then on-shell equivalent to the ones in Eq. (D.5). Note that they resemble the local operators introduced already in Eq. (2.4).

The field redefinitions also introduce $c_1^{(2)}$ dependent three- and four-body terms for sectors like $D^0\bar{D}^0\pi^0$, $D^0\pi^0\pi^0$, $D^0\bar{D}^0\pi^0\pi^0$, etc. Since the Lagrangian in principle already contains all interactions allowed by Galilean invariance, these terms are absorbed by existing ones. For further details, we refer to Ref. [165].

D.2 D^{0*} self-energy

In this section we calculate the self-energy loop in Fig. 3.8 using a cutoff, the MS scheme, and the PDS scheme. Let $\xi \equiv m_D/M_{D\pi} \approx 0.93$, p^μ be the total $D^0\pi^0$ four-momentum, $l^\mu \equiv \xi l_\pi^\mu - (1-\xi) l_D^\mu$ the undetermined relative $D^0\pi^0$ four-momentum, and $i, i' \in \{1,\, 2,\, 3\}$ the incoming/outgoing D^{0*} polarizations. By applying the Feynman rules in the caption of Fig. 3.6, we obtain the bare self-energy integral

$$-i\Sigma_*^{(\mathrm{b})}(E_\mathrm{cm})\,\delta^{ii'} = \int \frac{\mathrm{d}^4 l}{(2\pi)^4} \frac{i^2 \left(+g\, l^i\right)\left(-g\, l^{i'}\right)}{\left[(\xi p^0 - l^0) - \frac{(\xi \boldsymbol{p} - \boldsymbol{l})^2}{2m_D} + i\epsilon \right] \left[((1-\xi)p^0 + l^0) - \frac{((1-\xi)\boldsymbol{p} + \boldsymbol{l})^2}{2m_\pi} + i\epsilon \right]} \tag{D.8a}$$

$$= ig^2 \int \frac{\mathrm{d}^3 l}{(2\pi)^3} \frac{l^i\, l^{i'}}{\frac{\boldsymbol{l}^2}{2\mu_{D\pi}} + \frac{\boldsymbol{p}^2}{2M_{D\pi}} - p^0 - i\epsilon} \tag{D.8b}$$

$$= ig^2\, 2\mu_{D\pi} \frac{\delta^{ii'}}{3} \int \frac{\mathrm{d}^3 l}{(2\pi)^3} \frac{\boldsymbol{l}^2}{\boldsymbol{l}^2 - 2\mu_{D\pi}(E_\mathrm{cm} + i\epsilon)}\,. \tag{D.8c}$$

As follows from Galilean invariance, the bare self-energy is a function of the center-of-mass energy $E_\mathrm{cm} = p^0 - \boldsymbol{p}^2/(2M_{D\pi})$ only. The l^0 integral of Eq. (D.8a) has been performed using the residue theorem as explained in App. B.1. In order to simplify the integral over $\boldsymbol{l}$ in Eq. (D.8b), we distinguish between the two cases $i \neq i'$ and $i = i'$. For $i \neq i'$, the integral is asymmetric under $l^i \to -l^i$ and thus vanishes. For $i = i'$, the integral is independent of i because of rotational symmetry. Thus, we can replace $l^i l^{i'} \to \boldsymbol{l}^2\, \delta^{ii'}/3$.

The integral of Eq. (D.8c) is cubically divergent as can be seen by applying a cutoff $\lambda > |\boldsymbol{l}|$. In terms of the on-shell relative momentum $\bar{k} = i\,[-2\mu_{D\pi}(E_{\text{cm}} + i\epsilon)]^{1/2}$, this specific regularization scheme yields

$$\begin{aligned}\Sigma_*^{(\text{cutoff})}(E_{\text{cm}}) &= -g^2\,\frac{\mu_{D\pi}}{3\pi^2}\left(\frac{\lambda^3}{3} + \lambda\,\bar{k}^2 + i\bar{k}^3\,\operatorname{atan}\left(\frac{\lambda}{-i\bar{k}}\right)\right) && \text{(D.9a)}\\ &= -g^2\,\frac{\mu_{D\pi}}{6\pi}\left(\frac{2}{3\pi}\lambda^3 + \frac{2}{\pi}\lambda\,\bar{k}^2 + i\bar{k}^3 + \mathcal{O}\left(\lambda^{-1}\right)\right) && \text{(D.9b)}\\ &\equiv -g^2\,\frac{\mu_{D\pi}}{6\pi}\left(\frac{2}{3\pi}\lambda^3 + \frac{2}{\pi}\lambda\,2\mu_{D\pi}(E_{\text{cm}} + i\epsilon)\right) + \Sigma_*(E_{\text{cm}})\,, && \text{(D.9c)}\end{aligned}$$

where vanishing parts in λ^{-1} in Eq. (D.9b) can be neglected. In Eq. (D.9c), nondivergent terms yield the self-energy $\Sigma_*(E_{\text{cm}})$ as given in Eq. (3.38a). Divergent parts can be removed if one allows for cutoff dependent Lagrangian parameters $\Delta_0(\lambda)$ and $g(\lambda)$. One sees that already at LO, one needs two Lagrangian parameters (and thus two ERE coefficients a_*, $r_*/2$) to describe a shallow resonance.

A more convenient regularization scheme for the integral in Eq. (D.8c) is dimensional regularization. By turning to d spatial dimensions and introducing an arbitrary mass scale Λ_{PDS}, one obtains

$$\begin{aligned}\Sigma_*^{(\text{dimreg})}(E_{\text{cm}}) &= -g^2\,\frac{2\mu_{D\pi}}{3}\left(\frac{\Lambda_{\text{PDS}}}{2}\right)^{3-d}\int\frac{\mathrm{d}^d l}{(2\pi)^d}\,\frac{\boldsymbol{l}^2}{\boldsymbol{l}^2 - 2\mu_{D\pi}(E_{\text{cm}} + i\epsilon)} && \text{(D.10a)}\\ &= -g^2\,\frac{2\mu_{D\pi}}{3}\,J_{d,1}\Big(-2\mu_{D\pi}(E_{\text{cm}} + i\epsilon)\Big)\,. && \text{(D.10b)}\end{aligned}$$

In Eq. (D.10b), we recover the generic momentum integral of Appendix B.2. This expression has no pole in $d = 3$, but it does have one in $d = 2$. In the MS scheme, only poles in $d = 3$ are removed by counter terms and thus one directly obtains the self-energy given in Eq. (3.38a). Note that neither Δ_0 nor g have to absorb unphysical parameters in the MS scheme. They are directly given by ERE coefficients as shown in Eqs. (3.41a)-(3.41b).

In order to gain a deeper understanding of the necessity of Galilean invariance for scheme-independent renormalization, we compute the self-energy in a third scheme, PDS. Here, one explicitly removes the $d = 2$ pole of Eq. (D.10a) [19]. Using the results of Appendix B.2, the respective counter term reads

$$\Delta\Sigma_*^{(\text{PDS})}(E_{\text{cm}}) = g^2\,\frac{2\mu_{D\pi}}{6\pi}\,\frac{\Lambda_{\text{PDS}}}{d-2}\,[-2\mu_{D\pi}(E_{\text{cm}} + i\epsilon)]\,. \tag{D.11}$$

For $d = 3$ (physical case), the PDS result then reads

$$\Sigma_*^{(\text{PDS})}(E_{\text{cm}}) = -g^2\,\frac{\mu_{D\pi}}{6\pi}\Lambda_{\text{PDS}}\,2\mu_{D\pi}(E_{\text{cm}} + i\epsilon) + \Sigma_*(E_{\text{cm}})\,. \tag{D.12}$$

If one now allowed for a general kinetic D^{0*} mass m_{kin} and neglected higher-order parameter Δ_n, the full propagator would be inversely proportional to

$$\begin{aligned}&\Delta_0 + \Delta_1\left(p^0 + i\epsilon - \frac{\boldsymbol{p}^2}{2m_{\text{kin}}}\right) - g^2\frac{\mu_{D\pi}}{6\pi}\Lambda_{\text{PDS}}\,2\mu_{D\pi}\left(p^0 + i\epsilon - \frac{\boldsymbol{p}^2}{2M_{D\pi}}\right) - \Sigma_*(E_{\text{cm}}) && \text{(D.13a)}\\ &\equiv -g^2\frac{\mu_{D\pi}}{6\pi}\left(-a_*^{-1} + \frac{r_*}{2}\bar{k}^2 - i\bar{k}^3\right). && \text{(D.13b)}\end{aligned}$$

In order to eliminate the Λ_{PDS} using g^2 for general $\boldsymbol{p}$, one needs to choose $m_{\text{kin}} = M_{D\pi}$. Galilean invariance thus demands conservation of kinetic mass. The renormalization condition for $r_*/2$ then reads

$$\frac{r_*}{2} = -\left(\frac{6\pi}{\mu_{D\pi}}\,\frac{\Delta_1}{2\mu_{D\pi}\,g^2(\Lambda_{\text{PDS}})} + \Lambda_{\text{PDS}}\right). \tag{D.14}$$

The respective relation in MS in Eq. (3.41b) can be recovered by sending $\Lambda_{\text{PDS}} \to 0$. Neglecting radiative decays ($W_n = 0\,\forall n \geq 0$), the Lagrangian has to be Hermitian and thus $g^2 > 0$. Moreover, we know that $r_* < 0$ for a shallow resonance. As a consequence, in the MS scheme one obtains $\Delta_1 = +1$ as proposed in Sec. 3.1.4. The same holds in the PDS scheme for not too large Λ_{PDS} fulfilling $0 \leq \Lambda_{\text{PDS}} < -r_*/2$. This restriction is reasonable since $|r_*/2| \approx 17\,\text{GeV}$ is much larger than the natural scale $K_{\text{hi}} \sim m_\pi$.

D.3 Relativistic corrections

In this section, we investigate at which power counting order relativistic corrections enter the theory. The discussion is inspired by the one on nucleon-nucleon scattering in Ref. [112].

Relativistic corrections to the nonrelativistic propagators iG_{D^0}, iG_{π^0} of the pseudoscalars D^0 ($\bar{D}^0$) and π^0 can be identified by comparing them to exact Klein-Gordon propagators. Let $\kappa^\mu \equiv (k^0 + m_a,\, \boldsymbol{k})$ be the relativistic four-momentum of the meson ($a \in \{D, \pi\}$). In the on-shell case, $k^0 = \kappa^0 - m_a$ is the energy with respect to the relativistic rest mass m_a, i.e., the kinetic energy. The relativistic meson propagator then reads

$$iG_a(\kappa^\mu) = i\left[\kappa^\mu \kappa_\mu - m_a^2\right]^{-1} = \frac{1}{2m_a}\, i\left[k^0 - \frac{\boldsymbol{k}^2}{2m_a} + \frac{(k^0)^2}{2m_a}\right]^{-1}, \quad (a \in \{D, \pi\}). \tag{D.15}$$

The prefactor $1/(2m_a)$ in Eq. (D.15) can be eliminated by redefining the meson fields like $D^{0(\dagger)} \to (2m_D)^{1/2} D^{0(\dagger)}$ (similarly for $\bar{D}^0, \pi^0$). The Klein-Gordon propagators can then be described by the kinetic terms

$$\mathscr{L}_{\text{kin}} = D^{0\dagger}\left[i\partial_0 + \frac{\boldsymbol{\nabla}^2}{2m_D} + \frac{(i\partial_0)^2}{2m_D}\right] D^0 + \text{c.c.} + \pi^{0\dagger}\left[i\partial_0 + \frac{\boldsymbol{\nabla}^2}{2m_\pi} + \frac{(i\partial_0)^2}{2m_\pi}\right]\pi^0 \,. \tag{D.16}$$

Compared to Eq. (3.31), this Lagrangian exhibits terms quadratic in the energy derivative $i\partial_0$. They summarize all relativistic corrections to the respective one-body propagators. In principle, one could convert each kinetic term into the well-known nonrelativistic expansion form, i.e.,

$$D^{0\dagger}\left[i\partial_0 + \frac{\boldsymbol{\nabla}^2}{2m_D} + \frac{(i\partial_0)^2}{2m_D}\right] D^0 \to D^{0\dagger}\left[i\partial_0 + \frac{\boldsymbol{\nabla}^2}{2m_D} + \frac{\boldsymbol{\nabla}^4}{8m_D^3} + \cdots\right] D^0 \,, \tag{D.17}$$

by applying field redefinitions

$$D^{0\dagger} \to \left(1 - \frac{\boldsymbol{\nabla}^2}{4m_D^2} + \cdots\right) D^{0\dagger} \tag{D.18}$$

(similar for $\bar{D}^0, \pi^0$); see Refs. [112, 166].

Each $(i\partial_0)^2$ term in Eq. (D.16) is suppressed by a factor $k^0/(2m_a)$ compared to the linear $i\partial_0$ term. Relativistic corrections to D^0 ($\bar{D}^0$) propagators in the Faddeev equation are thus suppressed by factors $\sim \delta/(2m_D) \approx 0.002$ (N^{3}LO). For pion exchanges, suppression of relativistic contributions is much weaker. Let $\boldsymbol{p}_{\text{in/out}}$ be the incoming/outgoing relative DD^* momentum in a pion exchange interaction. The kinetic energy of the exchanged pion is then given by $k^0 = E - (p_{\text{in}}^2 + p_{\text{out}}^2)/(2m_D)$. For both low-momentum scales $p_{\text{in/out}} \sim P_X \sim 11\,\text{MeV}$ and $p_{\text{in/out}} \sim P_* = 117\,\text{MeV}$ of the three-body sector, this energy lies in the range $[0, E]$ and thus $k^0 \leq E \sim \delta$. For this reason, relativistic corrections in exchanged pions are suppressed by a factor $k^0/(2m_\pi) \leq \delta/(2m_\pi) = \chi_2$. Given the fact that pion exchanges are of NLO, relativistic pion corrections first enter at N^{2}LO.

Relativistic corrections to the vector meson propagators deserve a more detailed discussion. Let us consider a $D\pi$ pair moving at a total kinetic energy energy p^0 and a total momentum $\boldsymbol{p}$. As in the two-nucleon case [112], Lorentz invariance ensures that p^0 and $\boldsymbol{p}$ are related to the center-of-mass kinetic energy p_{cm}^0 via

$$p^0 - \frac{\boldsymbol{p}^2}{2M_{D\pi}} + \frac{(p^0)^2}{2M_{D\pi}} = p_{\text{cm}}^0 + \frac{(p_{\text{cm}}^0)^2}{2M_{D\pi}} \,. \tag{D.19}$$

The D^* pole position lies at $(p_{\text{cm}}^0)^{(\text{pole})} = E_*$. By plugging this condition into Eq. (D.19) and using $\boldsymbol{p}^2 \ll |M_{D\pi} + E_*|^2$, the pole position in the general frame yields

$$(p^0)^{(\text{pole})} = E_* + \frac{\boldsymbol{p}^2}{2(M_{D\pi} + E_*)} - \frac{\boldsymbol{p}^4}{8(M_{D\pi} + E_*)^3} + \dots \,. \tag{D.20}$$

Near the pole, the full D^* propagator can thus be written like

$$i\,G_*(p^\mu) = \frac{i\,Z(p^0)}{p^0 - (p^0)^{(\text{pole})}} + \text{reg}\,, \tag{D.21}$$

with $p^0 = E - \boldsymbol{p}^2/(2m_D) + \boldsymbol{p}^4/(8m_D^3) - \ldots$ in the DD^* system. In the nonrelativistic limit, the difference $p^0 - (p^0)^{(\text{pole})}$ must recover the Galilean-invariant expression $E_{\text{cm}} - E_* = E - \boldsymbol{p}^2/(2\mu_*) - E_*$, frequently used in this thesis. Indeed, we obtain this expression by expanding at $E_*/M_{D\pi} \approx 0$. That gives

$$p^0 - (p^0)^{(\text{pole})} = E - \frac{\boldsymbol{p}^2}{2\mu_*}\Bigg(1 - \underbrace{\frac{2\mu_* E_*}{M_{D\pi}^2}}_{\sim E_*/M_{D\pi}} - \underbrace{\frac{2\mu_*\boldsymbol{p}^2}{8M_{D\pi}^3} + \frac{2\mu_*\boldsymbol{p}^2}{8m_D^3}}_{\sim \boldsymbol{p}^2/M_{D\pi}^2} + \ldots\Bigg) - E_*\,, \tag{D.22}$$

where we used $2\mu_* \sim M$. All corrections in the parenthesis are suppressed by the total $D\pi$ mass and are thus extremely small. The first one ($\sim E_*/M_{D\pi} \sim \chi_2^3 + i\mathcal{N}\chi_2^3$) is of N^{3}LO size. The second and third ones are even smaller. We conclude that relativistic corrections can be neglected at NLO.

The conclusion that relativistic corrections in the two-body sector are suppressed by the total mass is a remarkable finding. We have validated this strong statement explicitly by recalculating the $D\pi$ self-energy loop using the relativistic Klein-Gordon propagators above. Terms involving the small three-momenta $\boldsymbol{p}^2$ indeed turn out to be suppressed by powers of the total mass.

D.4 Partial wave projection of the pion exchange potential

In this section, we perform the partial wave projection of the pion exchange potential in Eq. (3.68).

Following the projection prescription of Eq. (C.12), the partial wave potentials are given by

$$\begin{aligned} V^{{}^3L_1,{}^3L_1'}(p,q;E) &= \Big\langle P_{{}^3L_1,{}^3L_1'} \Big| V \Big\rangle (p,q;E) \\ &= \frac{1}{(4\pi)^2\,3} \sum_{i,j} \int_{\Omega_{\boldsymbol{p}},\Omega_{\boldsymbol{q}}} P^{ji}_{{}^3L_1',{}^3L_1}(\hat{\boldsymbol{q}},\hat{\boldsymbol{p}})\; V^{ij}(\boldsymbol{p},\boldsymbol{q};E)\,. \end{aligned} \tag{D.23}$$

The pion exchange potential has the form

$$V^{ij}(\boldsymbol{p},\boldsymbol{q};E) = -g^2\,m_\pi \frac{(\xi\boldsymbol{p}+\boldsymbol{q})^i\,(\xi\boldsymbol{q}+\boldsymbol{p})^j}{U_{\pi;D,D}(p,q;E) + \boldsymbol{p}\cdot\boldsymbol{q}}\,, \tag{D.24}$$

with $U_{\pi;D,D}$ defined in Eq. (C.14). The calculations of the partial wave potentials are straight-forward but lengthy. Thus, we only exemplify the procedure for the simplest case $L = L' = 0$.

First, we calculate the projector $P_{{}^3S_1,{}^3S_1}$ in the cartesian representation using the definitions of Eq. (C.2), (C.3), and (C.7). We obtain

$$P^{ij}_{{}^3S_1,{}^3S_1}(\hat{\boldsymbol{p}},\hat{\boldsymbol{q}}) = 4\pi \sum_{m_J} \sum_{m_L,m_S} \mathrm{C}^{1m_J}_{0m_L,1m_S}\, Y_0^{m_L}(\hat{\boldsymbol{p}})\,\big(\boldsymbol{\chi}_1^{m_S}\big)^i \sum_{m_{L'},m_{S'}} \mathrm{C}^{1m_J}_{0m_{L'},1m_{S'}}\, Y_0^{m_{L'}\,*}(\hat{\boldsymbol{p}})\,\big(\boldsymbol{\chi}_1^{m_{S'}}\big)^{j\,*} \tag{D.25a}$$

$$= \sum_{m_J}\sum_{m_S} \mathrm{C}^{1m_J}_{00,1m_S}\,\big(\boldsymbol{\chi}_1^{m_S}\big)^i \sum_{m_{S'}} \mathrm{C}^{1m_J}_{00,1m_{S'}}\,\big(\boldsymbol{\chi}_1^{m_{S'}}\big)^{j\,*} \tag{D.25b}$$

$$= \sum_{m_J} \big(\boldsymbol{\chi}_1^{m_J}\big)^i \big(\boldsymbol{\chi}_1^{m_J}\big)^{j\,*} = \delta^{ij}\,. \tag{D.25c}$$

The last equation follows from the fact that the spin functions represent a $\mathbb{C}^3$ basis. The other three projection operators are given in Eq. (3.74b).

Evaluating Eq. (D.23) then gives

$$
\begin{aligned}
V^{{}^3S_1,{}^3S_1}(p,q;E) &= -\frac{1}{(4\pi)^2 3}\, g^2 m_\pi \int_{\Omega_{\boldsymbol{p}},\Omega_{\boldsymbol{q}}} \frac{\xi\left(p^2+q^2\right)+\left(1+\xi^2\right)\boldsymbol{p}\cdot\boldsymbol{q}}{U_{\pi;D,D}(p,q;E)+\boldsymbol{p}\cdot\boldsymbol{q}} && \text{(D.26a)}\\
&= -\frac{1}{6}\, g^2 m_\pi \int_{-1}^{1} \mathrm{d}x\, \frac{\xi\left(p^2+q^2\right)P_0(x)+\left(1+\xi^2\right)pq\,P_1(x)}{U_{\pi;D,D}(p,q;E)+pqx} && \text{(D.26b)}\\
&= -\frac{1}{6}\, g^2 m_\pi \left[\xi\left(p^2+q^2\right) I^{(0)}_{\pi;D,D} + \left(1+\xi^2\right)pq\, I^{(1)}_{\pi;D,D}\right](p,q;E)\,. && \text{(D.26c)}
\end{aligned}
$$

The integrals $I^{(l)}_{\pi;D,D}$ are given in App. C.2. The other three partial wave potentials are given in Eqs. (3.79b)-(3.79d).

D.5 Numerical solution of the Faddeev amplitude

Let $\{q_i,\ 1\le i\le N\}\subseteq\mathbb{C}$ be quadrature points of the interval $[0,\Lambda]$ with associated weights $\{w_i,\ 1\le i\le N\}\subseteq\mathbb{C}$. The Faddeev equation then takes the approximate form

$$
\begin{aligned}
\mathscr{T}_i(p';E) &\equiv \vec{T}^{\,1^+}\left(q_i,p';E\right) && \text{(D.27a)}\\
&\approx -\underline{\underline{K}}^{1^+}\left(q_i,p';E\right)\cdot\vec{e}_1 + \frac{1}{2\pi^2}\sum_{j=1}^{N} w_j q_j^2\, \underline{\underline{K}}^{1^+}\left(q_i,q_j;E\right) \mathscr{G}^{(\mathrm{f})}_{*}\left(q_j;E\right)\cdot\vec{T}^{\,1^+}\left(q_j,p';E\right) && \text{(D.27b)}\\
&\equiv -\mathscr{V}_i(p';E)+\sum_{j=1}^{N}\mathscr{K}^{(\Lambda,C_0)}_{ij}(E)\,\mathscr{T}_j(p';E) \quad (1\le i\le N) && \text{(D.27c)}\\
\Leftrightarrow \sum_{j=1}^{N}&\left(\mathscr{K}^{(\Lambda,C_0)}(E)-\mathbb{1}\right)_{ij}\mathscr{T}_j(p';E)\approx\mathscr{V}_i(p';E)\,, && \text{(D.27d)}
\end{aligned}
$$

where the integration kernel and the inhomogeneity are defined as

$$
\begin{aligned}
\mathscr{K}^{(\Lambda,C_0)}_{ij}(E) &\equiv \frac{w_j q_j^2}{2\pi^2}\,\underline{\underline{K}}^{1^+}\left(q_i,q_j;E\right)\mathscr{G}^{(\mathrm{f})}_{*}\left(q_j;E\right), && \text{(D.28a)}\\
\mathscr{V}_i(p';E) &\equiv \underline{\underline{K}}^{1^+}\left(q_i,p';E\right)\cdot\vec{e}_1\,. && \text{(D.28b)}
\end{aligned}
$$

For the following discussion, we made the dependence of the integration kernel on Λ and C_0 explicit.

The linear Eq. (D.27d) can be solved numerically for the amplitude vector $(\mathscr{T}_i)_{1\le i\le N}$ for fixed p' and E. Note that the loop integral of the Faddeev equation does not involve a singularity on the real axis since the pole of the D^{0*} ($\bar{D}^{0*}$) propagator lies in the complex plain at

$$
q_{\mathrm{pole}} = \sqrt{2\mu_*\left(E+i\epsilon-E_*\right)}\,. \tag{D.29}
$$

Thus, we do not have to split the equation into a principle value integral and an imaginary part.

D.5.1 Renormalization for a bound $X(3872)$

In the vicinity of the $X(3872)$ pole, i.e., at $E\approx E_X$, the inhomogeneous term of Eq. (D.27d) can be neglected against the diverging amplitude vector. The equation then looses its dependence on p' and becomes homogeneous. It follows that the Fredholm determinant

$$
\mathscr{F}^{(\Lambda,C_0)}(E)\equiv\lim_{N\to\infty}\det\left(\mathscr{K}^{(\Lambda,C_0)}(E)-\mathbb{1}\right)\in\mathbb{C} \tag{D.30}
$$

of the Faddeev equation has a root at E_X.

For fixed Λ, we renormalize the Faddeev equation onto a certain binding energy $\delta_X > 0$ of the $X(3872)$. That is achieved by tuning the three-body force $C_0 \in \mathbb{R}$. In doing so, we obtain a prediction for the imaginary part of the pole, i.e., for the width Γ_X. More precisely, we search the two-dimensional root of the function

$$\mathbb{R}^2 \ni \begin{pmatrix} C_0 \\ \Gamma_X \end{pmatrix} \mapsto \begin{pmatrix} \operatorname{Re} \mathscr{F}^{(\Lambda,C_0)}(\delta - \delta_X - i\Gamma_X/2) \\ \operatorname{Im} \mathscr{F}^{(\Lambda,C_0)}(\delta - \delta_X - i\Gamma_X/2) \end{pmatrix} \in \mathbb{R}^2 . \tag{D.31}$$

In repeating this procedure for many cutoffs $\Lambda \gg (2\mu_* \delta)^{1/2} \approx 117\,\text{MeV}$ and $\delta_X > 0$, we obtain a curve $\Gamma_X(\delta_X)$, which should become independent of the cutoff as $\Lambda \to \infty$.

D.6 Analytic expressions for NLO width corrections

In this section, we derive analytic expressions for the NLO width corrections caused by single self-energy insertions and the charged meson loop.

D.6.1 Self-energy correction

The width correction $\Delta\Gamma_X^{(1\bar{\Sigma}_*)}$ due to single self-energy corrections in the D^{0*} ($\bar{D}^{0*}$) propagator can be obtained by calculating the loop integral in Fig. 3.20(a). For that, we insert the definition of the self-energy insertion $\bar{\Sigma}_*$ given in Fig. 3.12. The integral is then given by two terms, of which the first contains the dynamical $D\pi$ and the second the self-energy evaluated at $E_\text{cm} = E_*$.

Let i (i') be the incoming (outgoing) polarization. Moreover, let $(q^0, \boldsymbol{q})$ and $(s^0, \boldsymbol{s})$ be the four-momenta of the outer DD^* loop and the inner $D\pi$ self-energy loop, respectively. In $D = 1+d$ dimensions, we then obtain the integral

$$\begin{aligned}
&\left(iT_{00}^{(\text{LO})}(E)\right)^2 \left(\frac{\Lambda_\text{PDS}}{2}\right)^{4-D} \int \frac{\mathrm{d}^D q}{(2\pi)^D} \frac{i^3}{\left[q^0 - \frac{\boldsymbol{q}^2}{2m_D} + i\epsilon\right]\left[E - q^0 - \frac{\boldsymbol{q}^2}{2M_{D\pi}} - E_* + i\epsilon\right]^2} \\
&\qquad \times \left[-i\bar{\Sigma}_*\left(E - q^0 - \frac{\boldsymbol{q}^2}{2M_{D\pi}}\right)\right]
\end{aligned} \tag{D.32}$$

with self-energy insertion

$$-i\bar{\Sigma}_*\left(E - q^0 - \frac{\boldsymbol{q}^2}{2M_{D\pi}}\right)\delta^{ii'} = \left[-i\Sigma_*\left(E - q^0 - \frac{\boldsymbol{q}^2}{2M_{D\pi}}\right) + i\Sigma_*(E_*)\right]\delta^{ii'} \tag{D.33a}$$

$$\begin{aligned}
&= \left(\frac{\Lambda_\text{PDS}}{2}\right)^{4-D} \int \frac{\mathrm{d}^D s}{(2\pi)^D} \Bigg[\frac{i^2\left(+g\, s^i\right)\left(-g\, s^{i'}\right)}{\left[E - q^0 - s^0 - \frac{(\xi(-\boldsymbol{q})-\boldsymbol{s})^2}{2m_D} + i\epsilon\right]\left[s^0 - \frac{((1-\xi)(-\boldsymbol{q})+\boldsymbol{s})^2}{2m_\pi} + i\epsilon\right]} \\
&\qquad\qquad - \left[E - q^0 - \frac{\boldsymbol{q}^2}{2M_{D\pi}} \to E_*\right] \Bigg]
\end{aligned} \tag{D.33b}$$

$$= -ig^2 \frac{\delta_{ii'}}{d} \left(\frac{\Lambda_\text{PDS}}{2}\right)^{3-d} \int \frac{\mathrm{d}^d s}{(2\pi)^d} \left[\frac{\boldsymbol{s}^2}{E + i\epsilon - q^0 - \frac{\boldsymbol{q}^2}{2M_{D\pi}} - \frac{\boldsymbol{s}^2}{2\mu_{D\pi}}} - \frac{\boldsymbol{s}^2}{E_* + i\epsilon - \frac{\boldsymbol{s}^2}{2\mu_{D\pi}}}\right] \tag{D.33c}$$

$$= ig^2 \frac{\delta_{ii'}}{d} \left(\frac{\Lambda_\text{PDS}}{2}\right)^{3-d} \int \frac{\mathrm{d}^d s}{(2\pi)^d} \frac{\boldsymbol{s}^2\left[E - q^0 - \frac{\boldsymbol{q}^2}{2M_{D\pi}} - E_* + i\epsilon\right]}{\left[q^0 + \frac{\boldsymbol{q}^2}{2M_{D\pi}} + \frac{\boldsymbol{s}^2}{2\mu_{D\pi}} - (E + i\epsilon)\right]\left[\frac{\boldsymbol{s}^2}{2\mu_{D\pi}} - (E_* + i\epsilon)\right]} . \tag{D.33d}$$

In Eq. (D.33c), the residue theorem was used to solve the s^0 integral. After applying the residue theorem for q^0 in Eq. (D.32), we obtain the overall expression

$$-ig^2\frac{1}{d}\left(T_{00}^{(\mathrm{LO})}(E)\right)^2\left(\frac{\Lambda_{\mathrm{PDS}}}{2}\right)^{2(3-d)}\int\frac{\mathrm{d}^d q}{(2\pi)^d}\int\frac{\mathrm{d}^d s}{(2\pi)^d} \\ \times\frac{\boldsymbol{s}^2}{\left[\frac{\boldsymbol{q}^2}{2\mu_*}-(E-E_*+i\epsilon)\right]\left[\frac{\boldsymbol{q}^2}{2\mu_*}+\frac{\boldsymbol{s}^2}{2\mu_{D\pi}}-(E+i\epsilon)\right]\left[\frac{\boldsymbol{s}^2}{2\mu_{D\pi}}-(E_*+i\epsilon)\right]} \tag{D.34}$$

After introducing and solving a Feynman parameter integral we obtain for $d\to 3$ the result

$$-i\frac{g^2}{3\pi^3}\left(T_{00}^{(\mathrm{LO})}(E)\right)^2\,\mu_*^4\,r^{5/2} \\ \times\Bigg[\frac{1}{2}(E-4E_*)\left(\frac{1}{d-3}+\gamma-2+\ln\left(-\frac{\sqrt{r}}{4\pi}\frac{2\mu_*(E+i\epsilon)}{(\Lambda_{\mathrm{PDS}}/2)^2}\right)\right) \\ -E_*\left(1+\frac{\sqrt{E_*+i\epsilon}}{\sqrt{E+i\epsilon-E_*}}\tan^{-1}\left(\frac{\sqrt{E+i\epsilon-E_*}}{\sqrt{E_*+i\epsilon}}\right) \\ -3\frac{\sqrt{E+i\epsilon-E_*}}{\sqrt{E_*+i\epsilon}}\tan^{-1}\left(\frac{\sqrt{E_*+i\epsilon}}{\sqrt{E+i\epsilon-E_*}}\right)\right)\Bigg] \tag{D.35}$$

with $r=\mu_*/\mu_{D\pi}$ and Euler-Mascheroni constant γ. This expression (without the two LO amplitudes and the prefactor i) has to be evaluated at $E=E_X^{(\mathrm{LO})}=E_*-\delta_X$ in order to obtain the coefficient $\bar{b}^{(1\bar{\Sigma}_*)}$.

The overall width shift then reads

$$\Delta\Gamma_X^{(1\bar{\Sigma}_*)}(\delta_X) = -2Z^{(\mathrm{LO})}\,\mathrm{Im}\,\bar{b}^{(1\bar{\Sigma}_*)} \tag{D.36a}$$

$$= -\Gamma_{D^0\pi^0}\left(1+\theta(\delta-\delta_X)\left(-1+3\left(\frac{\delta_X}{\delta}\right)^{1/2}-3\frac{\delta_X}{\delta}+\left(\frac{\delta_X}{\delta}\right)^{3/2}\right)\right)\left(1+\mathcal{O}(\mathcal{N})\right) \tag{D.36b}$$

$$\approx -3\sqrt{\frac{\delta_X}{\delta}}\,\Gamma_{D^0\pi^0}\,, \tag{D.36c}$$

where we neglected higher orders in $\mathcal{N}$ and $\chi_3=(\delta_X/\delta)^{1/2}$. Note that dependences of $\mathrm{Im}\,\bar{b}^{(1\bar{\Sigma}_*)}$ on the Λ_{PDS} subtractions scale are suppressed by $\mathcal{N}$. Thus, a respective counter part is not needed at NLO.

Interestingly, in the (unphysical) case $\delta_X>\delta$, the shift identically cancels the partial width $\Gamma_{D^0\pi^0}$ the $X(3872)$ receives from its constituent D^{0*} ($\bar{D}^{0*}$). This observation, however, is not surprising. For $\delta_X>\delta$, the $X(3872)$ turns into a three-body bound state below the $D^0\bar{D}^0\pi^0$ threshold. Thus, it can no more decay to $D^0\bar{D}^0\pi^0$ and consequently must not exhibit a partial width for this channel.

D.6.2 Charged meson correction

The width shift caused by charged mesons can be calculated by iterating the effective interaction $\mathcal{J}_{\mathrm{c}}(E)$ of Eq. (3.108b) alongside C_0 (without pion exchange counterterm $+V^{(\infty)}$). The respective diagram series can be obtained from Fig. 3.16 by neglecting pion exchanges and choosing LO propagators $iG_*^{(\mathrm{LO})}$ everywhere. The corresponding Faddeev equation reads

$$T_{00}^{(\mathcal{J}_{\mathrm{c}})}(E) = -(C_0(\Lambda)+\mathcal{J}_{\mathrm{c}}(E))+\frac{1}{2\pi^2}\int_0^{\Lambda}\mathrm{d}q\,q^2\frac{C_0(\Lambda)+\mathcal{J}_{\mathrm{c}}(E)}{E-\frac{q^2}{2\mu_*}-E_*+i\epsilon}\,T_{00}^{(\mathcal{J}_{\mathrm{c}})}(E)\,. \tag{D.37}$$

It has the (unrenormalized) solution

$$T_{00}^{(\mathcal{J}_c)}(E) = -\left[\frac{1}{C_0(\Lambda)+\mathcal{J}_c(E)} + 2\mu_* J_{3,0}^{(\Lambda)}\Big(2\mu_*\left(E_* - E - i\epsilon\right)\Big)\right]^{-1} \tag{D.38}$$

with s-wave integral function $J_{3,0}^{(\Lambda)}$ defined in Eq. (B.11f). Moreover, we the effective interaction is given by

$$\mathcal{J}_c(E) = -4\,C_0^2\,2\mu_{*,c}\,J_{3,0}^{(\Lambda)}\Big(2\mu_{*,c}\left(\delta+\nu-E-i\epsilon\right)\Big). \tag{D.39}$$

We renormalize the amplitude by demanding a pole at $E_X^{(\mathcal{J}_c)} = E_X^{(\mathrm{LO})} - i\Delta\Gamma_X^{(\mathcal{J}_c)}/2$. Using the short-hand notations

$$J \equiv 2\mu_*\,J_{3,0}^{(\Lambda)}\Big(2\mu_*\left(E_* - E_X^{(\mathcal{J}_c)} - i\epsilon\right)\Big), \tag{D.40a}$$

$$J_c \equiv 2\mu_{*,c}\,J_{3,0}^{(\Lambda)}\Big(2\mu_{*,c}\left(\delta+\nu-E_X^{(\mathcal{J}_c)} - i\epsilon\right)\Big), \tag{D.40b}$$

one then obtains the quadratic equation

$$C_0^{-2} + J C_0^{-1} - 4 J J_c = 0 \tag{D.41}$$

for C_0^{-1}. It has the two solutions

$$C_0^{-1} = -\frac{J}{2}\left(1 \pm \sqrt{1+16 J_c/J}\,\right) \in \mathbb{R}. \tag{D.42}$$

The solution we are interested in is the "+" solution since it recovers the old result $C_0^{(\mathrm{LO})\,-1} = -J$ in the limit $J_c \to 0$.

Note that $J, J_c \in \mathbb{C}$, but $C_0 \in \mathbb{R}$ if no inelastic three-body channels are present. Thus, Eq. (D.42) actually represents the equation system

$$C_0^{-1} = -\mathrm{Re}\,\frac{1}{J}\left(1+\sqrt{1+16 J_c/J}\,\right), \tag{D.43a}$$

$$0 = -\mathrm{Im}\,\frac{1}{J}\left(1+\sqrt{1+16 J_c/J}\,\right) \tag{D.43b}$$

for the two unknowns C_0 and $\Delta\Gamma_X^{(\mathcal{J}_c)}/2$. It can be solved approximately for not too small δ_X using the relations $\Delta\Gamma_X^{(\mathcal{J}_c)}/2 \ll \delta_X$ and $(\Gamma_{0*} + \Delta\Gamma_X^{(\mathcal{J}_c)})/2 \ll \nu$. That yields

$$C_0^{(\mathcal{J}_c)\,-1} = -\frac{1+\sqrt{1+16\,\mu_{*,c}/\mu_*}}{2}\,\frac{\mu_*}{2\pi}\left(\frac{2}{\pi}\Lambda - \sqrt{2\mu_*\delta_X}\,(1-\eta) - \eta\sqrt{2\mu_{*,c}\nu} + \mathcal{O}\left(\Lambda^{-1}\right)\right), \tag{D.44a}$$

$$\Delta\Gamma_X^{(\mathcal{J}_c)} = -\frac{\eta}{1-\eta}\sqrt{\frac{\mu_{*,c}}{\mu_*}}\sqrt{\frac{\delta_X}{\nu}}\,\Gamma_{0*}\,, \tag{D.44b}$$

where

$$\eta \equiv \frac{1}{2}\,\frac{16\,\mu_{*,c}/\mu_*}{\sqrt{1+16\,\mu_{*,c}/\mu_*}\,\left(1+\sqrt{1+16\,\mu_{*,c}/\mu_*}\right)} \xrightarrow{\mu_{*,c}\to 0} 0\,. \tag{D.45}$$

These solutions fulfill the conditions $C_0^{(\mathcal{J}_c)\,-1} \to C_0^{(\mathrm{LO})\,-1}$ and $\Delta\Gamma_X^{(\mathcal{J}_c)} \to 0$ in the limit of no charged mesons, i.e., for $\mu_{*,c} \to 0$. Given Eq. (D.44b), the assumption $\Delta\Gamma_X^{(\mathcal{J}_c)}/2 \ll \delta_X$ is fulfilled for all $\delta_X > 0.04\,\mathrm{keV}$.

The $\mu_{*,c}$ dependent prefactor in Eq. (D.44a) suppresses the three-body force C_0 globally by a factor of ≈ 0.4. This suppression is in agreement with numerical calculations shown in Fig. 3.24.

D.7 Line shape integral

In this section, we calculate the $D^0\bar{D}^0\pi^0$ production rate $\mathrm{d}\Gamma/\mathrm{d}E$ from the matrix element in Fig. 3.25.

D.7.1 Matrix element

In Fig. 3.25, either the outgoing D^0 or $\bar{D}^0$ stems from the ultimate $D^* \to D\pi$ decay. Both possibilities have to be taken into account. Thus, before calculating the matrix element itself, we first calculate the transition from the initial short-distance channel $|\phi_+\rangle$, a $C = +$ eigenstate, to a specific DD^* flavor eigenstate [see notation of Eq. (3.66)]. Moreover, we define

$$|\psi_\pm\rangle \equiv \frac{1}{\sqrt{2}}\big(|\psi\rangle \pm |\bar{\psi}\rangle\big). \tag{D.46}$$

We first consider transition to the outgoing flavor eigenstate $|\psi\rangle$. Let i, i' be the polarizations in $|\phi_+\rangle$ and $|\psi\rangle$. The short-range vertex (crossed circle) is defined in the ${}^3S_1$ channel of the $X(3872) \equiv \psi_+$. Its Feynman rule thus reads $F\,\delta^{ii'}$ with $F \in \mathbb{R}$. In addition to the short-range vertex, we have to consider rescattering in the DD^* sector (second diagram in Fig. 3.25). For that, let $\boldsymbol{p}_{D^0}$ be the outgoing D^0 momentum. We then obtain

$$\begin{aligned}
iT^{ii'}_{\phi_+\psi}(\boldsymbol{p}_{D^0};E) &\equiv \langle\psi|\,i\hat{T}\,|\phi_+\rangle^{ii'}(\boldsymbol{p}_{D^0};E) &\text{(D.47a)}\\
&= \left[\frac{1}{\sqrt{2}}\Big(\langle\psi_+| + \langle\psi_-|\Big)\,i\hat{T}\,|\phi_+\rangle\right]^{ii'}(\boldsymbol{p}_{D^0};E) &\text{(D.47b)}\\
&= \frac{1}{\sqrt{2}}\,\langle\psi_+|\,i\hat{T}\,|\phi_+\rangle^{ii'}(\boldsymbol{p}_{D^0};E) &\text{(D.47c)}\\
&= \frac{F\,\delta^{ii'}}{\sqrt{2}} - \frac{F\,\delta^{ij}}{\sqrt{2}}\int\frac{\mathrm{d}^3q}{(2\pi)^3}\,\mathscr{G}^{(\mathrm{f})}_*(|-\boldsymbol{q}|;E)\,T^{ji'}(\boldsymbol{q},\boldsymbol{p}_{D^0};E) &\text{(D.47d)}\\
&= \frac{F\,\delta^{ii'}}{\sqrt{2}}\left(1 - \frac{1}{2\pi^2}\int_0^\Lambda \mathrm{d}q\,q^2\,\mathscr{G}^{(\mathrm{f})}_*(q;E)\,T_{00}(q,p_{D^0};E)\right), &\text{(D.47e)}
\end{aligned}$$

Equation (D.47c) follows from conservation of C parity. For Eq. (D.47d), we have directly performed the q^0 integral in the usual way. Moreover, Eq. (D.47e) follows from the definition of the short-range factor in the ${}^3S_1$ channel. In the same way, we obtain

$$iT^{ii'}_{\phi_+\bar{\psi}}(\boldsymbol{p}_{\bar{D}^0};E) = \frac{F\,\delta^{ii'}}{\sqrt{2}}\left(1 - \frac{1}{2\pi^2}\int_0^\Lambda \mathrm{d}q\,q^2\,\mathscr{G}^{(\mathrm{f})}_*(q;E)\,T_{00}(q,p_{\bar{D}^0};E)\right). \tag{D.48}$$

The final matrix element is given by a sum over the two possible transitions and attaching a final $D^* \to D\pi$ vertex. In the center-of-mass system ($\boldsymbol{p}_{\pi^0} \equiv -\boldsymbol{p}_{D^0} - \boldsymbol{p}_{\bar{D}^0}$), we obtain

$$\begin{aligned}
i\mathscr{M}^{i}_{\to D^0\bar{D}^0\pi^0}(\boldsymbol{p}_{D^0},\boldsymbol{p}_{\bar{D}^0},\boldsymbol{p}_{\pi^0};E) &\equiv \left\langle D^0\bar{D}^0\pi^0\right|\,i\hat{T}\,|\phi_+\rangle^{i}(\boldsymbol{p}_{D^0},\boldsymbol{p}_{\bar{D}^0},\boldsymbol{p}_{\pi^0};E) &\text{(D.49a)}\\
&= iT^{ij}_{\phi_+\psi}(\boldsymbol{p}_{D^0};E)\;i\mathscr{G}^{(\mathrm{f})}_*(|-\boldsymbol{p}_{D^0}|;E)\;g\,(\xi\boldsymbol{p}_\pi - (1-\xi)\boldsymbol{p}_{\bar{D}^0})^j\\
&\quad + iT^{ij}_{\phi_+\bar{\psi}}(\boldsymbol{p}_{\bar{D}^0};E)\;i\mathscr{G}^{(\mathrm{f})}_*(|-\boldsymbol{p}_{\bar{D}^0}|;E)\;g\,(\xi\boldsymbol{p}_\pi - (1-\xi)\boldsymbol{p}_{D^0})^j &\text{(D.49b)}\\
&= -ig\,\frac{F}{\sqrt{2}}\,\Big(\boldsymbol{p}_{D^0} + \xi\boldsymbol{p}_{\bar{D}^0}\Big)^i\,\mathscr{G}^{(\mathrm{f})}_*(p_{D^0};E)\\
&\qquad\times\left(1 - \frac{1}{2\pi^2}\int_0^\Lambda \mathrm{d}q\,q^2\,\mathscr{G}^{(\mathrm{f})}_*(q;E)\,T_{00}(q,p_{D^0};E)\right) &\text{(D.49c)}\\
&\quad + \Big[\boldsymbol{p}_{D^0} \longleftrightarrow \boldsymbol{p}_{\bar{D}^0}\Big]. &\text{(D.49d)}
\end{aligned}$$

D.7.2 $D^0\bar{D}^0\pi^0$ production rate

The rate $\mathrm{d}\Gamma/\mathrm{d}E$ can be calculated from the matrix element by averaging over incoming degrees of freedom (polarization i) and integrating over outgoing momenta, i.e.,

$$\begin{aligned}\frac{\mathrm{d}\Gamma}{\mathrm{d}E} = \int \frac{\mathrm{d}^3 p_{D^0}}{(2\pi)^3} \int \frac{\mathrm{d}^3 p_{\bar{D}^0}}{(2\pi)^3} \int \frac{\mathrm{d}^3 p_{\pi^0}}{(2\pi)^3} (2\pi)^4 \, \delta^{(3)}\Big(\boldsymbol{p}_{D^0} + \boldsymbol{p}_{\bar{D}^0} + \boldsymbol{p}_{\pi^0}\Big) \, \delta\left(E - \frac{\boldsymbol{p}_{D^0}^2 + \boldsymbol{p}_{\bar{D}^0}^2}{2m_D} - \frac{\boldsymbol{p}_{\pi^0}^2}{2m_\pi}\right) \\ \times \frac{1}{3} \sum_i \left|\mathscr{M}^i_{\to D^0\bar{D}^0\pi^0}(\boldsymbol{p}_{D^0}, \boldsymbol{p}_{\bar{D}^0}, \boldsymbol{p}_{\pi^0}; E)\right|^2 . \end{aligned} \tag{D.50}$$

The momentum conserving delta function can be performed right away by setting $\boldsymbol{p}_{\pi^0} = -\boldsymbol{p}_{D^0} - \boldsymbol{p}_{\bar{D}^0}$ everywhere. The energy conserving delta function then takes the form

$$\delta\left(E - \frac{\boldsymbol{p}_{D^0}^2 + \boldsymbol{p}_{\bar{D}^0}^2}{2m_D} - \frac{(-\boldsymbol{p}_{D^0} - \boldsymbol{p}_{\bar{D}^0})^2}{2m_\pi}\right) = \delta\left(E - \frac{\boldsymbol{p}_{D^0}^2 + \boldsymbol{p}_{\bar{D}^0}^2}{2\mu_{D\pi}} - \frac{\boldsymbol{p}_{D^0} \cdot \boldsymbol{p}_{\bar{D}^0}}{m_\pi}\right) \tag{D.51a}$$

$$= \frac{m_\pi}{p_{D^0} p_{\bar{D}^0}} \, \delta(x - x_0) \tag{D.51b}$$

with $x \equiv \boldsymbol{p}_{D^0} \cdot \boldsymbol{p}_{\bar{D}^0} / (p_{D^0} p_{\bar{D}^0})$ and

$$x_0 \equiv \frac{m_\pi}{p_{D^0} p_{\bar{D}^0}} \left(E - \frac{p_{D^0}^2 + p_{\bar{D}^0}^2}{2\mu_{D\pi}}\right). \tag{D.52}$$

Moreover, the sum over the squared matrix element in the center-of-mass system reads

$$\begin{aligned} &\sum_i \left[\mathscr{M}^i_{\to D^0\bar{D}^0\pi^0} \mathscr{M}^{*i}_{\to D^0\bar{D}^0\pi^0}\right](\boldsymbol{p}_{D^0}, \boldsymbol{p}_{\bar{D}^0}, -\boldsymbol{p}_{D^0} - \boldsymbol{p}_{\bar{D}^0}; E) \\ &\quad = g^2 \frac{F^2}{2} \Bigg[\Big(\boldsymbol{p}_{D^0} + \xi \boldsymbol{p}_{\bar{D}^0}\Big)^2 \, |\mathcal{J}_*(p_{D^0}; E)|^2 + \Big[\boldsymbol{p}_{D^0} \leftrightarrow \boldsymbol{p}_{\bar{D}^0}\Big] \\ &\qquad + \Big(\boldsymbol{p}_{D^0} + \xi \boldsymbol{p}_{\bar{D}^0}\Big) \cdot \Big(\boldsymbol{p}_{\bar{D}^0} + \xi \boldsymbol{p}_{D^0}\Big) 2 \, \mathrm{Re} \, \Big(\mathcal{J}_*(p_{D^0}; E) \mathcal{J}_*^*(p_{\bar{D}^0}; E)\Big) \Bigg] \end{aligned} \tag{D.53}$$

with $\mathcal{J}_*$ defined in Eq. (3.116a).

By expressing the momentum integrals of Eq. (D.50) in terms of x, we find

$$\begin{aligned} \frac{\mathrm{d}\Gamma}{\mathrm{d}E} &= \frac{1}{(2\pi)^6} \, 4\pi \int_0^\infty \mathrm{d}p_{D^0} \, p_{D^0}^2 \, 2\pi \int_0^\infty \mathrm{d}p_{\bar{D}^0} \, p_{\bar{D}^0}^2 \int_{-1}^1 \mathrm{d}x \, 2\pi \, \frac{m_\pi}{p_{D^0} p_{\bar{D}^0}} \delta(x - x_0) \\ &\qquad \times \frac{1}{3} \sum_i \left|\mathscr{M}^i_{\to D^0\bar{D}^0\pi^0}(\boldsymbol{p}_{D^0}, \boldsymbol{p}_{\bar{D}^0}, -\boldsymbol{p}_{D^0} - \boldsymbol{p}_{\bar{D}^0}; E)\right|^2 \end{aligned} \tag{D.54a}$$

$$\begin{aligned} &= \frac{g^2 F^2 m_\pi}{24\pi^3} \int_0^\infty \mathrm{d}p_{D^0} \, p_{D^0} \int_0^\infty \mathrm{d}p_{\bar{D}^0} \, p_{\bar{D}^0} \, \theta(1 - x_0) \, \theta(1 + x_0) \\ &\qquad \times \Bigg[\Big(p_{D^0}^2 + \xi^2 p_{\bar{D}^0}^2 + 2\xi \, p_{D^0} p_{\bar{D}^0} \, x_0\Big) \, |\mathcal{J}_*(p_{D^0}; E)|^2 + \Big[p_{D^0} \leftrightarrow p_{\bar{D}^0}\Big] \\ &\qquad + \Big(\xi \left(p_{D^0}^2 + p_{\bar{D}^0}^2\right) + (1 + \xi^2) \, p_{D^0} p_{\bar{D}^0} \, x_0\Big) 2 \, \mathrm{Re} \, \Big(\mathcal{J}_*(p_{D^0}; E) \mathcal{J}_*^*(p_{\bar{D}^0}; E)\Big) \Bigg]. \end{aligned} \tag{D.54b}$$

Due to the two Heaviside functions, representing energy conservation, the two momenta p_{D^0} and $p_{\bar{D}^0}$ can maximally be $(2\mu_* E)^{1/2}$. Finally, by inserting x_0 as defined above, we obtain the rate as given in Eq. (3.115).

In numerical calculations, we first discretize the interval $[0, \Lambda]$ to a set of momenta $A \equiv \{q_i, 1 \leq i \leq N\}$. Afterwards, we solve the Faddeev equation for all outgoing momenta $p' \in A$ separately after the amplitude vector $\{T_{00}(q_i, p'; E), 1 \leq i \leq N\}$. The integrals $\mathcal{J}_*(q_i; E)$ are then simply given by sums over the discretized amplitudes. In order to calculate the rate properly, one needs to choose a cutoff $\Lambda > (2\mu_* E)^{1/2}$.

E Calculations for nuclear (d, p) reactions (Chapter 4)

In this chapter, we present calculations for the study of $^{10}\mathrm{Be}\,(\mathrm{d},\,\mathrm{p})\,^{11}\mathrm{Be}$ in Halo EFT.

E.1 Self-energies

In the following, we give insights into the calculation of the p-n (c-n) self-energies in EFT($\not\pi$) (Halo EFT).

E.1.1 Proton-neutron sector

The p-n self-energy loops $-i\Sigma_b$ ($b \in \{\mathrm{d}, \mathrm{v}\}$) of the dibaryon fields d_m ($^3s_1$) and v ($^1s_0$) are shown in Fig. 4.5. In order to calculate them correctly, we have to consider the anticommutation relation $\{p_\alpha,\, n_\beta\} = 0$, which follows from Eq. (4.5b). In fact, we will show that this relation has no influence on the overall sign of the self-energies and we may switch to commutation relations $[p_\alpha,\, n_\beta] = 0$ between proton and neutron.

The self-energy loops represent interactions which are second order in the couplings g_b. For the deuteron case, we have to evaluate the matrix element

$$
\begin{aligned}
&\frac{1}{2!}\left\langle d_{m',p'}\right| \, T\Bigg[\, i\int \mathrm{d}^4x\left(-g_\mathrm{d}\, \mathrm{C}^{1m_1}_{1/2\alpha_1,1/2\beta_1}\left[d^\dagger_{m_1}\, p_{\alpha_1}\, n_{\beta_1}\right](x) + \text{H.c.}\right) \\
&\qquad\qquad \times i\int \mathrm{d}^4y\left(-g_\mathrm{d}\, \mathrm{C}^{1m_2}_{1/2\alpha_2,1/2\beta_2}\left[d^\dagger_{m_2}\, p_{\alpha_2}\, n_{\beta_2}\right](y) + \text{H.c.}\right)\Bigg]\left|d_{m,p}\right\rangle\Bigg|_{\substack{\text{amp.}\\ \text{conn.}}} \qquad \text{(E.1a)}\\
&= -g_\mathrm{d}^2\, \mathrm{C}^{1m_1}_{1/2\alpha_1,1/2\beta_1}\mathrm{C}^{1m_2}_{1/2\alpha_2,1/2\beta_2} \\
&\quad \times \frac{1}{2!}\left\langle d_{m',p'}\right| \, T\Bigg[\int \mathrm{d}^4x\int \mathrm{d}^4y\Bigg(\left[d^\dagger_{m_1}\, p_{\alpha_1}\, n_{\beta_1}\right](x)\left[n^\dagger_{\beta_2}\, p^\dagger_{\alpha_2}\, d_{m_2}\right](y) \\
&\qquad\qquad + \left[n^\dagger_{\beta_1}\, p^\dagger_{\alpha_1}\, d_{m_1}\right](x)\left[d^\dagger_{m_2}\, p_{\alpha_2}\, n_{\beta_2}\right](y)\Bigg)\Bigg]\left|d_{m,p}\right\rangle\Bigg|_{\substack{\text{amp.,}\\ \text{conn.}}} \qquad \text{(E.1b)}
\end{aligned}
$$

where T is the time ordering operator and "amp., conn." stands for "amputated, connected". In Eq. (E.1b), terms proportional to $d_{m_1}d_{m_2}$ and $d^\dagger_{m_1}d^\dagger_{m_2}$ vanish because of particle number conservation. Using Wick's theorem, we can translate the two terms of Eq. (E.1b) into a sum of contractions.

$$
\begin{aligned}
&\contraction{\langle}{d_{m',p'}}{|[}{d^\dagger_{m_1}}
\contraction[2ex]{\langle d_{m',p'}|[d^\dagger_{m_1}\,}{p_{\alpha_1}}{\,n_{\beta_1}](x)[n^\dagger_{\beta_2}\,}{p^\dagger_{\alpha_2}}
\contraction{\langle d_{m',p'}|[d^\dagger_{m_1}\,p_{\alpha_1}\,}{n_{\beta_1}}{](x)[}{n^\dagger_{\beta_2}}
\contraction{\langle d_{m',p'}|[d^\dagger_{m_1}\,p_{\alpha_1}\,n_{\beta_1}](x)[n^\dagger_{\beta_2}\,p^\dagger_{\alpha_2}\,}{d_{m_2}}{](y)\,|}{d_{m,p}}
\langle d_{m',p'}|[d^\dagger_{m_1}\,p_{\alpha_1}\,n_{\beta_1}](x)[n^\dagger_{\beta_2}\,p^\dagger_{\alpha_2}\,d_{m_2}](y)\,|d_{m,p}\rangle \\
&+\langle d_{m',p'}|[n^\dagger_{\beta_1}\,p^\dagger_{\alpha_1}\,d_{m_1}](x)[d^\dagger_{m_2}\,p_{\alpha_2}\,n_{\beta_2}](y)\,|d_{m,p}\rangle \sim (-1)^2 + (-1)^2(-1)^2 = +2\,. \qquad \text{(E.2)}
\end{aligned}
$$

By untangling the p-p and n-n contractions in the first term, we pick up the factor $(-1)^2 = +1$. That holds for the second term, but we additionally have to anticommute the n-n and p-p pairs, respectively.

Thus, we obtain $(-1)^2(-1)^2 = +1$ as well. The deuteron fields always commute since they represent bosons. The overall factor $+2$ then cancels the $1/(2!)$ factor of Eq. (E.1b). For the virtual state case, one obtains the same result. Thus, protons and neutrons might as well be treated like distinguishable particles, whose fields commute.

Let $l^\mu = (l_\mathrm{p}^\mu - l_\mathrm{n}^\mu)/2$ and $p^\mu = l_\mathrm{p}^\mu + l_\mathrm{n}$ be the relative and total p-n four-momenta in $D = 1+d$ dimensions. Moreover, we write ${}^{2j+1}s_j \in \{{}^3s_1,\ {}^1s_0\}$ for the general case $b \in \{\mathrm{d}, \mathrm{v}\}$. The bare self-energy loop integral at a p-n center-of-mass energy $E_\mathrm{cm} = p^0 - \boldsymbol{p}^2/(4m_\mathrm{N})$ then reads

$$
\begin{aligned}
&-i\Sigma_b^{(\mathrm{b})}(E_\mathrm{cm})\,\delta^{m_j m_j'} \\
&\quad = +\left(\frac{\Lambda_\mathrm{PDS}}{2}\right)^{4-D} \int \frac{\mathrm{d}^D l}{(2\pi)^D} \frac{i^2\left(-ig_b\,\mathrm{C}_{1/2\alpha,1/2\beta}^{jm_j}\right)\left(-ig_b\,\mathrm{C}_{1/2\alpha,1/2\beta}^{jm_j'}\right)}{\left[(p^0/2 - l^0) - \frac{(\boldsymbol{p}/2-\boldsymbol{l})^2}{2m_\mathrm{N}} + i\epsilon\right]\left[(p^0/2 + l^0) - \frac{(\boldsymbol{p}/2+\boldsymbol{l})^2}{2m_\mathrm{N}} + i\epsilon\right]} && \text{(E.3a)} \\
&\quad = ig_b^2\, m_\mathrm{N}\, \delta^{m_j m_j'} \left(\frac{\Lambda_\mathrm{PDS}}{2}\right)^{3-d} \int \frac{\mathrm{d}^d l}{(2\pi)^d} \frac{1}{\boldsymbol{l}^2 - m_\mathrm{N}(E_\mathrm{cm} + i\epsilon)}\,. && \text{(E.3b)} \\
&\quad = ig_b^2\, m_\mathrm{N}\, \delta^{m_j m_j'}\, J_{d,0}\Big(-m_\mathrm{N}(E_\mathrm{cm} + i\epsilon)\Big) && \text{(E.3c)}
\end{aligned}
$$

In Eq. (E.3b), we used the completeness relations of the Clebsch-Gordan coefficients (For $b = \mathrm{v}$ the projections are zero, i.e., $m_j = 0 = m_j'$). We recover the s-wave integral function $J_{d,0}$ given in Eq. (B.7a). It exhibits a divergence in $d = 2$ dimensions, which is removed in the PDS scheme. The final result $\Sigma_b^{(\mathrm{PDS})}$ is given in Eq. (4.23a).

E.1.2 Core-neutron sector

The core ^{A}X and the neutron represent distinguishable particles, whose fields commute. As usual, we define $p^\mu \equiv l_\mathrm{n}^\mu + l_\mathrm{c}^\mu$ and $l^\mu \equiv \xi l_\mathrm{n}^\mu - (1-\xi) l_\mathrm{c}^\mu$ to be the total and relative c-n four-momenta and $E_\mathrm{cm} = p^0 - \boldsymbol{p}^2/(2M_\mathrm{Nc})$ be the c-n center-of-mass energy. Here, $\xi = 1/(1+1/A)$. We consider the bare self-energy loop $-i\Sigma_\mathrm{h}$ in $d = 3$ spatial dimensions first, since otherwise we would need to generalize the spherical harmonics in the h ⟷ nc vertices to d dimensions. Given the Feynman rules of Eqs. (4.45a)-(4.45b), the bare self-energy loop then reads

$$
\begin{aligned}
&-i\Sigma_\mathrm{h}^{(\mathrm{b})}(E_\mathrm{cm})\,\delta^{m_j m_j'} \\
&\quad = \int \frac{\mathrm{d}^4 l}{(2\pi)^4} \frac{i^2\left(-ig_\mathrm{h}\,\mathrm{C}_{1/2\alpha,lm_l}^{jm_j}\,\{\boldsymbol{l}\}_{lm_l}^*\right)\left(-ig_\mathrm{h}\,\mathrm{C}_{1/2\alpha,lm_l'}^{jm_j'}\,\{\boldsymbol{l}\}_{lm_l'}\right)}{\left[(\xi p^0 - l^0) - \frac{(\xi\boldsymbol{p}-\boldsymbol{l})^2}{2m_\mathrm{N}} + i\epsilon\right]\left[((1-\xi)p^0 + l^0) - \frac{((1-\xi)\boldsymbol{p}+\boldsymbol{l})^2}{2m_\mathrm{c}} + i\epsilon\right]} && \text{(E.4a)} \\
&\quad = ig_\mathrm{h}^2\, 2\mu_\mathrm{Nc}\, \mathrm{C}_{1/2\alpha,lm_l}^{jm_j}\, \mathrm{C}_{1/2\alpha,lm_l'}^{jm_j'} \frac{4\pi}{2l+1} \int \frac{\mathrm{d}^3 l}{(2\pi)^3} \frac{|\boldsymbol{l}|^{2l}\, Y_l^{m_l\,*}(\hat{\boldsymbol{l}})\, Y_l^{m_l'}(\hat{\boldsymbol{l}})}{\boldsymbol{l}^2 - 2\mu_\mathrm{Nc}(E_\mathrm{cm} + i\epsilon)}\,. && \text{(E.4b)} \\
&\quad = ig_\mathrm{h}^2\, 2\mu_\mathrm{Nc}\, \mathrm{C}_{1/2\alpha,lm_l}^{jm_j}\, \mathrm{C}_{1/2\alpha,lm_l'}^{jm_j'} \frac{4\pi}{2l+1}\, \delta^{m_l m_l'} \int_0^\infty \frac{\mathrm{d}l\, l^2}{(2\pi)^3} \frac{l^{2n}}{l^2 - 2\mu_\mathrm{Nc}(E_\mathrm{cm} + i\epsilon)} && \text{(E.4c)} \\
&\quad = ig_\mathrm{h}^2\, 2\mu_\mathrm{Nc}\, \delta^{m_j m_j'} \frac{1}{2l+1} \int \frac{\mathrm{d}^3 l}{(2\pi)^3} \frac{\boldsymbol{l}^{2n}}{\boldsymbol{l}^2 - 2\mu_\mathrm{Nc}(E_\mathrm{cm} + i\epsilon)} && \text{(E.4d)} \\
&\quad = ig_\mathrm{h}^2\, 2\mu_\mathrm{Nc}\, \delta^{m_j m_j'} \frac{1}{2l+1} J_{3,l}\Big(-2\mu_\mathrm{Nc}(E_\mathrm{cm} + i\epsilon)\Big) && \text{(E.4e)}
\end{aligned}
$$

Due to the orthogonality of the spherical harmonics, the angular part of the integral in Eq. (E.4b) gives $\delta^{m_l m_l'}$. In Eq. (E.4c), we have expressed the factor 4π by yet another angular integral. such that we recover the integral function $J_{3,l}$ defined in Eq. (B.7a). This function can easily be generalized to d dimensions. The respective integral function $J_{d,l}$ is solved in Appendix B.2. The final self-energy in the PDS scheme is given in Eq. (4.46a).

E.2 Neutron exchange potentials

We provide details on the derivation of the neutron exchange potentials for a generic halo state.

E.2.1 Transfer from halo state to deuteron

The tensor structure of the neutron exchange potentials V_{hd} and V_{dh} follows from a sum over four Clebsch-Gordan coefficients. Two stem from the interaction vertices and the other two couple the single-particle spins to total spins S, S'. For V_{hd}, the sum reads

$$\sum_{\alpha,m_j,\epsilon,m'} \mathrm{C}^{Sm_S}_{1/2\alpha,jm_j}\,\mathrm{C}^{S'm_{S'}}_{00,1m'} \times \mathrm{C}^{jm_j}_{1/2\epsilon,lm_l}\,\mathrm{C}^{1m'}_{1/2\alpha,1/2\epsilon} = \delta^{S'1} \sum_{\alpha,m_j,\epsilon} \mathrm{C}^{Sm_S}_{1/2\alpha,jm_j}\,\mathrm{C}^{jm_j}_{1/2\epsilon,lm_l}\,\mathrm{C}^{1m_{S'}}_{1/2\alpha,1/2\epsilon}\,. \tag{E.5}$$

After applying symmetry relation

$$\mathrm{C}^{s_3m_3}_{s_1m_1,s_2m_2} = (-1)^{s_1+s_2-s_3}\,\mathrm{C}^{s_3m_3}_{s_2m_2,s_1m_1} \tag{E.6}$$

of the Clebsch-Gordan coefficients of Eq. (10) in Chapter 8.4.3 of Ref. [142], we can expresses the sum in terms of a $6j$ symbol. Using Eq. (12) in Chapter 8.7.3 of Ref. [142], we obtain

$$\delta^{S'1} \sum_{\alpha,m_j,\epsilon} \mathrm{C}^{Sm_S}_{1/2\alpha,jm_j}\,\mathrm{C}^{jm_j}_{1/2\epsilon,lm_l}\,\mathrm{C}^{1m_{S'}}_{1/2\alpha,1/2\epsilon} = (-1)^{1/2+j-S}\,\delta^{S'1} \sum_{\alpha,m_j,\epsilon} \mathrm{C}^{1m_{S'}}_{1/2\epsilon,1/2\alpha}\,\mathrm{C}^{Sm_S}_{jm_j,1/2\alpha}\,\mathrm{C}^{jm_j}_{1/2\epsilon,lm_l} \tag{E.7a}$$

$$= (-1)^{1/2+j-S}\,\delta^{S'1}\,(-1)^{3/2+j+l}\,\mathrm{C}^{Sm_S}_{1m_{S'},lm_l}\,\sqrt{3(2j+1)} \begin{Bmatrix} 1/2 & 1/2 & 1 \\ S & l & j \end{Bmatrix} \tag{E.7b}$$

$$= \sqrt{3(2j+1)}\,\mathrm{C}^{m_S}_{lm_l,1m_{S'}} \begin{Bmatrix} 1/2 & 1/2 & 1 \\ S & l & j \end{Bmatrix} \delta^{S'1}\,. \tag{E.7c}$$

where in the last step we used the fact that $2j$ is odd.

The h → cn vertex introduces a momentum tensor $\{-\xi \boldsymbol{p} - \boldsymbol{q}\}^*_{lm_l} = (-1)^l \{\xi \boldsymbol{p} + \boldsymbol{q}\}^*_{lm_l}$ to V_{hd}. Before we can perform the partial wave projection, we must disentangle the two vectors $\xi \boldsymbol{p}$ and $\boldsymbol{q}$. That can be achieved using the relation

$$\{\boldsymbol{a} + \boldsymbol{b}\}_{lm_l} \propto Y_l^{m_l}\left(\widehat{\boldsymbol{a} + \boldsymbol{b}}\right) |\boldsymbol{a} + \boldsymbol{b}|^l = \sum_{l_1+l_2=l} a^{l_1}\, b^{l_2} \sqrt{\frac{4\pi(2l+1)!}{(2l_1+1)!\,(2l_2+1)!}}\, \mathscr{Y}^{lm_l}_{l_1l_2}\left(\hat{\boldsymbol{a}}, \hat{\boldsymbol{b}}\right) \tag{E.8}$$

in Eq. (A.8) of Ref. [167]. It involves coupled spherical hermonics

$$\mathscr{Y}^{lm_l}_{l_1l_2}\left(\hat{\boldsymbol{a}}, \hat{\boldsymbol{b}}\right) \equiv \sum_{m_1,m_2} \mathrm{C}^{lm_l}_{l_1m_1,l_2m_2}\, Y_{l_1}^{m_1}(\hat{\boldsymbol{a}})\, Y_{l_2}^{m_2}\left(\hat{\boldsymbol{b}}\right). \tag{E.9}$$

Following the projection prescription in Appendix C.1, we have to calculate

$$V_{\mathrm{hd}}^{{}^{2S+1}L_J,{}^3L'_J}(p,q;E) = \frac{1}{(4\pi)^2(2J+1)} \sum_{m_S,m_{S'}} \int_{\Omega_{\boldsymbol{p}},\Omega_{\boldsymbol{q}}} P^{m_{S'}m_S}_{{}^{2S'+1}L'_J,{}^{2S+1}L_J}(\hat{\boldsymbol{q}},\hat{\boldsymbol{p}})\; V_{\mathrm{hd}}^{Sm_S,S'm_{S'}}(\boldsymbol{p},\boldsymbol{q};E) \tag{E.10a}$$

$$\propto \int_{\Omega_{\boldsymbol{p}},\Omega_{\boldsymbol{q}}} \sum_{m_L,m_{L'},m_l} Y_{L'}^{m_{L'}}(\hat{\boldsymbol{q}})\, Y_L^{m_L\,*}(\hat{\boldsymbol{p}})\, \{\xi\boldsymbol{p}+\boldsymbol{q}\}^*_{lm_l}$$

$$\times \sum_{m_S,m_{S'},m_J} \mathrm{C}^{Jm_J}_{L'm_{L'},1m_{S'}}\,\mathrm{C}^{Jm_J}_{Lm_L,Sm_S}\,\mathrm{C}^{Sm_S}_{lm_l,1m_{S'}}\,. \tag{E.10b}$$

The sum over Clebsch-Gordan coefficients can be simplified to

$$\sum_{m_S,m_{S'},m_J} \mathrm{C}^{Jm_J}_{L'm_{L'},1m_{S'}} \mathrm{C}^{Jm_J}_{Lm_L,Sm_S} \mathrm{C}^{Sm_S}_{lm_l,1m_{S'}} = (-1)^{L'+J+1}\sqrt{\frac{2S+1}{2L'+1}}\,(2J+1)\,\mathrm{C}^{L'm_{L'}}_{lm_l,Lm_L} \begin{Bmatrix} S & 1 & l \\ L' & L & J \end{Bmatrix} \tag{E.11}$$

using Eq. (E.6). Using Eq. (E.8), the momentum-dependent part of Eq. (E.10b) involves the product

$$Y^{m_L\,*}_{L}(\hat{\boldsymbol{p}})\,Y^{m_1\,*}_{l_1}(\hat{\boldsymbol{p}})\,Y^{m_{L'}}_{L'}(\hat{\boldsymbol{q}})\,Y^{m_2\,*}_{l_2}(\hat{\boldsymbol{q}}) = (-1)^{m_2}\,Y^{m_L\,*}_{L}(\hat{\boldsymbol{p}})\,Y^{m_1\,*}_{l_1}(\hat{\boldsymbol{p}})\,Y^{m_{L'}}_{L'}(\hat{\boldsymbol{q}})\,Y^{-m_2}_{l_2}(\hat{\boldsymbol{q}})\,. \tag{E.12}$$

The dependence on $\hat{\boldsymbol{p}}$ ($\hat{\boldsymbol{q}}$) of this expression can be absorbed in a single spherical harmonic using Eq. (9) in Chapter 5.6.2 of Ref. [142]. It gives

$$Y^{m_L\,*}_{L}(\hat{\boldsymbol{p}})\,Y^{m_1\,*}_{l_1}(\hat{\boldsymbol{p}}) = \sum_{k_1 m_{k_1}} \sqrt{\frac{(2L+1)(2l_1+1)}{4\pi(2k_1+1)}}\,\mathrm{C}^{k_1 0}_{L0,l_1 0}\,\mathrm{C}^{k_1 m_{k_1}}_{Lm_L,l_1 m_1}\,Y^{m_{k_1}\,*}_{k_1}(\hat{\boldsymbol{p}}) \tag{E.13}$$

and similar for $Y^{m_{L'}}_{L'}(\hat{\boldsymbol{q}})\,Y^{-m_2}_{l_2}(\hat{\boldsymbol{q}})$.

To finish the partial wave projection, we express the remaining Clebsch-Gordan sum in terms of yet another $6j$ symbol using Eq. (E.6) and the relations Eq. (10) in Chapter 8.4.3 and Eq. (8) in Chapter 9.1.1 of Ref. [142]. We then arrive at Eq. (4.75).

E.2.2 Transfer from halo state to proton-neutron virtual state

The neutron exchange potentials for transfer between a generic halo state and the p-n virtual state, V_{hv} and V_{vh} can be calculated in complete analogy to the ones involving the deuteron. Even though they are not used in this thesis, we provide their analytic forms in this subsection.

The unprojected exchange diagrams are obtained by replacing $S' = 1 \to 0$ in the Clebsch-Gordan coefficient, the $6j$ symbol, and the Kronecker delta of Eq. (4.74a) and $2S'+1 = 3 \to 1$ in the square root. Moreover, one has to replace $g_{\mathrm{d}} \to g_{\mathrm{v}}$ and multiply by -1. One then obtains

$$-iV^{Sm_S,S'm_{S'}}_{\mathrm{hv}}(\boldsymbol{p},\boldsymbol{q};E) = i g_{\mathrm{v}} g_{\mathrm{h}} m_{\mathrm{N}} (-1)^{l+1}\sqrt{2j+1}\,\mathrm{C}^{Sm_S}_{lm_l,00} \begin{Bmatrix} S & l & 0 \\ 1/2 & 1/2 & j \end{Bmatrix} \delta^{S'0}\,\delta^{m_{S'}0} \times \frac{\{\xi\boldsymbol{p}+\boldsymbol{q}\}^*_{lm_l}}{\boldsymbol{p}\cdot\boldsymbol{q} + U_{\mathrm{n;p,c}}(p,q;E)}\,, \tag{E.14a}$$

$$-iV^{Sm_S,S'm_{S'}}_{\mathrm{vh}}(\boldsymbol{p},\boldsymbol{q};E) = -i\left[V^{S'm_{S'},Sm_S}_{\mathrm{hv}}(\boldsymbol{q},\boldsymbol{p};E)\right]^*. \tag{E.14b}$$

Partial wave projections can be obtained by performing the same replacements in Eq. (4.75), expect multiplying by -1. We find

$$\begin{aligned} V^{{}^{\hat{S}}L_J,{}^{\hat{S}'}L'_J}_{\mathrm{hv}}(p,q;E) = {} & \frac{g_{\mathrm{v}} g_{\mathrm{h}} m_{\mathrm{N}}}{2}(-1)^{J+l}\sqrt{\hat{S}\,\hat{L}\,\hat{L}'\,\hat{j}\,(\hat{l}\,!)} \begin{Bmatrix} S & 0 & l \\ L' & L & J \end{Bmatrix} \begin{Bmatrix} S & l & 0 \\ 1/2 & 1/2 & j \end{Bmatrix} \delta^{S'0} \\ & \times \sum_{l_1+l_2=l} (\xi p)^{l_1}\, q^{l_2} \frac{1}{\sqrt{(2l_1!)(2l_2!)}} \\ & \times \sum_k (-1)^k\,\mathrm{C}^{k0}_{l_1 0,L0}\mathrm{C}^{k0}_{l_2 0,L'0} \begin{Bmatrix} l_1 & l_2 & l \\ L' & L & k \end{Bmatrix} I^{(k)}_{\mathrm{n;p,c}}(p,q;E)\,, \end{aligned} \tag{E.15a}$$

$$V^{{}^{\hat{S}}L_J,{}^{\hat{S}'}L'_J}_{\mathrm{vh}}(p,q;E) = V^{{}^{\hat{S}'}L'_J,{}^{\hat{S}}L_J}_{\mathrm{hv}}(q,p;E)\,. \tag{E.15b}$$

E.3 The core excitation $^{10}\text{Be}^*$

In the main text we mention that ^{11}Be also couples to a $^{10}\text{Be}^*$-n pair (d-wave), where $^{10}\text{Be}^*$ denotes the 2^+ core excitation; see Fig. 4.7. In this section, we categorize breakup towards this channel within the Halo EFT power counting. Moreover, we demonstrate that residual effects of this combination in the ^{11}Be pole region are automatically taken care of by renormalizing onto low-energy observables.

We analyze core excitation effects by introducing an explicit $^{10}\text{Be}^*$ field C_m to the theory. A similar approach has been chosen by Zhang *et al.* to analyze effects of the core excitation $^7\text{Li}^*$ on the $^7\text{Li}(\text{n},\gamma)^8\text{Li}$ reaction [168]. Moreover, Zhang *et al.* and Ryberg *et al.* used a $^7\text{Be}^*$ core excitation field in their calculation of the S-factor of $^7\text{Be}(\text{p},\gamma)^8\text{B}$ [169,170]. In both systems, the core excitation occurs at low energies. In our case, however, it occurs at the natural (high) energy $E_\text{x} = 3.37\,\text{MeV}$, i.e., at the natural relative momentum $(2\mu_\text{Nc}E_\text{x})^{1/2} \sim R_\text{c}^{-1}$.

The core excitation kinetic term reads

$$\mathscr{L}_{\text{kin},^{10}\text{Be}^*} = C_m^\dagger\left[i\partial_0 + \frac{\boldsymbol{\nabla}^2}{2m_\text{c}} - E_\text{x}\right]C_m\,, \tag{E.16}$$

where $m \in \{2, 1, 0, -1, -2\}$ stands for the polarization of the 2^+ state. The kinetic mass does not involve the excitation energy since $E_\text{x} \ll m_\text{c}$. Together with a neutron, $^{10}\text{Be}^*$ couples to ^{11}Be in a d-wave. In terms of the redefined field $\tilde{\sigma}_\alpha$, we thus write

$$\mathscr{L}_{\text{cn},^{10}\text{Be}^*} = -\sum_{s\in\{3/2,5/2\}} \frac{g_{\sigma,\text{x}}^{(s)}}{g_\sigma} \text{C}_{1/2\alpha,2m}^{sm_s}\text{C}_{sm_s,2m_l}^{1/2\alpha'}\left[\tilde{\sigma}_{\alpha'}^\dagger\left(n_\alpha\left\{-i\overleftrightarrow{\nabla}\right\}_{2m_l}C_m\right) + \text{H.c.}\right]. \tag{E.17}$$

The d-wave nature of the vertex manifests itself in the $l=2$ tensor structure defined in Eq. (4.43). Note that angular momentum conservation allows total $^{10}\text{Be}^*$-n spins $s \in \{3/2, 5/2\}$. The couplings $g_{\sigma,\text{x}}^{(s)}$ of ^{11}Be to these states could in principle be different.

Breakup towards $^{10}\text{Be}^*$

Due to the large energy difference $E_\text{x} + B_\sigma$, the couplings $g_{\sigma,\text{x}}^{(s)}$ should both be of natural size $g_{\sigma,\text{x}}^{(s)} \sim R_\text{c}^{3/2}$. This scaling scheme follows from the assumption of minimal fine-tuning. The overall coupling $g_{\sigma,\text{x}}^{(s)}/g_\sigma \sim R_\text{c}^2$ is then natural as well since $g_\sigma \sim r_\sigma^{-1/2} \sim R_\text{c}^{-1/2}$; see Eqs. (4.48a)-(4.48b).

Due to the small overall couplings, ^{11}Be breakup (and recombination) towards $^{10}\text{Be}^*$-n is highly suppressed at low energies. In particular, each corresponding vertex scales like $k^2R_\text{c}^2 \sim (R_\text{c}/R_\text{h})^2$, where k is a small reative momentum. One breakup and one recombination yields an overall suppression $(R_\text{c}/R_\text{h})^4$ (N^{4}LO). Note that the scaling scheme $k \sim R_\text{h}^{-1}$ might become inappropriate for the energies $E \gtrsim E_\text{x}$ used in the experiment by Schmitt *et al.*.

Contributions of $^{10}\text{Be}^*$ to the ^{11}Be propagator

The core excitation modifies the ^{11}Be propagator through the $^{10}\text{Be}^*$-neutron self-energy loop $-i\Sigma_{\sigma,\text{x}}\,\delta^{\alpha\alpha'}$. It resembles the neutron-core self-energy loop in Fig. 4.9(a), but the internal core lines (dashed) has to be replaced by a core excitation line. Using the PDS scheme, we obtain

$$\begin{aligned}\Sigma_{\sigma,\text{x}}(E_\text{cm}) = -\sum_s\left(\frac{g_{\sigma,\text{x}}^{(s)}}{g_\sigma}\right)^2 \frac{\mu_\text{Nc}}{10\pi}\,[2\mu_\text{Nc}(E_\text{cm} - E_\text{x} + i\epsilon)]^2 \\ \times\left(\Lambda_\text{PDS} - [-2\mu_\text{Nc}(E_\text{cm} - E_\text{x} + i\epsilon)]^{1/2}\right).\end{aligned} \tag{E.18}$$

The function $\Sigma_{\sigma,\mathrm{x}}$ is analytic in the low-energy region of the pole, i.e., for $E_{\mathrm{cm}} < E_{\mathrm{x}}$. Thus, it can be expanded at $E_{\mathrm{cm}} = 0$ yielding the sum

$$\Sigma_{\sigma,\mathrm{x}}(E_{\mathrm{cm}}) = -g_\sigma^{-2} \sum_{n\geq 0} \Delta_{\sigma,\mathrm{x}}^{(n)} (E_{\mathrm{cm}} + i\epsilon)^n . \tag{E.19}$$

The coefficients $\Delta_{\sigma,\mathrm{x}}^{(n)}$ contribute to the unrenormalized parameters $\Delta_\sigma^{(n)}$ ($\Delta_\sigma^{(1)} \equiv -1$) of the bare ^{11}Be propagator; see Eq. (4.90). Low-energy ERE coefficients must not be affected by the new parameters. Thus, in the matching equation (4.48a) we have to replace $\Delta_\sigma^{(n)} \to \Delta_\sigma^{(n)} + \Delta_{\sigma,\mathrm{x}}^{(n)}$. Alternatively, one can take the stand point that the $\Delta_{\sigma,\mathrm{x}}^{(n)}$ have been part of the $\Delta_\sigma^{(n)}$ all the time. In either case, the propagator expansion around the pole is the same as without the core excitation field.

We conclude that renormalization onto observables γ_σ (or a_σ), r_σ, etc. automatically takes care of core excitation effects at small E_{cm}, where the pole is located. In other words, C_m does not introduce any new information to the pole region.

E.4 Higher-order Coulomb diagrams for ^{10}Be(d, p)^{11}Be

We give expressions for the full (off-shell) c-p Coulomb amplitude, which was calculated by König *et al.*; see Ref. [145]. Afterwards, it is used to calculate bubble and box diagrams with multi-photon exchange. At the end of the section, we estimate the importance of Coulomb box diagrams involving the excited state ^{11}Be* in Fig. 4.20(a).

E.4.1 Core-proton Coulomb scattering

The full c-p Coulomb amplitude of Fig.4.10 was calculated by König *et al.*. It is given by the expression

$$it_{\mathrm{cp}}^{(\mathrm{C})}\left(\mathbf{k}, \mathbf{k}'; E_{\mathrm{cm}}\right) = -iV_{\mathrm{C}}\left(\mathbf{k}, \mathbf{k}'\right)\left[1 - 2i\eta \int_1^\infty \mathrm{d}s \left(\frac{s+1}{s-1}\right)^{-i\eta} \frac{1}{s^2 - 1 - \epsilon_\lambda + \zeta_\lambda(s)}\right] \tag{E.20}$$

with $\eta \equiv p_{\mathrm{C}}/\bar{k}$ and

$$\epsilon_\lambda \equiv \frac{\left(k^2 - \bar{k}^2\right)\left(k'^2 - \bar{k}^2\right)}{\bar{k}^2\left[(\mathbf{k}-\mathbf{k}')^2 + \lambda^2\right]}, \tag{E.21a}$$

$$\zeta_\lambda(s) \equiv \frac{\left(\bar{k}^2 - k^2\right)\left(\lambda^2 - 2i\lambda\bar{k}s\right)}{\bar{k}^2\left[(\mathbf{k}-\mathbf{k}')^2 + \lambda^2\right]}. \tag{E.21b}$$

This form shows that multi-photon exchanges are suppressed by the Sommerfeld parameter η. The integral in Eq. (E.20) can be expressed in terms of Hypergeometric functions. This form reads

$$it_{\mathrm{cp}}^{(\mathrm{C})}\left(\mathbf{k}, \mathbf{k}'; E_{\mathrm{cm}}\right) = -iV_{\mathrm{C}}\left(\mathbf{k}, \mathbf{k}'\right)\left[1 - \Delta_\lambda^{-1}\left({}_2F_1\left(1, i\eta; 1+i\eta; X_\lambda^-\right) - {}_2F_1\left(1, i\eta; 1+i\eta; X_\lambda^+\right)\right)\right] \tag{E.22}$$

with

$$\Delta_\lambda^2 \equiv 1 + \frac{\left(\bar{k}^2 - k^2\right)\left(\bar{k}^2 - k'^2 - \lambda^2\right)}{\bar{k}^2\left[(\mathbf{k}-\mathbf{k}')^2 + \lambda^2\right]} - \lambda^2 \frac{\left(\bar{k}^2 - k^2\right)^2}{\bar{k}^2\left[(\mathbf{k}-\mathbf{k}')^2 + \lambda^2\right]^2}, \tag{E.23a}$$

$$X_\lambda^\pm \equiv \frac{2\bar{k}^2\left[(\mathbf{k}-\mathbf{k}')^2 + \lambda^2\right](1 \pm \Delta_\lambda) + \left(\bar{k}^2 - k^2\right)\left(\bar{k}^2 - k'^2 - \lambda^2\right)}{\left(\bar{k}^2 - k^2\right)\left[\left(\bar{k} + i\lambda\right)^2 - k'^2\right]}. \tag{E.23b}$$

E.4.2 Diagrams with multi-photon exchange

In order to check the suppression of multi-photon suppressions numerically, we calculate the bubble diagram of Fig. 4.18, which involves the full Coulomb amplitude. Let $\boldsymbol{Q}$ be the neutron's three-momentum in the loop. Following Ref. [145], we obtain

$$\begin{aligned}\Gamma_{\mathrm{dd}}^{(\infty\gamma\text{-bubble})\,1m_S,1m_{S'}}(\boldsymbol{p},\boldsymbol{q};E) &= m_{\mathrm{N}}^2\delta^{m_S m_{S'}}\int\frac{\mathrm{d}^3Q}{(2\pi)^3}\,t_{\mathrm{cp}}^{(\mathrm{C})}\left(\boldsymbol{p},\boldsymbol{q};E-\frac{Q^2}{2\mu_{\mathrm{n(cp)}}}\right)\\ &\quad\times\left[A_p+B_p\,\hat{\boldsymbol{p}}\cdot\hat{\boldsymbol{Q}}\right]^{-1}\left[A_q+B_q\,\hat{\boldsymbol{q}}\cdot\hat{\boldsymbol{Q}}\right]^{-1}\end{aligned}\tag{E.24}$$

with short-hand notations

$$A_p\equiv\frac{1+y}{2}p^2+Q^2-m_{\mathrm{N}}(E+i\epsilon)\,,\quad A_q\equiv\frac{1+y}{2}q^2+Q^2-m_{\mathrm{N}}(E+i\epsilon)\,,\tag{E.25a}$$

$$B_p\equiv pQ\,,\quad B_q\equiv qQ\,.\tag{E.25b}$$

The angular part of the $\boldsymbol{Q}$ integration can be performed analytically since the Coulomb two-body amplitude only depends on $Q=|\boldsymbol{Q}|$. We find

$$\begin{aligned}\Gamma_{\mathrm{dd}}^{(\infty\gamma\text{-bubble})\,1m_S,1m_{S'}}(\boldsymbol{p},\boldsymbol{q};E) &= m_{\mathrm{N}}^2\frac{\delta^{m_S m_{S'}}}{4\pi^2}\int_0^\infty\mathrm{d}Q\,Q^2\,t_{\mathrm{cp}}^{(\mathrm{C})}\left(\boldsymbol{p},\boldsymbol{q};E-\frac{Q^2}{2\mu_{\mathrm{n(cp)}}}\right)\\ &\quad\times\frac{1}{\sqrt{F}}\left[\ln\left(\frac{A_p+B_p}{A_p-B_p}\right)-\ln\left(\frac{B_p(C+D)-A_p(D+B_q^2)+\sqrt{F}\left(A_q+B_qx\right)}{B_p(C-D)-A_p(D-B_q^2)+\sqrt{F}\left(A_q-B_qx\right)}\right)\right],\end{aligned}\tag{E.26}$$

where $\mu_{\mathrm{n(cp)}}\equiv m_{\mathrm{N}}(m_{\mathrm{N}}+m_{\mathrm{c}})/(2m_{\mathrm{N}}+m_{\mathrm{c}})=\mu_\sigma$ and $x\equiv\hat{\boldsymbol{p}}\cdot\hat{\boldsymbol{q}}$. Moreover,

$$C\equiv A_q^2-B_q^2\left(1-x^2\right),\tag{E.27a}$$

$$D\equiv A_qB_qx\,,\tag{E.27b}$$

$$F\equiv B_p^2C+A_p^2B_p^2-2A_pB_pD\,,\tag{E.27c}$$

and $y=m_{\mathrm{N}}/m_{\mathrm{c}}=1/A=0.1$.

The expression for $\Gamma_{\sigma\sigma}^{(\infty\gamma\text{-bubble})\,Sm_S,S'm_{S'}}$ can be obtained similarly. All one has to do is replacing the overall factor $m_{\mathrm{N}}^2\delta^{m_S m_{S'}}\to(2\mu_{\mathrm{Nc}})^2\delta^{SS'}\delta^{m_S m_{S'}}$ and redefining the above short-hand notations to

$$A_p\equiv p^2+Q^2-2\mu_{\mathrm{Nc}}(E+i\epsilon)\,,\quad A_q\equiv q^2+Q^2-2\mu_{\mathrm{Nc}}(E+i\epsilon)\,,\tag{E.28a}$$

$$B_p\equiv\frac{2y}{1+y}pQ\,,\quad B_q\equiv\frac{2y}{1+y}qQ\,.\tag{E.28b}$$

Box diagrams with multi-photon exchanges have the form

$$\begin{aligned}\Gamma_{\sigma\mathrm{d}}^{(\infty\gamma\text{-box})\,Sm_S,1m_{S'}}(\boldsymbol{p},\boldsymbol{q};E) &= m_{\mathrm{N}}(2\mu_{\mathrm{Nc}})\delta^{S1}\delta^{m_S m_{S'}}\int\frac{\mathrm{d}^3Q}{(2\pi)^3}\,t_{\mathrm{cp}}^{(\mathrm{C})}\left(-\boldsymbol{p}-\boldsymbol{Q},\boldsymbol{q};E-\frac{Q^2}{2\mu_{\mathrm{n(cp)}}}\right)\\ &\quad\times\left[A_p+B_p\,\boldsymbol{p}\cdot\hat{\boldsymbol{Q}}\right]^{-1}\left[A_q'+B_q'\,\boldsymbol{q}\cdot\hat{\boldsymbol{Q}}\right]^{-1},\end{aligned}\tag{E.29a}$$

$$\Gamma_{\mathrm{d}\sigma}^{(\infty\gamma\text{-box})\,1m_S,S'm_{S'}}(\boldsymbol{p},\boldsymbol{q};E)=\Gamma_{\sigma\mathrm{d}}^{(\infty\gamma\text{-box})\,S'm_{S'},1m_S}(\boldsymbol{q},\boldsymbol{p};E)\tag{E.29b}$$

with

$$A_p\equiv p^2+Q^2-2\mu_{\mathrm{Nc}}(E+i\epsilon)\,,\quad A_q'\equiv\frac{1+y}{2}q^2+Q^2-m_{\mathrm{N}}(E+i\epsilon)\,,\tag{E.30a}$$

$$B_p\equiv\frac{2y}{1+y}pQ\,,\quad B_q'\equiv qQ\,.\tag{E.30b}$$

E.4.3 Box diagrams including ^{11}Be*

Let us consider the box diagram in Fig. 4.20(a). If we choose the intermediate neutron three-momentum $\boldsymbol{Q}$ as integration variable, we find

$$\begin{aligned}\Gamma_{\mathrm{d}\pi}^{(\mathrm{LO})\,1m_S,S'm_{S'}}(\boldsymbol{p},\boldsymbol{q};E) &= m_{\mathrm{N}}(2\mu_{\mathrm{Nc}})\sqrt{6}\begin{Bmatrix} S' & 1 & 1 \\ 1/2 & 1/2 & 1/2\end{Bmatrix}\sum_{m_l}\mathrm{C}_{1m_l,1m_S}^{Sm_{S'}} \\ &\times\int\frac{\mathrm{d}^3Q}{(2\pi)^3}\frac{4\pi Q_{\mathrm{c}}\alpha}{(\boldsymbol{Q}+\boldsymbol{p}+\boldsymbol{q})^2+\lambda^2-i\epsilon}\frac{\left\{\boldsymbol{Q}+\frac{y}{1+y}\boldsymbol{q}\right\}_{1m_l}}{\left[A_p+B_p\,\hat{\boldsymbol{p}}\cdot\hat{\boldsymbol{Q}}\right]\left[A'_q+B'_q\,\hat{\boldsymbol{p}}\cdot\hat{\boldsymbol{Q}}\right]}\end{aligned}\tag{E.31}$$

with

$$A_p\equiv\frac{1+y}{2}p^2+Q^2-m_{\mathrm{N}}(E+i\epsilon)\,,\quad A'_q\equiv q^2+Q^2-2\mu_{\mathrm{Nc}}(E+i\epsilon)\,,\tag{E.32a}$$

$$B_p\equiv pQ\,,\quad B'_q\equiv\frac{2y}{1+y}qQ\,.\tag{E.32b}$$

After introducing Feynman parameters, each box diagram can be simplified to a sum of one-dimensional integrals. We obtain

$$\begin{aligned}\Gamma_{\mathrm{d}\pi}^{(\mathrm{LO})\,1m_S,S'm_{S'}}(\boldsymbol{p},\boldsymbol{q};E) &= \sqrt{6}\begin{Bmatrix} S' & 1 & 1 \\ 1/2 & 1/2 & 1/2\end{Bmatrix}\sum_{m_l}\mathrm{C}_{1m_l,1m_S}^{S'm_{S'}} \\ &\times\left[f_1\{\boldsymbol{p}\}_{1m_l}+f_2\{\boldsymbol{q}\}_{1m_l}\right]\end{aligned}\tag{E.33}$$

with coefficients

$$f_1\equiv Q_{\mathrm{c}}\alpha\,m_{\mathrm{N}}\mu_{\mathrm{Nc}}\int_0^1\mathrm{d}u\left[-\frac{1}{(a+b)\sqrt{b}}+\frac{1+u}{2}\left(\frac{1}{a\sqrt{b}}-a^{-3/2}\,\mathrm{atan}\left(\sqrt{\frac{a}{b}}\right)\right)\right],\tag{E.34a}$$

$$f_2\equiv Q_{\mathrm{c}}\alpha\,m_{\mathrm{N}}\mu_{\mathrm{Nc}}\int_0^1\mathrm{d}u\left[-\frac{1/(1+y)}{(a+b)\sqrt{b}}+\left(1-\frac{y}{1+y}u\right)\left(\frac{1}{a\sqrt{b}}-a^{-3/2}\,\mathrm{atan}\left(\sqrt{\frac{a}{b}}\right)\right)\right],\tag{E.34b}$$

$$a\equiv\left|\frac{1}{2}\boldsymbol{p}+\boldsymbol{q}+u\left(\frac{1}{2}\boldsymbol{p}-\frac{y}{1+y}\boldsymbol{q}\right)\right|^2,\tag{E.34c}$$

$$\begin{aligned}b\equiv{}&u^2\left(\frac{1}{2}\boldsymbol{p}-\frac{y}{1+y}\boldsymbol{q}\right)^2+u\left(q^2-\frac{1+y}{2}p^2+\boldsymbol{p}\cdot\left(\frac{1}{2}\boldsymbol{p}-\frac{y}{1+y}\boldsymbol{q}\right)-\frac{1-y}{1+y}m_{\mathrm{N}}(E+i\epsilon)\right)\\&+\frac{1+2y}{4}p^2-m_{\mathrm{N}}(E+i\epsilon)\,.\end{aligned}\tag{E.34d}$$

In order to estimate the importance of the box diagram, we compare it numerically to the neutron exchange potential $V_{\mathrm{d}\pi}$, which can be written in the similar form

$$\begin{aligned}V_{\mathrm{d}\pi}^{1m_S,S'm_{S'}}(\boldsymbol{p},\boldsymbol{q};E) &= \sqrt{6}\begin{Bmatrix} S' & 1 & 1 \\ 1/2 & 1/2 & 1/2\end{Bmatrix}\sum_{m_l}\mathrm{C}_{1m_l,1m_S}^{S'm_{S'}} \\ &\times\left[g_1\{\boldsymbol{p}\}_{1m_l}+g_2\{\boldsymbol{q}\}_{1m_l}\right]\end{aligned}\tag{E.35}$$

with coefficients

$$g_1\equiv\frac{m_{\mathrm{N}}}{\boldsymbol{p}\cdot\boldsymbol{q}+\frac{1+y}{2}p^2+q^2-m_{\mathrm{N}}(E+i\epsilon)}\tag{E.36a}$$

$$g_2\equiv\frac{1}{1+y}g_1\,.\tag{E.36b}$$

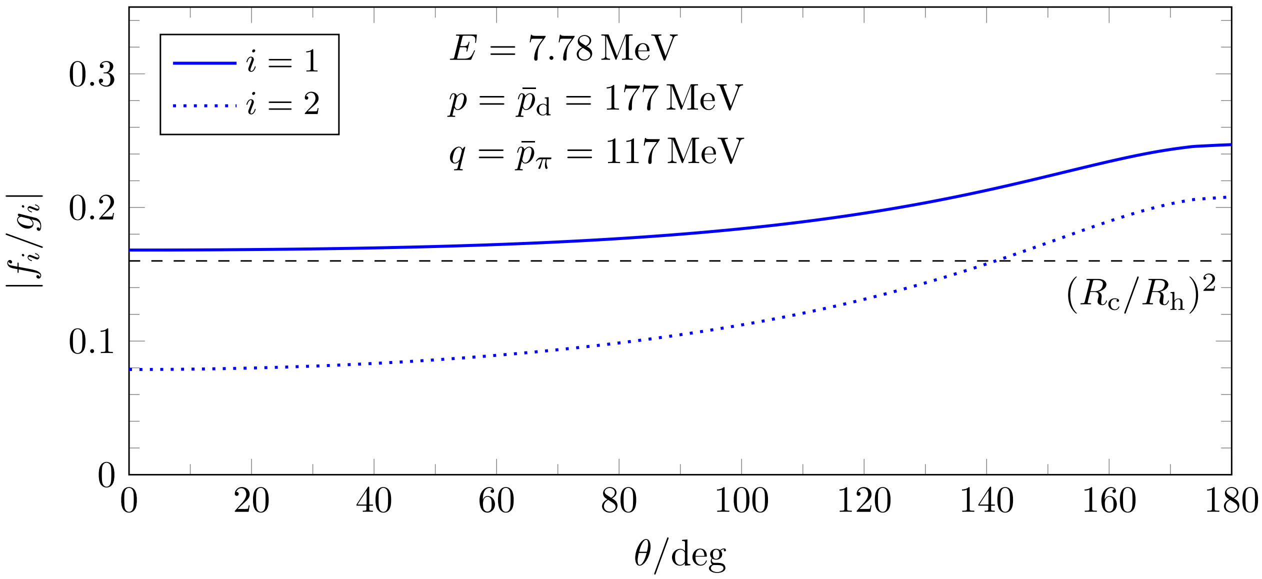

Figure E.1.: Ratios $|f_i/g_i|$ between the coefficients f_i, g_i of the one-photon box diagram $-i\Gamma^{(\mathrm{LO})}_{\mathrm{d}\pi}$ and the neutron exchange diagram $-iV_{\mathrm{d}\pi}$; see Eqs. (E.33)-(E.34b) and (E.35)-(E.36b).. The ratios are shown as functions of the scattering angle θ at the lowest experimental energy $E = 7.78\,\mathrm{MeV}$ (momenta are on shell).

In particular, we plot the ratios $|f_1/g_1|$ and $|f_2/g_2|$ of the coefficients for the lowest experimental energy [momenta on shell; see Eqs. (4.94a)-(4.94c)], as functions of the angle θ between $\boldsymbol{p}$ and $\boldsymbol{q}$. The results are shown in Fig. E.1. Apparently, the two ratios are of the order $0.16 = (R_\mathrm{c}/R_\mathrm{h})^2$ over the whole angular range. Given the fact that the box diagram comes along with a suppressed $^{11}\mathrm{Be}^*$ propagator ($\sim R_\mathrm{c}/R_\mathrm{h}$), we conclude that the overall influence of $\Gamma^{(\mathrm{LO})}_{\mathrm{d}\pi}$ (and $\Gamma^{(\mathrm{LO})}_{\pi\mathrm{d}}$) is of N^{3}LO.

E.5 Asymptotic analyses

We analyze the UV behaviors of the LO transfer amplitude and how it is modified by effective range corrections and the excited state $^{11}\mathrm{Be}^*$.

E.5.1 LO systems

In order to demonstrate the necessity of a three-body force for the LO Faddeev equation (4.109), we perform an asymptotic analysis for large incoming and loop momenta $p, q \gg (2m_\mathrm{N}E)^{1/2} > \gamma_\mathrm{d}, \gamma_\sigma, p_\mathrm{C}$, similar to Ref. [146].

In this limit, we may send $\gamma_\mathrm{d}, \gamma_\sigma \to 0$. Moreover, the Coulomb diagrams can be neglected compared to the neutron exchange diagrams since they are suppressed by a factor p_C/q. We can further neglect the inhomogeneity of the Faddeev equation, which alone depends on the outgoing momentum p'. We also omit the three-body force and send $\Lambda \to \infty$. The LO Faddeev equation (4.109) then reduces to the homogeneous form

$$\begin{pmatrix} T^{(\mathrm{LO})\,{}^3L_J,{}^3L_J}_{\mathrm{dd}} \\ T^{(\mathrm{LO})\,{}^3L_J,{}^3L_J}_{\sigma\mathrm{d}} \end{pmatrix}(p,0;0) = \frac{p^{-1}(-1)^L}{\pi\sqrt{1+2y}} \int_0^\infty \mathrm{d}q \begin{pmatrix} (1+y)^2\, Q_L\left(\frac{q}{p} + \frac{(1+y)}{2}\frac{p}{q}\right) T^{(\mathrm{LO})\,{}^3L_J,{}^3L_J}_{\sigma\mathrm{d}}(q,0;0) \\ 4\,Q_L\left(\frac{p}{q} + \frac{(1+y)}{2}\frac{q}{p}\right) T^{(\mathrm{LO})\,{}^3L_J,{}^3L_J}_{\mathrm{dd}}(q,0;0) \end{pmatrix}. \tag{E.37}$$

A more symmetric equation can be obtained by defining new amplitudes

$$T_1^{(L)}(p) \equiv p\sqrt{\frac{2}{1+y}}\, T_{\mathrm{dd}}^{(\mathrm{LO})\,{}^3L_J,{}^3L_J}\left(p\sqrt{\frac{2}{1+y}}, 0; 0\right), \quad T_2^{(L)}(p) \equiv p\, T_{\sigma\mathrm{d}}^{(\mathrm{LO})\,{}^3L_J,{}^3L_J}(p, 0; 0)\,. \tag{E.38}$$

That yields

$$\begin{pmatrix} T_1^{(L)} \\ T_2^{(L)} \end{pmatrix}(p) \approx \frac{(-1)^L}{\pi\sqrt{1+2y}} \int_0^\infty \frac{\mathrm{d}q}{q}\, Q_L\left(\sqrt{\frac{1+y}{2}}\left(\frac{q}{p}+\frac{p}{q}\right)\right) \begin{pmatrix} 0 & (1+y)^2 \\ 4 & 0 \end{pmatrix} \begin{pmatrix} T_1^{(L)} \\ T_2^{(L)} \end{pmatrix}(q)\,. \tag{E.39}$$

Equation (E.39) is invariant under the transformation $p \to p^{-1}$. Therefore, its solutions exhibit a power law behavior [21]. In the following, we derive a governing equation for the respective exponents. We observe that Eq. (E.39) can be diagonalized using

$$\begin{pmatrix} 0 & (1+y)^2 \\ 4 & 0 \end{pmatrix} \equiv S^{-1} J S = \begin{pmatrix} -\frac{1+y}{2} & \frac{1+y}{2} \\ 1 & 1 \end{pmatrix} \cdot \begin{pmatrix} -2(1+y) & 0 \\ 0 & 2(1+y) \end{pmatrix} \cdot \begin{pmatrix} -\frac{1}{1+y} & \frac{1}{2} \\ \frac{1}{1+y} & \frac{1}{2} \end{pmatrix} \tag{E.40}$$

Setting

$$S \begin{pmatrix} T_1^{(L)} \\ T_2^{(L)} \end{pmatrix}(p) \equiv \begin{pmatrix} p^{-s_1} \\ p^{-s_2} \end{pmatrix} \tag{E.41}$$

with $s_{1/2} \in \mathbb{C}$ and $q \equiv p\,x$, we find

$$\mp 1 = \frac{2(1+y)(-1)^L}{\pi\sqrt{1+2y}} \underbrace{\int_0^\infty \mathrm{d}x\, x^{-s_{1/2}-1}\, Q_L\left(\sqrt{\frac{1+y}{2}}\left(x+\frac{1}{x}\right)\right)}_{\equiv \mathscr{M}^{(L)}(s_{1/2})} \tag{E.42}$$

The integral on the right-hand side is a Mellin transform. As shown in Ref. [146], it can be solved analytically and reads

$$\begin{aligned} \mathscr{M}^{(L)}(s) = {} & \frac{\sqrt{\pi}}{2(1+y)} \left(\frac{1+y}{2}\right)^{-\frac{L-1}{2}} 2^{-L} \frac{\Gamma\left(\frac{L+s+1}{2}\right)\Gamma\left(\frac{L-s+1}{2}\right)}{\Gamma\left(L+\frac{3}{2}\right)} \\ & \times {}_2F_1\left(\frac{L+s+1}{2}, \frac{L-s+1}{2}; L+\frac{3}{2}; \frac{1}{2(1+y)}\right). \end{aligned} \tag{E.43}$$

The original amplitudes contain contributions from both s_1 and s_2, of which the exponent with the smallest allowed real part determines the asymptotic behavior. In order to find this value, we summarize the two conditions in Eq. (E.42) into one for $s \in \{s_1, s_2\}$ by taking the square on both sides. The governing equation then reads

$$1 = \frac{4(1+y)^2}{\pi^2(1+2y)} \left[\mathscr{M}^{(L)}(s)\right]^2 \tag{E.44a}$$

$$\begin{aligned} &= \frac{1}{\pi(1+2y)} \left(\frac{2}{1+y}\right)^{L-1} 2^{-2L} \\ &\quad \times \left[\frac{\Gamma\left(\frac{L+s+1}{2}\right)\Gamma\left(\frac{L-s+1}{2}\right)}{\Gamma\left(L+\frac{3}{2}\right)}\, {}_2F_1\left(\frac{L+s+1}{2}, \frac{L-s+1}{2}; L+\frac{3}{2}; \frac{1}{2(1+y)}\right)\right]^2 . \end{aligned} \tag{E.44b}$$

This equation is invariant under $s \to -s$. Thus, if s solves the equation, so does $-s$. Let $M^{(L)} \subseteq \mathbb{C}$ be the set of all solutions s. For each L, we search for the complex values $s^{(L)}$ in

$$\left\{ s^{(L)} \in M^{(L)} : \operatorname{Re} s^{(L)} = \min\{ s \in M^{(L)} : \operatorname{Re} s + 1 > 0 \} \right\}, \tag{E.45}$$

which have the smallest possible real part. They determine the asymptotic behaviors $\sim p^{-1-s^{(L)}}$ of the original amplitudes. For $L \leq 3$ we find

$$s^{(0)} \approx \pm 0.6357 i \equiv \pm i s_0 , \quad s^{(1)} \approx 1.6387 , \quad s^{(2)} \approx 2.8087 , \quad s^{(3)} \approx 3.8875 . \tag{E.46}$$

For $L \geq 1$, the amplitudes have unique solutions. For $L = 0$, however, $s^{(0)}$ can be one of the two solutions $\pm i s_0$. Thus, the rescaled amplitudes $T_{1/2}(p)$ are superpositions of the periodic functions $p^{\pm i s_0} = \exp(\pm i s_0 \ln(p))$. One of the two respective coefficients is fixed by the inhomogeneity of the Faddeev equation. In order to fix the second one, we need a three-body force. This quantity will then exhibit a limit-cycle behavior with scaling factor

$$\exp(\pi / s_0) \approx 140.091 . \tag{E.47}$$

This value coincides with the result of Braaten and Hammer [21]. It is much larger than the scaling factor 22.69 of three identical bosons.

E.5.2 Effective range modifications

Effective range corrections are implemented by replacing $\mathscr{G}_a^{(\mathrm{LO})}$ ($a \in \{\mathrm{d}, \sigma\}$) with NLO propagator functions $\mathscr{G}_a^{(\mathrm{NLO})}$ given in Eqs. (4.116a)-(4.116b). As mentioned in the text, this approach leads to a modification of the UV behavior of the Faddeev kernel. In particular, we find

$$\frac{\mathscr{G}_{\mathrm{d}}^{(\mathrm{NLO})}(q;0)}{\mathscr{G}_{\mathrm{d}}^{(\mathrm{LO})}(q;0)} \xrightarrow{q \gg r_{\mathrm{d}} > \gamma_{\mathrm{d}}} \frac{r_{\mathrm{d}}}{2} \frac{\sqrt{1+2y}}{2} q \equiv \rho_{\mathrm{d}} q \sqrt{\frac{1+y}{2}} \gg 1 , \tag{E.48a}$$

$$\frac{\mathscr{G}_{\sigma}^{(\mathrm{NLO})}(q;0)}{\mathscr{G}_{\sigma}^{(\mathrm{LO})}(q;0)} \xrightarrow{q \gg r_{\sigma} > \gamma_{\sigma}} \frac{r_{\sigma}}{2} \frac{\sqrt{1+2y}}{1+y} q \equiv \rho_{\sigma} q \gg 1 . \tag{E.48b}$$

As a consequence, the new asymptotic Faddeev equation reads

$$\begin{pmatrix} T_1^{(L)} \\ T_2^{(L)} \end{pmatrix}(p) \approx \frac{(-1)^L}{\pi \sqrt{1+2y}} \int_0^\infty \mathrm{d}q \, Q_L \left(\sqrt{\frac{1+y}{2}} \left(\frac{q}{p} + \frac{p}{q} \right) \right) \begin{pmatrix} 0 & (1+y)^2 \rho_\sigma \\ 4\rho_{\mathrm{d}} & 0 \end{pmatrix} \begin{pmatrix} T_1^{(L)} \\ T_2^{(L)} \end{pmatrix}(q) . \tag{E.49}$$

The definition of the amplitudes $T_i^{(L)}$ is the same as in Eq. (E.38).

The new asymptotic equation is not invariant under $p \to p^{-1}$ anymore. Thus, we cannot expect a simple power law behavior. Instead, we allow for p-dependent exponents $\tilde{s}_{1/2}$ and set

$$\tilde{S} \begin{pmatrix} T_1^{(L)} \\ T_2^{(L)} \end{pmatrix}(p) \equiv \begin{pmatrix} p^{-\tilde{s}_1(p)} \\ p^{-\tilde{s}_2(p)} \end{pmatrix} . \tag{E.50}$$

The new transformation matrix

$$\tilde{S} \equiv \begin{pmatrix} -\frac{1}{1+y}\sqrt{\frac{\rho_{\mathrm{d}}}{\rho_\sigma}} & \frac{1}{2} \\ \frac{1}{1+y}\sqrt{\frac{\rho_{\mathrm{d}}}{\rho_\sigma}} & \frac{1}{2} \end{pmatrix} = \begin{pmatrix} -\frac{1+y}{2}\sqrt{\frac{\rho_\sigma}{\rho_{\mathrm{d}}}} & \frac{1+y}{2}\sqrt{\frac{\rho_\sigma}{\rho_{\mathrm{d}}}} \\ 1 & 1 \end{pmatrix}^{-1} \tag{E.51}$$

diagonalizes the kernel matrix

$$\begin{pmatrix} 0 & (1+y)^2\rho_\sigma \\ 4\rho_\mathrm{d} & 0 \end{pmatrix} \equiv \tilde{S}^{-1} \begin{pmatrix} -2(1+y)\sqrt{\rho_\mathrm{d}\rho_\sigma} & 0 \\ 0 & 2(1+y)\sqrt{\rho_\mathrm{d}\rho_\sigma} \end{pmatrix} \tilde{S}\,. \tag{E.52}$$

The new exponents $\tilde{s}(p) \in \{\tilde{s}_1(p), \tilde{s}_2(p)\}$ are now governed by the equation

$$1 = \frac{4(1+y)^2}{\pi^2(1+2y)} \left(p\sqrt{\rho_\mathrm{d}\rho_\sigma}\right)^2 \left[\mathscr{M}^{(L)}(\tilde{s}(p)-1)\right]^2 \tag{E.53}$$

with

$$\sqrt{\rho_\mathrm{d}\rho_\sigma} = \frac{\sqrt{r_\mathrm{d} r_\sigma}}{2} \left(\frac{1+2y}{2(1+y)} \sqrt{\frac{2}{1+y}} \right)^{1/2} \approx 1.06\,\mathrm{fm} = (186\,\mathrm{MeV})^{-1}\,. \tag{E.54}$$

We see that the old equation for s can be restored by setting $p\,(\rho_\mathrm{d}\rho_\sigma)^{1/2} \equiv 1$ and replacing $\tilde{s}(p) \to s+1$. Thus, we expect the new amplitudes to fall off roughly one order faster in p (for not too large p) compared to the old amplitudes. Moreover, if $\tilde{s}(p)$ is a solution, so are the values $\tilde{s}^*(p)$, $-\tilde{s}(p)+2$, and $-\tilde{s}^*(p)+2$. That is a consequence of the symmetry relations

$$\Gamma(z^*) = [\Gamma(z)]^*\,, \tag{E.55a}$$

$${}_2F_1(a^*, b^*; c^*; z^*) = [{}_2F_1(a, b; c; z)]^* \quad (z \notin (1, \infty))\,, \tag{E.55b}$$

$${}_2F_1(a, b; c; z) = {}_2F_1(b, a; c; z)\,. \tag{E.55c}$$

Let $\tilde{M}^{(L)}(p)$ be the set of solutions $\tilde{s}(p)$ for fixed $L \geq 0$ and $p \geq (\rho_\mathrm{d}\rho_\sigma)^{-1/2}$. Again, we search for the values $\tilde{s}^{(L)}(p) \in \tilde{M}^{(L)}(p)$ with minimal allowed real part. Numerical results for $L \leq 3$ are shown in Fig. E.2. The $L = 0$ system has again two solutions $\tilde{s}^{(0)}(p) = 1 \pm i\tilde{s}_0(p)$ (complex conjugates) and still needs a three-body force. As opposed to the LO system, the new imaginary part $\tilde{s}_0(p)$ is logarithmically increasing in p, starting at $\tilde{s}_0(p = (\rho_\mathrm{d}\rho_\sigma)^{-1/2}) = s_0 \approx 0.6357$. It follows that $T_{1/2}(p) \sim p^{-1 \pm i\tilde{s}_0(p)} \sim \exp([\ln(p)]^2)/p$.

More remarkably, the $L \geq 1$ solutions resemble $\tilde{s}^{(0)}(p)$ for large p, i.e., above $p \approx 4\,(\rho_\mathrm{d}\rho_\sigma)^{-1/2} \approx 744\,\mathrm{MeV}$ ($L = 1$), $p \approx 17\,(\rho_\mathrm{d}\rho_\sigma)^{-1/2} \approx 3.16\,\mathrm{GeV}$ ($L = 2$), and $p \approx 60\,(\rho_\mathrm{d}\rho_\sigma)^{-1/2} \approx 11.2\,\mathrm{GeV}$ ($L = 3$). As a consequence, these channels now in principle also need a three-body force, at least if $\Lambda \sim p$ becomes very large. In NLO calculations, however, we choose cutoffs $\Lambda \leq 1500\,\mathrm{MeV}$, for which only the $L = 0$ and $L = 1$ sectors have more than one amplitude solution. We can thus neglect three-body forces in the $L \geq 2$ sectors. Moreover, it turns out that cutoff dependences of the $L = 1$ amplitudes are very small over the large range $\Lambda \in [500, 1500]\,\mathrm{MeV}$; see main text.

E.5.3 NLO systems

For completeness, we note that asymptotic analyses can also be done for the full NLO systems (including $^{11}\mathrm{Be}^*$). The exponents $\tilde{s}(p)$ in the $L_\mathrm{d} = J \pm 1$ can be determined from

$$\begin{aligned} 1 = \frac{4(1+y)^2}{\pi^2(1+2y)} \Bigg(&\left(p\sqrt{\rho_\mathrm{d}\rho_\sigma}\right)^2 \left[\mathscr{M}^{(L_\mathrm{d})}(\tilde{s}(p)-1)\right]^2 \\ &+ \left(p\sqrt{\rho_\mathrm{d}\rho_\pi}\right)^2 \left[\xi\mathscr{M}^{(L_\mathrm{d})}(\tilde{s}(p)-1) - \sqrt{2\xi}\,\mathscr{M}^{(J)}(\tilde{s}(p)-2)\right] \\ &\times \left[\xi\mathscr{M}^{(L_\mathrm{d})}(\tilde{s}(p)-1) - \sqrt{2\xi}\,\mathscr{M}^{(J)}(\tilde{s}(p))\right] \Bigg) \quad (L_\mathrm{d} = J \pm 1)\,, \end{aligned} \tag{E.56}$$

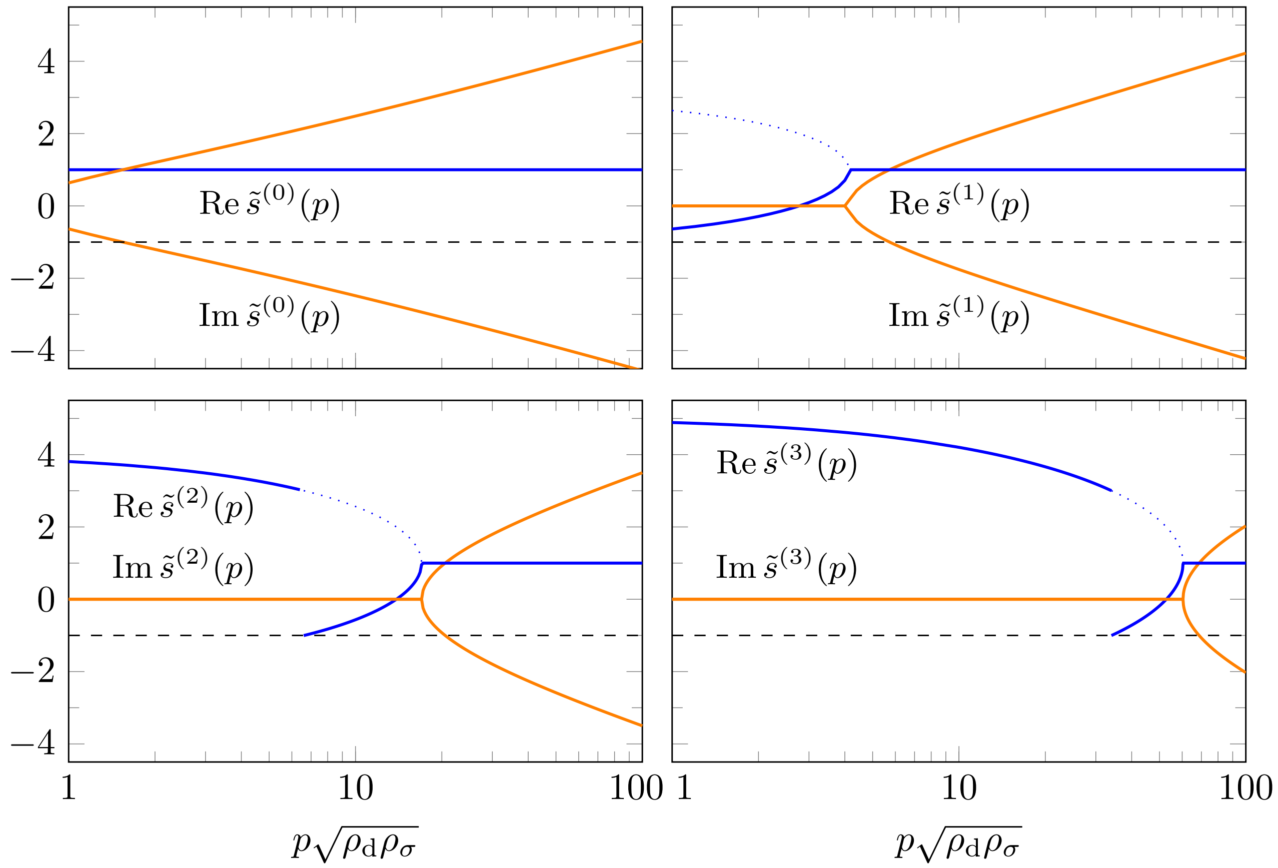

Figure E.2.: Solutions $\tilde{s}^{(L)}$ ($L \leq 3$) after inclusion of the effective ranges r_d, r_σ as functions of the rescaled momentum $p\,(\rho_\mathrm{d}\rho_\sigma)^{1/2} \approx p/(217\,\mathrm{MeV})$. Real (imaginary) parts are drawn in blue (orange). Dashed grid lines indicate the lower bound for the real part, i.e., Re$\,\tilde{s}^{(L)} > -1$.

and in the $L_\mathrm{d} = J$ systems we find

$$\begin{aligned} 1 = \frac{4(1+y)^2}{\pi^2(1+2y)}\Bigg(&\left(p\sqrt{\rho_\mathrm{d}\rho_\sigma}\right)^2 \left[\mathscr{M}^{(L_\mathrm{d})}(\tilde{s}(p)-1)\right]^2 \\ &+ \left(p\sqrt{\rho_\mathrm{d}\rho_\pi}\right)^2 \sum_{i=\pm1} w_i(J)\left[\xi\mathscr{M}^{(L_\mathrm{d})}(\tilde{s}(p)-1) - \sqrt{2\xi}\,\mathscr{M}^{(L_\mathrm{d}+i)}(\tilde{s}(p)-2)\right] \\ &\times \left[\xi\mathscr{M}^{(L_\mathrm{d})}(\tilde{s}(p)-1) - \sqrt{2\xi}\,\mathscr{M}^{(L_\mathrm{d}+i)}(\tilde{s}(p))\right]\Bigg) \quad (L_\mathrm{d} = J), \end{aligned} \tag{E.57}$$

where $\xi = 1/(1+y)$ and

$$\rho_\pi \equiv \frac{2}{-r_\pi}\,\frac{1+y}{\sqrt{1+2y}} \approx 1.21\rho_\sigma\,, \tag{E.58a}$$

$$w_{\pm1}(J) \equiv \left(\frac{J}{J+1}\right)^{\pm1} \frac{\max\{J, J\pm1\}}{2J+1}\,. \tag{E.58b}$$

The NLO elastic and transfer amplitudes then scale like $\sim p^{-1-\tilde{s}^{(L)}(p)}$ with $\tilde{s}^{(L)}(p)$ having minimally allowed real part. The previous equations obtained without the excited state are recovered by sending $\rho_\pi \to 0$, i.e., $r_\pi^{-1} \to 0$.

The qualitative behaviors of the new exponent solutions $\tilde{s}^{(L)}$ is the same as without the excited state. In particular, their real parts all approach 1, now even earlier in p than before. The imaginary parts are again logarithmically increasing in p.

E.6 Differential cross section

The transfer amplitude $T_{\sigma\mathrm{d}}^{Sm,1m'}$ can be used to calculate the differential cross section for the reaction $^{10}\mathrm{Be}\,(\mathrm{d},\,\mathrm{p})\,^{11}\mathrm{Be}$. The general expression for a spin-averaged nonrelativistic two-body cross section $\mathrm{d}\sigma$ with incoming (outgoing) momenta $\boldsymbol{p}_1$, $\boldsymbol{p}_2$ ($\boldsymbol{p}_1'$, $\boldsymbol{p}_2'$) and total spin S (S') reads

$$\mathrm{d}\sigma = \frac{1}{\sum_S (2S+1)} \sum_{Sm_S, S'm_{S'}} \frac{\mathrm{d}^3 p_1'}{(2\pi)^3} \frac{\mathrm{d}^3 p_2'}{(2\pi)^3} \cdot (2\pi)^4 \, \delta^{(4)}\left(p_1'^{\,\mu} + p_2'^{\,\mu} - p_1^{\mu} - p_2^{\mu}\right) \\ \times \frac{\left| \mathcal{M}^{Sm_S, S'm_{S'}} \left(p_1^{\mu}, p_2^{\mu} \to p_1'^{\,\mu}, p_2'^{\,\mu}\right) \right|^2}{|\boldsymbol{v}_1 - \boldsymbol{v}_2|} \,. \tag{E.59}$$

The energies $p_1^0, p_2^0, p_1'^{\,0}, p_2'^{\,0}$ are on shell. Moreover, $\mathcal{M}^{Sm_S, S'm_{S'}}\left(p_1^{\mu}, p_2^{\mu} \to p_1'^{\,\mu}, p_2'^{\,\mu}\right)$ is the matrix element of the process. The expression which depends on the velocities $\boldsymbol{v}_i = \boldsymbol{p}_i / m_{\mathrm{kin},i}$ of the incident particles is called flux factor.

We consider the reaction $^{10}\mathrm{Be}\,(\mathrm{d},\,\mathrm{p})\,^{11}\mathrm{Be}$ in the center-of-mass frame at energy E. The initial $^{10}\mathrm{Be}$ core and the deuteron have on-shell momenta $\boldsymbol{p}_{\mathrm{c}} \equiv \bar{\boldsymbol{p}}_{\mathrm{d}} = \bar{p}_{\mathrm{d}}\, \hat{\boldsymbol{p}}_{\mathrm{c}}$ and $\boldsymbol{p}_{\mathrm{d}} = -\bar{\boldsymbol{p}}_{\mathrm{d}}$. The flux factor then reads

$$|\boldsymbol{v}_{\mathrm{c}} - \boldsymbol{v}_{\mathrm{d}}|^{-1} = \left| \frac{\bar{\boldsymbol{p}}_{\mathrm{d}}}{m_{\mathrm{c}}} - \frac{-\bar{\boldsymbol{p}}_{\mathrm{d}}}{2m_{\mathrm{N}}} \right|^{-1} = \frac{\mu_{\mathrm{d}}}{\bar{p}_{\mathrm{d}}} \,. \tag{E.60}$$

In the outgoing channel, we set $\boldsymbol{p}_{\mathrm{p}}' \equiv \boldsymbol{p}' = p'\, \hat{\boldsymbol{p}}_{\mathrm{p}}'$ for the proton. The momentum-conserving delta function then yields $\boldsymbol{p}_{\sigma}' \to -\boldsymbol{p}'$ for $^{11}\mathrm{Be}$. Moreover, the energy-conserving delta function

$$\delta\left(\frac{\boldsymbol{p}'^2}{2\mu_{\sigma}} - B_{\sigma} - E \right) = \frac{\mu_{\sigma}}{\bar{p}_{\sigma}}\, \delta\left(p' - \bar{p}_{\sigma}\right) \tag{E.61}$$

ensures on-shell evaluation in the outgoing channel, i.e., it sets $\boldsymbol{p}' \to \bar{\boldsymbol{p}}_{\sigma} \equiv \bar{p}_{\sigma}\, \hat{\boldsymbol{p}}_{\mathrm{p}}'$.

The scattering angle θ_{cm} is defined via $\cos\theta_{\mathrm{cm}} \equiv \hat{\boldsymbol{p}}_{\mathrm{d}} \cdot \hat{\boldsymbol{p}}_{\mathrm{p}}'$. We set $\mathrm{d}^3 p' \equiv \mathrm{d}p'\, p'^2\, \mathrm{d}(\cos\theta_{\mathrm{cm}})\, \mathrm{d}\varphi \equiv \mathrm{d}p'\, p'^2\, \mathrm{d}\Omega$ and integrate over the delta functions. The matrix element is then replaced by the transfer amplitude as follows,

$$\left| \mathcal{M}^{Sm_S, S'm_{S'}} \left(p_1^{\mu}, p_2^{\mu} \to p_1'^{\,\mu}, p_2'^{\,\mu}\right) \right|^2 \xrightarrow{\delta^{(3)}} \left| \sqrt{Z_{\mathrm{d}} Z_{\sigma}}\; T_{\mathrm{d}\sigma}^{1m_S, S'm_{S'}} \left(\bar{\boldsymbol{p}}_{\mathrm{d}},\, \boldsymbol{p}';\, E\right) \right|^2 \tag{E.62a}$$

$$\xrightarrow{\delta} \left| \sqrt{Z_{\mathrm{d}} Z_{\sigma}}\; T_{\mathrm{d}\sigma}^{1m_S, S'm_{S'}} \left(\bar{\boldsymbol{p}}_{\mathrm{d}},\, \bar{\boldsymbol{p}}_{\sigma};\, E\right) \right|^2 \tag{E.62b}$$

$$= \left| \sqrt{Z_{\mathrm{d}} Z_{\sigma}}\; T_{\sigma\mathrm{d}}^{S'm_{S'}, 1m_S} \left(\bar{\boldsymbol{p}}_{\sigma},\, \bar{\boldsymbol{p}}_{\mathrm{d}};\, E\right) \right|^2 . \tag{E.62c}$$

In the last step we used time reversal invariance. The final cross section is then given by Eq. (4.114).

F Calculations for fermionic three-body losses (Chapter 5)

In the following, we expand on the calculation of the two-fermion self-energy and the exchange diagram.

F.1 Diatom self-energy

The ${}^6\mathrm{Li}_2(\mathrm{e})$ self-energy loop of Fig. 5.2 can be calculated using second order perturbation theory as done in Appendix E.1.1 for the p-n ${}^3s_1$ sector. We consider incoming/outgoing ${}^6\mathrm{Li}_2(\mathrm{e})$ states with four-momentum p^μ (conserved) and polarizations $m_l, m_l' \in \{1, 0, -1\}$. Considering all possible contractions of e_{m_l} and ψ fields, we find

$$
\begin{aligned}
&-i\Sigma_{\mathrm{e}}\Big(p^0-\boldsymbol{p}^2/(4m)\Big)\,\delta^{m_l m_l'}\\
&\quad= 2\,\frac{1}{2!}\left(-i\frac{g_{\mathrm{e}}}{\sqrt{2}}\right)^2 \Big\langle e_{m_l',\boldsymbol{p}}\Big|\Big[e^\dagger_{m_1}\Big(\psi\left\{-i\overleftrightarrow{\boldsymbol{\nabla}}\right\}_{1m_1}\psi\Big)\Big](x)\Big[\Big(\psi\left\{-i\overleftrightarrow{\boldsymbol{\nabla}}\right\}_{1m_2}\psi\Big)^\dagger e_{m_2}\Big](y)\Big|e_{m_l,\boldsymbol{p}}\Big\rangle\\
&\qquad+ 2\,\frac{1}{2!}\left(-i\frac{g_{\mathrm{e}}}{\sqrt{2}}\right)^2 \Big\langle e_{m_l',\boldsymbol{p}}\Big|\Big[e^\dagger_{m_1}\Big(\psi\left\{-i\overleftrightarrow{\boldsymbol{\nabla}}\right\}_{1m_1}\psi\Big)\Big](x)\Big[\Big(\psi\left\{-i\overleftrightarrow{\boldsymbol{\nabla}}\right\}_{1m_2}\psi\Big)^\dagger e_{m_2}\Big](y)\Big|e_{m_l,\boldsymbol{p}}\Big\rangle \qquad \text{(F.1a)}\\
&\quad\sim -\frac{g_{\mathrm{e}}^2}{2}\int\frac{\mathrm{d}^4 l}{(2\pi)^4}\Big[\ \{\boldsymbol{l}\}_{1m_l'}\{\boldsymbol{l}\}^*_{1m_l}(-1)^0+\{\boldsymbol{l}\}_{1m_l'}\{-\boldsymbol{l}\}^*_{1m_l}(-1)^1\ \Big]\\
&\qquad\qquad\times iG_\psi\left(p^\mu/2+l^\mu\right)\ iG_\psi\left(p^\mu/2-l^\mu\right) \qquad \text{(F.1b)}\\
&\quad= -g_{\mathrm{e}}^2\int\frac{\mathrm{d}^4 l}{(2\pi)^4}\{\boldsymbol{l}\}^*_{1m_l}\{\boldsymbol{l}\}_{1m_l'}\ iG_\psi\left(p^\mu/2+l^\mu\right)\ iG_\psi\left(p^\mu/2-l^\mu\right). \qquad \text{(F.1c)}
\end{aligned}
$$

In Eq. (F.1a), the arguments “(x)” and “(y)” indicate the double-integral origin of the respective two Lagrangian terms $\Psi^{(\dagger)}(x) \equiv \left[e^\dagger_m\Big(\psi\left\{-i\overleftrightarrow{\boldsymbol{\nabla}}\right\}_{1m}\psi\Big)\right]^{(\dagger)}(x)$. Note that we only made combinations of the form $\Psi(x)\Psi^\dagger(y)$ explicit. Contractions for $\Psi^\dagger(x)\Psi(y)$ give same results and are taken care of by the prefactors “2”. Matrix elements with $\Psi(x)\Psi(y)$ or $\Psi^\dagger(x)\Psi^\dagger(y)$ cannot be fully contracted.

Contractions of the e_{m_l} fields yield factors $\delta^{m_l' m_1}$ and $\delta^{m_l m_2}$. Each ψ contraction is related to a propagating ${}^6\mathrm{Li}$ atom (off shell). In our convention, the two atoms have off-shell momenta $l^\mu_{\psi,1/2} = p^\mu/2 \pm l^\mu$ with total and relative four-momenta $p^\mu = (p^0, \boldsymbol{p})$ and $l^\mu = (l^0, \boldsymbol{l})$, respectively. The tensors $\left\{-i\overleftrightarrow{\boldsymbol{\nabla}}\right\}_{1m}$ then yield $(\boldsymbol{l}_{\psi,1}-\boldsymbol{l}_{\psi,2})/2 = \pm\boldsymbol{l}$, depending on which fields they act. In the second row of Eq. (F.1a), the ψ fields are automatically disentangled since the Hermitian conjugate of $\Psi^\dagger(y)$ exchanges the order of the ψ fields. In the third row, one anticommutation is needed.

We observe that the vertex factor $1/\sqrt{2}$ properly accounts for the two possible contractions. The final expression resembles the D^0 self-energy loop in (D.8a) if $g \to g_{\mathrm{e}}$, $m_\pi, m_D \to m$, $\xi \to 1/2$ and $l_i \to \{\boldsymbol{l}\}_{1m_l}$, $l_{i'} \to \{\boldsymbol{l}\}_{1m_l'}$. Consequently, the self-energy in PDS reads

$$
\begin{aligned}
\Sigma_{\mathrm{e}}(E_{\mathrm{cm}}) &= -g_{\mathrm{e}}^2\frac{m}{12\pi}\left(\Lambda_{\mathrm{PDS}}\,m(E_{\mathrm{cm}}+i\epsilon)+[-m(E_{\mathrm{cm}}+i\epsilon)]^{3/2}\right) \qquad \text{(F.2a)}\\
&= -g_{\mathrm{e}}^2\frac{m}{12\pi}\left(\Lambda_{\mathrm{PDS}}\bar{k}^2+i\bar{k}^3\right). \qquad \text{(F.2b)}
\end{aligned}
$$

F.2 Fermion exchange potential

The tree-level fermion exchange diagram in Fig. 5.5 is a matrix element between two atom-diatom states. The respective momenta be $\pm\boldsymbol{p}$ ($\pm\boldsymbol{q}$). The exchanged ^{6}Li atom then has a momentum $-\boldsymbol{p}-\boldsymbol{q}$. We proceed similar to the self-energy calculation above and find

$$
\begin{aligned}
-iV_{\mathrm{e}}^{1m_l,1m_l'}(\boldsymbol{p},\boldsymbol{q};E) = 2\,\frac{1}{2!}\left(-i\frac{g_{\mathrm{e}}}{\sqrt{2}}\right)^2 \sum_{\substack{\psi\text{-}\\ \text{contractions}}} \\
\times \left\langle \psi_{\boldsymbol{q}}\, e_{m_l',-\boldsymbol{q}} \middle| \left[e^\dagger_{m_1}\left(\psi\left\{-i\overleftrightarrow{\boldsymbol{\nabla}}\right\}_{1m_1}\psi\right)\right](x)\left[\left(\psi\left\{-i\overleftrightarrow{\boldsymbol{\nabla}}\right\}_{1m_2}\psi\right)^\dagger e_{m_2}\right](y) \middle| \psi_{\boldsymbol{p}}\, e_{m_l,-\boldsymbol{p}} \right\rangle \qquad \text{(F.3a)}
\end{aligned}
$$

$$
\begin{aligned}
\sim -\frac{g_{\mathrm{e}}^2}{2}\Bigg[&-\left\{\frac{(-\boldsymbol{p}-\boldsymbol{q})-\boldsymbol{p}}{2}\right\}_{1m_l'}\left\{\frac{(-\boldsymbol{p}-\boldsymbol{q})-\boldsymbol{q}}{2}\right\}^*_{1m_l} \\
&+\left\{\frac{(-\boldsymbol{p}-\boldsymbol{q})-\boldsymbol{p}}{2}\right\}_{1m_l'}\left\{\frac{\boldsymbol{q}-(-\boldsymbol{p}-\boldsymbol{q})}{2}\right\}^*_{1m_l} \\
&+\left\{\frac{\boldsymbol{p}-(-\boldsymbol{p}-\boldsymbol{q})}{2}\right\}_{1m_l'}\left\{\frac{(-\boldsymbol{p}-\boldsymbol{q})-\boldsymbol{q}}{2}\right\}^*_{1m_l} \\
&-\left\{\frac{\boldsymbol{p}-(-\boldsymbol{p}-\boldsymbol{q})}{2}\right\}_{1m_l'}\left\{\frac{\boldsymbol{q}-(-\boldsymbol{p}-\boldsymbol{q})}{2}\right\}^*_{1m_l}\Bigg]\, iG_\psi\left(E-\frac{p^2+q^2}{2m};-\boldsymbol{p}-\boldsymbol{q}\right) \qquad \text{(F.3b)}
\end{aligned}
$$

$$
= +2ig_{\mathrm{e}}^2\frac{\{\boldsymbol{q}+\boldsymbol{p}/2\}^*_{1m_l}\{\boldsymbol{p}+\boldsymbol{q}/2\}_{1m_l'}}{E-\frac{p^2+q^2}{m}-\frac{\boldsymbol{p}\cdot\boldsymbol{q}}{m}+i\epsilon} \qquad \text{(F.3c)}
$$

Note that this result is qualitatively different from the one-pion exchange diagram between $D^0\bar{D}^{0*}$ and $\bar{D}^0D^{0*}$ pairs; cf. Eq. (3.68). Firstly, there is a symmetry factor 2 in front of the expression. Secondly (and more importantly, the diagram exhibits a different overall sign due to anticommutation. This sign changes the UV behavior of the integral kernel such that the spectrum is qualitatively different from the one of the $D^0\bar{D}^0\pi^0$ system.

Bibliography

[1] C. P. Burgess and G. D. Moore. *The standard model: A primer*. Cambridge University Press (2006).

[2] K. G. Wilson. *Confinement of Quarks*. Phys. Rev. D **10**, 2445–2459 (1974).

[3] S. Durr *et al.* *Ab-Initio Determination of Light Hadron Masses*. Science **322**, 1224–1227 (2008).

[4] Z. Davoudi. *Light Nuclei from Lattice QCD: Spectrum, Structure and Reactions*. arXiv:1902.04959 [hep-lat].

[5] S. Prelovsek and L. Leskovec. *Evidence for X(3872) from DD* scattering on the lattice*. Phys. Rev. Lett. **111**, 192001 (2013).

[6] H. Georgi. *Effective field theory*. Ann. Rev. Nucl. Part. Sci. **43**, 209–252 (1993).

[7] C. P. Burgess. *Introduction to Effective Field Theory*. Ann. Rev. Nucl. Part. Sci. **57**, 329–362 (2007).

[8] S. Weinberg. *Phenomenological Lagrangians*. Physica A **96**, 327–340 (1979).

[9] E. Epelbaum, H.-W. Hammer, and U.-G. Meissner. *Modern Theory of Nuclear Forces*. Rev. Mod. Phys. **81**, 1773–1825 (2009).

[10] R. Machleidt and D. R. Entem. *Chiral effective field theory and nuclear forces*. Phys. Rept. **503**, 1–75 (2011).

[11] J. Gasser and H. Leutwyler. *Chiral Perturbation Theory to One Loop*. Annals Phys. **158**, 142 (1984).

[12] J. Gasser and H. Leutwyler. *Chiral Perturbation Theory: Expansions in the Mass of the Strange Quark*. Nucl. Phys. B **250**, 465–516 (1985).

[13] E. E. Jenkins and A. V. Manohar. *Baryon chiral perturbation theory using a heavy fermion Lagrangian*. Phys. Lett. B **255**, 558–562 (1991).

[14] V. Bernard, N. Kaiser, J. Kambor, and U.-G. Meissner. *Chiral structure of the nucleon*. Nucl. Phys. B **388**, 315–345 (1992).

[15] V. Bernard, N. Kaiser, and U.-G. Meissner. *Chiral dynamics in nucleons and nuclei*. Int. J. Mod. Phys. E **4**, 193–346 (1995).

[16] H. Hergert, S. Binder, A. Calci, J. Langhammer, and R. Roth. *Ab Initio Calculations of Even Oxygen Isotopes with Chiral Two-Plus-Three-Nucleon Interactions*. Phys. Rev. Lett. **110**, 242501 (2013).

[17] K. Hebeler, J. M. Lattimer, C. J. Pethick, and A. Schwenk. *Equation of state and neutron star properties constrained by nuclear physics and observation*. Astrophys. J. **773**, 11 (2013).

[18] P. L. Cho. *Heavy hadron chiral perturbation theory*. Nucl. Phys. B **396**, 183–204 (1993). [Erratum: Nucl. Phys. B **421**, 683 (1994)].

[19] D. B. Kaplan, M. J. Savage, and M. B. Wise. *A New expansion for nucleon-nucleon interactions*. Phys. Lett. B **424**, 390–396 (1998).

[20] H. A. Bethe. *Theory of the Effective Range in Nuclear Scattering*. Phys. Rev. **76**, 38–50 (1949).

[21] E. Braaten and H.-W. Hammer. *Universality in few-body systems with large scattering length*. Phys. Rept. **428**, 259–390 (2006).

[22] H.-W. Hammer, C. Ji, and D. R. Phillips. *Effective field theory description of halo nuclei*. J. Phys. G **44**, 103002 (2017).

[23] E. Braaten and M. Kusunoki. *Low-energy universality and the new charmonium resonance at 3870 MeV*. Phys. Rev. D **69**, 074005 (2004).

[24] C. Ji, C. Elster, and D. R. Phillips. *^{6}He nucleus in halo effective field theory*. Phys. Rev. C **90**, 044004 (2014).

[25] M. J. Savage, K. A. Scaldeferri, and M. B. Wise. *$n + p \to d + \gamma$ in Effective Field Theory*. Nucl. Phys. A **652**, 273–286 (1999).

[26] J.-W. Chen and M. J. Savage. *$np \to d\gamma$ for Big-Bang Nucleosynthesis*. Phys. Rev. C **60**, 065205 (1999).

[27] G. Rupak. *Precision Calculation of $np \to d\gamma$ Cross Section for Big-Bang Nucleosynthesis*. Nucl. Phys. A **678**, 405–423 (2000).

[28] S.-K. Choi *et al.* (Belle Collab.). *Observation of a Narrow Charmoniumlike State in Exclusive $B^\pm \to K^\pm \pi^+ \pi^- J/\psi$ Decays*. Phys. Rev. Lett. **91**, 262001 (2003).

[29] D. Acosta *et al.* (CDF Collab.). *Observation of the narrow state $X(3872) \to J/\psi \pi^+ \pi^-$ in $\bar{p}p$ collisions at $\sqrt{s} = 1.96$ TeV*. Phys. Rev. Lett. **93**, 072001 (2004).

[30] S.-K. Choi *et al.* (Belle Collab.). *Bounds on the width, mass difference and other properties of $X(3872) \to \pi^+ \pi^- J/\psi$ decays*. Phys. Rev. D **84**, 052004 (2011).

[31] T. Barnes and S. Godfrey. *Charmonium options for the X(3872)*. Phys. Rev. D **69**, 054008 (2004).

[32] K. Terasaki. *A New tetra-quark interpretation of X(3872)*. Prog. Theor. Phys. **118**, 821–826 (2007).

[33] K. Terasaki. *Tetra-Quark Interpretation of X(3872) and Z_c(3900) Revisited*. arXiv:1611.02825 [hep-ph].

[34] R. Aaij *et al.* (LHCb Collab.). *Determination of the X(3872) meson quantum numbers*. Phys. Rev. Lett. **110**, 222001 (2013).

[35] A. Tomaradze, S. Dobbs, T. Xiao, and K. K. Seth. *Precision Measurement of the Mass of the D^{*0} Meson and the Binding Energy of the $X(3872)$ Meson as a $D^0\overline{D^{*0}}$ Molecule*. Phys. Rev. D **91**, 011102 (2015).

[36] M. Tanabashi *et al.* (Particle Data Group). *Review of Particle Physics*. Phys. Rev. D **98**, 030001 (2018).

[37] F. E. Close and P. R. Page. *The $D^{*0}\bar{D}^0$ threshold resonance*. Phys. Lett. B **578**, 119–123 (2004).

[38] S. Pakvasa and M. Suzuki. *On the hidden charm state at 3872 MeV*. Phys. Lett. B **579**, 67–73 (2004).

[39] M. B. Voloshin. *Interference and binding effects in decays of possible molecular component of X(3872)*. Phys. Lett. B **579**, 316–320 (2004).

[40] C.-Y. Wong. *Molecular states of heavy quark mesons*. Phys. Rev. C **69**, 055202 (2004).

[41] E. S. Swanson. *Short range structure in the X(3872)*. Phys. Lett. B **588**, 189–195 (2004).

[42] M. B. Voloshin and L. B. Okun. *Hadron Molecules and Charmonium Atom*. JETP Lett. **23**, 333–336 (1976). [Pisma Zh. Eksp. Teor. Fiz. **23**, 369 (1976)].

[43] E. Braaten. *Effective field theories for the X(3872)*. PoS **EFT09**, 065 (2009).

[44] E. Braaten and M. Lu. *Line shapes of the X(3872)*. Phys. Rev. D **76**, 094028 (2007).

[45] E. Braaten. *Galilean-invariant effective field theory for the X(3872)*. Phys. Rev. D **91**, 114007 (2015).

[46] V. Baru, A. A. Filin, C. Hanhart, Yu. S. Kalashnikova, A. E. Kudryavtsev, and A. V. Nefediev. *Three-body $D\bar{D}\pi$ dynamics for the X(3872)*. Phys. Rev. D **84**, 074029 (2011).

[47] I. Tanihata. *Nuclear Physics with RIB's: How it all started*. Eur. Phys. J. Plus **131**, 90 (2016).

[48] P. G. Hansen and B. Jonson. *The Neutron Halo of Extremely Neutron-Rich Nuclei*. Europhys. Lett. **4**, 409–414 (1987).

[49] M. V. Zhukov *et al.* *Bound state properties of Borromean halo nuclei: ^{6}He and ^{11}Li*. Phys. Rept. **231**, 151–199 (1993).

[50] P. G. Hansen, A. S. Jensen, and B. Jonson. *Nuclear halos*. Ann. Rev. Nucl. Part. Sci. **45**, 591–634 (1995).

[51] B. Jonson. *Light dripline nuclei*. Phys. Rep. **389**, 1–59 (2004).

[52] A. S. Jensen, K. Riisager, D. V. Fedorov, and E. Garrido. *Structure and reactions of quantum halos*. Rev. Mod. Phys. **76**, 215–261 (2004).

[53] W. Nörtershäuser *et al.* *Nuclear Charge Radii of ^{7,9,10}Be and the one-neutron halo nucleus ^{11}Be*. Phys. Rev. Lett. **102**, 062503 (2009).

[54] H.-W. Hammer and D. R. Phillips. *Electric properties of the Beryllium-11 system in Halo EFT*. Nucl. Phys. A **865**, 17–42 (2011).

[55] C. Fahlander and B. Jonson, editors. *Proceedings, Nobel Symposium 152: Physics with Radioactive Beams* **152** (2013).

[56] Y. Blumenfeld, T. Nilsson, and P. Van Duppen. *Facilities and methods for radioactive ion beam production*. Phys. Scripta T **152**, 014023 (2013).

[57] K. L. Jones. *Transfer reaction experiments with radioactive beams: from halos to the r-process*. Phys. Scripta T **152**, 014020 (2013).

[58] K. Wimmer. *Nucleon transfer reactions with radioactive beams*. J. Phys. G **45**, 033002 (2018).

[59] K. T. Schmitt *et al.* *Halo Nucleus ^{11}Be: A Spectroscopic Study via Neutron Transfer*. Phys. Rev. Lett. **108**, 192701 (2012).

[60] K. T. Schmitt *et al.* *Reactions of a ^{10}Be beam on proton and deuteron targets*. Phys. Rev. C **88**, 064612 (2013).

[61] A. E. Lovell and F. M. Nunes. *Systematic uncertainties in direct reaction theories*. J. Phys. G **42**, 034014 (2015).

[62] G. B. King, A. E. Lovell, and F. M. Nunes. *Uncertainty quantification due to optical potentials in models for (d,p) reactions*. Phys. Rev. C **98**, 044623 (2018).

[63] P. Navrátil *et al.* *Unified ab initio approaches to nuclear structure and reactions*. Phys. Scripta **91**, 053002 (2016).

[64] P. Capel, D. R. Phillips, and H.-W. Hammer. *Dissecting reaction calculations using halo effective field theory and ab initio input*. Phys. Rev. C **98**, 034610 (2018).

[65] C. Chin, R. Grimm, P. Julienne, and E. Tiesinga. *Feshbach resonances in ultracold gases*. Rev. Mod. Phys. **82**, 1225–1286 (2010).

[66] M. Bartenstein *et al.* *Precise Determination of ^{6}Li Cold Collision Parameters by Radio-Frequency Spectroscopy on Weakly Bound Molecules*. Phys. Rev. Lett. **94**, 103201 (2005).

[67] J. Zhang *et al.* *P-wave Feshbach resonances of ultracold ^{6}Li*. Phys. Rev. A **70**, 030702 (2004).

[68] M. Holland, S. J. J. M. F. Kokkelmans, M. L. Chiofalo, and R. Walser. *Resonance Superfluidity in a Quantum Degenerate Fermi Gas*. Phys. Rev. Lett. **87**, 120406 (2001).

[69] W. Yi and L.-M. Duan. *BCS-BEC crossover and quantum phase transition for ^{6}Li and ^{40}K atoms across the Feshbach resonance*. Phys. Rev. A **73**, 063607 (2006).

[70] M. Waseem, J. Yoshida, T. Saito, and T. Mukaiyama. *Unitarity-limited behavior of three-body collisions in a p-wave interacting Fermi gas*. Phys. Rev. A **98**, 020702 (2018).

[71] T. Schaetz. *Trapping ions and atoms optically*. J. Phys. B **50**, 102001 (2017).

[72] P. F. Bedaque, E. Braaten, and H.-W. Hammer. *Three-body Recombination in Bose Gases with Large Scattering Length*. Phys. Rev. Lett. **85**, 908–911 (2000).

[73] E. Braaten and H.-W. Hammer. *Efimov Physics in Cold Atoms*. Annals Phys. **322**, 120–163 (2007).

[74] E. Braaten and H.-W. Hammer. *Three body recombination into deep bound states in a Bose gas with large scattering length*. Phys. Rev. Lett. **87**, 160407 (2001).

[75] E. Braaten, H.-W. Hammer, D. Kang, and L. Platter. *Three-Body Recombination of Identical Bosons with a Large Positive Scattering Length at Nonzero Temperature*. Phys. Rev. A **78**, 043605 (2008).

[76] H. Suno, B. D. Esry, and C. H. Greene. *Recombination of Three Ultracold Fermionic Atoms*. Phys. Rev. Lett. **90**, 053202 (2003).

[77] B. D. Esry, C. H. Greene, and H. Suno. *Threshold laws for three-body recombination*. Phys. Rev. A **65**, 010705 (2001).

[78] J. J. Sakurai. *Modern Quantum Mechanics*. Addison-Wesley (1994).

[79] C. A. Bertulani, H.-W. Hammer, and U. Van Kolck. *Effective field theory for halo nuclei*. Nucl. Phys. A **712**, 37–58 (2002).

[80] J. Braun, W. Elkamhawy, R. Roth, and H.-W. Hammer. *Electric structure of shallow D-wave states in Halo EFT*. arXiv:1803.02169 [nucl-th].

[81] J. M. Blatt. *On the Neutron-Proton Force*. Phys. Rev. **74**, 92–96 (1948).

[82] J. Schwinger. *On the Charge Independence of Nuclear Forces*. Phys. Rev. **78**, 135–139 (1950).

[83] J. R. Taylor. *The Quantum Theory of Nonrelativistic Collisions*. Dover (2006).

[84] P. Zhang, P. Naidon, and M. Ueda. *Scattering amplitude of ultracold atoms near the p-wave magnetic Feshbach resonance*. Phys. Rev. A **82**, 062712 (2010).

[85] P. F. Bedaque, H.-W. Hammer, and U. van Kolck. *Narrow resonances in effective field theory*. Phys. Lett. B **569**, 159–167 (2003).

[86] J. J. de Swart, C. P. F. Terheggen, and V. G. J. Stoks. *The Low-Energy Neutron-Proton Scattering Parameters and the Deuteron*. arXiv:nucl-th/9509032.

[87] S. König, H. W. Grießhammer, H.-W. Hammer, and U. van Kolck. *Effective theory of* ^3H *and* ^3He. J. Phys. G **43**, 055106 (2016).

[88] H.-W. Hammer and D. Lee. *Causality and the effective range expansion*. Annals Phys. **325**, 2212–2233 (2010).

[89] R. B. Wiringa, V. G. J. Stoks, and R. Schiavilla. *Accurate nucleon-nucleon potential with charge-independence breaking*. Phys. Rev. C **51**, 38–51 (1995).

[90] R. Machleidt. *High-precision, charge-dependent Bonn nucleon-nucleon potential*. Phys. Rev. C **63**, 024001 (2001).

[91] F. Halzen and A. D. Martin. *Quarks and Leptons: An Introductory Course in Modern Particle Physics*. Wiley (1984).

[92] E. Braaten and M. Kusunoki. *Factorization in the production and decay of the X(3872)*. Phys. Rev. D **72**, 014012 (2005).

[93] M. Schmidt, M. Jansen, and H.-W. Hammer. *Threshold Effects and the Line Shape of the X(3872) in Effective Field Theory*. Phys. Rev. D **98**, 014032 (2018).

[94] E. Braaten, H.-W. Hammer, and G. P. Lepage. *Open Effective Field Theories from Deeply Inelastic Reactions*. Phys. Rev. D **94**, 056006 (2016).

[95] M. B. Wise. *Chiral perturbation theory for hadrons containing a heavy quark*. Phys. Rev. D **45**, R2188 (1992).

[96] G. Burdman and J. F. Donoghue. *Union of chiral and heavy quark symmetries*. Phys. Lett. B **280**, 287–291 (1992).

[97] T.-M. Yan, H.-Y. Cheng, C.-Y. Cheung, G.-L. Lin, Y. C. Lin, and H.-L. Yu. *Heavy quark symmetry and chiral dynamics*. Phys. Rev. D **46**, 1148–1164 (1992). [Erratum: Phys. Rev. D **55**, 5851 (1997)].

[98] J. Hu and T. Mehen. *Chiral Lagrangian with heavy quark-diquark symmetry*. Phys. Rev. D **73**, 054003 (2006).

[99] P. L. Cho. *Chiral perturbation theory for hadrons containing a heavy quark: The Sequel*. Phys. Lett. B **285**, 145–152 (1992).

[100] C. E. Thomas and F. E. Close. *Is X(3872) a molecule?* Phys. Rev. D **78**, 034007 (2008).

[101] E. Braaten, H.-W. Hammer, and T. Mehen. *Scattering of an Ultrasoft Pion and the X(3872)*. Phys. Rev. D **82**, 034018 (2010).

[102] S. Fleming, M. Kusunoki, T. Mehen, and U. van Kolck. *Pion interactions in the* $X(3872)$. Phys. Rev. D **76**, 034006 (2007).

[103] P. F. Bedaque and H. W. Griesshammer. *Quartet S wave neutron deuteron scattering in effective field theory*. Nucl. Phys. A **671**, 357–379 (2000).

[104] R. J. Furnstahl, H.-W. Hammer, and N. Tirfessa. *Field redefinitions at finite density*. Nucl. Phys. A **689**, 846–868 (2001).

[105] G. 't Hooft. *Naturalness, chiral symmetry, and spontaneous chiral symmetry breaking*. NATO Sci. Ser. B **59**, 135–157 (1980).

[106] D. Becirevic and F. Sanfilippo. *Theoretical estimate of the $D^* \to D\pi$ decay rate*. Phys. Lett. B **721**, 94–100 (2013).

[107] M. Jansen, H.-W. Hammer, and Y. Jia. *Light quark mass dependence of the X(3872) in an effective field theory*. Phys. Rev. D **89**, 014033 (2014).

[108] M. Jansen. *Effective field theory approaches for tensor potentials*. PhD thesis, Technische Universität Darmstadt (2016).

[109] M. A. Efremov, L. Plimak, M. Y. Ivanov, and W. P. Schleich. *Three-Body Bound States in Atomic Mixtures With Resonant p-Wave Interaction*. Phys. Rev. Lett. **111**, 113201 (2013).

[110] E. Braaten, P. Hagen, H.-W. Hammer, and L. Platter. *Renormalization in the Three-body Problem with Resonant P-wave Interactions*. Phys. Rev. A **86**, 012711 (2012).

[111] E. Prencipe, J. S. Lange, and A. Blinov ($\bar{\text{P}}$ANDA Collab.). *New spectroscopy with $\bar{P}ANDA$ at FAIR: X, Y, Z and the F-wave charmonium states*. AIP Conf. Proc. **1735**, 060011 (2016).

[112] J.-W. Chen, G. Rupak, and M. J. Savage. *Nucleon-nucleon effective field theory without pions*. Nucl. Phys. A **653**, 386–412 (1999).

[113] M. Schmidt, L. Platter, and H.-W. Hammer. *Neutron transfer reactions in halo effective field theory*. Phys. Rev. C **99**, 054611 (2019).

[114] J. Braun and H.-W. Hammer. *Electric Properties of One-Neutron Halo Nuclei in Halo EFT*. Few Body Syst. **58**, 94 (2017).

[115] D. R. Phillips and T. D. Cohen. *How short is too short? Constraining contact interactions in nucleon-nucleon scattering*. Phys. Lett. B **390**, 7–12 (1997).

[116] V. G. J. Stoks, R. A. M. Klomp, C. P. F. Terheggen, and J. J. de Swart. *Construction of high-quality NN potential models*. Phys. Rev. C **49**, 2950–2962 (1994).

[117] B. Acharya and D. R. Phillips. *^{19}C in halo EFT: Effective-range parameters from Coulomb dissociation experiments*. Nucl. Phys. A **913**, 103–115 (2013).

[118] J. Braun, H.-W. Hammer, and L. Platter. *Halo structure of ^{17}C*. Eur. Phys. J. A **54**, 196 (2018).

[119] A. O. Bouzas. *Addition theorems for spin spherical harmonics: II. Results*. J. Phys. A: Math. Theor. **44**, 165302 (2011).

[120] TUNL Nuclear Data Evaluation Project. *Energy Level Diagram, ^{11}Be (2012)*. [`http://www.tunl.duke.edu/nucldata/figures/11figs/11_02_2012.pdf`].

[121] TUNL Nuclear Data Evaluation Project. *Energy Level Diagram, ^{10}Be (2004)*. [`http://www.tunl.duke.edu/nucldata/figures/10figs/10_04_2004.pdf`].

[122] TUNL Nuclear Data Evaluation Project. *Energy Level Diagram, ^{11}B (2012)*. [`http://www.tunl.duke.edu/nucldata/figures/11figs/11_04_2012.pdf`].

[123] D. R. Goosman, E. G. Adelberger, and K. A. Snover. *$T = \frac{3}{2}$ Levels in ^{11}Be from the ^{10}Be$(p,\gamma_0)^{11}$B Reaction*. Phys. Rev. C **1**, 123–128 (1970).

[124] N. Soic *et al.* *Three-centre cluster structure in ^{11}C and ^{11}C*. J. Phys. G **31**, S1701–S1704 (2005).

[125] S. Typel and G. Baur. *Effective-range approach and scaling laws for electromagnetic strength in neutron-halo nuclei*. Phys. Rev. Lett. **93**, 142502 (2004).

[126] A. Deltuva, A. Ross, E. Norvaivsas, and F. M. Nunes. *Role of core excitation in (d, p) transfer reactions*. Phys. Rev. C **94**, 044613 (2016).

[127] M. Gomez-Ramos and A. M. Moro. *Influence of target deformation and deuteron breakup in (d, p) transfer reactions*. Phys. Rev. C **95**, 044612 (2017).

[128] V. Pesudo *et al.* *Scattering of the Halo Nucleus ^{11}Be on ^{197}Au at Energies around the Coulomb Barrier*. Phys. Rev. Lett. **118**, 152502 (2017).

[129] P. Descouvemont. *Four-body extension of the continuum-discretized coupled-channels method*. Phys. Rev. C **97**, 064607 (2018).

[130] A. Deltuva. *Core-excitation effects in three-body breakup reactions studied using the Faddeev formalism*. Phys. Rev. C **99**, 024613 (2019).

[131] A. Macchiavelli *et al.* *Analysis of spectroscopic factors in ^{11}Be and ^{12}Be in the Nilsson Strong-Coupling Limit*. Phys. Rev. C **97**, 011302 (2018). [Erratum: Phys. Rev. C **97**, 049902 (2018)].

[132] A. Calci, P. Navràtil, R. Roth, J. Dohet-Eraly, S. Quaglioni, and G. Hupin. *Can Ab Initio Theory Explain the Phenomenon of Parity Inversion in ^{11}Be?* Phys. Rev. Lett. **117**, 242501 (2016).

[133] J. Yang and P. Capel. *Systematic analysis of the peripherality of the ^{10}Be$(d, p)^{11}$Be transfer reaction and extraction of the asymptotic normalization coefficient of ^{11}Be bound states*. Phys. Rev. C **98**, 054602 (2018).

[134] L. Moschini and P. Capel. *Reliable extraction of the $dB(E1)/dE$ for ^{11}Be from its breakup at 520 MeV/nucleon*. Phys. Lett. B **790**, 367–371 (2019).

[135] M. E. Peskin and D. V. Schroeder. *An Introduction to Quantum Field Theory*. Addison-Wesley Reading, USA (1995).

[136] H.-W. Hammer and S. König. *General aspects of effective field theories and few-body applications*. Lect. Notes Phys. **936**, 93–153 (2017).

[137] J. C.Y. Chen and A. C. Chen. *Nonrelativistic Off-Shell Two-Body Coulomb Amplitudes*. Adv. At. Mol. Phys. **8** (1972).

[138] L. Hostler. *Coulomb Green's Functions and the Furry Approximation*. J. Math. Phys. **5**, 591–611 (1964).

[139] X. Kong and F. Ravndal. *Proton-proton scattering lengths from effective field theory*. Phys. Lett. B **450**, 320–324 (1999). [Erratum: Phys. Lett. B **458**, 565 (1999)].

[140] S. König. *Effective quantum theories with short- and long-range forces*. PhD thesis, Rheinische Friedrich-Wilhelms-Universität Bonn (2013).

[141] N. Curtis *et al.* *α + Li and H + Be decay of ^{10,11,12}B*. Phys. Rev. **72**, 044320 (2005).

[142] D. A. Varshalovich, A. N. Moskalev, and V. K. Khersonskii. *Quantum Theory of Angular Momentum*. World Scientific (1988).

[143] G. Rupak and X. Kong. *Quartet S-wave p-d scattering in EFT*. Nucl. Phys. A **717**, 73–90 (2003).

[144] S. König and H.-W. Hammer. *Low-energy p-d scattering and ^{3}He in pionless effective field theory*. Phys. Rev. C **83**, 064001 (2011).

[145] S. König, H. W. Grießhammer, and H.-W. Hammer. *The proton-deuteron system in pionless EFT revisited*. J. Phys. G **42**, 045101 (2015).

[146] H. W. Grießhammer. *Naïve dimensional analysis for three-body forces without pions*. Nucl. Phys. A **760**, 110–138 (2005).

[147] V. Efimov. *Energy levels arising form the resonant two-body forces in a three-body system*. Phys. Lett. **33B**, 563–564 (1970).

[148] P. Naidon and S. Endo. *Efimov physics: a review*. Rept. Prog. Phys. **80**, 056001 (2017).

[149] TUNL Nuclear Data Evaluation Project. *Energy Level Diagram, ^{12}B (2017)*. [`http://www.tunl.duke.edu/nucldata/figures/12figs/12_02_2017.pdf`].

[150] P. F. Bedaque, G. Rupak, H. W. Grießhammer, and H.-W. Hammer. *Low-energy expansion in the three-body system to all orders and the triton channel*. Nucl. Phys. A **714**, 589–610 (2003).

[151] C. Ji, D. R. Phillips, and L. Platter. *The three-boson system at next-to-leading order in an effective field theory for systems with a large scattering length*. Annals Phys. **327**, 1803–1824 (2012).

[152] C. Ji and D. R. Phillips. *Effective Field Theory Analysis of Three-Boson Systems at Next-To-Next-To-Leading Order*. Few Body Syst. **54**, 2317–2355 (2013).

[153] H.-W. Hammer and T. Mehen. *Range corrections to doublet S-wave neutron-deuteron scattering*. Phys. Lett. B **516**, 353–361 (2001).

[154] J. R. de Laeter *et al.* *Atomic weights of the elements: Review 2000 (IUPAC Technical Report)*. Pure Appl. Chem. **75**, 683–800 (2003).

[155] T. Nakasuji, J. Yoshida, and T. Mukaiyama. *Experimental determination of p-wave scattering parameters in ultracold ^{6}Li atoms*. Phys. Rev. A **88**, 012710 (2013).

[156] S. Gautam and D. Angom. *Scattering length for fermionic alkali atoms*. Eur. Phys. J. D **56**, 173–179 (2010).

[157] J. Levinsen, N. R. Cooper, and V. Gurarie. *Stability of fermionic gases close to a p-wave Feshbach resonance*. Phys. Rev. A **78**, 063616 (2008).

[158] G. M. Bruun, A. D. Jackson, and E. E. Kolomeitsev. *Multichannel scattering and Feshbach resonances: Effective theory, phenomenology, and many-body effects*. Phys. Rev. A **71**, 052713 (2005).

[159] J. P. D'Incao, H. Suno, and B. D. Esry. *Limits on Universality in Ultracold Three-Boson Recombination*. Phys. Rev. Lett. **93**, 123201 (2004).

[160] B. D. Esry, C. H. Greene, and J. P. Burke. *Recombination of Three Atoms in the Ultracold Limit*. Phys. Rev. Lett. **83**, 1751–1754 (1999).

[161] H. Suno, B. D. Esry, and C. H. Greene. *Three-body recombination of cold fermionic atoms*. New J. Phys. **5**, 53–53 (2003).

[162] G. Gokhroo *et al.* (Belle Collab.). *Observation of a Near-Threshold $D^0\bar{D}^0\pi^0$ Enhancement in $B \to D^0\bar{D}^0\pi^0 K$ Decay*. Phys. Rev. Lett. **97**, 162002 (2006).

[163] T. Aushev *et al.* (Belle Collab.). *Study of the $B \to X(3872)(\to D^{*0}\bar{D}^0)K$ decay*. Phys. Rev. D **81**, 031103 (2010).

[164] M. Abramowitz and I. A. Stegun. *Handbook of Mathematical Functions*. Dover, New York (1964).

[165] M. Schmidt. *The $X(3872)$ as $D\bar{D}\pi$ Resonance*. Master's thesis, Technische Universität Darmstadt (2016).

[166] M. E. Luke and M. J. Savage. *Power counting in dimensionally regularized NRQCD*. Phys. Rev. D **57**, 413–423 (1998).

[167] W. Glöckle. *The Quantum Mechanical Few-Body Problem*. Springer (1983).

[168] X. Zhang, K. M. Nollett, and D. R. Phillips. *Marrying ab initio calculations and Halo-EFT: the case of $^7Li + n \rightarrow {}^8Li + \gamma$*. Phys. Rev. C **89**, 024613 (2014).

[169] X. Zhang, K. M. Nollett, and D. R. Phillips. *Combining ab initio calculations and low-energy effective field theory for halo nuclear systems: The case of $^7Be + p \rightarrow {}^8B + \gamma$*. Phys. Rev. C **89**, 051602 (2014).

[170] E. Ryberg, C. Forssén, H.-W. Hammer, and L. Platter. *Constraining low-energy proton capture on beryllium-7 through charge radius measurements*. Eur. Phys. J. A **50**, 170 (2014).

Marcel Daniel Schmidt

Bismarckstraße 21 | 64293 Darmstadt
+49 151 50700749 | marcel.d.schmidt@gmx.net

Education

	Technische Universität Darmstadt, Darmstadt (GER)
06/16–06/19	Ph.D. in Theoretical Nuclear Physics, *summa cum laude*
10/13–05/16	M.Sc. in Physics, final grade 1.0 (excellent)
10/10–08/13	B.Sc. in Physics, final grade 1.33 (excellent)
06/09	**Modellschule Obersberg**, Bad Hersfeld (GER) German Abitur, final grade 1.1 (excellent)

Working experience

03/15–04/15	**d-fine GmbH**, Frankfurt am Main (GER) Consulting internship in market risk segment of a major bank
04/13–05/16	**Technische Universität Darmstadt**, Darmstadt (GER) Student teaching assistant

Publications

near future	***Three-body losses of a polarized Fermi gas in effective field theory*** M.S., L. Platter, and H.-W. Hammer (to be published)
06/19	***Neutron transfer reactions in halo effective field theory*** M.S., L. Platter, and H.-W. Hammer, Physical Review C 99, 054611 (2019)
07/18	***Threshold effects and the line shape of the X(3872) in effective field theory*** M.S., M. Jansen, and H.-W. Hammer, Physical Review D 98, 014032 (2018)

Research stays and conference talks

05/19	**XIII Int. Workshop on Heavy Quarkonium**, Turin (ITA) Invited talk, through SFB 1245 Travel Prize (see below)
07/18	**XXII Int. Conference on Few-Body Problems in Physics**, Caen (FRA)
06/18	**2018 NUCLEI Collaboration Meeting**, Knoxville (USA)
05/18	**IV Int. Workshop on “State of the Art in Nuclear Cluster Physics”**, Galveston (USA)
03/18–06/18	**The University of Tennessee**, Knoxville (USA) Research stay
10/17	**Critical Stability of Quantum Few-Body Systems**, Dresden (GER)
03/17	**INT-17-1a: Toward Predictive Theories of Nuclear Reactions [...]**, Seattle (USA)
08/13–01/14	**Danmarks Tekniske Universitet**, Copenhagen (DNK) ERASMUS semester

Awards

05/19	**SFB 1245 Travel Prize** Travel grant from the Deutsche Forschungsgemeinschaft (DFG)
10/14–09/15	**Deutschlandstipendium** Scholarship from the German government

Danksagung

Diese Dissertationsschrift ist den Menschen gewidmet,
die mich auf meinem Weg durch Studium und Promotion begleitet haben.

Zunächst gilt ein besonderer Dank meinem Doktorvater Hans-Werner Hammer. Schon während der Arbeit an meiner Master-Thesis war Hans-Werner viel daran gelegen, Lösungswege nicht vorzuschreiben, sondern im gemeinsamen physikalischen Diskurs zu erarbeiten. Hierfür stand seine Tür in den vergangenen vier Jahren im wahrsten Sinn des Wortes immer offen, was ich als großes Privileg empfinde. Weiter danke ich Hans-Werner dafür, mich auf eine Vielzahl physikalischer Fragestellungen von Teilchen- bis Atomphysik aufmerksam gemacht zu haben. So entstand nicht nur letzten Endes diese Dissertationsschrift; auch lernte ich eine Vielzahl herausragender Physiker kennen. Hervorzuheben sind dabei Lucas Platter, Eric Braaten und Daniel Phillips, denen ich auf diesem Weg für wertvolle Kommentare und Diskussionen im Rahmen meiner Publikationen danke.

Die Quantenfeldtheorie-Vorlesungen von Jens Braun bestärkten mich nachhaltig in meinem Wunsch, auf diesem spannenden Gebiet zu promovieren. Ihm danke ich herzlich für seine Ratschläge während der regelmäßigen Promotionskomitee-Meetings und für die Erstellung eines Dissertationsgutachtens.

Meiner Arbeitsgruppe im IKP-Theoriezentrum danke ich für die vielen schönen Stunden beim Wandern, Kaffeetrinken und gemeinsamen Geschenkgutscheine-Einlösen, für die lockere Arbeitsatmosphäre und die große Bereitschaft, sich gegenseitig bei physikalischen Problemen zu unterstützen. Fabian Hildenbrandt und Artem Volosniev (die ich beide zuweilen öfter sah als meine eigene Wohnung) danke ich vielmals für das Korrekturlesen dieser Dissertationsschrift. Beiden, sowie gleichermaßen Wael Elkamhawy und Matthias Göbel, danke ich außerdem für etliche gemeinsame Stunden angestrengten Grübelns und Kreideverschleißens. *Jedem* Mitglied meiner Arbeitsgruppe wünsche ich für die persönliche Zukunft alles erdenklich Gute.

Bei meinem Koautor Lucas Platter möchte ich mich ausdrücklich für die großartige Möglichkeit eines viermonatigen Forschungsaufenthalts an der University of Tennessee in Knoxville bedanken. Durch die netten Kollegen im Physics Department, Besuche im Oak Ridge National Laboratory, Wanderungen in den Smoky Mountains und vor allem die Gastfreundschaft von Lucas Familie war diese Zeit sicher der Höhepunkt meiner Promotion.

Zu guter Letzt gilt mein größter Dank meinen Eltern Sabine und Jörg, meinem Bruder Maurice und meiner Verlobten Anne. Eure unentwegte und bedingungslose Unterstützung in jeder Lebenslage haben diese Dissertationsschrift erst ermöglicht. Anne, danke für deine unerschütterliche Geduld mit mir und meiner Arbeit und für jedes aufmunternde Lächeln.